Âge, durée et enregistrement du métamorphisme de haute pression dans le massif Central

Caroline Lotout

ANNÉE 2017

THÈSE / UNIVERSITÉ DE RENNES 1
sous le sceau de l'Université Bretagne Loire

pour le grade de

DOCTEUR DE L'UNIVERSITÉ DE RENNES 1

Mention : Sciences de la Terre

Ecole doctorale EGAAL

Caroline Lotout

Préparée à l'unité de recherche UMR- CNRS 6118
Géosciences Rennes
Observatoire des Sciences de l'Univers de Rennes

Age, durée et enregistrement du métamorphisme de haute pression dans le Massif Central, Chaîne Varisque

Thèse soutenue à Rennes
le 24 novembre 2017

devant le jury composé de :

Stéphanie DUCHENE / *rapporteur*
Professeur, Université Paul Sabatier, Toulouse

Jean-Marc LARDEAUX / *rapporteur*
Professeur, Université Nice Sophia Antipolis

Jean-Pierre BURG / *examinateur*
Professeur, ETH Zurich, Suisse

Loic LABROUSSE / *examinateur*
Professeur, UPMC, Paris VI

Daniela RUBATTO / *examinateur*
Professeur, Université de Bern, Suisse

Valérie BOSSE / *invitée*
Maître de Conférences, Université Clermont Ferrand

Pavel PITRA / *directeur de thèse*
Maître de Conférences, Université Rennes 1

Jean VAN DEN DRIESSCHE / co-*directeur de thèse*
Professeur, Université Rennes 1

A Sylvia & Walt

Ce n'est qu'en essayant continuellement que l'on finit par réussir :
donc plus ça rate et plus on a de chances que ça marche !

Jacques Rouxel,
Shadoks et al.

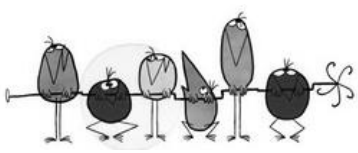

Remerciements

Dans un premier temps, je remercie Stéphanie et Jean-Marc d'avoir accepté de rapporter le manuscrit, et de façon si rapide !! Et bien sûr, Jean-Pierre, Loïc et Daniela pour avoir accepté de faire partie du jury. Merci à vous cinq pour l'intérêt porté à ce travail…. Et pour ces trois heures d'échanges qui m'auront laissé assoiffée !

Valérie, merci pour les supers discussions, et d'avoir accepté l'invitation à la soutenance ! Tu as d'ailleurs admirablement clos la série de questions ;) ! Eloïse, t'étais bien funky comme stagiaire ! Robert, merci pour ton accueil à Cracovie et ta disponibilité par mail pour toutes ces histoires de grenats ! Pavel, Jean, je tiens à vous remercier de m'avoir proposé ce sujet de thèse à la suite de mes stages de master 1 & 2. Jean, merci pour l'aspect « premier ordre, grande échelle, majeure ! » ;), Pavel, grâce à toi, Thermocalc & Theriak/Domino, n'ont plus (autant) de secrets pour moi ! Merci à vous deux pour ces trois années de liberté ! Gilles, merci de m'avoir initié à la datation argon, et de m'avoir fait confiance avec le Spectro ! Marc, merci pour tout : des premiers pas d'U-Pbiste au soutien de fin de thèse ! Et n'oublions pas l'akessent du midi à Lévézou pardi !!

Michel, Paola, c'est promis, plus de glissade intempestive près du Mont Gelé ou ailleurs ;) et un grand merci pour votre soutien et toutes ces nombreuses discussions ! Pierre, il est loin le temps où tu me lançais des craies pour cause de bavardage intensif (intempestif ?) en licence ! Philippe, merci pour tes conseils avisés en toutes situations ! Sans toi, Marc et Pierre, pas sûr que j'eu switché vers les cailloux en fin de L2!! Pips, le premier à m'avoir parlé du Lévézou (« Ne passe pas par là pour la coupe, personne n'y comprend rien », L3, janv. 2012). Jean-Pierre, j'attends avec impatience la dédicace de la photo… ;) Et un grand merci à l'azote liquide, sponsor de magnifiques après-midi au premier étage ! De façon plus générale, je remercie tous les permanents avec qui j'ai pu échanger, au cours de cette thèse et avant (c'est qu'à faire L3, master et thèse au même endroit, on deviendrait presque un meuble !), tant en science, qu'en pédagogie, qu'en bavardage ; alors merci à Sylvie, Marc, Thibault, Kerry, Erwan, François, Cécile, Thierry, Marie-Pierre, Yves, Fred, Anne-Catherine, Philippe, Didier, Jacques, Jean-Noël, Virginie…

Aline, Marie-Anne, Chantal, Jessica, Xavier, Yann, David, Catherine, Isabelle, Eddie merci pour l'aide apportée lors de ces trois années, tant dans les plannings d'enseignement, les missions, la fabrication des lames minces, la microsonde, le broyage, retrouver des documents perdus au fin fond du compactus,… Et bien sûr Dominique, toujours présent pour m'aider à agrandir des lames minces, réparer des pompes à poissons ou parler minions !

Audrey, Colin, Romain GTV, Romain, Giclure (quel beau surnom !), Vivi, Popo, Sassou, Tienou, Sissi : ma team brestoise au soutien infaillible, où le minuscule microb' que je suis se sent tellement à sa place ! Merci pour tout ce que vous m'apportez depuis tant d'années !

Flofloow, merci pour ce soutien inconditionnel !! Que de délires depuis le fin fond du Maine à regarder des Disney en 3D à Ranger John (on est des Rangers Junior !!), des boutures de tamaya à l'apprentissage du lasso chez les cow-boys, de la ford focus 4x4 à Buzz (je n'étalerais pas plus, ça va devenir ridicule), Schmeu !! Cocoooow (CoCaCoLo Team) & Rémi le Poney (adepte de la cuniculture moyenâgeuse), amis & trio infernal depuis la licence, je ne désespère pas qu'on réussisse à écrire & publier sur les demi-ânes… Ou qu'on ouvre cette fichue auberge de « l'akène chêneux » ;) ! Envelou & Nestor l'alligator invisible, Trugarez-vras et « Prenez garde à vos proches » ;) !

Claire & Laurent (et Charlotte, si calme à la soutenance !), Laura, Anne, Anne-Laure, Xavier, Guillaume, il s'en est passé du temps depuis notre plus petit collège costarmoricain & notre contrée trégoroise! Périg, tu aurais sans aucun doute adoré ce manuscrit…

Et bien sur les copains du labo… Géosciences, c'est un peu un temple d'entente et de bien-être, un peu comme un spa où on passerait le plus clair de notre temps à boire des pintes, refaire le monde (ou ses ongles), manger des crêpes et se taquiner d'une façon à la fois si charmante et malveillante ! Et oui, il n'y a pas que la thèse dans la vie (ni au labo d'ailleurs) !

Le p'tit pingouin râleur qui a élu domicile dans notre cher Bureau 127 a été une révélation de bêtise et de bonne humeur (chose assez étonnante pour un dark-penguin). Dans toute cette noirceur un brin stupide que tu sub-diffuses, on a vraiment bien rigolé ! Solenn, merci pour ces années au B127 et ailleurs (Mickeyyy, chapeau-chapeau, tutuuuure) ! Dupraaaaaaat l'éternel papillon à la joie de vivre débordante, hippie de toutes heures et co-fan inconditionnelle d'une certaine photo à Dignes en 1967 avec JPB & PC (anonymat oblige) ! Geminou ma compère chanteuse en trois langues d'hakunamatata et fière catalane au caractère si bien trempé; Pochon –Popoche, Pochonne ou Pochon d'Inde pour les intimes- la poulette rougissante, Vicky (depuis la licence !!), RDV au Congo, j'ai déjà fixé les dates en 2019 (et arrête d'offrir des cadeaux bizarre à Pochon, ça le fait rougir :p) !! Ce bureau feuillu & poissonneux (RIP gros suceur, tu auras bien vécu) en aura vu de toutes les couleurs… Merci à vous toutes (ici pas d'écriture inclusive ou d'accord en genre ; c'est accord en nombre !) pour ces supers moments, le B127 me manque déjà (larmiche émue)!

*Marie, petit « sac à puces » chantang le sud dans nos loooongues discussiong, merci pour ta présence et ton écoute (car même si tu parles beaucoup, ben… je parle tout autant) ! Marie-Francoise, faut-il vraiment que je te -Atchoo- ré-explique ce que sont des –Atchoo-hippopotames #TMTC#YOLO ? Merci pour -Atchoo- toutes ces soirées -Atchoo- cocktails mythiques –Atchoo Atchoo Atchoo! Dianou l'amatrice de vidéos de chats à l'accent si perfetto tutto bene, Eliot Pr. Grosmatou la gentillesse incarnée à l'humour si… « fin » ?! Encore Merci !!! Jéjé le saltimbanque en col blanc et sa fabuleuse LIMOO-KANGOO, Emma & Jon', colocs d'un temps polyglottes :) ! Rominouuu le gourmet à la mauvaise fois **carabinée**, Jeannette (qui n'a rien à faire dans ce paragraphe, mais qui fait partie de « mon » Géosciences malgré/bon gré sa thèse sur le théâtre) et nos si longs apéros-discussions-débats à toutes heures, Céline & Guilhem, J² ; Loulou la révolutionnaire féministe avec qui les sit-in place Ste Anne ont une tout autre signification !! Bochet le social-traître sub-partenaire malfaiteur ! Redj, team 22 For Ever, même si le FCNA passera toujours avant l'EAG! Dani como como como, nooooooooo ;) ; Justine, Caro le coup de foudre amical, Camille, Lorraine qui partage mon amour inconditionnel des éclogites & des vernis à ongles, Alicia, Nikol & les concerts de Ska à Prague, Cochelin & tes allergies PPP ! CristauxF' essaye donc de me rattraper la prochaine fois que je glisse ! On en aura traîné des kg d'éclogites depuis le Lago di Cignana ! Tofou, le karaoké avec micro-serpillère, il n'y a que ça de vrai ! Thomous le vrai Swanson ! Guillaume toujours prêt à acclimater ses plats façon végétarien :p, Jipé & Virginie, Feña, Riccardo, Lucas, Carlos (el padré dé Paco, Si !), Johny la banane caféinée, Anne-Morwenn la tamponneuse, Nath' qui ne sait pas où j'habite, Ch'Carole & Ch'marylou, La burte, Aurélie & Amaury, Luc double particule et sa super baignoire, Charline, Flore, Romain, Alix, Laurie, Mark, Polo, La que, Kashka, Akeek, Rémi, Seconde, Gloria, Jojo, Mag, Brendan, … Et le Tournebride ! J'ai sans doutes oublié du monde, damned (et milles excuses) !*

Un grand merci à tous mes gardiens de chat qui m'auront permis de partir sereine en terrain, congrès, vacances, weekend, tournée,… Avec une mention particulière pour Malika ! La meilleure pour la fin ? Pristie évidemment !!

« La notion de passoire est indépendante de la notion de trous »
Shadoks et al. (1966-BUMEUZOZOMEUZO)

L'ensemble des données présentées dans ce manuscrit, sauf indication contraire, ont été acquises et traitées par l'auteure.

Ce manuscrit présente le travail de thèse effectué pendant 3 ans au laboratoire Géosciences Rennes (Université Rennes 1), et a bénéficié d'un financement du Ministère de l'Enseignement Supérieur et de la Recherche de octobre 2014 à septembre 2017.

Les fonds de recherches nécessaire à son déroulement ont été pris sur nos soutiens de bases (Caroline Lotout, Pavel Pitra et Jean Van Den Driessche) au cours des années 2015, 2016, 2017. Un financement interne de l'Observatoire des Sciences de l'Univers de Rennes (OSUR) en 2016 et un financement externe de l'INSU en 2017 nous ont également été alloués.

Cette thèse a été effectuée avec la collaboration de Marc Poujol (maître de conférence, Géosciences Rennes, Université Rennes 1), Gilles Ruffet (chargé de recherches CNRS, Géosciences Rennes), Robert Anczkiewicz (équivalent chargé de recherche, Institut des Sciences de la Terre de Cracovie) et Valérie Bosse (Maître de conférences, Laboratoire Magma et Volcan, Clermont-Ferrand) pour les analyses géochronologiques.

Résumé

Les processus de subduction sont une étape clé de la formation des orogènes et induisent un métamorphisme de haute pression, localisé dans les faciès des schistes bleus et éclogites. Caractériser la durée et l'intensité de ce métamorphisme est ainsi une étape cruciale puisque amenant des contraintes quantitatives sur la géodynamique d'un orogène.

Par une étude pétrologique et géochronologique, cette thèse a ainsi pour objectif de préciser les conditions et durées du métamorphisme de haute pression dans le sud du Massif Central Français (chaîne Varisque), à travers l'étude des massifs de Najac, de la Montagne Noire et du Lévézou. Cette thèse associe ainsi une géochronologie multiméthodes (U-Pb sur zircon, rutile et apatite, Lu-Hf et Sm-Nd sur grenat, ^{40}Ar-^{39}Ar sur biotite et muscovite) à des analyses pétrologiques impliquant des modélisations numériques d'équilibres de phases (Theriak-Domino et THERMOCALC).

L'étude d'une éclogite du massif de Najac a ainsi permis de déterminer des conditions de 15 à 20 kbar et 560 à 630°C pour le métamorphisme de haute pression. Le début du faciès éclogite y est daté à ~383 Ma, tandis que le pic du métamorphisme éclogitique est atteint à 375.7 ± 1.2 Ma. La datation des éclogites de la Montagne Noire n'a pas permis de préciser un âge solide de l'évènement de haute pression. Néanmoins, les conditions de pression et température du faciès éclogite y sont estimées à ~ 21 kbar et ~ 750°C. L'étude des massifs de Najac et de la Montagne Noire a mis en évidence de potentiels découplages entre les systèmes de terres rares et le système isotopique U-Pb. Les protolithes des terrains éclogitiques du massif du Lévézou, tant mafiques que felsiques, se sont mis en place à ca. 470 Ma. Le métamorphisme éclogitique affectant les roches mafiques est estimé à 18-23 kbar pour 680-800°C et atteint à ~358 Ma. L'exhumation y est bien caractérisée : les terrains éclogitiques atteignent 8-9.5 kbar et ~600°C à ~352 Ma, impliquant une exhumation très rapide, suivie d'un refroidissement de plus de 50°C/Ma. Les granites du massif du Lévézou présentent des pseudomorphoses de cordiérite à disthène-grenat-muscovite-quartz, développées lors du métamorphisme de haute pression et équilibrées à ca. 15-17 kbar et ~670°C. La déformation majeure observée dans ces granites peut s'accompagner de fusion localisée, et semble se produire en différentes étapes, depuis ~352 Ma à ~340 Ma.

Replacées dans un contexte général, ces données s'inscrivent pleinement dans les gammes d'âges de la haute pression décrites pour la chaîne varisque et permettent de reconsidérer la tectonique du Massif Central.

Abstract

Subduction is one of the key stages of the mountain building processes. It leads to the development of high-pressure (HP) metamorphism in the rocks that typically equilibrate in the blueschist or eclogite-facies conditions. Dating the HP metamorphism and estimating its intensity is therefore a major challenge when reconstructing geodynamics through time.

Through a petrological and geochronological study, this PhD dissertation aims to better constrain conditions, durations and timings of HP metamorphism in the southern French Massif Central (European Variscan Belt). The massifs of Najac, Montagne Noire and Lévézou were investigated by a multi-method geochronological approach (zircon, rutile and apatite U-Pb dating, garnet Lu-Hf and Sm-Nd dating, biotite and muscovite ^{40}Ar-^{39}Ar dating) associated with a petrological analysis including numerical modelling of phase equilibria (Theriak-Domino and THERMOCALC).

The Najac eclogites reached 560-630 °C at 15-20 kbar and the prograde part of the high-pressure metamorphic event lasted for ~ 7 Myr starting at ~ 383 and peaking at ~ 376 Ma. Eclogites hosted in sillimanite-bearing migmatites in the Montagne Noire dome (French Massif Central) reached c. 750°C, 21 kbar before significant decompression at high temperatures. However, none of the obtained geochronological dates could be associated with the HP event. The study of the Najac massif and the Montagne Noire Dome highlight potential decoupling between the REE and the U-Pb isotopic systems.

The emplacement of the protoliths of felsic and mafic HP rocks in the Lévézou Massif was estimated at ca. 470 Ma. HP metamorphism peaked at 18-23 kbar and 680-800°C at ~358 Ma. The subsequent fast exhumation reached 8-9.5 kbar and ~600°C at ~352 Ma, highlighting a very fast exhumation followed by a cooling rate of 50°C/Ma. Granites from the Lévézou massif display kyanite-garnet-muscovite-quartz pseudomorphs after cordierite that equilibrated at ca. 15-17 kbar and ~670°C. The major deformation in these granites is associated with the exhumation stage, locally accompanied by partial melting, and seems to occur in different episodes, from ~352 Ma to ~340 Ma.

On a larger scale, these results are fully in line with the HP ages described in the Variscan Belt and allow to reconsider the tectonics in the French Massif Central.

Table des matières

Introduction Générale

1. Le métamorphisme de haute pression : une clé pour la compréhension de la géodynamique des orogènes

Les chaînes de montagnes résultent de grands mouvements de convergence de plaques lithosphériques continentales via les phénomènes de subduction, au cours desquels se développe un métamorphisme de haute pression. À terme, ces mouvements aboutissent à la collision des continents.

Comprendre la géodynamique globale d'une chaîne de montagnes nécessite de déterminer le cheminement des roches, depuis leur mise en place, leur enfouissement jusqu'à leur exhumation. Cela implique d'estimer à la fois la cinématique des déformations majeures, les pressions et températures subies par les roches au cours de leur histoire. En particulier, la combinaison des durées et de l'intensité du métamorphisme permet in fine de placer des contraintes quantitatives, ce qui est essentiel pour appréhender la géodynamique générale d'une chaîne de montagnes. Préciser les caractéristiques pétrologiques et géochronologiques du métamorphisme de haute-pression, stigmates des processus de subduction, est ainsi d'une importance capitale.

La « datation du métamorphisme de haute pression » reste encore actuellement un défi, puisqu'en l'occurrence plusieurs points posent problèmes :

(i) la préservation du chemin pression-température (P-T) : Les roches subissent divers rééquilibrages minéralogiques plus ou moins complets ainsi que de nombreuses modifications texturales et parfois chimiques, tant sur le chemin prograde, pendant la décompression ou le chemin rétrograde. La décompression subie par la roche est d'autant plus problématique qu'elle s'accompagne généralement d'une augmentation de la température induisant aussi des rééquilibrages venant fausser les estimations des conditions P-T de la haute pression.

(ii) la préservation des chronologies du métamorphisme lors du cheminement des roches, et plus particulièrement l'enregistrement géochronométrique de la haute pression et sa préservation : La rétromorphose ou les événements métamorphiques plus tardifs peuvent en effet facilement perturber les différents systèmes isotopiques avec plus ou moins d'intensité.

(iii) l'interprétation des dates obtenues, c'est-à-dire le fait qu'un résultat analytique devienne un âge ayant une signification géologique, est indispensable mais reste particulièrement complexe : un minéral datable, qu'il soit une phase accessoire ou majeure de la paragenèse, peut ainsi cristalliser de façon ponctuelle ou plus ou moins continue sur le chemin prograde, au pic du métamorphisme, pendant la décompression ou sur le chemin rétrograde.

Déchiffrer l'évolution P-T-t d'une roche est une étape exigeante. Elle nécessite d'allier des études pétrologiques et géochronologiques rigoureuses afin de placer la croissance et le rééquilibrage du minéral daté dans l'évolution temporelle de la roche. En l'occurrence, les signatures en éléments traces dans les différents minéraux peuvent parfois apporter (i) des contraintes qualitatives, en informant sur le type de paragenèse dans laquelle le minéral a cristallisé ou (ii) des contraintes quantitatives, en précisant des pressions ou températures auxquels se sont stabilisés les minéraux. L'utilisation de différents chronomètres est aussi source d'informations capitales, puisque outre le fait d'apporter de nombreuses contraintes temporelles et de les associer éventuellement à différentes parties du trajet P-T, elle permet aussi de vérifier la cohérence de l'ensemble des résultats et leur validité géologique individuelle.

Enfin, le terme « datation du métamorphisme de haute pression » est très général et peut à la fois correspondre à la datation de l'entrée dans les faciès dits de haute pression (schiste bleu ou éclogite), du pic de pression ou encore du début de la décompression ou rétromorphose (c'est-à-dire la fin du faciès éclogitique). Ainsi il va de soi que les différents âges et estimations P-T obtenus doivent être traités au cas par cas pour en extraire des bilans plus globaux, tels que des vitesses d'enfouissement ou d'exhumation, voire même la durée du métamorphisme éclogitique.

2. Zone d'étude : le Massif Central français

La chaîne varisque est considérée comme le résultat d'une collision continentale entre deux mégacontinents Laurussia et Gondwana, suivant des mécanismes comparables à la formation de la chaîne himalayenne (e.g. Bard et al. 1980, Matte et Burg 1981, Matte 1986). À grande échelle, la dynamique générale de cette chaîne fait globalement consensus. Cependant, de nombreuses controverses persistent, en particulier sur le nombre de domaines

océaniques et de zones de suture associées (e.g. Matte 2001, Ballèvre et al. 2009, 2014 ; Martinez Catalan 2011, Kroner et Romer 2013, Franke et al. 2017). En l'occurrence, le Massif Central est un parfait exemple de ce genre de problématique : l'âge du métamorphisme de haute pression (et plus largement des différents évènements métamorphiques) et le nombre de sutures y sont toujours débattus.

Trois massifs ont ainsi été sélectionnés pour tenter d'y appréhender au mieux les durées et conditions du métamorphisme : les massifs du Lévézou et de Najac, présentant respectivement des éclogites de haute et basse températures peu étudiées tant d'un point de vue pétrologique que géochronologique, et le massif de la Montagne Noire, où les données récentes sur le métamorphisme de haute pression portent à controverse (Faure et al. 2014 ; Whitney et al. 2015). J'ai systématiquement abordé ce travail par une étude pétrologique, en alliant observations pétrographiques, analyses des compositions chimiques minérales et modélisations de diagrammes de phases (Theriak-Domino et THERMOCALC), tant pour les roches mafiques que felsiques. Dans un deuxième temps, j'ai réalisé une étude géochronologique multiméthodes sur les roches mafiques comme felsiques en alliant, quand cela était possible, différents systèmes chronométriques complémentaires : U-Pb sur zircon, rutile, apatite ; Lu-Hf et Sm-Nd sur grenat ; ^{40}Ar-^{39}Ar sur amphibole, muscovite et biotite. Enfin, pour associer au mieux les dates obtenues à des phases du métamorphisme, la teneur en éléments en traces des minéraux a également pris en compte. Cela a permis d'accéder à des informations quantitatives (thermo(baro)mètres Zr-in-titanite, Zr-in-rutile) ou qualitatives comme la mise en évidence, via les spectre de terres rares, de la croissance synchrone de phases accessoires datables et phases majeures du métamorphisme.

3. Structuration du manuscrit

Ce manuscrit se structure en quatre parties, subdivisées en chapitres principalement composés d'articles publiés, soumis ou en préparation. La plupart de ces articles sont précédés de préambules et/ou de discussions complémentaires.

La **partie I** vise à présenter succinctement le cadre géologique de cette étude. Elle se structure ainsi autour de l'évolution des modèles géodynamiques de la chaîne varisque et aborde plus spécifiquement le Massif Central Français. Les occurrences de roches de haute pression dans le Massif Central y seront discutées tant sur le plan des estimations des

conditions P-T existantes que sur celui de l'âge du métamorphisme. Cette première partie met finalement en évidence les controverses et inconnues entourant encore le métamorphisme de haute pression dans le Massif Central.

La **partie II** se concentre sur l'enregistrement du métamorphisme éclogitique dans les roches mafiques, en utilisant une approche pétrologique et géochronologique sur les massifs de Najac, du Lévézou et de la Montagne Noire. Le **chapitre 1** se focalise ainsi sur le massif de Najac et se structure sous la forme d'un article accepté à *Lithos.* Ce dernier propose, par une étude pétrochronologique fine, le premier âge de la haute-pression à ca. 376 Ma pour des conditions P-T au pic de pression de 15-20 kbar et 560-630°C dans ce massif, ainsi qu'une durée du métamorphisme éclogitique prograde de 6.1 ± 4.3 Ma. La discussion complémentaire, basée sur les analyses des éléments traces, tente de préciser le chemin P-T-t. Le **chapitre 2** correspond à l'étude d'une éclogite de la Montagne Noire, qui a en partie fait l'objet du stage recherche de Master 2 d'Eloïse Bretagne que j'ai co-supervisé au cours de cette thèse en 2017. Il se compose, en outre d'un préambule sur les données existantes, d'un article en préparation pour *EPSL* remettant en question les âges récemment obtenus dans le massif de la Montagne Noire. Le **chapitre 3** se concentre sur le massif du Lévézou et fait l'objet d'un article en préparation à *Journal of Petrology*. Il correspond à l'étude d'une éclogite fraîche et d'une éclogite rétromorphosée en réalisant un panel complet de datations (U-Pb sur zircon, rutile, apatite; Lu-Hf et Sm-Nd sur grenat), une étude pétrologique précise des deux échantillons, ainsi que l'analyse des spectres de terre rares. Cette étude propose notamment un nouvel âge de la haute pression à ~358 Ma pour des pressions de ca. 18-23 kbar, suivie d'une exhumation rapide à 8-9.5 kbar et ~600°C.

La **partie III** se focalise sur les granites du massif du Lévézou situés de part et d'autres des roches mafiques (étudiées en partie II). Le **chapitre 1** se compose d'un article publié à *International Journal of Earth Sciences*. Il correspond à l'étude géochronologique et géochimique de ces granites, et présente notamment un âge de mise en place à 470 Ma. Il propose également que les granites situés de part et d'autre de la ceinture mafique sont en réalité une seule et même intrusion tectoniquement dupliquée. Le **chapitre 2** correspond à l'étude pétrologique de pseudomorphoses de cordiérites présentes dans ces granites. Cette étude propose que ces granites aient subi des pressions de près de 15-17 kbar, impliquant donc la subduction de croûte continentale. Ce résultat est de prime importance puisqu'il révèle l'occurrence de subduction de roches continentales lors de l'orogenèse Varisque dans le Massif Central. Enfin, le **chapitre 3** présente une étude large via ^{40}Ar-^{39}Ar sur les différents

faciès granitiques et permet de discuter la chronologie des évènements métamorphiques postérieurs à l'évènement métamorphique de haute pression.

La **partie IV** présente une synthèse des principaux résultats obtenus, tant d'un point de vue « thématique » que « varisque ». Elle intègre ainsi ces résultats à l'échelle du Massif Central et à l'échelle de la chaîne varisque, en abordant la question du nombre d'océans et en proposant un modèle géodynamique. Enfin, cette partie propose quelques unes des perspectives les plus intéressantes de mon travail de thèse.

PARTIE I

Contexte Géologique Général

1. La chaine varisque

La chaîne varisque est un orogène Paléozoique qui s'étend depuis les Appalaches au Caucase et à l'Oural, sur près de 8000 km. En Europe, cette chaîne de montagnes affleure sporadiquement depuis le massif Ibérique jusqu'au massif de Bohême, sur près de 4000 km. Cette chaîne, classiquement comparée à l'actuelle chaîne himalayenne, résulte au premier ordre de la collision entre les mégacontinents Laurussia au nord (résultant lui-même de la convergence des continents Laurentia et Baltica) et Gondwana au sud (Fig. 1). Un certain nombre de micro-blocs continentaux intermédiaires, tels qu'Avalonia ou Armorica, participent à cette collision (e.g. Dewey et Burke 1973 ; Bard et al. 1980 ; Matte et Burg, 1981 ; Matte 1986 ; Fig. 1). La disparition par subduction des domaines ou micro-domaines océaniques entraîne l'amalgamation de ces blocs continentaux, et à terme la formation du supercontinent Pangée.

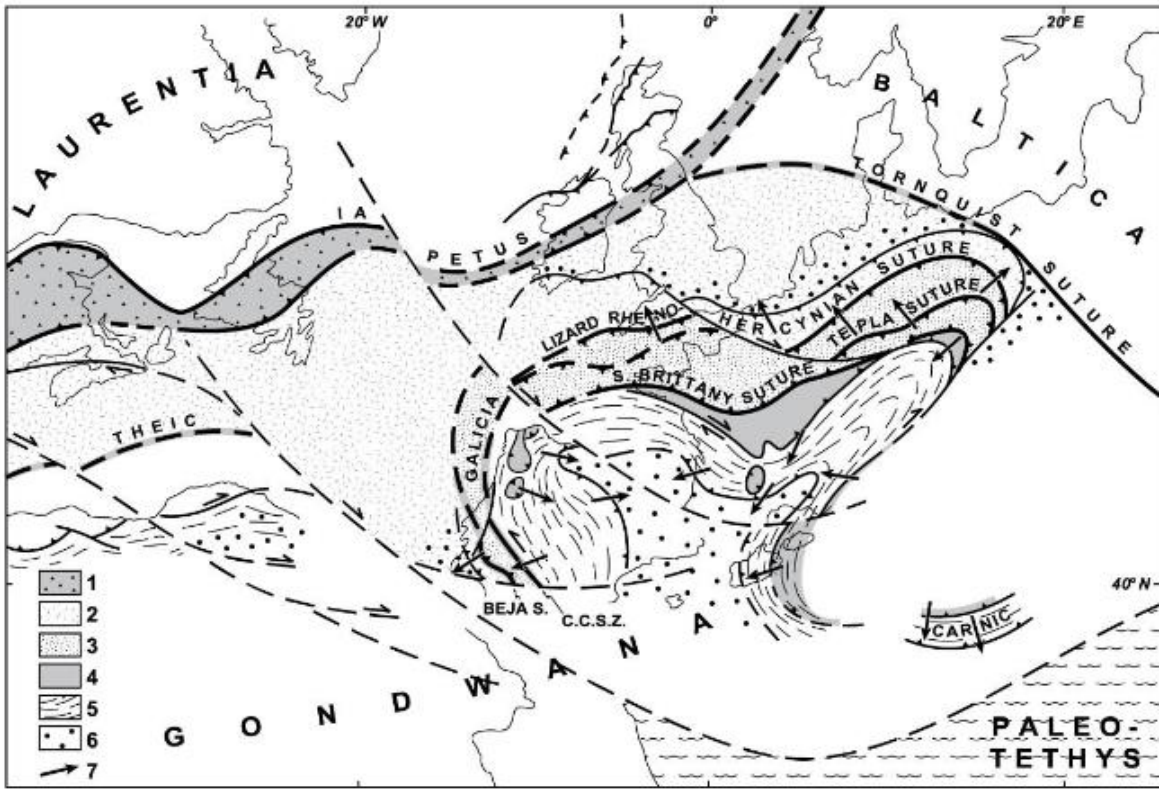

Figure 1 - Configuration de la chaîne varisque européenne au Permien (Matte 2001). 1. Suture de l'océan Iapetus ; 2. Avalonia, 3. Armorica, 4. Nappes ophiolitiques, 5. Nappes sud de la chaîne, 6. Bassins d'avant pays carbonifères, 7 Vergence des nappes.

Des unités d'affinité océanique pouvant être composées de gabbros ± métamorphisés, péridotites ± serpentinisées, pyroxénites ou amphibolites sont identifiées dans la plupart des

massifs de la chaîne. Des reliques de métamorphisme de haute pression (éclogites et schistes bleus ± rétromorphosées) y sont parfois préservées. Ces zones sont interprétées comme les témoins exhumés de subductions océaniques et donc comme les marqueurs des limites des blocs continentaux. Ces zones de sutures font l'objet de nombreuses controverses. À l'heure actuelle, il n'y a aucun réel consensus concernant le nombre de blocs continentaux ou d'arcs magmatiques impliqués dans la construction de l'orogène, la durée ou la dimension réelle des domaines océaniques, voire dans certains cas, la chronologie des subductions océaniques.

Ainsi différents modèles proposent l'existence de plusieurs continents et micro-continents impliqués dans la construction de la chaîne (e.g. Matte 2001; Ballèvre et al. 2009, 2014; Franke et al. 2017; Fig. 2 & 3). Suivant ces différents travaux, il est ainsi possible de dénombrer une multitude de zones de sutures qui résulteraient de la fermeture de différents domaines océaniques (océan Rhéique ou océan Rhéno-Hercynien, océan Saxo-Thuringien, océan Galice-Massif Central - aussi appelé Galice-Moldanubien ou océan Médio-Européen), et autant de continents ou micro-continents impliqués dans la formation de la chaîne (Fig. 2 & 3).

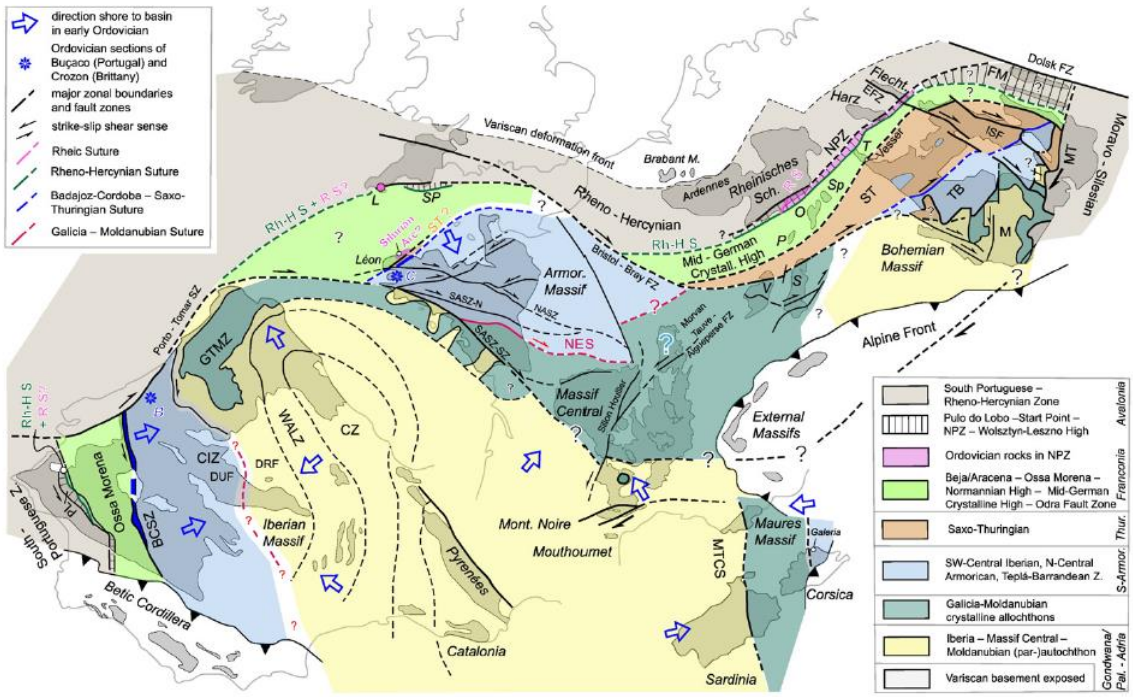

Figure 2 – Répartitions et affiliation des différents domaines varisques et sutures associées, d'après Franke et al. (2017).

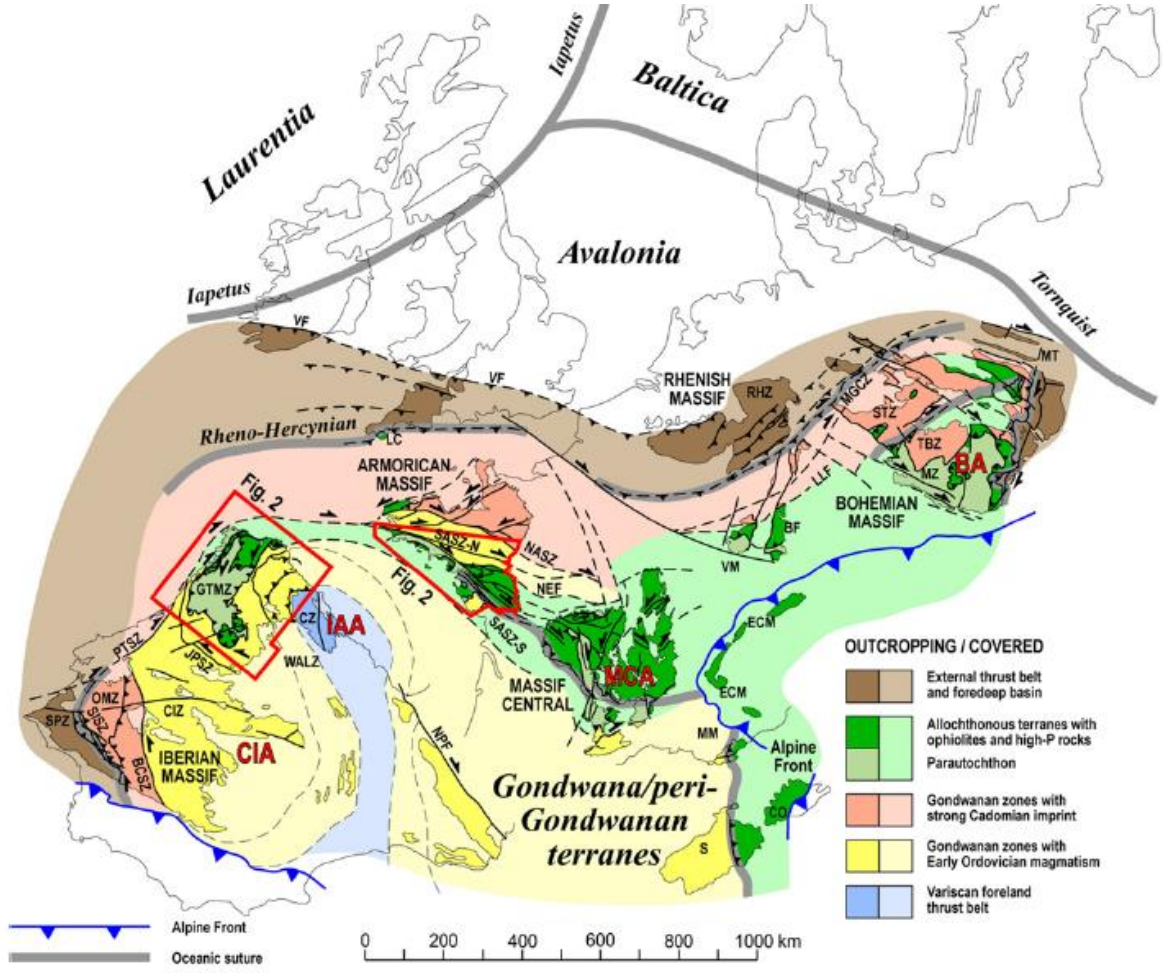

Figure 3- Répartitions et affiliation des différents domaines varisques et sutures associées, d'après Ballèvre et al. (2014), Martinez-Catalan 2007

À l'inverse, d'autres modèles proposent que la chaîne Varisque ne résulte que de la fermeture d'un seul océan majeur, l'océan Rhéique, et n'implique ainsi que la convergence de deux méga-plaques continentales *sensu stricto* (e.g. Martinez-Catalan 2011 ; Kroner et Romer 2013 ; Fig. 4). Par exemple, pour Kroner et Romer (2013), ce serait l'amincissement extrême des marges de l'océan Rhéique au Cambro-Ordovicien qui conduirait à la formation de différents microblocs continentaux « résistant à la subduction » (Massif Armoricain, Galice, Massif Central, Massif de Bohême, etc), séparés les uns des autres par des domaines de croûte continentale extrêmement amincie pouvant être subductés. Les subductions successives de ces domaines très amincis au cours de la convergence permettent, à terme, l'accrétion des différents micro-blocs continentaux et ainsi la formation de la chaîne.

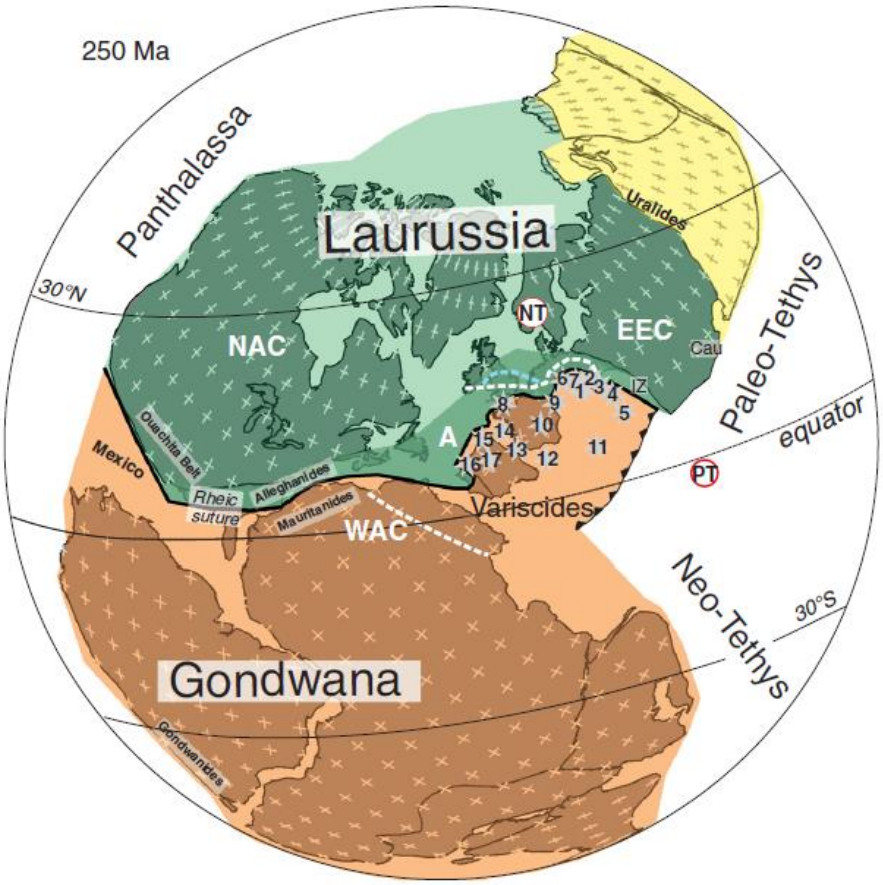

Figure 4 – La chaîne Varisque à la fin du Permien (Kroner et Romer 2013). Les nombres étoilés correspondent à la présence de reliques de haute-pression liées à des zones de subduction. Abréviations: NAC: North American Craton; EEC: East European Craton; WAC: West African Craton; A: Avalonia; IZ: Istanbul Zone; Cau: Caucasus. Numérotation des unités de haute-pression: 1: Moldanubian Zone — Bohemian Massif; 2: Sudetes; 3: Moravia; 4: W-Carpathian; 5: S-Carpathian; 6: Mid-German Crystalline Zone; 7: Saxo-Thuringian Zone; 8: Leon Domain; 9: Vosges–Schwarzwald; 10: N-French Massif Central; 11: Austro-Alpine; 12: Argentera — Corsica–Sardinia; 13: S-French Massif Central; 14: South Armorican Domain; 15: Galicia; 16: Ossa Morena Zone; 17: Spanish Central System.

Ces débats sur le nombre d'océans et de sutures associées sont étroitement liés au problème de l'affiliation de chaque massif Varisque à un continent ou micro-continent, c'est-à-dire à l'origine des unités de part et d'autre des roches d'affinité océanique. Les figures 2 & 3 illustrent par exemple les difficultés de filiation entre les unités du Massif Armoricain et de celui de Bohème.

Aussi, la chronologie et les conditions du métamorphisme de haute pression subi par les roches d'affinité océanique lors de leur subduction sont capitales pour déchiffrer l'évolution géodynamique de la chaîne Varisque. La dernière synthèse des âges du métamorphisme de haute pression (Paquette et al. accepté ; Fig. 5) met en évidence des âges allant de 400 à 360 Ma dans l'ensemble de la chaîne, à l'exception du Massif Central dans

lequel des âges de 430 à 410 Ma sont décrits. Cependant les unités allochtones regroupant le sud du Massif Armoricain et le Massif Central sont censées appartenir, dans la plupart des reconstructions géodynamiques, au même bloc continental. Ces unités enregistrent ainsi deux âges distincts du métamorphisme de haute pression, tous deux interprétés comme témoin de la fermeture de l'océan Médio-Européen. Un âge Dévonien supérieur à Carbonifère inférieur est ainsi bien documenté pour les zones de Groix ou Champtoceaux dans le Massif Armoricain (370-360 Ma - Paquette 1987; Bosse et al. 2000, 2005; Paquette et al. accepté), tandis qu'un âge Silurien à Dévonien inférieur est décrit dans le Massif Central (430-408 Ma – Pin et Lancelot 1982; Ducrot et al. 1983; Paquette et al. 1995; Berger et al. 2010).

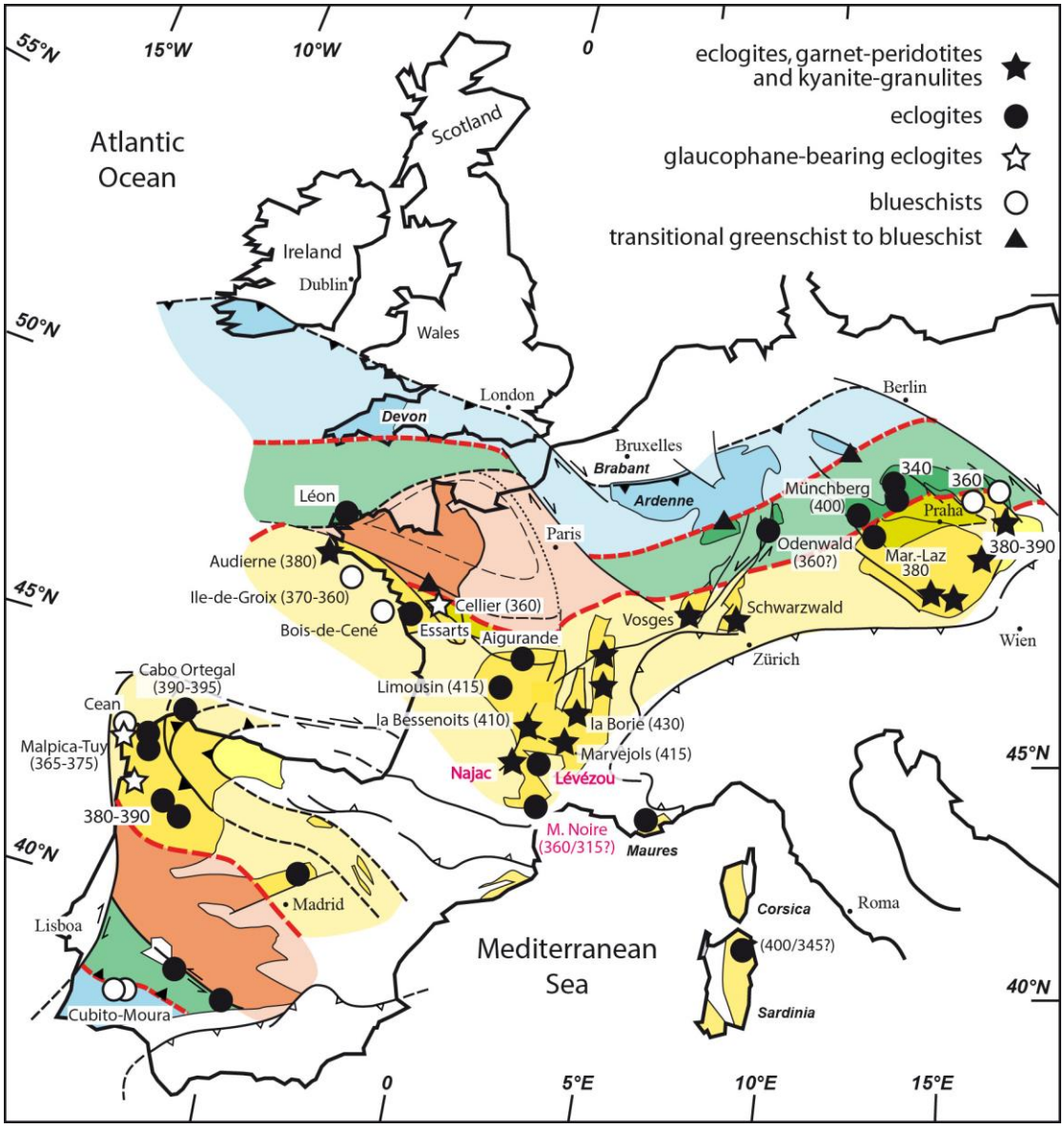

Figure 5 : Carte synthétisant les âges interprétés comme datant le métamorphisme de haute pression dans la chaîne varisque, modifiée d'après Paquette et al.(accepté). Les zones étudiées dans ce manuscrit sont mises en évidence.

Ainsi, si au premier ordre l'assemblage géodynamique de deux mégacontinents apparaît bien établi dans la tectonique Varisque, l'enchaînement des étapes intermédiaires de la construction de cette chaîne et la chronologie des évènements associés restent largement débattus.

2. Le Massif Central : évolution des modèles

Le Massif Central est une zone d'étude privilégiée car la chaîne Varisque d'Europe y affleure d'une façon quasi continue, sur près de 500 km. C'est notamment à travers son étude qu'ont été argumentés les premiers modèles de collision continentale de « type himalayen » au début des années 80. Ces modèles identifiaient une grande nappe cristalline, en partie ophiolitique, (e.g. Bard et al. 1980 ; Burg et al. 1984 ; Matte 1986), considérée comme ayant valeur de suture, où les roches situées de part et d'autre représentaient deux continents différents. Des modèles plus complexes impliquant au minimum cinq unités métamorphiques ont par la suite été proposés (*e.g.* Ledru et al. 1989 ; Faure et al. 2009 ; Lardeaux et al. 2014). Cette suture supposée enracinée au nord du Massif Central (suture « éo-Varisque »), celui-ci est dès lors considéré comme dérivant entièrement du continent Gondwana (Fig. 6 & 7).

.

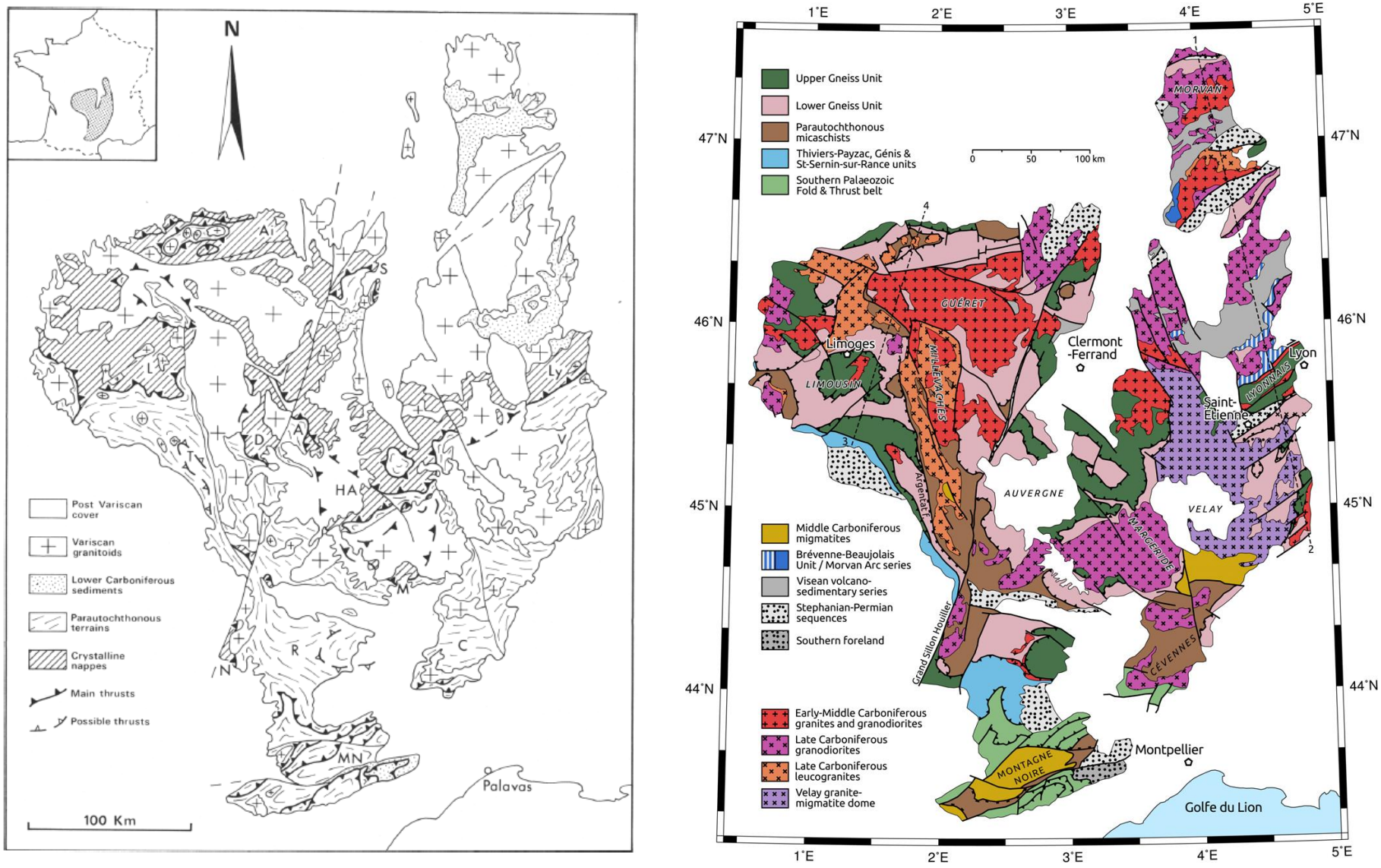

Figure 6 - Répartition des unités tectoniques majeures dans le Massif Central d'après Burg et al. *1984 (à gauche) et d'après* Lardeaux et al. *2014 (à droite)*

Les études les plus récentes subdivisent le Massif Central comme suit (Fig. 6B, 7 ; *e.g.* Faure et al. 2009 ; Lardeaux 2014 ; Lardeaux et al. 2014 ;):

(i) L'Unité du Parautochtone (*Parautochtonous Unit*, PAU), qui présente le grade métamorphique le plus faible, est principalement composée de méta-pélites, grauwackes, quartzites et méta-rhyolites (localement nommées « porphyroïdes »), métamorphisés en faciès schiste vert. Cette unité est située à la base des nappes du Massif Central et est considérée comme chevauchante sur le socle Gondwanien.

(ii) L'Unité Inférieure des Gneiss (*Lower Gneiss Unit*, LGU), chevauchant le PAU, est constituée de métasédiments métamorphisés en faciès schiste vert – amphibolite, et est intrudée par de nombreux granitoïdes dont les protolithes sont datés du Cambro-Ordovicien (e.g. Chelle-Michou et al. 2017)

(iii) L'Unité Supérieure des Gneiss (*Upper Gneiss Unit*, UGU) se compose de para- et orthogneiss plus ou moins migmatitiques, contenant rarement des enclaves de haute pression (e.g. Massif du Lévézou - Delor et al. 1985). Les composantes ortho-dérivées de l'UGU sont globalement ordoviciennes (e.g. Chelle-Michou et al. 2017) tandis que l'évènement de fusion partielle serait daté à ca. 390-370 Ma (e.g. 384 ± 16 Rb-Sr sur roche totale, Duthou et al. 1994 ; 374 ± 6 Ma, Faure et al. 2008)

(iv) Le Groupe Leptyno-Amphibolitique (*Leptyno-Amphibolitic Group*, LAG) est situé à l'interface entre l'UGU et la LGU, et correspond à une association bimodale de roches mafiques à ultra-mafiques (métagabbros, péridotites ± serpentinisées, amphibolites, pyroxénites, éclogites) et des roches felsiques (méta-rhyolites, leptynites). Les protolithes sont datés de l'Ordovicien (e.g. Pin et Lancelot 1982 ; Paquette et al. 1995 ; Berger et al. 2010 ; Chelle Michou et al. 2017). Cette unité porte les traces d'un métamorphisme de haute à ultra-haute pression daté du Silurien au Dévonien inférieur (Pin et Lancelot 1982 ; Ducrot et al. 1983 ; Paquette et al. 1995 ; Berger et al. 2010). Cette unité est discutée plus en détails dans les sections suivantes.

(v) Enfin, au sommet de ces séries se retrouvent les unités de la Brévenne et du Morvan, correspondant respectivement à un complexe ophiolitique et des roches

volcaniques datées à 366 ± 5 Ma (Pin et Paquette 1998). Un second complexe ophiolitique est également identifié dans le Limousin (e.g. Mercier et al. 1985) et correspond à l'unité du Génis.

L'évolution géodynamique généralement admise considère qu'après l'extension ordovicienne à l'origine de l'ouverture de l'océan Galice-Massif Central (aussi nommé océan Médio-Européen ou Galice-Moldanubien selon les auteurs), la subduction qui entraîne sa disparition se marque par le développement d'un métamorphisme de haute à ultra-haute pression dans les roches océaniques et continentales enfouies (e.g. Pin et Vielzeuf 1988 ; Lardeaux et al. 2001 ; Berger et al. 2010) du Silurien au Dévonien inférieur (de 432 ± 20 Ma 408 ± 7 Ma ; Pin et Lancelot 1982 ; Ducrot et al. 1983 ; Paquette et al. 1995 ; Berger et al. 2010). L'exhumation de ces terrains vers 390-370 Ma est contemporaine d'un évènement de migmatisation affectant l'UGU (e.g. Duthou et al. 1994 ; Faure et al. 2008). Au nord du Massif Central, la subduction de l'océan Saxo-Thuringien (ou Rhéique selon les auteurs) qui se développe vers 370 Ma entraîne la formation du bassin d'arrière arc de la Brévenne auquel est associé le magmatisme d'arc du Morvan (e.g. Faure et al. 2009).

Suivant les modèles géodynamiques, la collision continentale *s.s.* débute entre 380 et 350 Ma. Elle est marquée par le développement d'un métamorphisme inverse et l'injection de granites le long des grands chevauchements crustaux (e.g. Pin 1981). Enfin, vers 320 Ma l'ensemble du Massif Central est soumis à une tectonique extensive qui s'accompagne d'un métamorphisme HT et BP et d'une fusion partielle de la croûte à l'origine de dômes migmatitiques. En surface, dans le même temps, des bassins Permo-Carbonifères se développent. La plupart des modèles considèrent cette extension comme la conséquence directe de la collision et de l'épaississement crustal qui s'en est suivi, probablement accompagné d'une délamination du manteau continental (e.g. Malavieille 1993 ; Burg et al. 1994 ; Faure 1995 ; Laurent et al. 2017).

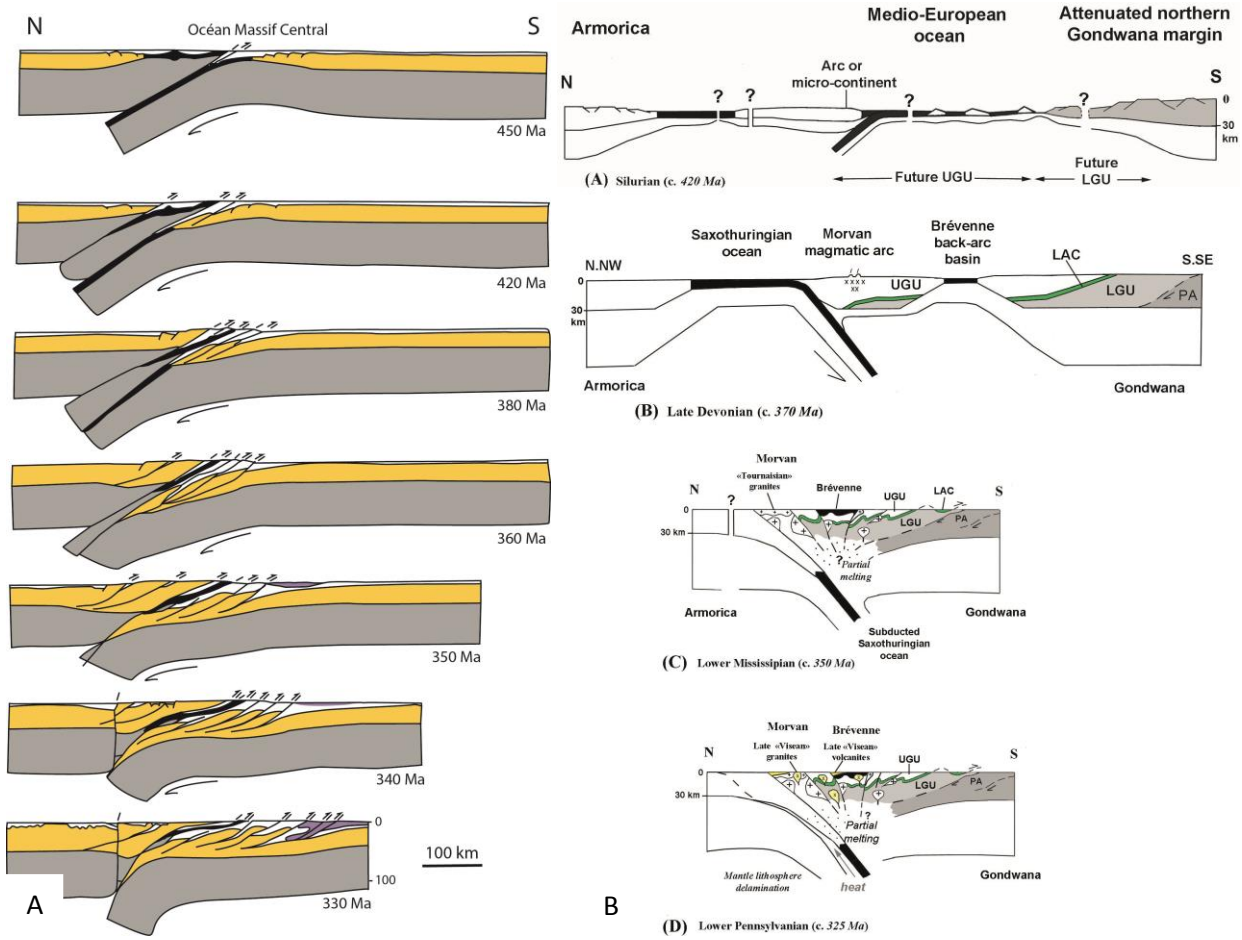

Figure 7 - Deux modèles de la tectonique varisque du Massif central à l'échelle lithosphérique, d'après A. Matte (1986) et B. Lardeaux (2014)

3. Les occurrences d'éclogites dans le Massif Central

Différents types de roches de haute pression coexistent dans le Massif Central. On observe ainsi des éclogites de haute température dans la plupart des massifs (Limousin, Monts du Lyonnais, Haut Allier, Sioule, Vivarais, Marvejols, Rouergue, Montagne Noire). Des éclogites de basse température sont décrites dans une unique localité, la klippe de Najac (Delor et al. 1986).

Ces roches, qui affleurent sous forme de reliques au sein d'ensembles massivement rétromorphosés en faciès amphibolite, appartiennent au LAG. Elles sont pour la plupart situées à l'interface entre l'UGU et la LGU. Seules les éclogites du massif de la Montagne Noire affleurent dans un contexte tectonique apparemment différent, dans les migmatites datées de la fin du Carbonifère (e.g. Roger et al. 2015 ; Poujol et al. 2017)

Forestier (1961) est le premier à décrire le LAG dans la zone de Brioude. Initialement nommé Groupe Leptyno-Amphibolitique Brivadois, cet ensemble correspond à l'association complexe de roches felsiques déformées, à grain fin (appelées « leptynites ») et de roches métamorphiques mafiques à ultramafiques (amphibolites, péridotites ± serpentinisées, pyroxénites) qu'il apparente à des termes éruptifs acides associés à des niveaux basiques, ultérieurement métamorphisés. Le terme est par la suite généralisé à toutes les occurrences de matériel mafique à ultramafique dans l'ensemble de la chaîne.

3.1. Composition géochimique et signification

Les roches composant le LAG ont une composition chimique très variable, depuis des compositions de MORB tholéiitique à des tholéiites continentales. Certaines roches du LAG présentent également un caractère composite (e.g. Briand et al. 1988, Massif du Lévézou), en associant des séries calco-alcalines continentales et des séries tholéitiques.

Le LAG a ainsi pu être interprété, selon les localités où il affleure, comme une relique de séquence ophiolitique (Nicollet 1978 ; Berger et al. 2005), la trace d'un ancien bassin d'arrière arc ou d'un ancien arc magmatiqu (e.g. Briand et al. 1988 ; Giraud et al. 1984 ; Bodinier et al. 1988), ou encore comme la trace d'une zone de rifting continentale (Pin et Lancelot 1982 ; Pin et Piboule 1979 ; Pin 1990).

Tous ces auteurs s'accordent néanmoins sur le fait que quel que soit l'environnement tectonique initial du protolithe du LAG, l'océan médio-européen n'a jamais atteint un stade d'océanisation avancé.

Plus récemment, Lardeaux (2014) et Lardeaux et al. (2014) ont proposé que le LAG et l'UGU soient les vestiges de la marge hyper-amincie du Gondwana, formée à l'Ordovicien (Fig. 8). Suivant cette interprétation, le LAG ne correspondrait pas à un véritable plancher océanique.

*

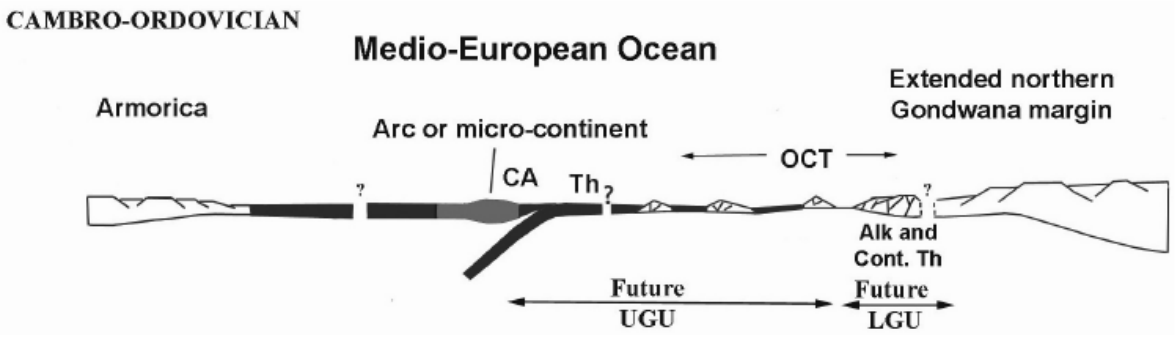

Figure 8 – Schéma interprétatif de la marge Nord de Gondwana au Cambro-Ordovicien, d'après Lardeaux et al. (2014)

3.2. Estimations des pressions et des températures

Les pressions enregistrées par la plupart des éclogites du LAG vont de 15 à 30 kbar, pour des températures de 660°C à près de 900°C (e.g. Lasnier 1977 ; Bouchardon et al. 1987 ; Briand et al. 1988 ; Mercier et al. 1989 ; Lardeaux et al. 2001 ; Bellot et Roig 2007 ; Berger et al. 2010 ; Whitney et al. 2015 ; Fig. 9). Les éclogites de Najac se démarquent par l'estimation de leur pression potentiellement plus basse (<12 kbar) pour des températures inférieures à 600°C (Delor et al. 1986 ; Fig 9).

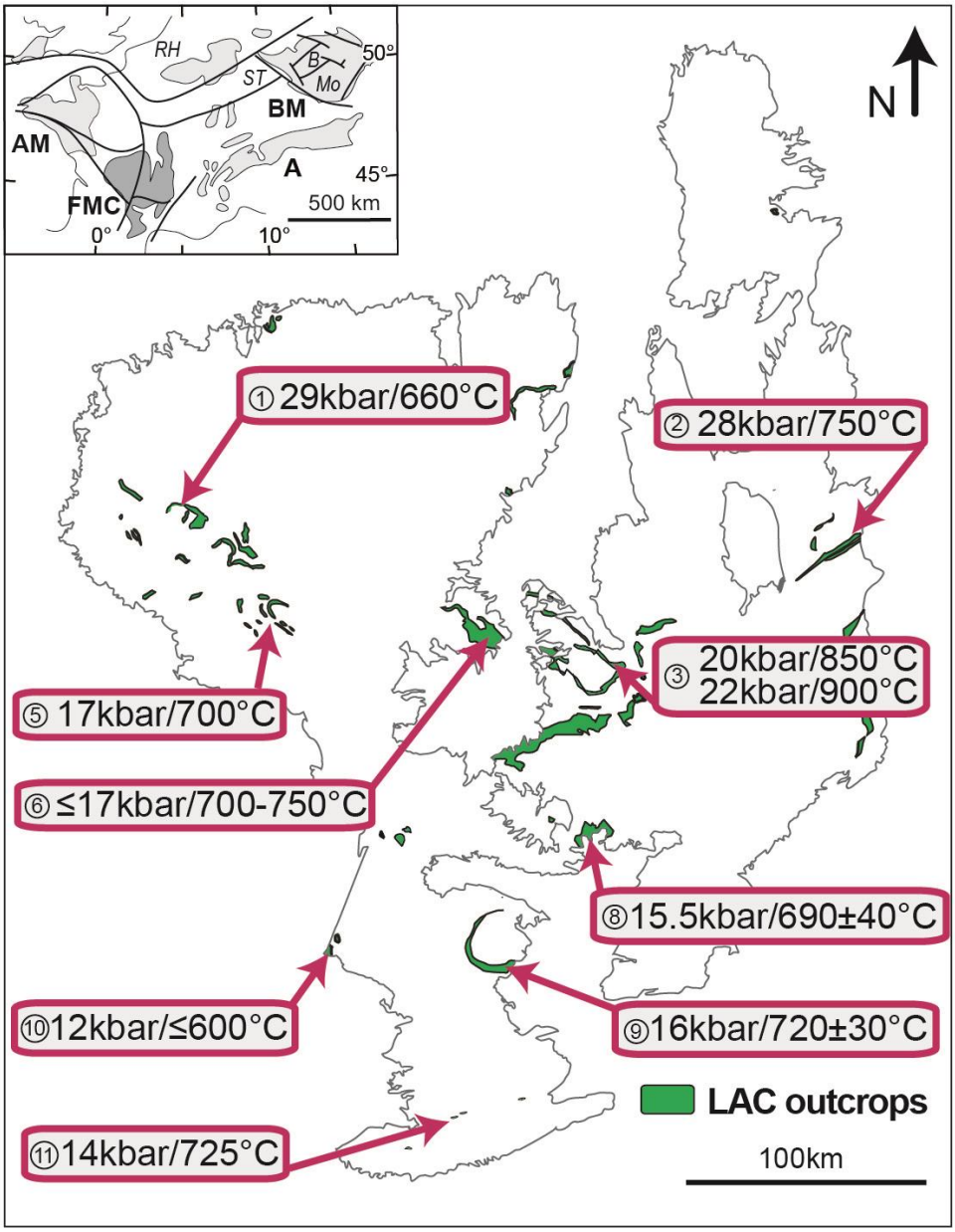

Figure 9 – Synthèse des données pressions et températures disponibles dans le Massif Central. 1. Berger et al. 2010 ;2. Lardeaux et al. 2001 ; 3. Lasnier 1977 ; 5. Bellot et Roig 2007 ; 6. Mercier et al. 1989 ; 8. Briand et al. 1988 ; 9. Bouchardon et al. 1987 ; 10. Delor et al. 1986 ; 11. Whitney et al. 2015

3.3. Age de l'évènement de haute-pression

Quatre âges obtenus sur des roches du LAG sont attribués au métamorphisme de haute pression et sont donc rattachés à une phase de subduction, du Silurien au Dévonien inférieur (Fig. 10, 11) :

(i) Pin et Lancelot (1982) ont daté une trondhjémite de haute pression à Marvejols (12.5-20 kbar, 750-850°C, Nicollet et al. 1979) par dilution isotopique de 4 fractions de zircons. Les données définissent une discordia dont l'intercept supérieur détermine une date à 415 ± 6 Ma, interprétée comme l'âge de cristallisation des zircons, i.e. l'âge du métamorphisme de haute pression.

(ii) Ducrot et al. (1983) ont daté une éclogite à quartz dans le Haut Allier (La Borie) par dilution isotopique de 7 fractions de zircons. Les fractions analysées sont toutes discordantes, mais s'alignent et permettent de définir une discordia, dont l'intercept supérieur révèle un âge de 432 ± 20 Ma interprété comme l'âge de la haute pression.

(iii) Paquette et al. (1995) ont réalisé une double étude géochronologique sur une gabbronorite du massif de La Bessenoit. Une fraction de grenat et une fraction de roche totale de deux éclogites fournissent deux âges Sm-Nd de 405 ± 5 Ma et 392 ± 29 Ma. En faisant l'hypothèse que les deux roches sont cogénétiques, les auteurs ont calculé un âge Sm-Nd, à partir d'une isochrone à 4 points, à 408 ± 7 Ma. La datation U-Pb (dilution et évaporation de monograin) a fourni un âge moyen à 413 ± 23 Ma. Ils interprètent ces deux âges, similaires dans l'erreur, comme datant le métamorphisme de haute pression.

(iv) Berger et al. (2010) ont plus récemment daté par LA-ICPMS les zircons d'une éclogite à disthène et zoïsite. Trois analyses définissent un âge concordant à 412 ± 6 Ma (MSWD = 0.29), tandis que 3 autres analyses concordantes définissent une date plus jeune à 382 ± 7 Ma (MSWD = 0.11). Les auteurs interprètent l'âge de 412 ± 6 Ma comme datant le métamorphisme de haute pression, en se basant sur sa similarité avec les trois études précédentes et considèrent l'âge de 382 ± 7 Ma comme relié à l'évènement plus tardif de haute température.

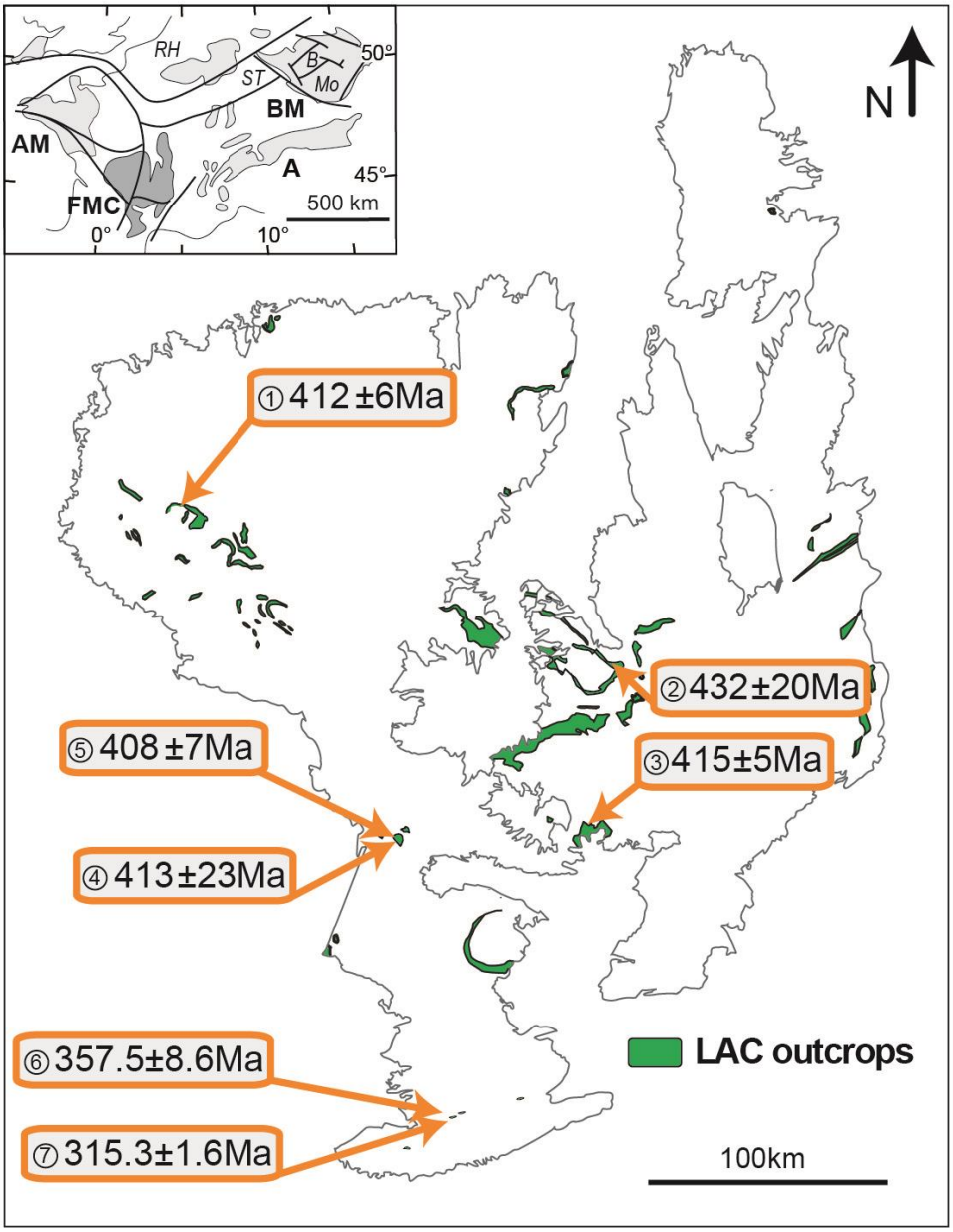

Figure 10 – Carte représentant les affleurements du Groupe Leptyno-Amphibolitique et les âges interprétés comme datant l'âge de la haute-pression. 1. U-Pb sur zircon, LA-ICP-MS, Berger et al. 2010, 2. U-Pb sur zircon, TIMS, Ducrot et al. 1983, 3. U-Pb sur zircon, TIMS, Pin et Lancelot 1982, 4. Sm-Nd sur grenat, TIMS, Paquette et al. 1995, 5. Pb-Pb sur zircon, TIMS, Paquette et al. 1995, 6. Sm-Nd sur grenat, TIMS, Faure et al. 2014, 7. U-Pb sur zircon, LA-ICP-MS, Whitney et al. 2015.

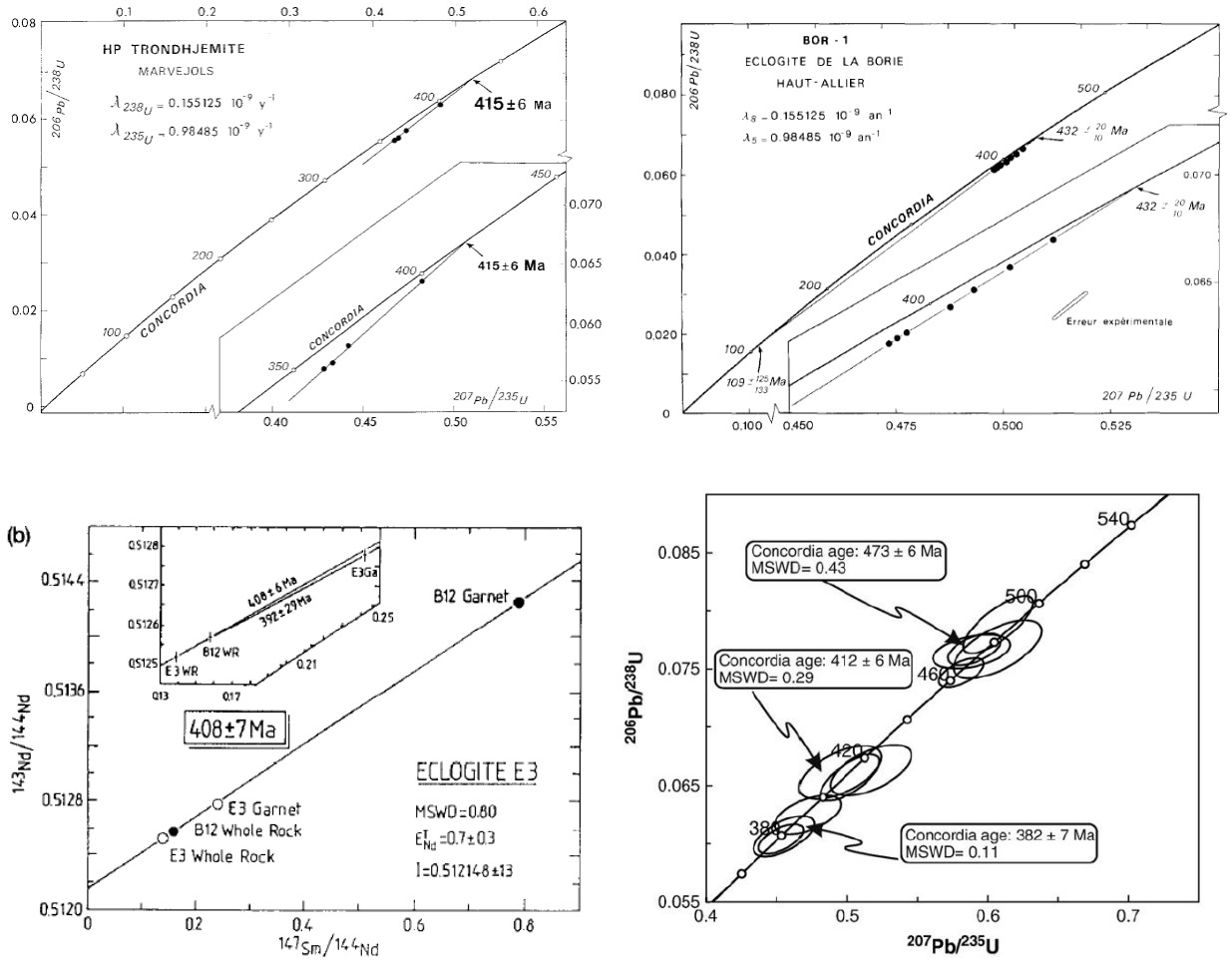

Figure 11- Synthèse des datations de la haute pression disponibles dans le Massif Central. A. Marvejols, Pin et Lancelot 1982 ; B. Haut-Allier, Ducrot et al. 1983 ; C.D. La Bessenoit, Paquette et al. 1995 ; E. Limousin, Berger et al. 2010.

Enfin, dans la Montagne Noire, deux études réalisées sur les éclogites de Peyrambert-Terme de Fourcaric proposent deux âges distincts de la haute pression (Fig. 10, 12):

(i) Faure et al. (2014) ont réalisé une étude géochronologique par Sm-Nd sur grenat et U-Pb sur zircons et rutiles. Deux plots de zircons ont fourni des intercepts inférieurs à 314 ± 2.5 Ma (N = 12, MSWD = 0.33) et 311 ± 2 Ma (N = 24, MSWD = 0.88), tandis que le rutile a fourni un âge concordant à 308 ± 4 Ma (N = 71, MSWD = 2). Les datations Sm-Nd sur une fraction de grenat, omphacite et roche totale ont fourni une date de 357.5 ± 8.6 Ma (MSWD = 0.89). Les auteurs interprètent la datation des grenats comme reflétant un stade de haute pression lié à une subduction continentale dévonienne, tandis que les âges obtenus sur zircons et rutiles sont considérés refléter des circulations tardives de fluides hydrothermaux.

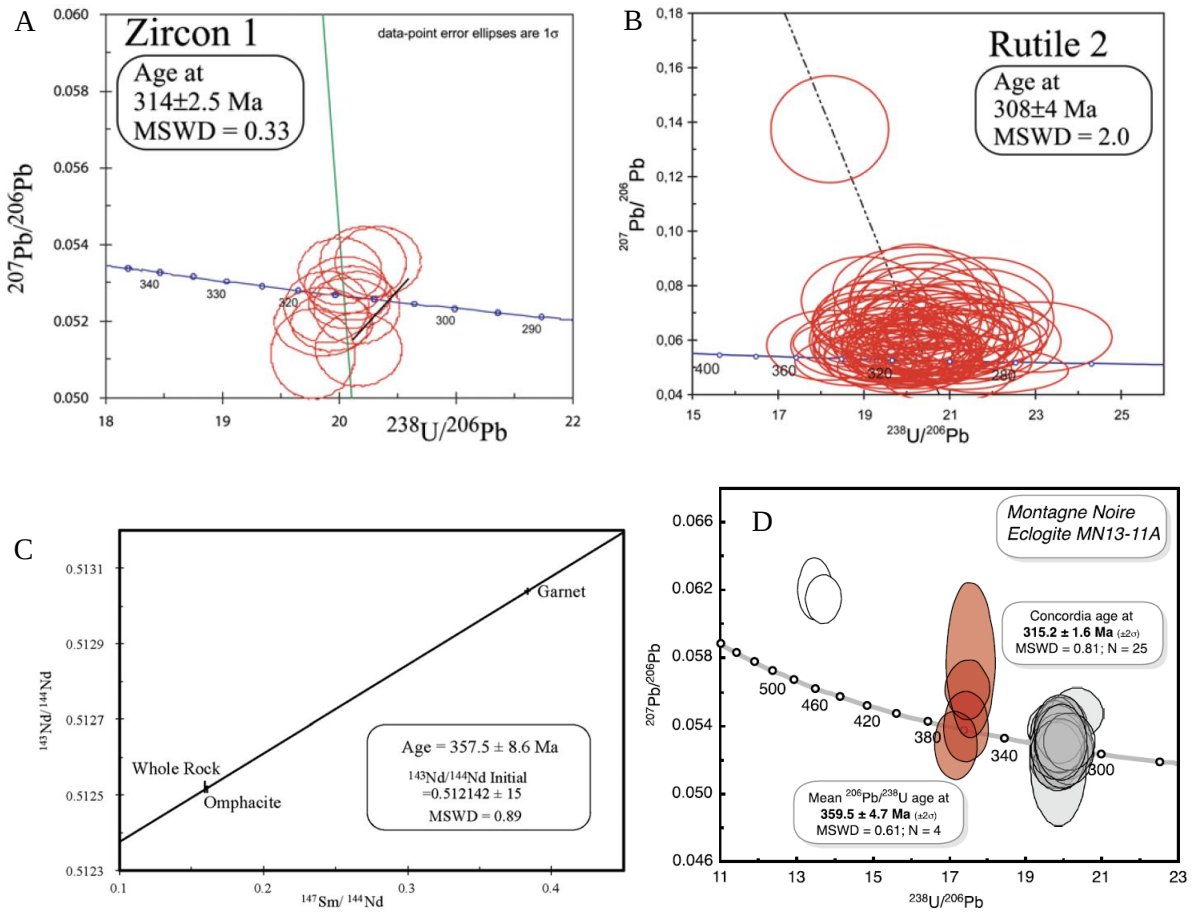

Figure 12- Synthèse des datations de la haute pression disponible dans le massif de la Montagne Noire. A. U-Pb sur zircon, LA-ICPMS, Faure et al. 2014, B. U-Pb sur zircon, LA-ICPMS, Faure et al. 2014, C. Sm-Nd sur grenat, TIMS, Faure et al. 2014, D. U-Pb sur zircon, LA-ICPMS, Whitney et al. 2015.

(ii) Whitney et al. (2015) ont effectué une étude U-Pb sur zircon et ont obtenu une date concordante à 315.3 ± 1.6 Ma (MSWD = 0.81, N = 25) et un âge moyen à 359.5 ± 4.7 Ma (MSWD = 0.61 ; N = 4). Basée sur l'analyse des spectres de terre rares dans les zircons, ils interprètent l'âge 359.5 ± 4.7 Ma comme celui du protolithe ou d'un stade métamorphique pré-éclogitique sur le chemin prograde, tandis que l'âge 315.3 ± 1.6 Ma est censé refléter l'âge du métamorphisme de haute pression.

3.4. Controverses et inconnues

Santallier et al. (1988) ont alerté sur l'utilisation abusive du terme Groupe Leptyno-Amphibolitique tout en synthétisant ses nombreux usages. Il peut à la fois signifier la

présence de reliques de haute pression ± rétromorphosées, caractériser un caractère bimodal de cette unité, correspondre à un mélange de subduction ou marquer de grands chevauchements d'échelle crustale, selon les auteurs (e.g. Nicollet 1978 ; Burg et al. 1983 ; Piboule et Briand 1985 ; Matte 1986).

A ces différents usages vient également s'ajouter la problématique de la position tectonique du protolithe du LAG, puisque toute occurrence de roche mafique n'est pas synonyme de croûte océanique.

La présence d'éclogites de basse température dans la région de Najac soulève également des questions, puisque ces dernières témoignent de conditions P-T différentes (cf. section 3.2). Certains auteurs suggèrent notamment que leur métamorphisme pourrait être rattaché à celui des éclogites de basse température et schistes bleus visibles dans le Massif Armoricain, lié à une subduction tardi-dévonienne (e.g. Lardeaux 2014)

Les études géochimiques et géochronologiques menées par Pin et Lancelot (1982), Ducrot et al. (1983) et Paquette et al. (1995) ont permis de mieux contraindre les modèles tectoniques et sont encore aujourd'hui à la base des modèles d'évolution géologique proposés dans le Massif Central. Néanmoins, ces âges obtenus par dilution isotopique de fractions de zircon doivent être reconsidérés, puisqu'ils amalgament de potentiels cœurs magmatiques ou hérités, et des surcroissances métamorphiques. L'étude *in situ* de Berger et al. (2010) est ainsi la seule étude géochronologiques solide disponible dans le Massif Central, bien que ses résultats puissent être discutés (voir Paquette et al. accepté).

Enfin, les âges récemment obtenus dans la Montagne Noire (Faure et al. 2014 ; Whitney et al. 2015) remettent fondamentalement en question la dynamique admise jusqu'alors de la chaîne Varisque du Massif Central. Que ce soit un âge Dévonien supérieur ou un âge Carbonifère supérieur, aucune autre occurrence de métamorphisme de haute pression datée de cette période n'est pour l'instant connue dans le Massif Central.

Partie II

Le Métamorphisme de haute pression : Enregistrement dans les roches mafiques des massifs de Najac, de la Montagne Noire et du Lévézou

Chapitre 1 – le massif de Najac

Table of content

Timing and duration of Variscan high-pressure metamorphism in the French Massif Central: a multimethod geochronological study from the Najac Massif

Lithos, accepted

Caroline Lotout [a], Pavel Pitra [a,b], Marc Poujol [a], Robert Anczkiewicz [c], Jean Van Den Driessche [a]

[a] Univ Rennes, CNRS, Géosciences Rennes - UMR 6118, F-35000 Rennes, France

[b] Česká geologická služba, Klárov 3, CZ-118 21 Praha 1, Česká republika

[c] Institute of Geological Sciences, Polish Academy of Sciences, Kraków Research Center, Senacka 1, PL 31-002, Kraków, Poland

Highlights of the paper

- First zircon and garnet petrochronological study of the eclogite metamorphic peak (376.6 ± 3.3 Ma) and duration (~6.1 ± 4.3 Myr) in the French Massif Central

- New P-T estimates (15-20 kbar and 560-630 °C) for the eclogite of the Najac Massif

- Zircon crystallization prior and during incipient garnet growth, recording the early stage of the eclogite-facies metamorphism.

Résumé

La datation précise du métamorphisme éclogitique est d'une importance capitale pour comprendre l'évolution d'un orogène. Nous présentons dans cette étude les résultats d'une investigation géochronologique multiméthodes réalisée sur une éclogite du massif de Najac (sud Massif Central, chaîne Varisque). Cette éclogite présente une paragenèse de haute pression à grenat-omphacite-amphibole-rutile-quartz. Les modélisations d'équilibre de phase permettent d'encadrer les conditions de ce métamorphisme de haute pression à 15-20kbar et 560-630°C. Les grenats présentent des cœurs enrichis en Lu tandis que les bordures sont enrichies en Sm. Les datations Lu-Hf et Sm-Nd ont permis d'obtenir des âges de 382.8 ± 1.0 Ma et 376.6 ± 3.3 Ma, respectivement. L'âge Lu-Hf est interprété comme marquant le début de la croissance prograde du grenat et l'entrée dans le faciès éclogite. L'âge Sm-Nd est quant à lui interprété comme reflétant la cristallisation des bordures du grenat, et par conséquent correspond au pic de température et de pression subit par la roche. Les zircons de cette eclogite présentent des spectres d'éléments de terres rares normalisés aux chondrites ayant des anomalies en Eu positives, négatives voir absentes ainsi que des enrichissements variables en terre rares lourdes. Néanmoins, malgré cette variabilité d'éléments de terres rares, toutes les zones analysées enregistrent un unique âge U-Pb de 385.5 ± 2.3 Ma. Les zonations en Lu et Zr dans le grenat, associées à la diversité des spectres d'éléments de terres rares suggèrent que le zircon a cristallisé avant et pendant la croissance du grenat, sur le trajet prograde, enregistrant ainsi les stades initiaux du faciès éclogitique. Par conséquent l'âge de 385.5 ± 2.3 Ma obtenu sur zircon, identique dans l'erreur à celui obtenu par Lu-Hf sur grenat, est interprété comme reflétant le début du faciès éclogite. La durée du métamorphisme éclogitique prograde est ainsi estimée à 6.1 ± 4.3 Myr. L'exhumation reste mal contrainte, à ~ 369 ± 13 Ma par la datation U-Pb des apatites de la roche.

Mot-clés : Datation U-Pb sur zircon et apatite, datation Lu-Hf et Sm-Nd sur grenat, éléments trace, modélisation P-T, pétrochronologie, datation du faciès éclogite, Massif Central français, chaîne varisque

Abstract

Accurate dating of eclogite-facies metamorphism is of paramount importance in order to understand the tectonic evolution of an orogen. An eclogite sample from the Najac Massif (French Massif Central, Variscan belt) displays a zircon-bearing garnet-omphacite-amphibole-rutile-quartz peak assemblage. Pseudosection modeling suggests peak pressure conditions of 15-20 kbar, 560-630 °C. Eclogite-facies garnet displays Lu-enriched cores and Sm-rich rims and yields a Lu-Hf age of 382.8 ± 1.0 Ma and a Sm-Nd age of 376.6 ± 3.3 Ma. The ages are interpreted as marking the beginning of the prograde garnet growth during the initial stages of the eclogite-facies metamorphism, and the high-pressure (and temperature) peak reached by the rock, respectively. Zircon grains display chondrite-normalized REE spectra with variably negative, positive or no Eu anomalies and are characterized by either enriched or flat HREE patterns. However, they yield a well constrained in situ LA-ICP-MS U-Pb age of 385.5 ± 2.3 Ma, despite this REE pattern variability. Zr zonation in garnet, Y content in zircon and the diversity of zircon HREE spectra may suggest that zircon crystallized prior to and during incipient garnet growth on the prograde P-T path, recording the initial stages of the eclogite-facies conditions. Consequently, the zircon age of 385.5 ± 2.3 Ma, comparable within error with the Lu-Hf age obtained on garnet, is interpreted as dating the beginning of the eclogite-facies metamorphism. Accordingly, the duration of the prograde part of the eclogite-facies event is estimated at 6.1 ± 4.3 Myr. Subsequent exhumation is constrained by an apatite U-Pb age at 369 ± 13 Ma.

Keyword: U-Pb zircon and apatite geochronology, Lu-Hf and Sm-Nd garnet dating, Trace Elements, P-T modeling, petrochronology, eclogite facies dating, French Massif Central, Variscan belt

1. Introduction

The occurrence of eclogites at the Earth surface is generally considered to record ancient subduction zones. Dating the high-pressure (HP) metamorphism that these rocks experienced is therefore a key step in the reconstruction of geodynamics through time. However, overprint of early HP metamorphic assemblages and geochronometers by subsequent metamorphic stages may hamper the measurement of an accurate age for the HP metamorphism and consequently the overall geodynamic interpretation. The late Paleozoic, European Variscan belt contains rocks that present such a challenge: available geodynamic models involve two or more subducted oceanic domains, depending on the interpretation of the geochronological results obtained on HP metamorphic rocks (e.g. Ballèvre et al., 2009, 2014; Martínez Catalán et al., 2009; Faure et al., 2009; Franke, 2006; Lardeaux et al., 2014; Matte, 1986; Schulmann et al., 2014).

Used independently or in combination, U-Pb on zircon, Lu-Hf and Sm-Nd on garnet have been used successfully for dating HP metamorphism (e.g. Anczkiewicz et al., 2004, 2007, 2012; Bingen et al., 2001; Duchêne et al., 1997, Kylander-Clark et al., 2007; Rubatto, 2002; Rubatto and Hermann, 2003; Smit et al., 2013). The multimethod approach is an excellent way to attribute ages to specific metamorphic stages, to access burial or exhumation rates, to evaluate the geological accuracy of each chronometer and to avoid misinterpreting geologically meaningless dates. It can also be used to test the validity of these different methods (e.g. REE eclogitic-like spectra in zircon dating granulite-facies rocks, Štípská et al., 2016).

Eclogites in the Najac area, in the south-western French Massif Central, are considered to be related to an oceanic suture (e.g. Delor et al., 1986). However, the methods used to estimate their P-T conditions (Delor et al., 1986, 1987) are now judged unreliable and the eclogites have never been dated. In this work, metamorphic P-T conditions are re-evaluated through a petrographical analysis and numerical modeling of phase equilibria. The age and duration of the HP metamorphism is investigated using several independent and complementary geochronological tools – Lu-Hf and Sm-Nd on garnet, and U-Pb on zircon and apatite – coupled to trace element analyses on the dated minerals.

2. Geological Context

In the French Massif Central (FMC), eclogite relics are mostly found associated with other mafic (amphibolites, gabbros), ultramafic (peridotites), felsic (fine-grained orthogneisses, traditionally termed "leptynites") and metasedimentary rocks, commonly strongly deformed. In the literature, this association is known as the "Leptyno-Amphibolitic Complex" (LAC) (e.g. Forestier et al., 1973; Lasnier, 1968, Fig. II.1.1A). The significance of the LAC is a controversial subject, as it has been successively interpreted as the relic of (i) a true ocean, (ii) a subduction mélange, (iii) a back-arc basin, or (iv) an ocean-continent transition zone (e.g. Bodinier et al., 1986; Bouchardon et al., 1989; Lardeaux, 2014; Piboule and Briand, 1985; Santallier et al., 1988). However, independently of the true nature of the protolith and its emplacement setting, the LAC is considered as a geotectonic marker of a subduction stage during the Variscan orogeny (e.g. Ledru et al., 1989; Ballèvre et al., 2009; Lardeaux, 2014 and references therein).

Only four studies have attempted to date the HP event in the LAC of the French Massif Central (Fig. II.1.1A). Pin and Lancelot (1982) dated four zircon fractions (U-Pb by ID-TIMS) from a HP trondhjemite sample in the Marvejols area. The data are discordant and define an upper intercept date of 415 ± 6 Ma. This trondhjemite is considered to result from melt crystallization at high-pressure. This date was interpreted as the age of the crystallization of the rock and consequently, as the age of the high-pressure event. Ducrot et al. (1983) studied a quartz-eclogite from the Haut-Allier. Seven zircon fractions analyzed by ID-TIMS are all discordant and point to an upper intercept date of 432 ± 20 Ma. The date was interpreted as reflecting the re-equilibration of the eclogite at high pressure, and consequently, as the age of the high-pressure event. An eclogitized gabbronorite from La Bessenoit Massif was dated at 408 ± 7 Ma (Sm-Nd on garnet) and 413 ± 23 Ma (U-Pb by ID-TIMS on zircon; Paquette et al., 1995). The Sm-Nd study was realized on garnet and whole rock from two distinct samples: a Ti-eclogite yielded a date of 392 ± 29 Ma while a Mg-eclogite yielded a date of 408± 5 Ma. Based on the assumption that both samples are cogenetic, they were plotted in the same diagram and yielded a date of 408± 8 Ma, mostly controlled by the garnet fraction from the Mg-eclogite sample. A recent geochronological re-investigation of the zircon age does not confirm the ca. 400 Ma date, and the authors conclude that the data may have been over-interpreted (Paquette et al., 2017). Finally, Berger *et al.* (2010) performed in-situ LA-ICP-MS dating on zircon from a kyanite-zoisite bearing eclogite from the Limousin area. The authors attributed the age of 412 ± 6 Ma (N=3) to the HP event by analogy with the

results from the three aforementioned studies, although they also obtained 3 younger concordant analyses yielding a concordia date of 382 ± 7 Ma. It has to be noted that the three zircon dating studies (Pin and Lancelot, 1982; Ducrot *et al*., 1983; Berger *et al*., 2010) do not demonstrate that the dated zircon grains belong to the eclogite-facies paragenesis. Consequently, the Sm-Nd study of Paquette et al. (1995) is so far the only one that dated minerals clearly associated with the HP event in the FMC, and this result is further discussed in the Discussion section.

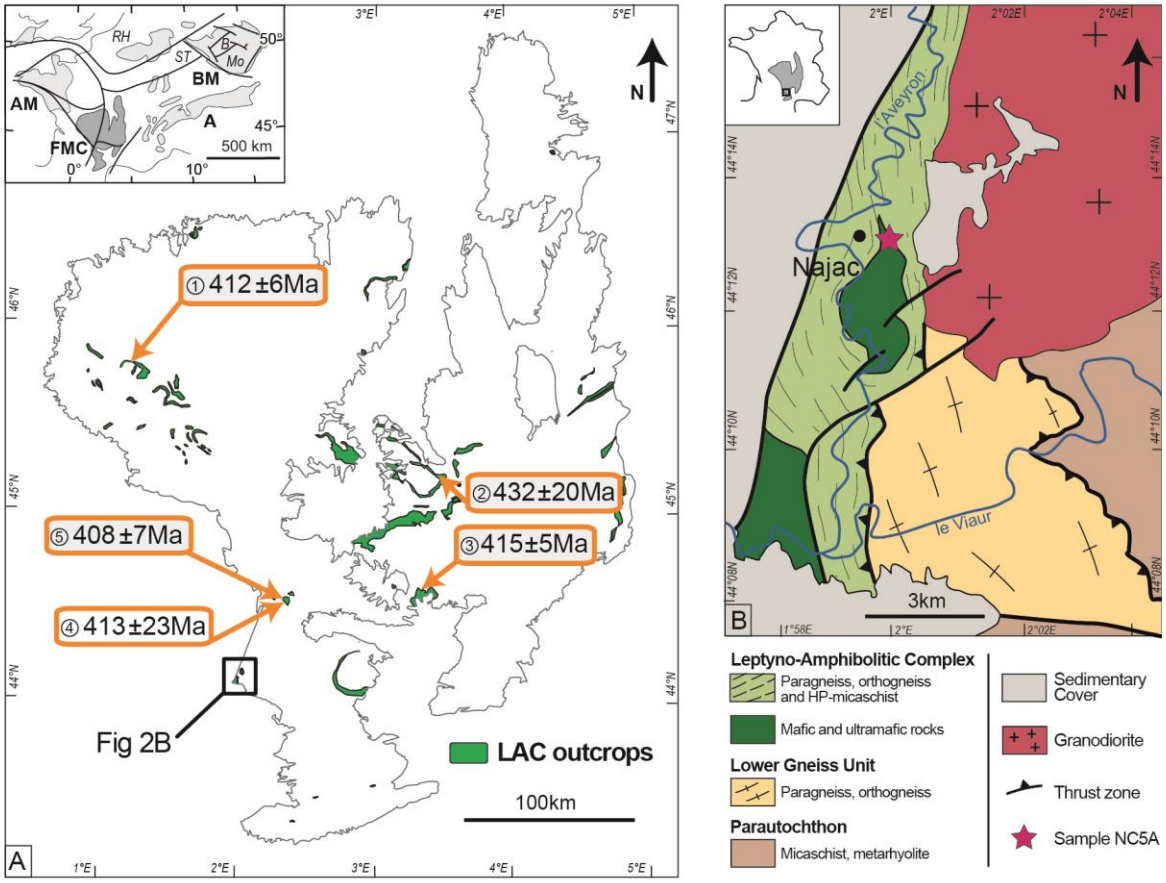

Figure II.1.1: A. Schematic map of the Leptyno-Amphibolitic Complex (LAC) outcrops in the French Massif Central, with the location of the study area and the previous geochronological studies. (1) Berger et al., 2010 (U-Pb, LA-ICP-MS dating on zircon), (2) Ducrot et al., 1983 (U-Pb, zircon isotopic dilution), (3) Pin and Lancelot, 1982 (U-Pb, zircon isotopic dilution), (4) Paquette et al., 1995 (Pb/Pb, zircon evaporation), (5) Paquette et al., 1995 (Sm-Nd - garnet & WR). Inset shows the location of the study area within the European Variscan belt A - Alps, AM - Armorican Massif, BM - Bohemian Massif, FMC – French Massif Central. B - Teplá-Barrandian, Mo - Moldanubian, ST - Saxothuringian, RH – Rhenohercynian. B: Schematic map of the Najac Massif (modified after Burg and Bodinier 1980-1981; Burg et al., 1989). Purple star indicates the sample location.

The Najac Massif (Fig. II.1.1B), located in the south-western part of the FMC, is a nappe-stack of three units (Burg et al., 1989; Delor et al., 1987) and a typical example of the Variscan architecture. (i) The Parautochthon comprises low-grade biotite-chlorite-bearing metasediments and felsic volcanic rocks ("porphyroids"). (ii) The lower allochthonous unit (Lower Gneiss Unit) is composed of felsic orthogneisses and biotite-bearing paragneisses. (iii) The upper allochthonous unit is composed of felsic orthogneisses and garnet-biotite bearing paragneisses that enclose lenses of phengite-chloritoid-garnet-staurolite-kyanite bearing micaschists, and mafic and ultramafic rocks (glaucophane-bearing eclogites, kyanite-bearing amphibolites, metagabbros, peridotites, serpentinites). The mafic rocks are of tholeiitic affinity (Bodinier, 1983). The presence of relics of high-pressure metamorphism allows to ascribe this unit to the LAC in the tectonic sense (Santallier et al., 1988).

Pressure-temperature conditions for the glaucophane-bearing eclogite have been estimated at P ~ 12 kbar and T ≤ 600°C for the pressure peak, followed by an increase in temperature up to ~ 730°C during the exhumation stage (Delor et al., 1986). Similarly, the minimum P-T conditions in the phengite-chloritoid-garnet-staurolite-kyanite bearing micaschists are estimated at P > 11 kbar and T < 600°C (Delor et al., 1987). There are, to date, no geochronological constrains available for the eclogitic rocks in the Najac massif.

3. Analytical procedure

3.1. Chemical analyses, mineral composition and P-T modeling

The sample was first cleaned from any weathered material, then crushed in a jaw crusher and in an agate mortar in order to obtain a fine powder. Major and trace elements analyses were performed by Inductively Coupled Plasma Atomic Emission Spectrometry (ICP-AES) and Inductively Coupled Plasma Mass Spectrometry (ICP-MS), respectively, at the Geochemical and Petrographical Research Center (SARM laboratory, CNRS-CRPG) in Nancy, following the procedure described in Carignan et al. (2001). FeO (vs. Fe2O3) was analyzed by wet titration.

Mineral analyses were carried out with a Cameca SX100 electron microprobe (Microsonde Ouest, IFREMER, Plouzané, France) operating in a wavelength-dispersive mode (for the complete analytical procedure, see Pitra et al., 2008). Data are plotted using the software GCDkit (Janoušek et al., 2006).

Pressure-Temperature pseudosections have been calculated in the model system Na2O–CaO–FeO–MgO–Al2O3–SiO2–H2O–TiO2–Fe2O3 (NCFMASHTO) using the software Theriak/Domino (de Capitani and Petrakakis 2010), and the internally consistent thermodynamic data set 5.5 (Holland and Powell 1998; updated Nov. 2003). Mixing models for solid solutions were taken from Diener and Powell (2012) – amphibole (amp), clinopyroxene (cpx), White et al. (2007) – garnet (g), Holland et al. (1998) – chlorite (chl), Holland & Powell (2003) – plagioclase (pl), Holland and Powell (1998) – talc (ta), epidote (ep), and White et al. (2000) – hematite (hem), ilmenite (ilm). Albite (ab), lawsonite (law), quartz (q), rutile (ru) and titanite (sphene, sph) are considered as pure end members. Doug Tinkham kindly provided the conversion of the mixing models for Theriak/Domino.

Other symbols (mole/atomic proportions) used are: XMg = Mg/(Fe2++Mg) (garnet, clinopyroxene, amphibole), XNa = Na/(Ca+Na+K) (plagioclase), XGrs = Ca/(Ca+Mn+Fe2++Mg), XPrp = Ca/(Ca+Mn+Fe2++Mg), XAlm = Fe2+/(Ca+Mn+Fe2++Mg), XSps = Mn/(Ca+Mn+Fe2++Mg) (garnet), wt% – weight per cent, mol.% – mole per cent, pfu – per formula unit. The bulk rock composition used to calculate the P-T diagrams was corrected for the presence of apatite, not considered in the calculations. K2O was removed from the bulk, since (i) no K-bearing phase was observed in the thin section, (ii) the amount of K2O in the bulk rock composition is low (0.14 wt%), and (iii) the amphibole model used does not allow to incorporate potassium. H2O was considered in excess.

3.2. U-Pb dating

A mineral separation procedure has been applied to concentrate zircon and apatite grains for U-Pb dating using the facilities available at Géosciences Rennes (University of Rennes 1). The sample was crushed and only the powder fraction with a diameter < 250 µm was kept. Heavy minerals were first concentrated by Wilfley table, then magnetic minerals were removed with an isodynamic Frantz separator. Heavy minerals were afterwards separated with heavy liquids. Zircon grains were handpicked under a binocular microscope. The selected minerals were then embedded in epoxy mounts, which were polished on a lap wheel. Zircon and apatite grains were imaged by cathodoluminescence (CL) using a Reliotron CL system equipped with a digital color camera available at Géosciences Rennes.

U-Pb geochronology of zircon and apatite grains was conducted by in-situ laser ablation inductively coupled plasma mass spectrometry (LA-ICP-MS) at Géosciences Rennes using a ESI NWR193UC Excimer laser coupled to an Agilent quadripole 7700x ICP-MS equipped with a dual pumping system to enhance sensitivity. The instrumental conditions are reported in the supplementary Table II.1.1. Further information on the zircon dating protocol can be found in Ballouard et al. (2015) and in Pochon et al. (2016) for apatite.

Ablation spot diameters of 35 µm (zrn) and 45 µm (ap) with repetition rates of 3 Hz (zrn) and 5 Hz (ap) and a fluence of 8.5 J/cm² were used. Data were corrected for U-Pb and Th-Pb fractionation and for the mass bias by standard bracketing with repeated measurements of the GJ-1 zircon standard (Jackson et al., 2004) or Madagascar apatite standard (Cochrane et al., 2014). Along with the unknowns, the zircon standard Plešovice (Sláma et al., 2008), the apatite standards McClure (Schoene and Bowring, 2006) and Durango (McDowell et al., 2005) were measured to monitor precision and accuracy of the analyses and produced ages of 337.8 ± 4.7 Ma (Plešovice, N = 6, MSWD = 0.013), 529 ± 16 (McClure, N = 4, MSWD = 1.7) and 33.3 ± 2.6 Ma (Durango, N = 5, MSWD = 2.7) during the course of the analyses.

Data reduction was carried out with the GLITTER® software package developed by the Macquarie Research Ltd. (Van Achterbergh et al., 2001) for zircon and the data reduction scheme VizualAge_UcomPbine, a set of Iolite procedures that work with Igor Pro (Chew et al., 2014) for apatite. Reproducibility and age uncertainty of reference material Plešovice were propagated by quadratic addition to the analyzed zircon grains according to Horstwood et al. (2016). Concordia ages and diagrams were generated using Isoplot 4.15 (Ludwig, 2012). All errors given in supplementary Table II.1.2 are listed at one sigma, but where data are combined for concordia age or weighted mean calculations, the final results are provided with 95% confidence limits.

3.3. Sm-Nd and Lu-Hf dating

Mineral separation was carried out at Géosciences Rennes. Rocks were crushed and from the fraction < 500 µm about 70 mg of amphibole and 200 mg of relatively pure garnet were handpicked under a binocular microscope. Garnet fraction was subsequently split into three roughly equal aliquots. Additionally, about 100 mg of representative whole rock powder was prepared and subjected together with garnet and amphibole to Lu-Hf and Sm-Nd dating

conducted at the Institute of Geological Sciences, Polish Academy of Sciences, Kraków Research Centre. Leaching, sample dissolution and columns chemistry follow procedures outlined in Anczkiewicz and Thirlwall (2003) and Anczkiewicz et al. (2004). All measurements were carried out in a static mode using a MC-ICP-MS Neptune applying the protocols similar to those outlined in Thirlwall and Anczkiewicz (2004). Procedure blanks, standards reproducibility, decay constants and reference isotopic ratios used for the calculations are given in the footnote to Table 1. Ages and $^{176}Hf/^{177}Hf$ and $^{143}Nd/^{144}Nd$ initial ratio calculations were conducted by Isoplot 4.15 (Ludwig, 2012). Errors for isotopic ratios are given at the 2 se (standard error) level. Age errors are quoted at 95% confidence level.

3.4. Trace element analyses

Trace element analyses in garnet and zircon were conducted at the Institute of Geological Sciences, Polish Academy of Sciences, Kraków Research Centre, using an Excimer laser (193 nm) RESOlution M50 by Resonetics (now Australian Scientific Instruments) equipped with S150 dual volume sample cell. Laser ablation was coupled with an ICP-MS XSeriesII by Thermo Fisher. Fluence of about 8 J/cm², and 10 Hz repetition rate were applied during the measurements. Analyses of zircon were performed in spot mode with beam size of 29 or 43 µm diameters. The results were normalized to the NIST612 primary standard using recommended values of Jochum et al. (2011). MPI DING glasses served as secondary standards for data quality control. Silicon content was used as an internal standard (fixed at 31.5%). Analyses of garnet profiles were performed in raster mode with a stage speed of 0.250 mm/min and a slit size of 40 µm. More details on analytical conditions can be found in Anczkiewicz and Anczkiewicz (2012). Data reduction was carried out using Iolite 3.0 (Paton et al., 2011) with the "trace element" data reduction scheme (Woodhead et al., 2007).

4. Pressure and temperature estimations

4.1. Sample description

Sample NC5A is a Fe-Ti eclogite outcropping in the north of a large (ultra)mafic body (Fig. II.1.1B; 44°13'7.27"N 1°59'20.19"E). The sample is a dark medium-grained eclogite dominated by garnet, clinopyroxene and amphibole, with minor titanite, rutile, ilmenite, epidote, albite, apatite, magnetite, sulfides (pyrite, chalcopyrite) and zircon.

Subhedral garnet (up to 3 mm) is fractured and contains inclusions of omphacite (cpx1), amphibole, rutile, quartz, apatite and zircon (Fig. II.1.2). It displays a slight rimward decrease in spessartine and grossular (XAlm = 0.54-0.63, XGrs = 0.30□0.24, XPrp = 0.08-0.15, XSps = 0.04□0.01, XMg = 0.15-0.21; Fig. 2D, E, F; Fig. 3A, supplementary table 3).

Clinopyroxene occurs in two textural positions. Anhedral unzoned omphacite (up to 0.6 mm, XJd = 0.28-0.34; XAe = 0.14-0.20; XMg = 0.63-0.73, "cpx1" in Fig. II.1.2B, 3C supplementary table 3) is surrounded by fine-grained symplectites of plagioclase ± amphibole ± diopside (XJd = 0.07-0.33; XAe = 0-0.21, "cpx2" in Fig. II.1.2A, B, C, E, 3C; supplementary table II.1.3)

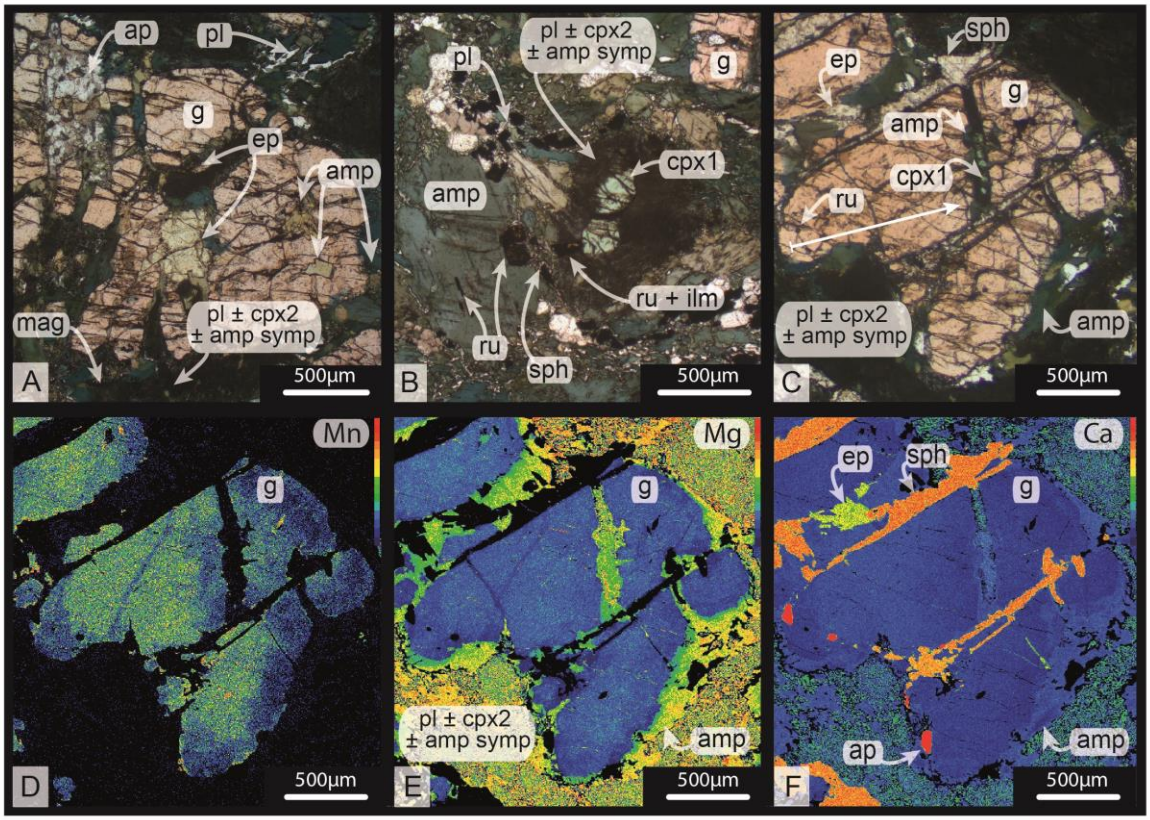

Figure II.1.2: *A. B. D Photomicrographs of the NC5A sample. X-ray maps for Mn (D), Mg (E) and Ca (F) of the garnet in C. Note the rimward decrease of Mn and Ca.*

Amphibole can be found in four textural positions. (1) Small subhedral crystals are locally included in garnet (0.02-0.2 mm, Fig. II.1.2A). (2) Large euhedral to subhedral crystals (up to 1 mm) commonly contain inclusions of tiny elongated rutile and magnetite (Fig. II.1.2B). Small anhedral crystals are found (3) in the matrix or surrounding the large subhedral crystals of amphibole 2 (up to 0.3 mm), and (4) in fine-grained symplectites surrounding omphacite

(Fig. II.1.2A, B, C, E) (Fig. II.1.3D; supplementary table II.1.3). The chemical compositions are very heterogeneous although individual crystals are unzoned. Amphiboles are calcic to sodic-calcic (CaB = 1.13-1.97, (Na+K)A = 0.48-0.86, Ti = 0.01-0.10 pfu) and span a compositional space from ferropargasite to magnesiohornblende (Si = 5.55-7.32 pfu, XMg = 0.23-0.65, Fig. II.1.3D;.supplementary table II.1.3). No correlation could be established between the chemical composition and the textural position.

Rutile occurs as brownish rounded grains (up to 0.3 mm) in the matrix, and as inclusions (7-20 µm) in garnet and amphibole 1 (Fig. II.1.2B, C). Ilmenite (1-10 mol.% haematite, 1-4 mol.% pyrophanite) commonly partly replaces rutile.

Titanite forms (i) elongated grains (up to ~1 mm) in garnet fractures (Fig. 2C) (ii) thin rims surrounding rutile ± ilmenite aggregates (Fig. II.1.2B) and (iii) anhedral crystals (~0.3-0.8 mm) in the matrix (Fig. II.1.2B). Large anhedral epidote (□0.4-0.5 mm; XFe3+ = 0.71-0.75) is locally found in garnet fractures or as 1 mm large patches in the matrix (Fig. II.1.2A, C).

Plagioclase (XNa = 0.95-0.99) forms rounded fine elongated grains (up to 400 µm x 25 µm) intergrown with amphibole (Fig. II.1.2A), surrounding titanite or ilmenite grains in the matrix (Fig. 2B), or as anhedral crystals in symplectites (Fig. II.1.2A, B, C).

Apatite forms (i) small inclusions in garnet (~40 µm, Fig. II.1.2F), (ii) large aggregates of ~1 mm, and (iii) anhedral grains (up to 0.2 mm) locally associated with titanite in garnet fractures. Rare quartz crystals are found in the matrix or as inclusions in garnet.

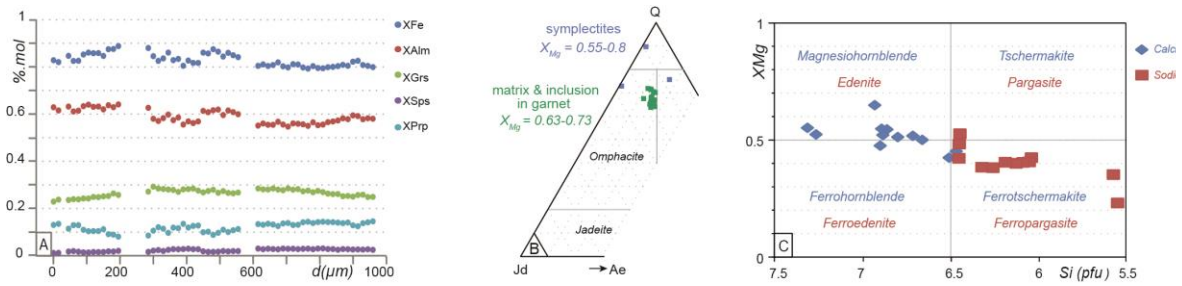

Figure II.1.3: *(A) Chemical profile across garnet from Fig. 2C, showing a homogeneous composition with local variations and a slight rimward decrease of grossular. Compositional diagram of clinopyroxene (B) and amphibole (C). Amphibole nomenclature follows the classification of Leake et al. (1997).*

We interpret the large crystals of garnet and omphacite as belonging to the main metamorphic assemblage, together with quartz and rutile that can be found in garnet. At the first order, they are indicative of the eclogite facies. Amphibole forms inclusions in garnet (amp 1) and large crystals (amp 2) that include rutile needles and are locally surrounded or partly replaced by small crystals of amphibole 3. Based on these observations, amphibole 1 and 2 are also interpreted as part this eclogite-facies assemblage. Subsequent decompression is suggested by the development of fine-grained symplectites involving plagioclase, amphibole and diopside at the expense of garnet and omphacite and the partial replacement of rutile by ilmenite. The observed scatter in the composition of amphibole can be attributed to partial reequilibration probably also associated with this metamorphic stage. Coarse crystals of apatite and titanite form late in garnet fractures. The position of epidote is unclear: grains associated with garnet fractures are probably late and accompany titanite and apatite while large crystals in the matrix could be part of or precede the eclogite-facies assemblage.

4.2. P-T modeling

The eclogite-facies assemblage comprises garnet, omphacite, amphibole, quartz and rutile. In the pseudosection (Fig. II.1.4), the corresponding stability field is located at T >~550°C and P ~13-23 kbar, and delimited by the appearance/disappearance of quartz and epidote at low temperature, amphibole at high pressure and temperature, talc at high pressure and ilmenite at low pressure (Fig. II.1.4A). Garnet appears at relatively high pressure and marks the beginning of the eclogite facies on the prograde path (garnet appearance/disappearance highlighted in Fig. II.1.4C). The amount of amphibole decreases with increasing pressure (Fig. II.1.4C). Compositional isopleths for garnet and clinopyroxene are used to define tighter constraints on the equilibration conditions of the assemblage. Isopleths of the proportion of grossular in garnet (X_{Grs}, Fig. II.1.4B) are temperature-dependent, which allows to bracket the temperatures to 560-660°C, but does not help to constrain the pressure. Isopleths for pyrope or the X_{Mg} ratio (not shown) follow a similar trend and the modelled values are compatible with the observed ones, but do not bring additional constraints. X_{Mg} isopleths for clinopyroxene are pressure-dependent (Fig. II.1.4C) and the observed X_{Mg} range (0.63-0.73) allows to constrain the equilibration conditions of the eclogite-facies assemblage between 15-20 kbar and 560-630°C.

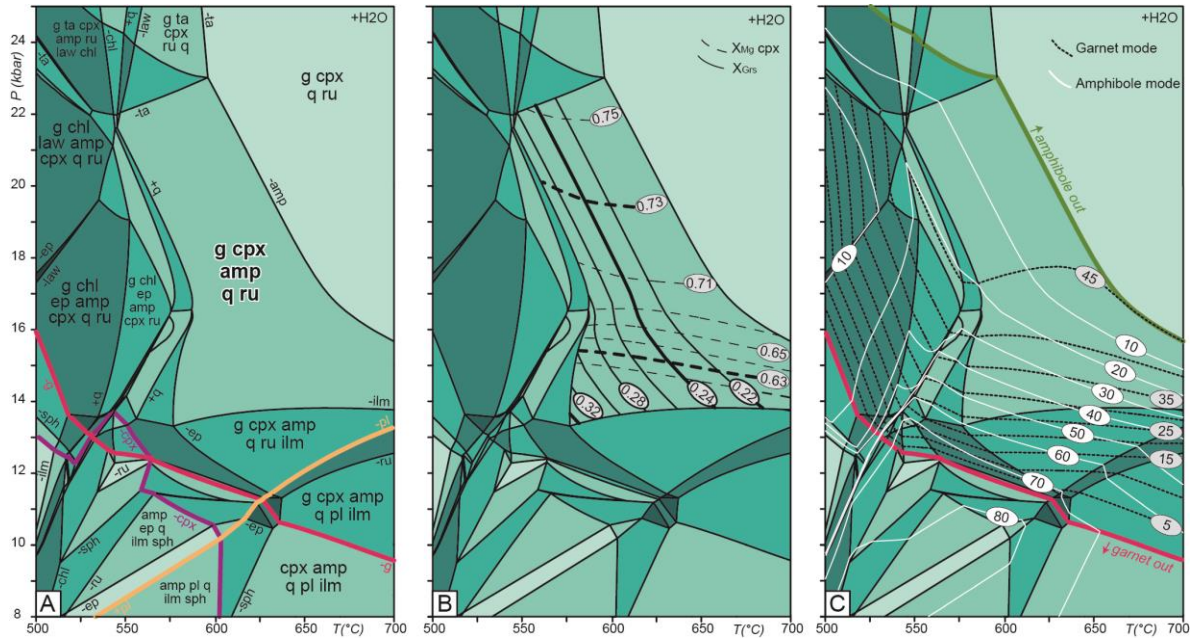

Figure II.1.4: *P-T pseudosection for the sample NC5A. The rock composition, given as mol.% oxide, is SiO2(48.28)–TiO2(3.92)–Al2O3(8.36)–Fe2O3(1.67)–FeO(15.18)–MgO(9.09)–CaO(10.17)–Na2O(3.23). Fields are colored with respect to their variance, darker colours indicate lower-variance assemblages. A. P-T diagram calculated with H2O saturation and 18.1% Fe3+ (of total iron), corresponding to the analysed amount. The peak high-pressure assemblage is highlighted. B. Modeled compositional isopleths for garnet (XGrs) and clinopyroxene (XMg), with bold lines marking the observed range. C. Mode isopleths for garnet and amphibole showing that garnet only grows along the prograde P-T path. Garnet and amphibole disappearance are highlighted.*

Overprinting the eclogite-facies assemblage leads to the development of plagioclase-amphibole-diopside-bearing symplectites, as well as ilmenite, titanite and epidote. In the pseudosection (Fig. II.1.4A), these minerals are stable together in a small field at ~11 kbar, 620 °C, suggesting decompression without significant cooling. However, these indications should be taken qualitatively, since the development of the symplectites, ilmenite replacing rutile, and titanite crystallizing in garnet fractures are not necessarily contemporaneous. Furthermore, they are governed by local equilibria, for which the pseudosection, calculated for the bulk-rock composition, is not necessarily strictly appropriate.

5. Trace elements mineral chemistry

5.1. Garnet

Trace element profiles were performed in 7 garnet crystals from one thin section. Because of the selected beam size, Hf could not be measured. Instead, we measured Zr whose abundance in garnet is much larger and its distribution mimics that of Hf. Trace element

abundances suggest that five out of the seven measured garnet profiles correspond to sections through the edge of the crystals and are not discussed further. The remaining two profiles are similar and are presented below. The terminology “core”, “mantle” and “rim” is based on the Lu zoning and is defined in Fig. II.1.5.

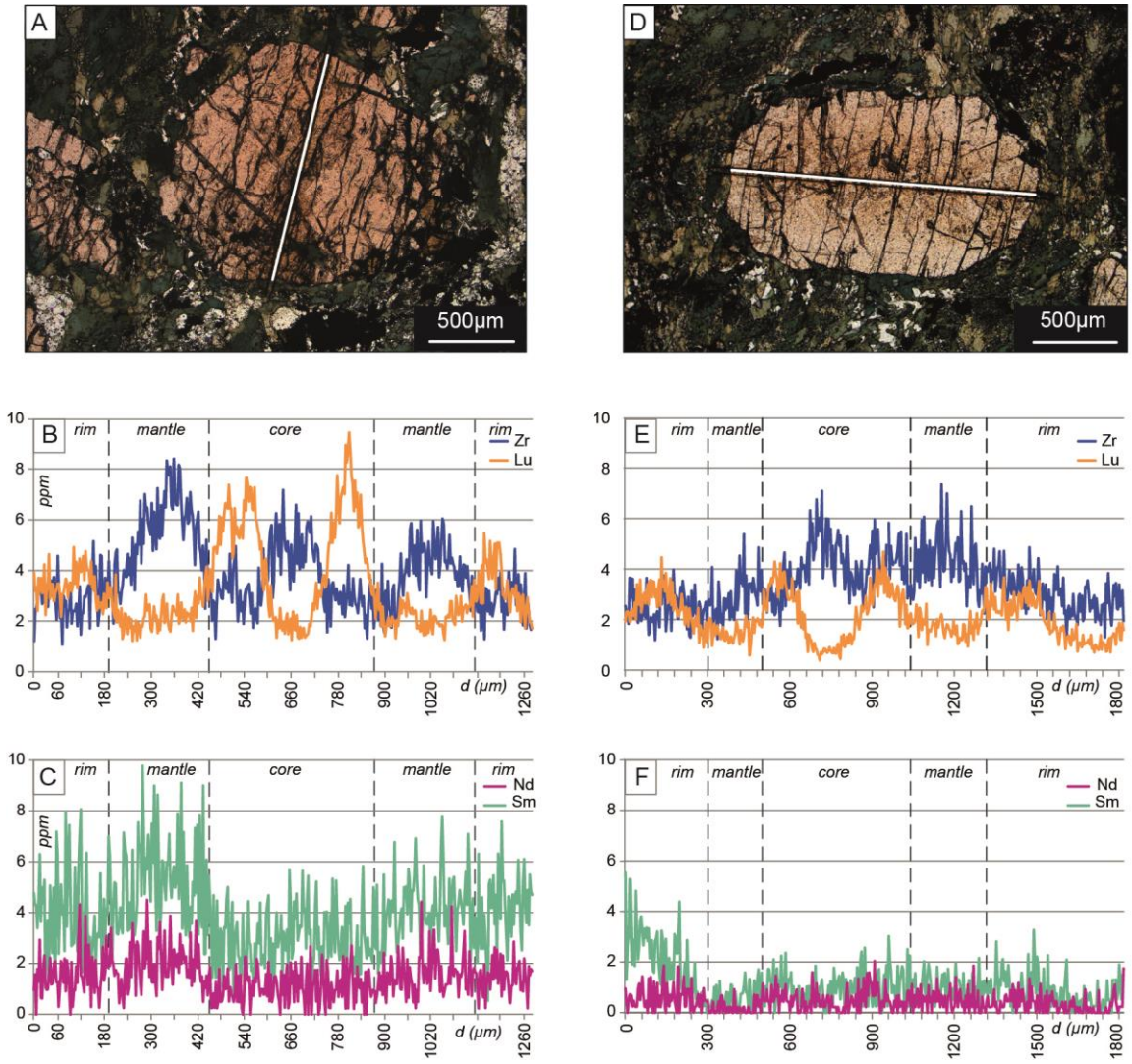

Figure II.1.5: *A, D. Photomicrograph of analyzed garnet, exhibiting the LA-ICP-MS mark of the REE profile analysis. B, E. Lu and Zr contents (ppm) along the profile marked in A, D. C, F. Sm and Nd (ppm) profile.*

The garnet crystals, analyzed directly in thin section, (Fig. II.1.5A, D). The crystals display an “oscillatory-type zoning” (Fig. II.1.5B, C, E, F). The center is characterized by a very narrow central domain with the lowest content in Lu (~2 ppm and <1 ppm), surrounded by two relatively high Lu peaks (up to ca. 8 ppm; Fig. II.1.5B, E). This core is surrounded by

a mantle area, which contains about 1-2 ppm Lu. The inner part of the rim displays an increase in Lu up to about 5 ppm before a final decrease to about 1-2 ppm in the outer rim. The same zonation trend is seen for Y, Yb, Er, Ho (supplementary table II.1.4). Concentration in Zr shows an opposite behavior (Fig. II.1.5B, E): the narrow central region shows high Zr content of up to 7 ppm that decreases in the external part of the core. The mantle displays a peak of up to ca. 8 ppm, followed by a decrease in the rims to 2-3 ppm. The Nd and Sm contents seem to gently increase from core to rim with a notable "bulge" in the mantle of one of the crystals (Fig. II.1.5C). In the other garnet grain, the Sm content is low and constant in the core and mantle zones (0.5-2 ppm), and strongly increases in one of the outer rims up to 5 ppm (Fig. II.1.5F). REE values normalized to chondrite range Sm_N = 1-41, Nd^N = 0.8-4.8, Yb_N = 22-251, Lu_N = 21-240 (Fig. II.1.7) and display a flat HREE pattern. Due to the oscillatory zonation, no classic core-to-rim depletion is seen.

5.2. Zircon

Zircon grains are elongated, subhedral to euhedral, colorless and translucentwith sizes ranging from100 to 340 μm. Cathodoluminescence (CL) imaging revealed various textures. Dark and bright CL domains characterize grains with patchy sector zoning, whereas other crystals are homogeneous and bright in CL. The analyzed zones are hereafter referred to as CL-dark and CL-bright (Fig. II.1.6). The U-Pb and trace element measurements were performed in two different spots during two distinct sessions, but these spots were carefully selected in order to analyze the same CL domain.When a positive Eu* anomaly was found, we checked that this anomalywas not due to the presence of small inclusions. Finally, since the U contents are correlated with the CL domains (dark domains are richer in U than bright domains; see Section 6.2), we verified that the uranium contents were comparable between the two analyzed spots (U-Pb and trace element analyses) in a given zone in order to check that different domains were not analyzed. All the presented REE patterns were then carefully investigated, even though the presence of micro-inclusions cannot be completely ruled out. Two different populations of spectra can be highlighted: (A) HREE-depleted spectra without Eu anomaly and (B) HREE-enriched spectra displaying various Eu anomalies (negative, positive or absence of anomaly).

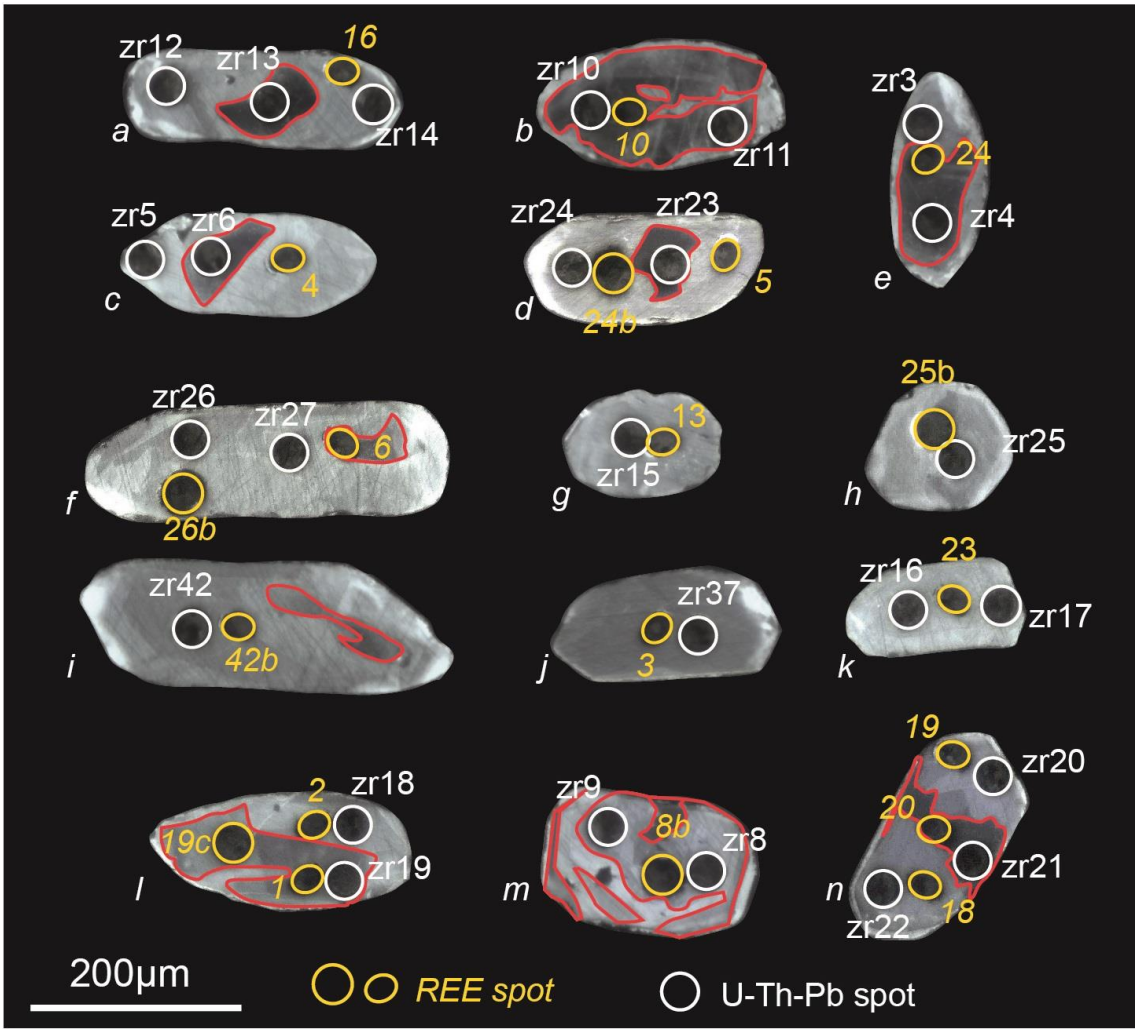

Figure II.1.6: *Selected cathodoluminescence images of zircon crystals, displaying the various textures observed. White (35 µm) and orange (40 and 26 µm) circles show the location of the U-Pb and REE analyses, respectively, and their corresponding analysis number.*

Population A (9 spectra, Fig. II.1.7A) displays no Eu anomaly (Eu/Eu* = 0.8-1., av. 1.02), a high positive anomaly in Ce (Ce/Ce* = 10.5-66.6) and a weak enrichment in HREE (Lu_N/Sm_N = 7-79, av. 33.5; Yb_N/Gd_N = 1-11, av. 6.5). All these spectra were obtained in CL-bright zircon zones (see section 6.2). They display the same general trend as the garnet REE patterns (Fig. II.1.7).

Population B (20 spectra, Fig. II.1.7B) shows a strong variable enrichment in HREE (Lu_N/Sm_N = 106-3134, av. 504; Yb_N/Gd_N = 23-437, av. 79). The Eu anomaly is highly variable showing either negative anomaly (Eu/Eu* = 0.3-0.7, 12 spectra), absence of anomaly (Eu/Eu* = 0.9-1.3, 5 spectra), or positive anomaly (Eu/Eu* = 1.6-2.6, 3 spectra). The positive Ce anomaly is variable (Ce/Ce* = 2.9-47.6). Fifteen of these spectra were obtained in CL-

dark zircon domains, while the five remaining analyses were performed in CL-bright zircon domains (see section 6.2 and Fig. II.1.6). These enriched patterns are significantly different from the ones observed in garnet (Fig. II.1.7).

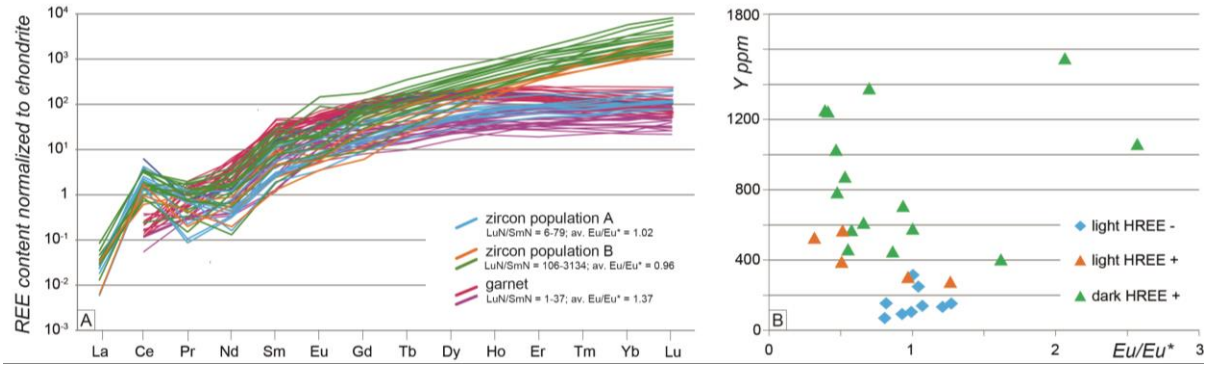

Figure II.1.7: *REE content normalized to chondrite values for garnet from Fig.5 (A. purple, D, violet) and dated zircons (blue – HREE depleted pattern; green –HREE enriched), with highlighted Eu/Eu* and LuN/SmN values (B) Y (ppm) vs. Eu/Eu* anomaly diagram, with the CL textures highlithed; blue – CL bright, HREE depleted; orange – CL bright, HREE enriched; green – CL dark, HREE enriched. See text for details.*

Analyses obtained in the zircon CL-bright zones systemically show low Y content (Y = 69-315 ppm) and no Eu anomaly (Eu/Eu* = 0.8-1.3) (Fig. II.1.7B). On the contrary, all the analyses performed in the CL-dark zones show higher Y contents (~402-1377 ppm) and various – but mostly negative – Eu anomalies (Eu/Eu* = 0.4-2.6). Finally, analyses performed in CL-bright zones and displaying a HREE enrichment show intermediate Y contents (Y = 276-567 ppm). Their corresponding Eu anomaly is variable (Eu/Eu* = 0.3-1.3).

6. Geochronology

6.1. Garnet

Garnet is a ubiquitous mineral of eclogite-facies rocks. The complementary Lu-Hf and Sm-Nd isotopic systems, combined with the analysis of trace element distribution can bring quantitative constraints on the timing and duration of metamorphism.

6.1.1. Lu-Hf isotopes

The Lu and Hf contents in the garnet fractions are very similar (Table II.1.1). Lu content in the three aliquots is equal within error (3.20 ppm), which indicates that our aliquots

represent the same averaged garnet fraction. Abundance of Hf is very low (0.08-0.10 ppm) and typical of metamorphic garnets, which suggests that our analyses were not significantly influenced by Hf rich inclusions. Thus, all three garnet fractions yielded high $^{176}Lu/^{177}Hf$ ratios (4.4 to 5.6), which together with amphibole and whole rock analyses define a precise age of 383.2 ± 1.0 Ma, MSWD = 0.6 (Fig. II.1.8A). Notably, the obtained analytical precision on age error is high and may not be representative of the duration of garnet crystal growth (if garnet crystallization was slow). We discuss this issue in the context of trace elements analyses in the next sections.

Table II.1.1: Summary of the Lu–Hf and Sm–Nd dating results

Fraction	Weight *mg*	Sm *ppm*	Nd *ppm*	$^{147}Sm/^{144}Nd$	$^{143}Nd/^{144}Nd$	Age *Ma*	Lu *ppm*	Hf *ppm*	$^{176}Lu/^{177}Hf$	$^{176}Hf/^{177}Hf$	Age *Ma*
Grt 1	69.78	2.724	1.45	1.1364	0.515367±9	376.7 ± 3.3	3.204	0.087	5.253	0.320579±22	382.8 ± 1.0
Grt 2	66.07	2.711	1.201	1.3655	0.515945±9		3.205	0.081	5.635	0.323249±27	
Grt 3	62.24	2.674	1.121	1.4434	0.516133±13		3.199	0.104	4.395	0.314443±23	
Amph	72.21	3.094	8.343	0.2242	0.513117±6		0.11	0.884	0.018	0.282997±5	
WR	100.4	9.988	31.85	0.1896	0.513047±7		1.062	0.664	0.226	0.284485±8	

All errors are 2 se (standard errors) and relate to the last significant digits. $^{176}Lu/^{177}Hf$ errors are 0.5% and $^{147}Sm/^{144}Nd$ errors are 0.3%. Reproducibility of JMC475 yielded 0.282166±4 (N = 4) over the period of analyses, while JNd-1 gave 0.512098 ± 5 (N = 7). Hf and Nd mass bias were corrected to $^{179}Hf/^{177}Hf = 0.7325$ and $^{146}Nd/^{144}Nd = 0.7219$, respectively. Decay constants applied to age calculations: $\lambda^{176}Lu = 1.865x10^{-11}\ yr^{-1}$ (Scherer et al., 2001) and $\lambda^{147}Sm = 6.54x10^{-12}\ yr^{-1}$ (Lugmair and Marti, 1978). Procedure blanks for all elements were below 30 pg.

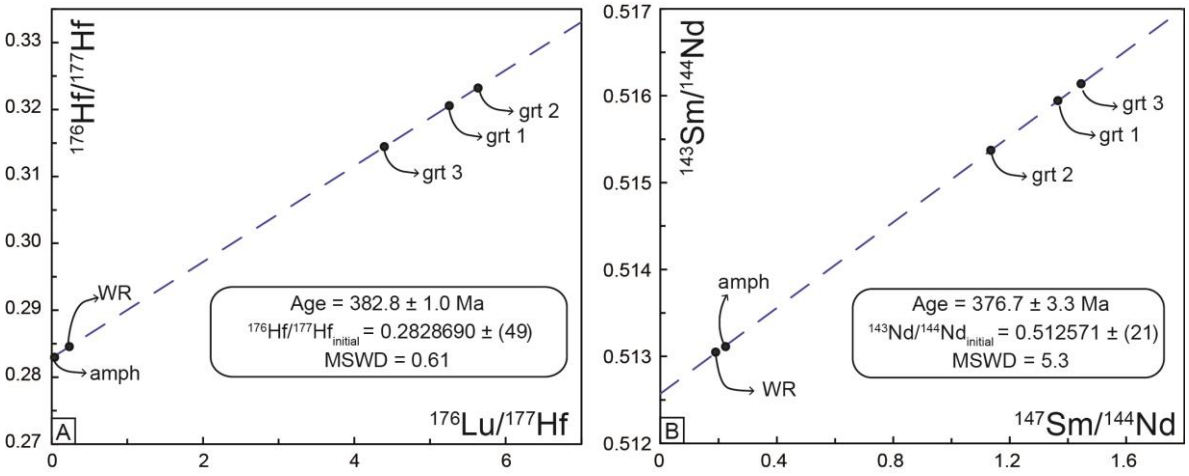

Figure II.1.8: *A. Lu–Hf (A) and Sm–Nd (B) isochron diagrams. WR – whole rock, grt 1-3 – garnet fractions, amph - amphibole. Errors of analyses were too small to be visible, consequently data points were increased.*

6.1.2. Sm-Nd isotopes

The three analyzed garnet fractions also show very consistent abundances in Sm (from 2.67 to 2.72 ppm) in all the isotope dilution analyses. Slightly larger "spread" is found in the Nd content, which varies from 1.12 to 1.45 ppm. Again, such values are very typical of pure metamorphic garnet, which is reflected in the fairly high $^{147}Sm/^{144}Nd$ ratios varying from 1.1 to 1.4 (Table II.1.1 and Fig. II.1.8B). All three garnet fractions along with amphibole and whole rock define an isochron age of 376.7 ± 3.3 Ma (MSWD = 5.3) with an initial 143Nd/144Nd = 0.512571 ± 21.

6.2. Zircon

Thirty-six analyses were performed out of 25 zircon grains (Fig. II.1.6, supplementary table II.1.2). The Th/U ratios vary from 0.03 to 1, while the U contents vary from 4.8 to 429.4 ppm. The maximum U contents are systematically found in the CL-dark zones (U = 15.3-429.4 ppm, av. 121.2 ppm), while CL-bright zones display low U contents (U = 3-63 ppm, av. 18.1 ppm). The data plot in a concordant to slightly discordant position (Fig. II.1.9A). Thirty-three concordant analyses (solid line ellipses) allow to calculate a concordia date (as of Ludwig, 1998) of 385.5 ± 2.3 Ma (MSWD = 0.43, Fig. II.1.9A). Two analyses (dashed line) are slightly discordant but provide $^{238}U/^{206}Pb$ apparent ages equivalent to the concordant ones (see supplementary table II.1.2). Their position is attributed to a slight amount of common Pb. The last analysis (zr-20, grey ellipse) is concordant and yields a $^{238}U/^{206}Pb$ apparent age of 424 ± 6 Ma (Fig. II.1.9.A and supplementary table II.1.2).

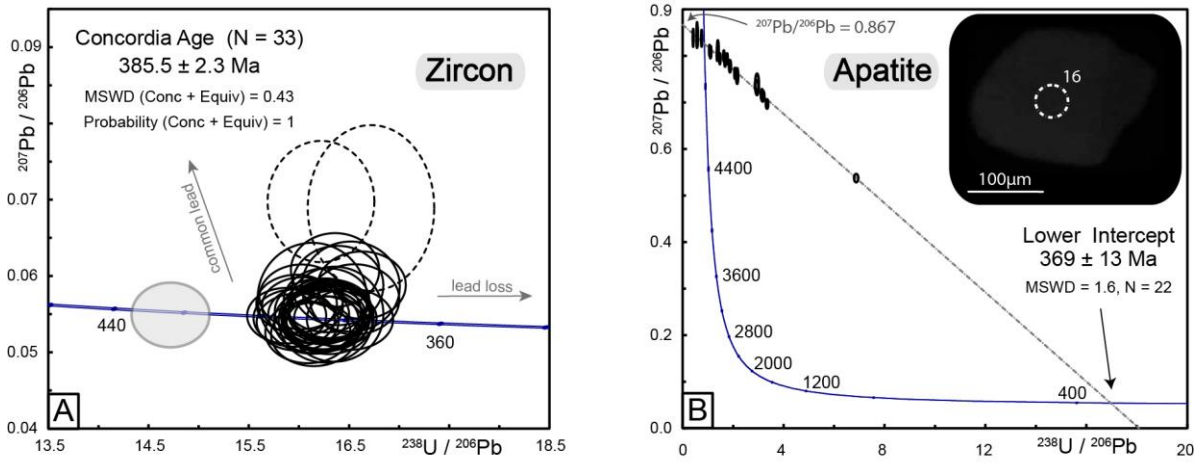

Figure 9: *A. Tera–Wasserburg ($^{207}Pb/^{206}Pb$ vs. $^{238}U/^{206}Pb$) diagram displaying all dates obtained on zircon. B. Tera–Wasserburg ($^{207}Pb/^{206}Pb$ vs. $^{238}U/^{206}Pb$) diagram displaying all analyses obtained on apatite and the $^{207}Pb/^{206}Pb$ initial ratio. An example of apatite grain (CL image) is shown.*

6.3. Apatite

Twenty-two U-Pb analyses were performed out of 22 grains (supplementary table II.1.2). These apatite grains are very homogeneous in cathodoluminescence (Fig. II.1.9B) and characterized by low U (0.1-7 ppm) and Pb (0.9-4.4 ppm) contents. In a Tera-Wasserburg diagram (Fig. II.1.9B), the data plot in a very discordant position indicative of a high proportion of common Pb. They define a lower intercept date of 369 ± 13 Ma (MSWD = 1.6) with a $^{207}Pb/^{206}Pb$ initial value of 0.867 which is in a good agreement with the Stacey and Kramers (1975) terrestrial Pb evolution model. The weighted average ^{207}Pb-corrected date (calculated at 370 Ma using Stacey and Kramers (1975) terrestrial Pb evolution model) is equivalent within error at 360 ± 11 Ma (MSWD = 2.5; not shown).

7. Discussion

7.1. Validity of the pressure-temperature estimates

The H_2O content in the P-T calculation was considered in excess, given the dehydration character of most metamorphic reactions during prograde metamorphism, which quickly leads to H_2O saturation. The general fit between the model and the observed mineral assemblages and mineral compositions supports a posteriori the validity of this choice.

Garnet mostly lacks major element zoning, with the exception of the slight rimward decrease of Mn and Ca. This could suggest that thermal diffusion may have occurred and influenced the estimated pressures and temperatures. Isopleths of garnet mode (Fig. II.1.4C) indicate that garnet grew only with increasing pressure and temperature, during prograde metamorphism. The preserved rimward decrease of Mn and Ca, although limited, is compatible with such an evolution, and argues against a total diffusional resetting. Despite numerous fractures, garnet lack signs of significant resorption (widespread symplectitic coronae or Mn increase in the outermost rim, typical of retrograde diffusional zoning). Moreover, garnet grains display strong zonation in Lu that argues against thermal resetting.The post-eclogitic mineral assemblage and its very fine-grained character suggest P-T conditions lower than the metamorphic peak and a rapid P-T evolution. Such conditions are not favorable for diffusional reequilibration. Consequently, if diffusional reequilibration occurred, this would have been close to the metamorphic peak, strengthening the conditions for a robust estimation of the P-T conditions.

7.2. From date to age

7.2.1. Garnet

7.2.1.1. Lu-Hf dating

The interpretation of Lu-Hf dates strongly depends on the parent element distribution in garnet. The core of the analyzed garnet is enriched in Lu (Fig. II.1.5) which is a classical characteristic for this highly compatible element (e.g. Anczkiewicz *et al*., 2007; Kohn, 2009). As detailed in section 4.2, garnet nucleation also marks the initial stages of the eclogite-facies metamorphism, during the prograde P-T path. Consequently in can be proposed that the date of 382.8 ± 1.0 Ma closely approximates the age of the early growth of garnet and the beginning of eclogite facies metamorphism (Fig. II.1.10). However, cores and rims could not be distinguished during garnet picking. Considering the rim contribution, the age of 382.8 ± 1.0 Ma is then biased toward the age of the core. The ± 1.0 Ma uncertainty, reflecting analytical errors only, then testifies to an efficient analytical procedure, but might be underestimated in terms of its geological significance.

7.2.1.2. Sm-Nd dating

Although the error on the calculated age is less than 1% (2 sigma), the elevated MSWD value suggests some scatter among the analyzed fractions. As a matter of fact, a close inspection of the data reveals that excess scatter seems to be related to the initial ratio correction. However, differences in calculations may suggest that equilibrium was not achieved between whole rock and amphibole. This is supported by the presence of several textural varieties and a large compositional range of amphibole in the rock (see also petrographic description). Even though primary amphibole was preferentially selected during the mineral separation, it is possible that some retrograde amphibole was present in the mineral separate, which affected the analyses and could result in the data scattering observed along the isochron.

Rare small apatite crystals are included in garnet (Fig. II.1.2F), even though the majority of apatite is inferred to crystallize on the retrograde P-T path, based on petrographic observations. Epidote occurs both in garnet fractures and in the matrix, and might have crystallized both early and late during the metamorphic evolution. Nevertheless, the Sm/Nd ratios based on the concentrations obtained from dilution analysis and LA-ICP-MS profiles are similar and consequently, inclusions did not contribute to the Sm-Nd budget.

By contrast to Lu, and due to its highly refractory character, Sm shows a slight enrichment toward the rim, a feature typically observed in garnet (e.g. Anczkiewicz *et al.*, 2012; Kohn, 2009; Smit *et al.*, 2013). Rims and mantles are volumetrically more significant than garnet cores, hence Sm-Nd dates tend to be biased towards the time of rim formation.

The temperature for the peak of the eclogite metamorphism is estimated at 560-630°C, which is too low to open the Sm-Nd chronometer by diffusion (e.g. Tirone *et al.*, 2005). Furthermore, there is no evidence for further heating during the decompression. Consequently, we can admit that there was no re-opening of the Sm-Nd system.

We then infer that the date of 376.7 ± 3.3 Ma, calculated including whole rock and amphibole fractions, closely approximates the crystallization of the garnet rims, which corresponds to the peak temperature (and pressure) conditions (Fig. II.1.10).

7.2.2. Zircon

The growth of metamorphic zircon may occur in a large range of pressures and temperatures and along different segments of the P-T path: during the prograde path (e.g. Bingen et al., 2001; Fraser et al., 1997; Harley et al., 2007), at the HP peak (e.g. Rubatto, 2002; Rubatto, 2017 and references therein), or during decompression and the retrograde path (e.g. Harley et al., 2007; Hermann et al., 2001; Kohn et al., 2015; Kohn, 2016; Whitehouse and Platt, 2003). According to Rubatto (2002) and Hoskin and Schaltegger (2003), the absence of an Eu anomaly and a flat HREE pattern are considered to reflect zircon growth in a plagioclase-free garnet-bearing assemblage, typical for the eclogite facies. By contrast, REE spectra from igneous zircon usually exhibit a negative Eu anomaly and a strong enrichment in HREE.

We obtained one coherent concordia date at 385.5 ± 2.3 Ma (Fig. II.1.9A), although we analyzed different zircon domains (CL-dark and CL-bright zones), with variable REE signatures (Fig. II.1.6, 7). In the first instance, the similarity between the U-Pb zircon date and the Lu-Hf garnet age (382.8 ± 1.0 Ma), along with the zircon HREE depleted patterns are robust arguments to interpret this date as the age of the eclogitic stage. Despite this result, the diversity of trace element signatures in the zircon grains testifies to the complexity of natural samples and call for a detailed investigation.

The crystallization of zircon prior to the garnet growth should result in a HREE enrichment. On the contrary, synchronous growth or growth after garnet crystallization should result in depleted and flat HREE patterns (e.g. Rubatto, 2002). As illustrated in Fig. II.1.7A, both tendencies are recorded in the zircon grains from sample NC5A, although they yielded comparable apparent ages. No correlation can therefore be established between apparent ages and zircon chemistry. This could imply (i) local equilibria, the REE signature recorded depending on the local chemical composition or (ii) multiple stages of zircon growth prior to and during the nucleation and growth of garnet. Because of the analytical uncertainties intrinsic to LA-Q-ICP-MS analyses (a few Myr), the distinction between the different ages of zircon growth might not be possible to achieve.

Zirconium zoning observed in the garnet profile (Fig. II.1.5B) could be attributed to equilibrium with a mineral growing or destabilized in a close vicinity (Yang and Rivers, 2002). Since the Zr budget in a rock is mainly controlled by zircon (Rubatto and Hermann,

2003), the outwards Zr decrease observed in the garnet core (Fig. II.1.5B) could be the consequence of synchronous zircon crystallization.

In the Y vs Eu/Eu* diagram (Fig. II.1.7B), the highest Y contents are found in CL-dark domains enriched in HREE, while the lowest Y contents correspond to CL-bright domains, depleted in HREE. Intermediate Y contents are found in CL-bright domain enriched in HREE. In the presence of garnet, HREE are more fractionated into zircon than Y and MREE (see partition coefficient from Rubatto and Hermann, 2007). The observed variation of the Y contents in zircon could therefore reflect progressive crystallization of zircon just before and alongside with garnet, along the prograde P-T path, in a progressively depleted HREE reservoir.

Finally, the rare positive Eu anomalies could be the result of local redox conditions, Eu3+ being easily substituted in the zircon lattice contrary to Eu2+ (e.g. Whitehouse 2003). Moreover, since zircon does not fractionate Eu, any Eu anomaly, either positive or negative, is directly inherited from the Eu available in the environment during crystallization.

To ascertain the processes involved in the peculiar trace elements pattern highlighted in this study, more analyses are needed. Especially, in context (i.e. in thin section) in situ trace element analyses in zircon and surrounding minerals could potentially help to identify if local equilibrium processes did occur.

7.2.3. Apatite

Apatite grains were mostly found in garnet fractures and are inferred to have formed late in the metamorphic history. The relatively imprecise date of 369 ± 13 Ma is, within error, comparable with both the Lu-Hf and Sm-Nd ages obtained on garnet. Closure temperature for Pb diffusion in apatite is estimated between ca. 375 and 550 °C (Chamberlain and Bowring, 2001; Cherniak et al., 1991; Cochrane et al., 2014; Harrison et al., 2002; Schoene and Bowring, 2007). The maximum temperature reached by the rock was estimated at 630°C, i.e. slightly above the maximum closure temperature of apatite. Therefore, we consider that this date of 369 ± 13 Ma marks the early retrograde stage of the metamorphic evolution (Fig. II.1.10).

7.2.4. Summary: from age to stage

According to the petrological and geochronological results, together with the trace elements analyses in both garnet and zircon, we propose that the garnet Lu-Hf age and the zircon U-Pb age (382.8 ± 1.0 Ma and 385.5 ± 2.3 Ma, respectively) record the beginning of the eclogite facies at ~ 383 Ma, whereas the Sm-Nd garnet age at 376.7 ± 3.3 Ma closely approaches the end of garnet crystallization, i.e. approximates the high-pressure metamorphic peak (Fig. II.1.10). It implies that garnet crystallized during 6.1 ± 4.3 Myr and that the terranes experienced eclogitic conditions during at least the same period on the prograde path. The retrogression event is constrained by U-Pb apatite dating at 369 ± 13 Ma, which does not allow to estimate any exhumation rate.

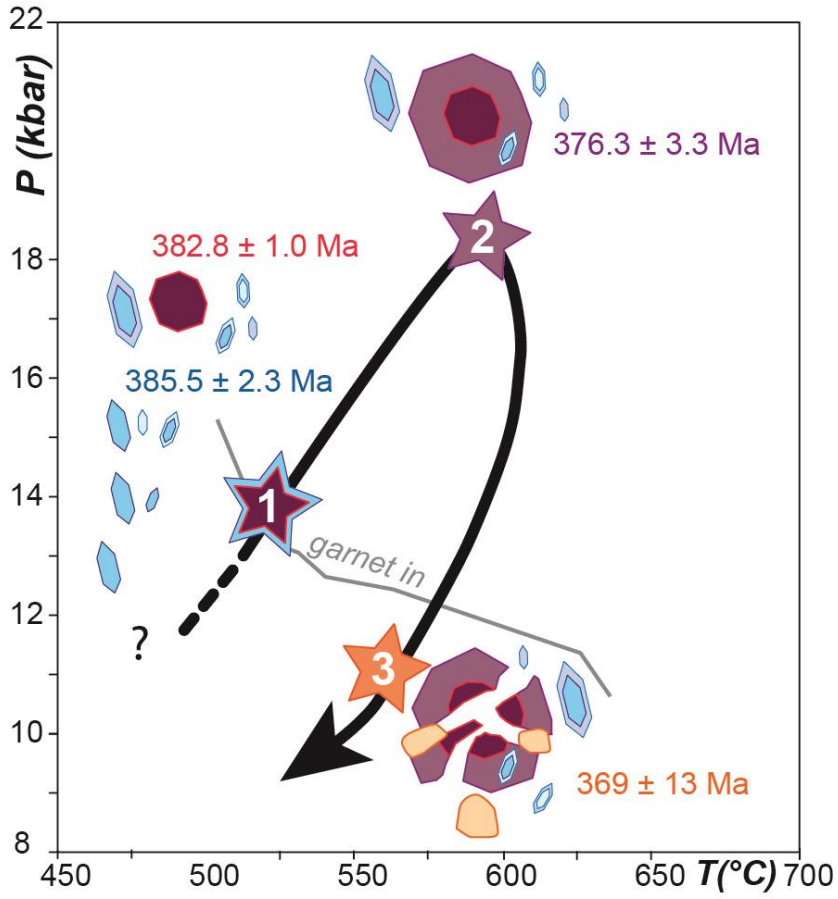

Figure II.1.10: *P-T-t sketch illustrating the growth of the dated minerals. Blue – zircon(U-Pb); violet and purple – garnet core (Lu-Hf) and rim (Sm-Nd), respectively; orange – apatite (U-Pb). Different zircon growth stages, prior and during the beginning of the eclogite-facies metamorphism are represented. The growth of garnet core, recorded by the Lu-Hf age of 382.8 ± 1.0 Ma, marks the initial stages of the eclogite facies. The Sm-Nd age of 376.6 ± 3.3 Ma corresponds to the crystallization of the rim and the HP-peak. Apatite, crystallizing in garnet fractures constrains the exhumation at 369 ± 13 Ma.*

It is quite uncommon to preserve traces of the prograde path, the equilibration at the metamorphic peak, exhumation and subsequent retrogression tending to erase any prior metamorphic record. But when the prograde path can be reconstructed, it gives access to information of paramount importance, as the duration of metamorphism or burial rates (e.g. Tual et al., 2017). In our case, the geochronological analysis allowed to estimate the duration of the prograde part of the eclogite-facies P-T path. Unfortunately, the poor preservation of the petrological record of this prograde P-T segment did not provide enough constraints to calculate the burial rates.

7.3. Larger framework

Dating eclogites, including their prograde path and amphibolite-facies retrogression sheds light on the early stages of an orogen. Indeed, the fact that eclogites end up at the Earth surface implies that subduction ceased and that the initially buried terranes were more or less rapidly exhumed. Depending on the time lag between burial and exhumation, as well as the rate of exhumation, different tectonic models could be proposed, but this is behind the scope of the present work.

As detailed in the geological context, only four studies attempted to date eclogite-facies rocks from the LAC in the Massif Central, and suggested a Silurian age (~415 Ma) for the HP event. Three of them are currently outdated due to analytical limitations (Pin and Lancelot, 1982; Ducrot et al., 1983; Paquette et al., 1995), as they used aliquots made of a population of zircon grains (i.e. they mixed different grains with potentially different or complex histories). Moreover, none of these studies described concordant datasets, all of the calculated dates corresponding to upper intercepts. Paquette et al. (2017) re-dated by in-situ LA-ICP-MS zircon from the same, previously dated sample separate of the La Bessenoit area (Paquette et al. 1995) and did not find any ca. 415 Ma dates. They conclude that this date has probably been over-interpreted. The recent U-Pb LA-ICP-MS study of Berger et al. (2010) suggests that the date of 412 ± 6 Ma (N=3) corresponds to the age of the HP metamorphism, based on the similarity with the previous HP ages proposed in the MCF. There is, however, no evidence in this study for the association of the dated zircon with the HP paragenesis and the significance of the date of ca. 415 Ma should be considered with caution.

The 408± 8 Ma Sm-Nd date obtained on garnet by Paquette et al. (1995) is significantly older than the 376.7 ± 3.3 Ma obtained by the same method in this study. Paquette et al. (1995)

described the presence of zoisite ± apatite in the two samples used to build the isochron. Moreover, the Nd content in the garnet fraction from the Fe-Ti sample is high (8.06 ppm) while the $^{147}Sm/^{144}Nd$ ratio is low (0.2416), which is a common feature for garnet contaminated by inclusions (see Baxter et al., 2017). The Mg-eclogite also shows a low $^{147}Sm/^{144}Nd$ ratio of 0.7893. No in situ analysis was performed on garnets from these samples to evaluate if the separates were pure enough. Consequently, until further investigations in this locality, the Sm-Nd date from the Paquette et al. (1995) study should be considered with caution.

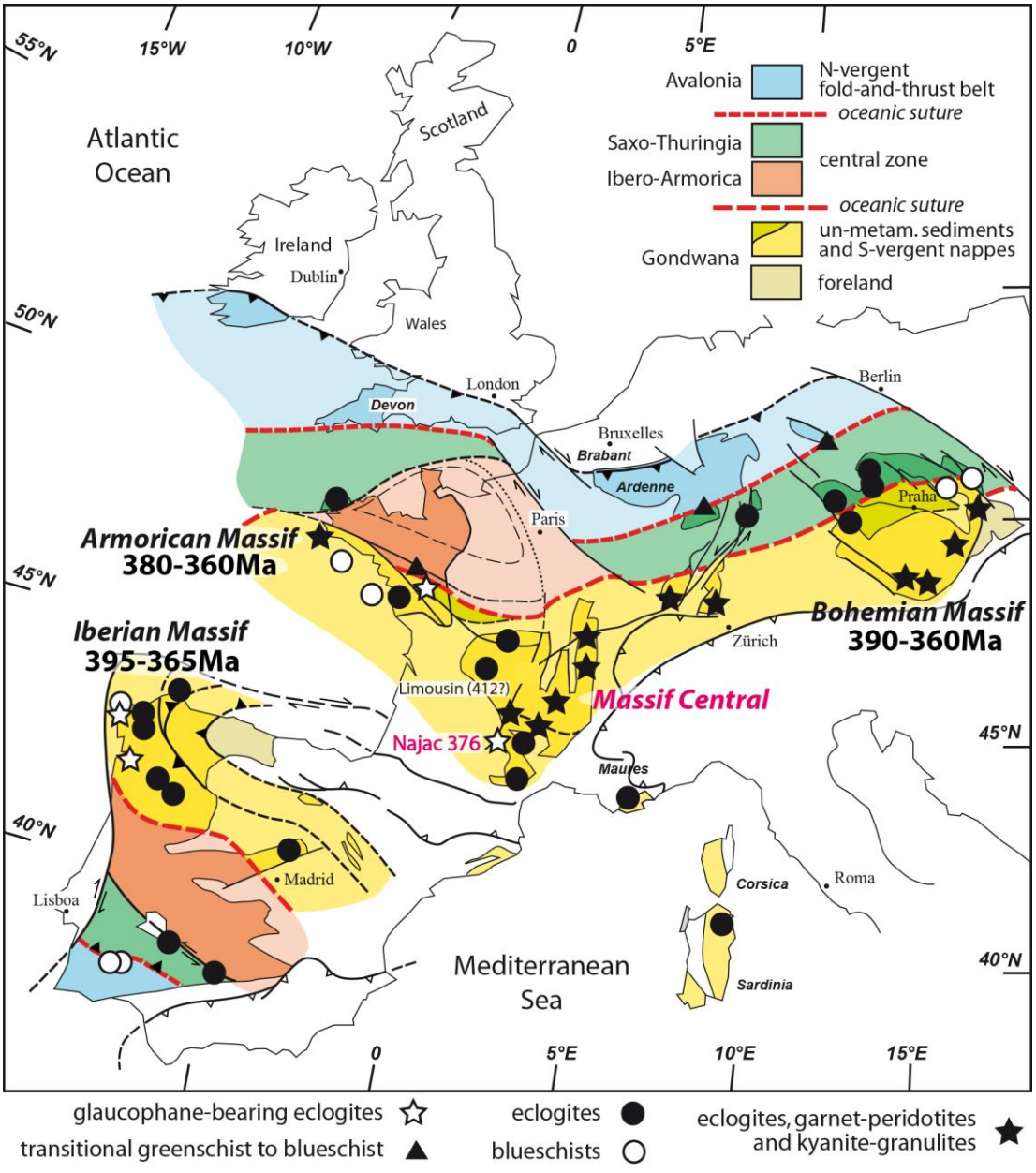

Figure 11: Ages of the high pressure metamorphic rocks in the European Variscide, (modified from Paquette et al., 2017). Result from this study is highlighted.

Despite the robustness of our petrochronological study on the eclogitic event in the Najac area, the lack of modern and reliable data on the high-pressure event in the LAC cannot lead us to discuss a large-scale model, given the existing uncertainties on the geodynamic setting of the French Massif Central within the Variscan belt framework. In the adjacent Armorican Massif, the high-pressure event is well constrained at 380-360 Ma (Bosse et al., 2000; Bosse et al., 2005; Paquette, 1987, Paquette et al., 2017; Fig. II.1.11). Similarly, the HP ages recorded in the Bohemian Massif and the Iberian Massif span 395-360 Ma and 390-365 Ma, respectively (see the recent review of Paquette et al., 2017 for the source of the HP data). The HP age recorded in the Najac massif is therefore fully in line with the HP ages reported from the other parts of the European Variscan belt. The concept of the ca. 415 Ma HP event described in the French Massif Central is then based on data that can be now considered as unreliable and do probably not have any geological significance. As in the other Variscan massifs, the HP event is expected to spread over a more or less long period of time, and distinct HP ages are expected in the different HP localities. Dating the high-pressure event provides a key constraint on the evolution of orogenic terranes. Consequently, the use of dates that were obtained by outdated methods, or that cannot be clearly attributed to the high-pressure assemblage, should be avoided. We caution against the use of the three above-mentioned zircon studies (Pin and Lancelot, 1982; Ducrot et al. 1983; Berger et al., 2010) to infer any geodynamic evolution for the French Massif Central and call for new geochronological studies in the different HP areas.

8. Conclusion

Based on a geochronological multi-method study and thermodynamic modeling, we show that the Najac eclogites reached 560-630 °C at 15-20 kbar and that the prograde part of the high-pressure metamorphic event lasted for 6.1 ± 4.3 Myr starting at ~ 382.8 ± 1 Ma and peaking at 376.7 ± 3.3 Ma. Subsequent exhumation is constrained by the apatite dating at 369 ± 13 Ma. This study is the first investigation of the HP-event in the French Massif Central using a petrochronological approach. Garnet dating appears fundamental to obtain temporal information on the rock history. Indeed, zircon dating alone would have led to significant uncertainty on the meaning of the obtained dates, considering the diversity of the REE spectra. In subducted rocks, the multi-method geochronological approach is better suited to unravel their complex metamorphic history.

Acknowledgments

We sincerely thank X. Le Coz for thin section preparation, Y. Lepagnot for sample crushing, M. Smędra and D. Sala for the help with the Sm-Nd and Lu-Hf chemical procedure. M. Ballèvre, P. Boulvais, V. Bosse, J. Andersson and D. Rubatto are thanked for interesting discussions about the Variscan geodynamics, the HP-dating challenge, zircon textures and the REE behavior. We thank M. Ballèvre for kindly providing the file of Fig. 11. Constructive comments from Stéphanie Duchêne and an anonymous reviewer helped to improve the manuscript. We are grateful to Marco Scambelluri for his editorial handling. This work was partly financed by an internal grant from the OSUR (Université Rennes 1), and an INSU-CNRS (TelluS 2017) project accorded to P. Pitra. This study is a part of the PhD thesis of C. Lotout, funded by the French Ministry of higher education and research..

Bibliography

Anczkiewicz, A.A., Anczkiewicz, R., 2012. U–Pb zircon geochronology and anomalous Sr-Nd-Hf isotope systematics of late orogenic andesites: Pieniny Klippen Belt, Western Carpathians, South Poland. Chemical Geology 427, 1-6.

Anczkiewicz, R., Platt, J.P., Thirlwall, M.F., Wakabayashi, J., 2004. Franciscan subduction off to a slow start: evidence from high-precision Lu–Hf garnet ages on high grade-blocks. Earth and Planetary Science Letters 225, 147-61.

Anczkiewicz, R., Szczepański, J., Mazur, S., Storey, C., Crowley, Q., Villa, I.M., Thirlwall, M.F., Jeffries, T.E., 2007. Lu–Hf geochronology and trace element distribution in garnet: implications for uplift and exhumation of ultra-high pressure granulites in the Sudetes, SW Poland. Lithos 95, 363-80.

Anczkiewicz, R., Thirlwall, M.F., 2003. Improving precision of Sm-Nd garnet dating by H2SO4 leaching: a simple solution to the phosphate inclusion problem. Geological Society, London, Special Publications 220, 83-91.

Anczkiewicz, R., Thirlwall, M., Alard, O., Rogers, N.W., Clark, C., 2012. Diffusional homogenization of light REE in garnet from the Day Nui Con Voi Massif in N-Vietnam: Implications for Sm-Nd geochronology and timing of metamorphism in the Red River shear zone. Chemical Geology 318, 16-30.

Ballèvre, M., Bosse, V., Ducassou, C., Pitra, P., 2009. Palaeozoic history of the Armorican Massif: models for the tectonic evolution of the suture zones. Comptes Rendus Geosciences 341, 174–201

Ballèvre, M., Martínez Catalán, J.R., López-Carmona, A., Pitra, P., Abati, J., Díez Fernández, R., Ducassou, C., Arenas, R., Bosse, V., Castiñeiras, P., Fernández-Suárez, J., Gómez Barreiro, J., Paquette, J.L., Peucat, J.J., Poujol, M., Ruffet, G., Sánchez Martínez, S. 2014. Correlation of the nappe stack in the Ibero-Armorican arc across the Bay of Biscay: a joint French-Spanish project. In: Schulmann, K., Martínez Catalán, J.R., Lardeaux, J.M., Janoušek, V., Oggiano, G., (eds) The Variscan orogeny: extent, timescale and the formation of the European Crust. Geological Society London 405, 77-113.

Ballouard, C., Boulvais, P., Poujol, M., Gapais, D., Yamato, P., Tartèse, R., Cuney, M. 2015. Tectonic record, magmatic history and hydrothermal alteration in the Hercynian Guérande leucogranite, Armorican Massif, France. Lithos 220-223, 1-22.

Berger, J., Féménias, O., Ohnenstetter, D., Bruguier, O., Plissart, G., Mercier, J.C., Demaiffe, D., 2010. New occurrence of UHP eclogites in Limousin (French Massif Central): Age, tectonic setting and fluid–rock interactions. Lithos 118, 365-382.

Bingen, B., Austrheim, H., Whitehouse, M., 2001. Ilmenite as a source for zirconium during high-grade metamorphism? Textural evidence from the Caledonides of Western Norway and implications for zircon geochronology. Journal of Petrology 42, 355-75.

Bodinier, J.L., 1983. Etude geochimique du massif basique et ultrabasique de Najac (Aveyron); Consequences geotectoniques. Bulletin de la Société Géologique de France 7, 185-93.

Bodinier, J.L., Giraud, A., Dupuy, C., Leyreloup, A., Dostal, J., 1986. Caracterisation geochimique des metabasites associees a la suture meridionale hercynienne; Massif Central francais et Chamrousse (Alpes). Bulletin de la Société Géologique de France 2, 115-23.

Bosse, V., Feraud, G., Ruffet, G., Ballèvre, M., Peucat, J.J., De Jong, K., 2000. Late Devonian subduction and early-orogenic exhumation of eclogite-facies rocks from the Champtoceaux Complex (Variscan belt, France). Geological Journal 35, 297-325.

Bosse, V., Féraud, G., Ballèvre, M., Peucat, J.J., Corsini, M., 2005. Rb–Sr and 40 Ar/39 Ar ages in blueschists from the Ile de Groix (Armorican Massif, France): implications for closure mechanisms in isotopic systems. Chemical Geology 220, 21-45.

Bouchardon, J.L., Santallier, D., Briand, B., Ménot, R.P., Piboule, M., 1989. Eclogites in the French Palaeozoic Orogen: geodynamic significance. Tectonophysics 169, 317-332.

Boynton, W.V., 1983. Cosmochemistry of the rare earth elements: meteorite studies, in: P. Henderson (Ed.), Rare Earth Element Geochemistry. Elsevier, pp 63-114.

Burg, J.P., Delor, C.P., Leyreloup, A.F., Romney, F., 1989. Inverted metamorphic zonation and Variscan thrust tectonics in the Rouergue area (Massif Central, France): PTt record from mineral to regional scale. Evolution of metamorphic belts 1, 423-39.

Capitani, C.D., Petrakakis, K., 2010. The computation of equilibrium assemblage diagrams with Theriak/Domino software. American Mineralogist 95, 1006-16.

Carignan, J., Hild, P., Mevelle, G., Morel, J., Yeghicheyan, D., 2001. Routine analyses of trace elements in geological samples using flow injection and low pressure on-line liquid chromatography coupled to ICP-MS: a study of geochemical reference materials BR, DR-N, UB-N, AN-G and GH. Geostandards Newsletter 25, 187-198.

Chamberlain, K.R., Bowring, S.A., 2001. Apatite–feldspar U–Pb thermochronometer: a reliable, mid-range (~ 450° C), diffusion-controlled system. Chemical Geology 172, 173-200.

Cherniak, D.J., Lanford, W.A., Ryerson, F.J., 1991. Lead diffusion in apatite and zircon using ion implantation and Rutherford backscattering techniques. Geochimica et Cosmochimica Acta 55, 1663-73.

Chew, D.M., Petrus, J.A., Kamber, B.S., 2014. U–Pb LA-ICPMS dating using accessory mineral standards with variable common Pb. Chemical Geology 363, 185-199

Cochrane, R., Spikings, R.A., Chew, D., Wotzlaw, J.F., Chiaradia, M., Tyrrell, S., Schaltegger, U., Van der Lelij, R., 2014. High temperature (> 350 C) thermochronology and mechanisms of Pb loss in apatite. Geochimica et Cosmochimica Acta 127, 39-56.

Delor C., Leyreloup, A., Bodinier, J.L., Burg, J.P., 1986. Découverte d'éclogites à glaucophane dans la klippe de Najac (Massif Central, France): nouveaux témoins océaniques d'un stade haute pression dans la chaîne de collision varisque. Comptes rendus de l'Académie des sciences, 302, 739-44.

Delor, C., Burg, J.P., Guiraud, M., Leyreloup, A., 1987. Les métapélites à phengite-chloritoïde-grenat-staurotide-disthène de la klippe de Najac-Carmaux: nouveaux marqueurs d'un métamorphisme de haute pression varisque en Rouergue occidental. Comptes rendus de l'Académie des sciences, 305, 589-95.

Diener, J.F., Powell, R. 2012., Revised activity–composition models for clinopyroxene and amphibole. Journal of Metamorphic Geology 30, 131-42.

Duchêne, S., Blichert-Toft, J., Luais, B., Télouk, P., 1997. The Lu-Hf dating of garnets and the ages of the Alpine high-pressure metamorphism. Nature 387(6633), 586.

Ducrot, J., Lancelot, J.R., Marchand, J., 1983. Datation U-Pb sur zircons de l'éclogite de la Borie (Haut-Allier, France) et conséquences sur l'évolution anté-hercynienne de l'Europe occidentale. Earth Planetary Science Letters 18, 97-113.

Faure, M., Lardeaux, J.M., Ledru, P., 2009. A review of the pre-Permian geology of the Variscan French Massif Central. Comptes Rendus Geoscience 341, 202-13.

Forestier, F.H., Lasnier, B., Leyreloup, A., Marchand, J., 1973. Vues nouvelles sur la catazone dans le Massif Central français et le Massif Armoricain de l'affleurement au Moho. Bulletin de la Société Géologique de France 15, 562-578.

Fraser, G., Ellis, D., Eggins, S., 1997. Zirconium abundance in granulite-facies minerals, with implications for zircon geochronology in high-grade rocks. Geology 25, 607-10.

Franke, W., 2006. The Variscan orogen in Central Europe: construction and collapse. Geological Society, London, Memoirs 32, 333-43.

Harley, S.L., Kelly, N.M., Möller, A., 2007. Zircon behaviour and the thermal histories of mountain chains. Elements 3, 25-30.

Harrison, T.M., Catlos, E.J., Montel, J.M., 2002. U-Th-Pb dating of phosphate minerals. Reviews in Mineralogy and Geochemistry 48, 524-558.

Hermann, J., Rubatto, D., Korsakov, A., Shatsky, V.S., 2001. Multiple zircon growth during fast exhumation of diamondiferous, deeply subducted continental crust (Kokchetav Massif, Kazakhstan). Contributions to Mineralogy and Petrology 141, 66-82.

Holland, T., Baker, J., Powell, R., 1998. Mixing properties and activity-composition relationships of chlorites in the system MgO-FeO-Al2O3-SiO2-H2O. European Journal of Mineralogy 22, 395-406.

Holland, T.J., Powell, R., 1998. An internally consistent thermodynamic data set for phases of petrological interest. Journal of Metamorphic Geology 16, 309-43.

Holland, T., Powell, R., 2003. Activity–composition relations for phases in petrological calculations: an asymmetric multicomponent formulation. Contributions to Mineralogy and Petrology 145, 492-501.

Horstwood, M.S.A., Košler, J., Gehrels, G., Jackson, S.E., McLean, N.M., Paton, C., Pearson, N.J., Sircombe, K., Sylvester, P., Vermeesch, P., Bowring, J.F., Condon, D.J., Schoene, B., 2016. Community-Derived Standards for LA-ICP-MS U-(Th-)Pb Geochronology – Uncertainty Propagation, Age Interpretation and Data Reporting. Geostandards and Geoanalytical Research 40, 311-332.

Hoskin, P.W., Black, L.P., 2000. Metamorphic zircon formation by solid-state recrystallization of protolith igneous zircon. Journal of Metamorphic Geology 18, 423-39.

Hoskin, P.W., Schaltegger, U., 2003. The composition of zircon and igneous and metamorphic petrogenesis. Reviews in Mineralogy and Geochemistry 53, 27-62.

Jackson, S.E., Pearson, N.J., Griffin, W.L., Belousova, E.A., 2004. The application of laser ablation-inductively coupled plasma-mass spectrometry to in situ U–Pb zircon geochronology. Chemical Geology 211, 47-69.

Janoušek, V., Farrow, C.M., Erban, V., 2006. Interpretation of whole-rock geochemical data in igneous geochemistry: introducing Geochemical Data Toolkit (GCDkit). Journal of Petrology 47, 1255-1259.

Jochum, K.P., Weis, U., Stoll, B., Kuzmin, D., Yang, Q., Raczek, I., Jacob, D.E., Stracke, A., Birbaum, K., Frick, D.A., Günther, D., 2011. Determination of reference values for NIST SRM 610–617 glasses following ISO guidelines. Geostandards and Geoanalytical Research 35, 397-429.

Kohn, M.J., 2009. Models of garnet differential geochronology. Geochimica et Cosmochimica Acta. 73, 170-82.

Kohn, M.J., Corrie S.L., Markley, C., (2015) The fall and rise of metamorphic zircon. American Mineralogist 100, 897-908.

Kohn, M.J., 2016. Metamorphic chronology—a tool for all ages: Past achievements and future prospects. American Mineralogist 101, 25-42.

Kylander-Clark, A.R., Hacker, B.R., Johnson, C.M., Beard, B.L., Mahlen, N.J., Lapen, T.J., 2007. Coupled Lu–Hf and Sm–Nd geochronology constrains prograde and exhumation histories of high-and ultrahigh-pressure eclogites from western Norway. Chemical Geology 242, 137-54.

Lardeaux, J.M., 2014. Deciphering orogeny: a metamorphic perspective Examples from European Alpine and Variscan belts Part II: Variscan metamorphism in the French Massif Central—a review. Bulletin de la Société Géolgique de France 185, 281-310.

Lardeaux, J.M., Schulmann, K., Faure, M., Janoušek, V., Lexa, O., Skrzypek, E., Edel, J.B., Štípská, P., 2014. The moldanubian zone in the French Massif Central, Vosges/Schwarzwald and Bohemian Massif revisited: differences and similarities. Geological Society, London, Special Publications 405, 7-44.

Lasnier, B., 1968. Découverte de roches éclogitiques dans le groupe leptyno-amphibolique des monts du Lyonnais (Massif Central Français). Bulletin de la Société Géolgique de France 7, 179-185.

Leake, B.E., Woolley, A.R., Arps, C.E., Birch, W.D., Gilbert, M.C., Grice, J.D., Hawthorne, F.C., Kato, A., Kisch, H.J., Krivovichev, V.G., Linthout, K., 1997. Report Nomenclature of Amphiboles: Report of the Subcommittee on Amphiboles of the International Mineralogical Association Commission on New Minerals and Mineral Names. Mineralogical Magazine 61, 295-321.

Ledru, P., Lardeaux, J.M., Santallier, D., Autran, A., Quenardel, J.M., Floc'h, J.P., Lerouge, G., Maillet, N., Marchand, J., Ploquin, A., 1989. Où sont les nappes dans le Massif Central Français? Bulletin de la Société Géolgique de France 3, 605–618.

Ludwig, K.R., 1998. On the treatment of concordant uranium-lead ages. Geochimica et Cosmochimica Acta 62, 665-76.

Ludwig, K.R., 2012. User's Manual for a geochronological toolkit for Microsoft Excel. Berkeley Geochronological Center 75.

Lugmair, G.W., Marti, K., 1978. Lunar initial 143Nd/144Nd: differential evolution of the lunar crust and mantle. Earth and Planetary Science Letters 39, 349-57.

Martínez Catalán, J.R., Arenas, R., Abati, J., Martínez, S.S., García, F.D., Suárez, J.F., Cuadra, P.G., Castiñeiras, P., Barreiro, J.G., Montes, A.D., Clavijo, E.G., 2009. A rootless suture and the loss of the roots of a mountain chain: the Variscan belt of NW Iberia. Comptes Rendus Geoscience 341, 114-26.

McDowell, F.W., McIntosh, W.C., Farley, K.A., 2005. A precise 40Ar–39Ar reference age for the Durango apatite (U–Th)/He and fission-track dating standard. Chemical Geology 214, 249-263.

Matte, P., 1986. Tectonics and plate tectonics model for the Variscan belt of Europe. Tectonophysics 126, 329-374.

Paquette, J.L., 1987. "Comportement des systèmes isotopiques U-Pb et Sm-Nd dans le métamorphisme éclogitique. Chaîne Hercynienne et chaîne Alpine." PhD dissertation, Université Rennes 1.

Paquette, J.L., Monchoux, P., Couturier, M., 1995. Geochemical and isotopic study of a norite-eclogite transition in the European Variscan Belt: Implications for U-Pb zircon systematics in metabasic rocks. Geochim. Cosmochim. acta 59, 1611-1622.

Paton, C., Woodhead, J.D., Hellstrom, J.C., Hergt, J.M., Greig, A., Maas, R., 2010. Improved laser ablation U-Pb zircon geochronology through robust downhole fractionation correction. Geochemistry, Geophysics, Geosystems, 11, Q0AA06, doi:10.1029/2009GC002618.

Piboule, M., Briand, B., 1985. Geochemistry of eclogites and associated rocks of the southeastern area of the French Massif Central: origin of the protoliths. Chemical geology 50, 189-99.

Pin, C., Lancelot, J., 1982. U–Pb dating of an early Paleozoïc bimodal magmatism in the French Massif Central and its further metamorphic evolution. Contribution to Mineralogy and Petrology 79, 1-12.

Pitra, P., Boulvais, P., Antonoff, V., Diot, H., 2008. Wagnerite in a cordierite-gedrite gneiss: Witness

of long-term fluid-rock interaction in the continental crust (Ile d'Yeu, Armorican Massif, France). American Mineralogist 93, 315-26.

Pochon, A., Poujol, M., Gloaguen, E., Branquet, Y., Cagnard, F., Gumiaux, C. Gapais, D. 2016. U-Pb LA-ICP-MS dating of apatite in mafic rocks: Evidence for a major magmatic event at the Devonian-Carboniferous boundary in the Armorican Massif (France). American Mineralogist 101, 2430-2442.

Rubatto, D., 2002. Zircon trace element geochemistry: partitioning with garnet and the link between U–Pb ages and metamorphism. Chemical geology 184, 123-38.

Rubatto, D., 2017. Zircon: the metamorphic mineral. Reviews in mineralogy and geochemistry 83, 261-95.

Rubatto, D., Hermann, J., 2003. Zircon formation during fluid circulation in eclogites (Monviso, Western Alps): implications for Zr and Hf budget in subduction zones. Geochimica et Cosmochimica Acta 67, 2173-87.

Rubatto, D., Hermann, J., 2007. Experimental zircon/melt and zircon/garnet trace element partitioning and implications for the geochronology of crustal rocks. Chemical Geology 241, 38-61.

Santallier, D.A., Briand, B.E., Menot, R.P., Piboule, M., 1988. Les complexes leptyno-amphiboliques (CLA): revue critique et suggestions pour un meilleur emploi de ce terme. Bulletin de la Société Géologique de France 1, 3-12.

Scherer, E., Münker, C., Mezger, K., 2001. Calibration of the lutetium-hafnium clock. Science 293, 683-7.

Schoene, B., Bowring, S.A., 2006. U–Pb systematics of the McClure Mountain syenite: Thermochronological constraints on the age of the 40Ar/39Ar standard MMhb. Contributions to Mineralogy and Petrology 151, 615–630.

Schulmann, K., Martínez Catalán, J.R., Lardeaux, J.M., Janoušek, V., Oggiano, G., 2014. The Variscan orogeny: extent, timescale and the formation of the European crust. Geological Society, London, Special Publication 405, 1–6.

Sláma, J., Košler, J., Condon, D.J., Crowley, J.L., Gerdes, A., Hanchar, J.M., Horstwood, M.S., Morris, G.A., Nasdala, L., Norberg, N., Schaltegger, U., 2008. Plešovice zircon—a new natural reference material for U–Pb and Hf isotopic microanalysis. Chemical Geology 249, 1-35.

Smit, M.A., Scherer, E.E., Mezger, K., 2013. Lu–Hf and Sm–Nd garnet geochronology: Chronometric closure and implications for dating petrological processes. Earth and Planetary Science Letters 381, 222-33.

Stacey, J.T., Kramers, J.D., 1975. Approximation of terrestrial lead isotope evolution by a two-stage model. Earth and planetary science letters 26, 207-21.

Štípská, P., Powell, R., Hacker, B.R., Holder, R., Kylander-Clark, A.R., 2016. Uncoupled U/Pb and REE response in zircon during the transformation of eclogite to mafic and intermediate granulite (Blanský les, Bohemian Massif). Journal of Metamorphic Geology 34, 551-72.

Sun, S.S., McDonough, W.S., 1989. Chemical and isotopic systematics of oceanic basalts: implications for mantle composition and processes. Geological Society, London, Special Publications 42, 313-45.

Tirel, C., Brun, J.P., Burov, E., Wortel, M.J., Lebedev, S., 2013. A plate tectonics oddity: Caterpillar-walk exhumation of subducted continental crust. Geology 41, 555-8.

Thirlwall, M.F., Anczkiewicz, R., 2004. Multidynamic isotope ratio analysis using MC–ICP–MS and the causes of secular drift in Hf, Nd and Pb isotope ratios. International Journal of Mass Spectrometry 235, 59-81.

Tirone, M., Ganguly, J., Dohmen, R., Langenhorst, F., Hervig, R., Becker, H.W., 2005 Rare earth diffusion kinetics in garnet: Experimental studies and applications: Geochimica et Cosmochimica Acta 69, 2385-2398.

Tual, L., Pitra, P., Möller, C., 2017. P–T evolution of Precambrian eclogite in the Sveconorwegian orogen, SW Sweden. Journal of Metamorphic Geology DOI: 10.1111/jmg.12242.

Van Achterbergh, E., Ryan, C.G., Jackson, S.E., Griffin, W.L., 2001. Data reduction software for LA-ICP-MS: appendix. In: Laser Ablation-ICP-Mass Spectrometry in the Earth Sciences: Principles and Applications. In Mineralog Assoc Canada (MAC) Short Courses Series (Sylvester, P.J., eds), Ottawa, Ontario, Canada 29, 239-243.

White, R.W., Powell, R., Holland, T.J., Worley, B.A., 2000. The effect of TiO~ 2 and Fe~ 2O~ 3 on metapelitic assemblages at greenschist and amphibolite facies conditions: mineral equilibria calculations in the system The effect of TiO2 and Fe2O3 on metapelitic assemblages at greenschist and amphibolite facies conditions: mineral equilibria calculations in the system K2O–FeO–MgO–Al2O3–SiO2–H2O–TiO2–Fe2O3. Journal of Metamorphic Geology 18, 497-512.

White R.W., Powell R., Holland T.J., 2007. Progress relating to calculation of partial melting equilibria for metapelites. Journal of Metamorphic Geology 25, 511-27.

Whitehouse, M.J., 2003. Rare earth elements in zircon: a review of applications and case studies from the Outer Hebridean Lewisian Complex, NW Scotland. Geological Society, London, Special Publications 220, 49-64.

Whitehouse, M.J., Platt, J.P., 2003. Dating high-grade metamorphism—constraints from rare-earth elements in zircon and garnet. Contributions to Mineralogy and Petrology 145, 61-74.

Yang, P., Rivers, T., 2002. The origin of Mn and Y annuli in garnet and the thermal dependence of P in garnet and Y in apatite in calc-pelite and pelite, Gagnon terrane, western Labrador. Geological Materials Research 4, 1-35.

Zhai, Q.G., Jahn, B.M., Li, X.H., Zhang, R.Y., Li, Q.L., Yang, Y.N., Wang, J., Liu, T., Hu, P.Y., Tang, S.H., 2017. Zircon U–Pb dating of eclogite from the Qiangtang terrane, north-central Tibet: a case of metamorphic zircon with magmatic geochemical features. International Journal of Earth Sciences. 106, 1239-55.

Supplementary Table II.1.1: Operating conditions for the LA-ICP-MS equipment

Laboratory & Sample Preparation	
Laboratory name	Géosciences Rennes, UMR CNRS 6118, Rennes, France
Sample type/mineral	Zircon (Zrn), Apatite (Ap)
Sample preparation	Conventional mineral separation, 1 inch resin mount, 1µm polish to finish
Imaging	CL: RELION CL instrument, Olympus Microscope BX51WI, Leica Color Camera DFC 420C
Laser ablation system	
Make, Model & type	ESI NWR193UC, Excimer
Ablation cell	ESI NWR TwoVol2
Laser wavelength	193 nm
Pulse width	< 5 ns
Fluence	8.5 J/cm-2
Repetition rate	3 Hz (Zrn) and 5Hz (Ap)
Spot size	35 µm (Zrn) and 45 µm (Ap)
Sampling mode / pattern	Single spot
Carrier gas	100% He, Ar make-up gas and N2 (3 ml/mn) combined using in-house smoothing device
Background collection	20 seconds
Ablation duration	60 seconds
Wash-out delay	15 seconds
Cell carrier gas flow (He)	0.75 l/min
ICP-MS Instrument	
Make, Model & type	Agilent 7700x, Q-ICP-MS
Sample introduction	Via conventional tubing
RF power	1350W
Sampler, skimmer cones	Ni
Extraction lenses	X type
Make-up gas flow (Ar)	0.85 l/min
Detection system	Single collector secondary electron multiplier
Data acquisition protocol	Time-resolved analysis
Scanning mode	Peak hopping, one point per peak
Detector mode	Pulse counting, dead time correction applied, and analog mode when signal intensity > ~ 10^6 cps
Masses measured	^{204}(Hg + Pb), ^{206}Pb, ^{207}Pb, ^{208}Pb, ^{232}Th, ^{238}U + ^{43}Ca (Ap)
Integration time per peak	10-30 ms
Sensitivity / Efficiency	28000 cps/ppm Pb (50µm, 10Hz)
Data Processing	
Gas blank	20 seconds on-peak
Calibration strategy	GJ1 zircon and Madagascar apatite standards used as primary reference material, Plešovice (Zrn) and McClure and Durango (Ap) used as secondary reference material (quality control)
Common-Pb correction, composition and uncertainty	No common-Pb correction. Analyses discarded of the age calculation when discordance >20%
Reference Material info	GJ1 (Jackson et al., 2004) Madagascar (Cochrane et al. 2014) Plešovice (Slama et al., 2008) McClure (Schoene and Bowring 2006) Durango (McDowell et al. 2005)
Data processing package used	Zrn : GLITTER ® (van Achterbergh et al., 2001) Ap : Iolite (Paton et al., 2010), VizualAge_UcomPbine (Chew et al., 2014)
Quality control / Validation	Plešovice: 337.8 ± 4.7 Ma (N=6; MSWD=0.013; probability=1.00) McClure: 529 ± 16 Ma (N=4, MSWD=7) Durango: 33.3 ± 2.6 Ma (N=5, MSWD=2.7)

Supplementary Table II.1.2: Summary of the U-Pb LA-ICP-MS analyses in zrn (bold – Silurian concordant date, italic – discordant date) and apatite

LA-ICPMS datas for zircons from sample NC5A																		
Zircon	Content (ppm)				Isotopic Ratios							Ages (Ma)						
Label	Pb	U	Th	Th/U	Pb^{206}/U^{238}	err%	Pb^{207}/Pb^{206}	err%	Pb^{207}/U^{235}	err%	rho	Pb^{207}/Pb^{206}	1σ	Pb^{206}/U^{238}	1σ	Pb^{207}/U^{235}	1σ	Conc.
5210916	9.3	156.4	29.6	0.19	16.23	1.30	0.05467	1.30	0.464	1.51	0.86	399	28	386	5	387	5	99.5
6210916	2.4	37.3	12.4	0.33	15.95	1.34	0.05448	1.89	0.471	2.03	0.66	391	42	392	5	392	7	100.1
7210916	1.4	22.3	9.3	0.42	16.63	1.41	0.05880	2.70	0.488	2.77	0.51	560	58	377	5	403	9	93.4
8210916	1.4	22.0	9.4	0.43	16.28	1.40	0.05682	2.59	0.481	2.67	0.53	484	56	384	5	399	9	96.4
10210916	2.8	44.3	17.9	0.40	16.31	1.34	0.05516	1.92	0.466	2.05	0.65	419	42	384	5	389	7	98.7
14210916	0.7	12.1	3.5	0.29	16.27	1.45	0.05462	3.44	0.463	3.47	0.42	397	75	385	5	386	11	99.6
15210916	0.7	11.7	3.2	0.28	16.56	1.46	0.05694	3.35	0.474	3.38	0.43	489	73	378	5	394	11	95.9
16210916	9.8	155.0	61.0	0.39	16.32	1.31	0.05534	1.32	0.468	1.52	0.86	426	29	384	5	390	5	98.4
17210916	5.8	93.8	31.2	0.33	16.36	1.31	0.05447	1.51	0.459	1.68	0.78	390	33	382	5	384	5	99.7
18210916	0.3	4.8	0.8	0.16	16.36	1.68	0.05499	6.22	0.464	6.18	0.27	412	133	383	6	387	20	98.9
19210916	11.0	172.4	70.0	0.41	16.28	1.30	0.05380	1.30	0.456	1.51	0.86	363	29	384	5	381	5	100.8
21210916	1.3	23.2	3.2	0.14	16.51	1.39	0.05432	2.56	0.454	2.62	0.53	384	56	379	5	380	8	99.8
25210916	0.4	5.8	1.5	0.26	16.52	1.67	0.05861	5.20	0.489	5.17	0.32	553	110	379	6	404	17	93.7
27210916	2.2	36.1	8.0	0.22	16.24	1.35	0.05427	2.23	0.461	2.33	0.58	382	49	385	5	385	7	100.1
28210916	3.1	49.3	19.0	0.39	16.31	1.32	0.05570	1.89	0.471	2.01	0.66	440	41	384	5	392	7	97.9
29210916	**0.9**	**13.6**	**3.9**	**0.29**	**14.72**	**1.41**	**0.05489**	**2.97**	**0.514**	**3.01**	**0.47**	**408**	**64**	**424**	**6**	**421**	**10**	**100.6**
30210916	1.0	15.3	5.7	0.37	16.36	1.46	0.06079	3.21	0.512	3.23	0.45	632	68	382	5	420	11	91.1
31210916	0.7	11.0	3.2	0.29	16.30	1.52	0.05453	4.03	0.461	4.03	0.38	393	87	384	6	385	13	99.7
5210916	8.7	113.9	114.8	1.01	15.88	1.29	0.05480	1.44	0.476	1.61	0.80	404	32	394	5	395	5	99.6
6210916	0.5	7.6	1.3	0.17	16.27	1.59	0.05416	5.30	0.459	5.27	0.30	377	115	385	6	384	17	100.3
7210916	0.9	16.4	0.5	0.03	16.18	1.39	0.05407	3.05	0.461	3.09	0.45	374	67	387	5	385	10	100.5
8210916	*0.2*	*3.0*	*0.6*	*0.20*	*16.72*	*2.27*	*0.06891*	*9.55*	*0.568*	*9.40*	*0.24*	*896*	*185*	*375*	*8*	*457*	*35*	*82.0*
10210916	*0.2*	*3.5*	*0.6*	*0.18*	*16.22*	*1.91*	*0.06976*	*6.28*	*0.593*	*6.18*	*0.31*	*921*	*124*	*386*	*7*	*473*	*23*	*81.6*
11210916	4.6	73.0	27.7	0.38	16.10	1.30	0.05496	1.75	0.471	1.88	0.69	410	38	389	5	392	6	99.2
15210916	0.3	5.7	0.3	0.05	16.13	1.98	0.05707	7.32	0.488	7.21	0.28	494	154	388	7	403	24	96.1
16210916	1.7	28.4	4.3	0.15	16.09	1.42	0.05262	2.95	0.451	2.98	0.48	312	65	389	5	378	9	102.9
17210916	0.5	9.4	0.6	0.06	16.39	1.52	0.05875	4.12	0.494	4.11	0.37	558	87	382	6	408	14	93.6
18210916	1.2	20.2	5.4	0.27	16.15	1.42	0.05234	3.21	0.447	3.24	0.44	300	71	387	5	375	10	103.3
19210916	7.4	113.4	60.8	0.54	16.24	1.30	0.05372	1.62	0.456	1.77	0.73	359	36	385	5	382	6	101.0
20210916	4.2	63.5	34.4	0.54	16.04	1.31	0.05602	1.73	0.482	1.88	0.70	453	38	390	5	399	6	97.7
21210916	2.0	31.2	11.6	0.37	16.19	1.42	0.05535	2.91	0.471	2.96	0.48	426	63	386	5	392	10	98.5
25210916	1.4	23.3	2.5	0.11	16.03	1.39	0.05726	2.60	0.493	2.67	0.52	501	57	390	5	407	9	95.9
26210916	16.0	267.0	60.1	0.22	16.26	1.30	0.05493	1.37	0.466	1.57	0.83	409	30	385	5	388	5	99.1
27210916	8.9	142.3	47.5	0.33	15.98	1.31	0.05636	1.63	0.486	1.80	0.73	466	36	391	5	402	6	97.3
28210916	4.0	63.9	23.8	0.37	15.99	1.34	0.05396	1.96	0.465	2.09	0.64	369	44	391	5	388	7	100.8
29210916	26.0	429.4	122.2	0.28	16.30	1.29	0.05511	1.27	0.466	1.48	0.87	417	28	384	5	389	5	98.8

LA-ICPMS datas for apatites from sample NC5A								
	Content (ppm)		Isotopic Ratios				Ages (Ma)	
Label	Pb	U	Pb^{206}/U^{238}	2σ	Pb^{207}/Pb^{206}	2σ	Pb^{207}/Pb^{206}	1σ
ap-01	3.8	3.9	3.34	0.039	0.697	0.008	382	23
ap-02	1.3	4.4	1.12	0.013	0.809	0.010	371	71
ap-03	0.5	1.5	1.39	0.028	0.812	0.018	289	97
ap-04	2.1	2.6	2.93	0.054	0.736	0.010	334	33
ap-05	0.3	1.8	0.75	0.017	0.838	0.015	220	190
ap-06	0.2	1.2	0.58	0.017	0.842	0.019	150	260
ap-07	1.3	3.2	1.48	0.02	0.794	0.010	358	57
ap-08	1.2	3.3	1.37	0.016	0.801	0.010	328	54
ap-09	2.0	3.6	2.07	0.022	0.763	0.010	369	38
ap-10	7.0	2.8	6.88	0.069	0.538	0.007	364	11
ap-11	1.0	1.6	2.16	0.035	0.757	0.014	383	58
ap-12	0.1	0.9	0.57	0.018	0.845	0.023	-90	280
ap-13	0.2	1.6	0.42	0.014	0.839	0.016	-90	340
ap-14	1.0	4.1	1.06	0.014	0.812	0.010	358	78
ap-15	1.7	4.2	1.68	0.023	0.789	0.010	340	55
ap-16	3.3	3.9	3.17	0.056	0.714	0.010	364	36
ap-18	1.2	4.3	1.10	0.014	0.806	0.010	386	73
ap-19	0.8	0.9	2.95	0.062	0.739	0.019	346	54
ap-20	3.2	3.5	3.14	0.034	0.718	0.009	352	26
ap-21	1.4	3.1	1.63	0.022	0.800	0.010	296	53
ap-22	1.5	3.3	1.76	0.023	0.794	0.010	302	48
ap-23	1.4	2.7	1.88	0.033	0.778	0.011	350	56

Supplementary Table II.1.3: Representative microprobe analyses of principal metamorphic minerals. The amount of ferric iron was calculated from stoichiometric constraints.

Clinopyroxene				
	NC5A-01-20	*NC5A-01-21*	*NC5A-01-24*	*NC5A-01-29*
	cpx 1	*cpx 1*	*cpx 1*	*cpx 2 symplectite*
SiO2	54.58	54.49	54.85	51.08
TiO2	0.11	0.08	0.05	0.19
Al2O3	7.95	6.92	7.49	3.16
Fe2O3	5.36	5.51	6.46	6.94
MgO	6.21	6.81	7.05	8.51
FeO	6.60	6.52	4.73	7.80
MnO	0.00	0.04	0.08	0.07
CaO	12.26	13.50	13.02	18.18
Na2O	6.90	6.29	6.81	3.21
K2O	0.00	0.01	0.01	0.01
Sum	99.97	100.18	100.55	99.15
Si	2.00	2.00	1.99	1.94
Ti	0.00	0.00	0.00	0.01
Al	0.34	0.30	0.32	0.14
Fe3	0.15	0.15	0.18	0.20
Mg	0.34	0.37	0.38	0.48
Fe2	0.20	0.20	0.14	0.25
Mn	0.00	0.00	0.00	0.00
Ca	0.48	0.53	0.51	0.74
Na	0.49	0.45	0.48	0.24
K	0.00	0.00	0.00	0.00
Sum	4.00	4.00	4.00	4.00
Xna	0.50	0.46	0.49	0.24
Xca	0.50	0.54	0.51	0.76
XMg	*0.63*	*0.65*	*0.73*	*0.66*
XFe3	0.42	0.43	0.55	0.45
Ca	0.24	0.27	0.25	0.38
Mg	0.17	0.19	0.19	0.25
Fe2+	0.10	0.10	0.07	0.13
2Na	0.49	0.45	0.48	0.24
Q	0.51	0.55	0.52	0.76
Jd	0.34	0.30	0.31	0.07
Ae	0.15	0.15	0.17	0.17

Plagioclase		
	NC5A-01-37	*NC5A-04-13*
SiO2	65.97	68.24
TiO2	0.01	0.00
Al2O3	19.02	19.59
MgO	0.78	0.00
FeO	1.67	0.52
MnO	0.00	0.00
CaO	1.04	0.19
Na2O	10.61	11.29
K2O	0.03	0.02
Sum	99.13	99.85
Si	2.94	2.99
Ti	0.00	0.00
Al	1.00	1.01
Mg	0.05	0.00
Fe2	0.06	0.02
Mn	0.00	0.00
Ca	0.05	0.01
Na	0.92	0.96
K	0.00	0.00
Sum	5.02	4.99
Xan	0.05	0.01
Xab	0.95	0.99
Xor	0.00	0.00

Epidote			
	NC5A-02-01	*NC5A02-02*	*NC5A-03-12*
SiO2	37.39	37.19	35.75
TiO2	0.12	0.21	0.10
Al2O3	24.30	23.82	22.45
Fe2O3	12.26	13.10	12.21
Mn2O3	0.04	0.06	0.00
MgO	0.09	0.02	0.15
CaO	22.39	21.54	19.73
Na2O	0.00	0.01	0.01
K2O	0.00	0.02	0.00
H2O	1.87	1.85	1.76
Sum	98.46	97.82	92.15
Si	3.00	3.00	3.05
Ti	0.01	0.01	0.01
Al	2.30	2.27	2.26
Fe3	0.74	0.80	0.78
Mn3	0.00	0.00	0.00
Mg	0.01	0.00	0.02
Ca	1.92	1.86	1.80
Na	0.00	0.00	0.00
K	0.00	0.00	0.00
OH	1.00	1.00	1.00
Sum	8.98	8.95	8.92
XF3	0.71	0.75	0.75

Garnet															
	NC5A 01	*NC5A 02*	*NC5A 03*	*NC5A 04*	*NC5A 05*	*NC5A 06*	*NC5A 07*	*NC5A 08*	*NC5A 09*	*NC5A 10*	*NC5A 11*	*NC5A 12*	*NC5A 13*	*NC5A 14*	*NC5A 15*
SiO2	37.50	38.15	37.88	37.70	38.16	37.74	37.73	37.88	37.96	37.94	37.81	37.79	37.85	37.58	37.90
TiO2	0.07	0.13	0.10	0.12	0.14	0.16	0.22	0.14	0.18	0.13	0.13	0.08	0.19	0.19	0.26
Al2O3	20.46	20.38	20.60	20.45	20.28	20.45	20.30	20.46	20.38	20.61	20.32	20.82	20.27	20.31	20.16
Fe2O3	1.39	0.63	1.61	1.04	0.75	1.21	1.14	1.31	1.18	1.07	1.33	0.77	1.38	1.47	1.03
MgO	3.07	3.45	3.49	2.81	3.29	2.93	2.71	3.25	3.17	3.23	3.02	2.57	3.40	3.06	3.20
FeO	26.78	25.57	25.06	26.77	25.46	25.54	25.90	25.03	25.29	25.13	25.21	26.25	24.69	24.62	24.86
MnO	1.04	1.31	1.25	0.94	1.28	1.30	1.26	1.36	1.36	1.36	1.38	1.18	1.41	1.41	1.44
CaO	8.90	9.75	9.93	9.58	10.13	10.14	10.32	10.17	10.21	10.18	10.33	10.26	10.32	10.45	10.33
Na2O	0.04	0.04	0.02	0.04	0.03	0.05	0.02	0.04	0.03	0.03	0.02	0.02	0.01	0.05	0.05
K2O	0.00	0.01	0.00	0.00	0.00	0.00	0.00	0.01	0.00	0.01	0.00	0.00	0.00	0.00	0.01
Sum	99.25	99.42	99.93	99.45	99.53	99.51	99.61	99.65	99.76	99.67	99.54	99.74	99.52	99.13	99.25
Si	2.99	3.02	2.99	3.00	3.02	3.00	3.00	3.00	3.01	3.00	3.00	3.00	3.00	3.00	3.01
Ti	0.00	0.01	0.01	0.01	0.01	0.01	0.01	0.01	0.01	0.01	0.01	0.01	0.01	0.01	0.02
Al	1.93	1.91	1.92	1.92	1.90	1.92	1.90	1.91	1.90	1.92	1.90	1.95	1.89	1.91	1.89
Fe3	0.08	0.04	0.10	0.06	0.05	0.07	0.07	0.08	0.07	0.06	0.08	0.05	0.08	0.09	0.06
Mg	0.37	0.41	0.41	0.33	0.39	0.35	0.32	0.38	0.37	0.38	0.36	0.30	0.40	0.36	0.38
Fe2	1.79	1.70	1.66	1.78	1.69	1.70	1.72	1.66	1.68	1.66	1.68	1.74	1.64	1.64	1.65
Mn	0.07	0.09	0.08	0.06	0.09	0.09	0.09	0.09	0.09	0.09	0.09	0.08	0.10	0.10	0.10
Ca	0.76	0.83	0.84	0.82	0.86	0.86	0.88	0.86	0.87	0.86	0.88	0.87	0.88	0.89	0.88
Na	0.01	0.01	0.00	0.01	0.01	0.01	0.00	0.01	0.01	0.01	0.00	0.00	0.00	0.01	0.01
K	0.00	0.00	0.00	0.00	0.00	0.00	0.00	0.00	0.00	0.00	0.00	0.00	0.00	0.00	0.00
Sum	8.00	8.00	8.00	8.00	8.00	8.00	8.00	8.00	8.00	8.00	8.00	8.00	8.00	8.00	8.00
XMg	0.17	0.19	0.20	0.16	0.19	0.17	0.16	0.19	0.18	0.19	0.18	0.15	0.20	0.18	0.19
XFe	0.83	0.81	0.80	0.84	0.81	0.83	0.84	0.81	0.82	0.81	0.82	0.85	0.80	0.82	0.81
Xalm	0.60	0.56	0.55	0.59	0.56	0.57	0.57	0.55	0.56	0.55	0.56	0.58	0.54	0.55	0.55
Xprp	0.12	0.13	0.14	0.11	0.13	0.12	0.11	0.13	0.12	0.13	0.12	0.10	0.13	0.12	0.13
Xgrs	0.26	0.27	0.28	0.27	0.28	0.29	0.29	0.29	0.29	0.29	0.29	0.29	0.29	0.30	0.29
Xsps	0.02	0.03	0.03	0.02	0.03	0.03	0.03	0.03	0.03	0.03	0.03	0.03	0.03	0.03	0.03

	Garnet													
	NC5A 16	*NC5A 17*	*NC5A 18*	*NC5A 19*	*NC5A 20*	*NC5A 21*	*NC5A 22*	*NC5A 23*	*NC5A 24*	*NC5A 25*	*NC5A 26*	*NC5A 27*	*NC5A 28*	*NC5A 29*
SiO2	37.51	37.46	37.97	37.76	37.67	37.68	37.77	37.75	38.09	38.01	37.71	37.80	37.75	37.73
TiO2	0.18	0.23	0.19	0.17	0.17	0.17	0.16	0.17	0.14	0.12	0.17	0.14	0.14	0.16
Al2O3	20.13	20.32	20.42	20.32	20.18	20.43	20.25	20.25	20.33	20.39	20.35	20.29	20.42	20.22
Fe2O3	1.35	1.74	1.21	1.12	1.41	1.43	1.83	1.38	1.18	1.42	1.47	1.68	1.78	1.39
MgO	2.48	2.65	3.41	3.26	3.21	3.32	3.21	3.09	3.41	3.45	3.06	3.22	3.25	3.17
FeO	25.69	25.43	24.53	24.66	24.90	24.46	24.63	24.87	24.89	24.82	25.04	25.20	24.73	25.02
MnO	1.32	1.36	1.51	1.50	1.38	1.51	1.51	1.49	1.47	1.42	1.28	1.38	1.38	1.33
CaO	10.44	10.41	10.34	10.30	10.26	10.15	10.29	10.36	10.16	10.08	10.30	9.96	10.30	10.28
Na2O	0.04	0.03	0.04	0.03	0.01	0.06	0.05	0.03	0.04	0.05	0.05	0.04	0.03	0.02
K2O	0.00	0.00	0.01	0.00	0.00	0.01	0.00	0.00	0.00	0.00	0.00	0.01	0.00	0.00
Sum	99.15	99.62	99.63	99.12	99.18	99.22	99.70	99.39	99.71	99.78	99.45	99.72	99.78	99.32
Si	3.00	2.98	3.00	3.01	3.00	3.00	2.99	3.00	3.01	3.00	3.00	3.00	2.99	3.00
Ti	0.01	0.01	0.01	0.01	0.01	0.01	0.01	0.01	0.01	0.01	0.01	0.01	0.01	0.01
Al	1.90	1.91	1.90	1.91	1.89	1.91	1.89	1.90	1.90	1.90	1.91	1.90	1.91	1.90
Fe3	0.08	0.10	0.07	0.07	0.08	0.09	0.11	0.08	0.07	0.09	0.09	0.10	0.11	0.08
Mg	0.30	0.32	0.40	0.39	0.38	0.39	0.38	0.37	0.40	0.41	0.36	0.38	0.38	0.38
Fe2	1.72	1.69	1.62	1.64	1.66	1.63	1.63	1.65	1.65	1.64	1.66	1.67	1.64	1.67
Mn	0.09	0.09	0.10	0.10	0.09	0.10	0.10	0.10	0.10	0.10	0.09	0.09	0.09	0.09
Ca	0.90	0.89	0.88	0.88	0.88	0.87	0.87	0.88	0.86	0.85	0.88	0.85	0.87	0.88
Na	0.01	0.00	0.01	0.00	0.00	0.01	0.01	0.00	0.01	0.01	0.01	0.01	0.01	0.00
K	0.00	0.00	0.00	0.00	0.00	0.00	0.00	0.00	0.00	0.00	0.00	0.00	0.00	0.00
Sum	8.00	8.00	8.00	8.00	8.00	8.00	8.00	8.00	8.00	8.00	8.00	8.00	8.00	8.00
XMg	0.15	0.16	0.20	0.19	0.19	0.20	0.19	0.18	0.20	0.20	0.18	0.19	0.19	0.18
XFe	0.85	0.84	0.80	0.81	0.81	0.81	0.81	0.82	0.80	0.80	0.82	0.82	0.81	0.82
Xalm	0.57	0.57	0.54	0.55	0.55	0.54	0.55	0.55	0.55	0.55	0.56	0.56	0.55	0.55
Xprp	0.10	0.11	0.13	0.13	0.13	0.13	0.13	0.12	0.13	0.14	0.12	0.13	0.13	0.12
Xgrs	0.30	0.30	0.29	0.29	0.29	0.29	0.29	0.29	0.29	0.28	0.29	0.28	0.29	0.29
Xsps	0.03	0.03	0.03	0.03	0.03	0.03	0.03	0.03	0.03	0.03	0.03	0.03	0.03	0.03

Garnet												
	NC5A 30	*NC5A 31*	*NC5A 32*	*NC5A 33*	*NC5A 34*	*NC5A 35*	*NC5A 36*	*NC5A 37*	*NC5A 38*	*NC5A 39*	*NC5A 40*	*NC5A 41*
SiO2	37.99	37.47	37.56	37.93	38.10	37.83	38.00	37.80	37.59	37.70	37.55	37.74
TiO2	0.10	0.13	0.09	0.06	0.09	0.08	0.09	0.05	0.07	0.07	0.09	0.17
Al2O3	20.56	20.30	20.48	20.47	20.50	20.49	20.68	20.58	20.63	20.52	20.54	20.37
Fe2O3	1.35	2.01	1.43	0.89	1.11	1.37	0.59	1.27	1.29	1.32	2.07	0.86
MgO	3.36	3.01	2.86	3.08	3.14	3.23	3.47	3.52	3.39	3.53	3.28	3.50
FeO	24.78	25.07	25.64	26.34	25.86	25.98	25.44	25.04	25.41	25.01	25.55	25.50
MnO	1.29	1.32	1.19	1.00	1.10	1.11	1.32	1.31	1.20	1.26	1.17	1.22
CaO	10.28	10.21	10.03	9.76	10.02	9.58	9.71	9.68	9.56	9.75	9.52	9.48
Na2O	0.05	0.01	0.04	0.01	0.05	0.04	0.02	0.04	0.02	0.01	0.04	0.04
K2O	0.01	0.00	0.01	0.00	0.00	0.00	0.00	0.01	0.00	0.00	0.00	0.00
Sum	99.78	99.53	99.33	99.54	99.96	99.71	99.33	99.30	99.17	99.18	99.81	98.90
Si	3.00	2.98	2.99	3.01	3.01	3.00	3.01	3.00	2.99	3.00	2.98	3.01
Ti	0.01	0.01	0.01	0.00	0.01	0.01	0.01	0.00	0.00	0.00	0.01	0.01
Al	1.91	1.90	1.92	1.92	1.91	1.92	1.93	1.93	1.94	1.92	1.92	1.92
Fe3	0.08	0.12	0.09	0.05	0.07	0.08	0.04	0.08	0.08	0.08	0.12	0.05
Mg	0.40	0.36	0.34	0.36	0.37	0.38	0.41	0.42	0.40	0.42	0.39	0.42
Fe2	1.64	1.67	1.71	1.75	1.71	1.72	1.69	1.66	1.69	1.66	1.69	1.70
Mn	0.09	0.09	0.08	0.07	0.07	0.07	0.09	0.09	0.08	0.09	0.08	0.08
Ca	0.87	0.87	0.86	0.83	0.85	0.81	0.83	0.82	0.82	0.83	0.81	0.81
Na	0.01	0.00	0.01	0.00	0.01	0.01	0.00	0.01	0.00	0.00	0.01	0.01
K	0.00	0.00	0.00	0.00	0.00	0.00	0.00	0.00	0.00	0.00	0.00	0.00
Sum	8.00	8.00	8.00	8.00	8.00	8.00	8.00	8.00	8.00	8.00	8.00	8.00
XMg	0.20	0.18	0.17	0.17	0.18	0.18	0.20	0.20	0.19	0.20	0.19	0.20
XFe	0.81	0.82	0.83	0.83	0.82	0.82	0.80	0.80	0.81	0.80	0.81	0.80
Xalm	0.55	0.56	0.57	0.58	0.57	0.58	0.56	0.56	0.57	0.55	0.57	0.57
Xprp	0.13	0.12	0.11	0.12	0.12	0.13	0.14	0.14	0.13	0.14	0.13	0.14
Xgrs	0.29	0.29	0.29	0.28	0.28	0.27	0.27	0.28	0.27	0.28	0.27	0.27
Xsps	0.03	0.03	0.03	0.02	0.02	0.02	0.03	0.03	0.03	0.03	0.03	0.03

Ilmenite			
	NC5A-02-15	*NC5A-01-28*	*NC5A-04-05*
SiO2	0.01	0.04	0.00
TiO2	47.68	50.48	52.09
Al2O3	0.05	0.01	0.00
Fe2O3	9.19	4.54	0.93
MgO	0.18	0.26	0.00
FeO	40.77	43.98	45.95
MnO	1.64	0.76	0.83
CaO	0.12	0.15	0.03
Na2O	0.00	0.00	0.00
K2O	0.00	0.01	0.00
Sum	99.64	100.22	99.84
Si	0.00	0.00	0.00
Ti	0.91	0.96	0.99
Al	0.00	0.00	0.00
Fe3	0.18	0.09	0.02
Mg	0.01	0.01	0.00
Fe2	0.87	0.93	0.97
Mn	0.04	0.02	0.02
Ca	0.00	0.00	0.00
Na	0.00	0.00	0.00
K	0.00	0.00	0.00
Sum	2.00	2.00	2.00
Xil	0.87	0.93	0.97
Xhm	0.09	0.04	0.01
Xgk	0.01	0.01	0.00
Xpy	0.04	0.02	0.02

Supplementary Table II.1.4: Non-exhaustive summary of the trace element analyses in garnet trend 1 and 2). Trace element contents are normalized to chondrite after Boyton (1984). Bdl – below detection limit.

trace element content (ppm)

	distance (µm)	La	Ce	Pr	Nd	Sm	Eu	Gd	Tb	Dy	Ho	Er	Yb	Lu	Y	Zr
garnet profile A	0	bdl	0.07	bdl	0.96	4.77	2.97	19.15	5.74	54.10	11.55	33.73	27.42	3.91	336.39	1.20
	60	bdl	bdl	0.11	1.27	6.17	3.43	18.61	6.27	55.63	13.13	36.00	31.07	3.49	369.89	4.56
	120	bdl	0.06	0.05	1.53	8.07	3.31	24.50	6.53	58.39	14.27	43.01	37.84	3.94	412.68	1.46
	180	bdl	0.11	0.04	1.32	4.53	3.92	25.34	5.75	65.58	12.68	32.01	25.43	3.08	358.76	2.80
	240	bdl	0.11	0.09	0.78	3.28	4.19	27.24	6.56	50.88	10.52	22.81	12.14	1.50	289.63	4.64
	300	bdl	0.05	0.09	2.86	4.44	4.80	30.65	7.29	65.49	11.58	26.81	15.47	1.71	332.29	5.40
	360	bdl	bdl	0.08	2.55	5.82	3.71	31.57	8.34	62.79	12.37	25.31	25.49	2.38	321.90	8.39
	420	bdl	bdl	0.04	1.83	7.45	2.82	26.66	8.02	63.63	11.36	25.58	22.46	2.99	332.02	5.97
	480	bdl	0.05	0.08	0.49	3.36	1.97	17.23	5.18	65.40	16.54	44.34	39.20	5.01	389.16	3.19
	540	bdl	0.05	0.13	0.53	2.10	2.11	17.68	5.85	60.84	16.11	54.50	43.16	6.77	436.34	1.89
	600	bdl	0.05	0.04	0.71	4.35	1.69	15.45	5.13	47.00	9.36	28.45	24.92	3.53	295.08	3.74
	660	bdl	bdl	0.04	2.03	4.35	2.90	18.08	5.04	41.50	8.37	23.14	17.11	2.10	243.03	3.21
	720	bdl	0.05	0.04	1.21	2.20	2.16	25.15	5.43	46.34	9.44	24.47	19.63	2.44	273.38	4.62
	780	bdl	0.16	0.04	1.72	3.64	1.74	18.81	6.52	65.10	15.55	49.39	52.57	7.75	450.84	3.27
	840	bdl	bdl	0.04	1.39	1.59	2.15	18.28	5.69	55.86	14.14	44.44	36.91	6.98	413.14	3.65
	900	bdl	bdl	0.08	2.41	5.49	2.82	17.91	5.67	52.74	10.93	31.80	19.76	1.87	312.16	1.81
	960	bdl	0.09	bdl	2.16	3.94	3.06	23.65	5.66	42.72	9.63	25.99	18.06	3.09	256.41	4.42
	1020	bdl	bdl	0.12	0.92	2.10	3.48	23.52	6.15	46.36	8.72	23.35	16.95	2.45	234.02	4.33
	1080	bdl	0.16	bdl	1.50	5.41	3.54	24.96	6.23	51.57	10.42	30.18	21.09	1.94	289.86	4.27
	1140	bdl	0.05	0.04	0.89	2.03	2.33	23.68	6.39	53.65	14.73	30.93	26.90	2.96	349.71	2.82
	1200	bdl	0.10	0.16	2.37	3.78	2.55	19.62	6.20	63.45	14.39	42.59	31.71	4.63	420.86	3.24
	1260	bdl	0.09	0.11	1.53	5.49	2.97	22.10	5.29	49.38	10.93	30.28	16.43	1.95	293.65	2.39

trace element content normalized to chondrite

	distance (µm)	LaN	CeN	PrN	NdN	SmN	EuN	GdN	TbN	DyN	HoN	ErN	YbN	LuN	Eu/Eu*	LuN/SmN
garnet profile A	0		0.1		1.6	24.5	40.5	73.9	121.1		160.9	160.6	131.2	121.3	1.0	5.0
	60			0.9	2.1	31.7	46.7	71.8	132.2	172.8	182.9	171.5	148.7	108.3	1.0	3.4
	120		0.1	0.4	2.6	41.4	45.1	94.6	137.7	181.3	198.7	204.8	181.1	122.3	0.7	3.0
	180		0.1	0.4	2.2	23.2	53.3	97.8	121.2	203.7	176.6	152.4	121.7	95.6	1.1	4.1
	240		0.1	0.7	1.3	16.8	57.0	105.2	138.5	158.0	146.6	108.6	58.1	46.5	1.4	2.8
	300		0.1	0.7	4.8	22.8	65.3	118.4	153.7	203.4	161.4	127.7	74.0	53.0	1.3	2.3
	360			0.6	4.3	29.8	50.5	121.9	176.0	195.0	172.4	120.5	122.0	74.0	0.8	2.5
	420			0.4	3.1	38.2	38.3	102.9	169.2	197.6	158.2	121.8	107.4	93.0	0.6	2.4
	480		0.1	0.7	0.8	17.2	26.8	66.5	109.3	203.1	230.4	211.2	187.6	155.7	0.8	9.0
	540		0.1	1.1	0.9	10.8	28.8	68.3	123.5	189.0	224.3	259.5	206.5	210.1	1.1	19.5
	600		0.1	0.3	1.2	22.3	23.0	59.6	108.3	146.0	130.4	135.5	119.2	109.8	0.6	4.9
	660			0.3	3.4	22.3	39.4	69.8	106.3	128.9	116.6	110.2	81.9	65.1	1.0	2.9
	720		0.1	0.3	2.0	11.3	29.3	97.1	114.5	143.9	131.5	116.5	94.0	75.8	0.9	6.7
	780		0.2	0.3	2.9	18.7	23.7	72.6	137.5	202.2	216.5	235.2	251.5	240.7	0.6	12.9
	840			0.3	2.3	8.1	29.2	70.6	120.1	173.5	197.0	211.6	176.6	216.7	1.2	26.6
	900			0.7	4.0	28.2	38.3	69.1	119.6	163.8	152.3	151.4	94.6	57.9	0.9	2.1
	960		0.1		3.6	20.2	41.6	91.3	119.4	132.7	134.2	123.7	86.4	96.1	1.0	4.8
	1020			1.0	1.5	10.8	47.3	90.8	129.7	144.0	121.4	111.2	81.1	76.0	1.5	7.1
	1080		0.2	0.0	2.5	27.8	48.2	96.4	131.5	160.2	145.1	143.7	100.9	60.1	0.9	2.2
	1140		0.1		1.5	10.4	31.7	91.4	134.8	166.6	205.2	147.3	128.7	92.1	1.0	8.9
	1200		0.1	1.3	3.9	19.4	34.7	75.7	130.8	197.1	200.5	202.8	151.7	143.7	0.9	7.4
	1260		0.1	0.9	2.6	28.2	40.4	85.3	111.6	153.4	152.3	144.2	78.6	60.7	0.8	2.2

trace element content (ppm)

	distance (µm)	La	Ce	Pr	Nd	Sm	Eu	Gd	Tb	Dy	Ho	Er	Yb	Lu	Y	Zr
	4	bdl	0.0	bdl	0.5	5.5	3.7	17.2	4.8	40.7	7.5	20.2	15.2	2.3	193.8	2.3
	60	bdl	0.1	0.0	1.4	3.8	3.2	16.3	4.7	42.1	9.3	24.1	21.1	2.6	202.3	2.1
	120	bdl	bdl	bdl	0.2	3.2	3.4	15.7	3.6	34.4	7.9	28.9	21.8	3.3	199.8	2.2
	180	bdl	0.0	0.1	0.5	1.3	2.5	10.8	2.7	21.8	6.0	20.4	16.9	2.9	148.8	3.0
	244	bdl	0.0	0.0	0.2	0.5	1.7	7.1	1.4	14.4	4.4	13.8	11.3	1.7	118.1	2.1
	316	bdl	0.1	0.0	0.2	0.3	0.6	3.4	0.9	7.3	2.4	8.5	6.9	1.0	55.1	4.1
	376	bdl	bdl	0.0	0.0	0.3	0.6	2.7	0.6	7.6	2.1	7.8	7.0	1.1	60.6	3.0
	436	bdl	0.1	bdl	bdl	1.1	1.0	3.6	1.1	12.4	3.1	10.0	12.2	2.0	72.5	2.2
	508	bdl	0.0	bdl	0.4	1.0	1.4	7.3	1.4	12.7	3.9	14.4	18.0	2.7	111.5	3.2
	556	bdl	0.1	0.0	1.1	1.7	2.2	6.5	1.7	16.9	4.5	17.9	24.2	2.9	130.9	2.7
	616	bdl	bdl	bdl	0.7	1.0	1.3	5.3	1.6	14.2	3.8	14.3	16.3	2.7	106.6	3.5
	692	bdl	bdl	0.0	1.2	1.8	1.1	1.2	0.8	8.0	2.0	3.6	5.0	0.8	45.4	6.8
	752	bdl	0.0	bdl	0.2	0.5	0.7	3.2	0.6	8.1	1.4	6.3	4.7	0.7	41.5	4.9
	804	bdl	0.1	bdl	1.2	1.3	0.9	2.2	0.9	7.4	2.3	7.7	6.5	1.3	51.0	5.3
garnet profile D	856	bdl	bdl	bdl	0.9	2.1	0.7	6.2	1.2	13.4	3.1	10.4	12.4	2.5	78.5	4.3
	924	bdl	bdl	bdl	bdl	1.7	1.1	5.8	1.2	18.6	5.1	14.0	19.9	3.5	115.4	3.7
	984	bdl	0.0	bdl	0.7	1.8	2.2	7.1	1.8	14.6	5.2	15.6	19.4	3.1	101.9	5.4
	1032	bdl	bdl	bdl	1.1	0.8	1.0	3.3	0.9	11.2	2.7	10.9	9.6	1.8	79.5	3.0
	1092	bdl	0.2	bdl	1.1	1.5	1.3	4.6	1.3	11.1	2.2	8.1	9.8	1.6	71.4	3.6
	1172	bdl	0.0	bdl	1.1	1.0	0.9	3.4	0.8	9.6	2.5	7.7	10.0	1.5	72.8	4.6
	1220	bdl	0.0	bdl	0.4	0.5	1.2	3.6	1.3	13.5	3.2	9.7	9.1	1.8	70.9	4.3
	1280	bdl	0.1	bdl	bdl	2.2	1.1	4.2	1.3	12.7	3.2	7.6	10.8	1.8	78.1	3.2
	1340	bdl	0.0	0.0	0.4	1.2	1.5	4.5	1.2	11.1	3.7	13.0	16.4	2.3	90.2	3.5
	1404	bdl	bdl	bdl	0.2	bdl	1.3	6.0	1.5	13.0	3.5	13.7	16.8	3.1	102.1	3.6
	1468	bdl	0.1	0.1	1.0	1.2	1.5	5.5	1.8	15.7	3.8	17.4	18.1	2.5	125.7	3.2
	1516	bdl	0.1	bdl	0.7	1.7	1.1	4.9	1.8	15.6	3.8	13.9	15.1	1.9	105.1	2.8
	1572	bdl	bdl	0.0	0.2	0.2	0.8	3.7	1.3	11.1	3.0	8.0	10.5	1.4	65.5	3.0
	1628	bdl	bdl	0.0	bdl	bdl	0.8	3.1	0.7	7.1	2.0	7.0	7.8	1.4	53.3	2.1
	1688	bdl	bdl	0.1	bdl	0.5	0.4	2.1	0.5	5.2	1.7	7.3	7.1	0.8	49.0	2.4
	1752	bdl	0.0	bdl	bdl	0.5	0.5	2.8	0.8	8.2	2.4	6.7	5.2	1.3	51.7	2.8
	1804	bdl	0.1	0.0	1.8	1.5	1.7	9.1	2.0	17.3	4.9	13.2	13.2	1.6	118.0	1.9

trace element content normalized to chondrite

	distance (µm)	LaN	CeN	PrN	NdN	SmN	EuN	GdN	TbN	DyN	HoN	ErN	YbN	LuN	Eu/Eu*	LuN/SmN
	4		0.1		0.8	28.4	50.4	66.4	100.6	126.4	104.1	96.0	72.8	71.4	1.2	2.5
	60		0.1	0.3	2.4	19.6	44.1	62.8	99.3	130.7	129.8	114.9	101.1	80.1	1.3	4.1
	120				0.4	16.4	46.2	60.5	75.0	106.8	110.1	137.5	104.1	101.8	1.5	6.2
	180				0.8	6.7	33.8	41.5	57.9	67.6	83.9	97.2	81.0	91.6	2.0	13.7
	244			0.3	0.4	2.8	23.0	27.4	28.9	44.6	61.8	65.9	54.0	53.8	2.7	19.5
	316		0.1	0.3	0.4	1.3	7.7	13.1	18.0	22.6	33.0	40.4	33.1	30.0	1.9	23.1
	376			0.3		1.3	8.8	10.5	13.7	23.5	29.4	37.3	33.7	33.0	2.4	24.9
	436		0.1			5.6	13.2	13.9	23.8	38.4	42.6	47.8	58.4	61.0	1.5	10.8
	508		0.1		0.7	5.2	19.6	28.3	30.6	39.3	53.7	68.8	85.9	84.0	1.6	16.2
	556		0.2	0.3	1.8	9.0	29.5	25.2	36.6	52.3	63.3	85.2	115.7	89.7	2.0	10.0
	616				1.1	5.3	18.2	20.6	32.9	44.1	52.5	67.9	78.0	85.0	1.7	16.0
	692		0.1		0.4	2.6	10.5	16.9	21.7	24.9	20.6	19.1	24.1	26.3	1.6	10.0
	752				1.1	6.3	6.4	11.6	19.9	29.1	28.4	26.8	22.3	21.7	0.7	3.4
	804			0.3	0.8		12.4	11.2	14.9	23.8	29.2	28.5	31.2	32.2		
garnet profile D	856		0.4	0.3		2.8	23.2	16.7	28.3	31.6	43.9	37.4	59.3	63.0		22.7
	924		0.1		1.2	8.3	32.0	35.2	30.4	53.4	68.7	78.0	95.1	122.4	1.9	14.7
	984		0.1		1.2	9.5	30.2	27.6	37.1	45.2	72.6	74.3	92.9	96.0	1.9	10.1
	1032				1.9	3.9	14.2	12.9	19.2	34.8	37.6	51.8	46.0	56.7	2.0	14.5
	1092		0.3		1.8	7.6	18.2	17.8	27.0	34.4	30.8	38.4	46.8	50.1	1.6	6.6
	1172		0.1		1.9	5.3	12.5	13.1	17.3	29.7	35.2	36.8	47.7	48.1	1.5	9.0
	1220		0.1		0.7	2.6	16.1	13.9	28.1	41.8	44.3	46.2	43.6	56.8	2.7	21.9
	1280		0.1			11.1	15.0	16.4	28.2	39.3	44.1	36.1	51.5	55.1	1.1	5.0
	1340		0.1	0.3	0.7	6.2	20.7	17.6	24.5	34.3	52.1	61.7	78.7	70.8	2.0	11.3
	1404				0.4		18.0	23.1	32.4	40.3	49.2	65.4	80.2	95.7		
	1468		0.2	0.6	1.7	6.0	20.8	21.2	37.9	48.9	53.5	83.0	86.7	79.1	1.8	13.2
	1516		0.1		1.1	8.9	14.7	18.8	38.6	48.6	53.2	66.0	72.2	59.6	1.1	6.7
	1572			0.3	0.3	1.2	11.3	14.5	27.2	34.6	41.7	38.1	50.1	43.6	2.8	37.3
	1628			0.3			10.3	11.9	14.6	22.0	27.6	33.2	37.3	43.3		
	1688			0.6		2.5	5.5	8.0	9.9	16.0	23.4	34.7	33.8	26.1	1.2	10.5
	1752		0.1			2.6	7.5	10.9	17.5	25.6	33.6	32.0	24.8	39.7	1.4	15.5
	1804		0.1	0.3	2.9	7.7	23.0	35.1	42.3	53.6	68.1	63.1	63.4	49.4	1.4	6.4

Supplementary Table II.1.5: Summary of the trace element analyses in zircon, with the analyzed texture specified. Trace element contents are normalized to chondrite after Sun and McDonough (1989). Bdl – below detection limit.

Label	NC5A1 19	NC5A1 7	NC5A1 14	NC5A1 11	NC5A1 08b	NC5A1 32B	NC5A 18	NC5A1 - 20	NC5A1 8	NC5A1 24	NC5A1 22	NC5A1 21	NC5A1 42b	NC5A1 23	NC5A 10b
CL texture	*light*	*dark*	*dark*	*dark*	*dark*	*light*	*light*	*dark*	*dark*	*dark*	*dark*	*dark*	*light*	*light*	*dark*
Trace element content (ppm)															
Y	527.25	1252.21	1245.09	1027.80	784.85	390.30	567.42	873.98	460.71	570.63	612.36	1376.71	69.55	153.93	448.41
La	bdl	bdl	bdl	0.02	0.01	bdl	bdl	0.01	bdl	bdl	bdl	0.01	bdl	0.01	bdl
Ce	1.08	1.99	1.95	2.02	1.17	1.03	0.95	0.98	1.05	0.84	1.90	2.20	0.77	1.55	1.19
Pr	0.07	0.16	0.19	0.09	0.04	0.02	0.11	0.10	0.07	0.08	0.09	0.13	0.08	0.08	0.07
Nd	0.41	1.46	1.84	1.32	0.80	0.28	0.75	0.78	0.25	0.87	0.77	0.68	0.08	0.24	0.30
Sm	1.51	3.59	4.34	2.89	1.82	0.72	1.27	2.36	0.68	1.17	2.22	1.97	0.30	0.86	0.70
Eu	0.39	1.10	1.40	1.07	0.72	0.33	0.60	1.04	0.37	0.63	1.18	1.31	0.20	0.67	0.47
Gd	9.42	20.43	24.75	16.77	11.75	5.58	9.98	15.16	6.06	9.57	13.47	16.65	1.93	7.29	3.93
Tb	3.48	7.49	8.92	6.65	4.71	2.12	3.80	5.52	2.51	3.88	4.59	6.16	0.66	2.35	1.76
Dy	45.52	97.38	112.12	81.52	62.26	29.07	48.92	72.29	36.68	48.43	55.14	94.14	7.17	19.78	29.30
Ho	17.81	40.71	43.08	34.22	25.07	12.22	20.12	30.53	15.78	20.82	20.84	42.95	2.31	5.22	13.77
Er	91.00	210.01	207.85	178.60	125.58	63.90	96.80	151.62	83.24	102.58	102.86	241.32	8.58	15.19	88.02
Tm	19.70	47.09	43.45	39.24	26.22	14.58	20.66	32.20	18.68	21.68	21.44	53.88	1.41	2.32	23.81
Yb	188.97	458.62	410.27	393.45	251.56	150.14	200.47	320.81	184.10	223.28	213.54	554.78	11.46	17.19	273.09
Lu	37.86	93.79	80.01	80.71	50.40	33.00	40.21	63.74	39.03	46.14	39.23	103.98	1.98	2.98	62.05
U	13.95	94.58	36.2	62.02	19.88	19.01	11.23	17.03	23.23	13.24	38.81	106.88	2.5	8.45	116.31

Label	NC5A15	NC5A11	NC5A1 2	NC5A115	NC5A118c	NC5A13	NC5A125B	NC5A113	NC5A128B	NC5A117	NC5A126	NC5A112	NC5A19	NC5A110
CL texture	*light*	*dark*	*light*	*light*	*dark*	*light*	*light*	*light*	*light*	*light*	*light*	*dark*	*dark*	*dark*
Trace element content (ppm)														
Y	92.38	708.63	303.29	103.83	578.51	314.92	248.24	139.42	132.48	276.46	151.76	402.67	1548.32	1060.14
La	bdl	0.01	0.01	bdl	0.01	bdl	bdl	0.01	bdl	0.01	0.00	bdl	0.01	bdl
Ce	1.38	0.62	0.37	1.08	0.45	3.82	2.50	2.58	0.86	0.58	0.92	0.15	0.97	0.84
Pr	0.06	0.13	0.09	0.12	0.04	0.07	0.02	0.11	0.01	0.04	0.01	0.03	0.17	0.11
Nd	0.18	0.82	0.20	0.23	0.54	0.63	0.37	0.56	0.16	0.09	0.15	0.06	1.37	1.07
Sm	0.67	1.68	0.37	0.42	1.19	2.38	1.06	1.73	0.46	0.19	0.38	0.28	4.33	2.61
Eu	0.45	1.34	0.30	0.36	0.99	2.15	0.98	1.39	0.50	0.20	0.46	0.38	8.48	5.21
Gd	3.26	11.40	2.35	2.86	7.70	17.99	7.79	9.10	3.46	1.25	3.20	1.88	36.41	14.71
Tb	1.21	4.49	1.41	1.05	3.27	5.28	2.57	2.22	1.19	0.87	1.30	1.13	13.38	6.51
Dy	11.91	61.60	20.74	10.94	45.27	44.51	26.76	19.12	12.98	16.42	14.01	21.41	157.99	89.58
Ho	3.08	24.83	10.05	3.46	18.66	9.93	7.68	4.50	4.03	8.92	4.55	12.84	56.62	35.74
Er	10.62	129.36	57.81	12.67	99.56	27.12	27.45	14.90	15.53	60.42	16.66	92.99	291.34	205.70
Tm	1.48	29.90	14.60	1.92	23.09	3.44	4.33	1.99	2.68	20.49	3.05	36.13	79.63	60.93
Yb	13.18	304.30	164.83	15.66	245.79	18.61	32.08	17.42	23.43	308.05	25.77	562.68	987.30	793.87
Lu	1.97	65.32	38.55	2.79	52.91	2.60	5.51	2.95	4.14	77.78	5.01	145.68	207.20	178.29
U	8.36	70.63	41.1	5.19	56.57	28.8	24.21	24.95	5.54	89.55	5.16	130.6	393.31	241.88

Label	NC5A1 19	NC5A1 7	NC5A1 14	NC5A1 11	NC5A1 08b	NC5A1 32B	NC5A 18	NC5A1 - 20	NC5A1 8	NC5A1 24	NC5A1 22	NC5A1 21	NC5A1 42b	NC5A1 23	NC5A 10b
CL texture	*light*	*dark*	*dark*	*dark*	*dark*	*light*	*light*	*dark*	*dark*	*dark*	*dark*	*dark*	*light*	*light*	*dark*
Trace element content normalised to chondrite (after Sun and McDonough (1989))															
LaN	bdl	bdl	bdl	0.08	0.02	0.01	bdl	0.03	0.01	bdl	bdl	0.06	0.02	0.04	bdl
CeN	1.77	3.25	3.19	3.30	1.91	1.69	1.55	1.61	1.72	1.37	3.10	3.59	1.26	2.53	1.94
PrN	0.69	1.64	1.95	0.96	0.39	0.20	1.17	1.01	0.73	0.79	0.95	1.37	0.80	0.81	0.73
NdN	0.89	3.13	3.94	2.83	1.71	0.59	1.61	1.67	0.54	1.86	1.65	1.46	0.16	0.52	0.63
SmN	9.87	23.46	28.37	18.89	11.90	4.73	8.30	15.42	4.41	7.65	14.51	12.88	1.94	5.62	4.58
EuN	6.76	18.88	24.14	18.40	12.41	5.76	10.31	17.93	6.29	10.90	20.34	22.59	3.45	11.55	8.09
GdN	45.84	99.42	120.44	81.61	57.18	27.15	48.56	73.77	29.49	46.57	65.55	81.02	9.39	35.47	19.12
TbN	93.05	200.27	238.50	177.81	125.94	56.71	101.60	147.59	67.11	103.74	122.73	164.71	17.70	62.83	47.06
DyN	179.21	383.39	441.42	320.94	245.12	114.45	192.60	284.61	144.41	190.67	217.09	370.63	28.23	77.87	115.35
HoN	314.66	719.26	761.13	604.59	442.93	215.90	355.48	539.40	278.80	367.84	368.20	758.83	40.81	92.23	243.29
ErN	549.85	1268.94	1255.89	1079.15	758.79	386.10	584.89	916.13	502.96	619.82	621.51	1458.13	51.84	91.78	531.84
TmN	772.55	1846.67	1703.92	1538.82	1028.24	571.76	810.20	1262.75	732.55	850.20	840.78	2112.94	55.29	90.98	933.73
YbN	1111.59	2697.76	2413.35	2314.41	1479.76	883.18	1179.24	1887.12	1082.94	1313.41	1256.12	3263.41	67.41	101.12	1606.41
LuN	1490.55	3692.52	3150.00	3177.56	1984.25	1299.21	1583.07	2509.45	1536.61	1816.54	1544.49	4093.70	77.95	117.32	2442.91
Eu/Eu*	0.32	0.39	0.41	0.47	0.48	0.51	0.51	0.53	0.55	0.58	0.66	0.70	0.81	0.82	0.86
Ce/Ce*				11.64	19.62	47.61		8.99	17.54			12.83	10.47	14.85	
LuN/SmN	151.03	157.37	111.05	168.22	166.81	274.94	190.72	162.69	348.30	237.55	106.44	317.94	40.16	20.87	533.95
YbN/GdN	29.31	32.80	24.22	34.28	31.28	39.32	29.35	30.92	44.39	34.09	23.17	48.69	8.68	3.45	101.54

Label	NC5A15	NC5A11	NC5A1 2	NC5A115	NC5A118c	NC5A13	NC5A125B	NC5A113	NC5A128B	NC5A117	NC5A126	NC5A112	NC5A19	NC5A110
CL texture	*light*	*dark*	*light*	*light*	*dark*	*light*	*light*	*light*	*light*	*light*	*light*	*dark*	*dark*	*dark*
Trace element content normalised to chondrite (after Sun and McDonough (1989))														
LaN	bdl	0.05	0.04	bdl	0.03	bdl	bdl	0.02	bdl	0.03	0.01	bdl	0.04	bdl
CeN	2.25	1.01	0.61	1.76	0.74	6.24	4.08	4.22	1.41	0.95	1.50	0.24	1.58	1.37
PrN	0.64	1.35	0.98	1.29	0.47	0.78	0.22	1.16	0.11	0.43	0.09	0.34	1.78	1.16
NdN	0.38	1.76	0.42	0.50	1.15	1.36	0.78	1.21	0.34	0.20	0.31	0.13	2.93	2.29
SmN	4.39	10.98	2.41	2.73	7.75	15.56	6.90	11.31	2.97	1.27	2.48	1.83	28.30	17.06
EuN	7.76	23.10	5.09	6.12	17.09	37.07	16.86	23.97	8.57	3.52	7.91	6.62	146.21	89.83
GdN	15.86	55.47	11.44	13.92	37.47	87.54	37.91	44.28	16.84	6.08	15.57	9.15	177.18	71.58
TbN	32.46	120.05	37.59	28.10	87.43	141.18	68.72	59.36	31.68	23.32	34.79	30.21	357.75	174.06
DyN	46.89	242.52	81.65	43.07	178.23	175.24	105.35	75.28	51.10	64.65	55.16	84.29	622.01	352.68
HoN	54.42	438.69	177.56	61.13	329.68	175.44	135.69	79.51	71.20	157.60	80.39	226.86	1000.35	631.45
ErN	64.17	781.63	349.31	76.56	601.57	163.87	165.86	90.03	93.84	365.08	100.66	561.87	1760.36	1242.90
TmN	58.04	1172.55	572.55	75.29	905.49	134.90	169.80	78.04	105.10	803.53	119.61	1416.86	3122.75	2389.41
YbN	77.53	1790.00	969.59	92.12	1445.82	109.47	188.71	102.47	137.82	1812.06	151.59	3309.88	5807.65	4669.82
LuN	77.56	2571.65	1517.72	109.84	2083.07	102.36	216.93	116.14	162.99	3062.20	197.24	5735.43	8157.48	7019.29
Eu/Eu*	0.93	0.94	0.97	0.99	1.00	1.00	1.04	1.07	1.21	1.27	1.27	1.62	2.06	2.57
Ce/Ce*		4.08	3.29		6.40			25.72		8.03	66.65		6.23	
LuN/SmN	17.66	234.20	631.01	40.30	268.73	6.58	31.43	10.27	54.81	2415.04	79.42	3134.00	288.24	411.48
YbN/GdN	5.91	39.01	102.49	8.00	46.64	1.51	6.02	2.80	9.90	360.11	11.77	437.35	39.62	78.86

Further discussion

Zr-in-rutile and Zr-in-Titanite to constrain the path of Najac Klippe's eclogite (French Massif Central)

Trace element thermometers are an useful tool when it comes to decipher the P-T-t path of metamorphic rocks. This complementary discussion brings preliminary results, based on rutile and titanite thermometers, on the P-T evolution of the NC5A sample discussed in the previous paper.

Rutile in the NC5A sample occurs in two textural positions: as inclusion, in garnet or in omphacite, or as large mineral in the matrix. It is commonly surrounded by ilmenite (Fig II.1.12B, F). Ilmenite is commonly dispersed in the matrix (Fig. II.1.12A, B). Titanite grains occur in three textural positions, in garnet fractures (Fig. II.1.12D, E), as anhedral grains in the matrix (Fig. II.1.12D), or surrounding ilmenite (Fig. II.1.12C). Finally zircon grains can be enclosed in garnet (Fig. II.1.12F) or dispersed in the matrix (Fig. II.1.12C, F).

According to P-T modelling (Fig. II.1.12G), rutile appears stable in almost all the pseudosections at pressures $P \geq 13$ kbar and temperatures $T \geq 520°C$. Titanite is stable at low temperatures $T \leq \sim 640°C$ and pressures $P \leq 13.5$kbar. As discussed in the previous paper, zircon is interpreted as equilibrating at the beginning of the eclogite facies on the prograde path, at ca. 14-16 kbar. According to petrographic observations, rutile is inferred to be a part of the high pressure assemblage, while titanite and ilmenite formed late during the exhumation stage. This interpretation is validated by P-T modelling (Fig. II.1.12G).

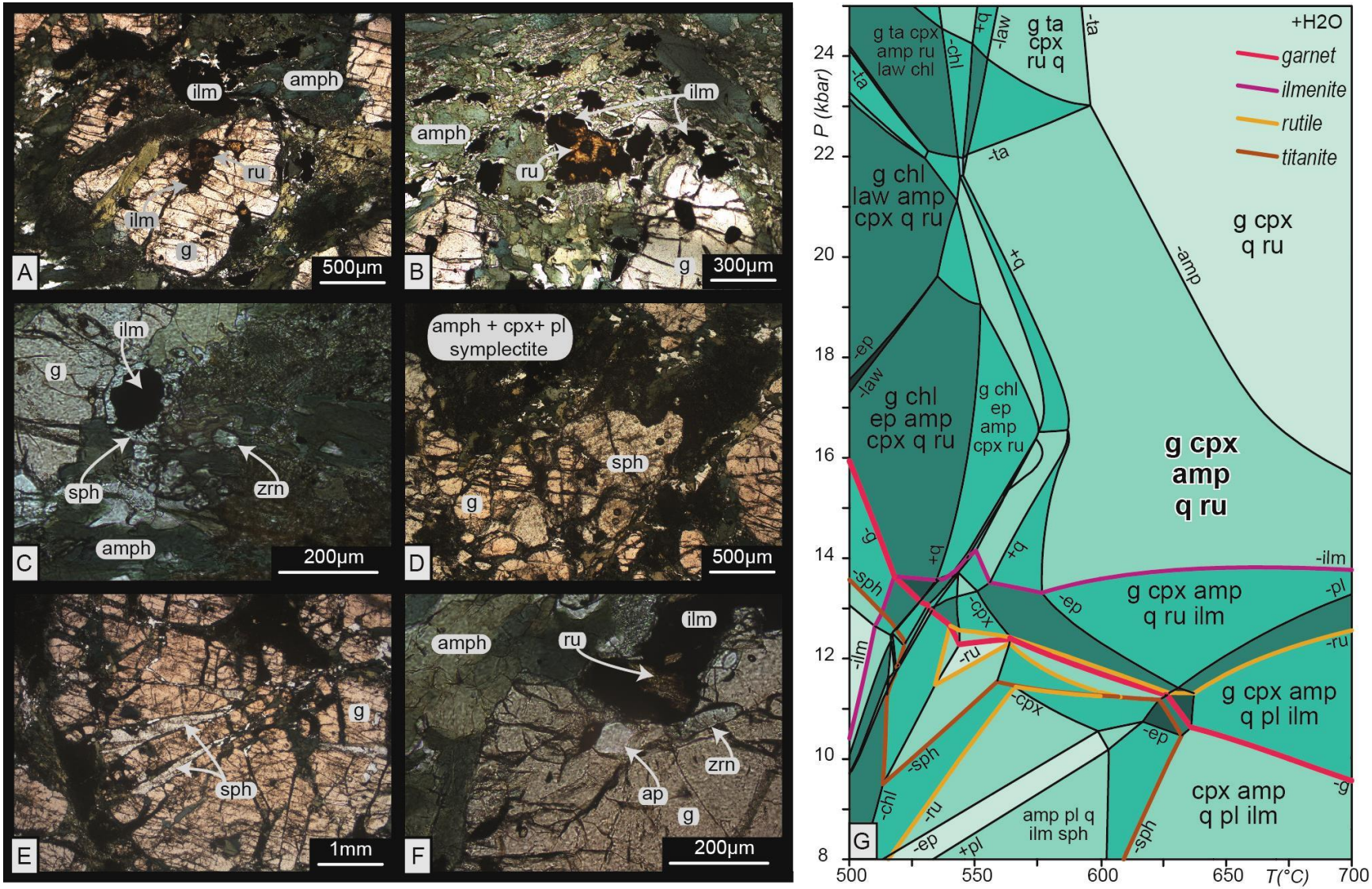

Figure II.1.12 – A, B, C, D, E, F photomicrograph ofNC5A sample. G P-T pseudosection for NC5A sample, with garnet, rutile, ilmenite and titanite appearance/disappearance line highlighted

1. Zr-in-Titanite

The Zirconium-in-titanite thermometer (Zr-in-titanite, Hayden et al. 2008) relies on equilibrium with rutile, quartz and zircon, and is based on the following equation:

$$T = \frac{7708 + 960P}{10.52 - \log(aTiO2) - \log(aSiO2) - \log(ZrSphene)} - 273$$

P – pressure (GPa), ZrSphene – Zr content in ppm, ($aSiO_2$) – quartz activity, set at 1, ($aTiO_2$) – rutile activity, set at 0.75 according to Kohn (2017).

We analyzed 12 grains by 18 spots of 50 µm by in-situ laser ablation inductively coupled plasma mass spectrometry (LA-ICP-MS) at Géosciences Rennes. Titanite grains were analyzed in their different textural positions, in core and rims of the titanite matrix grains, or garnet fractures (Fig. II.1.13). Pressure was constrained according to the P-T modelling and estimated at 10.5 kbar, i.e. the maximum modelled pressure for titanite.

Table II.1.2 : Summary of the Zr(ppm) in titanite results and calculated temperatures

Label	texturale position	Zr (ppm)	error	P input (Gpa)	Calculated temperature (°C)
sph_2	garnet fracture	9.56	0.18	1.05	629
sph_5	garnet fracture	9.54	0.16	1.05	629
sph_6	garnet fracture	13.16	0.28	1.05	642
sph_7	garnet fracture	7.78	0.14	1.05	621
sph_8	matrix	9.75	0.16	1.05	630
sph_9	close to garnet	10.03	0.19	1.05	631
sph_10	*close to matrix*	*24.16*	*0.43*	*1.05*	671
sph_11	*garnet fracture*	*30.79*	*0.56*	*1.05*	679
sph_12	garnet fracture	10.39	0.23	1.05	632
sph_13	garnet fracture	9.14	0.17	1.05	627
sph_14	*garnet fracture*	*20.6*	*1.4*	*1.05*	661
sph_15	*garnet fracture*	*22.72*	*0.41*	*1.05*	665
sph_16	garnet fracture	9.04	0.16	1.05	627
sph_17	garnet fracture	7.99	0.15	1.05	622
sph_18	garnet fracture	10.56	0.22	1.05	633
sph_19	garnet fracture	12.13	0.24	1.05	639
sph_20	matrix	6.91	0.13	1.05	616
sph_21	matrix	6.73	0.14	1.05	615

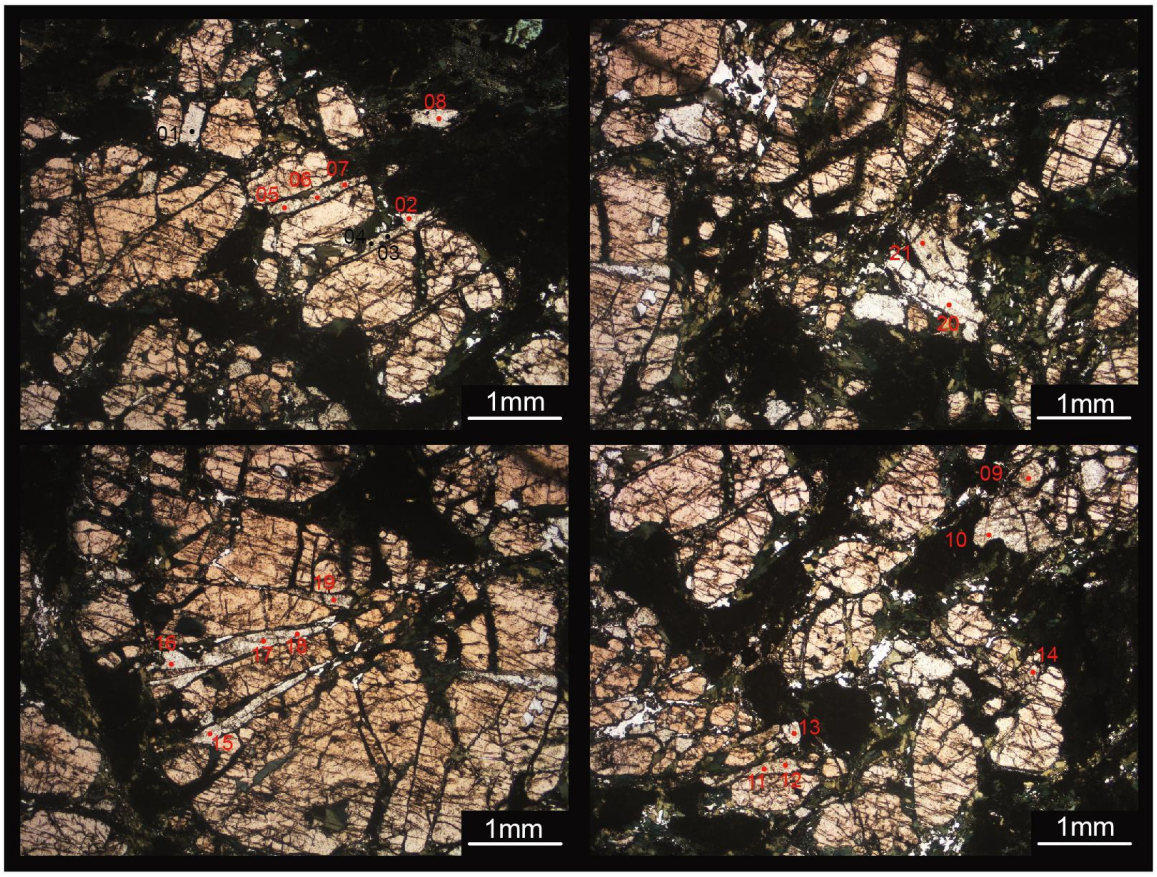

Figure II.1.13 - localization of analytical spots for Zr-in-Titanite thermometry and their analysis number. Black spots and analysis number correspond to rejected data due to low time analysis.

The results can be split in two categories that do not correlate with the textural position of the titanite grains:

(i) Low Zr content, from 6.73 to 13.16 ppm, in 14 titanite grains, that allows to calculate temperatures ranging from 615 to 642°C.

(ii) Moderately high Zr content, from 20.6 to 30.79 ppm, in 4 titanite grains, allowing to calculate temperatures ranging from 661-679°C.

When compared to the pseudosection, the first group of temperatures does correspond to the entrance in the stability field of titanite. The second group of temperatures appears more puzzling, since it yields temperatures (i) not reached by the rock (maximum temperature estimations at 660°C), and (ii) at which titanite is not stable, according to P-T modelling. Various explanations could justify these high temperatures, and should be investigated before further interpretations. First, the stability of titanite may be under-estimated, due to the use of pure pole solid solution. Second, sector zoning can occur in titanite resulting in different partition of trace elements (Hayden et al. 2008). Consequently, the use of the Hayden et al.'s

thermometer calibrated for the {111} crystal face will yield overestimated temperatures (see Hayden et al. 2008, Kohn 2017 for further details).

At the light of these preliminary results, we cannot conclude that the temperatures ranging from 615 to ~640°C may record the crystallization of titanite during the exhumation stage. Further investigation is needed to better constrain the rutile crystallization in the P-T-t history of the rock.

2. Zr-in-rutile

The Zirconium-in-rutile thermometer (Zr-in-rutile, Watson et al. 2006, Thomkins et al. 2007) is based on the following equation:

$$T = \frac{83.9 + 4.10P}{0.1428 - R\ ln(Zr\ Rutile)} - 273$$

P – pressure (GPa), ZrRutile – Zr content in ppm, R – gaz constant 0.0083144 kJ.K^{-1}

This thermometer relies on equilibrium with quartz and zircon. Based on petrographical observations and P-T modelling, rutile appears stable at high pressure, with quartz. The zircon stability has been investigated in the previous paper and is inferred to crystallize/equilibrate on the prograde path, contemporaneously with the garnet. Four rutile grains were analyzed by 20 spots for their Zr content, in different textural positions: enclosed in garnet, at the interface between garnet and matrix, and dispersed in the matrix (Fig.II.1.14). The setting of the spot (center, outer center and rim of the grain) is specified in Table II.1.3.

Rutile grains enclosed in garnet are considered to have equilibrated at the peak metamorphism (15-20 kbar) and consequently a mean pressure of 17 kbar was applied. Rutile grains from the matrix, massively associated with ilmenite, are considered to have re-equilibrated with the matrix during exhumation, and a pressure of 12 kbar (i.e. minimum pressure in the rutile stability field) was applied.

The central part of the rutile grains enclosed in garnet (rutiles 3 and 4) displays the highest Zr content, from ~322 to 350 ppm, while their rim shows a low Zr content ranging from 163 to 327 ppm. They yield temperatures ranging from 678 to 693°C, higher than those estimated for the peak assemblage (560-630°C).

Table II.1.3 : Summary of the Zr(ppm) results and calculated temperatures

Label	texturale position	Zr (ppm)	error	P input (Gpa)	Calculated temperature (°C)
ru2_1	rim	181.8	3.6	1.2	619
ru2_2	outer center	201	3.9	1.2	627
ru2_3	center	219	4.5	1.2	633
ru2_4	rim	188.9	3.8	1.2	622
ru2_5	outer center	216.4	3.9	1.2	632
ru2_6	rim matrix	176.5	3.5	1.2	617
ru3_1	rim	308.9	7	1.7	682
ru3_2	center	335.2	7.1	1.7	689
ru3_3	rim	326.9	7.4	1.7	687
ru3_4	rim	321.2	6.4	1.7	685
ru3_5	center	348.8	7.7	1.7	692
ru3_6	rim	163.1	4.1	1.7	632
ru3_7	outer center	349.3	7.7	1.7	693
ru4_3	center	334.5	7	1.7	689
ru4_4	outer center	322.3	6.5	1.7	686
ru4_5	rim	293.8	6.2	1.7	678
ru5_1	rim	81.9	1.8	1.2	564
ru5_2	rim	84.5	1.9	1.2	566

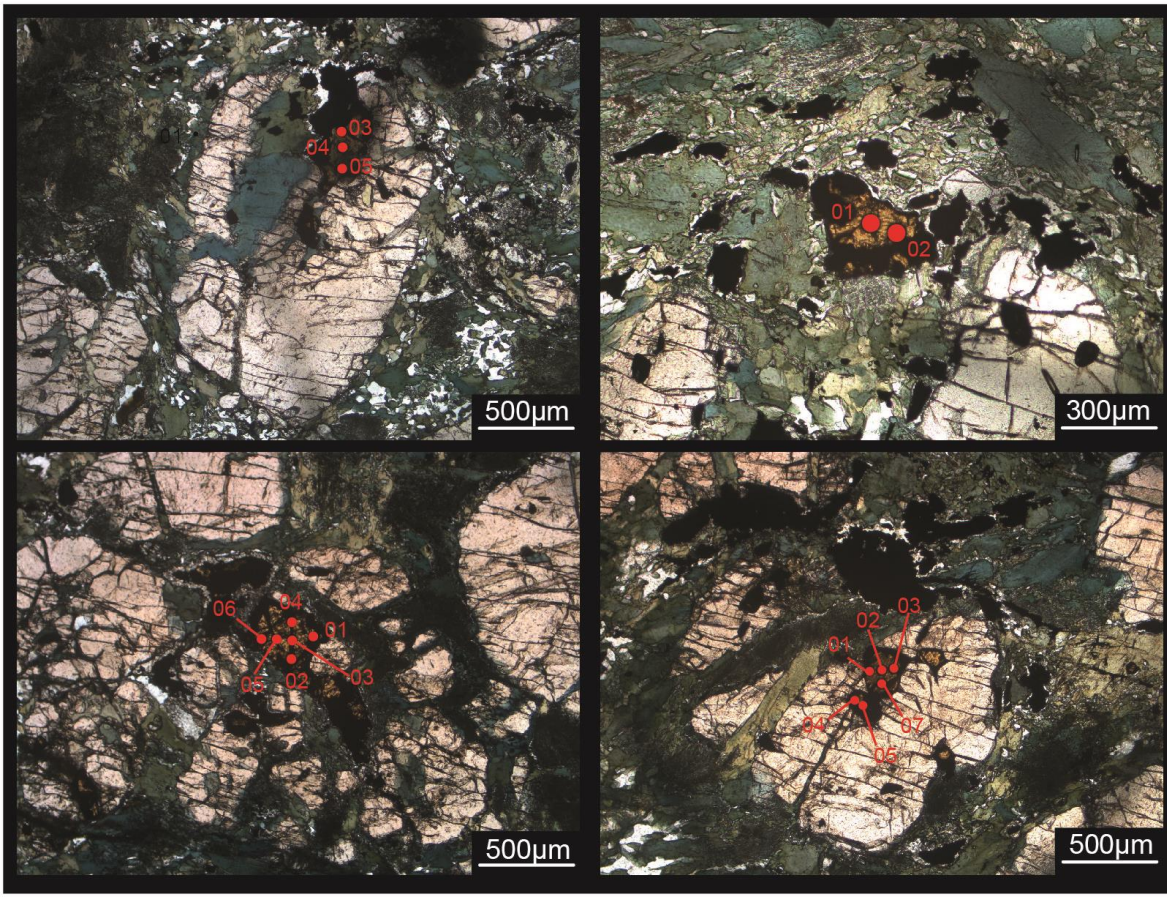

Figure II.1.14 – A, rutile 4, B. rutile 5, C rutile 2 D rutile 3

The large rutile grain in the matrix (rutile 2) displays also higher Zr content in the core (200-219 ppm), while the rim shows low Zr content (~176-190 ppm). The corresponding temperatures are 617-633°C. Finally, the small grain from the matrix displays the lowest Zr content (~82-85 ppm) and the lowest temperatures, between 564 and 566°C.

Different generations of rutile could co-exist, i.e. rutile crystallized at $P \geq 12$kbar and rutile recrystallized at lower pressure and lower temperature on the retrograde path ($T \leq 550$°C and $P \leq 11$ kbar). In particular, the smaller grain (ru5) analyzed in the matrix could reflect such an issue.

The important variability of the Zr content and consequently the temperature, combined with the limited number of rutile grains analyzed does not allow to propose a conclusive interpretation. An additional study on the rutile from this rock is needed, (i) by investigating a higher number of grains in different textural positions and (ii) by decreasing the beam spot to avoid mixing various domains. These preliminary results, nevertheless, suggest a potential over-estimation of the peak temperature reached by this rock.

3. Concluding remarks

These preliminary results need to be investigated by a larger study (higher number of analyses, smaller beam size and elemental maps to highlight potential zoning). They nevertheless seem promising and could precise the exhumation path of the Najac eclogite.

Chapitre 2 - le dôme de la Montagne Noire

Table of content

Preamble

The growth of metamorphic zircon may occur in a large range of pressures and temperatures: during the prograde path, at peak pressures, as well as during decompression or the retrograde path (Rubatto 2017 and references therein). In the absence of other indicators, the link between the growth of a specific zircon crystal and the eclogite-facies conditions can be validated using the analysis of its REE signature. The absence of a Eu anomaly is considered to reflect the growth in a plagioclase-free assemblage, while a flat HREE pattern is considered to reflect a growth in a garnet-bearing assemblage (e.g. Rubatto 2002). Zircon grains exhibiting this peculiar pattern are then supposed to date the eclogite facies.

The Montagne Noire Dome is a massively melted zone in the southern part of the French Massif Central. Numerous studies have dated the migmatization stage between ca. 330 Ma and 290 Ma (e.g. Faure et al. 2010, Roger et al. 2015, Poujol et al. 2017). Eclogites in the Montagne Noire (Demange 1985) are scarce. So far, only two studies have attempted to identify the age of the high-pressure metamorphism, both on samples from the same locality, at Peyrambert - Terme de Fourcaric.

Faure et al. (2014) have dated the eclogite by U-Pb on rutile and zircon, and Sm-Nd on garnet. Two zircon plots and rutile dating yield well-constrained dates of 314 ± 2.5 Ma (N = 12, MSWD = 0.33), 311 ± 2 Ma (N = 24, MSWD = 0.88) and 308 ± 4 Ma (N = 71, MSWD = 2) respectively. The Sm-Nd dating was performed using one garnet, omphacite and a whole-rock fraction and yields a date of 357.5 ± 8.6 Ma (MSWD = 0.89). Based on the garnet Sm-Nd dating results, the authors interpreted that the eclogite-facies stage occurred at ca. 360 Ma, while a hydrothermal event at ca. 315-310 Ma is recorded in zircon and rutile grains.

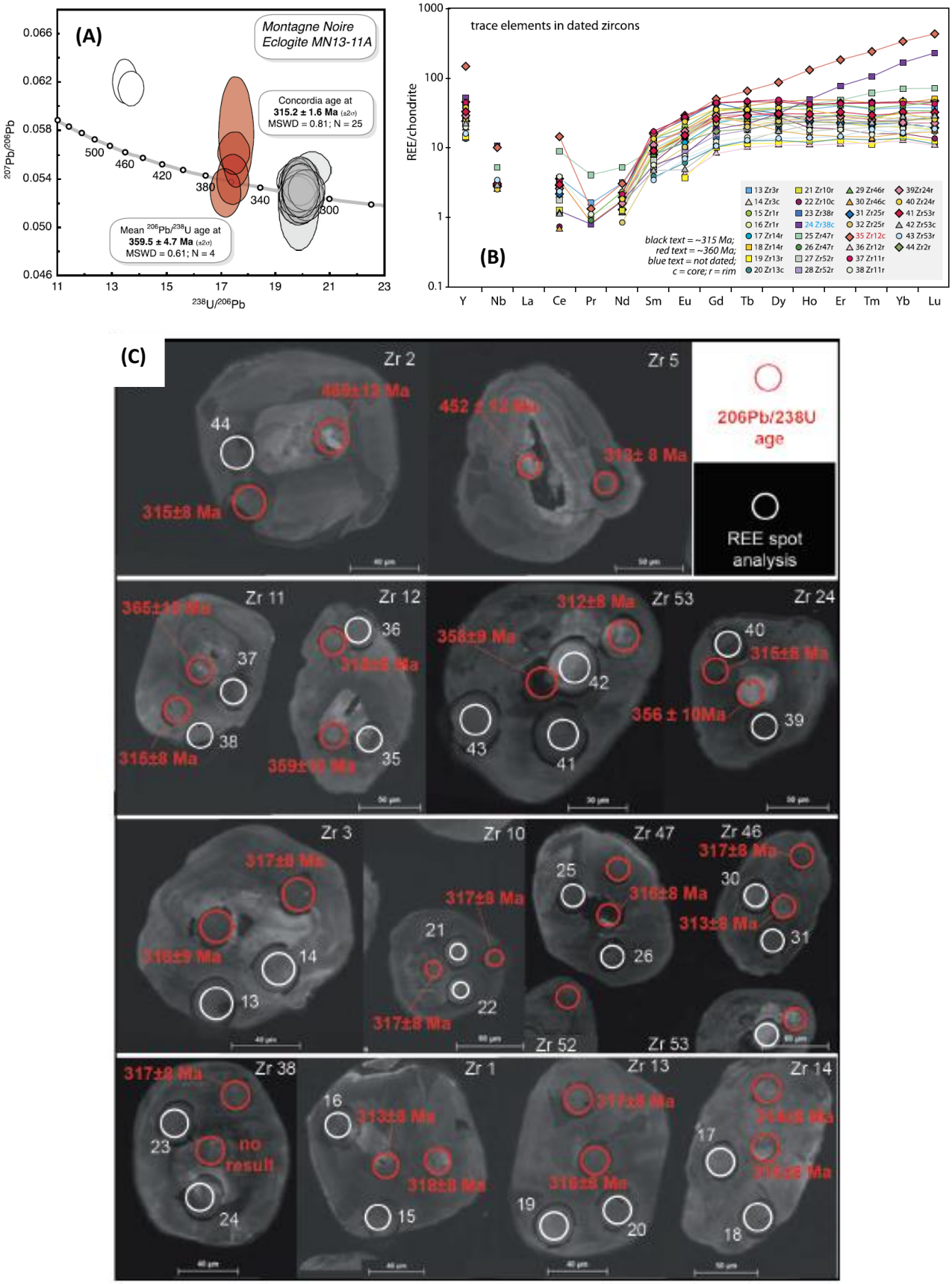

Figure II.2.1' :Data from Whitney et al. (2015). A.Tera-Wasserburg diagram, B. Chondrite-normalized REE plot for dated zircons, C. BSE images of zircon with ages in Ma, showing the location of analytical spots for geochronology (red

The second study available was realized by Whitney et al. (2015). They performed U-Pb dating on zircon and analysed the REE content in the same dated zones, when it was possible. Four zircon cores, to which corresponds one "magmatic-like" REE spectrum (spot #35), yield a mean date of 359.5 ± 4.7 Ma (MSWD = 0.61). A well recorded date of 315.2 ±1.6 Ma (MSWD = 0.81, N = 25) was also obtained, to which systematically correspond numerous flat HREE, i.e. "eclogitic-like", spectra. The authors conclude that 315.2 ±1.6 Ma corresponds to the age of the high-pressure event.

These two studies obtain similar results at ca. 315 Ma from zircon U-Pb dating on the same "Peyrambert - Terme de Fourcaric" eclogite. Nevertheless, their interpretations are dramatically opposed:

- Faure et al. (2014) propose a HP age at ca. 360 Ma based on Sm-Nd garnet dating and consider that the 315 Ma obtained on zircon reflects hydrothermal interaction
- Whitney et al. (2015) propose that the 315 Ma date obtained on zircon reflects the timing of high-pressure metamorphism, based on their eclogitic-like REE patterns. The 360 Ma is inferred to date either the protolith or the prograde pre-eclogitic metamorphism

The age of the massive LP-HT migmatitic event in the Montagne Noire is well constrained by numerous studies (Faure et al. 2010; Franke et al. 2011; Roger et al. 2015; Poujol et al. 2017) and considered to occur between 330 and 290 Ma. The interpretation of Whitney et al. would imply that HP metamorphism and the LP-HT event occurred in the same time and the same place. This interpretation is nevertheless founded on *a priori* solid arguments - the REE spectra of the analysed zircons. However, only one zircon core provided for a "magmatic-like" spectrum. Consequently, we decided to perform a new U-Pb and REE study on the same eclogite locality, with a particular focus on the REE content in zircon cores.

Deceiving zircon REE patterns and U-Pb dates from migmatite-hosted eclogites

In prep for EPSL

Eloïse Bretagne[1], Pavel Pitra[1,2], Jean Van Den Driessche[1], Caroline Lotout[1], Marc Poujol[1], Valérie Bosse[3], and Nathan Cogné[1]

[1]Géosciences Rennes UMR 6118, Université Rennes 1 and CNRS, Campus de Beaulieu, F-35042 Rennes CEDEX, France

[2]Česká geologická služba, Klárov 3, CZ-118 21 Praha 1, Česká republika

[3]Laboratoire magmas et volcans UMR 6524, Université Blaise Pascal and CNRS, Observatoire de physique du globe de Clermont-Ferrand, F-63000 Clermont-Ferrand, France

Résumé

Les spectres d'éléments de terres rares dans les zircons sont communément utilisés pour attribuer une date U-Pb au faciès éclogitique. Les éclogites du dôme de la Montagne Noire (Massif Central) sont empaquetées dans des migmatites à sillimanite et ont subi un métamorphisme de haute pression à 21 kbar et 750°C avant une décompression à haute température. Les zircons présents dans une éclogite de ce massif ont enregistrés trois groupes de dates à environ 360 Ma, 340 Ma et 315 Ma. Néanmoins, ils sont tous caractérisés par une même tendance de spectre d'éléments de terres rares ne présentant pas d'enrichissement en terres rares lourdes ou d'anomalie en Eu, ce qui est typique des zircons éclogitiques.

Nous proposons que lors de l'exhumation, les zircons éclogitiques ont subi une recristallisation partielle à complète, préservant les signatures de terres rares mais entraînant une remise à zéro plus ou moins complète du système U-Pb.

En absence d'autres critères, aucune de ces dates ne peut donc être attribuée sans ambiguïté à l'évènement de haute-pression. L'âge de 315 Ma enregistré par les zircons des migmatites environnantes -identique au plus jeune âge enregistré par les zircons des éclogites- est interprété comme datant le métamorphisme de haute pression et basse température.

Nous dissuadons fortement l'utilisation des tendances de spectres de terres rares pour interpréter l'âge du métamorphisme de haute pression dans des éclogites présentes dans des dômes migmatitiques. Nous proposons que la recristallisation post faciès éclogite puisse amener à un découplage entre les systèmes éléments de terres rares et le système isotopique U-Pb. L'interprétation incorrecte d'âges jeunes comme datant le faciès éclogite peut amener à proposer des taux d'exhumation erronés et des modèles géodynamiques en découlant discutables.

Abstract

Zircon REE patterns are widely used to attribute specific U-Pb dates to eclogite-facies metamorphism. Eclogites hosted in sillimanite-bearing migmatites in the Montagne Noire dome (French Massif Central) reached c. 750 °C, 21 kbar before significant decompression at high temperatures. Zircon crystals in eclogite yield three distinct age groups - 360 Ma, 340 Ma and 315 Ma. They are all characterized, however, by identical REE patterns (no Eu anomaly, flat HREE), typical for eclogite-facies equilibration.

It is inferred that during the subsequent exhumation, eclogite-facies zircons underwent partial to total solid-state recrystallization, leaving the REE system unmodified, but leading to a partial to total resetting of the U-Pb system and consequently the obtained dates. In the absence of other criteria, none of these dates can be unequivocally attributed to the HP event. The 315 Ma zircon dates from the embedding migmatitic rocks strongly suggest that this age is related to the HT-LP metamorphism.

We caution against the use of REE patterns to determine the age of HP metamorphism in eclogites occurring in migmatitic domes. We argue that post-eclogitic solid-state recrystallization can lead to uncorrelating the U-Pb and REE systems. Misinterpreted young ages may lead to inferring erroneous fast exhumation rates and consequently questionable geodynamic models.

1. Introduction

Eclogites at the Earth surface mostly testify to past subduction zones. Dating the HP metamorphism of these rocks is therefore a major challenge when reconstructing geodynamics through time. Closure temperatures of the U-Pb system in zircon are higher than the temperatures (i) encountered in most subduction zones and (ii) of zircon crystallization (e.g. Lee et al., 1997, Harley et al., 2007; Rubatto and Hermann, 2007). U-Pb dating of zircon is a powerful tool to retrace the timing of burial and exhumation of these rocks in a subduction wedge (Rubatto, 2002; Rubatto and Hermann, 2007). The main difficulty is the association of zircon with a particular part of the P-T path (e.g. Kohn et al., 2015). This results in conflicting interpretation of both the age of the HP metamorphism and the inferred geodynamics. For example, in the European Variscan belt, U-Pb dates on zircon from the same eclogite, embedded in migmatitic rocks, provided two conflicting interpretations (Faure et al., 2014; Whitney et al., 2015). Both works have obtained very similar dates of ca. 360 Ma and 315 Ma. Faure et al. (2014) consider that the 360 Ma date represents the age of the HP metamorphism, as recognized in other parts of the European Variscan belt (e.g. Bosse et al., 2000; Kroner and Romer, 2013), whereas the 315 Ma is related to the late HT-LP event, characteristic of the late evolution of the belt between 320-290 Ma (e.g. Poujol et al., 2017). By contrast, Whitney et al. (2015) claim that the 315 Ma date is the age of "the youngest Variscan eclogite", the 360 Ma date being the age of a "pre-eclogite facies metamorphism". The interpretation of Faure et al. (2014) is based on regional, mainly tectonic considerations, whereas Whitney et al. (2015) argue, following Rubatto (2002), that the REE patterns (absence of Eu anomaly and of enrichment in HREE) of the zircons dated at 315 Ma are characteristic of the eclogite facies. Although conflicting, both interpretations seem founded. Such a situation calls for a better understanding of the behavior of zircon in eclogites. We decided to approach this issue by re-analyzing the zircons from the same eclogites analyzed in these two previous works and by investigating the relations between zircon crystallization and metamorphism.

2. Petrology and P-T estimations

The Montagne Noire is a migmatitic dome where eclogites occur as boudins in sillimanite-bearing migmatites (Demange, 1985). Two eclogites and one migmatite were

sampled at the Terme de Fourcaric (Fig. II.2.DR1 in the GSA Data Repository[1]), the location of Faure et al. (2014) and Whitney et al. (2015).

Sample EP1 is a relatively fresh eclogite comprising garnet (~40 vol.%), omphacite (~25 vol.%), pargasitic amphibole (~5 vol.%), rutile and kyanite, interpreted as characteristic of the 'primary' eclogite-facies assemblage. Clinopyroxene marks a faint foliation. The primary minerals are surrounded by a very fine-grained symplectite, the mode of which varies even at the scale of a thin section (~10-30 vol.%). The symplectitic intergrowths are generally composed of plagioclase and amphibole, but locally contain various proportions of diopside, orthopyroxene and spinel. Garnet (1-5 mm) is subhedral and includes rutile, amphibole and rare quartz. It reveals a core-to-rim increase of pyrope (0.32→0.52 mol.%; X_{Mg} = 0.44→0.60) and decrease in spessartine (2→0 mol.%) and grossular (0.23→0.13 mol.%) (Fig. 1A and B; DR2), interpreted in terms of prograde growth zoning (e.g. Tracy, 1982). Unzoned anhedral omphacite (up to 8 mm) contains 35-40 mol.% jadeite. Pargasitic amphibole occurs in two textural settings: (i) large crystals (up to 5 mm) commonly associated with garnet and, (ii) fine-grained symplectitic intergrowth with plagioclase, typically surrounding omphacite relics. Kyanite was only found in separated minerals. In the thin sections, it is replaced by an extremely fine-grained spinel-plagioclase symplectite, commonly included in garnet (cf. e.g. Liati and Seidel, 1996). Mg-rich ilmenite (geikielite up to 35 mol.%) commonly surrounds or replaces rutile. Zircon is common in the matrix symplectites, and included in garnet rims or omphacite.

Sample MN12-03 is a strongly retrogressed eclogite that contains garnet (~30 vol.%), hornblende (~20 vol.%), biotite (~10 vol.%), and a relatively coarse-grained plagioclase-amphibole symplectite. Accessory minerals include quartz, rutile, ilmenite, titanite and apatite. Anhedral rounded garnet (up to 4 mm) includes rutile, quartz and pargasitic amphibole. It has a large unzoned core (pyrope 36-38 mol.%, grossular 12 mol.%, spessartine 4 mol%, X_{Mg} = 0.45-0.47) and a chemically zoned rim (~150 µm) marked by a rimward increase of spessartine (up to 8 mol.%) and a decrease in pyrope (36→20 mol.%; X_{Mg} = 0.45→0.26), interpreted in terms of diffusion zoning due to partial resorption of the garnet rim.

Sample EP5 is a biotite + garnet + sillimanite-bearing felsic migmatite. It has a regular foliation marked by the orientation of biotite, parallel to the alternation of biotite-rich layers and layers rich in quartz, plagioclase and K-feldspar. Sillimanite occurs in cm-sized nodules with quartz.

Pressure-temperature pseudosections (isochemical phase diagrams) and isopleths for some key chemical variables have been calculated using Theriak/Domino (de Capitani and Petrakakis, 2010) and the internally consistent thermodynamic data set 5.5 (Holland and Powell 1998; updated Nov. 2003) (Fig. II.2.DR2 and Appendix II.2.DR3). Using sample EP1 garnet zoning, it is inferred that garnet crystallized along a prograde P–T path that reached peak pressure conditions at ~21 kbar and 750°C ($X_{Mg}(g)$ = 0.58-60; $X_{Ca}(g)$ = 0.12-0.15) in the field g-cpx-amph-q-ru-ky (Fig. II.2.1C). Subsequent development of plagioclase-bearing symplectite testifies to decompression during exhumation. The replacement of rutile by ilmenite suggests pressures lower than ~9 kbar. The presence of orthopyroxene in the symplectites and the unusually high Mg content of ilmenite suggest high temperatures (e.g. Chu et al., 2016).

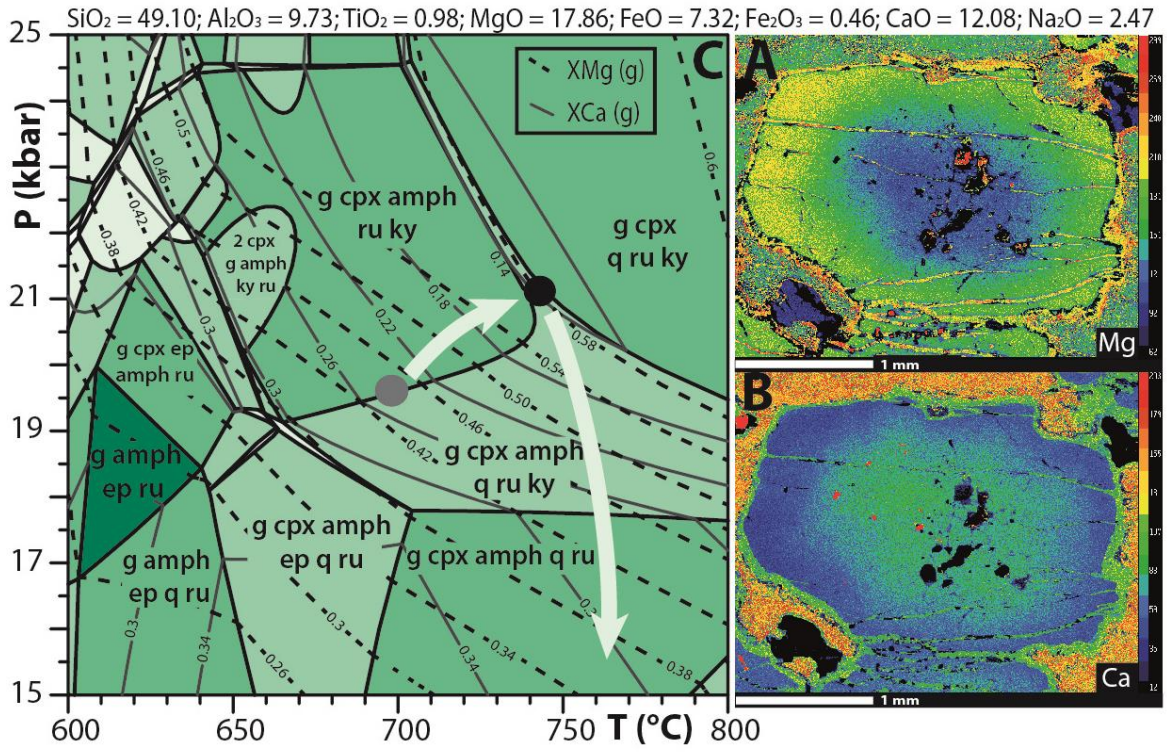

Figure II.2.1. A and B: X-ray maps for Mg and Ca in a selected garnet of the eclogite EP1. Rimward increase of Mg is characteristic of protrude zoning. C: P-T pseudosection and garnet compositional isopleths calculated for the bulk composition (indicated in mol.%) of the eclogite EP1, with excess H_2O. Only main fields are labeled. Darker field shading indicates higher variance of the assemblage. $X_{Mg}(g)$ = molar Mg/(Mg+Fe^{2+}), $X_{Ca}(g)$ = molar Ca/(Ca+Mg+Fe^{2+}). Arrow indicates the inferred P-T path based on the composition of the garnet core (grey dot) and rim (black dot) and the prograde garnet zoning. Decompression is qualitative only and is inferred from the development of plagioclase-bearing symplectites at the expense of garnet and clinopyroxene, and the replacement of rutile by ilmenite at P < 9 kbar (not shown).

3. U-Th-Pb zircon and monazite dating on eclogite

Zircon grains were analyzed as separated minerals mounted in epoxy pucks or *in context* directly in thin section. For both samples, cathodoluminescence imaging revealed that most zircon crystals are zoned with different internal structure in the inner and outer part. Others present only one type of zoning and are referred hereafter to as homogeneous crystals (Fig. II.2.DR9).

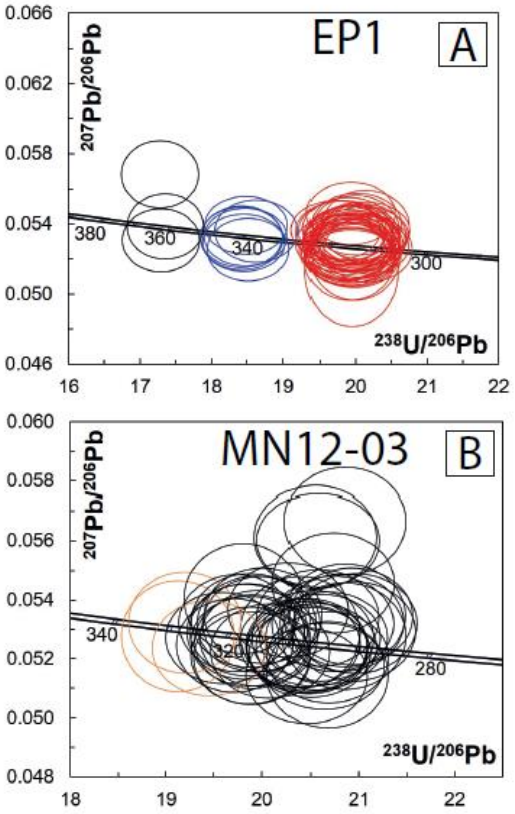

Figure II.2.2. Tera-Wasserburg $^{207}Pb/^{206}Pb$ versus $^{238}U/^{206}Pb$ Concordia diagram for zircons in the eclogites of the Montagne Noire gneiss dome. A: Zircon U-Pb dates obtained for the fresh eclogite EP1. Most values are concordant to sub-concordant except for one (black ellipse). Three age groups yield Concordia ages of 361.5 ± 6.3 Ma (black), 339.6 ± 3.2 Ma (blue) and 315.4 ± 1.2 Ma (red). B: Zircon U-Pb dates for the retrogressed eclogite MN12-03. Values are spread and not all concordant. Concordant results yield a Concordia age of 309.4 ± 1.6 Ma. Orange ellipses correspond to older outliers.

The apparent – since their ages were unknown at that stage – cores and rims were analyzed separately by U-Pb Laser Ablation Inductively Coupled Plasma Mass Spectrometry (LA ICP-MS) at Geosciences Rennes. Information about the analytical procedure can be found in Ballouard et al. (2015) and in supplementary Table II.2.DR4. Th/U ratios are < 0.1, a criterion often used as a discriminant for metamorphic zircon (Rubatto, 2002), although this should be treated with caution (Möller et al., 2003).

The fresh eclogite yields three distinct date groups with Concordia ages at 361.5 ± 6.3 Ma (MSWD = 0.32, N = 2), 339.6 ± 3.2 Ma (MSWD = 0.22, N = 7) and 315.4 ± 1.2 Ma (MSWD = 0.50, N = 42) (Fig. II.2.2A). Several situations are encountered. One zircon has a core dated at 360 Ma surrounded by a 316 Ma rim (Fig. II.2.3C and Fig. II.2.DR9). A homogeneous crystal included in a garnet rim was dated in context in the thin section at 360 Ma. Yet another grain, located in the fine-grained symplectitic intergrowth, is composed

of a 360 Ma core and a 315 Ma rim. Other zircon grains have 340 Ma cores and 316 Ma rims (Fig. II.2.3D). Finally, some crystals are homogeneous in terms of age at 340 Ma. The retrogressed eclogite (MN12-03), on the other hand, yields $^{206}Pb/^{238}U$ dates clustering between 320 to 300 Ma. They give a Concordia age at 309.4 ± 1.6 Ma (MSWD = 1.6, N = 36). Three slightly outlying analyses yield dates between 329 and 323 Ma (orange ellipses, Fig. II.2.2B). One crystal is characterized by three different dates with a core at 327 Ma, a first rim at 311 Ma and an outer rim at 300 Ma (Table II.2.DR7 and Fig. II.2DR9). There are also zircon grains with 315 Ma cores and rims around 300 Ma. Other crystals are homogeneous in terms of age at any value between 315 Ma and 300 Ma (Table II.2.DR7 and Fig. II.2DR9).

Monazite, also found in the retrogressed eclogite (MN12-03), yields a Concordia age of 311.4±1.2 Ma (MSWD = 1.2, N = 23) (Fig. II.2.DR5). Younger dates are discordant to sub-concordant due to Pb loss.

4. REE spectra

REE analyses have been obtained by LA-ICP-MS at the Magmas et Volcans Laboratory in Clermont-Ferrand. In order to get representative spectra, the REE have been measured for each dated zircon zone (analytical procedure can be found in Didier et al. (2015). With the exception of one analysis, all spectra in both the fresh eclogite EP1 and the retrogressed sample MN12-03 show similar patterns (Fig. II.2.4), marked by the absence of a negative Eu anomaly (Eu_N/Eu^* = 0.77-1.15) and a flat HREE tendency (Gd_N/Lu_N = 0.41-3.81). One zircon core has a negative Eu anomaly (Eu/Eu* = 0.15) and an HREE enriched spectrum (Gd_N/Lu_N = 0.06) (Fig. II.2.4A and Table II.2.DR8).

Reflecting on the whole set of data, we have three distinct dates (ca. 360 Ma, 340 Ma and 315 Ma) for one trend in REE spectra for the fresh eclogite (EP1) (Fig. II.2.3A-D). The same REE pattern is associated with dates ranging from 320 to 300 Ma in the retrogressed eclogite (MN12-03) (Fig. II.2.3E-F). The absence of interpretable data for the HREE enriched spectrum with a negative Eu anomaly (Fig. II.2.3A) is due to the presence of a fracture in the crystal, probably resulting in artificial fractioning of the different U and Pb isotopes.

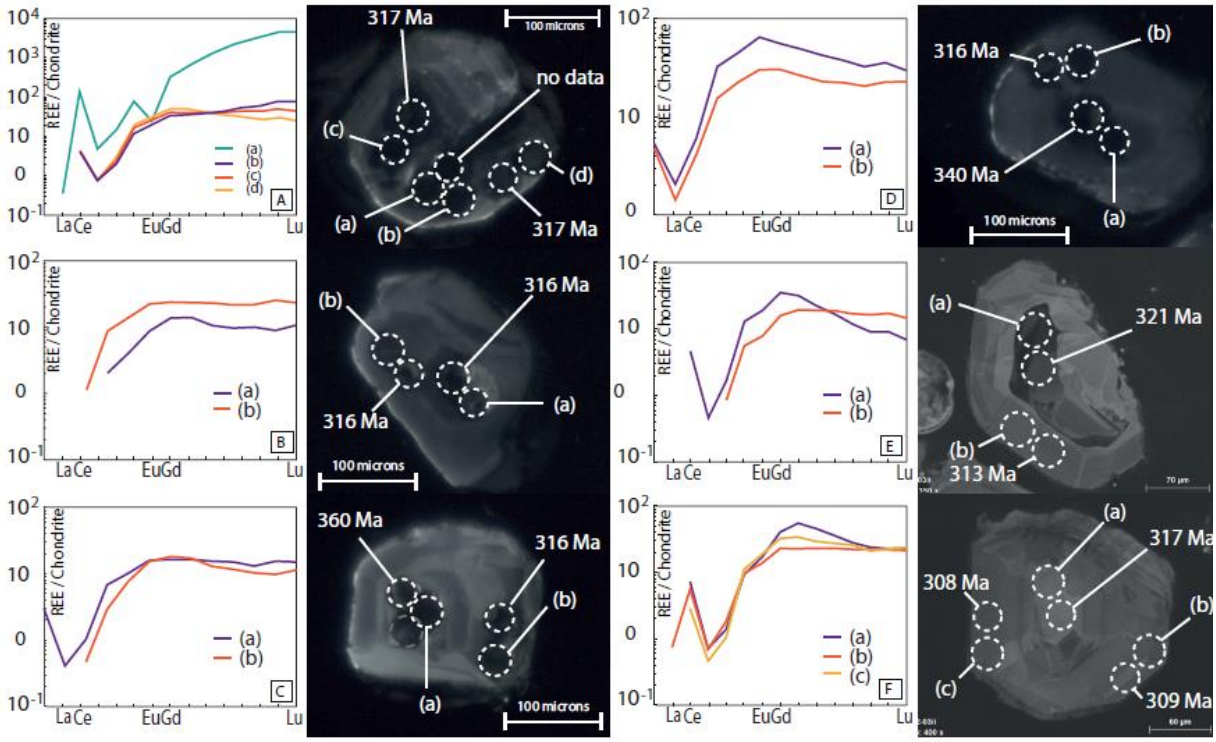

Figure 3. Absence of correlation between U-Pb dates and REE patterns in zoned zircons (EP1: A to D; and MN12-03: E and F). Zircon zones yield various dates, but similar REE patterns with flat HREE and no negative Eu anomaly, typical for eclogite-facies equilibration.

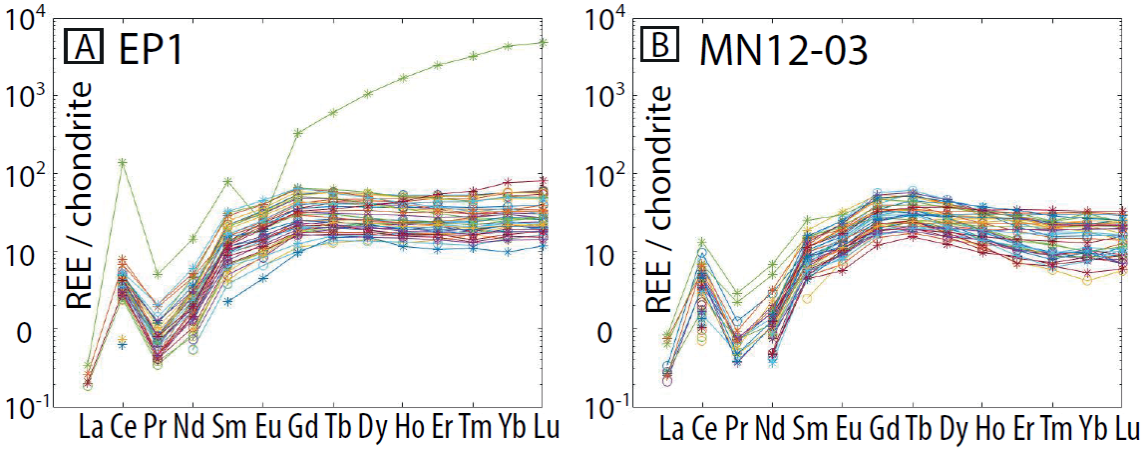

Figure 4. Chondrite-normalized REE spectra for all zircons from the fresh eclogite EP1 (A) and the retrogressed eclogite MN12-03 (B). All spectra are similar with flat HREE and no negative Eu anomaly except for one core analysis with a negative Eu anomaly and an enriched-HREE trend. Flat HREE spectra do not exceed 100 times chondrite values. Several spectra (in particular in B) have a slight bell shape with highest values at Gd and Tb and a weak negative slope towards heavier HREE.

5. U-Pb zircon dating on migmatite

Zircon U-Pb dating on migmatite (EP5) directly adjacent to eclogite boudins yields various date groups ranging from 2 517±18 Ma, which are clearly inherited, to 301±4 Ma (Fig. DR5). There are scattered groups of dates, one of which has a Concordia age of 315.3±2.2 Ma (MSWD = 0.93, N = 12). This date corresponds to the last overgrowth observed on zircon crystals. This means that it is the age of the last event the migmatite zircon recorded. No monazite was found in the sample.

6. Discussion

Following Rubatto (2002), the absence of Eu anomaly and flat HREE spectra testify to zircon crystallizing in eclogite facies conditions, implying that the studied sample (EP1) has been subjected to no less than three HP events within less than 45 Myr. This seems unlikely, and furthermore petrological data do not support successive burial/exhumation "yo-yo subduction" pattern (Rubatto et al., 2011). In our case we conclude that flat HREE patterns and the absence of negative Eu anomaly are not an irrefutable criterion to ascertain that the corresponding date is that of a HP event. There is no systematic coupling of the U-Pb system to the REE pattern in metamorphic zircon. The question remains however of the significance of eclogite zircon dates.

Elemental partitioning between coexisting minerals is well established and is also applicable to REE (e.g. Peucat et al., 1995; Schaltegger et al., 1999, Hoskin and Black, 2000). During crystallization, REE are incorporated following a mineral- and element-specific distribution coefficient. In the present case, the REE spectra indicate that partitioning occurred in the presence of garnet (flat HREE; Schaltegger et al., 1999) and absence of plagioclase (no negative Eu anomaly; Murali et al., 1983; Peucat et al., 1995). This implies that zircon crystallized in the eclogite facies (Rubatto, 2002).

REE and U in zircon are not subject to significant volume diffusion over long periods of time (Cherniak et al., 1997; Cherniak and Watson, 2001). Lead (Pb), which is entirely radiogenic in zircon, also has a very slow diffusion rate, but can be expelled during zircon recrystallization (Cherniak and Watson, 2001). This modifies the analyzed Pb/U ratio, yielding ages younger than those of zircon crystallization. The U-Pb system can evolve independently of the REE during the metamorphic evolution subsequent to zircon crystallization (e.g. Peters et al., 2013; Štípská et al., 2016). In particular, during solid-state

recrystallization of an existing zircon, Pb/U ratios are liable to be modified, whereas the REE patterns are not (Hoskin and Black, 2000).

Our interpretation is that in the studied samples zircon crystallized during the eclogite-facies metamorphism and acquired the "eclogitic" REE pattern. During the subsequent exhumation to low pressures, and in particular the associated melting of the host migmatites, zircon underwent partial to total solid-state recrystallization, leaving the REE system unmodified, but partially to totally resetting the U-Pb system and consequently the obtained dates.

Since we now do not have any criteria left to recognize HP zircons, we cannot determine which one of our dates truly corresponds to the HP event. We can, however, suggest with confidence that the 315 Ma date does not correspond to the timing of eclogite facies metamorphism, which conflicts with the assertion of Whitney et al. (2015). Identical U-Pb zircon ages (ca. 315 Ma) for eclogite boudins and their sillimanite-bearing host migmatite are indeed incompatible. This would imply that two dramatically different sets of metamorphic PT conditions occur at the same time in the same place. The coarse-grained character of the symplectites in the retrogressed eclogite MN12-03, as well as the abundance of biotite and monazite, unusual in this type of rocks, suggests that external fluids may have interacted with this eclogite at a late stage of the metamorphic evolution. Monazite is known to (re)crystallize easily in fluid-present environments (e.g. Parrish, 1990; Spear and Pyle, 2002; Kelly et al., 2012). Accordingly, dates of 311 Ma, provided by eclogite monazite, reinforce our opinion that the 315 Ma date is not that of the HP event. We conclude that the 315 Ma date in the Montagne Noire eclogite corresponds to the age of the late Carboniferous HT event, long recognized in the Variscan belt (e.g. Dewey and Burke, 1973).

To conclude, our results show that dating HP metamorphism in eclogites embedded in high-grade rocks is not straightforward. Using a particular REE pattern as the only criterion to attribute a U-Pb zircon date to a HP event may provide incorrect young ages influenced by the subsequent HT event. This has significant implications, since it may lead to inferring erroneous fast exhumation rates and consequently questionable geodynamic models.

Acknowledgements

E. Bretagne acknowledges internal research funds of CNRS UMR 6118 for salary. This research was supported by a CNRS-INSU grant (SYSTER program) to P. Pitra. Xavier Le Coz, Yann Lepagnot, and Nathan Hallot are thanked for making the thin sections, mineral separation and rock crushing, respectively.

Bibliography

Ballouard, C., Boulvais, P., Poujol, M., Gapais, D., Yamato, P., Tartèse, R. and Cuney, M., 2015, Tectonic record, magmatic history and hydrothermal alteration in the Hercynian Guérande leucogranite, Armorican Massif, France: Lithos, v. 220-223, p. 1-22, doi: 10.1016/j.lithos.2015.01.027.

Bosse, V., Féraud, G., Ruffet, G., Ballèvre, M., Peucat, J.-J., and de Jong, K., 2000, Late Devonian subduction and early-orogenic exhumation of eclogite-facies rocks from the Champtoceaux Complex (Variscan belt, France): Geological Journal, v. 35, p.297-305, doi: 10.1002/gj.864

Cherniak, D. J., and Watson, E. B., 2001, Pb diffusion in zircon: Chemical Geology, v. 172, p. 5-24, doi: 10.1016/S0009-2541(00)00233-3.

Cherniak, D. J., Hanchar, J. M., and Watson, E. B., 1997, Diffusion of tetravalent cations in zircon: Contributions to Mineralogy and Petrology, v. 127, p. 383-390, doi: 10.1007/s004100050287.

de Capitani, C., and Petrakakis, K., 2010, The computation of equilibrium assemblage diagrams with Theriak/Domino software: American Mineralogist, v. 95, p. 1006-1016, doi: 10.2138/am.2010.3354.

Demange, M., 1985, The eclogite-facies rocks of the Montagne Noire, France: Chemical geology, v. 50, p. 173-175, 179-188, doi: 10.1016/0009-2541(85)90119-6.

Dewey, J. F., and Burke, K. C. A., 1973, Tibetan, Variscan and Precambrian reactivation: Products of continental collision: Journal of Geology, v. 81, p. 683-692, doi: 10.1016/S0169-1368(01)00016-6.

Faure, M., Cocherie, A., Gaché, J., Esnault, C., Guerrot, C., Rossi, P., and Qiuli, L., 2014, Middle Carboniferous intracontinental subduction in the Outer zone of the Variscan belt (Montagne Noire axial zone, French Massif Central): Multimethod geochronological approach of polyphase metamorphism: Geological Society, London, Special Publications, v. 405, p. 289-311, doi: 10.1144/SP405.2.

Didier, A., Bosse, V., Bouloton, J., Mostefaoui, S., Viala, M., Paquette J. L., Devidal, J. L., and Duhamel, R., 2015, NanoSIMS mapping and LA-ICP-MS chemical and U–Th–Pb data in monazite from a xenolith enclosed in andesite (Central Slovakia Volcanic Field): Contribution to Mineralogy and Petrology, v. 170, p. 1-21, doi:10.1007/s00410-015-1200-1.

Harley, S. L., Kelly, N. M., and Möller, A., 2007, Zircon Behavior and the Thermal Histories of Mountain Chains: Elements, v. 3, p. 25-30, doi: 10.2113/gselements.3.1.25.

Holland, T. J. B., and Powell, R., 1998, An internally consistent thermodynamic data set for phases of petrological interest: Journal of metamorphic Geology, v. 16, p. 309-343, doi: 10.1111/j.1525-1314.2010.00923.x.

Hoskin, P. W. O., and Black, L. P., 2000, Metamorphic zircon formation by solid-state recrystallization of protolith igneous zircon: Journal of metamorphic Geology, v. 18, p. 423-439, doi: 10.1046/j.1525-1314.2000.00266.x.

Kelly, N. M., Harley, S. L., and Möller, A., 2012, Complexity in the behaviour and recrystallisation of monazite during high-T metamorphism and fluid infiltration: Chemical Geology, v. 322-323, p. 192-208, doi:10.1016/j.chemgeo.2012.07.001.

Kohn, M. J., Corrie, S. L., and Markley, C., 2015, The fall and rise of metamorphic zircon: American Mineralogist, v. 100, p. 897-908, doi:10.2138/am-2015-5064.

Kroner, U., and Romer, R. L., 2013, Two plates - Many subduction zones: The Variscan orogeny

reconsidered: Gondwana Research, v. 24, p. 298-329, doi: 10.1016/j.gr.2013.03.001.

Lee, J. K., Williams, I. S., and Ellis, D. J., 1997, Pb, U and Th diffusion in natural zircon: Nature, v. 390, p. 159-162, doi:10.1038/36554.

Liati, A., and Seidel, E., 1996, Metamorphic evolution and geochemistry of kyanite eclogites in central Rhodope, northern Greece: Contributions to Mineralogy and Petrology, v. 123, p. 293-307, doi: 10.1007/s004100050157.

Möller, A, O'Brien, PJ, Kennedy, A, and Kröner, A , 2003, Linking growth episodes of zircon and metamorphic textures to zircon chemistry: an example from the ultrahigh-temperature granulites of Rogaland (SW Norway): Geological Society of London Special Publication, v. 220, p. 65-81, doi.org/10.1144/GSL.SP.2003.220.01.04.

Murali, A. V., Parthasarathy, R., Mahadevan, T. M., and Das, M. S., 1983, Trace element characteristics, REE patterns and partition coefficients of zircons from different geological environments—a case study on Indian zircons: Geochimica et Cosmochimica Acta, v. 47, p. 2047-2052, doi: 10.1016/0016-7037(83)90220-X.

Parrish, R. R., 1990, U-Pb dating of monazite and its application to geological problems: Canadian Journal of Earth Sciences, v. 27, p. 1431-1450, doi.org/10.1139/e90-152.

Peters, T.J., Ayers, J.C., Gao, S., and Liu, X.M., 2013, The origin and response of zircon in eclogite to metamorphism during the multi-stage evolution of the Huwan Shear Zone, China: insights from Lu-Hf and U-Pb isotopic and trace element geochemistry: Gondwana Research, v. 23, p. 726–747, doi:10.1016/j.gr.2012.05.008.

Peucat, J. J., Hirata, T., and Nesbitt, R.W., 1995, REE fractionation (ICPMS LASER) evidence in metamorphic zircons during granulite facies metamorphism and anatectic processes: Terra Abstracts, v. 7, p. 346.

Poujol, M., Pitra, P., Van Den Driessche, J., Tartèse, R., Ruffet, G., Paquette, J. L., and Poilvet, J. C., 2016, Two-stage partial melting during the Variscan extensional tectonics (Montagne Noire, France): International Journal of Earth Sciences, v. 106, p. 477-500, doi: 10.1007/s00531-016-1369-1.

Rubatto, D., 2002, Zircon trace element geochemistry: partitioning with garnet and the link between U–Pb ages and metamorphism: Chemical Geology, v. 184, p. 123-138, doi: 10.1016/S0009-2541(01)00355-2.

Rubatto, D., and Hermann, J., 2007, Zircon Behavior in Deeply Subducted Rocks: Elements, v. 3, p. 31-35, doi: 10.2113/gselements.3.1.31.

Rubatto, D., Regis, D., Hermann, J., Boston, K., Engi, M., Beltrando, M., and McAlpine, S. R. B., 2011, Yo-yo subduction recorded by accessory minerals in the ItalianWestern Alps: Nature Geosciences, v. 4, p. 338-342, doi: 10.1038/NGEO1124

Schaltegger, U., Fanning, C. M., Günther, D., Maurin, J. C., Schulmann, K., and Gebauer, D., 1999, Growth, annealing and recrystallization of zircon and preservation of monazite in high-grade metamorphism: conventional and in-situ U-Pb isotope, cathodoluminescence and microchemical evidence: Contributions to Mineralogy and Petrology, v. 134, p. 186-201, doi: 10.1007/s004100050478.

Spear, F. S., and Pyle, J. M., 2002, Apatite, Monzanite and Xenotime in Metamorphic Rocks: Reviews in Mineralogy and Geochemistry, v. 48, p. 293-335, doi: 10.2138/rmg.2002.48.7.

Štípská, P., Powell, R., Hacker, B. R., Holder, R. and Kylander-Clark, A. R. C., 2016, Uncoupled U/Pb and REE response in zircon during the transformation of eclogite to mafic and intermediate granulite (Blanský les, Bohemian Massif): Journal of Metamorphic Geology, v. 34, p. 551-572, doi:10.1111/jmg.12193

Tracy, R. J., 1982, Compositional zoning and inclusions in metamorphic minerals: Reviews in Mineralogy and Geochemistry, v. 10, p. 355-397.

Whitney, D. L., Roger, F., Teyssier, C., Rey, P. F., and Respaut, J. P., 2015, Syn-collapse eclogite metamorphism and exhumation of deep crust in a migmatite dome: The P–T–t record of the youngest Variscan eclogite (Montagne Noire, French Massif Central): Earth and Planetary Science Letters, v. 430, p. 224-234, doi: 10.1016/j.epsl.2015.08.026.

Data Repository

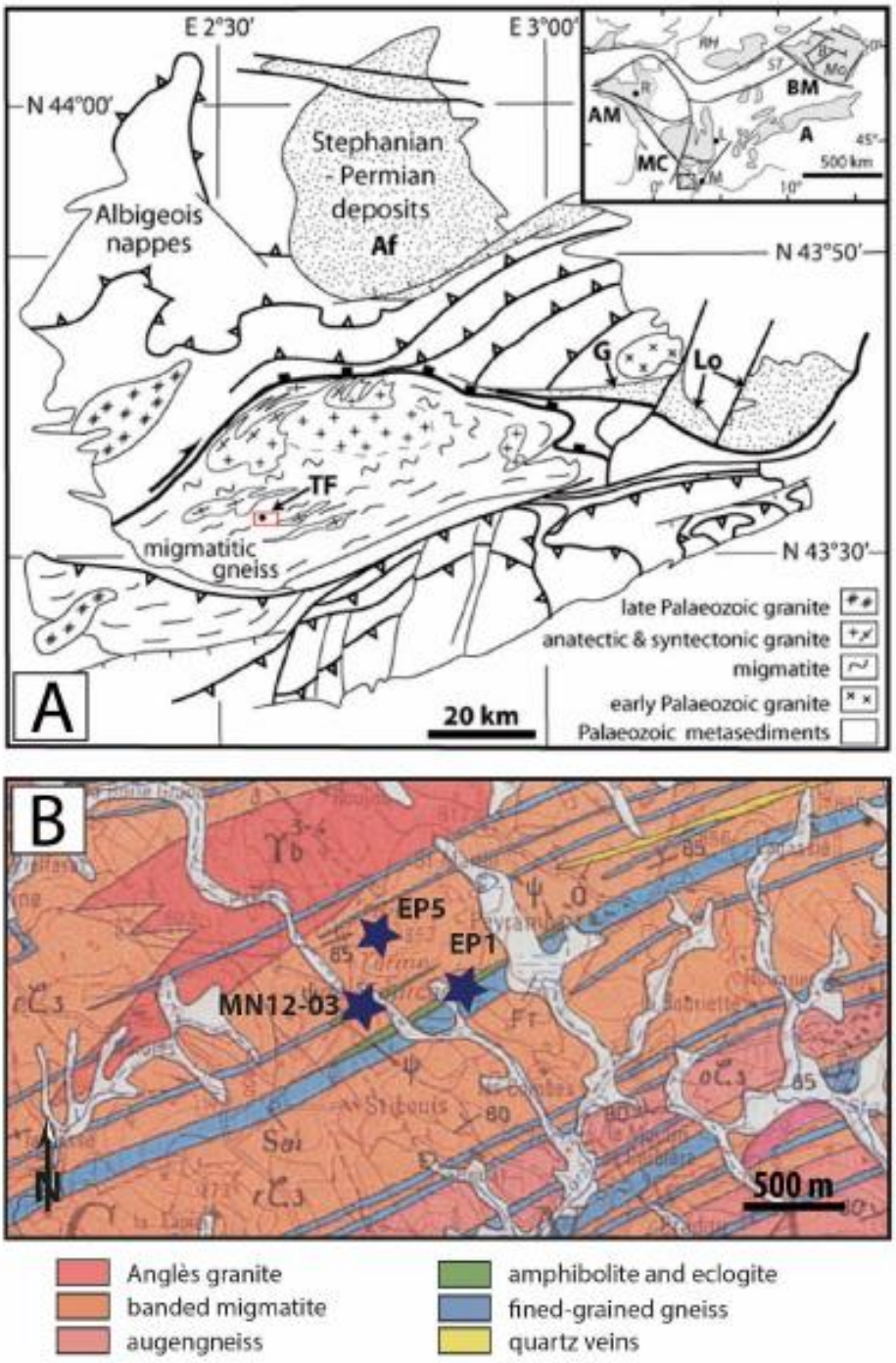

Figure II.2.DR1: (A) Structural map of the southern French Massif Central showing the relationships between the Montagne Noire gneiss dome, the Stephanian-Permian basins, and the Variscan thrusts and nappes (modified after Brun and Van Den Driessche, 1994). Af: St. Affrique basin, G: Graissessac basin, Lo: Lodève basin, TF: location of the Terme de Fourcaric area. Insert shows the location of the study area within the European Variscan belt (modified from Pitra et al. 2010). A - Alps, AM - Armorican Massif, BM - Bohemian Massif, MC - Massif Central. B - Teplá-Barrandian, Mo - Moldanubian, ST - Saxothuringian, RH - Rhenohercynian. L: Lyon; M: Montpellier; R: Rennes. (B) Geological map of the studied area with location of the sampled localities (modified after Alabouvette et al. 1993). EP1 - 'fresh' eclogite (N 43°33'5.21", E

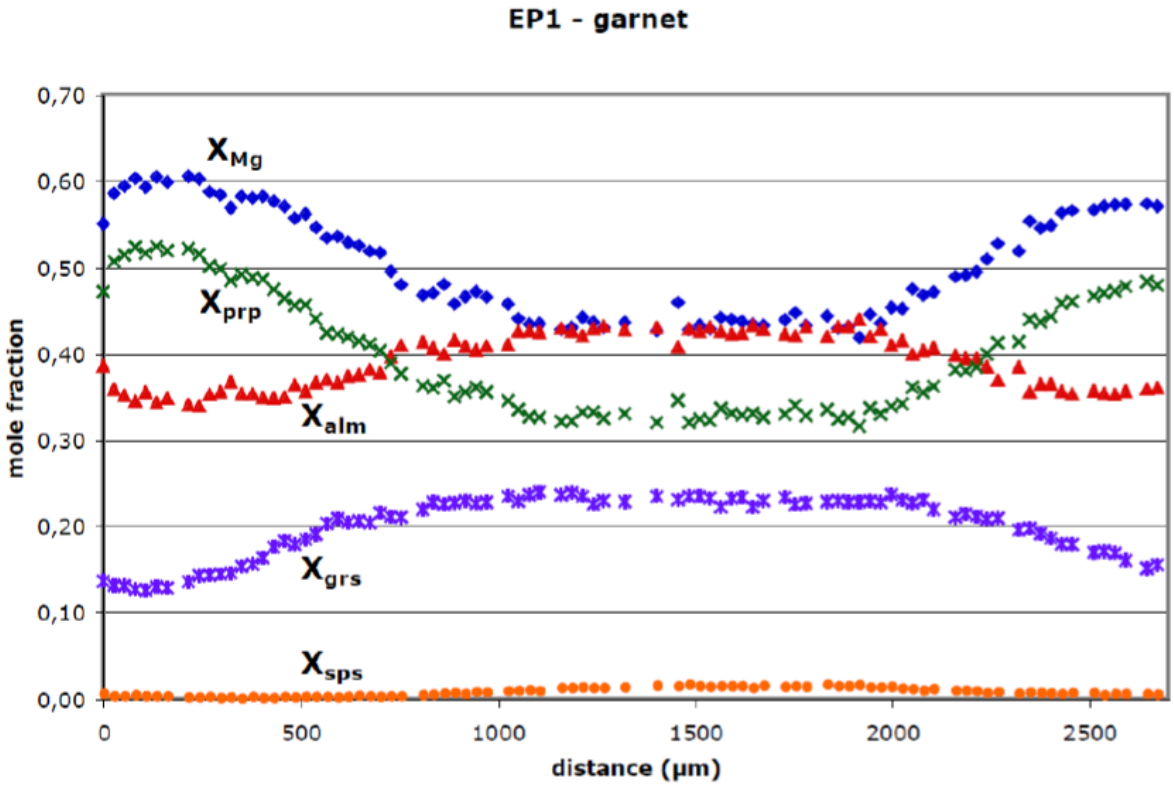

Figure DR2: Compositional zoning across the garnet shown in Figure 1A and B. Rimward decrease in spessartine and increase in pyrope and XMg are typical for prograde growth zoning. Zoning reversal in the outermost rim is related to limited garnet resoption during decompression. Component abbreviation: prp = pyrope; alm = almandine; grs = grossular, sps = spessartine.

DR3 : Petrological modeling

Pseudosections were calculated using both Theriak/Domino (de Capitani and Petrakakis, 2010) and THERMOCALC (Powell et al., 1998), and the internally consistent thermodynamic data set 5.5 (Holland and Powell 1998; updated Nov. 2003) in the system NCKFMASHTO (Na2O–CaO–K2O–FeO–MgO–Al2O3–SiO2–H2O–TiO2–Fe2O3). The phases considered in the calculations, and references to the activity-composition models used are amphibole, clinopyroxene (Diener and Powell, 2012), plagioclase (Holland and Powell, 2003), garnet (White et al., 2007), epidote (Holland &

Powell, 1998), chlorite (Holland et al., 1998), ilmenite, magnetite (White et al., 2000). Doug Tinkham kindly provided the conversion of the mixing models for Theriak/Domino. Bulk rock compositions and FeO (vs. Fe2O3) were analyzed at SARM (CRPG-CNRS, Nancy, France), from powders prepared at Géosciences Rennes using an agate mill.

Table DR4: Operating conditions for the LA-ICP-MS equipment

Laboratory & Sample Preparation	
Laboratory name	Géosciences Rennes, UMR CNRS 6118, Rennes, France
Sample type/mineral	Zircon (Zrn) and Monazite (Mnz)
Sample preparation	Conventional mineral separation, 1 inch resin mount, 1µm polish to finish Thin-sections
Imaging	CL: RELION CL instrument, Olympus Microscope BX51WI, Leica Color Camera DFC 420C
Laser ablation system	
Make, Model & type	ESI NWR193UC, Excimer
Ablation cell	ESI NWR TwoVol2
Laser wavelength	193 nm
Pulse width	< 5 ns
Fluence	6.7 J/cm^2 (Mnz) ou 8 J/cm^2 (Zrn)
Repetition rate	3 Hz
Spot size	10 µm (Mnz) et 25-30 µm (Zrn)
Sampling mode / pattern	Single spot
Carrier gas	100% He, Ar make-up gas and N2 (3 ml/mn) combined using in-house smoothing device
Background collection	20 seconds
Ablation duration	60 seconds
Wash-out delay	15 seconds
Cell carrier gas flow (He)	0.75 l/min
ICP-MS Instrument	
Make, Model & type	Agilent 7700x, Q-ICP-MS
Sample introduction	Via conventional tubing
RF power	1350W
Sampler, skimmer cones	Ni
Extraction lenses	X type
Make-up gas flow (Ar)	0.85 l/min
Detection system	Single collector secondary electron multiplier

Data acquisition protocol	Time-resolved analysis
Scanning mode	Peak hopping, one point per peak
Detector mode	Pulse counting, dead time correction applied, and analog mode when signal intensity > ~ 10^6 cps
Masses measured	^{204}(Hg + Pb), ^{206}Pb, ^{207}Pb, ^{208}Pb, ^{232}Th, ^{238}U
Integration time per peak	10-30 ms
Sensitivity / Efficiency	28000 cps/ppm Pb (50µm, 10Hz)
Data Processing	
Gas blank	20 seconds on-peak
Calibration strategy	GJ1 zircon and Moacir monazite standards used as primary reference materials, Plešovice zircon and Managoutry monazite used as secondary reference materials (quality control)
Reference Material info	GJ1 (Jackson et al., 2004) Moacir (Gasquet et al., 2010) Plešovice (Slama et al., 2008) Manangoutry (Paquette and Tiepolo, 2007)
Data processing package used	GLITTER ® (van Achterbergh et al., 2001)
Mass discrimination	Standard-sample bracketing with ^{207}Pb/^{206}Pb and ^{206}/^{238}U (^{208}Pb/^{232}Th for Mnz) normalized to reference material GJ1 and Moacir
Common Pb correction	No common Pb correction
Uncertainty level and propagation	Ages are quoted at 2sigma absolute, propagation is by quadratic addition according to Horstwood et al. (2003). Reproducibility and age uncertainty of reference material are propagated.
Quality control / Validation	Plešovice: 338.1 ± 1.9 Ma (N=18; MSWD=1.00) Manangoutry : 558.7 ± 4.1 Ma (N=6, MSWD=0.65)

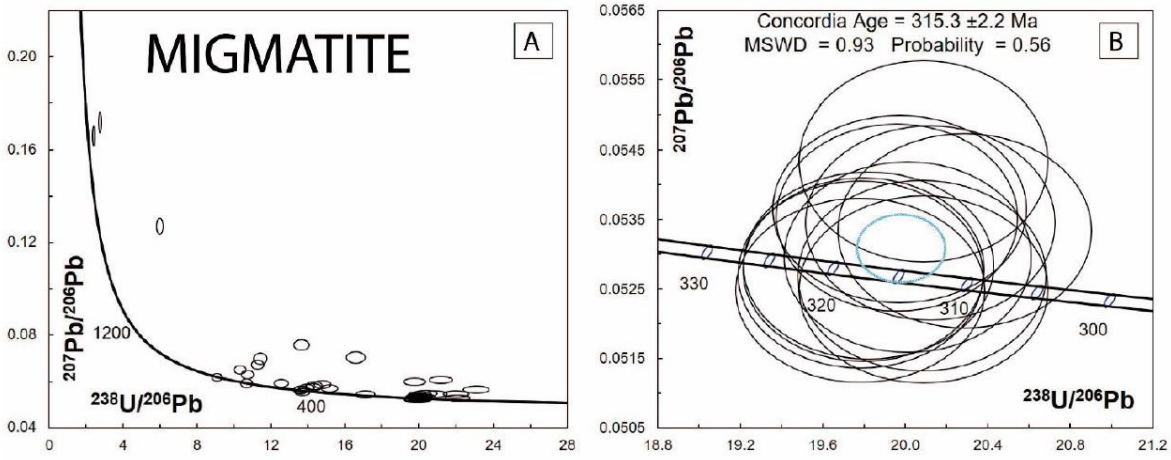

Figure DR5: 207Pb/206Pb versus 238U/206PbTera-Wasserburg diagram for zircons in the host migmatite (EP5). A : an overview of all the obtained dates; B: concordant 315 Ma date.

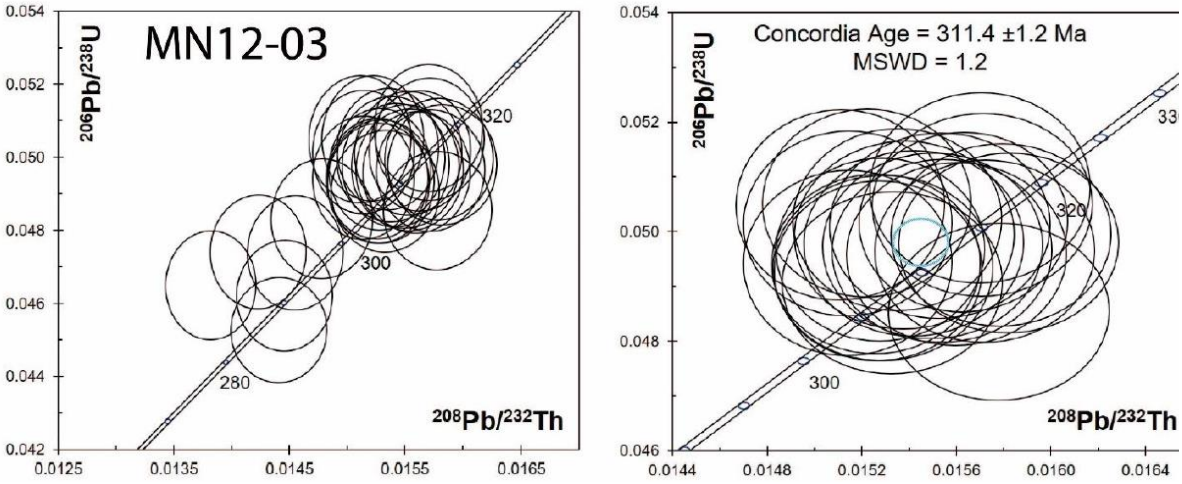

Figure DR6: 207Pb/206Pb versus 238U/206Pb Tera-Wasserburg diagram for monazites in the retrogressed eclogite (MN12-03). A: an overview of all dates obtained. Note how the younger ages tend to deviate upwards from the Concordia area due to common Pb; B: concordant 311 Ma dates.

					Isotopic Ratios										Apparent Ages					
Analysis #	Sample	Pb ppm	Uppm	Th/U	U238/Pb206	Err%	Pb207/Pb206	Err%	Conc.	Pb207/U235	Abs. Err	Pb206/U238	Abs. Err	rho	Pb207/Pb206		Pb206/U238		Pb207/U235	
S-270417a-01	EP1 IV 08 NW core	11	231	0.05	20.008	1.3	0.0525	1.3	100.3	0.3615	0.0052	0.04998	0.00063	0.87	306	28	314	4	313	4
S-270417a-02	EP1 IV 08 NW rim	13	278	0.07	20.125	1.2	0.0527	1.2	99.9	0.3611	0.0051	0.04969	0.00062	0.88	316	27	313	4	313	4
S-270417a-03	EP1 IV 08 NE core	9	199	0.06	19.900	1.3	0.0533	1.3	99.0	0.3694	0.0054	0.05025	0.00063	0.86	343	28	316	4	319	4
S-270417a-04	EP1 IV 08 NE rim	7	160	0.05	19.900	1.3	0.0525	1.4	100.3	0.3637	0.0056	0.05025	0.00063	0.82	307	31	316	4	315	4
S-270417a-05	EP1 IV 08 C core	12	256	0.07	20.133	1.3	0.0536	1.2	98.4	0.3671	0.0053	0.04967	0.00063	0.88	355	28	313	4	318	4
S-270417a-06	EP1 IV 08 C rim	8	176	0.05	19.920	1.3	0.0523	1.3	100.6	0.3622	0.0055	0.05020	0.00063	0.83	300	30	316	4	314	4
S-270417a-07	EP1 IV 09 SE core	13	271	0.08	19.920	1.3	0.0532	1.2	99.2	0.3683	0.0052	0.05020	0.00063	0.89	338	27	316	4	318	4
S-270417a-08	EP1 IV 09 SE rim	12	252	0.11	19.940	1.3	0.0534	1.2	98.8	0.3693	0.0053	0.05015	0.00063	0.88	347	28	315	4	319	4
S-270417a-09	EP1 IV 09 SW core	8	161	0.08	19.936	1.3	0.0546	1.3	97.0	0.3775	0.0057	0.05016	0.00063	0.83	396	29	316	4	325	4
S-270417a-10	EP1 IV 09 SW rim	11	236	0.02	19.996	1.3	0.0523	1.3	100.6	0.3608	0.0053	0.05001	0.00063	0.86	300	29	315	4	313	4
S-270417a-11	EP1 IV 09 N core	12	269	0.05	20.113	1.3	0.0534	1.3	98.8	0.3657	0.0053	0.04972	0.00063	0.87	344	28	313	4	317	4
S-270417a-12	EP1 IV 09 N rim	13	271	0.06	20.004	1.3	0.0531	1.2	99.3	0.3660	0.0053	0.04999	0.00063	0.88	333	28	315	4	317	4
S-270417a-13	EP1 IV 09 N rim 2	12	266	0.07	20.012	1.3	0.0529	1.2	99.6	0.3645	0.0052	0.04997	0.00063	0.88	325	28	314	4	316	4
S-270417a-14	EP1 IV 10 core	14	297	0.09	19.952	1.3	0.0524	1.3	100.5	0.3620	0.0054	0.05012	0.00063	0.84	302	30	315	4	314	4
S-270417a-15	EP1 IV 10 rim	12	252	0.05	19.786	1.3	0.0529	1.2	99.8	0.3685	0.0054	0.05054	0.00064	0.87	324	28	318	4	319	4
S-270417a-16	EP1 IV 12 N core	16	339	0.05	19.885	1.3	0.0529	1.2	99.6	0.3671	0.0052	0.05029	0.00063	0.89	326	27	316	4	318	4
S-270417a-17	EP1 IV 12 N rim	12	267	0.06	20.072	1.3	0.0530	1.3	99.5	0.3638	0.0053	0.04982	0.00063	0.87	327	28	313	4	315	4
S-270417a-18	EP1 IV 12 S core 1	13	254	0.07	18.625	1.3	0.0536	1.3	99.4	0.3967	0.0061	0.05369	0.00068	0.83	354	30	337	4	339	4
S-270417a-19	EP1 IV 12 S core 2	9	198	0.04	19.897	1.3	0.0537	1.4	98.4	0.3722	0.0057	0.05026	0.00064	0.83	359	30	316	4	321	4
S-270417a-20	EP1 IV 12 S rim 1	8	160	0.05	18.423	1.3	0.0532	1.4	100.2	0.3980	0.0063	0.05428	0.00069	0.81	337	31	341	4	340	5
S-270417a-21	EP1 IV 12 S rim 2	10	195	0.05	18.420	1.3	0.0532	1.3	100.1	0.3984	0.0060	0.05429	0.00069	0.84	339	30	341	4	341	4
S-270417a-22	EP1 IV 05 core	9	195	0.06	20.016	1.3	0.0540	1.3	97.9	0.3718	0.0056	0.04996	0.00064	0.84	370	30	314	4	321	4
S-270417a-23	EP1 IV 05 rim	9	200	0.07	19.976	1.3	0.0521	1.3	101.0	0.3593	0.0055	0.05006	0.00064	0.83	288	31	315	4	312	4
S-270417a-24	EP1 IV 05 rim 2	13	276	0.08	19.916	1.3	0.0521	1.3	101.0	0.3608	0.0054	0.05021	0.00064	0.86	291	29	316	4	313	4
S-270417b-01	EP1 III 101 core	8	165	0.04	19.728	1.3	0.0536	1.3	98.6	0.3748	0.0056	0.05069	0.00065	0.86	356	29	319	4	323	4
S-270417b-02	EP1 III 101 rim	10	226	0.04	19.904	1.3	0.0527	1.2	100.0	0.3652	0.0053	0.05024	0.00064	0.88	317	28	316	4	316	4
S-270417b-03	EP1 III 103 core	14	260	0.21	18.484	1.3	0.0539	1.2	99.0	0.4021	0.0058	0.05410	0.00069	0.88	367	28	340	4	343	4
S-270417b-04	EP1 III 103 rim	9	191	0.06	18.454	1.3	0.0529	1.3	100.6	0.3953	0.0058	0.05419	0.00069	0.87	325	29	340	4	338	4
S-270417b-05	EP1 III 113 core	11	223	0.06	18.477	1.3	0.0533	1.3	100.0	0.3974	0.0058	0.05412	0.00069	0.88	340	28	340	4	340	4
S-270417b-06	EP1 III 113 rim	11	234	0.05	19.928	1.3	0.0522	1.3	100.9	0.3607	0.0053	0.05018	0.00064	0.87	292	29	316	4	313	4
S-270417b-08	EP1 III 112 rim	10	219	0.05	19.940	1.3	0.0520	1.3	101.1	0.3598	0.0053	0.05015	0.00064	0.87	287	29	315	4	312	4
S-270417b-09	EP1 III 107 core	6	105	0.10	17.355	1.3	0.0538	1.4	99.9	0.4277	0.0067	0.05762	0.00073	0.80	364	32	361	4	362	5
S-270417b-10	EP1 III 107 rim	13	286	0.04	19.893	1.3	0.0529	1.2	99.7	0.3669	0.0053	0.05027	0.00063	0.87	326	28	316	4	317	4
S-270417b-11	EP1 III 94 core	10	207	0.05	19.865	1.3	0.0524	1.3	100.5	0.3639	0.0053	0.05034	0.00063	0.86	304	29	317	4	315	4
S-270417b-13	EP1 III 11 core	5	110	0.02	19.992	1.3	0.0524	2.2	100.4	0.3614	0.0081	0.05002	0.00066	0.59	304	48	315	4	313	6
S-270417b-14	EP1 III 11 core 2	3	64	0.02	19.916	1.3	0.0520	1.8	101.2	0.3597	0.0069	0.05021	0.00064	0.66	284	41	316	4	312	5
S-270417b-15	EP1 III 11 rim	11	244	0.04	19.964	1.2	0.0530	1.3	99.5	0.3659	0.0053	0.05009	0.00062	0.85	328	29	315	4	317	4
S-270417b-18	EP1 III 73 core 2	13	267	0.05	19.826	1.2	0.0525	1.3	100.4	0.3648	0.0052	0.05044	0.00062	0.86	306	28	317	4	316	4
S-270417b-19	EP1 III 73 rim	10	213	0.06	19.826	1.2	0.0536	1.3	98.7	0.3727	0.0056	0.05044	0.00063	0.84	354	30	317	4	322	4
S-270417b-20	EP1 III 71 core	14	295	0.06	19.996	1.2	0.0534	1.3	98.8	0.3684	0.0052	0.05001	0.00062	0.87	347	28	315	4	318	4
S-270417b-22	EP1 III 71 rim 2	9	191	0.05	20.000	1.2	0.0537	1.5	98.4	0.3700	0.0059	0.05000	0.00062	0.77	357	33	315	4	320	4
S-270417b-23	EP1 III 32 core	16	348	0.04	19.996	1.2	0.0530	1.3	99.6	0.3651	0.0053	0.05001	0.00062	0.85	327	29	315	4	316	4
S-270417b-24	EP1 III 32 rim	13	274	0.06	20.096	1.2	0.0534	1.3	98.8	0.3661	0.0055	0.04976	0.00061	0.82	345	30	313	4	317	4
S-220517e-01	EP1 Zr 03	10	182	0.12	17.292	1.3	0.0531	1.4	101.1	0.4232	0.0066	0.05783	0.00074	0.82	332	31	362	4	358	5
S-220517e-02	EP1 Zr 02	65	923	0.17	17.277	1.3	0.0568	1.4	95.5	0.4535	0.0070	0.05788	0.00074	0.83	484	30	363	4	380	5
S-220517e-03	EP1 Zr 04 core	13	256	0.04	18.512	1.3	0.0525	1.4	101.1	0.3914	0.0061	0.05402	0.00068	0.81	309	31	339	4	335	4
S-220517e-04	EP1 Zr 04 rim	10	222	0.03	19.786	1.3	0.0535	1.4	98.8	0.3727	0.0058	0.05054	0.00064	0.82	349	31	318	4	322	4
S-220517e-05	EP1 Zr 08	9	195	0.03	19.904	1.3	0.0529	1.6	99.6	0.3666	0.0063	0.05024	0.00064	0.74	326	36	316	4	317	5
S-220517e-06	EP1 Zr 09	13	273	0.10	20.048	1.3	0.0528	1.4	99.8	0.3630	0.0057	0.04988	0.00063	0.80	319	32	314	4	315	4
S-220517e-07	EP1 Zr 14	12	257	0.07	20.173	1.3	0.0525	1.4	100.1	0.3591	0.0057	0.04957	0.00062	0.79	309	33	312	4	312	4
S-220517e-09	EP1 Zr 16 core	4	75	0.23	19.948	1.3	0.0513	2.5	102.4	0.3544	0.0090	0.05013	0.00066	0.52	253	56	315	4	308	7
S-220517e-10	EP1 Zr 16 rim	10	217	0.05	20.137	1.2	0.0539	1.6	98.0	0.3688	0.0062	0.04966	0.00062	0.75	365	35	312	4	319	5

					Isotopic Ratios										Apparent Ages					
Analysis_#	Sample	Pb ppm	U ppm	Th/U	U238/Pb206	Err%	Pb207/Pb	Err%	Conc.	Pb207/U235	Abs. Err	Pb206/U23	Abs. Err	rho	Pb207/Pb206		Pb206/U238		Pb207/U235	
S-270417e-01	MN12-03 II 15W core	5	119	0.02	20.678	1.2	0.0515	1.4	101.7	0.3431	0.0054	0.04836	0.00060	0.79	262	33	305	4	300	4
S-270417e-02	MN12-03 II 15W rim	9	210	0.02	20.855	1.2	0.0535	1.3	98.2	0.3535	0.0053	0.04795	0.00059	0.83	349	30	302	4	307	4
S-270417e-03	MN12-03 II 15W rim 2	7	167	0.02	20.859	1.2	0.0567	1.3	93.5	0.3744	0.0055	0.04794	0.00059	0.84	477	29	302	4	323	4
S-270417e-04	MN12-03 II 15E core	18	406	0.03	20.636	1.2	0.0518	1.2	101.2	0.3458	0.0046	0.04846	0.00060	0.92	274	26	305	4	302	3
S-270417e-05	MN12-03 II 15E rim	21	476	0.03	20.563	1.2	0.0524	1.1	100.1	0.3514	0.0047	0.04863	0.00060	0.93	303	26	306	4	306	4
S-270417e-06	MN12-03 II 21 core	5	106	0.03	20.392	1.2	0.0529	1.5	99.4	0.3577	0.0057	0.04904	0.00061	0.78	325	33	309	4	311	4
S-270417e-07	MN12-03 II 21 rim	13	285	0.06	20.683	1.2	0.0521	1.2	100.7	0.3470	0.0048	0.04835	0.00060	0.89	288	28	304	4	302	4
S-270417e-08	MN12-03 II 22 core	6	135	0.05	20.851	1.3	0.0528	1.4	99.4	0.3489	0.0054	0.04796	0.00060	0.81	319	32	302	4	304	4
S-270417e-09	MN12-03 II 22 rim	12	252	0.04	20.008	1.2	0.0535	1.2	98.7	0.3683	0.0052	0.04998	0.00062	0.88	348	28	314	4	318	4
S-270417e-10	MN12-03 II 23 core	10	221	0.03	19.826	1.2	0.0529	1.2	99.7	0.3679	0.0053	0.05044	0.00063	0.87	325	28	317	4	318	4
S-270417e-11	MN12-03 II 23 rim	11	245	0.05	20.738	1.2	0.0546	1.3	96.6	0.3628	0.0052	0.04822	0.00060	0.87	395	28	304	4	314	4
S-270417e-12	MN12-03 II 24 core	14	300	0.04	19.988	1.2	0.0532	1.2	99.2	0.3669	0.0051	0.05003	0.00062	0.88	337	27	315	4	317	4
S-270417e-13	MN12-03 II 24 rim	13	282	0.03	19.900	1.2	0.0526	1.2	100.2	0.3643	0.0051	0.05025	0.00062	0.88	311	28	316	4	315	4
S-270417e-14	MN12-03 II 27 core	12	256	0.04	19.960	1.2	0.0527	1.3	100.0	0.3640	0.0052	0.05010	0.00062	0.86	316	28	315	4	315	4
S-270417e-15	MN12-03 II 27 rim	14	310	0.06	19.889	1.2	0.0520	1.2	101.1	0.3606	0.0051	0.05028	0.00062	0.88	287	28	316	4	313	4
S-270417e-16	MN12-03 II 29 core	17	355	0.03	19.592	1.2	0.0527	1.2	100.2	0.3709	0.0052	0.05104	0.00063	0.89	316	27	321	4	320	4
S-270417e-17	MN12-03 II 29 rim	17	369	0.03	20.080	1.2	0.0523	1.2	100.6	0.3588	0.0051	0.04980	0.00062	0.87	297	28	313	4	311	4
S-270417e-18	MN12-03 II 31 core	19	437	0.03	20.670	1.2	0.0527	1.2	99.5	0.3516	0.0049	0.04838	0.00060	0.89	316	27	305	4	306	4
S-270417e-19	MN12-03 II 31 rim	13	303	0.04	20.833	1.3	0.0532	1.3	98.6	0.3522	0.0051	0.04800	0.00060	0.87	339	28	302	4	306	4
S-270417e-20	MN12-03 II 46 core	15	339	0.03	20.458	1.2	0.0525	1.2	100.1	0.3535	0.0051	0.04888	0.00061	0.87	305	28	308	4	307	4
S-270417e-21	MN12-03 II 46 rim	14	316	0.05	20.921	1.3	0.0534	1.3	98.2	0.3522	0.0051	0.04780	0.00060	0.87	348	28	301	4	306	4
S-270417e-22	MN12-03 II 04 core	12	272	0.03	20.947	1.3	0.0529	1.3	99.0	0.3484	0.0051	0.04774	0.00060	0.85	326	29	301	4	304	4
S-270417e-23	MN12-03 II 04 rim	13	295	0.04	20.960	1.3	0.0532	1.3	98.6	0.3499	0.0051	0.04771	0.00060	0.86	337	29	300	4	305	4
S-270417e-24	MN12-03 II 04 rim 2	14	311	0.04	20.551	1.3	0.0561	1.3	94.4	0.3764	0.0055	0.04866	0.00061	0.86	456	28	306	4	324	4
S-270417f-01	MN12-03 II 07 core	13	283	0.03	19.873	1.3	0.0526	1.2	100.2	0.3648	0.0050	0.05032	0.00063	0.91	311	27	317	4	316	4
S-270417f-02	MN12-03 II 07 rim	14	306	0.06	20.471	1.2	0.0524	1.2	100.2	0.3531	0.0048	0.04885	0.00061	0.91	304	26	308	4	307	4
S-270417f-03	MN12-03 II 07 rim2	16	348	0.06	20.387	1.2	0.0525	1.2	100.0	0.3553	0.0048	0.04905	0.00061	0.92	309	26	309	4	309	4
S-270417f-04	MN12-03 II 13 core	19	421	0.03	20.602	1.2	0.0527	1.1	99.6	0.3528	0.0047	0.04854	0.00060	0.92	317	26	306	4	307	4
S-270417f-05	MN12-03 II 13 rim	9	203	0.05	20.576	1.3	0.0534	1.3	98.5	0.3577	0.0051	0.04860	0.00061	0.87	345	28	306	4	311	4
S-270417f-06	MN12-03 II 11 core	8	182	0.05	20.462	1.2	0.0514	1.3	101.9	0.3465	0.0051	0.04887	0.00061	0.85	260	29	308	4	302	4
S-270417f-07	MN12-03 II 11 rim	12	273	0.04	20.492	1.3	0.0522	1.2	100.5	0.3513	0.0049	0.04880	0.00061	0.90	295	27	307	4	306	4
S-270417f-08	MN12-03 II 11 rim 2	17	384	0.05	20.580	1.3	0.0560	1.1	94.6	0.3751	0.0050	0.04859	0.00061	0.94	452	25	306	4	323	4
S-270417f-09	MN12-03 III 15 core	7	154	0.02	19.194	1.2	0.0532	1.3	99.6	0.3824	0.0057	0.05210	0.00065	0.84	339	29	327	4	329	4
S-270417f-10	MN12-03 III 15 rim	12	264	0.02	20.268	1.3	0.0537	1.2	98.3	0.3649	0.0051	0.04934	0.00062	0.90	356	27	311	4	316	4
S-270417f-12	MN12-03 III 08 core	10	215	0.02	20.525	1.3	0.0527	1.3	99.7	0.3540	0.0051	0.04872	0.00061	0.87	316	28	307	4	308	4
S-270417f-13	MN12-03 III 08 rim	10	229	0.05	20.734	1.2	0.0532	1.2	98.7	0.3536	0.0050	0.04823	0.00060	0.87	337	28	304	4	308	4
S-270417f-14	MN12-03 III 08 rim 2	15	334	0.07	20.471	1.2	0.0523	1.2	100.3	0.3524	0.0048	0.04885	0.00061	0.92	300	26	308	4	307	4
S-270417f-15	MN12-03 III 04 core	5	110	0.04	19.124	1.3	0.0528	1.5	100.4	0.3804	0.0061	0.05229	0.00066	0.78	319	33	329	4	327	5
S-270417f-16	MN12-03 III 04 rim	8	181	0.03	19.736	1.2	0.0532	1.3	99.3	0.3718	0.0054	0.05067	0.00063	0.86	338	28	319	4	321	4
S-270417f-17	MN12-03 III 04 rim 2	9	192	0.02	19.448	1.2	0.0524	1.3	100.8	0.3712	0.0053	0.05142	0.00064	0.87	302	28	323	4	321	4
S-270417f-18	MN12-03 III 06 core	5	113	0.03	19.802	1.3	0.0540	1.4	98.0	0.3762	0.0059	0.05050	0.00064	0.81	373	31	318	4	324	4
S-270417f-19	MN12-03 III 06 rim	10	211	0.02	19.708	1.2	0.0525	1.2	100.5	0.3670	0.0052	0.05074	0.00063	0.87	306	28	319	4	317	4
S-270417f-20	MN12-03 III 06 rim 2	8	176	0.03	19.873	1.3	0.0521	1.3	101.0	0.3615	0.0053	0.05032	0.00063	0.86	290	29	317	4	313	4
S-270417f-21	MN12-03 III 03 core	12	268	0.06	19.936	1.3	0.0532	1.2	99.2	0.3677	0.0053	0.05016	0.00063	0.88	336	28	316	4	318	4
S-270417f-22	MN12-03 III 03 rim	12	265	0.05	19.877	1.3	0.0533	1.2	99.1	0.3697	0.0052	0.05031	0.00063	0.89	342	27	316	4	319	4
S-270417f-24	MN12-03 III 15	11	251	0.02	19.853	1.3	0.0530	1.2	99.6	0.3679	0.0051	0.05037	0.00063	0.90	328	27	317	4	318	4

					Isotopic Ratios									Apparent Ages					
Analysis_#	Sample	Pb ppm	U ppm	Th/U	U238/Pb206	Err%	Pb207/Pb206	Err%	Pb207/U235	Abs. Err	Pb206/U238	Abs. Err	rho	Pb207/Pb206		Pb206/U238		Pb207/U235	
S-220517c-02	EP5 IV 02 rim	22	224	0.60	10.737	1.27	0.0630	1.17	0.8090	0.0113	0.09314	0.00118	0.91	708	25	574	7	602	6
S-220517c-03	EP5 IV 02 rim 2	175	3883	0.01	19.972	1.26	0.0537	1.03	0.3704	0.0047	0.05007	0.00063	0.99	357	23	315	4	320	4
S-220517c-04	EP5 IV 01 core	14	194	0.25	13.659	1.27	0.0565	1.13	0.5704	0.0077	0.07321	0.00093	0.94	472	25	455	6	458	5
S-220517c-05	EP5 IV 01 rim	13	226	0.10	16.592	1.28	0.0704	1.42	0.5850	0.0093	0.06027	0.00077	0.81	940	29	377	5	468	6
S-220517c-06	EP5 IV 01 rim 2	265	5811	0.01	19.782	1.25	0.0525	1.03	0.3658	0.0046	0.05055	0.00063	0.98	307	23	318	4	317	3
S-220517c-07	EP5 IV 03 core	10	131	0.34	13.661	1.26	0.0759	1.15	0.7661	0.0105	0.07320	0.00092	0.92	1093	23	455	6	578	6
S-220517c-08	EP5 IV 03 rim	17	259	0.03	13.607	1.25	0.0564	1.15	0.5711	0.0078	0.07349	0.00092	0.92	466	25	457	6	459	5
S-220517c-10	EP5 IV 05 core	7	80	0.33	11.421	1.27	0.0698	1.42	0.8431	0.0133	0.08756	0.00111	0.80	924	29	541	7	621	7
S-220517c-11	EP5 IV 05 rim	20	320	0.04	14.795	1.24	0.0587	1.14	0.5471	0.0073	0.06759	0.00084	0.93	556	25	422	5	443	5
S-220517c-12	EP5 IV 05 rim 2	302	6494	0.02	19.822	1.25	0.0528	1.04	0.3675	0.0046	0.05045	0.00063	0.99	322	23	317	4	318	3
S-220517c-13	EP5 III 01 core	30	376	0.75	14.345	1.25	0.0583	1.18	0.5604	0.0077	0.06971	0.00087	0.91	541	26	434	5	452	5
S-220517c-14	EP5 III 01 rim	13	185	0.40	14.290	1.24	0.0576	1.16	0.5561	0.0075	0.06998	0.00087	0.92	516	25	436	5	449	5
S-220517c-16	EP5 III 02 core	18	161	0.37	9.083	1.24	0.0619	1.13	0.9388	0.0125	0.11009	0.00136	0.93	669	24	673	8	672	7
S-220517c-17	EP5 III 02 rim	18	192	0.23	11.287	1.23	0.0673	1.19	0.8223	0.0113	0.08860	0.00109	0.90	848	25	547	6	609	6
S-220517c-18	EP5 III 02 rim 2	124	2687	0.02	20.088	1.23	0.0543	1.09	0.3728	0.0048	0.04978	0.00061	0.96	385	24	313	4	322	4
S-220517c-19	EP5 III 03 core	15	142	0.57	10.330	1.23	0.0651	1.17	0.8692	0.0117	0.09681	0.00119	0.91	778	24	596	7	635	6
S-220517c-21	EP5 III 04 core	47	100	0.24	2.411	1.22	0.1659	1.08	9.4883	0.1210	0.41473	0.00507	0.96	2517	18	2237	23	2386	12
S-220517c-22	EP5 III 04 rim	41	98	0.39	2.762	1.22	0.1719	1.08	8.5802	0.1093	0.36209	0.00442	0.96	2576	18	1992	21	2295	12
S-220517c-24	EP5 III 05 core	6	57	0.81	10.671	1.23	0.0594	1.33	0.7672	0.0113	0.09371	0.00115	0.83	581	29	578	7	578	7
S-220517d-01	EP5 III 05 rim	131	2807	0.02	19.960	1.20	0.0535	1.03	0.3698	0.0045	0.05010	0.00060	0.99	351	23	315	4	320	3
S-220517d-02	EP5 III 05 rim 2	138	3284	0.02	22.090	1.19	0.0529	1.02	0.3301	0.0040	0.04527	0.00054	0.99	324	23	285	3	290	3
S-220517d-03	EP5 III 06 rim	165	3943	0.02	22.090	1.19	0.0530	1.02	0.3305	0.0040	0.04527	0.00054	0.99	327	23	285	3	290	3
S-220517d-04	EP5 III 06 rim 2	47	1151	0.00	23.100	1.20	0.0566	1.08	0.3377	0.0042	0.04329	0.00052	0.96	475	24	273	3	296	3
S-220517d-07	EP5 III 17 rim	20	300	0.08	13.930	1.21	0.0574	1.08	0.5684	0.0072	0.07179	0.00087	0.95	508	24	447	5	457	5
S-220517d-08	EP5 III 17 rim 2	149	3200	0.01	19.798	1.21	0.0528	1.02	0.3675	0.0045	0.05051	0.00061	0.99	319	23	318	4	318	3
S-220517d-09	EP5 III 18 rim	144	3263	0.02	20.907	1.21	0.0546	1.04	0.3597	0.0045	0.04783	0.00058	0.98	394	23	301	4	312	3
S-220517d-11	EP5 III 20 rim	137	3017	0.02	20.088	1.23	0.0525	1.05	0.3602	0.0045	0.04978	0.00061	0.98	307	24	313	4	312	3
S-220517d-12	EP5 III 13 rim	92	2028	0.01	20.080	1.22	0.0527	1.06	0.3617	0.0046	0.04980	0.00061	0.97	315	24	313	4	314	3
S-220517d-13	EP5 III 21 rim	14	204	0.10	13.701	1.22	0.0554	1.14	0.5576	0.0074	0.07299	0.00089	0.92	429	25	454	5	450	5
S-220517d-14	EP5 III 22 rim	116	2790	0.02	22.002	1.23	0.0548	1.06	0.3430	0.0043	0.04545	0.00056	0.98	402	23	287	3	300	3
S-220517d-15	EP5 III 23 rim	159	3488	0.02	20.012	1.22	0.0530	1.06	0.3648	0.0046	0.04997	0.00061	0.97	327	24	314	4	316	3
S-220517d-16	EP5 III 25 rim	143	3113	0.02	19.782	1.23	0.0527	1.04	0.3673	0.0046	0.05055	0.00062	0.97	316	24	318	4	318	3
S-220517d-17	EP5 III 26 rim	95	2120	0.01	20.121	1.23	0.0535	1.07	0.3662	0.0047	0.04970	0.00061	0.96	348	24	313	4	317	3
S-220517d-18	EP5 III 26 rim 2	113	2534	0.01	20.288	1.24	0.0533	1.07	0.3625	0.0047	0.04929	0.00061	0.96	343	24	310	4	314	3
S-220517d-19	EP5 III 27 rim	25	406	0.04	15.179	1.23	0.0571	1.12	0.5187	0.0069	0.06588	0.00081	0.92	495	25	411	5	424	5
S-220517d-20	EP5 III 27 rim 2	57	1220	0.02	19.771	1.25	0.0600	1.08	0.4185	0.0055	0.05058	0.00063	0.96	604	23	318	4	355	4
S-220517d-21	EP5 III 28 rim	21	292	0.04	12.549	1.24	0.0593	1.15	0.6510	0.0088	0.07969	0.00099	0.92	576	25	494	6	509	5
S-220517d-22	EP5 III 28 rim 2	79	1494	0.01	17.106	1.23	0.0545	1.08	0.4394	0.0057	0.05846	0.00072	0.94	393	24	366	4	370	4
S-220517d-24	EP5 II 01 core	32	146	0.93	5.988	1.25	0.1271	1.12	2.9272	0.0390	0.16701	0.00208	0.94	2059	20	996	11	1389	10

					Isotopic Ratios								Apparent Ages							
Analysis_#	Sample	Pb ppm	Uppm	Th/U	Pb208/Th232	Abs. Err	Pb206/U238	Abs. Err	Pb207/U235	Abs. Err	Pb206/U238	Abs. Err	Pb207/Pb206		Pb206/U238		Pb207/U235		Pb208/Th232	
S220517a-01	MN12-03 MON 01 core	1153.8	2275.8	32.77	0.01570	0.00019	0.05080	0.00071	0.4055	0.0062	0.05080	0.00071	526	27	319	4	346	4	315	4
S220517a-02	MN12-03 MON 01 rim	1281.9	2522.5	33.80	0.01529	0.00019	0.04934	0.00069	0.3986	0.0059	0.04934	0.00069	552	26	311	4	341	4	307	4
S220517a-03	MN12-03 MON 01 S core	1257.5	1592.2	54.56	0.01511	0.00018	0.05049	0.00071	0.4809	0.0072	0.05049	0.00071	901	25	318	4	399	5	303	4
S220517a-04	MN12-03 MON 01 S rim	1296.8	2297.9	37.53	0.01538	0.00019	0.04994	0.00070	0.4193	0.0062	0.04994	0.00070	636	25	314	4	356	4	309	4
S220517a-05	MN12-03 MON 02 core	1156.6	1718.4	46.01	0.01514	0.00018	0.04943	0.00069	0.4311	0.0062	0.04943	0.00069	717	24	311	4	364	4	304	4
S220517a-06	MN12-03 MON 02 rim	1310.1	2733.8	31.56	0.01533	0.00019	0.04907	0.00068	0.4107	0.0057	0.04907	0.00068	629	23	309	4	349	4	308	4
S220517a-07	MN12-03 MON 03 core	805.7	2159.4	23.48	0.01560	0.00019	0.04959	0.00068	0.3870	0.0055	0.04959	0.00068	476	25	312	4	332	4	313	4
S220517a-08	MN12-03 MON 03 rim	653.9	1922.8	21.27	0.01550	0.00019	0.04974	0.00069	0.3831	0.0055	0.04974	0.00069	447	25	313	4	329	4	311	4
S220517a-09	MN12-03 MON 04 core	1416.4	1242.7	79.47	0.01514	0.00018	0.05015	0.00069	0.4788	0.0071	0.05015	0.00069	906	25	315	4	397	5	304	4
S220517a-10	MN12-03 MON 05	1086.2	2472.8	28.38	0.01542	0.00019	0.04979	0.00069	0.4007	0.0057	0.04979	0.00069	544	25	313	4	342	4	309	4
S220517a-11	MN12-03 MON 06	1362.0	1199.4	78.67	0.01522	0.00018	0.05052	0.00070	0.4785	0.0072	0.05052	0.00070	890	25	318	4	397	5	305	4
S220517a-12	MN12-03 MON 07 core	1156.9	3249.4	22.30	0.01554	0.00019	0.04965	0.00068	0.3774	0.0053	0.04965	0.00068	418	24	312	4	325	4	312	4
S220517a-13	MN12-03 MON 07 rim	1508.7	4140.3	22.45	0.01579	0.00019	0.04994	0.00068	0.3822	0.0053	0.04994	0.00068	433	24	314	4	329	4	317	4
S220517a-14	MN12-03 MON 08 core	819.3	1285.4	41.92	0.01553	0.00019	0.05011	0.00069	0.4326	0.0063	0.05011	0.00069	695	25	315	4	365	4	312	4
S220517a-15	MN12-03 MON 08 rim	1210.0	3157.4	23.83	0.01572	0.00019	0.04964	0.00068	0.3904	0.0055	0.04964	0.00068	493	25	312	4	335	4	315	4
S220517a-16	MN12-03 MON 08 rim 2	1350.2	3349.5	25.16	0.01578	0.00019	0.04854	0.00066	0.3751	0.0053	0.04854	0.00066	454	25	306	4	323	4	316	4
S220517a-17	MN12-03 MON 09 core	1432.5	2886.8	32.58	0.01526	0.00018	0.04941	0.00067	0.3883	0.0057	0.04941	0.00067	491	27	311	4	333	4	306	4
S220517a-18	MN12-03 MON 09 rim	909.3	2103.3	28.98	0.01478	0.00018	0.04832	0.00067	0.4005	0.0067	0.04832	0.00067	608	31	304	4	342	5	297	4
S220517a-19	MN12-03 MON 10	1020.7	1073.6	64.66	0.01528	0.00018	0.04967	0.00068	0.4528	0.0069	0.04967	0.00068	811	27	313	4	379	5	307	4
S220517a-20	MN12-03 MON 11	1461.1	3501.1	25.89	0.01582	0.00019	0.04979	0.00067	0.3960	0.0056	0.04979	0.00067	518	26	313	4	339	4	317	4
S220517a-21	MN12-03 MON 12	1069.3	1912.9	36.88	0.01527	0.00018	0.04929	0.00067	0.4194	0.0061	0.04929	0.00067	665	26	310	4	356	4	306	4
S220517a-22	MN12-03 MON 13	926.3	1420.7	45.73	0.01455	0.00017	0.04739	0.00064	0.4142	0.0062	0.04739	0.00064	722	27	299	4	352	4	292	3
S220517a-23	MN12-03 MON 14	1372.4	3110.8	30.27	0.01446	0.00017	0.04621	0.00062	0.3680	0.0054	0.04621	0.00062	520	27	291	4	318	4	290	3
S220517a-24	MN12-03 MON 15	1089.1	2320.2	32.81	0.01423	0.00017	0.04741	0.00064	0.3954	0.0062	0.04741	0.00064	622	29	299	4	338	5	286	3
S220517b-02	MN12-03 MON 17	1288.1	2079.8	41.34	0.01535	0.00018	0.05022	0.00068	0.4255	0.0064	0.05022	0.00068	655	27	316	4	360	5	308	4
S220517b-03	MN12-03 MON 18 core	724.9	1064.8	44.11	0.01571	0.00019	0.05049	0.00068	0.4577	0.0071	0.05049	0.00068	798	28	318	4	383	5	315	4
S220517b-04	MN12-03 MON 18 rim	1094.1	2515.3	27.04	0.01563	0.00018	0.05017	0.00067	0.3940	0.0063	0.05017	0.00067	489	32	316	4	337	5	314	4
S220517b-05	MN12-03 MON 19	1435.0	2429.7	42.34	0.01382	0.00016	0.04650	0.00061	0.3921	0.0059	0.04650	0.00061	645	28	293	4	336	4	278	3
S220517b-06	MN12-03 MON 19 rim	1063.0	2724.7	25.67	0.01441	0.00017	0.04527	0.00059	0.3624	0.0056	0.04527	0.00059	532	30	285	4	314	4	289	3

Table II.2.DR8: REE data for EP1 zircon and MN12-03 zircon; statistics on REE concentrations. Chondrite normalization after Sun and McDonough (1989).

Element	06-ZR05iv	07-ZR05iv	08-ZR05iv	09-ZR08SEiv	10-ZR08SEiv	11-ZR08Eiv	12-ZR08Eiv	13-ZR08Civ	14-ZR08Civ	15-ZR09NWi	16-ZR09NWi	17-ZR09Siv	18-ZR09Siv	19-ZR09Siv	20-ZR09Civ	21-ZR09Civ	26-ZR10iv	27-ZR10iv	28-ZR12iv	29-ZR12iv	30-ZR12NWi	31-ZR12NWi	32-ZR12NWi	33-ZR12NWi	34-ZR113
Si29	14.82	14.84	14.82	15.19	14.99	15.02	15.17	14.91	15.09	15.06	15	15.2	14.61	15.21	15	15.27	14.96	14.83	15.07	15.05	14.92	16.29	15.06	15.12	15
Ca44	0.00275	0.00778	0.00706	0.00413	0.00746	0.00704	0.00777	0.00744	0.00713	0.00663	0.00624	0.0093	0.0074	0.00658	0.0076	0.00807	0.00389	0.00572	0.00429	0.00532	0.00525	0.0114	0.00571	0.00583	0.0067
Ti47	4.62	4.56	4.51	4.47	4.39	4.35	4.35	4.3	4.28	4.26	4.25	4.2	4.21	4.14	4.1	4.1	4.03	4	3.97	3.97	3.97	3.94	3.97	3.96	3.95
Ti49	0.0364	0.017	0.0317	0.0167	0.011	0.0252	0.0242	0.0294	0.0173	0.0173	0.0098	0.018	0.0333	0.0143	0.0117	0.0294	0.0295	0.0298	0.0183	0.03	0.0157	0.0182	0.0177	0.0164	0.033
Ti50	0	0	0	0	0	0	0	0	0	0	0	0	0	0	0	0	0	0	0	0	0	0	0	0	0
Y89	25	19.21	52.83	19.05	14.59	31.81	39.93	56.18	25.05	18.21	14.22	18.33	56.96	22.74	21.58	58.52	44.8	49.53	39.45	58.43	20.11	22.74	27.28	24.06	45.19
Zr90	127906.8	127906.8	127906.8	127906.8	127906.8	127906.8	127906.8	127906.8	127906.8	127906.8	127906.8	127906.8	127906.82	127906.8	127906.8	127906.8	127906.79	127906.79	127906.79	127906.79	127906.79	127906.79	127906.79	127906.79	127906.8
Nb93	2.89	2.5	2.69	2.39	2.48	2.31	2.36	2.18	1.78	1.97	2.13	2.23	2.07	1.93	1.85	1.9	1.93	1.82	2.08	1.98	1.59	1.71	1.81	1.52	1.7
La139	0	0	0	0	0	0	0	0	0.19	0	0	0	0	0	0	0	0.257	0	0	0	0	0	0	0	0
Ce140	7.8	3.95	5.45	3.05	2.302	4.25	4.96	4.82	2.568	3.46	2.94	2.681	4.95	3.52	4.92	4.53	6.65	4.09	4.6	4.09	4.16	2.85	3.93	2.385	5.27
Pr141	1.89	0.81	0.77	0	0	0.6	0.8	1.15	0.38	0.65	0	0.45	0.9	0.46	1.19	0.69	2.04	0.46	1.04	0.91	1.26	0	0.66	0.34	2.04
Nd146	4.58	2.55	2.66	0.97	0.53	2.05	3.24	4.62	0.79	1.7	0.54	1.46	3.48	1.75	3.55	2.97	5.15	2.43	3.04	2.83	3.03	0.72	2.16	0.86	6
Sm147	15.69	11.54	16.11	5.36	3.78	12.62	21.89	30.77	6.64	6.38	3.75	10.52	21.46	10.01	15.31	21.45	28.44	16.36	19.1	21.23	11.4	4.92	13.49	6.56	32.31
Eu153	21.44	14.25	24.88	10.4	6.45	19.64	30.13	40.16	9.39	8.46	6.47	13.91	32.95	14.56	17.97	32.94	39.65	23.57	28.36	31.92	15.62	8.24	19.05	9.83	44.81
Gd157	28.99	19.68	41.51	17.6	11.21	31.86	47.97	64.85	17.75	12.43	9.89	21.11	54.52	21.78	24.53	53.33	62.94	39.06	43.62	52.37	23.19	16.75	29.81	17.31	64.47
Tb159	27.12	20.06	46.04	17.11	12.64	30.71	46.74	61.92	20.77	15.64	13.54	21.56	55.4	23.89	23.42	57.34	58.59	43.89	40.94	56.41	21.64	18.75	29.68	19.33	55.34
Dy163	23.85	18.54	46.33	17.01	14.07	29.8	41.77	57.07	22.68	15.68	13.48	18.56	53.48	21.75	22.13	54.52	49.74	44.48	39.52	54.48	20.39	22.56	26.74	22.08	48.64
Ho165	23.27	16.25	47.9	16.96	12.76	28.8	37.72	49.55	22.66	16.98	13.09	16.7	50.18	18.73	19.05	52.09	40.36	43.42	35.03	50.05	17.87	21.62	24.17	22.87	42.11
Er166	23.72	16.57	49.86	16.63	13.89	27.27	34.54	48.41	24.1	18.29	12.48	16.24	49.3	20.56	18.63	52.26	34.83	47.62	33.67	50.35	17.52	22.85	23.27	23.64	37.37
Tm169	26.89	18.27	50.71	16.92	16.05	27.78	29.95	43.38	25.54	16.97	11.87	14.01	50.46	17.73	18.88	52.61	34.5	46.97	31.89	49.89	16.26	21.88	21.64	23.65	32.23
Yb172	33.96	17.79	56.48	20.43	14.27	29.48	31.02	50.09	26.57	18.83	14.49	16.25	53.59	22.08	20.94	56.34	34.45	55.61	32.18	57.02	17.54	23.12	24.56	25.97	35.4
Lu175	38.82	17.71	59.95	22.17	16.09	26.97	30.11	49.04	26.71	19.56	15.86	17.85	53.15	18.74	19.8	57.96	33.78	56.96	31.4	55.13	17.9	23.66	27.09	25.54	29.48
Hf178	100378.92	103357.01	102744.02	102799.32	104061.91	101644.45	99630.32	100317.95	104887.37	103513.31	104001.5	114023.23	100288.94	102832.7	103408.65	102083.26	101734.69	104507.41	101885.97	102811.34	105163.49	103129.19	103324.8	105308.9	101147.77
Ta181	12.86	5.44	5.24	6	4.66	3.44	4.71	6.63	0	4.48	5.74	5.94	4.51	5.28	4.94	6.03	5.16	4.25	5.17	4.1	0	0	0	3.37	0
Pb208	0.172	0.19	0.267	0.193	0.131	0.16	0.291	0.336	0.188	0.132	0.106	0.165	0.32	0.237	0.279	0.301	0.383	0.201	0.327	0.31	0.201	0.281	0.291	0.131	0.26
Th232	408.45	520.84	653.25	580.98	378.69	434.44	849.58	1013.24	387.89	368.23	280.54	391.49	883.32	595.68	897.23	897.4	1139.34	597.6	931.28	742.54	551.52	316.25	777.75	329.8	888.36
U238	21224	33193.37	42356.36	34044.05	24972.71	32539.93	40249.23	46067.24	24956.46	26336.14	34931.08	25605.24	48749.1	38993.36	39215.8	47006.52	46813.16	38489.19	68777.72	45044.64	36786.89	34754.28	40067.62	25469.43	49739.52

Element	35-ZR113	36-ZR112	37-ZR112	38-ZR103	39-ZR103	40-ZR101	41-ZR101	42-ZR107	43-ZR107	44-ZR107	45-ZR94	46-ZR94	51-ZR73	52-ZR73	53-ZR73	54-ZR73	55-ZR71	56-ZR71	57-ZR32	58-ZR32	59-ZR32	61-ZR11	62-ZR11	63-ZR11
Si29	15.15	15.41	15.22	15.06	15.3	15.07	15.25	15.28	15.34	15.31	15.12	15.04	15.6	15.07	15.12	15.34	14.98	15.02	15.06	15.13	15.25	14.83	15.03	14.71
Ca44	0.0077	0.0202	0.0044	0.009	0.0053	0.006	0.0067	0.0144	0.0084	0.00552	0.0062	0.00657	0.0196	0.0064	0.0059	0.0062	0.0058	0.0134	0.0067	0.008	0.0082	0.0052	0.0034	0.0077
Ti47	3.91	3.91	3.95	3.89	3.93	3.91	3.91	9.89	3.87	3.88	3.88	3.9	3.96	3.93	3.91	3.93	3.93	3.91	3.91	3.92	3.95	3.93	3.93	3.93
Ti49	0.0207	0.036	0.0229	0.013	0.0169	0.0192	0.0182	6.17	0.0116	0.0263	0.0163	0.0172	0.0357	0.0294	0.0242	0.0272	0.0322	0.0154	0.0174	0.0137	0.13	0.0282	0.0192	0.0298
Ti50	0	0	0	0	0	0	0	0	5.16	0	0	0	0	0	0	0	0	0	0	0	0	0	0	0
Y89	27.03	18.34	45.32	13.28	27.59	34.62	25	27.17	24.09	53.32	16.29	21.41	2036.08	47.7	51.9	38.99	56.24	23.04	25.98	46.76	17.91	37.62	14.81	40.53
Zr90	127906.79	127906.8	127906.79	127906.8	127906.8	127906.79	127906.8	127906.79	127906.79	127906.79	127906.78	127906.79	127906.79	127906.79	127906.78	127906.78	127906.8	127906.8	127906.79	127906.79	127906.8	127906.8	127906.79	127906.79
Nb93	1.58	1.59	1.61	1.64	1.69	1.82	1.89	1.44	1.25	1.31	1.4	1.78	121.12	1.81	2.36	1.64	1.74	1.63	1.42	1.84	1.76	1.96	1.56	1.3
La139	0	0.207	0	0	0	0	0	0.38	0	0	0	0	0.341	0	0	0	0	0	0	0	0	0	0	0
Ce140	4.7	2.93	3.59	0.623	3.24	2.71	2.98	1.336	0.734	3.66	2.96	3.03	135.72	3.95	4.2	4.42	3.72	2.98	3.17	3.01	2.97	0.64	0.824	2.75
Pr141	1.41	0.41	0.65	0	0	0.45	0	0.76	0	0.69	0.45	0.69	4.96	0.76	0.79	0.75	0.62	0.61	0.52	0.55	0.41	0	0	0
Nd146	4.08	1.43	1.91	0	1.23	1.65	1.28	1.26	0	3.04	1.31	1.84	14.41	2.32	1.94	3.09	2.61	1.32	1.73	1.2	1.03	0.66	0.47	1.79
Sm147	15.39	8.65	13.22	2.21	9.49	12.18	9.4	5.26	4.16	24.32	7.41	7.54	78.31	16.22	11.79	20.44	19.24	9.24	12.15	7.66	6.79	1.91	2.9	13.05
Eu153	22.45	11.4	22.95	4.42	15.15	21.18	12.72	10.06	8.65	35.59	0	12.14	23.33	24.79	19	30.55	29.04	13.48	18.19	12.57	10.12	4.91	7.6	20.8
Gd157	30.01	17.44	35.57	9.48	24.24	30.71	24.77	19.67	17.36	58.05	16.29	18.85	327.91	40.64	32.63	49.95	49.18	20.37	25.85	24.34	15.81	11.81	15.19	35.35
Tb159	30.15	17.55	41.76	14.85	25.88	33.06	25.12	26.26	23.16	55.27	15.71	20.17	604.93	40.32	34.85	47.57	52.49	21.63	26.2	30.68	16.4	20.86	18.04	37.63
Dy163	26.04	17.35	41	15.17	25.4	33.57	25.45	26.25	22.95	52.34	15	19.63	1062.94	41.03	38.55	41.76	52.17	20.85	24.73	36.7	16.37	26.93	17.17	36.92
Ho165	22.76	15.73	40.65	11.47	25.1	31.13	22.42	25.35	20.5	49.77	14.72	19.36	1676.49	41.25	43.55	35.49	50.52	19.95	23.09	44.32	15.42	34.41	12.88	36.25
Er166	22.14	16.27	43.23	10.5	23.45	31.81	21.78	23.82	21.74	45.92	13.99	17.86	2489.55	43.34	53.77	30.15	51.13	20.06	21.65	57.82	15.03	48.34	11.64	37.42
Tm169	20.44	15.88	43.4	10.83	23.73	30.26	17.99	23.75	19.46	44.8	12.78	19.27	3208.53	43.56	59.07	26.82	49.8	20.16	20.13	65.19	13.04	61.5	10.3	36.41
Yb172	22.51	19.23	50.27	9.66	27.58	32.84	21.79	24.34	21.5	46.86	13.83	21.22	4347.16	49.31	75.95	29.85	57.95	24.12	21.35	86.36	15.4	97.28	9.74	37.67
Lu175	22.68	18.51	54.13	11.66	25.32	32.59	20.67	27.7	21.6	46.38	14	19.35	4830.09	46.97	80.05	26.01	61.09	20.87	22.19	101.17	15.01	125.34	11.39	38.97
Hf178	102027.11	107455.96	104997.83	113770.14	100548.83	100705.2	103434.5	114922.94	113667.7	100949.32	103096.01	101640.32	126679.33	100391.43	98332.98	100730.55	100070.24	100804.96	100035.3	107794.67	99857.88	112155.23	108661.52	103367.7
Ta181	3.62	3.49	0	0	0	4.03	0	3.42	0	5.36	0	0	1763.78	3.7	17.07	0	4.74	0	0	6.47	4.85	8.45	0	0
Pb208	0.172	2.51	0.207	0.044	0.176	0.135	0.184	0.114	0.04	0.223	0.142	0.822	17.07	0.209	0.401	0.33	0.255	0.29	0.166	0.427	0.252	0.172	0	0.255
Th232	512.41	428.84	650.1	197.29	531.2	385.29	444.27	177.83	173.98	703.23	361.63	381.76	35761.75	569.05	794.13	908.18	663.77	573.81	429.02	758.9	463.14	416.17	78.4	369.58
U238	34943.86	23024.91	36217.47	17250.54	36749.63	30354.15	30031.33	16936.09	16090.47	43696.8	32078.14	27603.33	98441.23	40840.24	33894.89	40973.18	42057.82	27596.53	37778.69	27144.63	33972.18	25765.72	14531.86	34974.95

Element	07-Zr3w	08-Zr3w	09-Zr3w	10-Zr4	11-Zr4	12-Zr4	13-Zr6	14-Zr6	15-Zr6	16-Zr8	17-Zr8	18-Zr8	19-Zr15	20-Zr15	21-Zr15	26-Zr4ii	27-Zr4ii	28-Zr4ii	29-Zr7ii	30-Zr7ii	31-Zr7ii	32-Zr11ii	33-Zr11ii
Si29	167.11	162.24	167.07	161.93	161	164.85	163.1	162.29	162.55	161.28	161.45	164.76	161.8	158.74	161.88	163.25	163.18	163.54	163.18	160.11	161.5	161.83	163.3
Ca44	0.25	0.21	0.29	0.3	0.28	0.3	0.23	0.22	0.23	0.21	0.17	0.25	0.23	0.28	0.22	0.23	0.27	0.22	0.2	0.29	0.21	0.2	0.25
Ti47	5.58	5.5	5.54	5.5	5.43	5.4	5.35	5.33	5.29	5.31	5.29	5.25	5.23	5.23	5.18	5.08	5.04	5.03	5.05	4.97	4.97	4.96	5.03
Ti49	0.0236	0.0152	0.0372	0.0103	0.0116	0.0103	0.0094	0.0158	0.018	0.0134	0.0212	0.0183	0.016	0.0187	0.012	0.0199	0.0138	0.0216	0.0278	0.0153	0.0146	0.0138	0.0161
Ti50	0	0	0	0	0	0	0	0	0	0	0	0	0	0	0	0	0	0	0	0	0	0	0
Y89	16.72	23.34	24.86	13.34	14.76	11.11	27.36	14.54	24.85	36.59	35.67	16.19	28.98	19.26	18.08	19.5	18.11	33.44	39.88	26.44	32.84	14.28	22.01
Zr90	127906.8	127906.8	127906.8	127906.8	127906.8	127906.8	127906.8	127906.8	127906.8	127906.8	127906.8	127906.8	127906.8	127906.8	127906.8	127906.8	127906.8	127906.8	127906.8	127906.8	127906.8	127906.8	127906.8
Nb93	3.56	3.77	3.62	2.63	3.22	3.67	3.69	3.74	2.53	3.38	3.68	3.47	3.09	3.69	2.96	2.76	3.44	2.83	3.27	2.66	2.63	3.22	2.82
La139	0	0	0.635	0	0	0	0	0	0	0	0	0	0	0.275	0	0	0	0.267	0	0.738	0	0	0
Ce140	4.52	4.9	6.68	0.94	1.122	1.345	0.689	1.347	3.17	1.898	6.8	4.54	1.436	1.727	1.098	2.588	4.26	3.37	7.26	5.55	2.87	2.189	3.34
Pr141	0.67	0.72	2.17	0	0	0	0	0	0	0	0.55	0.36	0	0	0	0.72	0	0.38	0.71	0.69	0.46	0	0
Nd146	1.65	1.97	4.95	0	0.36	0.46	0	0.83	1.06	0.67	2.29	1.12	0.6	0.83	0.41	1.14	1.46	1.07	1.38	1.82	1.04	0.49	0.75
Sm147	11.42	8.06	15.52	4.72	4.89	4.39	2.44	4.34	6.79	7.95	18.33	7.33	9.91	7.8	6.88	6.02	8.64	8.6	9.3	9.67	11.04	6.74	5.3
Eu153	17.55	11.67	19.89	6.7	8.36	5.55	7.43	9.62	10.43	16.39	32.18	11.02	19.26	13.6	13.65	9.09	10.82	13.26	17	13.74	18.74	11.39	8.88
Gd157	32.91	17.92	26.92	14.73	18.48	11.88	17.03	19.45	20.38	40.93	52.5	16.3	42.22	28.64	29	19.54	19.18	25.82	40.47	22.85	32.5	22.34	16.8
Tb159	30.81	20.74	25.2	16.97	21.6	15.2	24.58	23.74	20.36	55.39	49.52	17.96	50.78	34.48	34.64	25.35	18.81	29.52	54.97	22.7	34.01	23.74	18.81
Dy163	22.05	19.56	23.03	14.02	16.41	12.18	25.76	19.29	20.83	49.06	39.77	15.15	39.93	27.08	26.2	22.77	17.39	29.73	45.51	22.95	29.25	18.2	19.34
Ho165	14.81	18.79	20.76	12.19	13.72	9.54	26.1	14.9	18.93	32.9	30.79	14.14	28.38	18.68	17.76	19.19	15.24	30.16	35.98	22.97	27.35	13.29	17.91
Er166	10.51	19.06	20.58	11.19	11.66	8.48	26.02	10.11	18.82	24.31	23.87	10.28	19.62	13.59	12.6	14.26	14.05	28.93	28.06	22.19	25.85	10.09	18.91
Tm169	9.42	18.18	20.1	8.99	9.38	6.71	20.69	7.73	19.57	17.29	19.94	8.63	15.03	11.92	9.24	12.18	13.42	29.46	23.88	22.29	21	8.97	18.91
Yb172	8.09	19.39	21.26	9.4	11.1	7.52	21.19	9.69	22.51	20.01	17.69	10.56	16.59	9.93	10.06	9.8	12.66	30.42	22.69	21.8	22.38	10.09	18.9
Lu175	11.25	19.26	20.5	12.57	10.37	8.84	16.79	6.8	21.87	24.45	13.78	6.82	15.85	11.33	9.76	11.46	15.49	28.57	23	21.31	23.65	9.01	19.65
Hf178	99242.52	94245.09	95794.21	105144.1	98519.88	100892.8	97042.34	95577.59	98933.98	98008.07	102400.2	101656.2	99765.41	94677.48	97159.93	103454.6	103138.3	105713.1	105707.9	100896.7	106023.5	102896.4	100924.4
Ta181	9.68	14.06	14.01	9.03	9.7	11.22	12.88	12.62	6.55	14.53	13.69	12.5	7.75	11.43	7.98	8.5	15.71	10.57	11.09	7.47	5.01	12.53	13.18
Pb208	0.274	0.289	0.692	0.07	0.086	0.169	0	0.086	0.115	0.099	0.57	0.271	0.062	0.432	0.057	0	0.268	0.203	0.113	0.731	0.247	0.239	0.179
Th232	752.75	573.21	855.52	180.33	284.8	287.31	135.18	236.58	320.34	268.53	1615.01	739.22	183.49	278.45	173.72	195.41	832.58	524.55	357.36	1354.22	558.8	586.58	440.67
U238	39453.82	38024.98	44471.5	16715.79	26357.51	28571.83	19267.97	40840.28	26657.93	40789.77	70059.73	43841.18	26412.14	36403.22	24399.54	25312.57	40330.08	41706.48	44863.01	57440.68	48584.41	49314.92	35035.34

Element	34-Zr11ii	35-Zr13ii	36-Zr13ii	37-Zr15iiE	37-Zr15iiW	38-Zr15iiW	40-Zr15iiE	45-Zr21ii	46-Zr21ii	47-Zr22ii	48-Zr22ii	49-Zr23ii	50-Zr23ii	51-Zr24ii	52-Zr24ii	53-Zr27ii	54-Zr27ii	55-Zr29ii	56-Zr29ii	57-Zr31ii	58-Zr31ii	59-Zr46ii	60-Zr46ii
Si29	162.74	161.66	173.12	162.84	161.41	173.83	165.86	167.23	164.18	163.99	162.53	157.82	161.37	159.76	160.01	159.73	160.23	161.58	161.28	160.62	161.2	160.52	162.91
Ca44	0.22	0.23	0.44	0.23	0.28	0.44	0.16	0.19	0.19	0.16	0.21	0.19	0.24	0.18	0.4	0.26	0.27	0.14	0.17	0.24	0.22	0.2	0.19
Ti47	4.95	4.99	5.03	4.96	4.97	4.99	4.94	4.89	4.92	4.86	4.89	4.82	4.78	4.8	5.08	4.82	4.78	4.74	4.72	4.71	4.72	4.74	4.72
Ti49	0.0198	0.0108	0.0142	0.0126	0.0117	0	0.0144	0.0221	0.0306	0.0122	0.0215	0.0127	0.0134	0.018	0.1794	0.0328	0.0366	0.0149	0.0155	0.0162	0.0192	0.0119	0.0252
Ti50	0	0	0	0	0	0	0	0	0	0	0	0	0	0	0.061	0	0	0	0	0	0	0	0
Y89	37.25	16.39	13.95	26.72	11.11	10.8	30.78	18.95	35.89	14.95	27.6	30.6	33.6	11.18	27.03	30.98	34.93	16.59	20.45	37.28	40.81	29.43	41.54
Zr90	127906.8	127906.8	127906.8	127906.8	127906.8	127906.8	127906.8	127906.8	127906.8	127906.8	127906.8	127906.8	127906.8	127906.8	127906.8	127906.8	127906.8	127906.8	127906.8	127906.8	127906.8	127906.8	127906.8
Nb93	3.01	3.9	3.21	3.92	2.64	3.67	3.41	3.94	3.59	2.5	3.02	2.96	2.59	2.54	3.75	4.19	4.78	2.95	2.64	2.64	2.74	2.58	3.26
La139	0	0	0	0	0	0	0	0.219	0.247	0	0	0	0	0	0.87	0.334	0.827	0	0	0	0	0	0
Ce140	4.18	1.406	1.636	3.02	1.036	1.118	4.46	3.55	6.39	0.781	3.86	1.519	1.657	1.987	4.81	9.46	13.2	4.65	3.02	3.02	3.67	1.573	5.11
Pr141	0	0	0	0	0	0	0.47	0.76	0.93	0	0	0.48	0	0	1.19	1.25	2.86	0.46	0	0	0	0	0
Nd146	1.68	0.42	0	1.22	0.47	0	1.28	1.59	3.14	0	0.86	1.02	1.07	0.84	1.47	2.85	6.72	1.67	0.85	1.4	1.23	0.8	1.51
Sm147	15.03	6.74	7.49	11.16	4.81	0	8.43	6.3	14.47	4.72	5.9	14.25	12.87	5.61	7.65	10.28	24.9	12.98	5.6	11.92	11.28	13.42	15.52
Eu153	21.04	14.55	15.12	19.44	10.24	9.31	11.38	11.15	18.98	10.27	11.27	25.15	22.57	9.05	12.46	15.45	29.2	19.01	7.81	22.88	16.74	22.47	24.44
Gd157	37.17	31.12	28.58	39.28	22.1	20.08	24.27	24.38	34.1	22.38	21.06	56.3	52.76	18.07	21.04	34.15	46.14	35.31	15.87	47.21	32.08	44.93	48.25
Tb159	39.68	33.51	29.47	39.34	24.49	23.09	28.9	31.04	34.52	24.51	24	60.22	56.31	19.6	25.21	44.84	43.53	31.76	19.44	52.65	36.5	51.96	50.61
Dy163	37.26	26.15	20.51	29.56	17	16.98	28.07	26.63	32.04	20.06	24.22	45.75	45.26	15.27	24.18	40.45	36.44	22.36	19.09	41.06	36.97	40.08	43.37
Ho165	33.13	17.54	13.57	22.71	11.64	11.19	27.02	18.57	32.1	14	23.39	30.11	32.66	10.43	22.47	30.97	31.21	16.81	18.79	32.78	33.52	29.1	37.17
Er166	30.54	12.05	8.68	18.06	6.89	7.11	26.08	12.88	30.79	11.28	24.97	23.01	27.18	8.02	22.91	20.47	27.91	11.87	16.99	27.63	34.38	24.3	33.71
Tm169	24.41	9.67	6.14	14.71	6.39	5.74	23.36	8.87	30.92	8.46	22.61	17.69	21.76	7.04	23.34	15.26	24.17	9.03	16.38	22.82	33.61	20.07	28.28
Yb172	30.24	9.5	7.34	14.57	5.23	4.14	22.18	7.79	31.47	8.5	24.33	17.38	21.26	8.33	22.07	15.57	27.45	9.07	17.18	23.2	32.55	20.36	26.33
Lu175	23.65	8.51	10.34	13.73	5.84	5.58	24.96	7.83	30.02	8.52	24.11	15.97	21.36	6.93	20.84	16.07	24.8	6.87	14.65	19.68	32.66	23.97	24.95
Hf178	105301.2	96597.65	98307.56	113486.1	102959.2	100943.9	106797.5	103510.9	104569.9	107103.3	100953.1	102121	104032.1	106210.2	106867.5	95817.6	106919.7	120950.3	109949.2	108271.2	105940.5	104245.7	103297.5
Ta181	13.39	17.55	12.62	22.15	12.49	7.8	17.44	15.33	18.17	11.36	11.27	10.37	12.82	13.41	16.79	12.41	14.95	13.28	8.54	9.7	8.34	10.28	16.69
Pb208	0.265	0.119	0	0.225	0.075	0.118	0.228	0.138	0.247	0.09	0.184	0.146	0.171	0.14	0.843	0.157	0.479	0.251	0.144	0.171	0.139	0.121	0.323
Th232	728.88	355.84	314.14	662.51	144.73	165.34	738.88	370.97	625.96	236.71	492.1	334.8	403.9	433.4	667.47	401.29	836.16	827.6	465.27	468.33	436.24	377.7	920.77
U238	51875.15	46315.5	27569.78	82104.02	22559.15	36306.99	66759.8	41323.57	38951.08	15945.02	38067.73	38137.6	43438.68	39380.2	57859.13	32376.53	59741.93	113764.7	45851.85	57964.37	38452.2	45694.28	57895.9

Sample		$(Eu/Eu^*)_{mean}$	$(Eu/Eu^*)_{min}$	$(Eu/Eu^*)_{max}$	$(Gd/Lu)_{mean}$	$(Gd/Lu)_{min}$	$(Gd/Lu)_{max}$
EP1	Core	0.96	0.83	1.06	0.99	0.62	1.92
	Rim	0.94	0.93	1.14	1.10	0.41	2.19
MN12-03	Core	0.92	0.80	1.15	2.40	1.01	3.66
	Rim	0.92	0.77	1.05	1.78	0.86	3.81

Figure DR9: Location of REE (white spots) and dating (blue, red, yellow spots) analyses in zircon. In the order: EP1 IV; EP1 III; MN12-03 III; MN12-03 II.

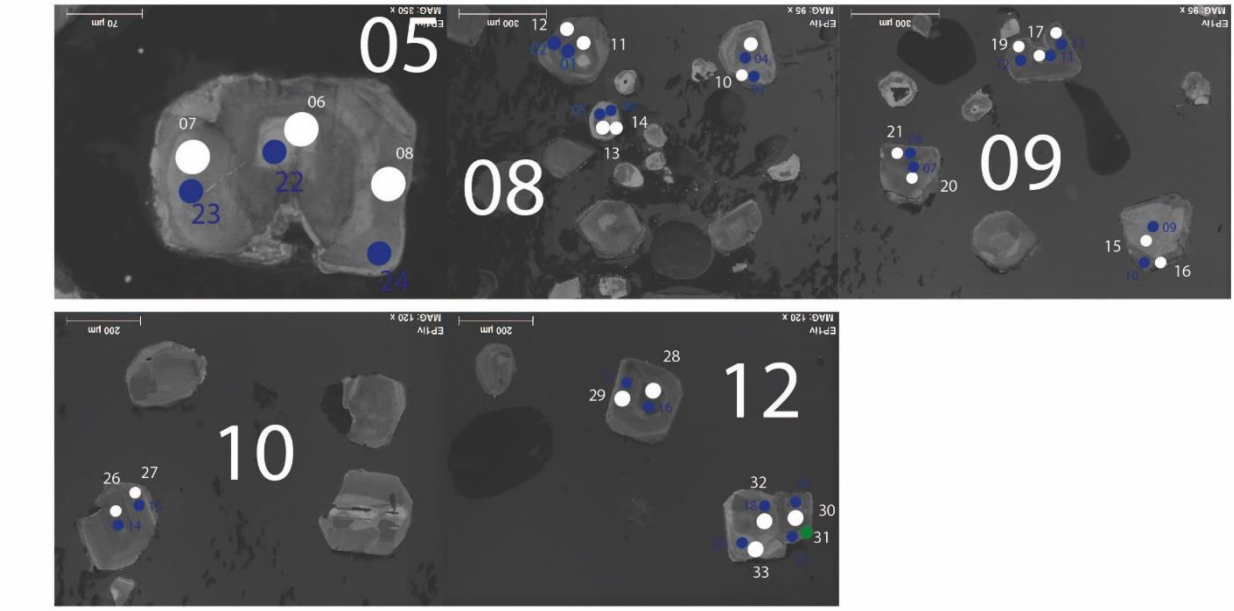

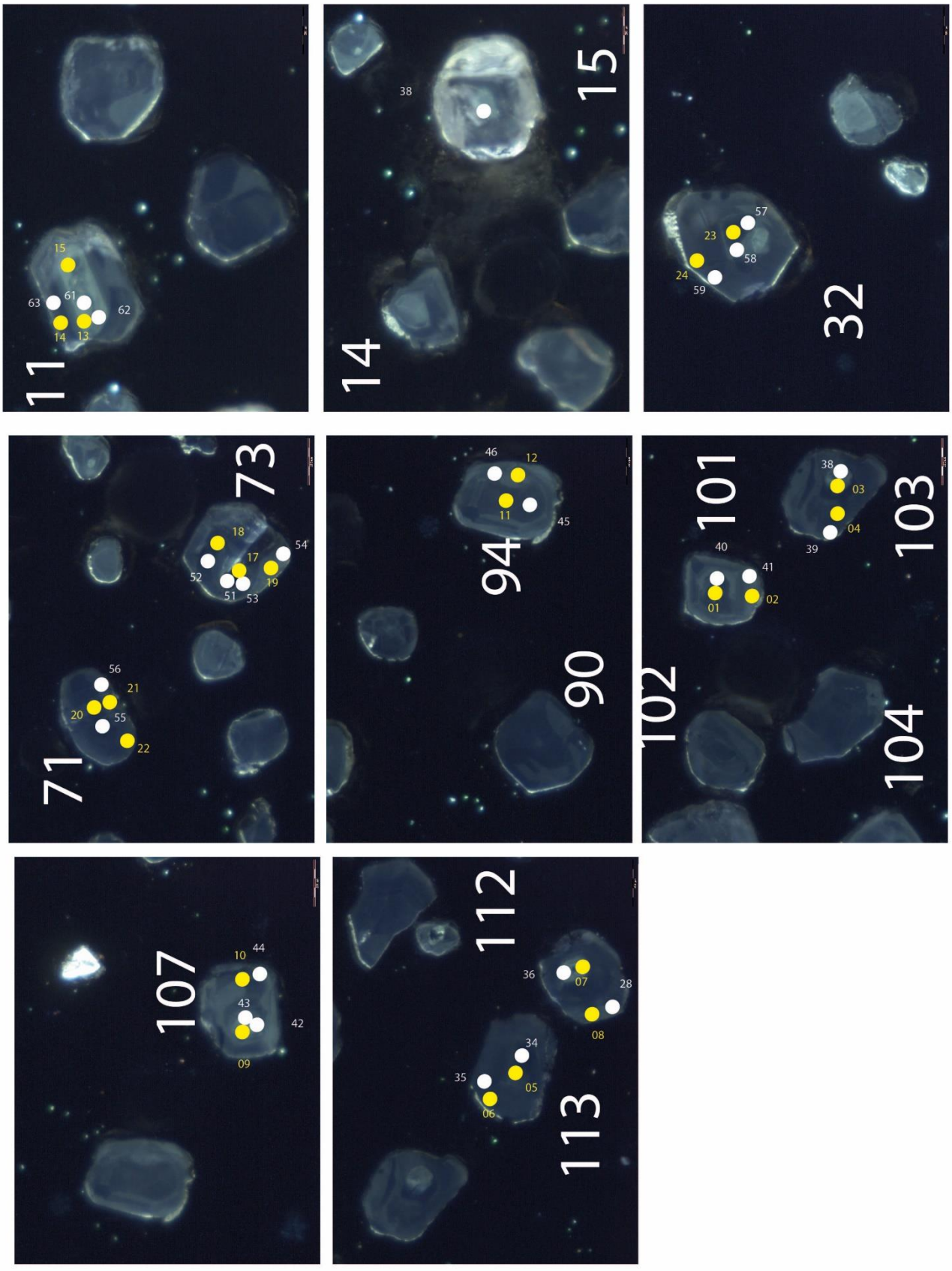
11
15
63
61
62
14
13
14
38
15
32
57
23
58
24
59
71
73
56
21
20
55
22
18
54
17
52
19
51
53
94
46
12
11
45
90
101
103
38
03
04
39
40
41
01
02
102
104
107
10
44
43
42
09
112
36
07
28
08
34
35
05
06
113

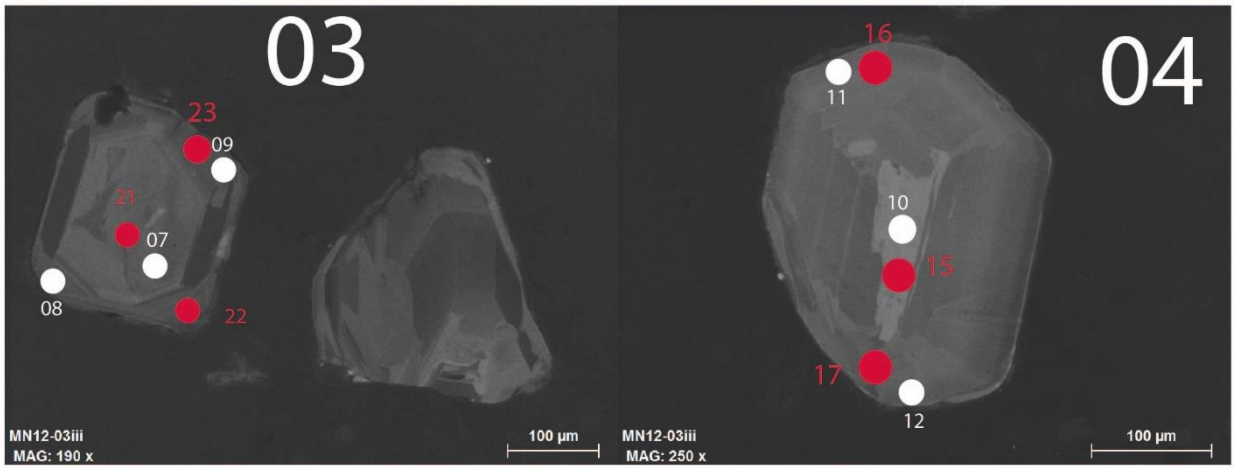
03
23
09
21
07
08
22
MN12-03iii
MAG: 190 x
100 µm
04
16
11
10
15
17
12
MN12-03iii
MAG: 250 x
100 µm

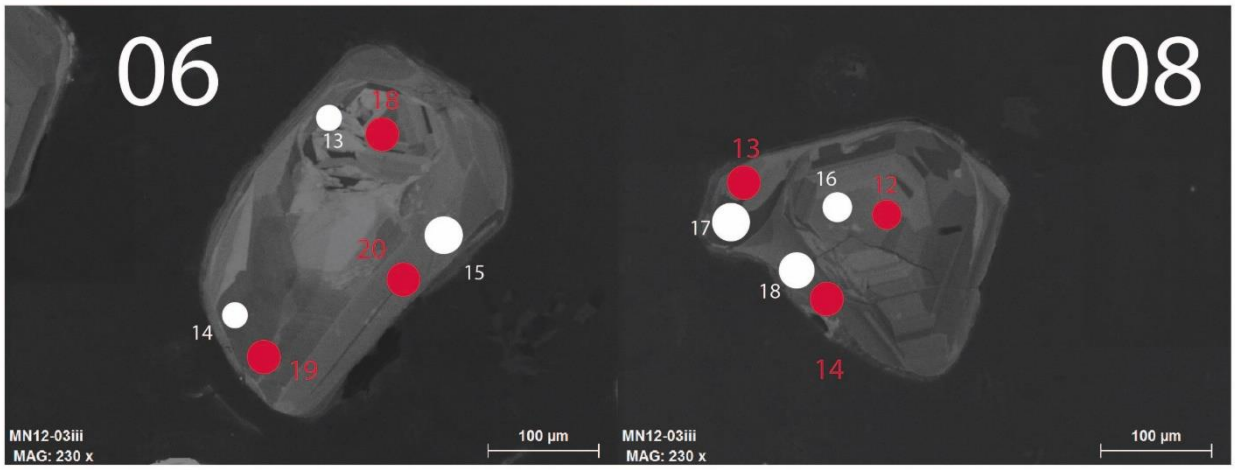
06
18
13
20
15
14
19
MN12-03iii
MAG: 230 x
100 µm
08
13
16
12
17
18
14
MN12-03iii
MAG: 230 x
100 µm

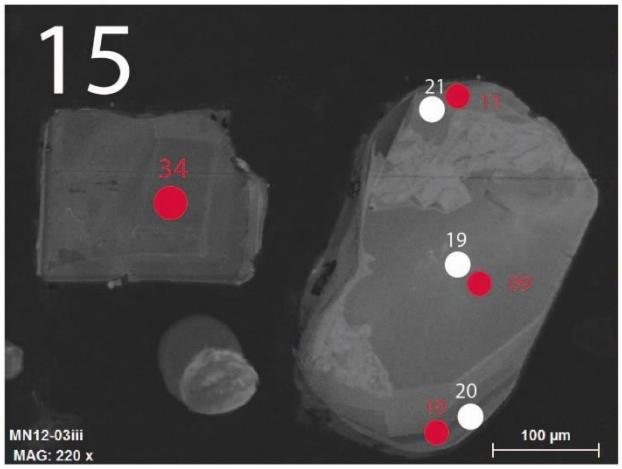
15
21
11
34
19
09
20
10
MN12-03iii
MAG: 220 x
100 µm

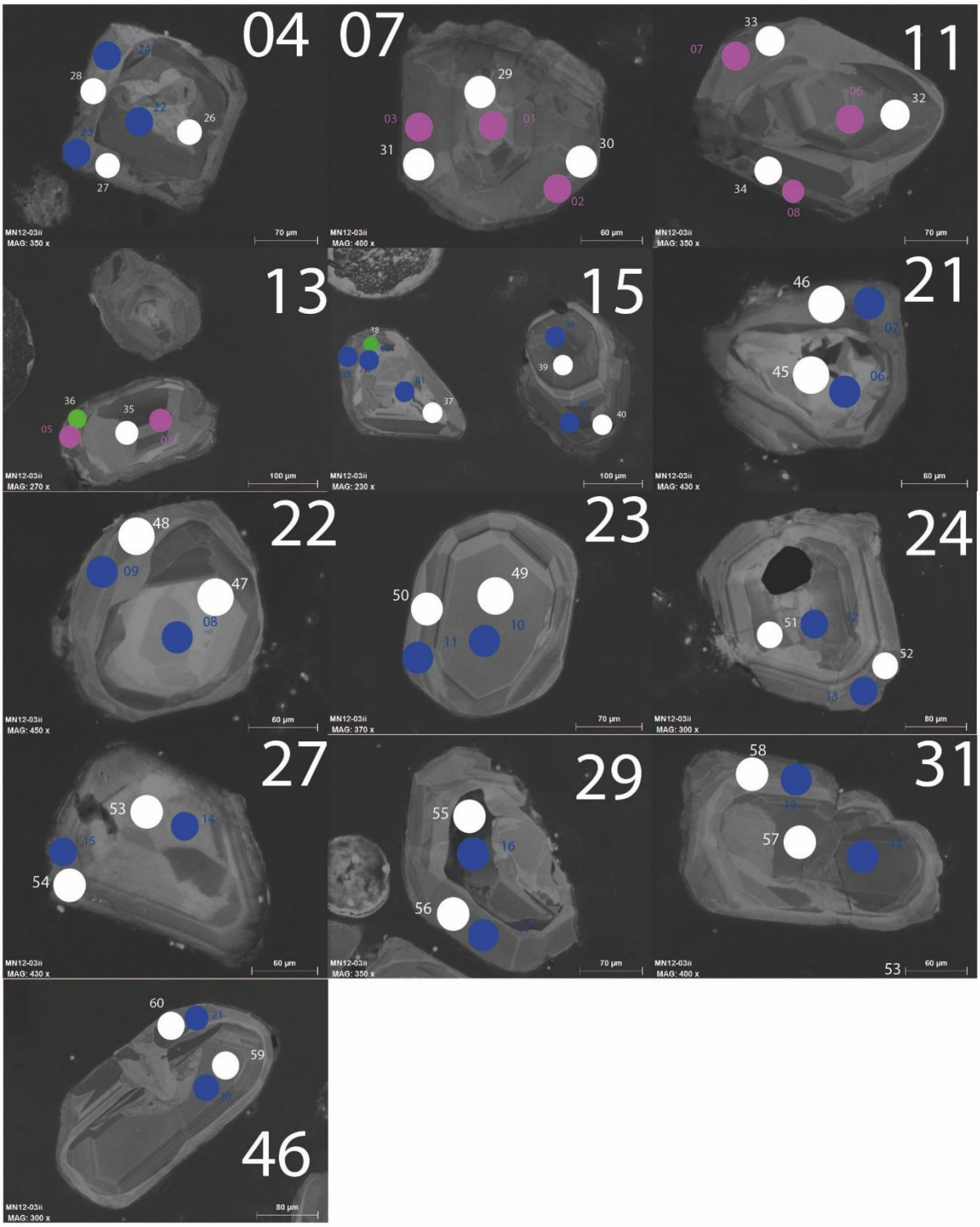
04
07
11
13
15
21
22
23
24
27
29
31
46
MN12-03ii
MAG: 350 x
MAG: 400 x
MAG: 270 x
MAG: 230 x
MAG: 430 x
MAG: 450 x
MAG: 370 x
MAG: 300 x
MAG: 350 x
MAG: 400 x
70 µm
60 µm
100 µm
80 µm
53

REFERENCES

Alabouvette, B., Demange, M., and Echtler, H., 1993, Carte géologique de la France (1/50 000), feuille Saint-Pons (1013), Bureau de Recherches Géologiques et Minières, Orléans, France, Notice explicative par Alabouvette, B., Demange, M. et coll., 1993, p. 123,

Brun, J.-P., and Van Den Driessche, J., 1994, Extensional gneiss domes and detachment fault systems: structure and kinematics: Bulletin de la Société Géologique de France, v. 165, p. 519-530.

de Capitani, C., and Petrakakis, K., 2010, The computation of equilibrium assemblage diagrams with Theriak/Domino software: American Mineralogist, v. 95, p. 1006-1016, doi: 10.2138/am.2010.3354.

Diener, J.F.A., and Powell, R., 2012, Revised activity–composition models for clinopyroxene and amphibole: Journal of Metamorphic Geology, v. 30, p. 131-142, doi: 10.1111/j.1525-1314.2011.00959.x.

Holland, T., and Powell, R., 2003, Activity–composition relations for phases in petrological calculations: an asymmetric multicomponent formulation: Contributions to Mineralogy and Petrology, v. 145, p. 492-501, doi: 10.1007/s00410-003-0464-z.

Holland, T., Baker, J., and Powell, R., 1998, Mixing properties and activity-composition relationships of chlorites in the system MgO-FeO-Al2O3-SiO2-H2O: European Journal of Mineralogy, v. 10, p. 395-406.

Holland, T.J.B., and Powell, R., 1998, An internally consistent thermodynamic data set for phases of petrological interest: Journal of Metamorphic Geology, v. 16, p. 309-343, doi: 10.1111/j.1525-1314.1998.00140.x.

Pitra, P, Poujol, M., Van den Driessche, J., Poilvet, J. C., and Paquette, J.L., 2012, Early Permian extensional shearing of an Ordovician granite: The Saint-Eutrope "C/S-like" orthogneiss (Montagne Noire, French Massif Central): Comptes Rendus Geosciences, v. 344, p. 377-384, doi: 10.1016/j.crte.2012.06.002.

Pitra, P., Ballèvre, M., and Ruffet, G., 2010, Inverted metamorphic field gradient towards a Variscan suture zone (Champtoceaux Complex, Armorican Massif, France): Journal of Metamorphic Geology, v. 28, p. 183-208, doi: 10.1111/j.1525-1314.2009.00862.x.

Powell, R., Holland, T., and Worley, B., 1998, Calculating phase diagrams involving solid solutions via non-linear equations, with examples using THERMOCALC: Journal of Metamorphic Geology, v. 16, p. 577-588, doi: 10.1111/j.1525-1314.1998.00157.x.

Sun, S.S. and McDonough, W.S., 1989. Chemical and isotopic systematics of oceanic basalts: implications for mantle composition and processes. Geological Society, London, Special Publications, 42(1), pp.313-345.

White, R.W., Powell, R., and Holland, T.J.B., 2007, Progress relating to calculation of partial melting equilibria for metapelit
Metamorphic Geology, v. 2[illegible]
10.1111/j.1525-1314.2007.0071

Chapitre 3 – le massif du Lévézou

Table of content

From burial to exhumation: evolution of eclogitic terranes through multimethod petrochronology, Lévézou Massif (French Massif Central)

In preparation for Journal of Petrology

[a] UMR CNRS 6118, Géosciences Rennes, OSUR, Université, Rennes 1, 35042 Rennes CEDEX, France

[b] Česká geologická služba, Klárov 3, 118 21 Praha 1, Česká republika

[c] Institute of Geological Sciences, Polish Academy of Sciences, Kraków Research Center, Senacka 1, PL 31-002, Kraków, Poland

Highlights:

- **First HP dating and new P-T condition for HP peak and retrogression in the Lévézou Massif, French Massif Central**
- **HP peak reached 18-23 kbar and 680-800°C at ca. 358 Ma**
- **Exhumation at 8-9.5 kbar and 600-620°C is reached at ca. 352 Ma**
- **Fast exhumation followed by a fast cooling of ca. 50°C/km**

Résumé

Pour déterminer l'évolution des roches métamorphiques, il est nécessaire de comprendre l'évolution et la croissance des minéraux au cours du temps. La datation des étapes métamorphiques précoces est un challenge, particulièrement du fait de la rétromorphose s'y surimposant. Une éclogite fraîche, indemne de toute trace de rétromorphose, et une éclogite rétromorphosée en faciès amphibolique (massif du Lévézou, chaîne varisque) ont ainsi été sélectionnées pour préciser les timing et durées des épisodes de haute pression et d'exhumation. Un large panel de géochronomètres a été utilisé (U-Pb sur zircon, rutile et apatite, Lu-HF et Sm-Nd sur grenat) à la lumière d'un contexte pétrologique détaillé par des observations pétrographiques, l'analyse des éléments traces ainsi que la modélisation d'équilibre de phases pour préciser timing de l'évènement de haute pression et le refroidissement au cours de l'exhumation. Les deux échantillons ont enregistrés des conditions de haute pression similaires à 18-23 kbar et 680-800°C, tandis que l'éclogite rétromorphosée s'est par la suite équilibrée à 8-9.5 kbar et ca. 600-620°C. Dans l'échantillon rétromorphosé, la plupart des grains de zircons sont caractérisés par des spectres de terres rares à anomalies négatives en Eu et sont enrichis en HREE ; ils ont été datés par U-Pb à 472.3 ± 1.7 Ma. Cet âge est interprété, en accord avec la littérature, comme reflétant la cristallisation du protolithe mafique, contemporaine de l'amincissement extrême des marges continentales lors d'une phase de rifting ou d'extension arrière-arc. Quelques bordures de zircons présentent des spectres de terres rares légèrement moins enrichis en HREE datées à 378 ± 5.7 Ma, et interprétés comme un âge prograde et anté-éclogitique. Les datations Lu-Hf des deux échantillons ont fourni des âges similaires de 357 ± 13 Ma et 357.5 ± 4 Ma, interprétés comme l'âge du pic de métamorphisme de haute pression. L'éclogite fraiche et l'éclogite rétromorphosée ont respectivement fourni des âges de 350.4 ± 7.7 Ma et 352 ± 20 Ma par datation Sm-Nd sur grenat, 367.8 ± 9.1 Ma et 354.9 ± 9.5 Ma par datation U-Pb sur rutile. Les apatites de l'échantillon rétromorphosé datent le refroidissement, post phase d'exhumation majeure, à 351.8 ± 2.8 Ma. Tous ces âges sont identiques dans l'erreur et, quand associés aux estimations P-T, mettent en évidence une phase de décompression majeure de 8.5 à 15kbar en moins de 10 My, suggérant des taux d'exhumation de 5 à plus de 10mm/an. La décompression est adiabatique, suivant des gradients de 7.8 à 1.3°C/km. Un refroidissement rapide, post phase d'exhumation majeure est estimé à près de 50°C/Ma.

Mots-clés: Datation du métamorphisme de haute pression; Géochronologie U-Pb sur zircon, rutile et apatite; Géochronologie Lu-Hf et Sm-Nd sur grenat; estimations P-T, éléments trace; Pétrochronologie

Abstract

To unravel the evolution of metamorphic rocks, the understanding of the mineral growth through time is required. However, dating early metamorphic stages is a challenge, due to subsequent retrograde overprinting.

A perfectly fresh eclogite and a former eclogite retrogressed under amphibolite facies from the southern French Massif Central (Lévézou massif, Variscan Belt), were investigated with a large panel of geochronometers (U-Pb on zircon, rutile and apatite, Lu-Hf and Sm-Nd on garnet) in a petrological context tightly constrained by petrographic observation, trace element analyses and phase equilibrium modelling.

Both samples recorded similar HP conditions at 18-23 kbar and 680-800°C, while the retrogressed eclogite later equilibrated at 8-9.5 kbar and ca. 620°C. In the retrogressed sample, most of the zircon grains are characterized by negative Eu anomalies and HREE enrichment, and yield an Ordovician U-Pb date of 472.3 ± 1.7 Ma. This is interpreted as the emplacement age of the mafic protoliths and, in agreement with other data available for the Variscan belt, is considered to represent the extreme thinning of continental margins during a rifting event or a back-arc extension. Few zircon rims show a weaker HREE enrichment and yield a date of 378 ± 5.7 Ma, interpreted as a prograde, pre-eclogitic, age. Lu-Hf garnet dating from both samples yields identical dates of 357 ± 13 Ma and 357.5 ± 4 Ma, that approximate the age of the high pressure metamorphic peak. Fresh and retrogressed samples respectively yield 350.4 ± 7.7 Ma and 352 ± 20 Ma dates for Sm-Nd garnet dating, and 367.8 ± 9.1 Ma and 354.9 ± 9.5 Ma for U-Pb rutile dating. Apatite grains from the retrogressed sample give a mean age of 351.8 ± 2.8 Ma. All these ages are identical within error and, when combined with P-T estimations, highlight a major decompression ranging from 8.5 to 15 kbar in less than 6 My, suggesting exhumation rates in excess of 5 mm up to more than 1 cm/yr. Decompression is nearly adiabatic with gradient ranging from 7.8 to 1.3°C/km, followed by cooling rates after major decompression exceeding 50°C/Ma.

Keywords: HP metamorphism dating; U-Pb zircon, rutile and apatite dating; Lu-Hf and Sm-Nd garnet dating; P-T estimates, Trace elements; Petrochronology.

1. Introduction

High pressure (HP) metamorphism testifies to mountain building processes, including oceanic subduction, crustal thickening and continental subduction. The subsequent exhumation of these HP rocks is accompanied with retrogression and re-equilibration, and is driven by a combination of erosion and tectonic processes. These processes of subduction, exhumation and cooling can be long-lived and protracted or can result from fast and short-lived event. To decipher the geodynamic evolution of mountain building, estimation of rates and duration of metamorphism, and in particular rates and duration of high pressure metamorphism, are then key parameters. Numerous studies have attempted to constrain the age of the HP event and the subsequent exhumation history, by combining several geochronometers as U-Pb on zircon, U-Pb on monazite, U-Pb on rutile, U-Pb on titanite, Lu-Hf on garnet and/or Sm-Nd on garnet (e.g. Anczkiewicz et al. 2007, 2012; Cheng et al. 2009, 2012; Kylander-Clark et al. 2007, 2008; Colett et al. 2018; Lotout et al. 2018; Butler et al. 2018). The link between theses ages and the metamorphic history of the rock, i.e between time and the Pressure-Temperature (P-T) evolution, is generally achieved through the trace element analysis of the dated minerals (e.g. linking the zircon and garnet growth through their REE patterns, e.g Rubatto 2002; Whitehouse and Platt, 2003).

In the Variscan belt, numerous controversies exist on the timing of the HP metamorphism and subsequent exhumation. The convergence between the two megacontinents, Laurussia to the north and Gondwana to the south, with contribution of microplates such as Armorica or Avalonia (e.g. Murphy et al. 2009) induced the closure of oceanic domains, while oceanic rocks were subducted and metamorphosed under HP to UHP conditions (e.g. Matte, 1986; Lardeaux et al. 2001; Ballèvre et al., 2009;). At the scale of the whole Variscan belt, the age of the high pressure metamorphism spreads from the middle to the upper Devonian (e.g. Paquette et al., 2017), with the exception of the French Massif Central (FMC). The metamorphic pressure peak in the FMC has long been considered to be late Silurian in age (410-430 Ma), based on only four studies (Pin and Lancelot, 1982; Ducrot et al., 1983; Paquette et al., 1995; Berger et al., 2010; Fig.II.3.1A). Nevertheless, a recent study from Lotout et al. (2018) question the validity of these HP ages, resulting from outdated method or over-interpreted results. Based on a multimethod geochronological approach (Lu-Hf and Sm-Nd on garnet; U-Pb on zircon and apatite) they demonstrate a HP age of 376 ± 3.3 Ma in the Najac massif. To decipher the processes involved in the building of the variscan

orogeny in the FMC and document the timing and duration of the high-pressure event, more petrochronological studies are required.

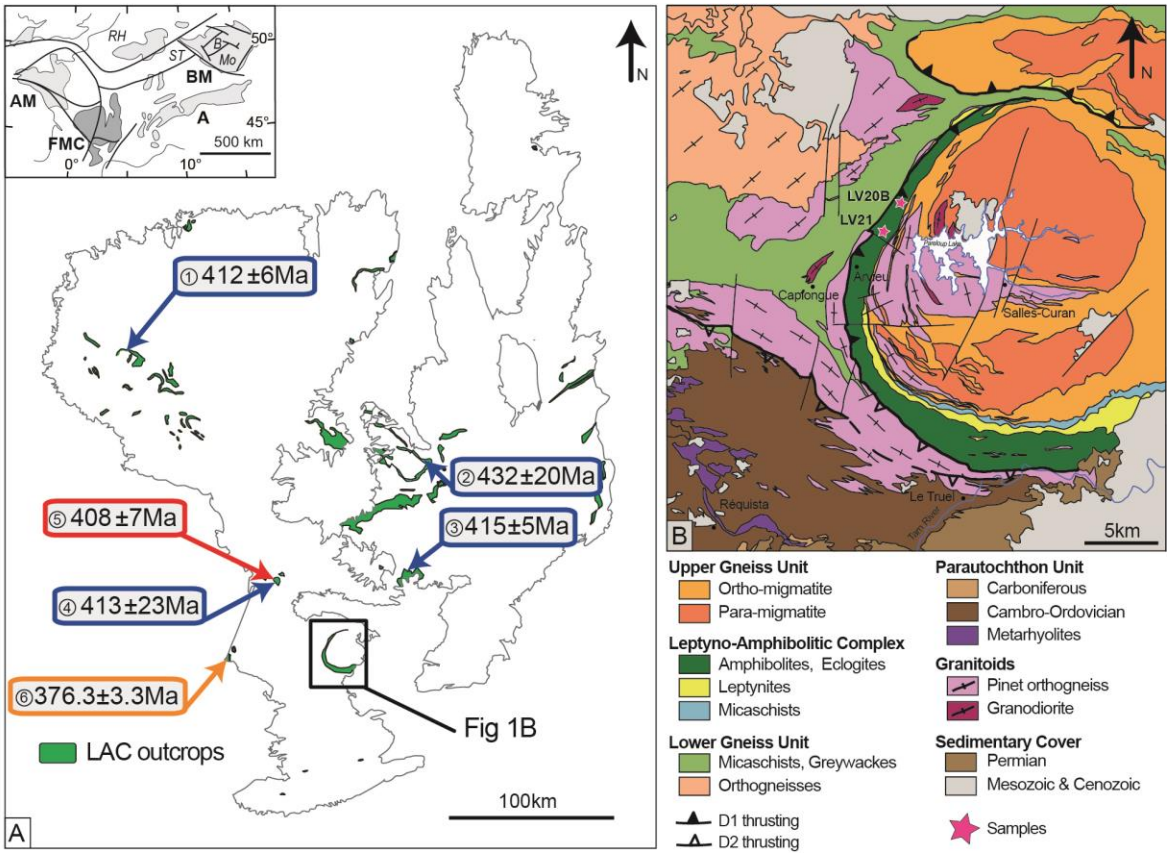

Figure II.3.1 : A. Schematic map of the Leptyno-Amphibolitic Complex (LAC) outcrops in the French Massif Central, with the location of the study area and the previous geochronological studies. (1) Berger et al., 2010 (U-Pb, LA-ICP-MS dating on zircon), (2) Ducrot et al., 1983 (U-Pb, zircon isotopic dilution), (3) Pin & Lancelot 1982 (U-Pb, zircon isotopic dilution), (4) Paquette et al., 1995 (Pb/Pb, zircon evaporation), (5) Paquette et al., 1995 (Sm-Nd - garnet & WR). (6) Lotout et al. 2018 (U-Pb, LA-ICP-MS dating on zircon; Lu-Hf and Sm-Nd dating on garnet). Blue :dating of zircon, no evidence on the belonging of the dated mineral to the HP paragenesis; Red: dating of garnet, Yellow : dating of garnet through a petrochronological approach. Inset shows the location of the study area within the European Variscan belt A - Alps, AM - Armorican Massif, BM - Bohemian Massif, FMC – French Massif Central. B - Teplá-Barrandian, Mo - Moldanubian, ST - Saxothuringian, RH – Rhenohercynian. B. Schematic map of the Lévézou Massif (modified after Lotout et al., 2017). Purple star indicates the samples location.

The Lévézou Massif, located only some 70 km east of the Najac Massif (south FMC), exposes some of the best-preserved eclogites from the FMC and was chosen to perform a multimethod geochronological study, to pursue the investigation on the timing of HP metamorphism in this portion of the European Variscan belt. The strategy is based on a detailed study of two samples from the same HP unit: a perfectly preserved eclogite and a former eclogite largely retrogressed under amphibolite-facies conditions. P-T conditions are

estimated through a petrographical analysis and numerical modelling of phase equilibria. We then use a large panel of geochronometers (U-Pb on zircon, rutile and apatite, Lu-Hf and Sm-Nd on garnet) combined with trace element analyses in some of the dated minerals (zircon, garnet) to decipher the timing of the HP metamorphism and the subsequent exhumation.

2. Geological context

In the French Massif Central, relics of high-pressure rocks are concentrated in the so-called "Leptyno-Amphibolitic Complex" (LAC) (e.g. Forestier 1971, Santallier et al. 1988, Ledru et al. 1989; Faure et al., 2009, Lardeaux 2014). In the Lévézou massif, these high-pressure terranes are dominated by mafic and ultramafic rocks with tholeiitic and calc-alkaline affinities (Nicollet 1978; Piboule 1979) and contain abundant lenses of eclogite, ± coronitic metagabbro, metadolerite, serpentinite, and peridotite. The emplacement of the tholeiitic suite was dated at ca. 485 ± 30 Ma (U/Pb on zircon population from a trondhjemite; Pin 1979). A gabbro from the calc-alkaline suite was dated at 367 ± 10 Ma with the same method (Pin and Piboule 1988). No dating of the HP-event was ever performed in this massif, but it has long been considered as Silurian in age (e.g. Duguet and Faure 2004; Faure et al. 2009; Lardeaux 2014) based on the similarity with the published HP ages in other localities of the MCF (Pin and Lancelot 1982; Ducrot et al., 1983; Paquette et al., 1995; Berger et al., 2010). The validity of these previous studies is now questioned (Lotout et al. 2018), and the age of the HP event in the Lévézou Massif is consequently unknown. The upper part of the Lévézou's LAC comprises micaschists, leucocratic paragneisses and quartzites (Fig.1B). Numerous interpretations have been proposed for the signification and the emplacement of the LAC in the Lévézou massif : (i) for Briand et al. (1988), the magmatic signature of the LAC is that of a back-arc basin environment; (ii) Piboule (1979) suggested an early intra-continental early marginal basin, not fully evolved to an oceanic stage; (iii) Nicollet et al. (1978) suggested that the LAC correspond to a subducted dislocated ophiolitic sequence (iv) Pin and Piboule (1988) proposed a collision between two independent magmatic suites to account for the composite character of the LAC; (v) Lardeaux (2014) finally reinterpreted the chemical composition of all the LAC occurrences from the French Massif Central as reflecting a hyper-extended continental margin. All the authors agree on the fact that the LAC does not correspond to a mature oceanic crust. Despite the controversies on the emplacement setting of the LAC, it is unanimously considered as the tectonic marker of a subduction stage during the Variscan orogeny (e.g. Ledru et al., 1989; Ballèvre et al., 2009; Lardeaux, 2014

and references therein). P-T conditions for the high pressure metamorphism in the Lévézou were first estimated at 12.5-20 kbar and 750-840°C (Nicollet and Leyreloup, 1978), then at 16 kbar and 720 ± 30°C (Bouchardon, 1987).

The Lévézou massif is classically subdivided into four superposed units, the Upper Gneiss Unit (UGU), the LAC, the Lower Gneiss Unit (LGU), and the Parautochthnous Unit (PAU), from the core to the outside of the massif. The LAC is separated from each gneissic unit by a major tectonic contact. (Fig. II.3.1B) The UGU is composed of paragneisses and felsic orthogneisses, migmatized to various degrees. Mafic enclaves with rare relics of HP mineral assemblages, interpreted as xenoliths, are locally found within the orthogneisses (Delor et al. 1985), recently dated at 470 Ma (Lotout et al. 2017). The Lower Gneiss Unit (LGU) is composed of amphibolite-facies metasedimentary rocks intruded by several granitoid bodies. The Parautochthonous Unit (PAU) is the most external and least metamorphosed unit (Fig. 1B), and is composed of quartzo-pelitic rocks, micaschists and quartzites with intercalated metarhyolites (Collomb 1970; Delbos et al. 1964). Thrusting of the LGU, and the overlying UGU and LAC, onto the PAU is responsible for an apparent inverted metamorphic zonation (Burg et al. 1989).

3. Analytical procedures

a. Chemical analyses, mineral composition and P-T modelling

The samples were first cleaned from any weathered material, then crushed in a jaw crusher and in an agate mortar in order to obtain a fine powder. Major and trace elements analyses were performed by Inductively Coupled Plasma Atomic Emission Spectrometry (ICP-AES) and Inductively Coupled Plasma Mass Spectrometry (ICP-MS), respectively, at the Geochemical and Petrographical Research Center (SARM laboratory, CNRS-CRPG) in Nancy, following the procedure described in Carignan et al. (2001). FeO (vs. Fe2O3) was analyzed by wet titration.

Mineral analyses were carried out with a Cameca SX100 electron microprobe (Microsonde Ouest, IFREMER, Plouzané, France) operating in a wavelength-dispersive mode (for the complete analytical procedure, see Pitra et al., 2008). Data are plotted using the software GCDkit (Janoušek et al., 2006).

P-T pseudosections have been calculated in the model system Na2O–CaO–(K2O)–FeO–MgO–Al2O3–SiO2–H2O–TiO2–Fe2O3 (NC(K)FMASHTO) using the software

Theriak/Domino (de Capitani and Petrakakis 2010), and the internally consistent thermodynamic data set 5.5 (Holland and Powell 1998; updated Nov. 2003). Mixing models for solid solutions were taken from Diener and Powell (2012) – amphibole (amp), clinopyroxene (cpx), White et al. (2007) – garnet (g), biotite (bi), Holland et al. (1998) – chlorite (chl), Holland & Powell (2003) – plagioclase (pl), Holland and Powell (1998) – talc (ta), epidote (ep), Coggon & Holland (2002) – muscovite (mu) and White et al. (2000) – hematite (hem), ilmenite (ilm). Albite (ab), lawsonite (law), quartz (q), rutile (ru) and titanite (sphene, sph) are considered as pure end members. Doug Tinkham kindly provided the conversion of the mixing models for Theriak/Domino.

Other symbols (mole/atomic proportions) used are: XMg = Mg/(Fe2++Mg) (garnet, clinopyroxene, amphibole), XNa = Na/(Ca+Na+K) (plagioclase), XGrs = Ca/(Ca+Mn+Fe2++Mg), XPrp = Ca/(Ca+Mn+Fe2++Mg), XAlm = Fe2+/(Ca+Mn+Fe2++Mg), XSps = Mn/(Ca+Mn+Fe2++Mg) (garnet), wt% – weight per cent, mol.% – mole per cent, pfu – per formula unit. The bulk rock composition used to calculate the P-T diagrams was corrected for the presence of apatite, not considered in the calculations.

b. LA-ICP-MS dating

A mineral separation procedure has been applied to concentrate zircon, rutile and apatite grains for U-Pb dating using the facilities available at Géosciences Rennes (University of Rennes 1). The sample was crushed and only the powder fraction with a diameter < 250 µm was kept. Heavy minerals were first concentrated by Wilfley table, then magnetic minerals were removed with an isodynamic Frantz separator. Heavy minerals were afterwards separated with heavy liquids. Zircon grains were handpicked under a binocular microscope. The selected minerals were then embedded in epoxy mounts, which were grounded and polished on a lap wheel. Zircon and apatite grains were imaged by cathodoluminescence (CL) using a Reliotron CL system equipped with a digital color camera available at Géosciences Rennes.

U-Pb geochronology of zircon and apatite grains was conducted by in-situ laser ablation inductively coupled plasma mass spectrometry (LA-ICP-MS) at Géosciences Rennes using a ESI NWR193UC Excimer laser coupled to an Agilent quadripole 7700x ICP-MS equipped with a dual pumping system to enhance sensitivity. The instrumental conditions are reported in the supplementary table II.3.1. Further information on the zircon dating protocol

can be found in Ballouard et al. (2015), in Boutin et al. (2016) for rutile and in Pochon et al. (2016) for apatite.

Ablation spot diameters of 35µm and 25µm (Zrn), 60µm (Ru) and 45 µm (Ap) with repetition rates of 3 Hz (Zrn) and 5 Hz (Ru, Ap) and a fluence of 8.7J/cm² were used. Data were corrected for U–Pb and Th–Pb fractionation and for the mass bias by standard bracketing with repeated measurements of the GJ-1 zircon (Jackson et al. 2004), R10b for rutile (Zack et al. 2011) and the Madagascar apatite (Cochrane et al., 2014). Along with the unknowns, zircon standard Plešovice (Slama et al., 2008), rutile standard R19 (Zack et al. 2011), apatite standards McClure (Schoene and Bowring, 2006) and Durango (McDowell et al., 2005) were measured to monitor precision and accuracy of the analyses and produced ages of 336.6 ± 4.1 Ma (Plešovice, N = 6, MSWD = 0.095), 491.8 ± 3.4 Ma (R19, N = 8, MSWD = 0.38), 532 ± 13 Ma (McClure, N = 4, MSWD = 4.4) and 32.5 ± 1.1 Ma (Durango, N = 5, MSWD = 0.34) during the course of the analyses.

Data reduction was carried out with the GLITTER® software package developed by the Macquarie Research Ltd. (Van Achterbergh et al., 2001) for zircon, and the data reduction scheme VizualAge_UcomPbine, a set of Iolite procedures that work with Igor Pro (Chew et al., 2014) for apatite and rutile. Concordia ages and diagrams were generated using Isoplot 4.15 (Ludwig, 2012). All errors given in supplementary table 2 are listed at two sigma, as well as concordia age or weighted mean calculations.

c. Sm-Nd and Lu-Hf dating

Mineral separation was carried out at Géosciences Rennes. Rocks were crushed and from the fraction <500 µm about 70 mg of amphibole and 200 mg of relatively pure garnet were handpicked under a binocular microscope. Garnet fraction was subsequently split into three roughly equal aliquots. Additionally, about 100 mg of representative whole rock powder was prepared and subjected together with garnet and amphibole to Lu-Hf and Sm-Nd dating conducted at the Institute of Geological Sciences, Polish Academy of Sciences, Kraków Research Centre. Leaching, sample dissolution and columns chemistry follow procedures outlined in Anczkiewicz and Thirlwall (2003) and Anczkiewicz et al. (2004). All measurements were carried out in a static mode using a MC-ICP-MS Neptune applying the protocols similar to those outlined in Thirlwall and Anczkiewicz (2004). Procedure blanks, standards reproducibility, decay constants and reference isotopic ratios used for the

calculations are given in the footnote to Table 1. Ages and 176Hf/177Hf and 143Nd/144Nd initial ratio calculations were conducted by Isoplot 4.15 (Ludwig, 2012). Errors for isotopic ratios are given at the 2 se (standard error) level. Age errors are quoted at 95% confidence level.

d. Trace element analyses in garnet and zircon

Trace element analyses in garnet and zircon were conducted at the Institute of Geological Sciences, Polish Academy of Sciences, Kraków Research Centre, using an Excimer laser (193 nm) RESOlution M50 by Resonetics (now Australian Scientific Instruments) equipped with S150 dual volume sample cell. Laser ablation was coupled with an ICP-MS XSeriesII by Thermo Fisher. Fluence of about 8 J/cm2, and 10 Hz repetition rate were applied during the measurements. Analyses of zircon were performed in spot mode with beam size of 29 or 43 μm diameters. The results were normalized to the NIST612 primary standard using recommended values of Jochum et al. (2011). MPI DING glasses served as secondary standards for data quality control. Silicon content was used as an internal standard (fixed at 31.5%). Analyses of garnet profiles were performed in raster mode with a stage speed of 0.250 mm/min and a slit size of 40 μm. More details on analytical conditions can be found in Anczkiewicz and Anczkiewicz (2012). Data reduction was carried out using Iolite 3.0 (Paton et al., 2010) with the "trace element" data reduction scheme (Woodhead et al., 2007).

4. Pressure and temperature estimations

Two eclogites with various degrees of retrogression were sampled in the Leptyno-Amphibolitic Complex of the Lévézou massif, in outcrops close to each other (LV21: 44°12'50"N, 2°40'48"E; LV20B : 44°14'7"N, 2°42'2"E, Fig. II.3.1B).

a. Fresh eclogite

Petrography

LV21 is a pale isotropic fine-grained eclogite, composed of garnet, omphacite, amphibole, kyanite and rutile. Garnet forms small subhedral grains (40-250 μm) in necklace textures along the clinopyroxene and amphibole grains boundaries (Fig. II.3.2A). They are rarely found as small inclusions in clinopyroxene and amphibole. Garnet is inclusion free,

homogeneous, magnesian and chemically unzoned in major elements (XMg = 0.59-0.65, XPrp = 0.48-0.52, XAlm = 0.27-0.34, XGrs = 0.17-0.22, XSps ≤ 0.01; Fig. II.3.3, supplementary table II.3.3). Clinopyroxene forms subhedral tabular grains (80-600 µm). It is unzoned in major elements and has mostly the composition of omphacite (Fig. II.3.3, supplementary table II.3.3, XJd = 0.27-0.31; XAe ≤ 0.05). Omphacite can include tiny crystals of garnet and elongated rutile needles, but occurs mostly without inclusions.

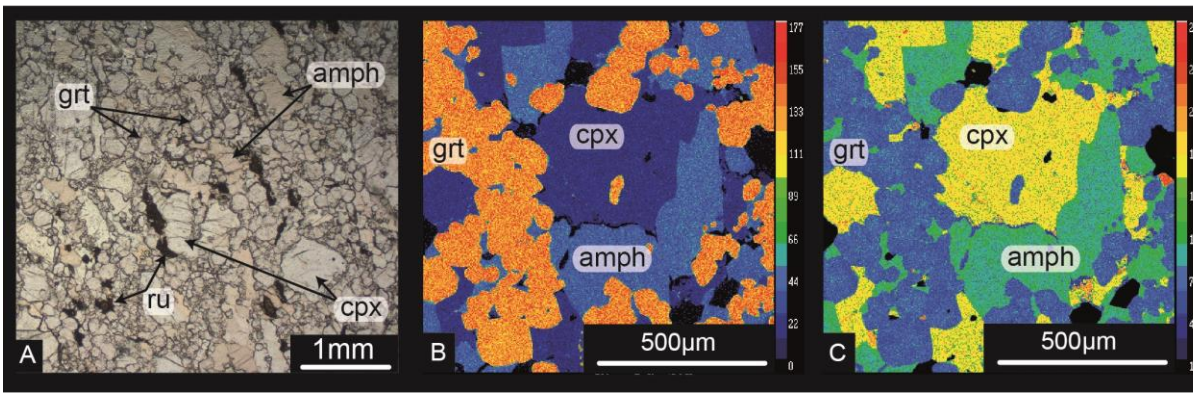

Figure 2 : A. Photomicrographs of the NC5A sample. B. X-ray map for Fe C. X-ray map for Ca.

Amphibole forms euhedral to subhedral crystals (50-500 µm), that are calcic, unzoned and chemically homogeneous and span a compositional space between edenite, tschermakite and magnesiohornblende (Si = 6.54-6.72 pfu, Ca = 1.57-1.78, (Na+K)A = 0.46-0.57, Ti = 0.05-0.09 pfu , XMg = 0.92-0.93, Fig. II.3.3, supplementary table II.3.3). They locally contain garnet and tiny rutile as inclusions. Rutile crystals occur as reddish to orange subhedral grains (50-250 µm) in the matrix, or as needles included in omphacite and amphibole. Rare elongate kyanite can be found in the matrix. Magnetite, sulfides (pyrite, chalcopyrite) and apatite constitute the accessory minerals.

No symplectites develop at the expense of the above minerals and the sample can be considered as a perfectly preserved, unretrogressed eclogite. The stable metamorphic assemblage is interpreted as garnet-omphacite-amphibole-kyanite-rutile.

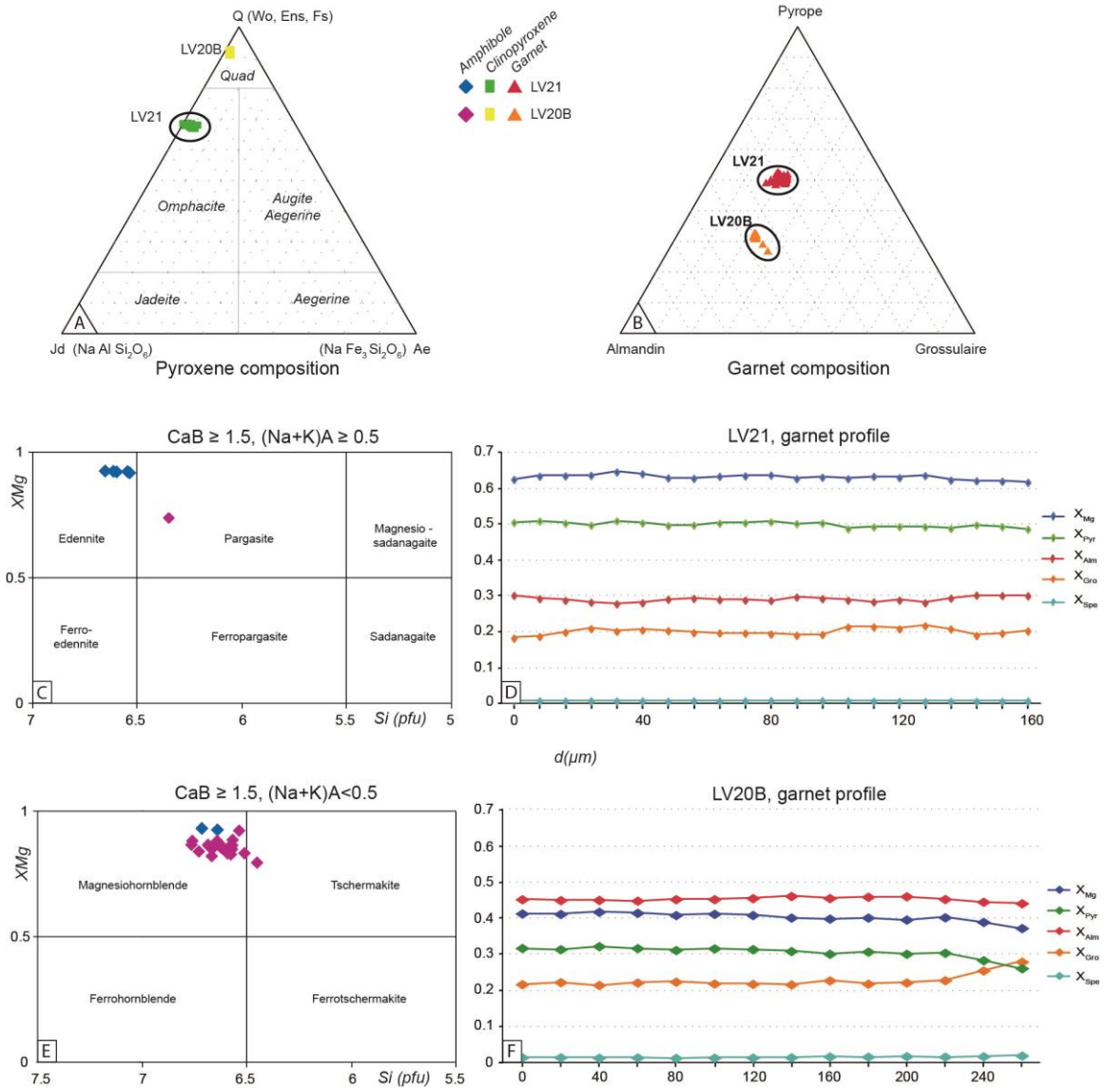

Figure II.3.3 : Compositional diagrams of clinopyroxene (A), garnet (B, D, F) and amphibole (C, E). Results are color coded according to their sample. Amphibole nomenclature follows the classification of Leake et al., (1997).

P-T estimates

In order to calculate P-T pseudosections, the bulk composition was reduced to the NCFMASHTO model system. In particular, K2O was removed from the bulk, since (i) no K-bearing phase was observed in the thin section, (ii) the amount of K2O in the bulk rock composition is very low (0.16 wt%), and (iii) the amphibole model used does not allow to incorporate potassium.

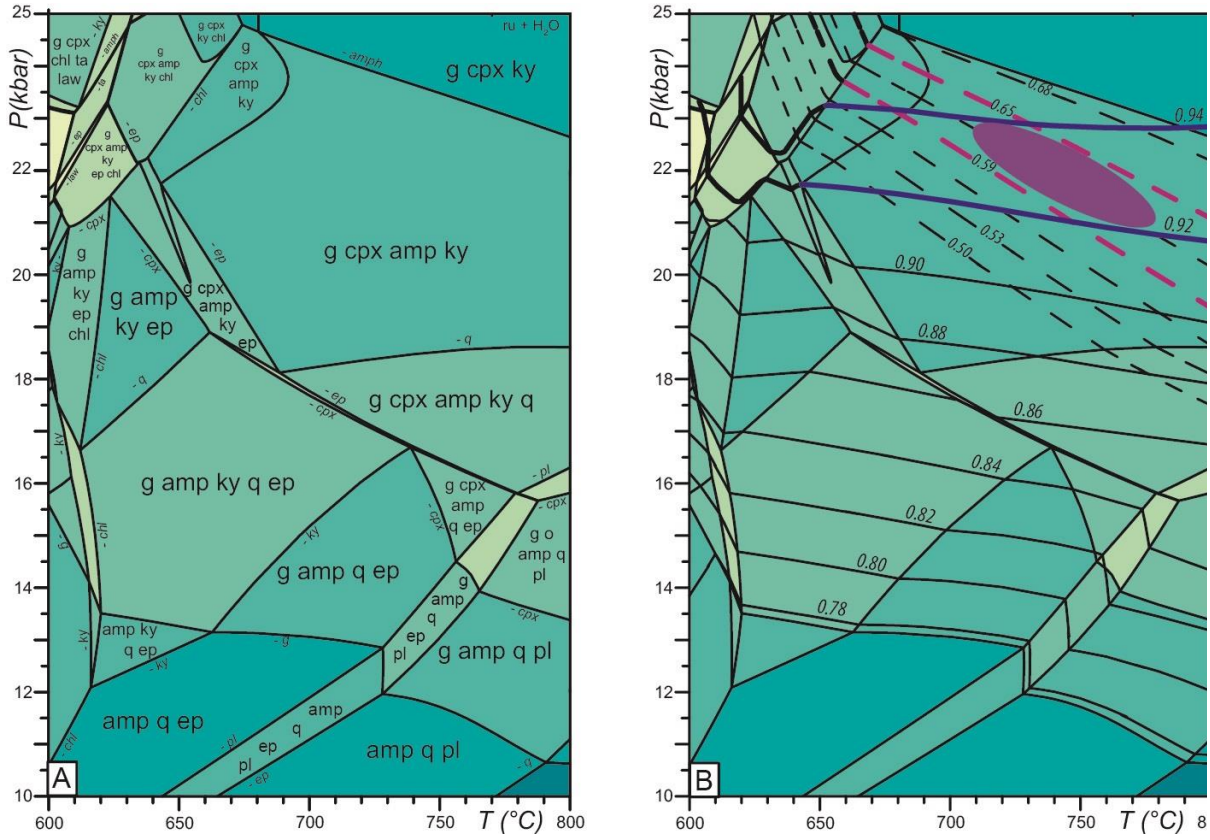

Figure II.3.4 : P-T pseudosection for the sample LV21. The rock composition, given as mol.% oxide, is SiO_2(48.87)–TiO_2(0.57)–Al_2O_3(11.71)–Fe_2O_3(0.24)–FeO(5.24)–MgO(18.22)–CaO(12.55)–Na_2O(2.49). Fields are colored with respect to their variance, darker colours indicate lower variance assemblage. A. P-T diagram calculated with H_2O saturation and 8.2% Fe^{3+} (of total iron), corresponding to the analyzed amount. The peak high-pressure assemblage is highlighted. B. Modeled compositional isopleths for garnet (X_{Mg}) and amphibole (X_{Mg}), with bold and dashed lines respectively marking the observed range.

In the pseudosection (Fig. II.3.4A), the stability field corresponding to the inferred eclogite-facies assemblage garnet-omphacite-amphibole-kyanite-rutile is located from ~18 to 24 kbar and 650 to >800°C. It is delimited by the appearance/disappearance lines of chlorite and epidote at low temperature, quartz at low pressure and amphibole at high pressure. Compositional isopleths and the observed XMg range for garnet (0.59-0.66) and amphibole (0.92-0.93) constrain the equilibration conditions at 21-23 kbar and 680-800 °C (Fig. II.3.4B).

b. Retrogressed eclogite

Petrography

LV20B is a light greenish fine-grained eclogite, dominated by garnet and relatively coarse amphibole surrounded by fine grained symplectites of amphibole, plagioclase and diopside. Also present are minor quartz, epidote, rutile, ilmenite, titanite, biotite, zircon and apatite.

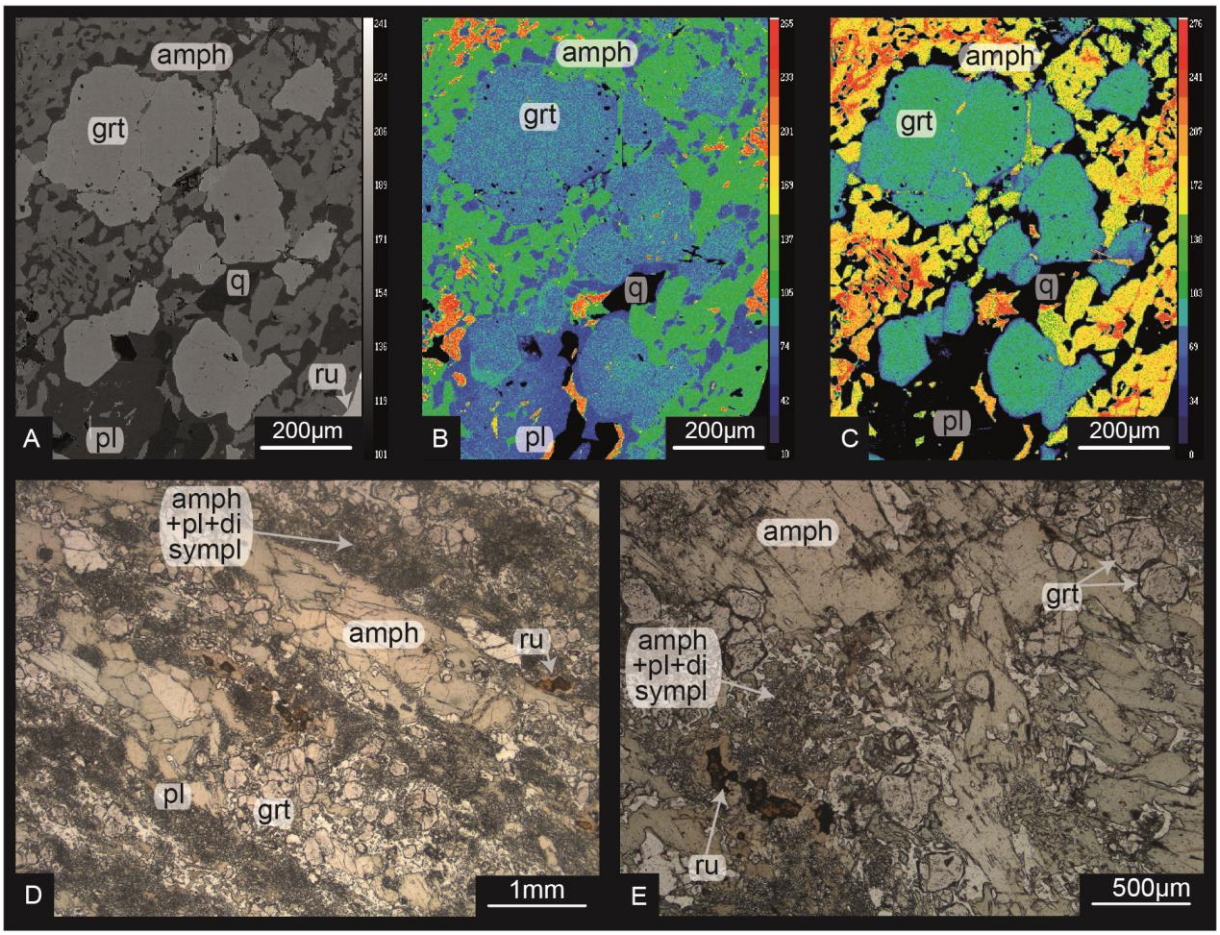

Figure II.3.5: A. SEM picture. B. X-ray map for Ca. C. X-ray map for Mg. D, E. Photomicrograph

Small subhedral garnet (60-260 µm) is homogeneous and chemically unzoned in major elements (XMg = 0.34-0.44, XAlm = 0.41-0.49, XPrp = 0.25-0.35, XGrs = 0.21-0.32, XSps ~ 0.01-0.02; Figs. II.3.3, 5, supplementary table II.3.3). Garnet locally contains inclusions (50-150 µm) of epidote or amphibole. Rare tiny inclusions of K-feldspar (< 20 µm) can also be found in garnet. Based on their textural position, three main types of amphibole can be described. (i) Amphibole 1 forms large anhedral green crystals (0.2-2 mm). They are calcic, magnesian (Ca = 1.80-1.85 pfu; XMg = 0.73-0.83; Si = 6.53-6.79 pfu; (Na+K)A =

0.42-0.56 pfu) and have a low Ti content (Ti = 0.04-0.11 pfu). (ii) Small brownish crystals of amphibole 2 (50-250 µm) are commonly closely associated with rutile or surround fine grained symplectites. They display a calcic and magnesian composition (Ca = 1.84-1.88 pfu; (Na+K)A = 0.47-0.55 pfu; XMg = 0.69-0.71, Si = 6.42-6.51 pfu), and show a higher Ti content (Ti = 0.17-0.2). (iii) Amphibole 3 forms tiny light green crystals (10-50 µm) in symplectites with plagioclase. They are also calcic (Ca = 1.90-1.96 pfu; (Na+K)A = 0.54-0.60 pfu, Si = 6.35-6.49 pfu), magnesian (XMg = 0.67-0.76) and display a variable content in Ti (Ti = 0.05-0.20 pfu). Garnet and amphibole 1 are commonly surrounded by coronae of amphibole 3 + diopside + plagioclase-bearing symplectites.

Epidote occurs as rounded grains disseminated in the matrix, locally as small inclusions (~ 50 µm) in amphibole. Plagioclase occurs as small subhedral crystals in the matrix (100-300 µm), and as tiny lamellae in symplectites (Fig. II.3.5, supplementary table II.3.3). Despite the different textural position, all crystals have the same composition (XAn = 0.30-0.41). Rutile forms tiny prismatic inclusions (10-75 µm) in amphibole 1 and anhedral grains (100-500 µm) in the matrix, locally closely associated with ilmenite (Fig. II.3.5). Brown small biotite crystals (50-200 µm) are localised close to amphibole and rutile (Fig. II.3.5, supplementary table II.3.3). Rounded quartz grains are found in the matrix. Amphibole 1 is interpreted as “primary” and as a part of the original high-pressure assemblage, containing also garnet and rutile. The dominant mineral assemblage is interpreted to comprise amphibole 2 and 3, plagioclase, titanite, epidote and biotite.

P-T estimates

Calculations were performed in the model system NCKFMASHTO, including K2O, since biotite is part of the dominant assemblage amphibole-plagioclase-titanite-epidote-biotite. The corresponding stability field is located at <8-12 kbar, <600-700°C (Fig. 6). It is delimited by the appearance/disappearance of garnet and epidote at high temperature and plagioclase at high pressure. Compositional isopleths were used to constraint the equilibration conditions of both the dominant retrogressed and the primary mineral assemblages. The intersection of the isopleths for the silicon content of amphibole 1 (Si = 6.5-6.8 pfu) and XMg of garnet (XMg = 0.34-0.44) suggests the equilibration of the primary assemblage under eclogite-facies conditions at 17.5-19 kbar and 680-750°C, in the stability field garnet-muscovite-amphibole-clinopyroxene-rutile-quartz ± kyanite. Due to the highly retrogressed character of the sample, we can not ascertain the presence or absence of kyanite to restrain the stability field.

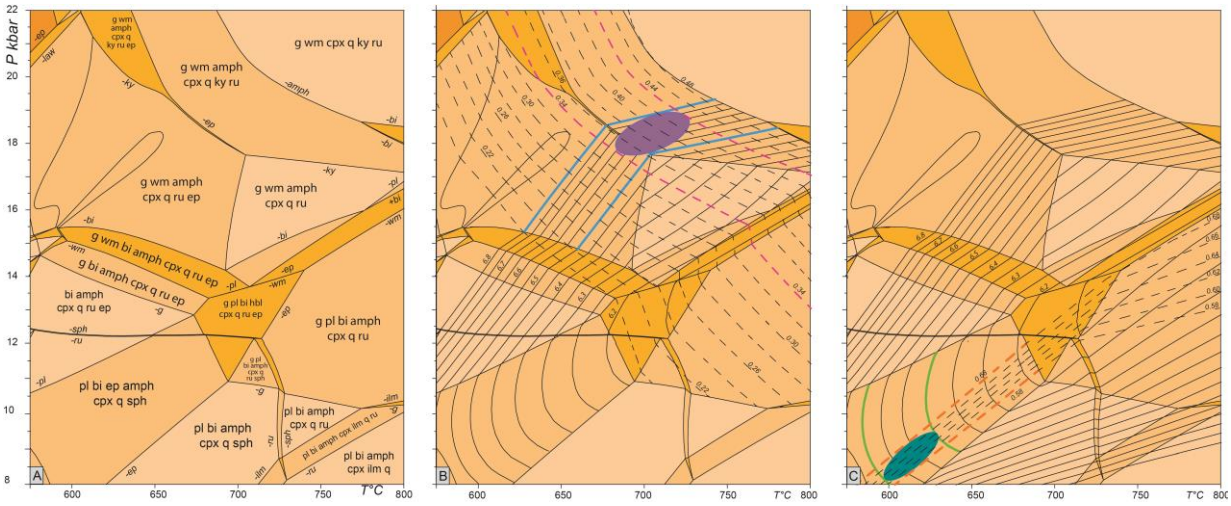

Figure II.3.6 - P-T pseudosection for the sample LV2B. The rock composition, given as mol.% oxide, is SiO_2(54.26)–TiO_2(0.82)–Al_2O_3(9.18)–Fe_2O_3(0.53)–FeO(6.95)–MgO(13.65)–CaO(11.68)–Na_2O(2.42). Fields are colored with respect to their variance, darker colors indicate lower variance assemblage. A. P-T diagram calculated with H_2O saturation and 13.3% Fe^{3+} (of total iron), corresponding to the analyzed amount. The peak high-pressure assemblage is highlighted. B. Modeled compositional isopleths for garnet (X_{Mg}) and amphibole (X_{Si}), with dashed and bold lines marking the observed range .C. Modeled compositional isopleths for plagioclase (X_{Na}) and amphibole (X_{Si}), with dashed and bold lines respectively marking the observed range.

The intersection of the isopleths for the secondary amphibole (Si = 6.35-6.50 pfu) and plagioclase (XCa = 0.58-0.68) suggests equilibration at 600-640°C and 8-9.5 kbar in the field plagioclase-biotite-epidote-amphibole-clinopyroxene-titanite-quartz.

5. Garnet dating

a. Lu-Hf dating

Lu and Hf contents from sample LV21 were low and practically the same in all the analyzed garnet fractions, with values ranging 0.59-0.60 ppm and 0.13-0.14 ppm, respectively (Table II.3.1). These contents are in a good agreement with the LA-ICP-MS measurements performed on garnet in thin section (see Garnet trace element chemistry below). The low Hf value measured is typical of metamorphic garnets, and suggest that no Hf-rich inclusions disturbed the analyses. The parent/daughter ratios are very low (0.629-0.670) but systematically higher than the ones from the WR or the clinopyroxene fractions (0.070 and 0.007 respectively). The isochron yields a date of 357 ± 13 Ma (MSWD = 22; Fig.II.3.7, Table II.3.1), the low precision being linked to the low parent/daughter ratio and to the excess scatter among the analyzed garnet fractions. The accuracy of the results is discussed in the interpretation section below.

Lu and Hf contents from sample LV20B were also low in all the isotope dilution analyses (Table II.3.1), Lu ranging 0.9-1.3 ppm, and Hf 0.08-0.10 ppm. Similarly, the low Hf values suggest that no Hf-rich inclusion disturbed the analyses. Parent/daughter ratios in garnet are higher in this sample (1.74 and 1.76), and significantly different from the parent/daughter ratios of WR and amphibole (0.08 and 0.07 respectively). They spread on an isochron and allow to define a date of 357.5 ± 4.0 Ma (MSWD = 16) with an initial $^{176}Hf/^{177}Hf$ = 0.282862 ±56. The isochron date, calculated without the WR, is similar but more precise at 356.9 ± 1.5 Ma (MSWD = 0.31), and the calculation including the WR and removing the amphibole fractions yields a date of 358.8 ± 1.5 Ma (MSWD = 0.30).

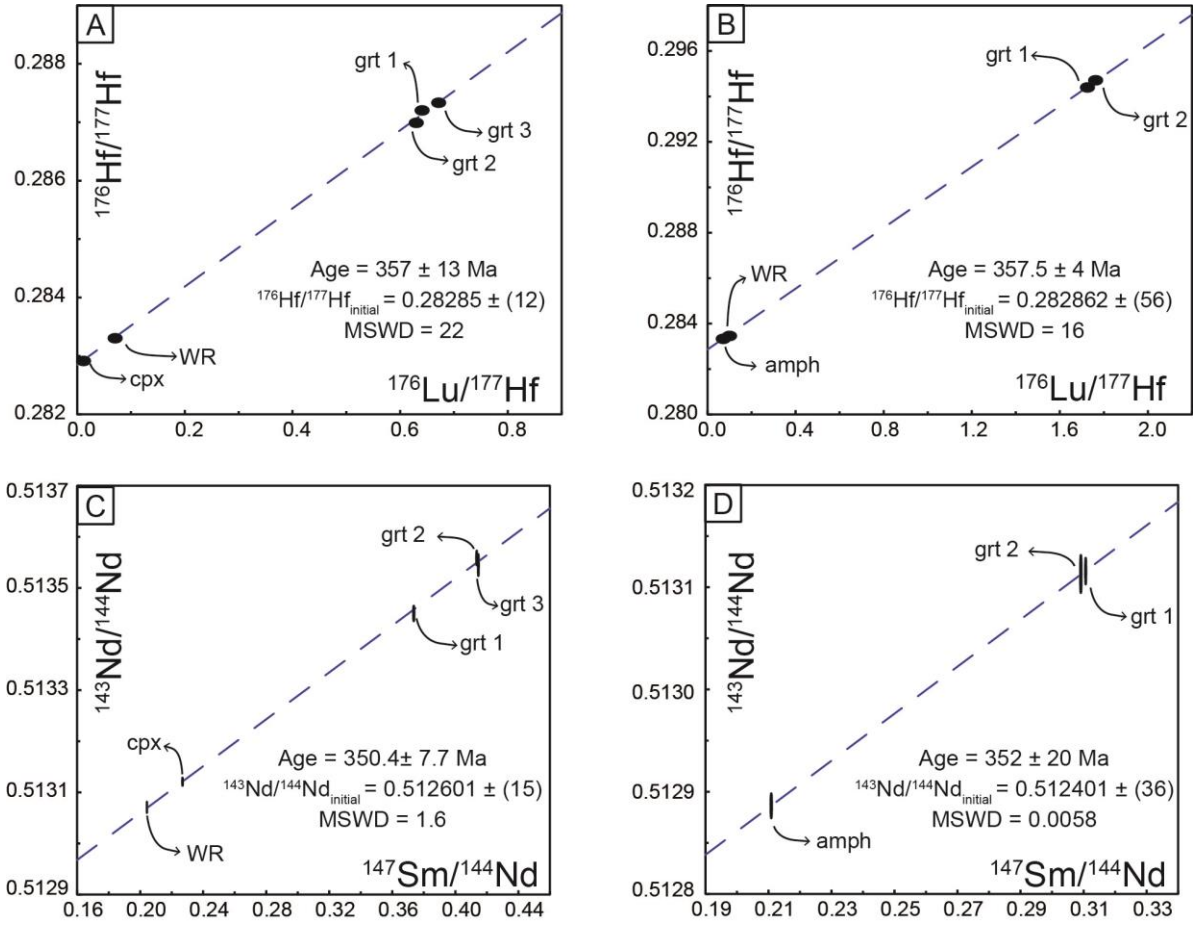

Figure II.3.7 - Lu–Hf (A, B) and Sm–Nd (C, D) isochron diagrams for samples LV21 and LV20B respectively. WR – whole rock, Grt – garnet, 1-3 – garnet fractions, Amph - amphibole. Cpx – clinopyroxene. Lu-Hf errors of analyses were too small to be visible, consequently data points were increased.

Table 1 : Summary of the Lu–Hf and Sm–Nd dating results.

fraction	Weight [mg]	Sm [ppm]	Nd [ppm]	$^{147}Sm/^{144}Nd$	2s	$^{143}Nd/^{144}Nd$	2s	Lu [ppm]	Hf [ppm]	$^{176}Lu/^{177}Hf$	2s	$^{176}Hf/^{177}Hf$	2s
Sample LV21													
G1	73.83	0.6908	1.1180	0.373618	0.000271	0.513450	0.000012	0.592	0.131	0.6419	0.0032	0.287209	0.000019
G2	70.93	0.6516	0.9528	0.413559	0.000184	0.513559	0.000012	0.598	0.135	0.6286	0.0031	0.286990	0.000016
G3	52.72	0.6314	0.9209	0.414617	0.000190	0.513545	0.000017	0.593	0.125	0.6700	0.0034	0.287331	0.000029
cpx	67.84	1.6321	4.3493	0.226896	0.000155	0.513121	0.000006	0.028	0.531	0.0073	0.0000	0.282911	0.000007
WR	101.68	1.9344	5.7249	0.204302	0.000027	0.513071	0.000009	0.225	0.453	0.0702	0.0004	0.283310	0.000006
Sample LV20B													
G1	68.54	0.6379	1.2416	0.3107	0.000107	0.513116	0.000011	0.924	0.075	1.737	0.0087	0.294480	0.000026
G2	65.09	0.6018	1.1771	0.3091	0.000170	0.513113	0.000015	1.269	0.102	1.755	0.0088	0.294631	0.000041
cpx	66.78	1.6609	4.7618	0.2109	0.000157	0.512886	0.000010	0.348	0.683	0.072	0.0004	0.283362	0.000009
WR	102.66	2.7591	8.9256	0.1869	0.000040	0.512815	0.000005	0.358	0.643	0.079	0.0004	0.283374	0.000007

Footnote to Table 1: All errors are 2 se (standard errors) and relate to the last significant digits. $^{176}Lu/^{177}Hf$ errors are 0.5% and $^{147}Sm/^{144}Nd$ errors are 0.3%. Reproducibility of JMC475 yielded 0.282166 ± 4 (N = 4) over the period of analyses, while JNd-1 gave 0.512098 ± 5 (N = 7). Hf and Nd mass bias were corrected to $^{179}Hf/^{177}Hf = 0.7325$ and $^{146}Nd/^{144}Nd = 0.7219$, respectively. Decay constants applied to age calculations: $\lambda^{176}Lu = 1.865x10^{-11}$ yr^{-1} (Scherer et al., 2001) and $\lambda^{147}Sm = 6.54x10^{-12}$ yr^{-1} (Lugmair and Marti, 1978). Procedure blanks for all elements were below 30 pg.

b. Sm-Nd dating

Sm and Nd contents in LV21 are low, ranging 0.634-0.69 ppm and 0.92-1.12 ppm, respectively (Table II.3.1). Parent/daughter ratios also display very low values of 0.3736-0.4136. Despite the fact that the Nd contents are higher than the Sm contents, they are nevertheless low, which is typical for metamorphic garnet and also suggests that no Nd-rich inclusions disturbed our analyses. All the garnet, clinopyroxene and WR fractions yields an isochron date of 350.4 ± 7.7 Ma (MSWD = 1.6) with an initial 143Nd/144Nd = 0.512601 ± 15 (Fig. II.3.7).

Sm and Nd contents are similarly very low in LV20B, displaying values of 0.60 and 0.64 ppm for Sm and 1.18 and 1.24 ppm for Nd (Table II.3.1). The parent/daughter ratios of the garnet aliquots are low, ranging 0.309-0.311. This ratio is also low for the amphibole and WR fractions, with values of 0.211 and 0.187, respectively. The Nd contents, although higher than the Sm contents, are very low and characterize pure metamorphic garnet. The two garnet fractions together with the WR and amphibole fractions define a date of 371 ± 12 Ma (MSWD = 2.8). Excluding the WR from the calculation yields a date of 352 ± 20 Ma (MSWD = 0.0058) (Fig. II.3.7), while excluding the amphibole fraction yields a date of 371 ±12 Ma (MSWD = 0.0095).

6. Zircon U-Pb dating

Sample LV20B was the only one to provide zircon grains. The crystals are colorless, mostly subhedral to euhedral and range in size from 40 to 350 µm (Fig. II.3.8). Few metamict crystals were avoided during the picking stage. Zircon grains display oscillatory zonation (Fig. II.3.8a, d), patchy zonation (Fig. II.3.8b, e, f) and core and rim textures (Fig. II.3.8c). When it was possible, the rims were analyzed. Sixty-six analyses were performed out of forty-five zircon grains. Three groups can be distinguished.

(i) A Cambrian group is composed of 11 analyses performed on 9 zircon grains. All the analyses are concordant to slightly discordant and 10 of them allow to calculate a Concordia date (as of Ludwig, 1998) of 511.2 ± 3.9 Ma (MSWD = 1.17, Fig. II.3.9A, B). The remaining analysis displays an older concordant date at ca. 570 Ma. Cambrian zircon grains display oscillatory zonation (e.g. Fig. II.3.8, zircon a, spot zr-05 and zr-54, zircon d, spot zr-11 and zr-12) and never exhibit patchy zonation. Their Th/U ratios vary from 0.3 to 0.9, while the U content varies from 63 to 799 ppm.

(ii) Ordovician grains define the second group, represented by 47 analyses obtained on 34 zircon grains. The analyses are concordant to discordant. Forty-four analyses provide a lower intercept date of 472.4 ± 1.7 (MSWD = 0.78, Fig. II.3.9A, supplementary table II.3.2), while the 32 most concordant analyses yield a concordia date of 473.4 ± 2 Ma (MSWD = 1.3, Fig. II.3.9C). Three remaining analyses (~450Ma, supplementary table II.3.2, zr-40, zr-51 and zr-56) are slightly subconcordant to discordant, and are best explained by variable lead loss and common lead enrichment. The Ordovician zircon dates can be found either in zircon cores (e.g. Fig. II.3.8, zircon c, spot zr-04), in grains characterized by oscillatory or patchy zoning (e.g. Fig. II.3.8, zircon e, spot zr-40, zr-41, zr-45; zircon f, spot zr-01, zr-02, zr-03). Their Th/U ratios are variable (0.3-1) with highly variable U contents between 63 and 799 ppm.

(iii) The last group yields Devonian dates, obtained on six analyses from five different zircon grains yielding a lower intercept date of 378.6 ± 5.7 Ma (MSWD = 0.96, Fig. II.3.9A, D). The four concordant analyses yield a concordia date of 382.3 ± 4.7 Ma (MSWD = 1.4, Fig. II.3.9D). Two analyses were obtained on zircon rims surrounding an Ordovician core (e.g. Fig. II.3.8, zircon c, spot zr-61), while four analyses correspond to different patchy zonings within grains that preserved an older Ordovician age (Fig. II.3.8, zr 63, 39) or on a solely Devonian zircon (e.g. Fig. II.3.8D, zircon b, spot zr-17 and zr-18). Therefore, the Devonian dates do not correspond to a specific zircon texture. Their Th/U ratios are distributed from 0.4 to 0.6, with U contents ranging from 66 to 220 ppm. No obvious correlation is seen between the U content or the Th/U ratios.

Finally, in the whole set of analyses, there is no evident pattern linking the texture of the zircon crystals to their apparent ages. Similarly, no obvious link exists between the dates and the U contents (from 28 to 799 ppm) or the Th/U ratios (from 0.3 to 1) (Supplementary Table II.3.2).

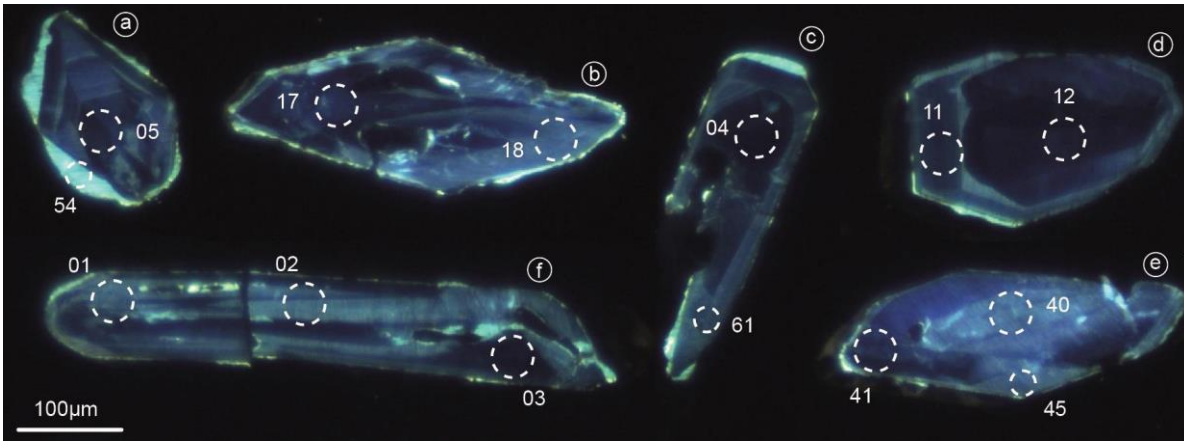

Figure II.3.8: Selected cathodoluminescence images of zircon crystals, displaying the various textures observed. White (35 and 25 µm) circles show the location of the U-Pb analyses and their corresponding analysis number.

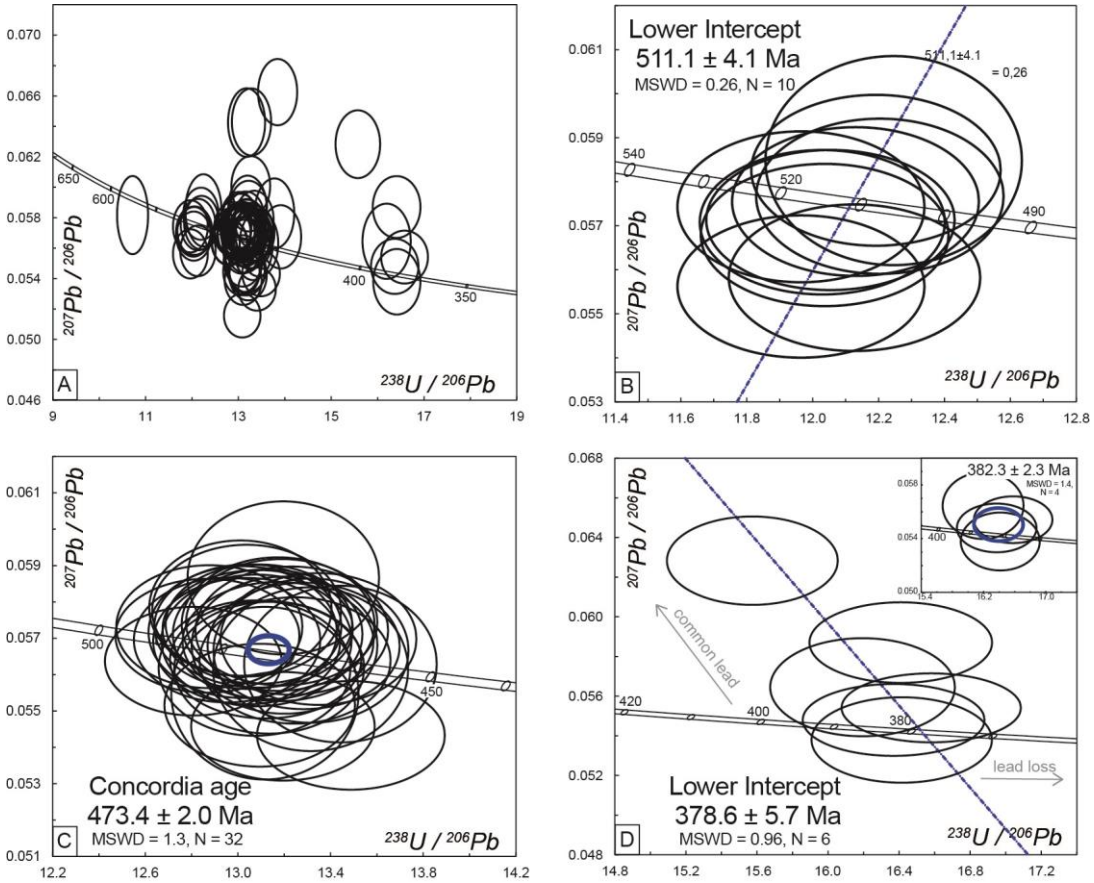

Figure II.3.9: A. Tera–Wasserburg ($^{207}Pb/^{206}Pb$ vs. $^{238}U/^{206}Pb$) diagram displaying all dates obtained on zircon. B. Tera–Wasserburg diagram displaying cambrian analyses C. Tera–Wasserburg diagram displaying concordant ordovician analyses D. Tera–Wasserburg diagram displaying all Devonian analyses, insert show the Concordia age.

7. Garnet and zircon trace element chemistry

a. Garnet

Four and seven REE profiles were performed in garnet crystals from samples LV21 and LV20B, respectively. They are very homogeneous, and two spectra from each sample were chosen to illustrate the REE variations in garnet. In both samples, the REE contents are very low.

LV21 garnet grains display very low REE contents, and various trends can be described (Fig. II.3.10A, B). The first profile displays an "oscillatory zonation". The core of the garnet is composed of a center characterized by a very low Lu content (down to 0.1 ppm) and surrounded by the highest Lu content (~1-1.5 ppm). The surrounding rims show Lu contents decreasing toward the edge (from ~1 to 0.3-0.4 ppm). The second type of profile displays an opposite trend, with very low Lu content in the inner part of the crystal that tends to increase toward the edge up to 1 ppm. The Sm and Nd contents in both crystal types are low, near or even below the detection limit with the applied analytical conditions, but since the Sm and Nd behaviors are strongly coupled, the zonation trends can be deciphered from Sm alone. The Sm contents show a slight rise towards the edges (up to 1-2.5 ppm) with the lowest content found in the inner part of the crystal (~0.4 ppm).

LV20B garnet grains are very homogeneous as it can be seen in the two profiles (Fig. II.3.10C, D, Supplementary Table II.3.4). The HREE contents are very low, the Lu contents barely exceeding 2 ppm. The cores of the crystals show the highest contents in Lu (~0.6-2.4 ppm), which decreases toward the rims down to 0.5 ppm. A slight increase can be seen toward one edge of profile 2, up to 1.5 ppm. Sm and Nd values are also very low, rarely higher than the detection limit. When detected, Sm shows contents ranging from 0.2 to 2 ppm throughout the crystals. Nd contents do not exceed 0.6 ppm in the core of the garnet crystals, but can reach up to ~1.6 ppm in the rims.

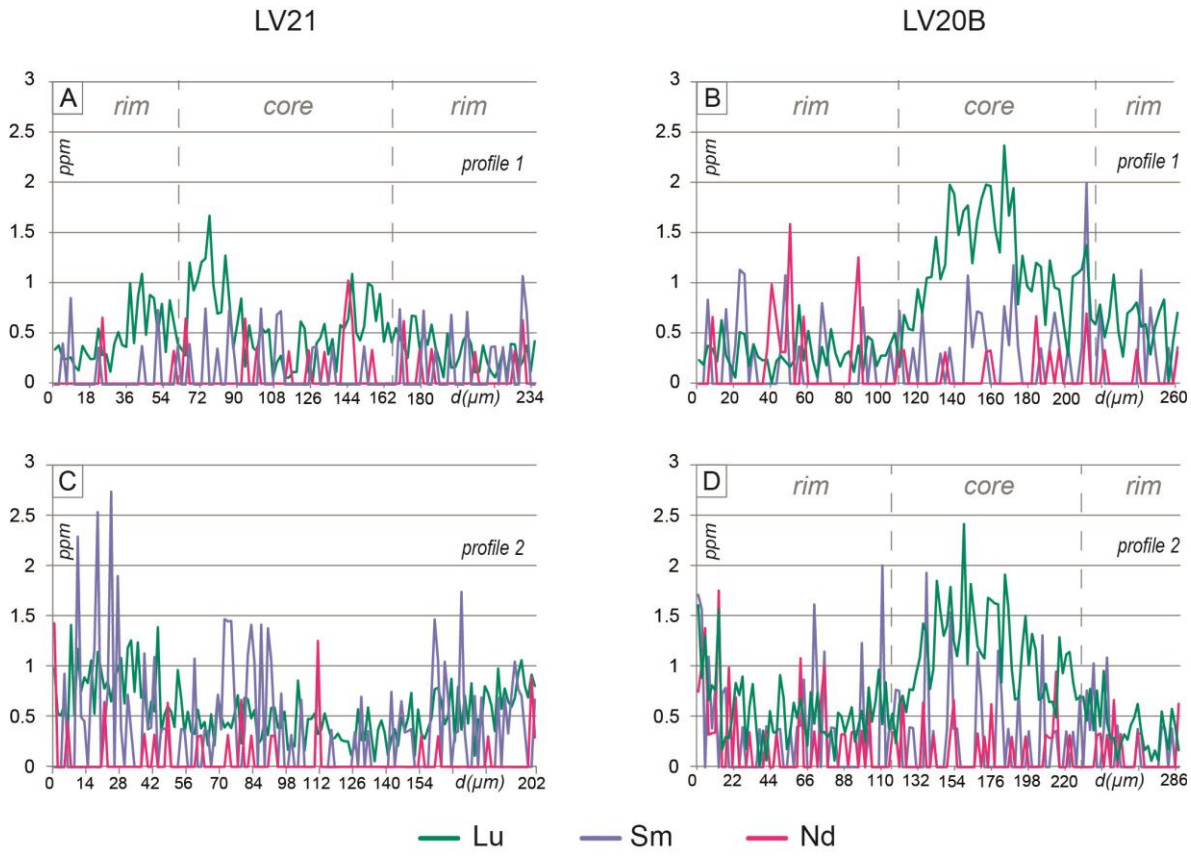

Figure II.3.10: Trace element profiles for garnet from samples LV21 (A, C) and LV20B (B, D). Lu – green, Sm – purple, Nd – pink.

b. Zircon

The three apparent ages groups (Cambrian, Ordovician and Devonian, see results in the geochronology section) were also analyzed for their trace elements contents, in different textural positions (core, rim, patchy and oscillatory zonation). All the REE spectra are variably enriched in HREE (LuN/SmN = 70.64-3871.89), and display various Eu anomalies (Eu/Eu* = 0.25-0.71, Fig. II.3.11A, Supplementary Table II.3.5). They are hereafter described according to their measured apparent ages.

Devonian zones were too small to be systematically analyzed and consequently only three spots were measured. They systematically display the lowest Ce/Ce* (1.6-6.08) and the highest Pr/Pr* (0.46-1.06). The Eu anomalies are variable (Eu/Eu* = 0.35-0.71), while HREE are enriched (LuN/SmN = 189.62-331.44; YbN/GdN = 44.25-78.59) (Fig. II.3.11A). This group nevertheless display the lowest HREE contents (SmN = 4.58-6.14; LuN = 1138.98-1892.99). Yttrium contents are low in this dataset (Y = 211.46-582.05 ppm, Fig. II.3.11B).

Ordovician zones are homogeneous with the exception of one analysis (Fig. II.3.11A). Almost all the analyses show high Ce anomalies (Ce/Ce* = 14.82-92.35), high negative Eu/Eu* (0.25-0.40), low Pr/Pr* (0.10-0.47) and a strong HREE enrichment (LuN/SmN = 70.64-323.38, av. 213.95; YbN/GdN = 13.25-38.05, av. 27.7). The Y contents are very high (Y = 736.34-3838.82 ppm, Fig. II.3.11B). HREE contents are high (SmN = 8.25-95.75; LuN = 2064.17-6764.17). The remaining analysis displays a low Ce anomaly (13.56), a relatively small negative Eu anomaly (0.74), as well as Pr anomaly (0.69) and a low enrichment in HREE (LuN/SmN = 274.46; YbN/GdN = 39.10). Nevertheless, as it was the case for the Devonian group, this remaining analysis displays low REE contents (SmN = 3.42; LuN = 938.19) and a depletion in Y (265.34 ppm, Fig. II.3.11B).

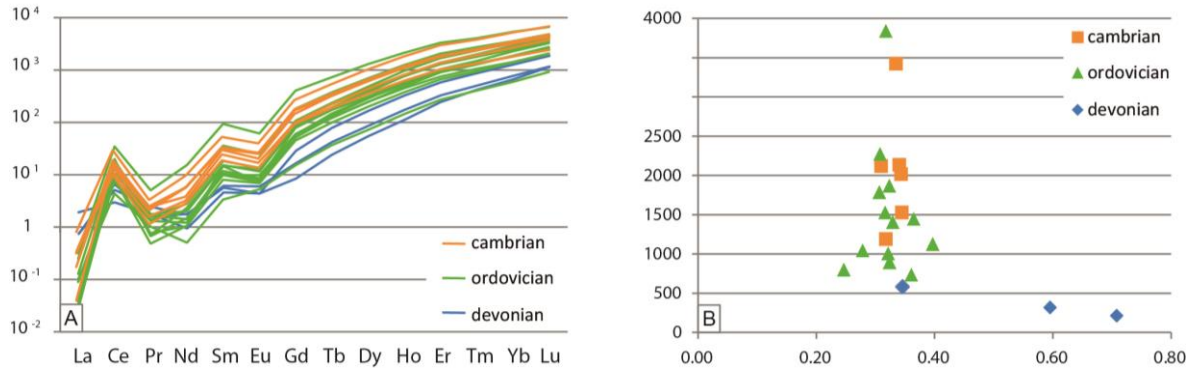

Figure II.3.11: A. Trace element chemistry for dated zircons. REE content normalized to chondrite for zircon displaying Devonian dates (blue), Ordovician dates (green), Cambrian dates (orange). B. Y (ppm) vs. Eu/Eu anomaly diagram, with the recorded dates highlighted. See text for details.*

Cambrian zones (Fig. II.3.11A) display high Ce anomalies (16.62-51.85), low negative Eu anomalies (0.31-0.34), and an enrichment in HREE (LuN/SmN = 130.4-160.89, av. 142.02; YbN/GdN = 18.83-27.87, av. 21.58). The Y contents are also very high (Y = 1188.14-3422.89 ppm, Fig. II.3.11B).

8. Rutile geochronology

In sample LV21, the dated rutile grains are subhedral, with a redish to orangish color, with sizes ranging from 80 to 230 µm (Fig. II.3.12A, B). Seventeen analyses were performed on fourteen rutile crystals. Plotted in a Tera-Wasserburg diagram, the 17 analyses are discordant because of the variable amounts of common Pb and rather low U contents (1.11-2.29 ppm). Nevertheless, all the analyses spread on a discordia and allow to calculate a lower intercept

date of 367.8 ± 9.1 Ma (MSWD = 1.5, Fig. II.3.12A, Supplementary Table II.3.2) with a $^{207}Pb/^{206}Pb$ initial value at 0.891. The weighted average ^{207}Pb-corrected date (calculated at 370 Ma using the Stacey and Kramers (1975) terrestrial Pb evolution model) is equivalent within error at 365.6 ± 8.4 Ma (MSWD = 1.7).

The dated rutile grains from LV20B are reddish to dark, anhedral, with sizes ranging from 80 to 190 µm. Eighteen analyses were conducted on 18 rutile grains. All the analyses are discordant because of the presence of variable amounts of common Pb. The U contents in rutile are very low, mostly ranging from 0.9-3.6 ppm except for one analysis with an uranium content of 9.6 ppm. The eighteen analyses allow to calculate a lower intercept date of 354.9 ± 9.5 Ma (MSWD = 2.1, Fig. II.3.12B) and a ^{207}Pb-corrected date of 350.6 ± 7.3 Ma (MSWD = 1.6).

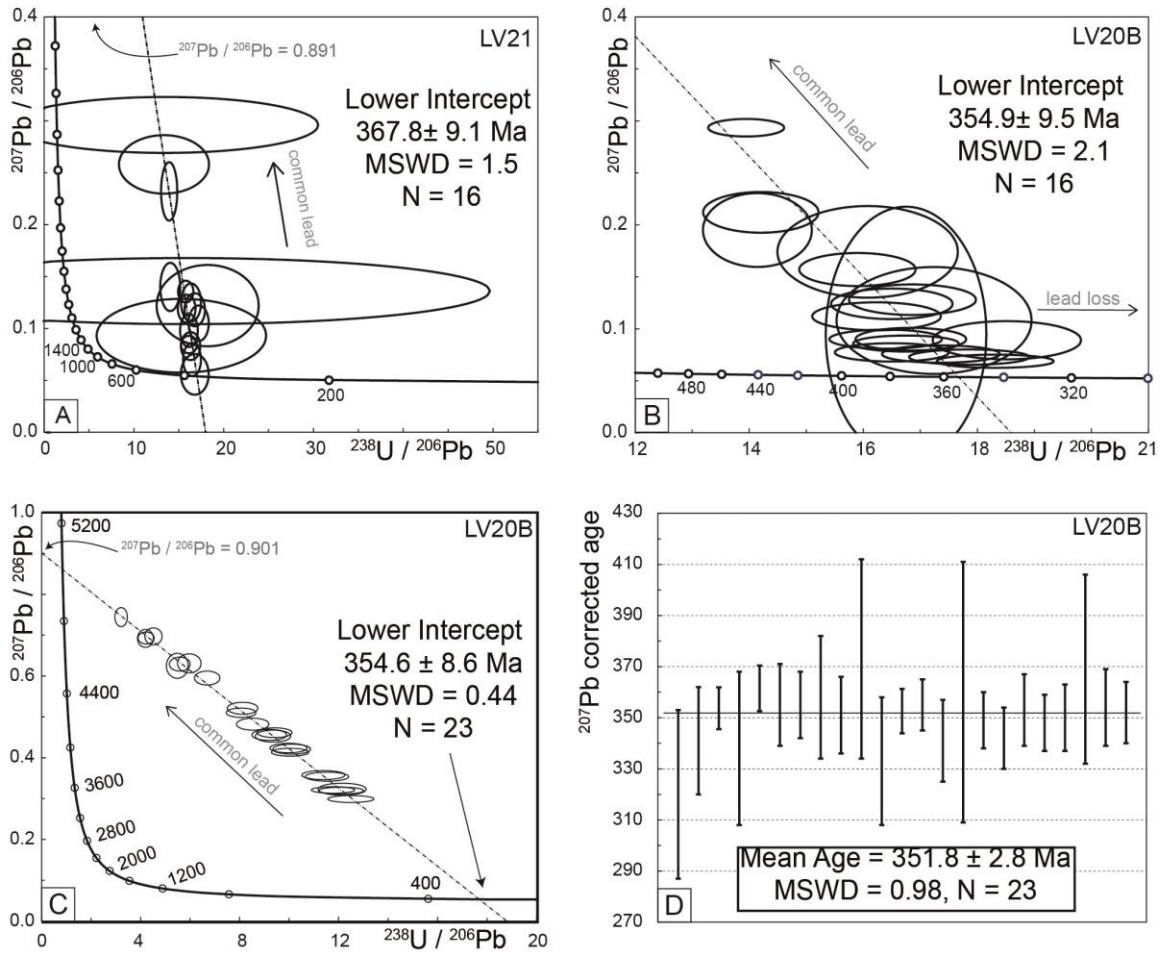

Figure II.3.12: Tera–Wasserburg ($^{207}Pb/^{206}Pb$ vs. $^{238}U/^{206}Pb$) diagram displaying all dates obtained on rutile from LV21 (A) and LV20B (B) and apatite from LV20B (C) and the mean age ^{207}Pb-corrected. (D).

9. Apatite geochronology

Apatite grains were found both in LV21 and LV20B samples but they were too small in sample LV21 to be analyzed. Apatite grains from LV20B are colorless and rounded, with sizes ranging from 100 to 200 µm. Twenty-three analyses were performed on 23 apatite grains (supplementary table II.3.2). The grains are very homogeneous in cathodoluminescence and characterized by low U (2.0-14.6 ppm) and Pb (0.8-4.2 ppm) contents. All the analyzed apatite grains contain some common Pb and therefore plot in a discordant position in a Tera-Wasserburg diagram (Fig. II.3.12C). The resulting discordia allows to calculate a lower intercept date of 354.6 ± 8.6 Ma (MSWD = 0.44) with a $^{207}Pb/^{206}Pb$ initial value of 0.901. The weighted average ^{207}Pb-corrected date (calculated at 350 Ma using the Stacey and Kramers (1975) terrestrial Pb evolution model) is equivalent within error at 351.8 ± 2.8 Ma (MSWD = 0.98, Fig. II.3.12D).

10. Interpretation and discussion

a. From dates to ages

Zircon

Th/U ratios range from 0.33 to 1.01, which is much higher than the usual values expected for metamorphic zircon (<0.1, Rubatto 2002). Nevertheless, the sample does not include Th-rich minerals such as monazite or allanite, which could explain these higher Th/U ratios as suggested by Harley et al. (2007).

The Cambrian and Ordovician dates display true “magmatic-like” spectra (high negative Eu anomaly and enrichment in HREE, e.g. Rubatto 2002) that imply that these dates should not be considered as dating a metamorphic event. The concordant date of 473.4 ± 2 Ma is well recorded by the majority of zircon grains from this sample and is a common age in the Variscan belt, either for mafic (e.g. Pin and Lancelot 1982; Villaseca et al., 2015; Chelle-Michou et al. 2017; Paquette et al. 2017) or felsic material (e.g. Ballèvre et al. 2012; Del Greco et al., 2016; Chelle-Michou et al. 2017; García-Arias et al., 2018). It is also equivalent to the emplacement age of the neighboring granites (ca 470 Ma, Lotout et al. 2017). We then propose that this 473.4 ± 2 Ma date corresponds to the emplacement and crystallization of the mafic material. The Cambrian date, older and less recorded could correspond to xenocrists – i.e contamination– from the intruded metasedimentary material (not dated but considered cambro-ordovician in the litterature).

The 378.6 ± 5.7 Ma date is poorly recorded and obtained in zircon zones displaying a less-enriched HREE pattern, a lower Eu anomaly (0.4-0.8), a lower Th/U ratio (0.34-0.59) and lower Y content (~200-600 ppm). This chemistry, although different from the magmatic zircon, is not characteristic of eclogitic zircon which is expected to display no HREE enrichment, no Eu anomaly, and Th/U < 0.1 (Rubatto, 2002). The spectra tendency is then likely to correspond to zircon growth or recrystallization during a metamorphic reaction on the prograde path, prior to the eclogite facies.

Garnet

Lu/Hf and Sm/Nd ratios are very similar, whether they were acquired by LA-ICP-MS or solution MC-ICP-MS which indicates that the garnet fractions were pure enough. The low contents are therefore inherent to the rock chemistry and not to the presence of inclusion or to analytical problems.

The first profile from sample LV21 (Fig. II.3.10A) shows, despite the low contents, a depleted inner core surrounded by Lu highs and a rimward depletion. The second profile from the same sample does not show the Lu highs in the garnet core. Instead, it shows that the edges are apparently slightly enriched in Lu, suggesting that the Lu zoning is not fully preserved and is probably modified due to diffusion. The temperature range reached by the rock (ca 680-800°C) is similar to the closure temperature estimated for the Lu-Hf system (ca. 750°C in these grains, following estimations from Smit et al. 2013). All Lu profiles in garnet LV20B show a systematic classic Rayleigh fractionation (enriched core evolving to depleted rim).

Garnet grains, in the two samples, belong to the high-pressure assemblage (peak estimated around 18-23 kbar) and grew on the prograde P-T path. Lu-Hf results in both samples yield comparable ages at ca. 358 Ma. Despite their poor precision, the fact that the Lu-Hf dates obtained on garnet from both the retrogressed and the fresh eclogitic samples are equivalent within error, suggesting that these dates are accurate. Considering the temperature reached by the rocks, this date is therefore the best estimate for the age of the HP peak.

In both samples, Sm and Nd show very low contents which, when successfully analyzed, lead to incomplete profiles, difficult to interpret. The possible diffusional disturbance of the Lu zoning (see above) might also be applied to Sm and Nd. Nevertheless, in all profiles, Nd and Sm contents appear to be slightly higher in the rims, which is a typical feature of

incompatible element behavior. LV21 yields a date of 350.4 ±7.7 Ma, which is equivalent, within error, to the Lu-Hf date in the same sample.

LV20B Sm-Nd data, when all fractions are used in the calculation, yield a date of 371 ± 12 Ma, by far older than the Lu-Hf date of 357 ± 4 Ma recorded on the same aliquots. Excluding the amphibole fraction from the calculation yields similar results, while excluding WR yields a poorly constrained date of 352 ± 20 Ma, similar to the one recorded in the fresh sample LV21. Considering the temperatures reached by the rocks, largely above the Sm-Nd closure temperature commonly accepted (ca. 650°C), we infer that both Sm-Nd dates of 350.4 ±7.7 Ma (LV21) and 352 ± 20 Ma (LV20B) correspond to cooling during exhumation.

Rutile

Rutile has been used in numerous studies as a geochronometer to constrain the cooling history of metamorphic terranes (e.g. Zack et al. 2004, 2011, Kooijman et al. 2010, Mezger et al. 1989, 1991; Kylander-Clark et al 2008). The closure temperature (Tc) of the U-Pb system in rutile is strongly controlled by the grain size and considered to be ~ 600-650°C in crystals with a size ranging from ~ 100 µm up to ~ 200 µm (Cherniak 2000). All the selected rutile grains were around 200 µm in size, implying that this Tc can apply. The recorded 367.8 ± 9.1 Ma (MSWD = 1.5, N = 16) date in the fresh sample is analytically good (good spread, valid 207Pb/206Pb initial value) and is equivalent within error to the date recorded in garnet from the same sample (Lu-Hf: 357 ± 13 Ma).

Similarly, rutile analyses from the retrogressed sample allow to calculate a lower intercept date of 354.9 ± 9.5 Ma (MSWD = 2.1), which is equivalent within error to the recorded garnet dates (Lu-Hf: 356.9 ± 1.5 Ma ; Sm-Nd: 352 ± 20 Ma) and the rutile date from the fresh sample. Petrographically, rutile from the retrogressed sample is not in equilibrium with the dominant assemblage and is interpreted as a relic of the HP paragenesis. Considering that the temperatures reached by the rock (680-800°C) are by far higher than the usual ca 600-650°C closure temperature considered for the U-Pb system in rutile, we infer that both these dates correspond to cooling during exhumation.

Apatite

Apatite grains are dispersed in the matrix and cannot be attributed to any part of the metamorphic history based on petrographical observations. They could have crystallized during the magmatic stage and been re-equilibrated during the metamorphic history of the rock, or crystallized during any part of the P-T path. U-Pb on apatite is considered as a medium temperature chronometer since its Pb closure temperatures are comprised between 375 and 500°C (e.g. Cherniak et al. 1991; Chamberlain and Bowring 2001; Harrisson et al. 2002; Schoene and Bowring 2007; Cochrane et al. 2014). The temperature reached by the rocks is very high (680-800°C) and consequently we consider that the date of 354.6 ± 8.6 Ma (mean age at 351.8 ± 2.8 Ma) corresponds to the cooling bellow the apatite Tc during the exhumation of the terranes.

b. Timing and duration: from age to stage

The well recorded 473.4 ± 2 Ma age in zircon is a new evidence of the magmatism related to the Ordovician rifting. Based on the younger dates recorded by zircon, it is plausible that this oceanic domain started to subduct around ~380 Ma.

Garnet Lu-Hf and Sm-Nd, rutile U-Pb and apatite U-Pb dating yield similar ages within error (Fig. II.3.13). Considering the temperature conditions at the peak pressure metamorphism, we infer that garnet Lu-Hf at ca. 358 Ma is the best approximation for the HP metamorphic peak at 18-23 kbar and 680-800°C. The garnet Sm-Nd and rutile U-Pb results are then considered to date the cooling during the exhumation stage until 8-9.5 kbar and 600-620°C, conditions of the development of the dominant retrogressive assemblage in LV20B. Apatite closure temperature being lower than these temperature conditions, the mean 351.8 ± 2.8 Ma date is then considered to reflect the subsequent cooling event.

The temperature decreased of 130 ± 70°C during major decompression, from 18-23 to 8-9.5 kbar (pressure drop of 11.75 ± 3.25 kbar) allow to calculate a low cooling rate of 21.5 ± 11.5°C/Ma. This low rate emphasizes a fast exhumation. The apatite dating highlight a fast cooling post major exhumation stage, of 80 ± 5°C/Ma (600-620°C and 8-9.,5 kbar at to 450°C at 351.8 ± 2.8 Ma). Since it can not be possible to infer any pressure to this temperature, we can not distinguish if this apatite dating emphasizes an ongoing fast decompression or if it highlights a fast cooling post major exhumation stage, of 80 ± 5°C/Ma.

We cannot constrain the P-T-t path of the rocks between 358 Ma and 352 Ma because of the large margins of error in the Sm-Nd and Lu-Hf dates, and the lack of pressure data at 352 Ma. However, we reasonably assume that the pressure value that corresponds to the temperature of 450°C was less than 8.5 - 9 kbar. So the pressure drop from 18-23 kbar to 8.5-9 kbar that starts at 358 Ma, was achieved at 352 Ma. Assuming lithostatic pressure, this provides minimum exhumation rates ranging from 7.25 mm/y to 4.5 mm/y, emphasizing fast exhumation.

These rates are markedly faster than mean erosion in mountain belts, suggesting that exhumation was driven by tectonic processes. The temperature decrease from 680-800°C to 450°C between 358 Ma and 352 Ma corresponds to mean cooling rates ranging from 38°C/Myr to 58°/Myr. However, P-T data show that decompression was accompanied by a relative low cooling (~130°C for 14, 5 to 9 kbar decompression, i.e. ~ 2,6 to 4°C/km), fitting with fast exhumation. This suggests that cooling rates were much higher after than during decompression, in excess of 58°C/Myr.

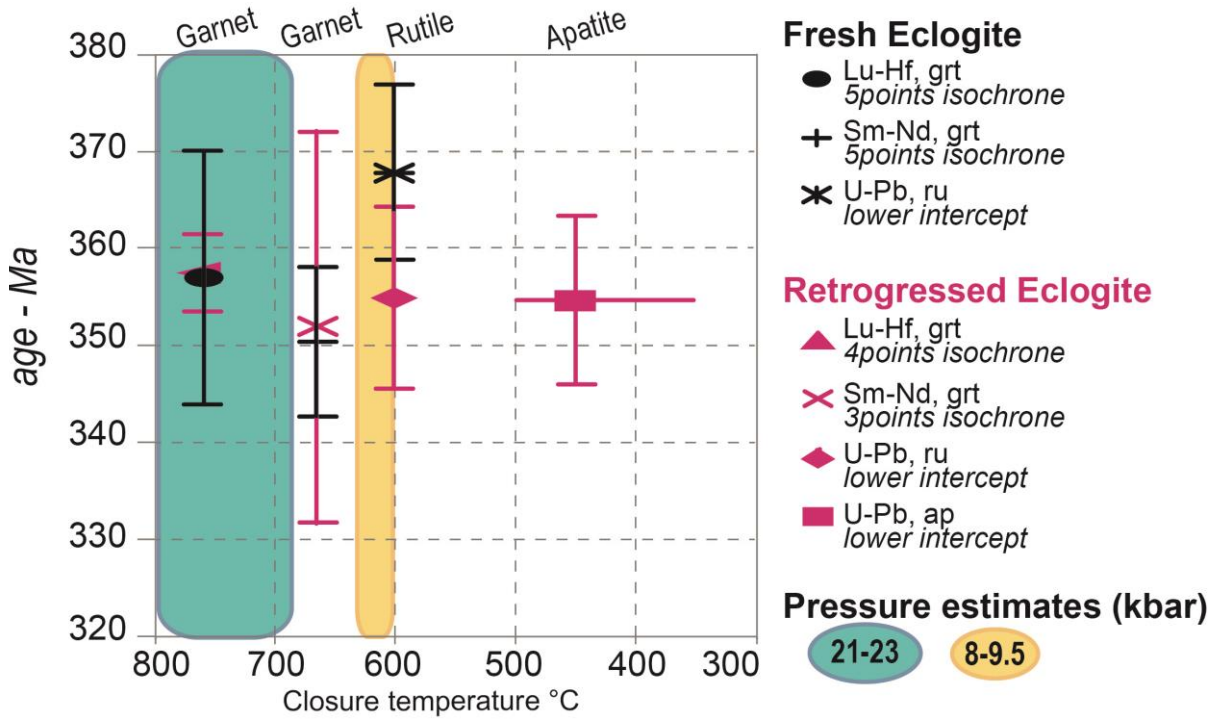

Figure II.3.13: Age (Ma) – Temperature (°C) diagram summarizing the chronological and petrological results from this study.

c. Implication for the French Massif Central

This is the first high-pressure age for the Lévézou Massif, by far younger than the commonly accepted Silurian age. This age This is the first age for the high-pressure event in the Lévézou Massif that is significantly younger than the recent high-pressure age described in the neighboring Najac massif, where the HP peak is estimated at 376 ± 3.3 Ma (Lotout et al., 2018). This diachronism can be explained by either (i) the dating of rocks in distinct initial tectonic settings (true oceanic crust vs. continental margin), (ii) closure of different oceanic domains, (iii) an irregular limit of the subducting plate inducing a diachronous closure of the ocean, or (iv) an active subduction zone where slices of buried crust are episodically exhumed.

(i) The first hypothesis implies that the older HP ages reflect true oceanic terranes, while the youngest recorded dates correspond to the subduction of more continental terranes. This hypothesis is hazardous since the Lévézou massif displays true tholeiitic MORB chemical compositions (Briand et al., 1988) and has been described as a dismembered ophiolitic sequence (Nicollet 1978). As detailed in the geological setting, the tectonic emplacement of the LAC protolith is an ongoing debate in the whole FMC and the interpretations on the true nature of these terranes has changed other the past decades. (ii) Different oceanic domains imply that different continental blocs are involved in the FMC architecture, and that each eclogite-bearing mafic outcrop should correspond to a suture zone. Such hypothesis is highly unlikely. (iii) A diachroneous closure of the oceanic domain could be plausible at the scale of the FMC, but this would imply the occurrence of major transfer faults, not yet identified. (iv) Finally, the episodic exhumation of HP terranes in an active subduction setting could be a likely explanation for the record of different HP ages. Indeed, 0 based on the HP P-T estimates described in this paper, we calculate that the geothermal gradient of 9.1-13.4°C/km in the Lévézou massif. When calculate from the data of Lotout et al. (2018), the geothermal gradient in the nearby Najac Massif is similar at 8.5-12.4°C/km. The similarity between these two gradients strongly suggests an identical tectonic context and favor the hypothesis of an active subduction setting.

11. Conclusion

Based on a geochronological multi-method study and thermodynamic modeling on an eclogite and a former eclogite retrogressed under amphibolite facies, we show that the Lévézou eclogites reached 680-800°C at 18-23 kbar. The age of the high-pressure peak is estimated at ~ 358 Ma, while subsequent exhumation to 8-9.5 kbar and 620-600°C is completed at ca. 352 Ma, suggesting fast exhumation rates, followed by a fast cooling after major decompression, in excess of 80°C/Ma. This study brings the first dating of the HP-event in the Lévézou massif. The geochronological multimethod approach and the use of metamorphic rocks equilibrated under different conditions are good strategy to unravel the history of high pressure terranes.

Acknowledgement

We sincerely thank X. Le Coz for thin section preparation, Y. Lepagnot for sample crushing, M. Smędra and D. Sala for the help with the Sm-Nd and Lu-Hf chemical procedure, and J. Langlade for the help with microprobe analysis. M. Ballèvre, P. Boulvais, V. Bosse, J. Andersson are thanked for interesting discussions about the Variscan geodynamics, the HP-dating challenge, zircon textures and the REE behavior. This work was partly financed by an internal grant from the OSUR (Université Rennes 1), and a INSU-CNRS (TelluS 2017) project accorded to P. Pitra. This study is a part of the PhD thesis of C. Lotout, founded by the French Ministry of higher education and research.

References

Anczkiewicz, A.A. & Anczkiewicz, R. (2012). U–Pb zircon geochronology and anomalous Sr-Nd-Hf isotope systematics of late orogenic andesites: Pieniny Klippen Belt, Western Carpathians, South Poland. Chemical Geology 427, 1-6.

Anczkiewicz, R., Platt, J.P., Thirlwall, M.F. & Wakabayashi, J. (2004). Franciscan subduction off to a slow start: evidence from high-precision Lu–Hf garnet ages on high grade-blocks. Earth and Planetary Science Letters 225, 147-161.

Anczkiewicz, R., Szczepański, J., Mazur, S., Storey, C., Crowley, Q., Villa, I.M., Thirlwall, M.F. & Jeffries, T.E. (2007). Lu–Hf geochronology and trace element distribution in garnet: implications for uplift and exhumation of ultra-high pressure granulites in the Sudetes, SW Poland. Lithos 95, 363-380.

Anczkiewicz, R. & Thirlwall, M.F. (2003). Improving precision of Sm-Nd garnet dating by H2SO4 leaching: a simple solution to the phosphate inclusion problem. Geological Society, London, Special Publications 220, 83-91.

Anczkiewicz, R., Thirlwall, M., Alard, O., Rogers, N.W. & Clark, C. (2012). Diffusional homogenization of light REE in garnet from the Day Nui Con Voi Massif in N-Vietnam: Implications for Sm-Nd geochronology and timing of metamorphism in the Red River shear zone. Chemical Geology 318, 16-30.

Ballèvre, M., Bosse, V., Ducassou, C. & Pitra, P. (2009). Palaeozoic history of the Armorican Massif: models for the tectonic evolution of the suture zones. Comptes Rendus Geosciences 341, 174–201

Ballèvre, M., Catalán, J.R.M., López-Carmona, A., Pitra, P., Abati, J., Díez Fernández, R., Ducassou, C., Arenas, R., Bosse, V., Castiñeiras, P., Fernández-Suárez, J., Gómez Barreiro, J., Paquette, J.L., Peucat, J.J., Poujol, M., Ruffet, G. & Sánchez Martínez, S. (2014). Correlation of the nappe stack in the Ibero-Armorican arc across the Bay of Biscay: a joint French-Spanish project. In: Schulmann, K., Catalán, J.R.M., Lardeaux, J.M., Janoušek, V., Oggiano, G., (eds) The Variscan orogeny: extent, timescale and the formation of the European Crust. Geological Society London 405, 77-113.

Ballevre, M., Fourcade, S., Capdevila, R., Peucat, J.J., Cocherie, A. & Fanning, C.M. (2012). Geochronology and geochemistry of Ordovician felsic volcanism in the Southern Armorican Massif (Variscan belt, France): Implications for the breakup of Gondwana. Gondwana Research 21, 1019-1036.

Ballouard, C., Boulvais, P., Poujol, M., Gapais, D., Yamato, P., Tartèse, R. & Cuney, M. (2015). Tectonic record, magmatic history and hydrothermal alteration in the Hercynian Guérande leucogranite, Armorican Massif, France. Lithos 220-223, 1-22.

Berger, J., Féménias, O., Ohnenstetter, D., Bruguier, O., Plissart, G., Mercier, J.C. & Demaiffe, D. (2010). New occurrence of UHP eclogites in Limousin (French Massif Central): Age, tectonic setting and fluid–rock interactions. Lithos 118, 365-382.

Bosse, V., Feraud, G., Ruffet, G., Ballèvre, M., Peucat, J.J. & De Jong, K. (2000). Late Devonian subduction and early-orogenic exhumation of eclogite-facies rocks from the Champtoceaux Complex (Variscan belt, France). Geological Journal 35, 297-325.

Bosse, V., Féraud, G., Ballèvre, M., Peucat, J.J. & Corsini, M. (2005). Rb–Sr and 40 Ar/39 Ar ages in blueschists from the Ile de Groix (Armorican Massif, France): implications for closure mechanisms in isotopic systems. Chemical Geology 220, 21-45.

Bouchardon, J.L., 1987. Evaluation des conditions de pression-temperature du “top” mttamorphique des eclogites du Levezou (Rouergue Massif Central Français). CR. Acad. Sci. Paris 305, 271-275.

Bouchardon, J.L., Santallier, D., Briand, B., Ménot, R.P. & Piboule, M. (1989). Eclogites in the French Palaeozoic Orogen: geodynamic significance. Tectonophysics 169, 317-332.

Capitani, C.D. & Petrakakis, K. (2010). The computation of equilibrium assemblage diagrams with Theriak/Domino software. American Mineralogist 95, 1006-1016.

Briand, B., Piboule, M. & Bouchardon, J.L. (1988). Diversité géochimique des métabasites des groupes leptyno-amphiboliques du Rouergue et de Marvejols (Massif central). Origine et implications. Bull. Soc. Géol. France 8, 489-498.

Carignan, J., Hild, P., Mevelle, G., Morel, J. & Yeghicheyan, D. (2001). Routine analyses of trace elements in geological samples using flow injection and low pressure on-line liquid chromatography coupled to ICP-MS: a study of geochemical reference materials BR, DR-N, UB-N, AN-G and GH. Geostandards Newsletter 25, 187-198.

Chamberlain, K.R. & Bowring, S.A. (2001). Apatite–feldspar U–Pb thermochronometer: a reliable, mid-range (~ 450° C), diffusion-controlled system. Chemical Geology 172, 173-200.

Chelle-Michou, C., Laurent, O., Moyen, J.F., Block, S., Paquette, J.L., Couzinié, S., Gardien, V., Vanderhaeghe, O., Villaros, A. & Zeh, A. (2017). Pre-Cadomian to late-Variscan odyssey of the eastern Massif Central, France: Formation of the West European crust in a nutshell. Gondwana Research 46, 170-190.

Cherniak, .DJ. (2000). Pb diffusion in rutile. Contributions to Mineralogy and Petrology 139, 198-207.

Cherniak, D.J., Lanford, W.A. & Ryerson, F.J. (1991). Lead diffusion in apatite and zircon using ion implantation and Rutherford backscattering techniques. Geochimica et Cosmochimica Acta 55, 1663-1673.

Chew, D.M., Petrus, J.A. & Kamber, B.S. (2014). U–Pb LA-ICPMS dating using accessory mineral standards with variable common Pb. Chemical Geology 363, 185-199

Cochrane, R., Spikings, R.A., Chew, D., Wotzlaw, J.F., Chiaradia, M., Tyrrell, S., Schaltegger, U. & Van der Lelij, R. (2014). High temperature (> 350 C) thermochronology and mechanisms of Pb

loss in apatite. Geochimica et Cosmochimica Acta 127, 39-56.

Coggon, R. & Holland, T.J. (2002). Mixing properties of phengitic micas and revised garnet-phengite thermobarometers. Journal of Metamorphic Geology 20, 683-96.

Collomb, P. (1970). Etude géologique du Rouergue cristallin. Mém. Expl. Serv. Carte géol. France, Paris.

Delbos, L., Lasserre, M. & Roques, M. (1964). Géochronologie et rétromorphose dans la série cristallophyllienne du Rouergue (Massif central français). Sciences de la Terre 10, 329–342.

Del Greco, K., Johnston, S. T. & Shaw, J., (2016). Tectonic setting of the North Gondwana margin during the Early Ordovician: A comparison of the Ollo de Sapo and Famatina magmatic events. Tectonophysics 681, 73-84.

Delor C., Leyreloup A. & Burg J.P. (1985). Nouveaux arguments pétrologiques enfaveur de l'allochtonie du Lévézou (Massif Central français): les enclaves basiques des granites calco-alcalins et les métacornéennes associées. C. R. Acad. Sci. Paris 301, 1037–1042.

Diener, J.F. & Powell, R. (2012). Revised activity–composition models for clinopyroxene and amphibole. Journal of Metamorphic Geology 30, 131-42.

Ducrot, J., Lancelot, J.R. & Marchand, J. (1983). Datation U-Pb sur zircons de l'éclogite de la Borie (Haut-Allier, France) et conséquences sur l'évolution anté-hercynienne de l'Europe occidentale. Earth Planetary Science Letters 18, 97-113.

Faure, M., Lardeaux, J.M. & Ledru, P. (2009). A review of the pre-Permian geology of the Variscan French Massif Central. Comptes Rendus Geoscience 341, 202-13.

Forestier, F.H. (1961). Métamorphisme hercynien et antéhercynien dans le bassin du Haut-Allier (Massif central français). Doctoral dissertation, Faculté des Sciences de l'Université de Clermont-Ferrand.

García-Arias, M., Díez-Montes, A., Villaseca, C. & Blanco-Quintero, I. F., (2018). The Cambro-Ordovician Ollo de Sapo magmatism in the Iberian Massif and its Variscan evolution: A review. Earth-Science Reviews 176, 345-372.

Harley, S.L., Kelly, N.M. & Möller, A. (2007). Zircon behaviour and the thermal histories of mountain chains. Elements 3, 25-30.

Harrison, T.M., Catlos, E.J. & Montel, J.M. (2002). U-Th-Pb dating of phosphate minerals. Reviews in Mineralogy and Geochemistry 48, 524-558.

Holland, T., Baker, J. & Powell, R. (1998). Mixing properties and activity-composition relationships of chlorites in the system MgO-FeO-Al2O3-SiO2-H2O. European Journal of Mineralogy 22, 395-406.

Holland, T. & Powell, R. (1998). An internally consistent thermodynamic data set for phases of petrological interest. Journal of Metamorphic Geology 16, 309-43.

Holland, T. & Powell, R. (2003). Activity–composition relations for phases in petrological calculations: an asymmetric multicomponent formulation. Contributions to Mineralogy and Petrology 145, 492-501.

Jackson, S.E., Pearson, N.J., Griffin, W.L. & Belousova, E.A. (2004). The application of laser ablation-inductively coupled plasma-mass spectrometry to in situ U–Pb zircon geochronology. Chemical Geology 211, 47-69.

Janoušek, V., Farrow, C.M. & Erban, V. (2006). Interpretation of whole-rock geochemical data in igneous geochemistry: introducing Geochemical Data Toolkit (GCDkit). Journal of Petrology 47, 1255-1259.

Jochum, K.P., Weis, U., Stoll, B., Kuzmin, D., Yang, Q., Raczek, I., Jacob, D.E., Stracke, A., Birbaum, K., Frick, D.A. & Günther, D. (2011). Determination of reference values for NIST SRM 610–617 glasses following ISO guidelines. Geostandards and Geoanalytical Research 35, 397-429.

Kohn, M.J. (2009). Models of garnet differential geochronology. Geochimica et Cosmochimica Acta 73, 170-82.

Kohn, M.J., Corrie S.L. & Markley, C. (2015). The fall and rise of metamorphic zircon. American Mineralogist 100, 897-908.

Kohn, M.J. (2016). Metamorphic chronology—a tool for all ages: Past achievements and future prospects. American Mineralogist 101, 25-42.

Kooijman, E., Mezger, K. & Berndt, J. (2010). Constraints on the U–Pb systematics of

metamorphic rutile from in situ LA-ICP-MS analysis. Earth and Planetary Science Letters 293, 321-330.

Kylander-Clark, A.R., Hacker, B.R., Johnson, C.M., Beard, B.L., Mahlen, N.J. & Lapen, T.J. (2007). Coupled Lu–Hf and Sm–Nd geochronology constrains prograde and exhumation histories of high-and ultrahigh-pressure eclogites from western Norway. Chemical Geology 242, 137-54.

Kylander-Clark, A.R.C., Hacker, B.R. & Mattinson, J.M. (2008). Slow exhumation of UHP terranes: titanite and rutile ages of the Western Gneiss Region, Norway. Earth and Planetary Science Letters 272, 531-540.

Lardeaux, J.M. (2014). Deciphering orogeny: a metamorphic perspective Examples from European Alpine and Variscan belts Part II: Variscan metamorphism in the French Massif Central—a review. Bulletin de la Société Géolgique de France 185, 281-310.

Lardeaux, J.M., Schulmann, K., Faure, M., Janoušek, V., Lexa, O., Skrzypek, E., Edel, J.B. & Štípská, P. (2014). The moldanubian zone in the French Massif Central, Vosges/Schwarzwald and Bohemian Massif revisited: differences and similarities. Geological Society, London, Special Publications 405, 7-44.

Leake, B.E., Woolley, A.R., Arps, C.E., Birch, W.D., Gilbert, M.C., Grice, J.D., Hawthorne, F.C., Kato, A., Kisch, H.J., Krivovichev, V.G. & Linthout, K. (1997). Report Nomenclature of Amphiboles: Report of the Subcommittee on Amphiboles of the International Mineralogical Association Commission on New Minerals and Mineral Names. Mineralogical Magazine 61, 295-321.

Ledru, P., Lardeaux, J.M., Santallier, D., Autran, A., Quenardel, J.M., Floc'h, J.P., Lerouge, G., Maillet, N., Marchand, J. & Ploquin, A. (1989). Où sont les nappes dans le Massif Central Français? Bulletin de la Société Géolgique de France 3, 605–618.

Li, Q.L., Lin, W., Su, W., Li, X.H., Shi, Y.H., Liu, Y. & Tang, G.Q. (2011). SIMS U–Pb rutile age of low-temperature eclogites from southwestern Chinese Tianshan, NW China. Lithos 122, 76-86.

Lotout, C., Pitra, P., Poujol, M. & Van Den Driessche, J. (2017). Ordovician magmatism in the Lévézou massif (French Massif Central): tectonic and geodynamic implications. International Journal of Earth Sciences 106, 501-515.

Ludwig, K.R. (2012). User's Manual for a geochronological toolkit for Microsoft Excel. Berkeley Geochronological Center 75.

Luvizotto, G.L., Zack, T., Meyer, H.P., Ludwig, T., Triebold, S., Kronz, A., Münker, C., Stockli, D.F., Prowatke, S., Klemme, S., Jacob, D.E. & von Eynatten, H. (2009). Rutile crystals as potential trace element and isotope mineral standards for microanalysis. Chemical Geology 261, 346–369.

McDowell, F.W., McIntosh, W.C. & Farley, K.A. (2005). A precise 40Ar–39Ar reference age for the Durango apatite (U–Th)/He and fission-track dating standard. Chemical Geology 214, 249-263.

Matte, P. (1986). Tectonics and plate tectonics model for the Variscan belt of Europe. Tectonophysics 126, 329-374.

Mezger, K., Hanson, G.N. & Bohlen S.R. (1989). High-precision U–Pb ages of metamorphic rutile: application to the cooling history of high-grade terranes. Earth and Planetary Science Letters 96, 106–118.

Mezger, K., Rawnsley, C.M., Bohlen, S.R. & Hanson, G.N. (1991). U-Pb garnet, sphene, monazite, and rutile ages: implications for the duration of high-grade metamorphism and cooling histories, Adirondack Mts., New York. The Journal of Geology 99, 15-428.

Nicollet, C. (1978). Pétrologie et tectonique des terrains cristallins antépermiens du versant sud du dôme du Lévezou (Rouergue, Massif central). Bull BRGM 3, 225–263.

Nicollet, C. & Leyreloup, A. (1978). Pétrologie des niveaux trondhjemitiques de haute pression et de leur encaissant éclogitique et amphibolitique (Levezou et Marvejols, Massif Central Francais). Conséquences sur la génèse des groupes leptyno-amphibolitiques. Can. Journal of Earth Sciences 15, 696-707.

Paquette, J.L., (1987). "Comportement des systèmes isotopiques U-Pb et Sm-Nd dans le métamorphisme éclogitique. Chaîne Hercynienne et chaîne Alpine." Doctoral dissertation, Université Rennes 1.

Paquette, J.L., Monchoux, P. & Couturier, M. (1995). Geochemical and isotopic study of a norite-eclogite transition in the European Variscan Belt: Implications for U-Pb zircon systematics in metabasic rocks. Geochim. Cosmochim. acta 59, 1611-1622.

Paton, C., Woodhead, J.D., Hellstrom, J.C., Hergt, J.M., Greig, A. & Maas, R. (2010). Improved laser ablation U-Pb zircon geochronology through robust downhole fractionation correction. Geochemistry, Geophysics, Geosystems, 11, Q0AA06, doi:10.1029/2009GC002618.

Piboule, M. (1979). L'origine des amphibolites: approche géochimique et mathématique. Application aux amphibolites du Massif central français. Thèse d'Etat, Lyon I University

Piboule, M. & Briand, B., (1985). Geochemistry of eclogites and associated rocks of the southeastern area of the French Massif Central: origin of the protoliths. Chemical geology 50, 189-99.

Pin, C. (1979). Géochronologie U–Pb et microtectonique des séries métamorphiques anté-stéphaniennes de l'Aubrac et de la région de Marvejols (Massif central). PhD Thesis, Montpellier University

Pin, C. & Piboule, M. (1988). Upper Devonian U–Pb zircon age of the calc-alkaline series in the Levezou mafic belt, Rouergue (Massif Central, France). A composite leptyno-amphibolitic association. Bull Soc Géol Fr 4, 261–265

Pin, C. & Lancelot, J. (1982). U–Pb dating of an early Paleozoïc bimodal magmatism in the French Massif Central and its further metamorphic evolution. Contribution to Mineralogy and Petrology 79, 1-12.

Pitra, P., Boulvais, P., Antonoff, V. & Diot, H. (2008). Wagnerite in a cordierite-gedrite gneiss: Witness of long-term fluid-rock interaction in the continental crust (Ile d'Yeu, Armorican Massif, France). American Mineralogist 93, 315-26.

Pochon, A., Poujol, M., Gloaguen, E., Branquet, Y., Cagnard, F., Gumiaux, C. & Gapais, D. (2016). U-Pb LA-ICP-MS dating of apatite in mafic rocks: Evidence for a major magmatic event at the Devonian-Carboniferous boundary in the Armorican Massif (France). American Mineralogist 101, 2430-2442.

Rubatto, D. (2002). Zircon trace element geochemistry: partitioning with garnet and the link between U–Pb ages and metamorphism. Chemical geology 184, 123-38.

Rubatto, D. (2017). Zircon: the metamorphic mineral. Reviews in mineralogy and geochemistry 83, 261-95.

Rubatto, D. & Hermann, J. (2003). Zircon formation during fluid circulation in eclogites (Monviso, Western Alps): implications for Zr and Hf budget in subduction zones. Geochimica et Cosmochimica Acta 67, 2173-2187.

Santallier, D.A., Briand, B.E., Menot, R.P. & Piboule, M. (1988). Les complexes leptyno-amphiboliques (CLA): revue critique et suggestions pour un meilleur emploi de ce terme. Bulletin de la Société Géologique de France 1, 3-12.

Scherer, E., Münker, C. & Mezger, K. (2001). Calibration of the lutetium-hafnium clock. Science 293, 683-687.

Schoene, B. & Bowring, S.A. (2006). U–Pb systematics of the McClure Mountain syenite: Thermochronological constraints on the age of the 40Ar/39Ar standard MMhb. Contributions to Mineralogy and Petrology 151, 615–630.

Sláma, J., Košler, J., Condon, D.J., Crowley, J.L., Gerdes, A., Hanchar, J.M., Horstwood, M.S., Morris, G.A., Nasdala, L., Norberg, N. & Schaltegger, U. (2008). Plešovice zircon—a new natural reference material for U–Pb and Hf isotopic microanalysis. Chemical Geology 249, 1-35.

Smit, M.A., Scherer, E.E. & Mezger, K. (2013). Lu–Hf and Sm–Nd garnet geochronology: Chronometric closure and implications for dating petrological processes. Earth and Planetary Science Letters 381, 222-33.

Stacey, J.T. & Kramers, J.D. (1975). Approximation of terrestrial lead isotope evolution by a two-stage model. Earth and planetary science letters 26, 207-21.

Thirlwall, M.F. & Anczkiewicz, R. (2004). Multidynamic isotope ratio analysis using MC–ICP–MS and the causes of secular drift in Hf, Nd and Pb isotope ratios. International Journal of Mass Spectrometry 235, 59-81.

Van Achterbergh, E., Ryan, C.G., Jackson, S.E. & Griffin, W.L. (2001). Data reduction software for LA-ICP-MS: appendix. In: Laser Ablation-ICP-Mass Spectrometry in the Earth Sciences: Principles and Applications. In Mineralog Assoc Canada (MAC) Short Courses Series (Sylvester, P.J., eds), Ottawa, Ontario, Canada 29, 239-243.

Villaseca, C., Castiñeiras, P. & Orejana, D., (2015). Early Ordovician metabasites from the Spanish Central System: A remnant of intraplate HP rocks in the Central Iberian Zone. Gondwana Research 27, 392-409.

Warren, C.J., Grujic, D., Cottle, J.M. & Rogers, N.W. (2012). Constraining cooling histories: rutile and titanite chronology and diffusion modelling in NW Bhutan. Journal of Metamorphic Geology 30, 113-30.

White, R.W., Powell, R., Holland, T.J. & Worley, B.A. (2000). The effect of TiO~ 2 and Fe~ 2O~ 3 on metapelitic assemblages at greenschist and amphibolite facies conditions: mineral equilibria calculations in the system The effect of TiO2 and Fe2O3 on metapelitic assemblages at greenschist and amphibolite facies conditions: mineral equilibria calculations in the system K2O–FeO–MgO–Al2O3–SiO2–H2O–TiO2–Fe2O3. Journal of Metamorphic Geology 18, 497-512.

White R.W., Powell R. & Holland T.J. (2007). Progress relating to calculation of partial melting equilibria for metapelites. Journal of Metamorphic Geology 25, 511-27.

Whitehouse, M.J. Platt, J.P. (2003). Dating high-grade metamorphism—constraints from rare-earth elements in zircon and garnet. Contributions to Mineralogy and Petrology 145, 61-74.

Woodhead, J.D., Hellstrom, J., Hergt, J.M., Greig, A. & Maas, R., (2007). Isotopic and elemental imaging of geological materials by laser ablation inductively coupled plasma-mass spectrometry. Geostandards and Geoanalytical Research 31, 331-343.

Zack, T., Moraes, R. & Kronz, A. (2004). Temperature dependence of Zr in rutile: empirical calibration of a rutile thermometer. Contributions to Mineralogy and Petrology 148, 471-88..

Supplementary Table II.3.1: Operating conditions for the LA-ICP-MS equipment

Laboratory & Sample Preparation	
Laboratory name	Géosciences Rennes, UMR CNRS 6118, Rennes, France
Sample type/mineral	Zircon (Zrn), Apatite (Ap), Rutile (Ru)
Sample preparation	Conventional mineral separation, 1 inch resin mount, 1µm polish to finish
Imaging	CL: RELION CL instrument, Olympus Microscope BX51WI, Leica Color Camera DFC 420C
Laser ablation system	
Make, Model & type	ESI NWR193UC, Excimer
Ablation cell	ESI NWR TwoVol2
Laser wavelength	193 nm
Pulse width	< 5 ns
Fluence	8.5 J/cm-2
Repetition rate	3 Hz (Zrn) and 5Hz (Ap, Ru)
Spot size	25 & 35 µm (Zrn) , 45 µm (Ap), 60µm(Ru)
Sampling mode / pattern	Single spot
Carrier gas	100% He, Ar make-up gas and N2 (3 ml/mn) combined using in-house smoothing device
Background collection	20 seconds
Ablation duration	60 seconds
Wash-out delay	15 seconds
Cell carrier gas flow (He)	0.75 l/min
ICP-MS Instrument	
Make, Model & type	Agilent 7700x, Q-ICP-MS
Sample introduction	Via conventional tubing
RF power	1350W
Sampler, skimmer cones	Ni
Extraction lenses	X type
Make-up gas flow (Ar)	0.85 l/min
Detection system	Single collector secondary electron multiplier
Data acquisition protocol	Time-resolved analysis
Scanning mode	Peak hopping, one point per peak
Detector mode	Pulse counting, dead time correction applied, and analog mode when signal intensity > ~ 10^6 cps
Masses measured	^{204}(Hg + Pb), ^{206}Pb, ^{207}Pb, ^{208}Pb, ^{232}Th, ^{238}U + ^{43}Ca (Ap)
Integration time per peak	10-30 ms
Sensitivity / Efficiency	28000 cps/ppm Pb (50µm, 10Hz)
Data Processing	
Gas blank	20 seconds on-peak
Calibration strategy	GJ1 zircon, R10 rutile and Madagascar apatite standards used as primary reference material, Plešovice (Zrn) , R19 (Ru) and McClure and Durango (Ap) used as secondary reference material (quality control)
Common-Pb correction, composition and uncertainty	No common-Pb correction. Analyses discarded of the age calculation when discordance >20%
Reference Material info	GJ1 (Jackson et al., 2004) Madagascar (Cochrane et al. 2014) R10b (Zack et al. 2011) Plešovice (Slama et al., 2008) R19 (Zack et al. 2011) McClure (Schoene and Bowring 2006) Durango (McDowell et al. 2005)
Data processing package used	Zrn : GLITTER ® (van Achterbergh et al., 2001) Ru, Ap : Iolite (Paton et al., 2010), VizualAge_UcomPbine (Chew et al., 2014)
Quality control / Validation	Plešovice: 337.8 ± 4.7 Ma (N=6; MSWD=0.013; probability=1.00) R19 : 491.8 ± 3.4 Ma (N = 8, MSWD = 0.38 McClure: 529 ± 16 Ma (N=4, MSWD=7) Durango: 33.3 ± 2.6 Ma (N=5, MSWD=2.7)

Supplementary Table II.3.1: Operating conditions for the LA-ICP-MS equipment

											zircons from sampleLV20B		
	content (ppm)				isotopic ratio								
num zr	Pb	U	Th	Th/U	238/206	err%	207/206	err%	Pb207/U235		Pb206/U238		rho
Ordovician dates													
1	10.3	131.1	53.7	0.41	13.17	1.29	0.0574	1.31	0.601	0.0091	0.07591	0.0010	0.85
2	13.1	161.9	89.3	0.55	13.35	1.29	0.057	1.30	0.589	0.00884	0.07492	0.0010	0.86
3	43.0	497.6	399.9	0.80	13.12	1.29	0.0564	1.17	0.593	0.00829	0.07622	0.0010	0.92
4	46.0	544.6	363.2	0.67	13.09	1.28	0.0573	1.15	0.603	0.00833	0.07642	0.0010	0.93
6	12.6	154.6	82.4	0.53	13.07	1.29	0.0562	1.35	0.593	0.00918	0.0765	0.0010	0.84
8	48.5	569.2	419.8	0.74	13.17	1.28	0.0569	1.18	0.596	0.00833	0.07591	0.0010	0.91
10	19.8	232.5	180.6	0.78	13.19	1.28	0.0574	1.24	0.6	0.0087	0.07582	0.0010	0.88
13	30.1	352.7	256.7	0.73	13.09	1.28	0.0552	1.25	0.581	0.00849	0.07637	0.0010	0.88
15	25.1	311.6	170.9	0.55	13.28	1.28	0.0568	1.25	0.589	0.00856	0.07528	0.0010	0.88
19	15.5	189.9	114.0	0.60	13.32	1.29	0.0567	1.43	0.587	0.00935	0.0751	0.0010	0.81
20	35.4	427.2	250.8	0.59	13.08	1.28	0.0569	1.30	0.6	0.00894	0.07645	0.0010	0.86
21	49.2	557.3	500.2	0.90	13.25	1.27	0.0564	1.26	0.587	0.00854	0.07549	0.0010	0.87
23	8.1	101.2	47.3	0.47	13.20	1.28	0.0587	1.47	0.613	0.01	0.07578	0.0010	0.78
24	48.2	549.3	448.3	0.82	13.09	1.26	0.0574	1.17	0.604	0.00833	0.07639	0.0010	0.91
26	20.8	237.9	186.9	0.79	13.04	1.26	0.0569	1.25	0.602	0.00867	0.0767	0.0010	0.88
28	16.2	204.3	91.4	0.45	13.14	1.27	0.0562	1.32	0.59	0.00889	0.07613	0.0010	0.85
29	4.9	64.7	21.4	0.33	13.31	1.29	0.0562	1.64	0.581	0.01033	0.07511	0.0010	0.73
30	74.3	799.6	807.2	1.01	12.87	1.26	0.0571	1.12	0.611	0.00822	0.07771	0.0010	0.94
31	23.0	275.5	179.6	0.65	13.13	1.27	0.0571	1.28	0.6	0.00881	0.07617	0.0010	0.87
33	16.2	198.0	105.2	0.53	13.04	1.28	0.0578	1.28	0.611	0.00899	0.0767	0.0010	0.87
34	20.1	235.1	164.5	0.70	13.02	1.28	0.0572	1.29	0.605	0.00903	0.0768	0.0010	0.86
35	40.6	460.4	388.6	0.84	13.04	1.27	0.0573	1.22	0.606	0.00863	0.07667	0.0010	0.89
36	26.2	328.0	143.1	0.44	12.95	1.27	0.057	1.23	0.606	0.00874	0.0772	0.0010	0.88
38	44.2	491.1	430.7	0.88	12.88	1.27	0.0573	1.20	0.614	0.00867	0.07766	0.0010	0.90
42	26.5	309.1	246.8	0.80	13.23	1.28	0.0572	1.26	0.596	0.00872	0.07557	0.0010	0.88
43	29.0	338.6	212.6	0.63	12.81	1.22	0.0564	1.08	0.607	0.00772	0.07808	0.0010	0.96
46	5.0	63.7	21.2	0.33	13.01	1.24	0.0578	1.31	0.613	0.0089	0.07686	0.0010	0.85
48	16.1	194.8	120.1	0.62	13.12	1.26	0.0555	1.75	0.583	0.0107	0.07624	0.0010	0.69
57	27.0	320.7	224.7	0.70	13.19	1.23	0.0546	1.12	0.57	0.00737	0.07579	0.0009	0.95
58	27.7	325.5	233.9	0.72	13.49	1.23	0.0543	1.12	0.555	0.00718	0.07414	0.0009	0.95
59	53.3	616.0	545.1	0.88	13.20	1.24	0.0568	1.36	0.593	0.00885	0.07575	0.0009	0.83
60	6.9	86.9	39.5	0.45	13.44	1.26	0.0563	1.56	0.577	0.0096	0.07439	0.0009	0.76
49	*5.2*	*66.8*	*23.3*	*0.35*	*13.15*	*1.22*	*0.0581*	*1.12*	*0.609*	*0.00788*	*0.07602*	*0.0009*	*0.95*
50	*21.3*	*257.7*	*150.4*	*0.58*	*13.22*	*1.23*	*0.0588*	*1.16*	*0.613*	*0.00815*	*0.07565*	*0.0009*	*0.92*
52	*16.2*	*196.8*	*112.6*	*0.57*	*13.07*	*1.23*	*0.0545*	*1.18*	*0.575*	*0.00771*	*0.07654*	*0.0009*	*0.92*
47	*10.2*	*125.3*	*62.2*	*0.50*	*13.17*	*1.22*	*0.0545*	*1.19*	*0.57*	*0.0077*	*0.07592*	*0.0009*	*0.91*
64	*44.4*	*523.5*	*411.0*	*0.79*	*13.21*	*1.24*	*0.0542*	*1.25*	*0.566*	*0.00792*	*0.07571*	*0.0009*	*0.89*
55	*15.0*	*193.1*	*71.5*	*0.37*	*13.08*	*1.23*	*0.0516*	*1.14*	*0.543*	*0.00715*	*0.07644*	*0.0009*	*0.93*
66	*11.5*	*148.1*	*62.7*	*0.42*	*13.10*	*1.24*	*0.0539*	*1.22*	*0.567*	*0.00782*	*0.07632*	*0.0010*	*0.90*
62	*7.6*	*100.0*	*37.3*	*0.37*	*13.40*	*1.23*	*0.0533*	*1.09*	*0.548*	*0.00696*	*0.07462*	*0.0009*	*0.97*
16	*16.1*	*193.3*	*131.1*	*0.68*	*13.34*	*1.28*	*0.0579*	*1.35*	*0.598*	*0.00919*	*0.07496*	*0.0010*	*0.83*
41	*18.8*	*226.3*	*139.6*	*0.62*	*13.27*	*1.29*	*0.0601*	*1.33*	*0.625*	*0.0095*	*0.07538*	*0.0010*	*0.85*
7	*15.3*	*183.0*	*114.8*	*0.63*	*13.28*	*1.30*	*0.0643*	*1.40*	*0.667*	*0.01056*	*0.07529*	*0.0010*	*0.82*
45	11.8	148.5	73.1	0.49	*13.18*	*1.24*	*0.0643*	*1.43*	*0.672*	*0.01046*	*0.0759*	*0.0009*	*0.80*
40	*6.6*	*90.1*	*36.8*	*0.41*	*13.91*	*1.29*	*0.0567*	*1.50*	*0.562*	*0.00939*	*0.07188*	*0.0009*	*0.77*
56	*7.6*	*101.0*	*43.0*	*0.43*	*13.78*	*1.27*	*0.0583*	*1.61*	*0.583*	*0.01*	*0.07259*	*0.0009*	*0.74*
51	*5.6*	*74.3*	*24.7*	*0.33*	*13.84*	*1.25*	*0.0663*	*1.34*	*0.66*	*0.00978*	*0.07223*	*0.0009*	*0.84*

zircons from sampleLV20B							
	Ages (Ma)						
num zr	Pb207/Pb206		Pb206/U238		Pb207/U235		conc
Ordovician dates							
1	506.2	28.5	471.7	5.9	477.6	5.8	98.8
2	490.2	28.7	465.7	5.8	470.0	5.7	99.1
3	467.7	25.9	473.5	5.9	472.6	5.3	100.2
4	501.0	25.3	474.7	5.9	479.3	5.3	99.0
6	458.9	29.9	475.2	5.9	472.5	5.9	100.6
8	487.3	26.1	471.7	5.8	474.4	5.3	99.4
10	507.9	26.9	471.1	5.8	477.5	5.5	98.7
13	418.5	27.6	474.4	5.9	465.0	5.5	102.0
15	482.9	27.7	467.9	5.8	470.5	5.5	99.4
19	477.7	31.4	466.8	5.8	468.7	6.0	99.6
20	488.5	28.7	474.9	5.9	477.3	5.7	99.5
21	467.1	27.8	469.2	5.8	468.9	5.5	100.1
23	554.7	31.8	470.9	5.8	485.4	6.3	97.0
24	506.0	25.4	474.5	5.8	480.0	5.3	98.9
26	487.7	27.5	476.4	5.8	478.4	5.5	99.6
28	458.9	29.2	473.0	5.8	470.7	5.7	100.5
29	457.9	35.6	466.9	5.8	465.4	6.6	100.3
30	493.8	24.8	482.4	5.9	484.5	5.2	99.6
31	495.0	28.1	473.2	5.8	477.0	5.6	99.2
33	520.4	28.0	476.4	5.8	484.0	5.7	98.4
34	497.4	28.6	477.0	5.9	480.6	5.7	99.3
35	503.2	26.6	476.2	5.8	480.9	5.5	99.0
36	489.0	27.4	479.4	5.9	481.1	5.5	99.6
38	503.2	26.2	482.1	5.9	485.9	5.5	99.2
42	499.1	27.7	469.6	5.8	474.7	5.6	98.9
43	466.1	24.1	484.6	5.7	481.4	4.9	100.7
46	523.1	28.6	477.4	5.7	485.2	5.6	98.4
48	431.8	37.9	473.6	5.8	466.5	6.9	101.5
57	394.9	24.8	470.9	5.6	458.1	4.8	102.8
58	384.5	25.1	461.1	5.5	448.4	4.7	102.8
59	483.6	30.1	470.7	5.7	472.9	5.6	99.5
60	463.2	34.3	462.5	5.6	462.6	6.2	100.0
49	*534.0*	*24.8*	*472.3*	*5.6*	*483.0*	*5.0*	*97.8*
50	*558.1*	*25.2*	*470.1*	*5.6*	*485.2*	*5.1*	*96.9*
52	*390.0*	*26.2*	*475.4*	*5.6*	*460.9*	*5.0*	*103.1*
47	*391.0*	*26.3*	*471.7*	*5.6*	*458.1*	*5.0*	*103.0*
64	*380.5*	*28.1*	*470.4*	*5.6*	*455.3*	*5.1*	*103.3*
55	*266.4*	*26.1*	*474.8*	*5.6*	*440.6*	*4.7*	*107.8*
66	*365.8*	*27.6*	*474.1*	*5.7*	*455.8*	*5.1*	*104.0*
62	*342.1*	*24.5*	*463.9*	*5.5*	*443.8*	*4.6*	*104.5*
16	*524.1*	*29.6*	*466.0*	*5.8*	*475.9*	*5.8*	*97.9*
41	*606.9*	*28.5*	*468.5*	*5.8*	*492.7*	*5.9*	*95.1*
7	*751.2*	*29.3*	*467.9*	*5.9*	*519.1*	*6.4*	*90.1*
45	*749.7*	*29.9*	*471.6*	*5.7*	*522.0*	*6.4*	*90.3*
40	*480.9*	*33.3*	*447.5*	*5.6*	*453.0*	*6.1*	*98.8*
56	*539.7*	*35.5*	*451.7*	*5.5*	*466.4*	*6.4*	*96.8*
51	*814.2*	*27.9*	*449.6*	*5.4*	*514.3*	*6.0*	*87.4*

zircons from sampleLV20B																			
	content (ppm)				isotopic ratio									Ages (Ma)					
num zr	Pb	U	Th	Th/U	238/206	err%	207/206	err%	Pb207/U 235		Pb206/U 238		rho	Pb207/ Pb206		Pb206/U 238		Pb207 /U235		conc
Devonian Dates																			
17	14.2	220.0	111.1	0.50	16.37	1.28	0.0548	1.35	0.462	0.0071	0.06109	0.0008	0.83	404.0	29.7	382.2	4.8	385.3	4.9	99.2
18	8.6	137.2	48.2	0.35	16.19	1.31	0.0565	1.79	0.481	0.0092	0.06175	0.0008	0.69	469.2	39.5	386.3	4.9	398.5	6.3	96.9
53	12.4	189.9	112.9	0.59	16.58	1.24	0.0554	1.28	0.461	0.00659	0.06031	0.0008	0.87	428.5	28.3	377.5	4.5	384.7	4.6	98.1
61	6.0	97.0	36.1	0.37	16.41	1.26	0.0538	1.64	0.452	0.00787	0.06092	0.0008	0.73	362.2	36.8	381.2	4.7	378.4	5.5	100.7
39	*10.3*	*158.5*	*86.0*	*0.54*	*16.41*	*1.28*	*0.0587*	*1.41*	*0.493*	*0.00787*	*0.06094*	*0.0008*	0.80	*555.9*	*30.7*	*381.4*	*4.8*	*407.1*	*5.4*	*93.7*
63	*4.5*	*66.0*	*25.8*	*0.39*	*15.57*	*1.26*	*0.0628*	*1.45*	*0.556*	*0.00873*	*0.06421*	*0.0008*	0.80	*702.4*	*30.6*	*401.2*	*4.9*	*448.9*	*5.7*	*89.4*
Cambrian Dates																			
5	18.9	201.9	143.2	0.71	11.96	1.28	0.0574	1.22	0.662	0.00946	0.08358	0.0011	0.90	507.7	26.3	517.5	6.4	515.7	5.8	100.3
9	47.4	503.8	382.7	0.76	12.05	1.28	0.0571	1.14	0.653	0.00896	0.08296	0.0011	0.93	496.0	25.3	513.8	6.3	510.6	5.5	100.6
11	23.2	259.4	154.1	0.59	12.13	1.29	0.0558	1.22	0.635	0.00906	0.08246	0.0011	0.90	445.1	26.3	510.8	6.3	499.0	5.6	102.4
12	28.7	319.0	181.5	0.57	11.96	1.28	0.0556	1.19	0.641	0.00904	0.08358	0.0011	0.91	437.0	25.9	517.5	6.4	502.9	5.6	102.9
27	5.7	69.0	23.6	0.34	12.25	1.30	0.0585	1.66	0.658	0.01185	0.08166	0.0011	0.72	547.9	35.9	506.0	6.3	513.7	7.3	98.5
14	55.4	569.5	513.1	0.90	12.04	1.28	0.0568	1.16	0.65	0.00904	0.08308	0.0011	0.92	482.8	25.9	514.5	6.3	508.8	5.6	101.1
22	17.5	200.0	102.4	0.51	12.20	1.26	0.0577	1.25	0.651	0.00939	0.08194	0.0010	0.87	516.9	27.3	507.7	6.2	509.4	5.8	99.7
25	23.1	249.1	180.7	0.73	12.13	1.26	0.0576	1.20	0.654	0.00919	0.08244	0.0010	0.90	512.5	25.8	510.6	6.2	511.0	5.6	99.9
32	30.6	338.6	199.3	0.59	12.03	1.26	0.0571	1.17	0.654	0.00907	0.08313	0.0011	0.91	493.9	26.0	514.8	6.3	511.0	5.6	100.7
37	42.1	449.9	360.9	0.80	12.19	1.27	0.0583	1.20	0.659	0.00932	0.08202	0.0010	0.90	538.8	26.7	508.1	6.2	513.8	5.7	98.9
54	2.8	28.3	10.0	0.35	10.72	1.28	0.0582	1.81	0.748	0.01417	0.0933	0.0012	0.67	535.5	39.7	575.0	7.0	567.1	8.2	101.4

apatites from sample LV20B						
	Content (ppm)		Isotopic Ratios			
Label	Pb	U	Pb^{206}/U^{238}	2σ	Pb^{207}/Pb^{206}	2σ
ap-01	1.7	2.2	4.523	0.29	0.697	0.02
ap-02	1.4	3.4	6.693	0.42	0.595	0.01
ap-03	1.1	9.9	12.500	0.77	0.299	0.01
ap-04	1.3	2.7	5.967	0.39	0.631	0.02
ap-05	1.4	10.4	11.779	0.72	0.321	0.01
ap-06	1.1	4.8	9.355	0.59	0.453	0.01
ap-07	1.9	5.6	8.065	0.49	0.510	0.01
ap-08	1.4	2.4	5.583	0.34	0.629	0.01
ap-09	0.8	6.3	12.151	0.80	0.323	0.01
ap-10	1.3	2.2	5.482	0.36	0.625	0.03
ap-11	4.2	5.0	4.225	0.27	0.693	0.01
ap-12	1.1	9.2	12.107	0.75	0.320	0.01
ap-13	2.7	14.6	10.040	0.61	0.413	0.01
ap-14	2.9	10.1	8.123	0.51	0.521	0.01
ap-15	2.1	2.0	3.216	0.21	0.744	0.02
ap-16	1.8	12.3	11.390	0.71	0.358	0.01
ap-17	1.8	7.8	9.416	0.58	0.461	0.01
ap-18	1.3	5.5	9.200	0.58	0.456	0.01
ap-19	1.2	8.7	11.534	0.72	0.354	0.01
ap-20	1.2	5.8	10.111	0.62	0.421	0.01
ap-21	1.7	2.1	4.198	0.26	0.692	0.02
ap-22	1.3	5.0	8.532	0.54	0.482	0.01
ap-23	1.5	7.2	9.980	0.62	0.424	0.01

rutiles from sample LV21				
	Isotopic Ratios			
Analysis_#	238/206	err%	207/206	err%
RutLV21_1	16.31	0.88	0.083	0.011
RutLV21_2	18.21	4.64	0.122	0.032
RutLV21_3	13.46	13.95	0.296	0.022
RutLV21_4	16.78	0.93	0.118	0.013
RutLV21_5	16.37	0.91	0.125	0.015
RutLV21_6	17.21	0.92	0.105	0.014
RutLV21_7	15.29	7.72	0.093	0.029
RutLV21_8	13.35	4.10	0.258	0.023
RutLV21_9	15.77	0.70	0.136	0.009
RutLV21_10	13.93	0.74	0.232	0.023
RutLV21_11	15.87	0.81	0.119	0.011
RutLV21_12	14.04	0.91	0.140	0.019
RutLV21_13	16.13	0.73	0.085	0.007
RutLV21_14	16.78	1.27	0.056	0.016
RutLV21_15	16.47	0.81	0.070	0.013
RutLV21_16	16.13	0.81	0.098	0.013
RutLV21_17	15.85	27.63	0.136	0.026

rutiles from sample LV20B				
	Isotopic Ratios			
Analysis_#	238/206	err%	207/206	err%
RutLV20B_1	16.50	0.82	0.077	0.007
RutLV20B_2	16.75	0.76	0.086	0.006
RutLV20B_3	16.84	0.79	0.090	0.009
RutLV20B_4	17.36	0.84	0.076	0.007
RutLV20B_5	17.24	1.40	0.108	0.042
RutLV20B_6	14.20	0.83	0.212	0.016
RutLV20B_7	16.86	0.91	0.128	0.012
RutLV20B_8	16.50	0.87	0.124	0.012
RutLV20B_9	16.23	0.92	0.112	0.011
RutLV20B_10	16.08	1.29	0.174	0.036
RutLV20B_11	18.32	0.84	0.069	0.005
RutLV20B_12	16.39	0.81	0.090	0.008
RutLV20B_13	16.75	1.15	0.095	0.100
RutLV20B_14	18.52	1.06	0.089	0.015
RutLV20B_15	17.86	0.86	0.073	0.006
RutLV20B_16	15.90	0.83	0.157	0.013
RutLV20B_17	14.14	0.78	0.195	0.029
RutLV20B_18	13.95	0.54	0.293	0.007

Supplementary Table II.3.3: Representative microprobe analyses of principal metamorphic minerals. The amount of ferric iron was calculated from stoichiometric constraints.

amphibole

	LV20B								LV21			
	LV20B zone B-8 secondary	LV20B zone A-9 secondary	LV20B zone A-11 symplectite	LV20B zone A-12 symplectite	LV20B zone A-18 primary	LV20B zone B-13 primary	LV20B zone B-14 primary	LV20B zone A-8 primary	67.00	77.00	81.00	82.00
SiO2	43.78	44.19	43.95	43.28	45.56	46.08	45.74	45.15	48.24	46.89	46.45	46.55
TiO2	1.87	1.77	1.52	1.81	0.98	0.34	0.41	0.84	0.50	0.56	0.44	0.52
Al2O3	12.68	12.37	12.18	12.10	10.97	11.08	11.14	11.39	12.28	12.32	13.05	13.09
MgO	12.95	13.08	12.83	12.46	14.28	14.93	13.98	13.94	18.23	17.97	17.79	17.84
FeO	11.34	10.98	11.54	11.67	10.66	10.47	11.22	11.05	4.78	5.07	4.82	4.80
MnO	0.06	0.09	0.04	0.10	0.07	0.00	0.07	0.02	0.03	0.05	0.04	0.04
CaO	11.93	12.00	12.04	12.00	11.65	11.58	11.84	11.88	10.56	11.51	11.61	11.81
Na2O	1.33	1.58	1.47	1.46	1.40	1.42	1.21	1.44	2.40	2.35	2.32	2.28
K2O	1.14	1.03	1.02	1.04	0.76	0.74	0.83	0.85	0.63	0.50	0.56	0.60
H2O	2.04	2.04	2.03	2.01	2.04	2.05	2.04	2.04	2.14	2.12	2.11	2.12
Sum	99.11	99.13	98.61	97.93	98.37	98.69	98.48	98.60	99.79	99.34	99.18	99.65
Si	6.42	6.48	6.49	6.45	6.66	6.67	6.68	6.61	6.72	6.60	6.55	6.54
Ti	0.21	0.20	0.17	0.20	0.11	0.04	0.05	0.09	0.05	0.06	0.05	0.06
Al	2.19	2.14	2.12	2.13	1.89	1.89	1.92	1.96	2.02	2.04	2.17	2.17
Fe3	0.15	0.07	0.10	0.07	0.26	0.37	0.29	0.22	0.00	0.00	0.00	0.00
Mg	2.83	2.86	2.82	2.77	3.11	3.22	3.04	3.04	0.28	0.28	0.26	0.23
Fe2	1.25	1.27	1.33	1.39	1.05	0.90	1.08	1.14	3.79	3.77	3.74	3.74
Mn	0.01	0.01	0.01	0.01	0.01	0.00	0.01	0.00	0.28	0.32	0.31	0.33
Ca	1.87	1.88	1.90	1.92	1.82	1.80	1.85	1.86	0.00	0.01	0.01	0.01
Na	0.38	0.45	0.42	0.42	0.40	0.40	0.34	0.41	1.58	1.74	1.75	1.78
K	0.21	0.19	0.19	0.20	0.14	0.14	0.16	0.16	0.65	0.64	0.63	0.62
Sum	15.50	15.55	15.54	15.56	15.43	15.43	15.42	15.49	0.11	0.09	0.10	0.11
XMg	0.69	0.69	0.68	0.67	0.75	0.78	0.74	0.73	15.46	15.54	15.56	15.57

	Garnet							
	LV20B				LV21			
	104.00	105.00	106.00	107.00	113.00	114.00	115.00	116.00
SiO2	39.27	39.07	38.73	38.71	39.81	40.28	40.60	40.07
TiO2	0.01	0.10	0.13	0.20	0.01	0.03	0.01	0.01
Al2O3	22.23	21.99	21.76	21.63	22.79	23.05	23.06	23.04
Fe2O3	0.38	1.35	1.73	1.49	2.66	1.98	1.58	2.04
MgO	7.41	8.05	7.73	7.35	13.47	13.37	13.56	13.53
FeO	22.83	21.27	21.62	22.16	13.42	14.00	14.27	13.90
MnO	0.74	0.71	0.77	0.85	0.39	0.35	0.42	0.36
CaO	7.94	8.12	7.95	8.00	7.64	7.64	7.53	7.40
Na2O	0.00	0.02	0.01	0.02	0.00	0.04	0.00	0.01
K2O	0.00	0.00	0.00	0.00	0.00	0.01	0.01	0.00
Sum	100.81	100.68	100.44	100.40	100.18	100.74	101.04	100.36
Si	2.99	2.97	2.96	2.97	2.94	2.95	2.96	2.95
Ti	0.00	0.01	0.01	0.01	0.00	0.00	0.00	0.00
Al	2.00	1.97	1.96	1.96	1.98	1.99	1.98	2.00
Fe3	0.02	0.08	0.10	0.09	0.15	0.11	0.09	0.11
Mg	0.84	0.91	0.88	0.84	1.48	1.46	1.48	1.48
Fe2	1.45	1.35	1.38	1.42	0.83	0.86	0.87	0.86
Mn	0.05	0.05	0.05	0.06	0.02	0.02	0.03	0.02
Ca	0.65	0.66	0.65	0.66	0.60	0.60	0.59	0.58
Na	0.00	0.00	0.00	0.00	0.00	0.01	0.00	0.00
K	0.00	0.00	0.00	0.00	0.00	0.00	0.00	0.00
Sum	8.00	8.00	8.00	8.00	8.00	8.00	8.00	8.00
XMg	0.37	0.40	0.39	0.37	0.64	0.63	0.63	0.63

	Plagioclase			
	LV20B			
	100.00	101.00	111.00 symplectite	114.00 symplectite
SiO2	59.93	59.83	60.29	58.75
TiO2	0.06	0.01	0.00	0.07
Al2O3	24.79	24.74	24.46	25.26
MgO	0.01	0.00	0.01	0.02
FeO	0.02	0.09	0.18	0.18
MnO	0.00	0.00	0.00	0.04
CaO	6.47	6.73	6.31	7.32
Na2O	7.91	7.53	7.80	7.32
K2O	0.22	0.19	0.30	0.20
Sum	99.42	99.13	99.34	99.16
Si	2.69	2.69	2.70	2.65
Ti	0.00	0.00	0.00	0.00
Al	1.31	1.31	1.29	1.34
Mg	0.00	0.00	0.00	0.00
Fe2	0.00	0.00	0.01	0.01
Mn	0.00	0.00	0.00	0.00
Ca	0.31	0.32	0.30	0.35
Na	0.69	0.66	0.68	0.64
K	0.01	0.01	0.02	0.01
Sum	5.01	4.99	5.00	5.01
Xna	0.31	0.33	0.30	0.35

	Pyroxene						
	LV21						LV20B
	1	16	17	19	20		88.00
SiO2	53.96	54.38	53.23	54.04	53.81		52.59
TiO2	0.21	0.2	0.19	0.16	0.2		0.09
Al2O3	9.78	9.75	12.43	9.61	9.43		3.03
Cr2O3	0.02	0.02	0.05	0.12	0.13		
Fe2O3	1.36	1.77	0	1.6	2.12		1.67
MgO	11.36	11.54	10.04	11.61	11.58		13.7
FeO	1.21	0.8	2.15	0.96	0.45		4.88
MnO	0.01	0.03	0.04	0	0.06		0.03
CaO	17.54	17.75	17.56	17.22	17.68		22.52
Na2O	4.42	4.54	4.22	4.54	4.47		1.03
K2O	0.09	0	0	0	0		0
Sum	99.96	100.78	99.92	99.85	99.92	99.53	
Si	1.925	1.923	1.895	1.927	1.921		1.945
Ti	0.006	0.005	0.005	0.004	0.005		0.002
Al	0.411	0.407	0.522	0.404	0.397		0.132
Cr	0.001	0.001	0.002	0.003	0.004		
Fe3	0.036	0.047	0	0.043	0.057		0.046
Mg	0.604	0.608	0.533	0.617	0.616		0.756
Fe2	0.036	0.024	0.064	0.029	0.014		0.151
Mn	0	0.001	0.001	0	0.002		0.001
Ca	0.67	0.673	0.67	0.658	0.676		0.892
Na	0.306	0.311	0.291	0.314	0.309		0.074
K	0.004	0	0	0	0		0
Sum	4	4	3.984	4	4		4
XFe	0.056	0.037	0.107	0.044	0.021		0.17
XJd	0.29	0.28	0.31	0.29	0.27		0.05
XAe	0.03	0.04	0.00	0.04	0.05		0.03

Supplementary Table II.3.4: Non-exhaustive summary of the trace element analyses in garnet.

LV21

profil 1				profil 2			
distance	Nd(ppm)	Sm (ppm)	Lu(ppm)	distance	Nd(ppm)	Sm (ppm)	Lu(ppm)
0.00	-0.01	-0.02	0.33	0.00	1.42	-0.01	0.98
1.94	-0.01	-0.02	0.37	1.40	-0.01	-0.01	0.53
3.88	-0.01	0.39	0.24	2.80	-0.01	-0.01	0.51
5.82	-0.01	-0.02	0.24	4.20	-0.01	0.92	0.62
7.76	-0.01	0.84	0.26	5.60	0.44	-0.01	0.31
9.70	-0.01	-0.01	0.17	7.00	-0.01	-0.01	1.41
11.64	-0.01	-0.02	0.12	8.40	-0.01	-0.01	0.50
13.58	-0.01	-0.02	0.37	9.80	-0.01	2.29	1.17
15.52	-0.01	-0.01	0.29	11.20	-0.01	0.49	0.75
17.46	-0.01	-0.02	0.24	12.60	-0.01	0.45	0.88
19.40	-0.01	-0.02	0.24	14.00	-0.01	-0.01	0.83
21.34	-0.01	0.35	0.54	15.40	-0.01	0.82	1.05
23.28	0.65	-0.01	0.28	16.80	-0.01	1.16	0.52
25.22	-0.01	-0.01	0.29	18.20	-0.01	2.53	1.14
27.16	-0.01	-0.01	0.11	19.60	-0.01	-0.01	0.95
29.10	-0.01	-0.01	0.39	21.00	0.64	0.36	0.77
31.04	-0.01	-0.01	0.51	22.40	-0.01	0.75	0.85
32.98	-0.01	-0.01	0.38	23.80	-0.01	2.74	0.64
34.92	-0.01	-0.02	0.36	25.20	-0.01	-0.01	0.87
36.86	-0.01	-0.01	0.99	26.60	-0.01	1.89	0.96
38.80	-0.01	-0.01	0.40	28.00	-0.01	0.37	1.08
40.74	-0.01	-0.01	0.86	29.40	-0.01	-0.01	0.62
42.68	-0.01	0.37	1.09	30.80	-0.01	0.71	1.18
44.62	-0.01	-0.01	0.48	32.20	-0.01	0.36	1.25
46.56	-0.01	-0.01	0.88	33.60	-0.01	-0.01	0.74
48.50	-0.01	-0.01	0.85	35.00	-0.01	-0.01	1.23
50.44	-0.01	0.73	0.50	36.40	-0.01	-0.01	0.68
52.38	-0.01	-0.02	0.79	37.80	0.32	1.12	0.79
54.32	-0.01	-0.01	0.31	39.20	-0.01	0.37	0.39
56.26	-0.01	-0.01	0.82	40.60	-0.01	0.38	0.64
58.20	0.32	-0.01	0.61	42.00	0.31	1.09	0.54
60.14	-0.01	0.36	0.39	43.40	-0.01	-0.01	1.38
62.08	-0.01	-0.01	0.34	44.80	-0.01	0.37	0.34
64.02	0.64	-0.01	0.27	46.20	-0.01	0.37	0.51
65.96	-0.01	0.39	1.20	47.60	0.63	0.36	0.60
67.90	-0.01	-0.01	0.92	49.00	-0.01	-0.01	0.54
69.84	-0.01	-0.02	1.02	50.40	-0.01	-0.01	0.39
71.78	-0.01	-0.01	1.20	51.80	-0.01	-0.01	0.96
73.72	-0.01	0.74	1.24	53.20	-0.01	0.37	0.68
75.66	-0.01	-0.02	1.67	54.60	-0.01	0.36	0.33
77.60	-0.01	-0.02	0.98	56.00	-0.01	-0.01	0.54
79.54	-0.01	0.34	0.69	57.40	-0.01	-0.01	0.34
81.48	-0.01	-0.01	0.70	58.80	-0.01	1.07	0.32
83.42	-0.01	-0.01	1.27	60.20	0.29	-0.01	0.56
85.36	-0.01	0.73	0.83	61.60	0.31	-0.01	0.37
87.30	-0.01	0.37	0.34	63.00	-0.01	0.36	0.44
89.24	-0.01	-0.02	0.58	64.40	-0.01	0.34	0.21

LV21

profil 1				profil 2			
distance	Nd(ppm)	Sm (ppm)	Lu(ppm)	distance	Nd(ppm)	Sm (ppm)	Lu(ppm)
91.18	-0.01	-0.01	0.84	65.80	-0.01	-0.01	0.52
93.12	0.64	-0.01	0.16	67.20	-0.01	0.34	0.21
95.06	-0.01	-0.02	0.57	68.60	-0.01	0.71	0.70
97.00	-0.01	-0.02	0.35	70.00	-0.01	0.37	0.50
98.94	0.36	-0.02	0.31	71.40	-0.01	1.46	0.38
100.88	-0.01	0.74	0.56	72.80	0.31	1.44	0.43
102.82	-0.01	-0.01	0.50	74.20	-0.01	1.45	0.38
104.76	-0.01	-0.01	0.54	75.60	-0.01	0.69	0.52
106.70	-0.01	-0.01	0.05	77.00	-0.01	-0.01	0.71
108.64	-0.01	0.68	0.21	78.40	0.66	-0.01	0.23
110.58	-0.01	0.72	0.27	79.80	-0.01	0.34	0.68
112.52	-0.01	-0.01	0.05	81.20	-0.01	1.11	0.67
114.46	0.31	-0.01	0.05	82.60	0.30	1.41	0.48
116.40	-0.01	-0.01	0.11	84.00	-0.01	1.02	0.56
118.34	-0.01	-0.02	0.11	85.40	-0.01	-0.01	0.22
120.28	-0.01	-0.01	0.61	86.80	-0.01	1.41	0.26
122.22	-0.01	-0.02	0.54	88.20	-0.01	-0.01	0.45
124.16	0.32	-0.02	0.11	89.60	-0.01	1.37	0.31
126.10	-0.01	0.35	0.00	91.00	0.30	1.06	0.58
128.04	-0.01	0.36	0.39	92.40	0.30	0.35	0.58
129.98	-0.01	-0.02	0.45	93.80	-0.01	-0.01	0.38
131.92	0.31	-0.01	0.59	95.20	-0.01	0.72	0.38
133.86	-0.01	-0.02	0.28	96.60	-0.01	-0.01	0.54
135.80	-0.01	0.35	0.44	98.00	-0.01	-0.01	0.16
137.74	-0.01	-0.02	0.11	99.40	-0.01	0.31	0.24
139.68	-0.01	-0.02	0.58	100.80	-0.01	-0.01	0.20
141.62	0.63	-0.01	0.54	102.20	-0.01	-0.01	0.85
143.56	1.02	-0.02	0.64	103.60	-0.01	0.66	0.50
145.50	0.63	-0.01	1.09	105.00	-0.01	-0.01	0.16
147.44	-0.01	-0.02	0.50	106.40	-0.01	-0.01	0.47
149.38	0.00	-0.01	0.42	107.80	-0.01	-0.01	0.47
151.32	-0.01	0.36	0.57	109.20	-0.01	-0.01	0.53
153.26	-0.01	-0.02	0.99	110.60	1.25	1.07	0.32
155.20	0.33	-0.02	0.96	112.00	-0.01	-0.01	0.36
157.14	-0.01	-0.02	0.62	113.40	-0.01	-0.01	0.53
159.08	-0.01	-0.02	0.89	114.80	-0.01	-0.01	0.40
161.02	-0.01	-0.02	0.41	116.20	-0.01	0.36	0.27
162.96	-0.01	-0.01	0.60	117.60	-0.01	-0.01	0.28
164.90	-0.01	-0.02	0.40	119.00	-0.01	-0.01	0.32
166.84	-0.01	-0.02	0.55	120.40	-0.01	-0.01	0.26
168.78	-0.01	0.73	0.45	121.80	-0.01	-0.01	0.25
170.72	0.62	-0.01	0.37	123.20	-0.01	-0.01	0.25
172.66	0.00	-0.01	0.25	124.60	-0.01	-0.01	0.11
174.60	-0.01	-0.02	0.67	126.00	-0.01	0.33	0.20
176.54	-0.01	-0.02	0.66	127.40	-0.01	-0.01	0.57
178.48	0.33	-0.02	0.34	128.80	-0.01	0.69	0.26
180.42	0.00	0.72	0.49	130.20	-0.01	-0.01	0.26

LV21

profil 1				profil 2			
distance	Nd(ppm)	Sm (ppm)	Lu(ppm)	distance	Nd(ppm)	Sm (ppm)	Lu(ppm)
182.36	0.00	-0.02	0.38	131.60	-0.01	0.35	0.58
184.30	0.34	-0.02	0.58	133.00	-0.01	-0.01	0.31
186.24	0.00	0.33	0.35	134.40	-0.01	-0.01	0.05
188.18	-0.01	-0.02	0.23	135.80	-0.01	-0.01	0.37
190.12	-0.01	-0.02	0.05	137.20	-0.01	-0.01	0.46
192.06	0.00	-0.02	0.49	138.60	-0.01	-0.01	0.33
194.00	0.00	0.68	0.15	140.00	-0.01	-0.01	0.10
195.94	0.00	-0.01	0.16	141.40	-0.01	0.74	0.28
197.88	0.00	-0.01	0.26	142.80	-0.01	-0.01	0.37
199.82	-0.01	-0.02	0.42	144.20	-0.01	0.33	0.20
201.76	0.00	0.71	0.48	145.60	-0.01	0.65	0.49
203.70	0.00	-0.02	0.38	147.00	-0.01	0.33	0.36
205.64	0.31	-0.01	0.11	148.40	-0.01	0.35	0.48
207.58	0.00	-0.02	0.11	149.80	-0.01	0.37	0.73
209.52	0.00	-0.02	0.38	151.20	-0.01	-0.01	0.10
211.46	0.00	-0.02	0.21	152.60	-0.01	-0.01	0.56
213.40	0.00	0.36	0.11	154.00	0.31	-0.01	0.32
215.34	0.00	0.36	0.06	155.40	-0.01	-0.01	0.27
217.28	0.00	-0.02	0.16	156.80	-0.01	-0.01	0.37
219.22	0.00	0.35	0.33	158.20	-0.01	0.70	0.47
221.16	0.00	-0.02	0.05	159.60	-0.01	1.46	0.77
223.10	0.00	0.36	0.39	161.00	0.30	1.04	0.78
225.04	0.32	-0.02	0.39	162.40	-0.01	-0.01	0.63
226.98	0.00	-0.01	0.15	163.80	-0.01	1.04	0.42
228.92	0.63	1.06	0.21	165.20	-0.01	0.67	0.50
230.86	0.00	0.70	0.37	166.60	-0.01	-0.01	0.87
232.80	0.00	-0.02	0.11	168.00	-0.01	0.32	0.25
234.74	0.00	-0.01	0.42	169.40	-0.01	0.35	0.79
				170.80	-0.01	1.74	0.36
				172.20	-0.01	0.33	0.70
				173.60	-0.01	-0.01	0.42
				175.00	-0.01	-0.01	0.83
				176.40	-0.01	0.70	0.10
				177.80	-0.01	-0.01	0.47
				179.20	-0.01	0.68	0.41
				180.60	-0.01	-0.01	0.80
				182.00	0.30	-0.01	0.73
				183.40	-0.01	-0.01	0.60
				184.80	-0.01	-0.01	0.35
				186.20	-0.01	0.68	0.97
				187.60	-0.01	-0.01	0.57
				189.00	-0.01	0.69	0.78
				190.40	-0.01	0.33	0.65
				191.80	-0.01	0.71	0.59
				193.20	-0.01	1.04	0.68
				194.60	-0.01	0.77	0.92
				196.00	-0.01	0.70	1.06

LV21

profil 2

distance	Nd(ppm)	Sm (ppm)	Lu(ppm)
197.40	-0.01	0.35	0.80
198.80	-0.01	-0.01	0.68
200.20	0.89	-0.01	0.91
201.60	0.29	0.66	0.80

LV20B

profil 1				profil 2			
distance	Nd(ppm)	Sm (ppm)	Lu(ppm)	distance	Nd(ppm)	Sm (ppm)	Lu(ppm)
0.00	bdl	-0.01	0.23	0.00	0.74	1.70	1.60
2.47	-0.01	-0.01	0.18	1.80	1.02	1.56	0.88
4.94	-0.01	0.83	0.37	3.60	1.38	-0.01	1.30
7.41	0.66	-0.01	0.34	5.40	0.31	1.09	0.66
9.88	-0.01	-0.01	0.21	7.20	0.33	0.38	0.81
12.35	-0.01	-0.01	0.63	9.00	0.33	0.77	0.76
14.82	-0.01	0.74	0.28	10.80	1.75	-0.01	1.56
17.29	-0.01	-0.01	0.17	12.60	-0.01	0.72	0.16
19.76	-0.01	0.37	0.05	14.40	-0.01	0.78	0.29
22.23	-0.01	1.13	0.51	16.20	0.98	-0.01	0.28
24.70	-0.01	1.08	0.49	18.00	-0.01	-0.01	0.51
27.17	-0.01	-0.01	0.17	19.80	0.69	-0.01	0.83
29.64	-0.01	0.37	0.39	21.60	-0.01	-0.01	0.71
32.11	-0.01	-0.01	0.26	23.40	-0.01	0.39	0.89
34.58	-0.01	-0.01	0.23	25.20	-0.01	-0.01	0.17
37.05	0.34	-0.01	0.23	27.00	0.34	-0.01	0.59
39.52	0.98	-0.01	0.00	28.80	-0.01	-0.01	0.82
41.99	0.64	-0.01	0.22	30.60	-0.01	-0.01	0.40
44.46	0.31	0.35	0.27	32.40	-0.01	0.37	0.00
46.93	0.31	1.07	0.21	34.20	-0.01	-0.01	0.35
49.40	1.58	-0.01	0.16	36.00	0.35	0.40	0.06
51.87	-0.01	-0.01	0.23	37.80	-0.01	-0.01	0.55
54.34	-0.01	0.37	0.78	39.60	-0.01	-0.01	0.34
56.81	0.66	-0.01	0.23	41.40	0.32	0.37	0.34
59.28	-0.01	-0.01	0.52	43.20	-0.01	0.37	0.91
61.75	-0.01	-0.01	0.23	45.00	-0.01	-0.01	0.68
64.22	-0.01	-0.01	0.06	46.80	-0.01	-0.01	0.17
66.69	-0.01	0.80	0.36	48.60	-0.01	0.37	0.34
69.16	-0.01	0.39	0.17	50.40	-0.01	-0.01	0.63
71.63	-0.01	-0.01	0.54	52.20	-0.01	0.39	0.48
74.10	-0.01	-0.01	0.30	54.00	1.08	0.40	0.68
76.57	-0.01	-0.01	0.16	55.80	-0.01	0.86	0.46
79.04	-0.01	-0.01	0.28	57.60	-0.01	-0.01	0.20
81.51	-0.01	-0.01	0.32	59.40	-0.01	-0.01	0.74
83.98	0.65	-0.01	0.11	61.20	0.35	1.61	0.42
86.45	1.25	-0.01	0.37	63.00	-0.01	0.75	0.73
88.92	-0.01	0.75	0.11	64.80	0.65	-0.01	0.34
91.39	-0.01	-0.01	0.46	66.60	1.00	1.14	0.34
93.86	-0.01	0.40	0.43	68.40	-0.01	-0.01	0.29
96.33	-0.01	-0.01	0.17	70.20	-0.01	0.38	0.35
98.80	-0.01	-0.01	0.27	72.00	-0.01	0.38	0.06
101.27	-0.01	-0.01	0.27	73.80	-0.01	-0.01	0.53
103.74	-0.01	0.37	0.39	75.60	0.32	-0.01	0.50
106.21	-0.01	-0.01	0.50	77.40	0.32	-0.01	0.34
108.68	0.31	0.72	0.16	79.20	-0.01	-0.01	0.45
111.15	0.33	-0.01	0.68	81.00	0.34	-0.01	0.59
113.62	-0.01	-0.01	0.54	82.80	0.35	-0.01	0.24

LV20B

profil 1				profil 2			
distance	Nd(ppm)	Sm (ppm)	Lu(ppm)	distance	Nd(ppm)	Sm (ppm)	Lu(ppm)
116.09	-0.01	0.35	0.52	84.60	-0.01	-0.01	0.40
118.56	-0.01	-0.01	0.94	86.40	0.35	1.22	0.55
121.03	-0.01	0.71	0.70	88.20	-0.01	-0.01	0.24
123.50	-0.01	-0.01	1.05	90.00	0.65	0.37	0.78
125.97	-0.01	-0.01	1.06	91.80	-0.01	-0.01	0.44
128.44	0.00	-0.01	1.45	93.60	-0.01	-0.01	0.65
130.91	0.00	0.30	1.03	95.40	-0.01	-0.01	0.96
133.38	0.31	-0.01	1.18	97.20	-0.01	2.00	0.42
135.85	-0.01	0.35	1.98	99.00	-0.01	-0.01	0.83
138.32	-0.01	-0.01	1.88	100.80	-0.01	0.35	0.37
140.79	0.00	-0.01	1.47	102.60	0.34	0.38	0.53
143.26	0.00	-0.01	1.71	104.40	0.33	0.76	0.23
145.73	-0.01	1.07	1.77	106.20	-0.01	0.75	0.62
148.20	-0.01	0.36	1.19	108.00	0.68	-0.01	0.70
150.67	-0.01	0.71	1.61	109.80	-0.01	-0.01	0.54
153.14	0.00	0.70	1.84	111.60	-0.01	0.39	0.77
155.61	0.31	0.35	1.98	113.40	-0.01	0.38	0.76
158.08	0.32	-0.01	1.96	115.20	-0.01	-0.01	0.93
160.55	0.00	-0.01	1.53	117.00	-0.01	-0.01	1.08
163.02	-0.01	-0.01	1.30	118.80	0.63	-0.01	1.42
165.49	-0.01	0.77	2.37	120.60	-0.01	1.92	1.33
167.96	-0.01	0.38	1.67	122.40	-0.01	-0.01	0.77
170.43	-0.01	1.17	1.94	124.20	0.31	0.35	0.96
172.90	-0.01	0.37	0.78	126.00	-0.01	-0.01	1.85
175.37	-0.01	-0.01	1.27	127.80	-0.01	-0.01	1.56
177.84	0.00	-0.01	0.96	129.60	-0.01	-0.01	1.30
180.31	0.00	-0.01	0.91	131.40	-0.01	0.37	1.40
182.78	0.66	-0.01	1.20	133.20	0.33	1.53	1.78
185.25	0.00	0.35	1.16	135.00	0.66	0.37	1.25
187.72	0.00	-0.01	0.58	136.80	-0.01	0.38	1.09
190.19	0.32	0.37	1.22	138.60	-0.01	-0.01	1.37
192.66	0.00	0.70	0.95	140.40	-0.01	-0.01	2.41
195.13	0.34	0.38	0.93	142.20	-0.01	-0.01	1.02
197.60	0.00	-0.01	0.59	144.00	-0.01	-0.01	1.81
200.07	0.00	0.36	0.27	145.80	-0.01	-0.01	1.49
202.54	-0.01	-0.01	1.06	147.60	0.33	1.13	1.19
205.01	-0.01	-0.01	1.09	149.40	-0.01	0.71	1.12
207.48	0.00	0.36	1.13	151.20	0.29	-0.01	1.07
209.95	0.69	1.99	1.37	153.00	-0.01	-0.01	1.68
212.42	-0.01	-0.01	0.64	154.80	0.62	-0.01	1.65
214.89	-0.01	-0.01	0.58	156.60	-0.01	-0.01	1.62
217.36	0.00	0.74	0.78	158.40	-0.01	1.15	1.61
219.83	0.33	-0.01	0.45	160.20	-0.01	0.74	0.83
222.30	0.00	-0.01	0.66	162.00	-0.01	-0.01	1.91
224.77	0.00	-0.01	1.08	163.80	-0.01	0.37	1.59
227.24	0.00	-0.01	0.51	165.60	0.29	-0.01	0.97
229.71	0.00	-0.01	0.26	167.40	-0.01	-0.01	0.66

LV20B

profil 1				profil 2			
distance	Nd(ppm)	Sm (ppm)	Lu(ppm)	distance	Nd(ppm)	Sm (ppm)	Lu(ppm)
232.18	0.00	-0.01	0.70	169.20	-0.01	0.75	0.68
234.65	0.00	-0.01	0.74	171.00	-0.01	-0.01	1.15
237.12	0.33	-0.01	0.80	172.80	0.29	-0.01	1.49
239.59	0.00	1.12	0.56	174.60	-0.01	0.35	1.01
242.06	-0.01	-0.01	0.59	176.40	-0.01	-0.01	1.32
244.53	0.00	0.75	0.28	178.20	-0.01	-0.01	1.16
247.00	0.00	0.36	0.55	180.00	-0.01	-0.01	0.66
249.47	0.00	-0.01	0.71	181.80	-0.01	1.30	0.68
251.94	0.00	-0.01	0.83	183.60	0.31	-0.01	0.82
254.41	0.00	0.35	0.00	185.40	0.28	-0.01	0.64
256.88	0.00	-0.01	0.41	187.20	0.28	0.32	0.64
259.35	0.31	0.36	0.70	189.00	0.94	0.35	0.48
				190.80	-0.01	-0.01	1.28
				192.60	-0.01	-0.01	0.92
				194.40	-0.01	0.35	1.11
				196.20	0.31	-0.01	1.14
				198.00	-0.01	0.34	0.84
				199.80	-0.01	-0.01	0.66
				201.60	-0.01	0.70	0.69
				203.40	-0.01	-0.01	0.69
				205.20	-0.01	0.75	0.45
				207.00	-0.01	0.36	0.77
				208.80	-0.01	1.02	0.36
				210.60	0.31	-0.01	0.75
				212.40	0.33	-0.01	0.40
				214.20	-0.01	0.36	0.95
				216.00	0.31	1.08	0.43
				217.80	-0.01	-0.01	0.27
				219.60	0.66	-0.01	0.28
				221.40	-0.01	0.41	0.06
				223.20	0.32	-0.01	0.22
				225.00	-0.01	-0.01	0.32
				226.80	-0.01	-0.01	0.26
				228.60	-0.01	-0.01	0.41
				230.40	-0.01	-0.01	0.49
				232.20	0.32	0.37	0.62
				234.00	0.33	-0.01	0.34
				235.80	-0.01	-0.01	0.16
				237.60	-0.01	-0.01	0.20
				239.40	-0.01	-0.01	0.05
				241.20	-0.01	-0.01	0.16
				243.00	-0.01	-0.01	0.06
				244.80	-0.01	0.40	0.54
				246.60	-0.01	0.37	0.34
				248.40	-0.01	-0.01	0.17
				250.20	-0.01	0.38	0.57
				252.00	-0.01	-0.01	0.41

Supplementary Table 5: Summary of the trace element analyses in zirconTrace element contents are normalized to chondrite after Sun and McDonough (1989). Bdl – below detection limit.

Date group	Devonian			Ordovician						
Label	18b - 1	17b -1	*17b - 2*	26b	36b	52b	04b	13b	15b	07b
Trace element content (ppm)										
Y	211.46	317.47	*582.05*	1866.42	1446.29	894.00	797.71	2272.85	1403.53	1044.28
La	0.46	0.18	*0.18*	0.05	0.06	0.01	0.01	0.01	bdl	0.01
Ce	1.81	3.14	*4.02*	5.97	11.65	6.35	4.77	9.14	6.71	6.38
Pr	0.17	0.23	*0.15*	0.20	0.17	0.17	0.08	0.23	0.13	0.16
Nd	0.44	0.81	*0.83*	2.97	0.96	0.66	0.50	2.87	1.01	0.68
Sm	0.70	0.94	*0.86*	5.39	2.33	1.54	2.28	5.63	2.34	1.85
Eu	0.26	0.35	*0.26*	1.41	0.76	0.43	0.43	1.48	0.73	0.50
Gd	1.73	3.39	*5.89*	32.72	17.20	10.77	12.29	38.30	19.40	16.50
Tb	0.90	1.58	*2.95*	11.47	6.96	4.77	4.62	14.33	7.33	6.63
Dy	13.82	21.82	*42.14*	145.43	98.47	63.47	63.82	179.49	103.42	80.31
Ho	6.34	9.79	*18.38*	58.00	44.14	27.97	25.85	71.49	44.08	34.09
Er	40.51	54.27	*96.59*	280.74	232.37	152.55	126.84	347.97	218.71	166.62
Tm	10.69	12.80	*22.17*	56.83	51.66	33.04	27.50	70.85	46.66	34.96
Yb	112.47	131.19	*215.62*	515.67	501.59	325.57	247.74	617.19	427.24	312.96
Lu	28.93	29.59	*47.32*	103.28	106.79	71.34	52.43	125.06	90.81	64.86
Trace element content normalised to chondrite (after after Sun and McDonough (1989))										
LaN	1.92	0.74	*0.74*	0.21	0.26	0.04	0.05	0.05		0.03
CeN	2.96	5.13	*6.57*	9.75	19.04	10.38	7.79	14.93	10.96	10.42
PrN	1.77	2.44	*1.58*	2.10	1.80	1.79	0.79	2.38	1.40	1.64
NdN	0.94	1.73	*1.78*	6.36	2.06	1.42	1.07	6.15	2.16	1.46
SmN	4.58	6.14	*5.62*	35.23	15.23	10.07	14.90	36.80	15.29	12.09
EuN	4.40	6.00	*4.40*	24.26	13.03	7.45	7.38	25.52	12.53	8.69
GdN	8.42	16.50	*28.66*	159.22	83.70	52.41	59.81	186.37	94.40	80.29
TbN	24.09	42.25	*78.88*	306.68	186.10	127.54	123.53	383.16	195.99	177.27
DyN	54.41	85.91	*165.91*	572.56	387.68	249.88	251.26	706.65	407.17	316.18
HoN	112.01	172.97	*324.73*	1024.73	779.86	494.17	456.71	1263.07	778.80	602.30
ErN	244.77	327.92	*583.63*	1696.31	1404.05	921.75	766.40	2102.54	1321.51	1006.77
TmN	419.22	501.96	*869.41*	2228.63	2025.88	1295.69	1078.43	2778.43	1829.80	1370.98
YbN	661.59	771.71	*1268.35*	3033.35	2950.53	1915.12	1457.29	3630.53	2513.18	1840.94
LuN	1138.98	1164.96	*1862.99*	4066.14	4204.33	2808.66	2064.17	4923.62	3575.20	2553.54
Eu/Eu*	0.71	0.60	*0.35*	0.32	0.37	0.32	0.25	0.31	0.33	0.28
Ce/Ce*	1.60	3.81	*6.08*	14.82	27.97	39.80	41.28	41.67		47.68
Pr/Pr*	1.06	0.82	0.46	0.27	0.29	0.47	0.27	0.25	0.29	0.42
LuN/SmN	248.95	189.62	*331.44*	115.42	276.08	279.04	138.52	133.80	233.76	211.18
YbN/GdN	78.59	46.78	*44.25*	19.05	35.25	36.54	24.37	19.48	26.62	22.93

	Ordovician						Cambrian					
Label	28b	19b	08B	40B	34B	35B	22b	09b	12b	14b	25B	37B
Trace element content (ppm)												
Y	1004.04	1786.29	1526.96	1126.16	736.34	3838.82	1526.15	2118.49	2133.44	2016.08	1188.14	3422.89
La	0.02	0.01	0.03	0.08	bdl	0.08	bdl	0.04	0.01	0.08	0.08	0.20
Ce	5.30	11.67	12.54	8.68	5.19	21.67	7.21	12.00	10.16	8.79	6.26	18.70
Pr	0.13	0.15	0.07	0.07	0.05	0.49	0.16	0.23	0.24	0.21	0.11	0.32
Nd	0.58	1.34	1.12	0.71	0.51	7.36	1.52	1.82	2.75	2.68	1.34	4.59
Sm	1.65	2.85	2.39	1.58	1.26	14.65	3.86	4.70	5.29	4.98	2.96	8.29
Eu	0.47	0.81	0.69	0.58	0.41	3.66	1.01	1.22	1.57	1.50	0.79	2.38
Gd	12.23	22.54	18.34	12.55	9.50	84.55	20.58	30.72	37.59	35.74	19.71	56.97
Tb	5.63	9.03	7.34	5.26	3.79	27.94	8.38	12.17	13.51	12.47	7.22	20.57
Dy	74.90	124.13	104.15	74.05	51.55	334.81	114.00	158.06	171.51	161.24	91.21	268.94
Ho	30.67	55.41	45.09	32.28	21.67	122.79	47.27	64.59	68.83	63.91	36.48	106.61
Er	160.61	285.09	234.93	175.30	111.97	558.52	234.96	320.24	322.61	309.36	176.03	511.12
Tm	34.53	61.27	49.72	38.71	24.51	105.43	50.71	66.57	65.97	63.46	35.19	101.20
Yb	318.55	575.40	471.29	394.99	245.01	926.45	474.42	621.02	585.61	563.32	320.64	924.70
Lu	67.29	120.71	96.13	84.93	53.72	171.81	100.00	125.54	118.38	114.06	64.08	181.69
Trace element content normalised to chondrite (after after Sun and McDonough (1989))												
LaN	0.09	0.03	0.13	0.32		0.34		0.18	0.04	0.35	0.32	0.82
CeN	8.66	19.07	20.49	14.18	8.48	35.41	11.78	19.61	16.60	14.36	10.23	30.56
PrN	1.34	1.58	0.73	0.69	0.49	5.19	1.64	2.45	2.56	2.16	1.16	3.39
NdN	1.24	2.87	2.39	1.52	1.09	15.76	3.25	3.90	5.89	5.74	2.87	9.83
SmN	10.78	18.63	15.62	10.34	8.25	95.75	25.23	30.72	34.58	32.55	19.35	54.18
EuN	8.16	13.88	11.83	9.98	7.05	63.10	17.33	20.98	27.07	25.86	13.69	41.05
GdN	59.51	109.68	89.25	61.07	46.23	411.44	100.15	149.49	182.92	173.92	95.91	277.23
TbN	150.53	241.44	196.26	140.64	101.34	747.06	224.06	325.40	361.23	333.42	193.05	550.00
DyN	294.88	488.70	410.04	291.54	202.95	1318.15	448.82	622.28	675.24	634.80	359.09	1058.82
HoN	541.87	978.98	796.64	570.32	382.86	2169.43	835.16	1141.17	1216.08	1129.15	644.52	1883.57
ErN	970.45	1722.60	1419.52	1059.21	676.56	3374.74	1419.70	1934.98	1949.31	1869.24	1063.63	3088.34
TmN	1354.12	2402.75	1949.80	1518.04	961.18	4134.51	1988.63	2610.59	2587.06	2488.63	1380.00	3968.63
YbN	1873.82	3384.71	2772.29	2323.47	1441.24	5449.71	2790.71	3653.06	3444.76	3313.65	1886.12	5439.41
LuN	2649.21	4752.36	3784.65	3343.70	2114.96	6764.17	3937.01	4942.52	4660.63	4490.55	2522.83	7153.15
Eu/Eu*	0.32	0.31	0.32	0.40	0.36	0.32	0.34	0.31	0.34	0.34	0.32	0.33
Ce/Ce*	24.64	92.35	66.27	30.07		26.65		29.71	51.85	16.62	16.74	18.29
Pr/Pr*	0.41	0.21	0.10	0.15	0.16	0.22	0.27	0.28	0.26	0.24	0.21	0.20
LuN/SmN	245.65	255.13	242.28	323.38	256.41	70.64	156.05	160.89	134.80	137.96	130.40	132.02
YbN/GdN	31.49	30.86	31.06	38.05	31.18	13.25	27.87	24.44	18.83	19.05	19.67	19.62

Partie III

Les granites du Levezou :

âge, métamorphisme et exhumation

Chapter 1 – Ordovician magmatism in the Lévézou massif (French Massif Central): tectonic and geodynamic implications

Table of content

Ordovician magmatism in the Lévézou massif (French Massif Central): tectonic and geodynamic implications

Published in International Journal of Earth Sciences

Caroline Lotout [a], Pavel Pitra [a,b], Marc Poujol [a] and Jean Van Den Driessche [a]

[a] UMR CNRS 6118, Géosciences Rennes, OSUR, Université, Rennes 1, 35042 Rennes CEDEX, France

[b] Česká geologická služba, Klárov 3, 118 21 Praha 1, Česká republika

corresponding author: Caroline Lotout

email: caroline.lotout@univ-rennes1.fr

Tel: + 33 223 236 783

Résumé

Nous présentons de nouveaux âges U-Pb sur zircon à environ 470 Ma pour les granitoïdes du Massif du Lévézou (Sud Massif Central). Ces nouvelles datations contredisent l'interprétation les considérant comme des intrusions syn-tectoniques mis en place lors des chevauchements fin-Dévonien à début Carbonifère, au cours du stade de la collision varisque. Ce magmatisme est relié à l'évènement magmatique majeur ayant cours à l'Ordovicien, présent dans toute la chaîne Varisque d'Europe et lié à l'amincissement extrême de marges continentales durant un rifting ou une extension d'arrière arc. La similarité des signatures isotopiques de ces granitoïdes situés de part et d'autre de l'unité éclogitique mafique, associé à un âge de mise en place commun, suggère fortement que ces granitoïdes appartenaient initialement à la même unité, dupliquée tectoniquement par plis isoclinal ou chevauchement lors de l'orogénèse Varisque.

Abstract

New U-Pb dating on zircon yielded ca. 470 Ma ages for the granitoids from the Lévézou massif in the southern French Massif Central. These new ages do not support the previous interpretation of these granitoids as syn-tectonic intrusions emplaced during the late Devonian-early Carboniferous thrusting. The geochemical and isotopic nature of this magmatism is linked to a major magmatic Ordovician event recorded throughout the European Variscan belt and related to extreme thinning of continental margins during a rifting event or a back arc extension. The comparable isotopic signatures of these granitoids on each side of the eclogite-bearing leptyno-amphibolitic complex in the Lévézou massif, together with the fact that they were emplaced at the same time, strongly suggest that these granitoids were originally part of a single unit, tectonically duplicated by either isoclinal folding or thrusting during the Variscan tectonics.

1. Introduction

Variscan tectonics during the Late Devonian-Early Carboniferous is classically viewed as the result of a continental collision following oceanic subduction (e.g. Dewey and Burke 1973). The close association of strongly deformed high-pressure/high-temperature (HP/HT) metamorphic mafic and felsic rocks within the so-called "leptyno-amphibolitic complex" (LAC; Forestier 1961; Lasnier 1968; Forestier et al. 1973; Santallier et al. 1988) is considered to be a tectonic mélange s.l. that formed during the closure of one or several oceans previously separating the continental blocks (e.g. Bard et al. 1980; Matte and Burg 1981; Pin and Vielzeuf 1983; Matte 1986). Different geodynamic interpretations have been proposed that commonly involve two major continents separated by magmatic arcs or several micro-blocks that resulted from the extreme stretching of the continental margins prior to oceanic subduction (e.g. Bard et al. 1980; Matte and Burg 1981; Matte 1986, 1991; Pin 1990; Franke 2006; Ribeiro et al. 2007; Martínez Catalán et al. 2009; Lardeaux 2014; Schulmann et al. 2014). All these interpretations agree, however, on the fact that the Variscan belt resulted from the final collage of two supercontinents, Laurussia to the north and Gondwana to the south (Fig. III.1.1).

The Early Palaeozoic pre-orogenic extensional event is recorded across the entire Variscan Belt by the formation of large Cambro-Ordovician sedimentary basins (e.g. Young 1990; Linnemann et al. 2004) and massive bimodal magmatism (e.g. Pin 1990; Pin and Marini 1993; Abati et al. 1999; Crowley et al. 2000; Sanchéz-García et al. 2003; Sanchéz-García et al. 2008). Among the most typical examples are the porphyritic granitic and rhyolitic orthogneisses with emplacement ages clustering between 490 and 450 Ma (e.g. Helbing and Tiepolo 2005; Solá et al. 2008; Montero et al. 2009; Ballèvre et al. 2012; Talavera et al. 2013; Del Greco et al. 2016 and references therein).

In the southern French Massif Central, the Lévézou is a dome-shaped massif that comprises migmatitic paragneisses and orthogneisses in the core, surrounded by the eclogite-bearing LAC, itself surrounded by lower-grade orthogneiss and micaschists (Fig. III.1.2). The occurrence of the LAC separating two gneissic units makes it a key-area, because it typifies the Variscan architecture, in particular in the Massif Central.

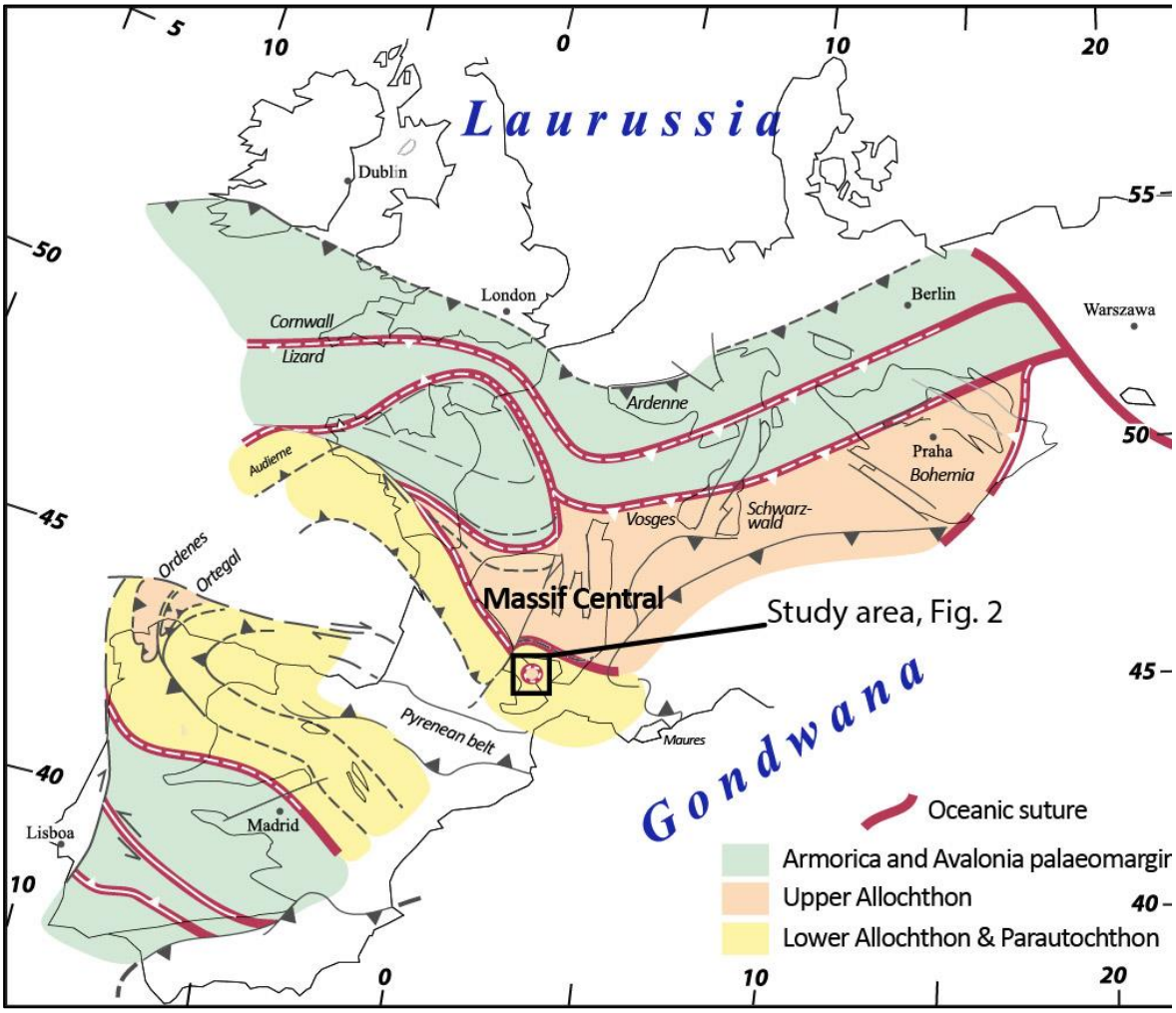

Figure III.1.1 - Tectonic sketch of the Variscan Belt (after Ballèvre et al. 2009). The study area in the French Massif Central is indicated.

The external (Pinet) orthogneiss has been interpreted as a syn-kinematic intrusion, emplaced and deformed during the Late Devonian-Early Carboniferous thrusting event (Pin 1981, Burg and Teyssier 1983; Burg 1987; Dutruge and Burg 1997; Duguet and Faure 2004). The petrology and the deformation patterns of this orthogneiss, however, strongly remind those of the Caroux and Espinouse massifs (Montagne Noire) located ~50 km farther to the south, and whose protoliths were recently dated at 450-455 Ma (Roger et al. 2004, Pitra et al. 2012). This lead us to reexamine the Lévézou orthogneisses from a petrological, geochemical, geochronological and finally tectonic point of view.

2. Geological Setting

The French Massif Central is traditionally subdivided into four Gondwana-derived units, based on their petrological characteristics: the Upper Gneiss Unit (UGU), the Leptyno-Amphibolitic Complex (LAC), the Lower Gneiss Unit (LGU) and the Parautochthon Unit (PAU) (e.g. Burg and Matte 1978; Matte 1986; Ledru et al. 1989; Figs. III.1.1, 2). Some authors refer to the Upper and Lower Gneiss Units as the Upper and Lower Allochthon, respectively (e.g. Ballèvre et al. 2009, 2014). Classically, the LGU and UGU correspond to two continents separated by an oceanic crust (LAC) before the Carboniferous collision (e.g. Burg et Matte 1978; Matte and Burg 1981; Matte 1986, 2001). A recent study (e.g. Lardeaux 2014) has re-interpreted the Upper and Lower Gneiss Unit as an extremely thinned margin of Gondwana; UGU corresponding to the more distal blocks and LGU to the proximal ones. The LGU and the PAU display low grade metamorphism, while the LAC and the UGU have recorded high-pressure (HP) and high-temperature (HT) metamorphism, respectively (e.g. Ledru et al. 1989). Granitoids close to the tectonic contact between the LGU and the LAC were interpreted as syn-tectonic intrusions (Ledru et al. 1989; Duguet and Faure 2004). The Lévézou massif comprises all of these units and represents therefore a classic example of the Variscan architecture (Fig. III.1.2).

The LAC in the Lévézou is dominated by amphibolites with tholeiitic and calc-alkaline affinities (Nicollet 1978; Piboule 1979). It contains abundant lenses of eclogite and locally peridotite. The emplacement of the tholeiitic suite was dated at ca. 485 ± 30Ma (U/Pb on zircon population from a trondhjemite; Pin 1979). A gabbro from the calc-alkaline suite was dated at 367 ± 10 Ma with the same method (Pin and Piboule 1988). The upper part of the LAC comprises micaschists, leucocratic paragneisses and quartzites. For Piboule (1979) and Briand et al. (1988), the magmatic signature of the LAC is that of a back arc basin environment rather than that of an oceanic one. Pin and Piboule (1988) proposed a collision between two independent magmatic suites to account for the composite character of the LAC. Finally, Lardeaux (2014) reinterpreted the REE spectrum of the tholeiitic suite as being compatible with an ocean-continent transition zone. The age of the eclogite-facies HP event in the Lévézou massif is unknown. In the whole French Massif Central, this age is considered to be Silurian (ca. 430-400 Ma; U/Pb on zircon population, Pin and Lancelot 1982; Ducrot et al. 1983; Sm/Nd on garnet, Paquette et al. 1995; in situ U/Pb on 2 zircon grains, Berger et al. 2010). Because of the oceanic affinity of its rocks and the presence of eclogite relics, the LAC is a key unit that has been interpreted as marking the orogenic suture between the UGU and

the LGU (e.g. Bard et al. 1980; Matte, 1986). In the Lévézou massif, the LAC forms a conspicuous arc that separates the inner (UGU) from the outer (LGU) part of the massif. It dips steeply to the south (beneath the LGU) in the southern part of the massif, and to the east, beneath the UGU, in the western part of the massif (Fig. III.1.2). This led to a large spectrum of tectonic interpretations (see below).

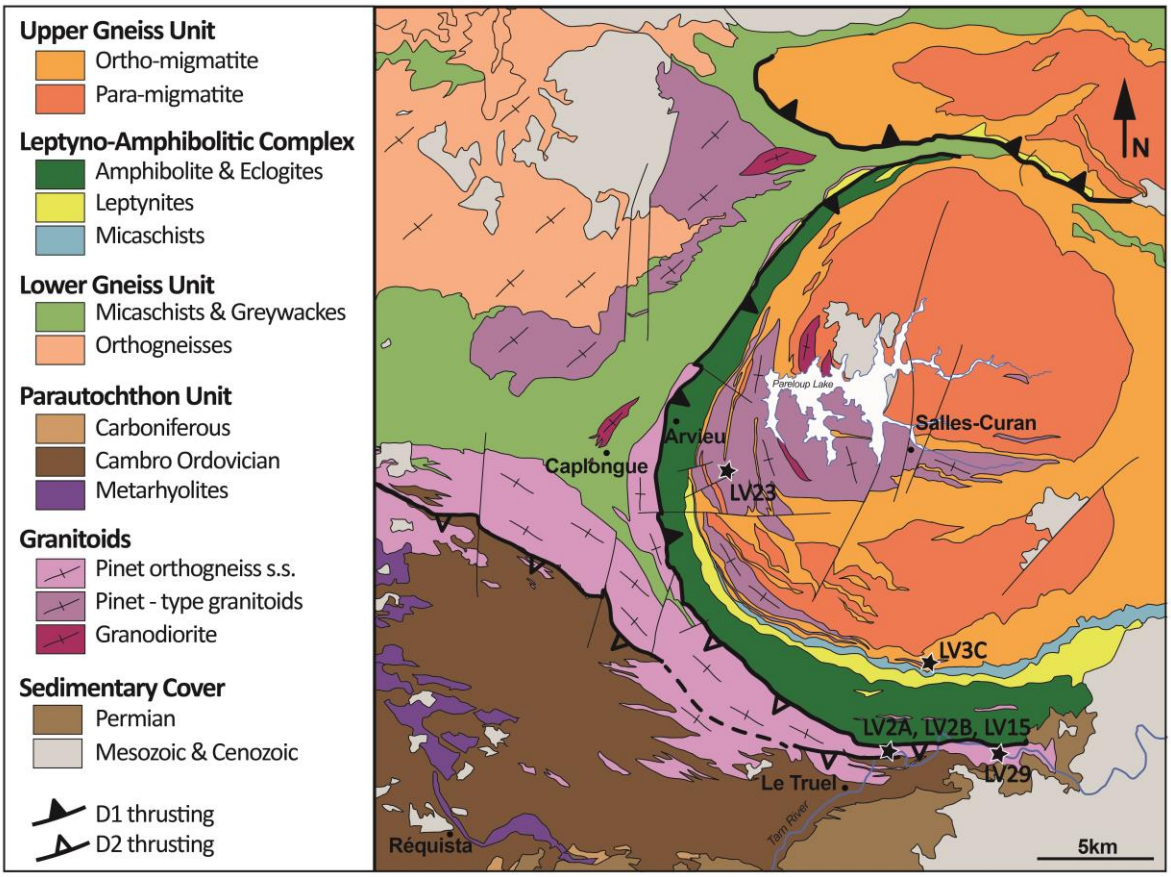

Figure III.1.2 - Simplified geological map of the Lévézou Massif (modified from Delor et al. 1989; Guérangé-Lozes et al. 1995; Duguet and Faure 2004). Black stars indicate sample locations.

The UGU forms the core of the Lévézou massif and is composed of paragneisses and felsic orthogneisses, migmatized to various degrees. The felsic orthogneisses, termed "Pinet-type granitoids" (cf. below) in the literature, are deformed calc-alkaline S-types granites (Nicollet 1978). Mafic enclaves with some relics of HP mineral assemblages, interpreted as xenoliths, are locally found within the orthogneisses (Delor et al. 1985) whose emplacement was considered to be Carboniferous in age (e.g. Pin 1981; Burg and Teyssier 1983).

The LGU outcrops in the western part of the massif. It is composed of amphibolite-facies metasedimentary rocks, mainly micaschists, metapelitic paragneisses, and metagreywackes, intruded by several granitoid bodies. The protholith ages of the Rodez

alkaline orthogneiss and the Caplongue metagranodiorite are considered to be Cambrian (U/Pb on zircon population, Lafon et al, 1984). The granitic Pinet orthogneiss s.s. forms an elongated body mostly parallel to the contact between the LAC and the LGU (Fig. III.1.2). Based on the analysis of the deformation patterns, Burg and Teyssier (1983), and Dutruge and Burg (1997) argued that this granite emplaced as a syntectonic laccolith. The emplacement of the granitic protolith of the Pinet orthogneiss was dated at ca. 360 Ma (Pin 1981). The combination of these two interpretations, if correct, is crucial since it linked the main episode of thrusting to the Variscan history of the Massif Central.

The PAU is the most external and less metamorphosed unit (Fig. III.1.2). It is composed of the so-called Saint-Sernin-sur-Rance nappe, including quartzo-pelitic rocks, micaschists and quartzites with intercalated Cambrian metarhyolites (Collomb 1970; Delbos et al. 1964). The presence of a contact metamorphism was described within the PAU along the contact with the Pinet orthogneiss (Nicollet 1978).

The different tectonic interpretations of the Lévézou massif all involve a first major thrusting event, responsible for the parallelism between foliations, lithological boundaries or major contacts, and related to the late Devonian – early Carboniferous Variscan collision that followed subduction of an oceanic crust and the related eclogite-facies metamorphism. Interpretations differ on the origin of the final dome-like shape of the massif, ranging from diapirism (Burg and Teyssier 1983; Burg 1987), recumbent fold nappe (Burg et al. 1986; Duguet and Faure 2004) or extensional gneiss dome (Burg et al. 1994).

3. Analytical procedures

Chemical and isotopic analyses

The samples were first cleaned from any weathered material, then crushed in a jaw crusher and in an agate mortar in order to obtain a fine powder. Major and trace elements analysis were performed by Inductively Coupled Plasma Atomic Emission Spectrometry (ICP-AES) and Inductively Coupled Plasma Mass Spectrometer (ICP-MS) respectively, at the Geochemical and Petrographical Research Center (SARM laboratory, CNRS-CRPG) in Nancy, following the procedure described in Carignan et al. (2001).

Whole rock Sm-Nd and Sr isotope analyses were carried out at the Geosciences Rennes Laboratory using a 7 collectors Finnigan MAT-262 mass spectrometer. For a complete procedure see Ballouard et al. (2015). The samples were analyzed together with the AMES Nd standard that yielded a mean $^{143}Nd/^{144}Nd$ ratio of 0.511973 (±4) and with the Sr

standard NBS 987 with a mean $^{87}Sr/^{86}Sr$ ratio of 0.710222 (±9). Blank analyses yield values of 160pg for Sr and 25pg for Nd and were therefore considered to be negligible. Data are plotted using the software GCDkit (Janoušek et al. 2006).

U-Th-Pb dating

A classic mineral separation procedure has been applied to concentrate the zircon grains for U-Pb dating using the facilities available at the University of Rennes. Rocks were crushed and only the powder fraction with a diameter < 250 µm has been kept. Heavy minerals were successively concentrated by Wilfley table and heavy liquids. Magnetic minerals were then removed with an isodynamic Frantz separator. Zircon grains were then handpicked under a binocular microscope. The selected grains were then embedded in epoxy mounts. The mounts were grounded and polished on a lap wheel. Zircon grains were imaged by cathodoluminescence (CL) using a Reliotron CL system equipped with a digital color camera available in Géosciences Rennes.

U-Pb geochronology of zircon grains was conducted by in-situ laser ablation inductively coupled plasma mass spectrometry (LA-ICP-MS) at Géosciences Rennes using a ESI NWR193UC Excimer laser coupled to an Agilent quadripole 7700x ICP-MS equipped with a dual pumping system to enhance sensitivity. The instrumental conditions are reported in the supplementary table III.1.1.

The ablated material is carried into helium, and then mixed with nitrogen (Paquette et al. 2014) and argon, before injection into the plasma source. The alignment of the instrument and mass calibration was performed before each analytical session using the NIST SRM 612 reference glass, by inspecting the ^{238}U signal and by minimizing the ThO+/Th+ ratio (<0.5%). During the course of an analysis, the signals of ^{204}(Pb+Hg), ^{206}Pb, ^{207}Pb, ^{208}Pb and ^{238}U masses are acquired. The occurrence of common Pb in the sample can be monitored by the evolution of the ^{204}(Pb+Hg) signal intensity, but no common Pb correction was applied owing to the large isobaric interference with Hg. The ^{235}U signal is calculated from ^{238}U on the basis of the ratio $^{238}U/^{235}U$=137.88. Single analyses consisted of 20s of background integration followed by 60s integration with the laser firing and then a 10 s delay to wash out the previous sample. Ablation spot diameters of 20 µm with repetition rates of 4 Hz were used. Data were corrected for U–Pb and Th–Pb fractionation and for the mass bias by standard bracketing with repeated measurements of the GJ-1 zircon standard (Jackson et al. 2004). Along with the unknowns, the zircon standard 91500 (1065 Ma, Wiedenbeck et al. 1995) was

measured to monitor precision and accuracy of the analyses and produced a concordia age of 1063.7 ± 4.8 Ma (N=27, MSWD=1.5) during the course of the analyses. Data reduction was carried out with the GLITTER® software package developed by the Macquarie Research Ltd. (Van Achterbergh et al. 2001). Concordia ages and diagrams were generated using Isoplot/Ex (Ludwig 2012). All errors given in supplementary table 2 are listed at one sigma, but where data are combined for concordia age or weighted mean calculations, the final results are provided with 95% confidence limits. Further information on the protocol can be found in Ballouard et al. (2015).

4. Petrography and geochemistry

Samples with various degrees of deformation were selected, in order to check the possible influence of the deformation on the geochemical and geochronological data: two macroscopically undeformed samples (LV3C, LV23) of the Pinet-type granitoids from the inner part (UGU) of the Lévézou massif, and one undeformed sample (LV2A), one augen orthogneisses (LV2B) and one mylonite (LV15) from the Pinet orthogneiss in the outer part (LGU) of the massif (Fig. III.1.2).

Inner undeformed porphyritic facies

Two rock samples from the core of the Lévézou massif (LV3C, LV23, Fig. III.1.2), although sampled at geographically distant locations (some 12 km apart), are petrographically almost identical. They represent a macroscopically undeformed isotropic coarse-grained porphyritic granite (Fig. III.1.3a) dominated by quartz, plagioclase, K-feldspar, biotite, and muscovite. The rocks appear undeformed, but thin section observations reveal abundant metamorphic textures. Quartz (up to 3 mm) forms recrystallized polycrystalline aggregates. Plagioclase forms polygonal to rectangular aggregates with straight outer limits, composed of a mosaic of granoblastic plagioclase interspersed with interstitial muscovite flakes (both ~0.1 mm). Subhedral K-feldspar phenocrysts (up to 3 cm) include crystals of biotite, and recrystallized quartz and plagioclase. K-feldspar is commonly surrounded by a rim of myrmekite. Biotite is present in two textural positions. Red-brown biotite (biotite 1) forms large thick flakes (up to 3 mm) and is locally surrounded by thin coronae of garnet (Fig. III.1.3e). Pale green biotite (biotite 2, up to 0.2 mm) is present in decussate sub-rectangular aggregates (up to 5 mm in size) with muscovite, garnet, kyanite, ±dravite, ±plagioclase,

±chlorite, ±hematite. These clusters are interpreted as pseudomorphs after cordierite (Fig. III.1.3f). In places, rutile (0.1 mm) builds up sub-rectangular aggregates (up to 0.5 mm) interpreted as pseudomorphs after ilmenite. Monazite, apatite and zircon are found as accessory minerals.

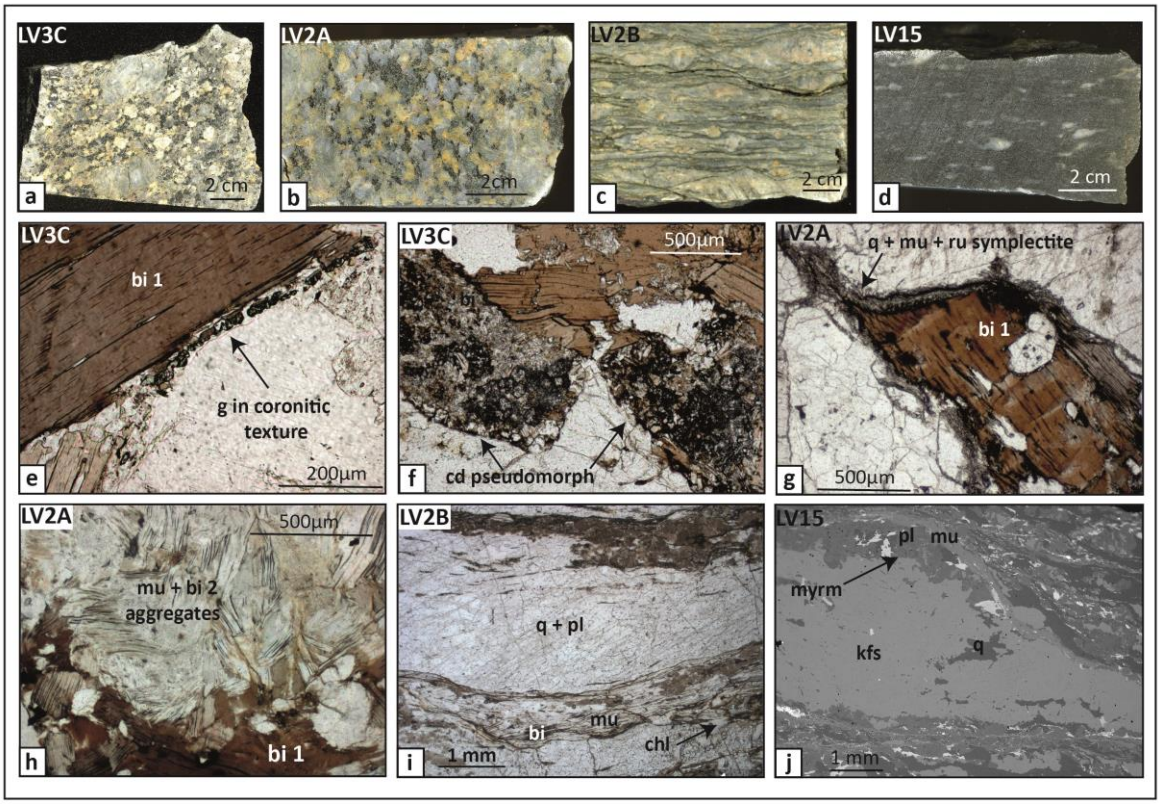

Figure 3*- a) Undeformed porphyritic facies of the inner Pinet-type granitoid (LV3C), b) undeformed porphyritic facies of the Pinet orthogneiss (LV2A), c) augen orthogneiss facies of the Pinet orthogneiss (LV2B), d) ultramylonite facies of the Pinet orthogneiss (LV15), e) garnet corona around primary biotite (bi 1; LV3C) f) cordierite pseudomorphed by fine-grained garnet + muscovite + kyanite in LV3C, g) quartz + muscovite + rutile symplectite surrounding a primary biotite crystal displaying several kink-bands (LV2A), h) muscovite and secondary biotite aggregate in LV2A, i) chlorite, muscovite and biotite foliation surrounding quartz, plagioclase and K-feldspar augen in LV2B, j) K-feldspar porphyroclast surrounded by myrmekite and muscovite-bearing foliation in LV15. bi – biotite, cd – cordierite, chl – chlorite, g – garnet, kfs – K-feldspar, mu – muscovite, myr – myrmekite, pl – plagioclase, q – quartz, ru – rutile.*

Outer undeformed porphyritic facies

Sample LV2A (Fig. III.1.3b) is a coarse-grained (2-10 mm) porphyritic granite mainly composed of quartz, plagioclase, porphyritic K-feldspar (up to 15 cm) and biotite. It bears some resemblance with the undeformed samples from the UGU (LV3, LV23), described above. Macroscopically, this sample appears isotropic, but various deformation and

recrystallization features can be observed in thin section. K-feldspar forms large subhedral crystals with undulose extinction, locally cut by fractures filled with fine-grained quartz. Plagioclase forms subhedral crystals (up to 10 mm) that are generally partly altered to a mixture of tiny crystals of muscovite. Quartz is present as remnants of large anhedral crystals (up to 10 mm) with undulous extinction systematically surrounded by a mosaic of recrystallized grains with irregular grain boundaries. Large thick red-brown biotite (biotite 1, up to 5 mm) displays undulous extinction, is in general affected by numerous kink-bands and locally surrounded by fine-grained symplectites containing quartz, rutile and muscovite (Fig. III.1.3g). It is interpreted as a primary magmatic phase. Smaller light green to pale brown biotite flakes (biotite 2, up to 0.3 mm), interpreted as secondary, are present in sub-rectangular cm-sized decussate aggregates with muscovite (0.05-2 mm), and locally garnet, quartz and plagioclase (Fig. 3h). These aggregates may represent pseudomorphs after another "primary" mineral, possibly cordierite. Rutile (~0.1 mm) forms polycrystalline sub-rectangular to polygonal aggregates (up to 1 mm), interpreted as pseudomorphs after ilmenite. Monazite, zircon and apatite are also present.

Outer augen orthogneiss (Pinet orthogneiss)

The rock (samples LV29 and LV2B, Fig. III.1.3c) is a well-foliated felsic augen orthogneiss containing porphyroclasts (up to several cm) of K-feldspar and plagioclase. It represents the most common facies of the Pinet-type granitoids. The foliation is defined by alternating layers, up to 2 mm thick, dominated either by quartz, or feldspar or phyllosilicates (biotite, muscovite and chlorite) and by the alignment of the latters (Fig. III.1.3i). The foliation wraps augen composed of subhedral relics of K-feldspar or plagioclase (up to 3 cm), commonly partly recrystallized in strain shadows. The porphyroclasts are locally broken with quartz and chlorite crystallizing in the fractures. Biotite is strongly chloritised and chlorite in the foliation is interspersed by numerous tiny needles of rutile (sagenite) suggesting that it developed at the expense of biotite. Muscovite forms either large crystals (up to 1 mm) that can be kinked and wrapped by the foliation, or small flakes (up to 0.1 mm) recrystallized in the foliation and commonly surrounding chloritised biotite. Allanite, titanite, apatite, zircon and rutile are also locally present.

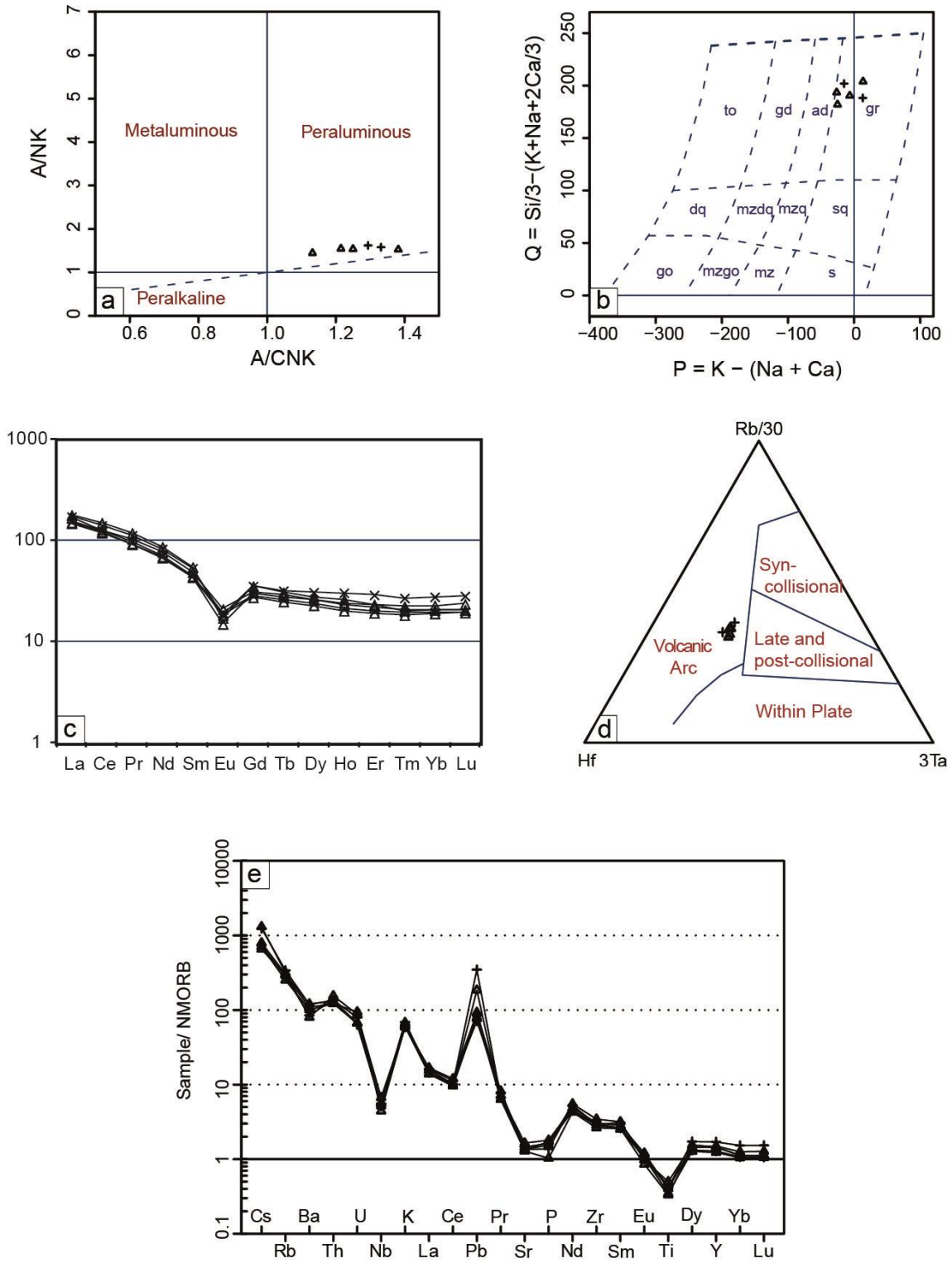

Figure III.1.4 - Geochemical characteristics of the studied samples. Triangles and crosses correspond to outer (LV2A, LV2B, LV15, LV29) and inner (LV3, LV23) samples, respectively. a) Shand (1943) diagram (A/CNK = Al_2O_3/(CaO + Na_2O + K_2O); A/NK = (Al_2O_3/Na_2O + K_2O)), b) P-Q diagram after Debon and Lefort (1982), gr – granite, ad – adamellite, c) chondrite-normalized REE distribution of all samples, values are normalized after Barrat et al. (2012), d) ternary tectonic discrimination diagram from Harris et al. (1986), e) N-MORB-normalized spider diagram after Sun and McDonough (1989).

Outer ultramylonitic facies

This sample (LV15) is a fine-grained ultramylonite with rare K-feldspar augen (Fig. 3d). The macroscopic fabric of the rock is defined by closely spaced (~5 mm) thin shear bands marked by very fine-grained (~0.01 mm) biotite, commonly associated with muscovite, quartz and feldspar. Thin (up to 0.3 mm) ribbons of strongly elongated quartz wrap small (up to 0.5 mm) crystals of K-feldspar and plagioclase. They are oblique to the shear-bands and together with crystals of muscovite (up to 0.5 mm long) define a foliation. K-feldspar forms rare porphyroclasts (up to 1 cm), commonly rimmed by myrmekite and recrystallized in strain shadows (Fig. III.1.3j). Chlorite is locally present in fractures in K-feldspar. Titanite, rutile, apatite, zircon and allanite are locally present.

Whole-rock compositions

These samples have the composition of a slightly peraluminous granite (A/CNK = 1.12-1.38; Fig. III.1.4 a,b; table III.1.1). They bear the general characteristics of the calc-alkaline series: (i) high abundances of Th and LREE (La_N ~145-180), (ii) moderate fractionation of LREE vs. HREE (La_N/Lu_N ~6.1-8.7) and a lack of important fractionation among the HREE (Fig. 4c), and (iii) significant negative (Ta, Nb, Ti) and positive (Pb) anomalies (Fig. III.1.4e). The chondrite-normalized REE patterns display the same trend for all the samples (including the same Eu anomaly range: Eu_N=0.022-0.032) regardless of the deformation intensity (Fig. III.1.4c). Taken together, the studied granites and granitic orthogneisses from the UGU and LGU have the same compositions, and deformation was not accompanied by a significant element mobility, with respect to the REE (Fig. III.1.4c). The homogeneity of the whole rock compositions of these different samples is also highlighted in the triangular Rb-Hf-Ta discrimination diagram (Harris et al. 1986, Fig III.1.4d). They fall into the “volcanic arc” domain, an expected result considering their calc-alkaline character (e.g. Ballèvre et al. 2012). Nevertheless, the tectonic setting can be either an active continental margin or the reworking of an older arc during a rifting event.

Table III.1.1 - Whole-rock chemical compositions of the samples from outer (LV2A, LV2B, LV15, LV29) and inner (LV3, LV23) samples

Sample		**Outer Samples**				**Inner Samples**	
		LV 2A	**LV 2B**	**LV 15**	**LV 29A**	**LV 23**	**LV 3C**
SiO2	wt.%	70.43	71.24	71.31	68.63	70.30	68.65
Al2O3	wt.%	14.59	14.39	13.64	14.36	14.34	14.61
Fe2O3	wt.%	3.55	3.20	3.24	4.34	3.82	3.80
MnO	wt.%	0.03	0.04	0.03	0.05	0.05	0.05
MgO	wt.%	1.13	0.95	0.94	1.42	1.20	1.14
CaO	wt.%	1.20	0.54	1.44	1.39	1.23	0.95
Na2O	wt.%	2.65	2.51	2.88	2.83	2.58	2.34
K2O	wt.%	4.73	4.90	4.34	4.29	4.25	4.98
TiO2	wt.%	0.51	0.44	0.42	0.63	0.52	0.55
P2O5	wt.%	0.21	0.20	0.12	0.18	0.16	0.19
LOI	wt.%	1.70	2.05	1.29	1.68	1.57	1.73
FeO	wt.%	2.31	1.86	2.48	X	2.68	2.62
As	ppm	6.14	10.76	2.43	7.70	3.49	13.87
Ba	ppm	760.70	685.30	635.00	503.80	535.20	748.60
Be	ppm	2.41	2.41	2.10	2.62	2.73	2.45
Bi	ppm	0.19	0.23	bdl	0.63	0.29	0.17
Cd	ppm	0.27	0.31	0.20	0.32	0.25	0.37
Ce	ppm	76.73	73.50	71.69	89.71	84.65	76.38
Co	ppm	6.01	6.12	5.02	8.45	6.32	6.05
Cr	ppm	49.31	56.71	39.03	67.31	41.15	48.47
Cs	ppm	5.57	4.60	4.98	9.16	5.13	8.72
Cu	ppm	14.46	12.77	7.11	26.71	16.35	11.96
Dy	ppm	6.58	5.78	6.52	7.08	7.83	6.01
Er	ppm	3.59	3.19	3.86	3.79	4.81	3.32
Eu	ppm	1.23	1.07	0.87	1.00	1.09	1.13
Ga	ppm	20.96	20.56	19.18	21.25	20.40	21.20
Gd	ppm	6.42	5.62	6.24	7.28	7.31	5.91
Ge	ppm	1.55	1.29	1.63	1.50	1.46	1.66
Hf	ppm	5.94	5.62	5.30	6.96	6.04	5.90
Ho	ppm	1.30	1.14	1.36	1.48	1.72	1.20
In	ppm	0.08	0.08	bdl	0.07	bdl	0.09
La	ppm	39.27	35.37	34.74	42.02	40.53	36.27
Lu	ppm	0.51	0.48	0.58	0.51	0.70	0.48
Mo	ppm	1.17	bdl	1.00	1.22	0.56	bdl
Nb	ppm	12.97	12.08	10.31	15.64	12.45	13.02
Nd	ppm	35.57	32.02	31.27	40.20	38.41	33.00
Ni	ppm	14.15	14.69	11.11	18.53	12.97	14.90
Pb	ppm	27.84	55.37	24.00	26.94	21.40	104.35
Pr	ppm	9.44	8.52	8.33	10.80	10.24	8.82
Rb	ppm	169.40	163.10	141.20	176.90	157.70	190.10
Sc	ppm	8.46	7.37	8.74	10.92	8.33	9.70
Sb	ppm	bdl	0.81	bdl	0.68	bdl	1.42
Sm	ppm	7.45	6.61	6.77	8.34	8.13	6.90
Sn	ppm	2.71	3.30	2.16	4.22	2.99	3.60
Sr	ppm	148.00	119.90	115.60	121.90	122.00	131.20
Ta	ppm	1.13	1.11	1.04	1.34	1.02	1.23
Tb	ppm	1.09	0.93	1.04	1.15	1.20	0.97
Th	ppm	15.76	14.69	14.62	18.64	16.48	16.21
Tm	ppm	0.54	0.48	0.58	0.53	0.71	0.51
U	ppm	3.18	3.12	4.44	4.11	3.00	3.73
V	ppm	45.00	37.76	31.54	51.61	41.75	48.41
W	ppm	1.62	4.13	0.95	1.22	1.25	1.72

Table III.1.1 - continued

Sample		Outer Samples				Inner Samples	
		LV 2A	**LV 2B**	**LV 15**	**LV 29A**	**LV 23**	**LV 3C**
Y	ppm	40.33	34.45	42.06	40.76	47.67	35.98
Yb	ppm	3.437	3.182	3.831	3.44	4.656	3.275
Zn	ppm	63.97	122.8	54.15	94.69	63.84	118.1
Zr	ppm	226.9	211.4	194.6	255	215.4	219.9
Total	%	100.74	100.45	99.65	99.79	100	98.97
A/NK		1.97	1.94	1.89	2.02	2.10	1.99
A/CNK		0.55	0.54	0.52	0.69	0.64	0.59

LOI: Loss on ignition, bdl: below detection limit; A/NK: molar $Al_2O_3/(Na_2O + K_2O)$; A/CNK: molar $Al_2O_3/(CaO + Na_2O + K_2O)$; Fe_2O_3 corresponds to total Fe; FeO to Fe^{2+} only, analysed by titration.

Rb-Sr and Sm-Nd radiogenic isotopes

Sr and Sm-Nd isotopic analyses for the 6 samples are listed in table 2 and reported in Fig. 5. The ε_{Nd} and $^{87}Sr/^{86}Sr$ (I_{Sr}) values have been recalculated for an age of 470 Ma (see part 6). ε_{Nd} values are comprised between -5.66 and -5.29 for the six samples. I_{Sr} vary from 0.705635 to 0.714268. The T_{DM} (model age, calculated after Liew & Hoffman 1988) values vary from 1567 to 1596 Ma.

The ε_{Nd} values display very little variation, as usually observed within the same pluton (e.g. Ballouard et al. 2015). In contrast, I_{Sr} values are more spread (Fig. III.1.6). Rubidium and strontium are known to be mobile under metamorphism, deformation or fluid alteration. Moreover, a large range of I_{Sr} can also reflect variable sedimentary sources involved in magma production. The range of values is then likely explained by the highly variable patterns of deformation that affected the different facies, by alteration, or by its sedimentary origin (see part 4 - Whole-rock compositions). Finally, the samples yield the same model age range. Considering the large range of inherited zircon cores (see part 5 - U-Th-Pb Dating) and the peraluminous character of the rocks (see part 4 - Whole-rock compositions), reworking of multiple sedimentary sources is the most likely explanation for these old ages, and these T_{DM} should then be seen as a mean age of the sedimentary source rather than as an extraction age from the mantle.

Table III.1.2 - Rb–Sr and Sm–Nd whole-rock data for the samples from outer (LV2A, LV2B, LV15, LV29) and inner (LV3, LV23) samples.

Sample	Rb (ppm)	Sr (ppm)	$^{87}Rb/^{86}Sr$	$^{87}Sr/^{86}Sr$	±	I Sr_{470}	Sm (ppm)	Nd (ppm)	$^{147}Sm/^{144}Nd$	$^{143}Nd/^{144}Nd$	±	$\varepsilon_{Nd\ (470)}$	T
Outer samples													
LV 2A	169.40	133.9	3.67	0.733146	10	0.708563	6.9	35.1	0.118651	0.512110	4	−5.62	1.
LV 2B	163.10	107.1	4.42	0.735226	10	0.705635	6.1	30.6	0.121020	0.512118	5	−5.61	1.
LV 15	115.60	105.7	3.17	0.734002	10	0.712742	6.5	31.6	0.124813	0.512141	4	−5.38	1.
LV 29A	176.90	117.2	4.38	0.736913	10	0.707572	8.1	42.0	0.116544	0.512117	5	−5.35	1.
Inner samples													
LV 3C	141.20	118.2	3.47	0.737488	10	0.714268	6.4	32.6	0.118418	0.512107	5	−5.66	1.
LV 23	157.70	117.9	3.88	0.733453	12	0.707455	7.5	38.7	0.116902	0.512122	4	−5.29	1.

Rb concentrations have been obtained by ICP-MS, other concentrations by isotopic dilution. ε_{Nd} and $^{87}Sr/^{86}Sr$ are calculated with an age of 470 Ma. $^{87}Rb/^{86}Sr$ ratios are calculated after Janoušek et al. (2015, p.54, equation 5.4) and the two stage T_{DM} model age after Liew and Hoffmann (1988)

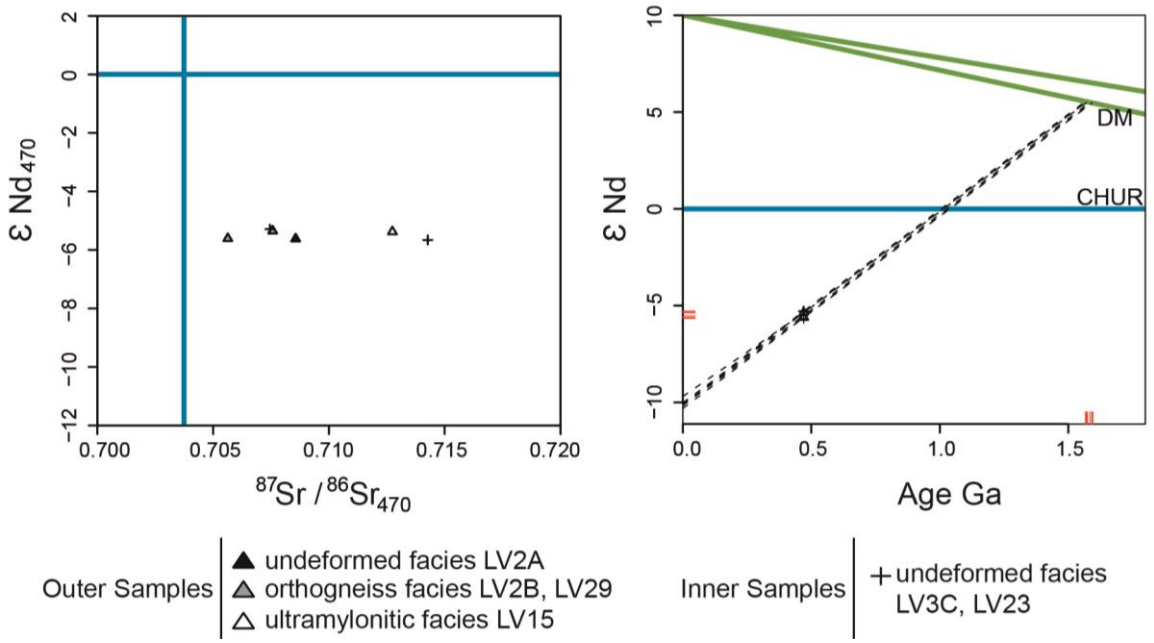

Figure III.1.5 - a) Sr and Nd isotope composition of the samples. ε_{Nd} and $^{87}Sr/^{86}Sr$ are calculated with an age of 470 Ma (see part 6). Crosses represent the undeformed samples outcropping in the inner part of the massif (LV3C, LV23) and triangles correspond to the samples from the outer part (Pinet orthogneiss s.s., LV2A, LV2B, LV29 and LV15). b) Two stage T_{DM} model age, calculated after Liew and Hoffmann (1988). Marks on x and y-axis correspond to the two stage Nd model age and ε_{Nd} initial values, respectively. CHUR – Chondritic Uniform Reservoir; DM – Depleted Mantle.

5. U-Th-Pb Dating

Zircon crystals were extracted from samples LV2A, LV2B, LV15 and LV3C, located on both sides of the LAC (Fig. III.1.2). All crystals were translucent and colorless, with heterogeneous shapes from rounded to euhedral, ranging from 100 to 400 µm in size. Most of the grains have inherited cores surrounded by magmatic rims (Fig.III.1. 6 a,b,d). Locally, inherited cores are surrounded by a primary zonation, and by a magmatic rim, as revealed by cathodolumiscence imaging (Fig. III.1.6b). Numerous purely magmatic zircon crystals are also found (Fig. III.1.6c).

Most of the inherited cores show high degrees of discordance (see supplementary table 2) and it is therefore impossible to discuss them in terms of provenance. All data that are more than 90% concordant (and less than 110%) are plotted in a kernel density estimates diagram (Fig. 7e). Apart from the magmatic rim that will be discussed later, a first group of inherited cores provides apparent ages between 500 and 760 Ma. A second group is bracketed around 1 Ga, while the remaining data yield apparent ages between 1700 and 3200 Ma.

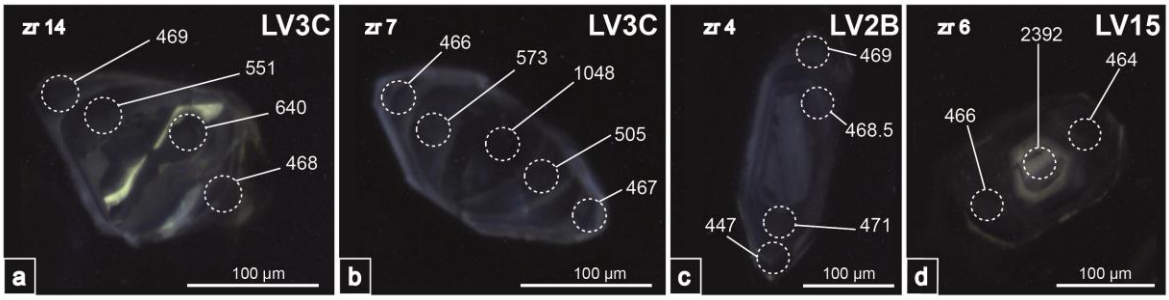

Figure III.1.6 - Selected cathodoluminescence images of zircon crystals from samples LV3C (a, b), LV2B (c) and LV15 (d). Dotted circles show the location of the LA-ICP-MS analyses and their corresponding $^{238}U/^{206}Pb$ ages.

Inner undeformed porphyritic facies

Sixty-six analyses were performed out of 18 different zircon grains from sample LV3C (supplementary table III.1.2). Apart from the inherited core discussed above, 33 analyses performed on magmatic zircon crystals without inherited core and/or on crystal rims plot in concordant to discordant position (Fig. 7a) due to various degrees of Pb loss and/or to the presence of common Pb. Nevertheless, all these analyses have very consistent $^{206}Pb/^{238}U$ dates and provide a lower intercept date of 466.6 ± 3.3 Ma (MSWD=0.14). The five most

concordant analyses yield a concordia date of 467.8 ± 2.3 Ma (MSWD=0.3). It has to be noticed that one single analysis performed on a rim (supplementary table 2, 18b) plots in an apparently concordant position at 414.1 ± 4.7 Ma. But another spot (18a) realized on the same rim from the same grain yields a concordant date of 468.7 ± 5.3 Ma. We conclude therefore that the younger date is linked to a slight Pb loss.

Outer undeformed porphyritic facies

Sixty-nine analyses were performed out of 38 zircon grains in sample LV2A (supplementary table 2). All magmatic rims yield $^{206}Pb/^{238}U$ dates bracketed around 470 Ma (Fig. III.1.7b and e) and allow to calculate a lower intercept date of 468.2 ± 2.7 Ma (MSWD=0.7; N=34). The 10 most concordant data (Fig. III.1.7b) yield a concordia date of 469.8 ± 1.6 Ma (MSWD=0.56) while the remaining analyses are slightly discordant due to the presence of a small amount of common Pb and/or Pb loss.

Outer orthogneissic facies (Pinet orthogneiss)

In the augen orthogneiss LV2B, 16 zircon grains were analyzed (supplementary table 2, Fig.7c). Most of the 30 analyses display discordant dates. The 4 youngest concordant analyses allow to calculate a concordia date of 469.8 ± 2.7 Ma (MSWD=0.26). Six concordant to discordant analyses allow to calculate a lower intercept date of 470.5 ± 5.2 Ma (MSWD=0.30), the same within error as the calculated concordia date. Eight of the remaining analyses are discordant, ranging from 420 to 480 Ma, and can be explained by variable lead loss and common lead enrichment. Twelve rim analyses range from 496 to 765 Ma.

Outer ultramylonitic facies

Eighty-two analyses on 30 different zircon crystals were performed for sample LV15. A group of 31 concordant to discordant analyses (common Pb and/or Pb loss) allow to calculate a lower intercept date of 465.6 ± 2.6 Ma (MSWD=0.66). An equivalent (within the error) concordia date was calculated with the 5 concordant spots, yielding a date of 468 ± 1.3 Ma (MSWD=0.98) (Fig. 7d). Three analyses display younger dates ranging from 427 to 311 Ma ($^{206}Pb/^{238}U$), which can be explained by a combination of lead loss and common lead enrichment.

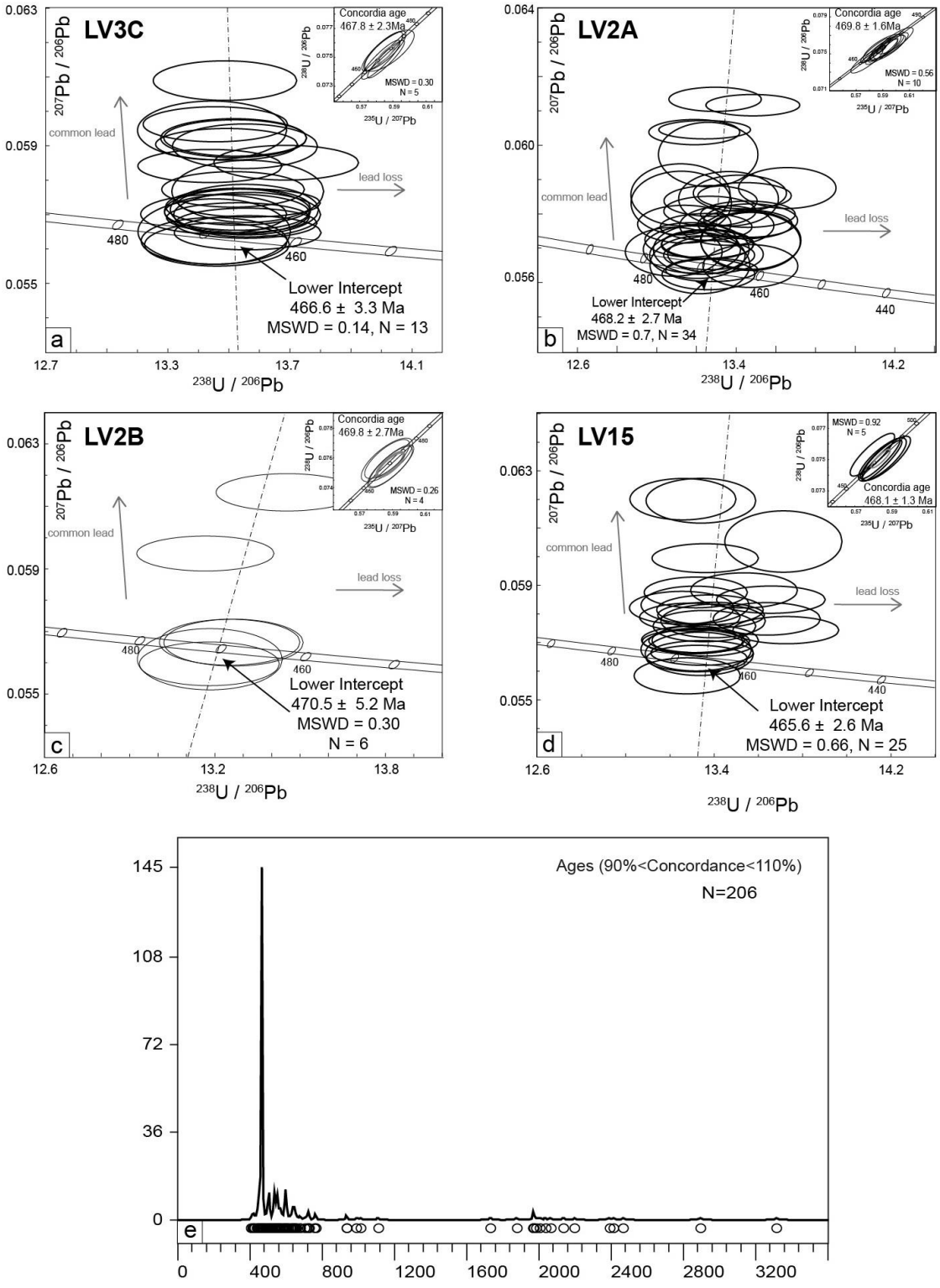

Figure III.1.7 - Tera-Wasserburg ($^{207}Pb/^{206}Pb$ vs $^{238}U/^{206}Pb$) and Wetherill ($^{238}U/^{206}Pb$ vs $^{235}U/^{207}Pb$) Concordia diagrams displaying Ordovician analyses made on zircon from samples a) LV3C, b) LV2A, c) LV2B, d) LV15. e) Kernel diagram (Vermeesch 2012) on the U/Pb data from this study (90% to 110% concordance only).

Inherited cores from all the four samples range from 500 Ma to 3 Ga, show various lead loss, and display concordant to discordant dates. Three populations can be distinguished in the inherited cores and primary zonation: (i) few Precambrian dates, from ca. 3.3 to 1 Ga, in discordant position, (ii) Precambrian dates from ca 770 to 550 Ma, in concordant to sub concordant position, and (iii) few Cambrian dates ranging from 550 to 500 Ma (Fig. 7e). All the rims of the zircon grains with inherited cores recorded an Ordovician event at ca. 470 Ma. Besides, all zircon crystals without inherited cores yield equivalent ages (within error) at ca. 470 Ma, obtained by lower intercepts in Tera-Wasserburg diagrams and by concordia dates (Fig. 7a-d). In conclusion, all analyzed samples, regardless of their position with respect to the LAC and the deformation intensity, yield the same Ordovician age of ca. 470 Ma, interpreted as the age of the emplacement of the granitic protoliths.

6. Discussion

The Pinet-type granitoids: Ordovician intrusions

An Ordovician event around 470 Ma is recorded by all the granitoid samples, independently from the facies from which they were extracted, the presence or absence of inherited cores in the studied zircon crystals, or the deformation intensity. As both undeformed and ultramylonitic samples provide the same age, the U-Pb chronometer has not been affected by deformation. Previous dating of the Pinet orthogneiss (ca. 360 Ma, Pin 1981) was performed on zircon fractions, meaning that a large amount of grains has been dissolved and then dated. Pin noticed the presence of inherited cores in some of the crystals, but, although he tried to avoid them during the picking, the data obtained plot systematically in a discordant position with evidence for mixing between a magmatic age and different apparent inherited ages. In addition, Pb-loss is evidenced by the lack of a simple linear array and the proposed age of ca. 360 Ma (lower intercept) is mostly constrained by the analysis of one fraction of apatite crystals that plots also in a discordant position. Consequently, the proposed ca. 360 Ma age for the emplacement of the protolith of the Pinet orthogneiss must be discarded and the Pinet orthogneiss cannot be syn-kinematic with respect to the late Devonian – early Carboniferous thrusting events as previously suggested (Burg and Teyssier 1983; Burg 1987; Dutruge and Burg 1997; Duguet and Faure 2004). Considering the gradual transition observed by Nicollet (1978) between the Pinet orthogneiss and the metarhyolite from the PAU, the Cambrian Rb/Sr age (Delbos et al. 1964) of the latter should also be reconsidered.

Tectonic and geodynamic implications for the Lévézou massif

Both the inner and the outer granitoids/orthogneisses display the same age, the same textures, the same chemical composition, the same REE spectrum, the same radiogenic isotope values and the same T_{DM} age. Consequently, all these granitoids originated from the same magmatic source. The Pinet-type granitoids therefore belong to the Ordovician magmatic event that is well-documented at the scale of the Variscan orogen (see Introduction). The precise geodynamic context of this event (i.e. extended continental margin, back arc basin) is debated, although most interpretations consider that magmatism resulted from extreme lithosphere thinning (Gondwana breakup, opening of the Rheic ocean) during Ordovician times (e.g. Lardeaux 2014). The 470 Ma age obtained on the granitoids of the Lévézou massif is markedly older than the 460-455 Ma age obtained on the orthogneisses from the Montagne Noire ~50 km farther to the south, suggesting a migration of the magmatic source during the Ordovician extension.

The occurrence of similar granitoids of the same age on each side of the LAC suggests two end-member interpretations. (1) The UGU and LGU in the Lévézou massif were originally two continental margins of an ocean or a back-arc basin during Ordovician times. The stacking of the UGU, LAC and LGU occurred during the Variscan tectonics. (2) The UGU and LGU were originally a single Ordovician unit (a continental margin or an arc) and the LAC represented the adjacent oceanic crust that was under- or overthrusted during early Variscan tectonics, resulting in a major tectonic contact. The occurrence of this single unit on each side of the LAC requires either isoclinal nappe refolding as previously proposed (Burg and Teyssier 1983) or tectonic duplication by superimposed shearing events during ongoing Variscan tectonics. The identical isotopic signature of the granitoids on each side of the LAC favours the single-unit hypothesis (2). However, in order to settle the tectonic interpretation, new quantitative PT and age data on other metamorphic rocks are required. This work, dedicated to comparing the metamorphic evolution of the orthogneisses and adjacent rocks on both sides of the LAC, is in progress.

7. Conclusion

New U-Pb ages of ca. 470 Ma of the granitoids from the Lévézou massif in the southern Massif Central reveal that these intrusions belong to the major magmatic event that developed throughout the European Variscan belt during the Early-Middle Ordovician extensional tectonics. As a consequence, the Pinet-type orthogneisses are not syn-tectonic intrusions emplaced during the late Devonian-Early Carboniferous Variscan collision, as previously thought. The similar ages, chemical compositions and isotopic signatures of these granitoids in the Lévézou massif as a whole strongly suggest that the Lower and Upper gneissic units (UGU and LGU), on each side of the leptyno-amphibolitic complex (LAC) were originally a single unit, tectonically duplicated either by isoclinal folding or thrusting during the Variscan tectonics.

Acknowledgements

We sincerely thank X. Le Coz and Y. Lepagnot for the sample preparation, J. Langlade for the assistance with microprobe analysis, and D. Vilbert for the Sm/Nd and Sr isotopic analysis. V. Janoušek and P. Boulvais are thanked for helpful discussions about the whole-rock and isotopic geochemistry. Constructive reviews of P. Jeřábek and J.M. Lardeaux helped to improve the manuscript.

References

Abati J, Dunning GR, Arenas R, García FD, Cuadra PG, Catalán JM, Andonaegui P (1999) Early Ordovician orogenic event in Galicia (NW Spain): evidence from U–Pb ages in the uppermost unit of the Ordenes Complex. Earth and Planetary Science Letters 165:213-28.

Ballèvre M, Bosse V, Ducassou C, Pitra P (2009) Palaeozoic history of the Armorican Massif: Models for the tectonic evolution of the suture zones. C. R. Geoscience 341:174-201.

Ballèvre M, Fourcade S, Capdevila R, Peucat JJ, Cocherie A, Fanning CM (2012) Geochronology and geochemistry of Ordovician felsic volcanism in the Southern Armorican Massif (Variscan belt, France): Implications for the breakup of Gondwana. Gondwana Research 21:1019-36.

Ballèvre M, Martínez Catalán JR, López-Carmona A, Pitra P, Abati J, Díez Fernández R, Ducassou C, Arenas R, Bosse V, Castiñeiras P, Fernández-Suárez J, Gómez Barreiro J, Paquette J-L, Peucat J-J, Poujol M, Ruffet G, Sánchez Martínez S (2014) Correlation of the nappe stack in the Ibero-Armorican arc across the Bay of Biscay: a joint French-Spanish project. In: Schulmann K, Martínez Catalán JR, Lardeaux J-M, Janoušek V, Oggiano G (eds) The Variscan Orogeny: Extent, Timescale and the Formation of the European Crust . Geol Soc London 405:77-113.

Ballouard C, Boulvais P, Poujol M, Gapais D, Yamato P, Tartèse R, Cuney M (2015) Tectonic record, magmatic history and hydrothermal alteration in the Hercynian Guérande leucogranite, Armorican Massif, France. Lithos 220–223:1–22.

Bard JP, Burg JP, Matte P, Ribeiro A, (1980) La Chaîne Hercynienne d'Europe Occidentale en termes de tectonique des plaques. Int. Geol. Congr., 26th, Mém. BRGM, Paris 108:233–246.

Barrat JA, Zanda B, Moynier F, Bollinger C, Liorzou C, Bayon G. (2012) Geochemistry of CI chondrites: Major and trace elements, and Cu and Zn Isotopes. Geochimica et Cosmochimica Acta 83:79-92.

Berger J, Féménias O, Ohnenstetter D, Bruguier O, Plissart G, Mercier JC, Demaiffe D (2010a) New occurrence of UHP eclogites in Limousin (French Massif Central): Age, tectonic setting and fluid–rock interactions. Lithos 118:365-382.

Briand B, Piboule M, Bouchardon JL (1988) Diversité géochimique des métabasites des groupes leptyno-amphiboliques du Rouergue et de Marvejols (Massif central). Origine et implications.Bull. Soc. Géol. France 8:489-498.

Burg JP, Ph. Matte P (1978) A cross section through the French Massif Central and the scope of its Variscan evolution. Z. Dtsch. Geol. Ges. 129:429–440.

Burg JP, Teyssier C (1983) Contribution à l'étude tectonique et microtectonique des séries cristallophyliennes du Rouergue oriental : la déformation des laccolites syntectoniques, type Pinet. Géol. France 1:3-30.

Burg JP, Delor C, Leyreloup A (1986) Le massif du Lévezou et les séries adjacentes du Rouergue oriental. Nouvelles données pétrographiques et structurales. Géol. France 3:229-272.

Burg JP (1987) Regional shear variation in relation to diapirism and folding. J. Struct. Geol. 9:925-934.

Burg JP, Van Den Driessche J, Brun JP (1994) Syn-to post-thickening extension in the Variscan Belt of Western Europe: modes and structural consequences. Géol. France 3:33-51.

Carignan J, Hild P, Mevelle G, Morel J, Yeghicheyan D (2001) Routine analyses of trace elements in geological samples using flow injection and low pressure on-line liquid chromatography coupled to ICP-MS: a study of geochemical reference materials BR, DR-N, UB-N, AN-G and GH. Geostandards Newsletter 25:187-198.

Collomb P (1970) Etude géologique du Rouergue cristallin. Mém. Expl. Serv. Carte géol. France, Paris.

Crowley QG, Floyd PA, Winchester JA, Franke W, Holland JG (2000) Early Palaeozoic rift-related magmatism in Variscan Europe: fragmentation of the Armorican Terrane Assemblage. Terra Nova 12(4):171-180

Debon F, Le Fort P. (1983) A chemical–mineralogical classification of common plutonic rocks and associations. Transactions of the Royal Society of Edinburgh: Earth Sciences 73:135-49.

Delbos L, Lasserre M, Roques M (1964) Géochronologie et rétromorphose dans la série cristallophyllienne du Rouergue (Massif central français). Sciences de la Terre 10:329–342.

Del Greco K, Johnston ST, Shaw J (2016) Tectonic setting of the North Gondwana margin during the Early Ordovician: A comparison of the Ollo de Sapo and Famatina magmatic events. Tectonophysics 681:73-84

Delor C, Leyreloup A, Burg JP (1985) Nouveaux arguments pétrologiques enfaveur de l'allochtonie du Lévézou (Massif Central français): les enclaves basiques des granites calco-alcalins et les métacornéennes associées. C. R. Acad. Sci. Paris 301:1037–1042.

Delor C, Burg JP, Leyreloup A, Teyssier C (1989) Carte géol France (1/50000), feuille Salles Curan(908). Orléans: BRGM

Dewey JF, Burke KCA (1973) Tibetan, Variscan, and Precambrian Basement Reactivation: Products of Continental Collision. The Journal of Geology 81:683-692.

Ducrot J, Lancelot JR, Marchand J (1983) Datation U-Pb sur zircons de l'éclogite de la Borie (Haut-Allier, France) et conséquences sur l'évolution anté-hercynienne de l'Europe occidentale. Earth Planet. Sci. Lett. 18:97-113.

Duguet M, Faure M (2004) Successive shearing tectonics during the hercynian collisional evolution of the southwestern French Massif Central. Bull. Soc. Geol. France 175:49–59.

Dutruge G, Burg JP (1997) Strain localisation in an orthogneiss laccolith (the Pinet massif, Aveyron, southern France). Tectonophysics 280:47–60.

Forestier FH (1961) Métamorphisme hercynien et antéhercynien dans le bassin du haut-Allier (Massif Central français), PhD Thesis, Clermont-Ferrand University .

Forestier FH, Lasnier B, Leyreloup A, Marchand J (1973) Vues nouvelles sur la catazone dans le Massif Central français et le Massif Armoricain de l'affleurement au Moho. Bull. Soc. Géol. France 15:562–578.

Franke W (2006) The Variscan orogen in Central Europe: construction and collapse. Memoirs Geol Soc London 32:333-343.

Guérangé-Lozes J, Burg JP, Vinchon C, Alabouvette B, Defaut B, Astruc JG, Galharague J, Leyreloup

A,Michard AG, Perrin C, Servelle S (1995), Carte géol France (1/50000), feuille Requista(934). Orléans: BRGM

Harris NB, Pearce JA, Tindle AG (1986) Geochemical characteristics of collision-zone magmatism. Geol Soc London, Special Publications 19:67-81.

Helbing H, Tiepolo M (2005) Age determination of Ordovician magmatism in NE Sardinia and its bearing on Variscan basement evolution. Journal of the Geological Society 162:689-700

Jackson SE, Pearson NJ, Griffin WL, Belousova EA (2004) The application of laser ablation-inductively coupled plasma-mass spectrometry to in situ U–Pb zircon geochronology. Chem. Geol. 211:47–69.

Janoušek V, Farrow CM, Erban V (2006) Interpretation of whole-rock geochemical data in igneous geochemistry: introducing Geochemical Data Toolkit (GCDkit). Journal of Petrology 47:1255-1259.

Janousek V, Moyen JF, Martin H, Erban V, Farrow C (2015) Geochemical Modelling of Igneous Processes–Principles And Recipes in R Language: Bringing the Power of R to a Geochemical Community. In Springer, 347p.

Lardeaux JM. (2014) Deciphering orogeny: a metamorphic perspective Examples from European Alpine and Variscan belts Part II: Variscan metamorphism in the French Massif Central–A review. Bull Soc Géol France 185:281-310.

Lasnier B (1968) Découverte de roches éclogitiques dans le groupe leptyno-amphibolique des monts du Lyonnais (Massif central français). Bull. Soc. Géol. de France, 7:179-185

Ledru P, Lardeaux JM, Santallier D, Autran A, Quenardel JM, Floc'h JP, Lerouge G, Maillet N, Marchand J, Ploquin A (1989) Où sont les nappes dans le Massif central français ? Bull. Soc. géol. Fr. 3:605-618.

Liew TC, Hofmann AW (1988) Precambrian crustal components, plutonic associations, plate environment of the Hercynian Fold Belt of central Europe: indications from a Nd and Sr isotopic study. Contributions to Mineralogy and Petrology 98:129-138.

Linnemann U, McNaughton NJ, Romer RL, Gehmlich M, Drost K, Tonk C (2004) West African provenance for Saxo-Thuringia (Bohemian Massif): Did Armorica ever leave pre-Pangean Gondwana? - U/Pb-SHRIMP zircon evidence and the Nd-isotopic record. Int. Journ. Earth Sciences 93(5):683-705

Ludwig KR (2012) User's Manual for a geochronological toolkit for Microsoft Excel. Berkeley Geochronological Cent. 75.

Martínez Catalán JR, Arenas R, Abati J, Sánchez Martínez S, Díaz García F, Fernández-Suárez J, González Cuadra P, Castiñeiras P, Gómez Barreiro J, Díez Montes A, Gónzalez Clavijo E, Pascual FJR, Andonaegui P, Jeffries TE, Alcock JE, Díez Fernández R, López Carmona A (2009) A rootless suture and the loss of the roots of a mountain chain: the Variscan belt of NW Iberia. Comptes Rendus Geoscience 341:114-126.

Matte P, Burg JP (1981) Sutures, thrusts and nappes in the Variscan arc of Western Europe: plate tectonic implication in McClay K, Price NJ (ed) Thrust and Nappe Tectonics, Geol. Soc. London Spec. Publ. 8:353–357.

Matte P (1986) Tectonics and plate tectonics model for the Variscan belt of Europe. Tectonophysics 126:329–374.

Matte P (1991) Accretionary history of the Variscan belt in western Europe. Tectonophysics, 196:309-337.

Matte P (2001) The Variscan collage and orogeny (480-290 Ma) and the tectonic definition of the Armorica microplate: a review. Terra Nova 13(2):122-128

Montero P, Talavera C, Bea F, Lodeiro FG, Whitehouse MJ (2009) Zircon Geochronology of the Ollo de Sapo Formation and the Age of the Cambro-Ordovician Rifting in Iberia. J. Geol. 117(2):174-191

Nicollet C (1978) Pétrologie et tectonique des terrains cristallins anté-permiens du versant sud du dôme du Lévezou (Rouergue, Massif central). Bull. BRGM 3:225-263.

Paquette JL, Monchoux P, Couturier M (1995) Geochemical and isotopic study of a norite-eclogite transition in the European Variscan Belt : Implications for U-Pb zircon systematics in metabasic rocks. Geochim. Cosmochim. acta 59:1611-1622.

Paquette JL, Piro JL, Devidal JL, Bosse V, Didier A, Sanac S, Abdelnour Y (2014) Sensitivity enhancement in LA-ICP-MS by N2 addition to carrier gas: Application to radiometric dating of U-Th-bearing minerals. Agilent ICP-MS Journal 58:1-5.

Piboule M (1979) L'origine des amphibolites: approche géochimique et mathématique. Application aux amphibolites du Massif central français. Thèse d'Etat, Lyon I University

Pin C (1979) Géochronologie U-Pb et microtectonique des séries métamorphiques anté-stéphaniennes de l'Aubrac et de la région de Marvejols (Massif central). PhD Thesis, Montpellier University.

Pin C (1990) Variscan oceans: ages, origins and geodynamic implications inferred from geochemical and radiometric data. Tectonophysics 177:215-227.

Pin C (1981) Old inherited zircons in two synkinematic variscan granitoids : the « granite du Pinet » and the « orthogneiss de Marvejols » (southern French Massif central). N. Jb. Miner. Abh. 142:27-48.

Pin C (1990) Variscan oceans: Ages, origins and geodynamic implications inferred from geochemical and radiometric data. Tectonophysics 177:215-227

Pin C, Marini F (1993) Early Ordovician continental break-up in Variscan Europe: Nd-Sr isotope and trace element evidence from bimodal igneous associations of the Southern Massif Central, France. Lithos 29(3):177-196

Pin C, Lancelot J (1982) U-Pb dating of an early Paleozoïc bimodal magmatism in the French Massif central and its further metamorphic evolution. Contrib. Mineral. Petrol. 79:1-12.

Pin C, Piboule M (1988) Upper Devonian U-Pb zircon age of the calc-alkaline series in the Levezou mafic belt, Rouergue (Massif Central, France). A composite leptyno-amphibolitic association. Bull. Soc. géol. Fr. 4:261-265.

Pin C, Vielzeuf D (1983) Granulites and related rocks in Variscan median Europe: a dualistic interpretation. Tectonophysics 93:47–74.

Pitra P, Poujol M, Van Den Driessche J, Poilvet JC, Paquette JL (2012) Early Permian extensional shearing of an Ordovician granite: The Saint-Eutrope "C/S-like" orthogneiss (Montagne Noire, French Massif Central). Comptes Rendus Géoscience 344:377-84.

Ribeiro A, Munhá J, Dias R, Mateus A, Pereira E, Ribeiro L, Fonseca P, Araújo A, Oliveira T, Romão J, Chaminé H, Coke C, Pedro J (2007) Geodynamic evolution of the SW Europe Variscides. Tectonics 26:1-24 TC6009.

Roger F, Respaut JP, Brunel M, Matte P, Paquette JL (2004) U-Pb dating of Augen orthogneisses from the axial zone of the Montague Noire (Southern of Massif Central): new witness of Ordovician magmatism into the Variscan Belt. Comptes Rendus Géoscience 336:19-28.

Sánchez-García T, Bellido F, Quesada C (2003) Geodynamic setting and geochemical signatures of Cambrian–Ordovician rift-related igneous rocks (Ossa-Morena Zone, SW Iberia). Tectonophysics 365(1-4):233-255

Sánchez-García T, Quesada C, Bellido F, Dunning GR, González del Tánago J (2008) Two-step magma flooding of the upper crust during rifting: The Early Paleozoic of the Ossa Morena Zone (SW Iberia). Tectonophysics 461(1-4):72-90

Santallier D, Briand B, Menot RP, Piboule M (1988) Les complexes leptyno-amphiboliques (C.L.A.); revue critique et suggestions pour un meilleur emploi de ce terme. Bull. Soc. Géol. France 4:3–12.

Shand SJ (1943) Eruptive rocks. Their genesis, composition, classification, and their relation to ore-deposits with a chapter on meteorite. In John Wiley & Sons, New York.

Schulmann K, Catalán JR, Lardeaux JM, Janoušek V, Oggiano G. (2014) The Variscan orogeny: extent, timescale and the formation of the European crust. Geol Soc London, Special Publications 405:1-6.

Solá AR, Pereira MF, Williams IS, Ribeiro ML, Neiva AM, Montero P, Bea F, Zinger T (2008) New insights from U–Pb zircon dating of Early Ordovician magmatism on the northern Gondwana margin: the Urra Formation (SW Iberian Massif, Portugal). Tectonophysics 461:114-29.

Sun SS, McDonough WF (1989) Chemical and isotopic systematics of oceanic basalts: implications for mantle composition and

processes. Geol Soc London, Special Publications 42:313-45.

Talavera C, Montero P, Bea F, González Lodeiro F, Whitehouse M (2013) U–Pb Zircon geochronology of the Cambro-Ordovician metagranites and metavolcanic rocks of central and NW Iberia. Int. Journ. Earth Sciences 102:1-23

Van Achterbergh E, Ryan CG, Jackson SE, Griffin WL (2001) Data reduction software for LA-ICP-MS: appendix. In: Laser Ablation-ICP-Mass Spectrometry in the Earth Sciences: Principles and Applications. In Mineralog Assoc Canada (MAC) Short Courses Series (Sylvester, P.J., eds), Ottawa, Ontario, Canada 29:239-243.

Vermeesch P (2012) On the visualisation of detrital age distributions. Chemical Geology 312-313:190-194.

Wiedenbeck M, Allé P, Corfu F, Griffin WL, Meier M, Oberli F, von Quadt A, Roddick JC, Spiegel W (1995) Three natural zircon standards for U-Th-Pb, Lu-Hf, trace element and REE analyses. Geostand Newsl 19:1–23.

Young TP (1990) Ordovician sedimentary facies and faunas of southwest Europe: palaeogeographic and tectonic implications. Geological Society, London, Memoirs 12(1):421-430

Supplementary Table III.1.1: Operating conditions for the LA-ICP-MS equipment

Laboratory & Sample Preparation	
Laboratory name	Géosciences Rennes, UMR CNRS 6118, Rennes, France
Sample type/mineral	zircon
Sample preparation	Conventional mineral separation, 1 inch resin mount, 1µm polish to finish
Imaging	CL: RELION CL instrument, Olympus Microscope BX51WI, Leica Color Camera DFC 420C
Laser ablation system	
Make, Model & type	ESI NWR193UC, Excimer
Ablation cell	ESI NWR TwoVol2
Laser wavelength	193 nm
Pulse width	< 5 ns
Fluence	7.5 J/cm-2
Repetition rate	4 Hz
Spot size	20 µm
Sampling mode / pattern	Single spot
Carrier gas	100% He, Ar make-up gas and N2 (3 ml/mn) combined using in-house smoothing device
Background collection	20 seconds
Ablation duration	60 seconds
Wash-out delay	15 seconds
Cell carrier gas flow (He)	0.75 l/min
ICP-MS Instrument	
Make, Model & type	Agilent 7700x, Q-ICP-MS
Sample introduction	Via conventional tubing
RF power	1350W
Sampler, skimmer cones	Ni
Extraction lenses	X type
Make-up gas flow (Ar)	0.85 l/min
Detection system	Single collector secondary electron multiplier
Data acquisition protocol	Time-resolved analysis
Scanning mode	Peak hopping, one point per peak
Detector mode	Pulse counting, dead time correction applied, and analog mode when signal intensity > ~ 10^6 cps
Masses measured	^{204}(Hg + Pb), ^{206}Pb, ^{207}Pb, ^{208}Pb, ^{232}Th, ^{238}U
Integration time per peak	10-30 ms
Sensitivity / Efficiency	20000 cps/ppm Pb (50µm, 10Hz)
Data Processing	
Gas blank	20 seconds on-peak
Calibration strategy	GJ1 zircon standard used as primary reference material, 91500 used as secondary reference material (quality control)
Reference Material info	GJ1 (Jackson et al., 2004) 91500 (Wiedenbeck et al., 1995)
Data processing package used	GLITTER ® (van Achterbergh et al., 2001)
Quality control / Validation	91500: concordia age = 1063.7 ±4.8 Ma (N=27; MSWD=1.5)

Supplementary table III.1.2: LA-ICPMS analyses on zircon from samples LV3C, LV2A, LV2B, LV15; data in bold represent the analyses used for the calculation of the concordia ages; zon.1 : primary zonation.

		Content (ppm)			**Isotopic Ratios**							**Ages (Ma)**						
Zircon		Pb	U	Th/U	$^{207}Pb/^{235}U$	1σ	$^{206}Pb/^{238}U$	1σ	rho	$^{207}Pb/^{206}Pb$	1σ	$^{207}Pb/^{206}Pb$	1σ	$^{206}Pb/^{238}U$	1σ	$^{207}Pb/^{235}U$	1σ	Conc
LV3C																		
1a	core	17	196	0.90	0.592	0.008	0.0726	0.0009	0.86	0.0591	0.0008	572.3	28.6	451.9	5.2	472.2	5.2	95.7
1b	rim	33	488	0.09	0.569	0.007	0.0707	0.0008	0.91	0.0584	0.0007	542.8	25.9	440.4	4.9	457.2	4.7	96.3
1c	rim	23	355	0.07	0.620	0.008	0.0671	0.0008	0.91	0.0671	0.0008	839.4	25.0	418.8	4.7	490.1	5.0	85.5
2a		32	440	0.19	0.589	0.007	0.0750	0.0009	0.92	0.0569	0.0007	487.7	26.2	466.4	5.2	470.0	4.8	99.2
2b		22	308	0.18	0.590	0.008	0.0750	0.0009	0.89	0.0571	0.0007	494.0	27.7	466.4	5.3	471.2	5.0	99.0
2c		29	407	0.10	0.613	0.008	0.0751	0.0009	0.89	0.0592	0.0007	575.8	26.4	466.6	5.2	485.5	5.0	96.1
2d		40	576	0.06	0.591	0.007	0.0748	0.0009	0.93	0.0574	0.0007	504.6	25.3	465.0	5.2	471.8	4.7	98.6
2e		**33**	**478**	**0.07**	**0.586**	**0.007**	**0.0749**	**0.0009**	**0.91**	**0.0568**	**0.0007**	**481.7**	**25.9**	**465.4**	**5.2**	**468.2**	**4.7**	**99.4**
3a	core	13	50	2.06	2.588	0.035	0.1739	0.0021	0.89	0.1080	0.0014	1765.1	24.0	1033.5	11.6	1297.1	10.0	73.5
3b	core	21	53	2.06	4.267	0.056	0.2607	0.0031	0.92	0.1187	0.0015	1936.8	22.3	1493.6	16.0	1686.9	10.8	87.1
3c	rim	25	360	0.03	0.598	0.008	0.0741	0.0009	0.90	0.0585	0.0007	549.4	26.3	461.0	5.2	476.0	4.9	96.8
3d	core	26	59	1.61	5.320	0.069	0.3190	0.0038	0.92	0.1210	0.0015	1970.7	21.7	1784.8	18.6	1872.1	11.1	95.0
3e	core	28	59	2.05	5.481	0.073	0.3115	0.0038	0.91	0.1276	0.0016	2065.8	22.2	1748.2	18.5	1897.7	11.4	91.9
3f	rim	33	466	0.03	0.612	0.008	0.0752	0.0009	0.91	0.0591	0.0007	569.2	25.3	467.6	5.2	485.1	4.9	96.4
4a	core	29	272	0.67	0.796	0.011	0.0977	0.0011	0.88	0.0591	0.0007	571.1	26.9	600.9	6.7	594.6	5.9	101.1
4b	rim	36	511	0.09	0.592	0.008	0.0750	0.0009	0.88	0.0572	0.0007	500.3	27.6	466.3	5.3	472.1	5.0	98.8
4c	rim	31	411	0.06	0.678	0.009	0.0802	0.0009	0.90	0.0614	0.0007	653.2	25.7	497.0	5.6	525.8	5.3	94.5
4d	zon.1	80	949	0.07	0.761	0.009	0.0887	0.0010	0.93	0.0623	0.0007	682.8	24.2	547.8	6.0	574.6	5.4	95.3
5a		24	178	1.62	0.831	0.011	0.0957	0.0011	0.88	0.0630	0.0008	707.8	27.1	589.1	6.6	614.1	6.2	95.9
5b		21	211	0.51	0.765	0.010	0.0934	0.0011	0.87	0.0594	0.0008	581.3	27.8	575.7	6.5	576.8	6.0	99.8
5c		15	121	1.20	0.831	0.012	0.0976	0.0012	0.84	0.0618	0.0009	666.3	29.4	600.0	6.8	614.0	6.6	97.7
5d		13	121	0.78	0.806	0.012	0.0962	0.0012	0.82	0.0607	0.0009	630.2	30.4	592.1	6.8	600.0	6.6	98.7

		Content (ppm)			Isotopic Ratios							Ages (Ma)						
Zircon		Pb	U	Th/U	$^{207}Pb/^{235}U$	1σ	$^{206}Pb/^{238}U$	1σ	rho	$^{207}Pb/^{206}Pb$	1σ	$^{207}Pb/^{206}Pb$	1σ	$^{206}Pb/^{238}U$	1σ	$^{207}Pb/^{235}U$	1σ	Conc
LV3C																		
7b	zon.1	37	405	0.07	0.979	0.014	0.0931	0.0011	0.84	0.0763	0.0011	1102.9	27.9	573.9	6.6	693.3	7.2	62.9
7c	rim	41	592	0.04	0.598	0.008	0.0751	0.0009	0.89	0.0577	0.0007	519.8	26.9	466.9	5.2	475.9	4.9	98.1
7d	zon.1	43	570	0.05	0.653	0.008	0.0816	0.0010	0.90	0.0581	0.0007	532.3	26.8	505.6	5.6	510.4	5.2	99.1
7e	rim	36	501	0.11	0.632	0.008	0.0753	0.0009	0.88	0.0609	0.0008	636.0	26.8	467.8	5.3	497.3	5.2	94.1
8a	core	18	70	0.47	3.499	0.051	0.2367	0.0029	0.85	0.1072	0.0015	1753.0	25.9	1369.4	15.3	1526.9	11.5	87.1
8b	zon.1	21	246	0.11	0.759	0.011	0.0878	0.0010	0.84	0.0627	0.0009	698.5	28.7	542.8	6.2	573.7	6.2	94.6
8c	rim	32	449	0.10	0.588	0.008	0.0749	0.0009	0.85	0.0570	0.0008	491.3	30.0	465.3	5.3	469.7	5.3	99.1
9a	core	32	94	0.48	4.873	0.064	0.3077	0.0036	0.90	0.1149	0.0014	1878.0	22.3	1729.3	17.9	1797.5	11.1	95.7
9b	rim	54	446	0.07	1.419	0.018	0.1236	0.0014	0.90	0.0833	0.0010	1274.8	23.6	751.4	8.3	896.8	7.7	70.3
9c	rim	37	348	0.08	1.203	0.016	0.1085	0.0013	0.87	0.0804	0.0011	1207.2	25.5	664.0	7.5	801.8	7.5	66.4
10a	core	23	257	0.16	0.869	0.012	0.0874	0.0011	0.85	0.0721	0.0010	989.1	27.7	540.1	6.2	634.8	6.7	85.1
10b	rim	26	335	0.40	0.590	0.009	0.0749	0.0009	0.82	0.0572	0.0008	497.0	31.5	465.6	5.4	471.0	5.6	98.9
11a		30	258	0.89	0.864	0.012	0.0997	0.0012	0.84	0.0629	0.0009	705.2	28.9	612.5	7.0	632.5	6.7	96.8
11b		27	239	0.55	0.887	0.013	0.1027	0.0012	0.84	0.0627	0.0009	696.3	28.8	630.0	7.1	644.6	6.7	97.7
12a	core	94	324	1.21	3.571	0.049	0.2217	0.0027	0.91	0.1168	0.0015	1908.5	23.1	1290.8	14.4	1543.2	10.8	80.9
12b	rim	22	318	0.09	0.613	0.008	0.0751	0.0009	0.88	0.0592	0.0007	575.6	27.1	466.8	5.4	485.6	5.2	96.1
12c	zon.1	15	181	0.06	0.752	0.012	0.0859	0.0011	0.76	0.0635	0.0011	726.1	34.5	531.3	6.5	569.6	7.2	93.3
13a	**rim**	**26**	**380**	**0.07**	**0.583**	**0.008**	**0.0748**	**0.0009**	**0.90**	**0.0565**	**0.0007**	**470.5**	**27.4**	**465.2**	**5.3**	**466.2**	**4.9**	**99.8**
13b	rim	29	414	0.11	0.593	0.008	0.0755	0.0009	0.88	0.0570	0.0007	491.7	28.5	469.0	5.4	473.0	5.2	99.2
13c	rim	27	352	0.12	0.660	0.009	0.0823	0.0010	0.89	0.0581	0.0007	534.3	27.7	510.1	5.8	514.6	5.4	99.1
14a	core	28	290	0.06	0.892	0.012	0.1045	0.0012	0.90	0.0619	0.0008	670.8	26.0	640.9	7.2	647.5	6.3	99.0
14b	zon.1	46	516	0.18	0.853	0.011	0.0893	0.0011	0.91	0.0693	0.0008	906.6	24.7	551.6	6.2	626.3	6.0	88.1
14c	rim	36	522	0.02	0.608	0.008	0.0755	0.0009	0.91	0.0584	0.0007	545.8	26.4	469.4	5.3	482.5	5.0	97.3
14d	rim	32	454	0.02	0.620	0.008	0.0754	0.0009	0.90	0.0596	0.0007	590.5	26.5	468.8	5.3	490.0	5.1	95.7
15a	core	26	58	0.93	6.962	0.090	0.3665	0.0044	0.92	0.1378	0.0017	2199.7	21.1	2012.9	20.5	2106.6	11.4	95.8
15b	core	13	33	0.22	6.538	0.089	0.3566	0.0044	0.90	0.1330	0.0018	2137.9	23.0	1966.1	20.7	2051.1	12.0	95.9

		Content (ppm)			Isotopic Ratios							Ages (Ma)						
Zircon		Pb	U	Th/U	$^{207}Pb/^{235}U$	1σ	$^{206}Pb/^{238}U$	1σ	rho	$^{207}Pb/^{206}Pb$	1σ	$^{207}Pb/^{206}Pb$	1σ	$^{206}Pb/^{238}U$	1σ	$^{207}Pb/^{235}U$	1σ	Conc
LV3C																		
16a	core	96	353	0.25	5.428	0.068	0.2447	0.0028	0.93	0.1609	0.0019	2465.3	19.6	1411.1	14.7	1889.4	10.7	76.6
16b	rim	25	365	0.10	0.585	0.008	0.0716	0.0009	0.86	0.0593	0.0008	576.7	28.7	445.8	5.1	467.6	5.2	95.3
16c	rim	23	323	0.09	0.595	0.010	0.0748	0.0009	0.77	0.0577	0.0009	517.7	35.0	465.2	5.5	474.1	6.1	98.1
17a		22	239	0.97	0.591	0.008	0.0750	0.0009	0.84	0.0571	0.0008	494.8	30.2	466.4	5.3	471.3	5.3	99.0
17b		**10**	**130**	**0.42**	**0.588**	**0.010**	**0.0755**	**0.0009**	**0.75**	**0.0565**	**0.0010**	**471.9**	**37.1**	**469.0**	**5.6**	**469.5**	**6.3**	**99.9**
17c		18	226	0.44	0.619	0.010	0.0755	0.0009	0.79	0.0595	0.0009	584.0	33.0	469.2	5.5	489.1	6.0	95.9
18a	**rim**	**32**	**456**	**0.03**	**0.584**	**0.008**	**0.0754**	**0.0009**	**0.85**	**0.0561**	**0.0008**	**457.6**	**29.5**	**468.7**	**5.3**	**466.8**	**5.2**	**100.4**
18b	rim	45	716	0.05	0.508	0.007	0.0663	0.0008	0.86	0.0561	0.0008	432.0	28.3	414.1	4.7	416.8	4.6	99.4
6a	core	15	132	0.55	0.900	0.013	0.1068	0.0013	0.82	0.0611	0.0009	643.8	30.3	653.9	7.5	651.5	7.0	100.4
6b	**rim**	**28**	**403**	**0.03**	**0.585**	**0.008**	**0.0755**	**0.0009**	**0.83**	**0.0563**	**0.0008**	**461.5**	**30.7**	**468.9**	**5.4**	**467.7**	**5.4**	**100.3**
6c	rim	24	340	0.09	0.609	0.008	0.0749	0.0009	0.85	0.0590	0.0008	566.9	28.1	465.6	5.3	483.0	5.3	96.4
7a	core	191	1098	0.11	2.572	0.031	0.1766	0.0020	0.94	0.1057	0.0012	1726.2	20.6	1048.3	11.1	1292.8	8.9	74.9

		Content (ppm)			Isotopic Ratios							Ages (Ma)						
Zircon		Pb	U	Th/U	$^{207}Pb/^{235}U$	1σ	$^{206}Pb/^{238}U$	1σ	rho	$^{207}Pb/^{206}Pb$	1σ	$^{207}Pb/^{206}Pb$	1σ	$^{206}Pb/^{238}U$	1σ	$^{207}Pb/^{235}U$	1σ	Conc
LV2A																		
1a	rim	26	379	0.11	0.602	0.008	0.0685	0.0008	0.87	0.0638	0.0008	734.4	27.5	427.2	4.9	478.8	5.2	89.2
1b	zon.1	62	406	0.09	1.554	0.019	0.1564	0.0018	0.94	0.0721	0.0008	987.7	23.1	936.8	10.1	952.1	7.6	98.4
1c	core	36	149	0.52	2.478	0.032	0.2103	0.0025	0.90	0.0855	0.0011	1325.9	24.1	1230.5	13.2	1265.6	9.5	95.5
1d	zon.1	79	528	0.05	1.542	0.019	0.1561	0.0018	0.94	0.0717	0.0008	976.0	23.2	935.2	10.1	947.3	7.6	98.7
2a	rim	24	348	0.08	0.576	0.008	0.0722	0.0009	0.86	0.0579	0.0008	525.4	29.2	449.4	5.1	462.0	5.2	97.3
2b	core	36	39	0.78	25.567	0.318	0.6825	0.0082	0.96	0.2717	0.0032	3316.1	18.3	3353.9	31.3	3330.1	12.1	100.4
2c	zon.1	52	289	0.08	2.604	0.033	0.1795	0.0021	0.92	0.1053	0.0013	1718.6	22.0	1064.0	11.6	1301.8	9.4	75.7
3a	rim	38	525	0.08	0.595	0.008	0.0749	0.0009	0.87	0.0577	0.0007	516.5	28.1	465.6	5.3	474.2	5.1	98.2
3b	core	75	701	0.39	0.856	0.011	0.1016	0.0012	0.93	0.0611	0.0007	644.0	24.8	623.8	6.9	628.1	5.9	99.3
3c	rim	35	482	0.05	0.605	0.008	0.0761	0.0009	0.88	0.0577	0.0007	518.1	27.9	472.9	5.4	480.7	5.1	98.4
4a	**rim**	**32**	**444**	**0.06**	**0.594**	**0.009**	**0.0756**	**0.0009**	**0.82**	**0.0570**	**0.0008**	**489.6**	**31.5**	**469.9**	**5.5**	**473.3**	**5.6**	**99.3**
4b	rim	44	557	0.43	0.593	0.008	0.0732	0.0009	0.87	0.0588	0.0008	557.9	28.0	455.5	5.2	472.8	5.2	96.3
4c	core	32	307	0.52	0.810	0.012	0.0965	0.0012	0.82	0.0609	0.0009	635.1	30.8	593.8	6.9	602.4	6.7	98.6
4d	rim	31	385	0.38	0.621	0.010	0.0754	0.0009	0.77	0.0597	0.0010	593.8	34.3	468.7	5.6	490.5	6.3	95.6
4e	rim	39	623	0.10	0.530	0.008	0.0653	0.0008	0.84	0.0588	0.0008	560.2	29.5	408.0	4.8	431.7	5.0	94.5
5a		40	576	0.07	0.586	0.009	0.0742	0.0009	0.79	0.0572	0.0009	500.0	33.7	461.5	5.5	468.0	5.9	98.6
5b		26	369	0.05	0.609	0.011	0.0736	0.0010	0.73	0.0600	0.0011	604.3	38.0	458.1	5.7	483.2	6.8	94.8
5c		38	537	0.07	0.585	0.009	0.0742	0.0009	0.78	0.0572	0.0009	498.5	33.5	461.6	5.5	467.8	5.9	98.7
6a	**rim**	**26**	**367**	**0.08**	**0.593**	**0.008**	**0.0757**	**0.0009**	**0.84**	**0.0568**	**0.0008**	**482.9**	**30.4**	**470.6**	**5.5**	**472.7**	**5.4**	**99.6**
6b	core	24	202	0.98	0.843	0.012	0.0989	0.0012	0.85	0.0619	0.0008	669.5	28.7	607.7	7.0	620.9	6.6	97.9
6c	**rim**	**36**	**505**	**0.07**	**0.589**	**0.008**	**0.0752**	**0.0009**	**0.88**	**0.0568**	**0.0007**	**484.0**	**28.1**	**467.5**	**5.4**	**470.3**	**5.1**	**99.4**
7a	rim	26	307	0.14	0.696	0.012	0.0860	0.0011	0.76	0.0587	0.0010	554.0	35.9	532.0	6.5	536.1	7.0	99.2
7b	core	7	60	0.68	0.993	0.019	0.1075	0.0015	0.69	0.0670	0.0013	837.6	40.8	658.1	8.4	700.1	9.8	94.0
7c	rim	27	363	0.08	0.620	0.009	0.0779	0.0010	0.84	0.0577	0.0008	517.2	30.6	483.7	5.7	489.6	5.7	98.8
8a	rim	39	415	0.11	0.806	0.011	0.0974	0.0012	0.88	0.0601	0.0008	605.3	27.6	599.1	6.9	600.4	6.2	99.8
8b	core	109	308	0.45	5.513	0.072	0.3185	0.0038	0.91	0.1256	0.0015	2036.6	21.4	1782.5	18.6	1902.6	11.3	93.4

		Content (ppm)			Isotopic Ratios							Ages (Ma)						
Zircon		Pb	U	Th/U	$^{207}Pb/^{235}U$	1σ	$^{206}Pb/^{238}U$	1σ	rho	$^{207}Pb/^{206}Pb$	1σ	$^{207}Pb/^{206}Pb$	1σ	$^{206}Pb/^{238}U$	1σ	$^{207}Pb/^{235}U$	1σ	Conc
LV2A																		
8c	rim	38	410	0.12	0.813	0.011	0.0970	0.0012	0.87	0.0608	0.0008	631.4	28.0	597.0	6.9	604.2	6.3	98.8
9a	core	14	141	0.15	0.785	0.013	0.0982	0.0012	0.77	0.0580	0.0009	528.0	35.1	604.1	7.2	588.3	7.3	102.7
9b	rim	18	248	0.11	0.620	0.010	0.0783	0.0010	0.77	0.0575	0.0009	510.3	35.1	485.8	5.9	490.1	6.3	99.1
9c	core	27	221	0.58	0.961	0.015	0.1113	0.0014	0.80	0.0626	0.0010	694.7	32.1	680.4	8.1	683.6	7.8	99.5
9d	rim	22	278	0.20	0.719	0.012	0.0805	0.0010	0.78	0.0648	0.0010	766.5	33.1	499.0	6.1	549.8	6.9	90.8
10a	rim	32	457	0.01	0.615	0.010	0.0762	0.0010	0.78	0.0586	0.0009	550.7	34.1	473.5	5.8	486.9	6.3	97.2
10b	core	63	324	0.82	1.674	0.024	0.1663	0.0020	0.85	0.0730	0.0010	1014.8	27.4	991.6	11.3	998.7	9.2	99.3
10c	**rim**	**35**	**498**	**0.02**	**0.599**	**0.009**	**0.0764**	**0.0009**	**0.83**	**0.0569**	**0.0008**	**487.0**	**31.2**	**474.7**	**5.6**	**476.9**	**5.6**	**99.5**
11a	rim	19	266	0.13	0.613	0.010	0.0762	0.0010	0.77	0.0583	0.0009	541.0	35.5	473.4	5.8	485.2	6.4	97.6
11b	core	5	61	0.19	0.742	0.016	0.0900	0.0013	0.65	0.0598	0.0013	597.3	46.9	555.4	7.4	563.6	9.3	98.5
11c	**rim**	**23**	**326**	**0.08**	**0.590**	**0.009**	**0.0757**	**0.0010**	**0.79**	**0.0565**	**0.0009**	**472.2**	**34.1**	**470.1**	**5.7**	**470.6**	**6.0**	**99.9**
12a	**rim**	**59**	**841**	**0.08**	**0.596**	**0.009**	**0.0759**	**0.0009**	**0.84**	**0.0570**	**0.0008**	**489.6**	**30.5**	**471.5**	**5.6**	**474.7**	**5.5**	**99.3**
12b	core	70	198	0.91	4.216	0.061	0.2885	0.0036	0.85	0.1060	0.0015	1731.9	25.0	1634.0	17.9	1677.2	11.9	97.4
12c	rim	35	502	0.07	0.603	0.009	0.0748	0.0009	0.81	0.0584	0.0009	546.4	31.7	465.2	5.6	479.1	5.9	97.1
13a	rim	27	321	0.14	0.720	0.008	0.0884	0.0010	0.98	0.0591	0.0006	570.4	23.2	546.3	6.1	550.9	5.0	99.2
13b	rim	32	310	0.44	0.818	0.010	0.0983	0.0011	0.95	0.0603	0.0007	614.3	24.0	604.7	6.7	606.7	5.6	99.7
14a	**rim**	**25**	**357**	**0.09**	**0.585**	**0.007**	**0.0754**	**0.0009**	**0.91**	**0.0562**	**0.0007**	**460.8**	**26.3**	**468.7**	**5.3**	**467.4**	**4.8**	**100.3**
15a	rim	30	438	0.10	0.594	0.007	0.0743	0.0009	0.94	0.0580	0.0007	529.0	25.5	462.0	5.2	473.4	4.7	97.6
15b	rim	27	338	0.19	0.649	0.008	0.0813	0.0010	0.94	0.0579	0.0007	526.0	25.2	503.9	5.6	507.9	5.0	99.2
16a	rim	24	336	0.12	0.592	0.007	0.0744	0.0009	0.93	0.0577	0.0007	518.1	25.9	462.5	5.2	471.9	4.8	98.0
17a	rim	34	484	0.06	0.625	0.008	0.0742	0.0009	0.96	0.0612	0.0007	645.0	23.6	461.2	5.2	493.2	4.7	93.5
17b	rim	33	450	0.10	0.629	0.007	0.0755	0.0009	0.97	0.0605	0.0007	619.6	23.2	469.4	5.2	495.7	4.7	94.7
18a	rim	29	374	0.15	0.654	0.008	0.0814	0.0009	0.97	0.0583	0.0006	538.5	24.3	504.5	5.6	510.7	4.8	98.8
19a	rim	21	290	0.14	0.606	0.008	0.0754	0.0009	0.92	0.0584	0.0007	543.9	25.8	468.3	5.3	481.3	4.9	97.3
20a	rim	45	671	0.04	0.585	0.007	0.0709	0.0008	0.96	0.0598	0.0007	596.6	23.9	441.6	4.9	467.4	4.5	94.5
21a	rim	29	372	0.08	0.679	0.008	0.0832	0.0010	0.94	0.0592	0.0007	575.4	24.5	515.0	5.7	526.2	5.0	97.9

		Content (ppm)			Isotopic Ratios							Ages (Ma)						
Zircon		Pb	U	Th/U	$^{207}Pb/^{235}U$	1σ	$^{206}Pb/^{238}U$	1σ	rho	$^{207}Pb/^{206}Pb$	1σ	$^{207}Pb/^{206}Pb$	1σ	$^{206}Pb/^{238}U$	1σ	$^{207}Pb/^{235}U$	1σ	Conc
LV2A																		
22a	rim	44	604	0.12	0.631	0.008	0.0758	0.0009	0.94	0.0604	0.0007	617.1	24.0	471.1	5.2	496.8	4.8	94.8
23a	rim	30	417	0.13	0.594	0.007	0.0755	0.0009	0.92	0.0571	0.0007	494.7	25.8	468.9	5.2	473.4	4.7	99.0
24a	**rim**	**24**	**341**	**0.10**	**0.585**	**0.007**	**0.0753**	**0.0009**	**0.95**	**0.0564**	**0.0006**	**465.9**	**25.0**	**468.2**	**5.2**	**467.9**	**4.6**	**100.1**
25a	rim	22	310	0.10	0.600	0.007	0.0755	0.0009	0.93	0.0576	0.0007	515.0	24.6	469.1	5.2	477.0	4.7	98.3
26a	rim	22	244	0.29	0.750	0.009	0.0919	0.0011	0.96	0.0592	0.0007	574.8	24.1	566.5	6.2	568.1	5.3	99.7
27a	rim	35	393	0.16	0.764	0.009	0.0927	0.0011	0.97	0.0598	0.0007	597.0	23.3	571.2	6.3	576.4	5.2	99.1
28a	rim	48	676	0.06	0.636	0.008	0.0752	0.0009	0.95	0.0613	0.0007	651.0	24.0	467.5	5.2	499.9	4.8	93.5
29a	rim	43	621	0.04	0.603	0.008	0.0754	0.0009	0.92	0.0581	0.0007	532.3	26.1	468.4	5.2	479.4	4.8	97.7
30a	rim	28	402	0.06	0.600	0.007	0.0744	0.0009	0.94	0.0585	0.0007	549.5	24.9	462.6	5.1	477.4	4.7	96.9
31a	rim	22	310	0.11	0.591	0.008	0.0742	0.0009	0.90	0.0578	0.0007	522.3	26.6	461.5	5.2	471.8	4.8	97.8
32a	**rim**	**23**	**332**	**0.09**	**0.578**	**0.008**	**0.0742**	**0.0009**	**0.85**	**0.0565**	**0.0008**	**470.4**	**29.4**	**461.6**	**5.2**	**463.2**	**5.1**	**99.7**
33a	rim	40	597	0.06	0.590	0.007	0.0724	0.0008	0.93	0.0591	0.0007	571.0	25.0	450.5	5.0	470.7	4.7	95.7
34a	rim	27	373	0.05	0.697	0.010	0.0774	0.0009	0.86	0.0654	0.0009	786.5	28.1	480.4	5.5	537.2	5.8	89.4
35a	rim	40	551	0.16	0.602	0.008	0.0745	0.0009	0.89	0.0586	0.0007	552.3	26.7	463.3	5.2	478.5	5.0	96.8
36a	rim	27	380	0.12	0.594	0.007	0.0754	0.0009	0.92	0.0571	0.0007	495.7	26.1	468.8	5.2	473.5	4.7	99.0
37a	rim	37	519	0.05	0.599	0.008	0.0759	0.0009	0.89	0.0572	0.0007	500.5	27.1	471.7	5.3	476.7	4.9	99.0
38a	**rim**	**29**	**410**	**0.06**	**0.590**	**0.007**	**0.0754**	**0.0009**	**0.92**	**0.0568**	**0.0007**	**483.2**	**25.8**	**468.5**	**5.2**	**471.1**	**4.7**	**99.4**

		Content (ppm)			Isotopic Ratios							Ages (Ma)						
Zircon		Pb	U	Th/U	$^{207}Pb/^{235}U$	1σ	$^{206}Pb/^{238}U$	1σ	rho	$^{207}Pb/^{206}Pb$	1σ	$^{207}Pb/^{206}Pb$	1σ	$^{206}Pb/^{238}U$	1σ	$^{207}Pb/^{235}U$	1σ	Conc
LV2B																		
1a	core	52	136	0.33	9.395	0.122	0.3293	0.0040	0.95	0.2069	0.0024	2881.7	18.8	1835.1	19.6	2377.4	11.9	82.5
1b	core	68	313	0.30	3.741	0.048	0.2034	0.0025	0.94	0.1334	0.0016	2143.1	20.2	1193.6	13.2	1580.1	10.4	73.7
2a	rim	36	483	0.22	0.630	0.009	0.0743	0.0009	0.89	0.0615	0.0008	655.5	27.2	462.2	5.4	496.0	5.4	93.2
2b	rim	34	450	0.22	0.623	0.008	0.0760	0.0009	0.89	0.0595	0.0008	585.6	27.0	471.9	5.5	491.8	5.3	96.0
3a	rim	45	709	0.07	0.564	0.007	0.0680	0.0008	0.91	0.0601	0.0007	606.7	26.2	424.3	4.9	453.9	4.9	93.5
3b	rim	35	544	0.07	0.590	0.008	0.0673	0.0008	0.88	0.0636	0.0008	729.0	26.9	420.0	4.9	471.2	5.2	89.1
4a		**44**	**624**	**0.06**	**0.589**	**0.009**	**0.0755**	**0.0009**	**0.82**	**0.0567**	**0.0008**	**477.9**	**31.9**	**469.0**	**5.6**	**470.5**	**5.7**	**99.7**
4b		**31**	**432**	**0.08**	**0.589**	**0.009**	**0.0754**	**0.0009**	**0.81**	**0.0567**	**0.0008**	**477.4**	**32.0**	**468.5**	**5.5**	**470.1**	**5.6**	**99.7**
4c		**40**	**564**	**0.06**	**0.587**	**0.010**	**0.0759**	**0.0010**	**0.74**	**0.0561**	**0.0010**	**456.9**	**37.4**	**471.3**	**5.8**	**468.9**	**6.5**	**100.5**
4d		43	632	0.07	0.569	0.008	0.0719	0.0009	0.84	0.0574	0.0008	507.7	30.1	447.5	5.2	457.5	5.3	97.8
8a	rim	21	241	0.40	0.828	0.012	0.0835	0.0011	0.88	0.0720	0.0010	984.5	26.7	517.0	6.4	612.5	6.7	84.4
8b	rim	31	426	0.16	0.919	0.012	0.0682	0.0009	0.95	0.0978	0.0011	1582.5	21.7	425.1	5.2	661.7	6.5	64.2
9a	rim	34	256	0.58	1.095	0.015	0.1261	0.0016	0.92	0.0630	0.0008	709.2	25.5	765.4	9.1	751.0	7.3	101.9
9b	rim	34	344	0.19	0.855	0.012	0.1048	0.0013	0.92	0.0592	0.0007	573.6	26.1	642.6	7.7	627.4	6.4	102.4
9c	core	15	107	0.74	1.099	0.016	0.1263	0.0016	0.87	0.0631	0.0009	713.0	28.4	766.4	9.2	752.7	7.8	101.8
10a	rim	17	206	0.14	0.694	0.010	0.0897	0.0011	0.88	0.0561	0.0007	457.6	28.3	553.8	6.7	535.3	6.0	103.5
10b	rim	16	201	0.11	0.691	0.010	0.0882	0.0011	0.86	0.0569	0.0008	485.1	30.1	545.0	6.6	533.6	6.1	102.1
10c	core	21	243	0.08	0.740	0.012	0.0915	0.0012	0.82	0.0587	0.0009	555.5	32.1	564.6	7.0	562.6	6.8	100.4
11a	rim	21	271	0.07	0.666	0.009	0.0849	0.0011	0.89	0.0570	0.0007	489.9	28.2	525.0	6.3	518.4	5.7	101.3
11b	rim	31	324	0.44	0.735	0.010	0.0914	0.0011	0.90	0.0584	0.0007	543.1	26.9	563.6	6.7	559.4	5.9	100.8
12a	core	70	348	0.10	3.810	0.050	0.1952	0.0024	0.94	0.1416	0.0017	2247.3	20.0	1149.3	12.9	1594.9	10.5	71.0
12b	rim	42	620	0.05	0.668	0.009	0.0695	0.0009	0.91	0.0697	0.0009	918.9	25.5	433.1	5.2	519.2	5.6	83.4
13a	rim	55	586	0.17	0.822	0.011	0.0959	0.0012	0.91	0.0622	0.0008	680.7	26.3	590.4	6.9	609.3	6.2	96.9
13b	rim	28	256	0.37	0.877	0.013	0.1049	0.0013	0.85	0.0606	0.0008	626.5	29.7	642.9	7.7	639.2	7.0	100.6
14a	**rim**	**29**	**414**	**0.06**	**0.586**	**0.009**	**0.0759**	**0.0010**	**0.84**	**0.0560**	**0.0008**	**452.3**	**31.0**	**471.5**	**5.7**	**468.2**	**5.6**	**100.7**
14b	rim	26	337	0.09	0.635	0.009	0.0808	0.0010	0.85	0.0571	0.0008	492.9	30.3	500.6	6.0	499.3	5.7	100.3

		Content (ppm)			Isotopic Ratios							Ages (Ma)						
Zircon		Pb	U	Th/U	$^{207}Pb/^{235}U$	1σ	$^{206}Pb/^{238}U$	1σ	rho	$^{207}Pb/^{206}Pb$	1σ	$^{207}Pb/^{206}Pb$	1σ	$^{206}Pb/^{238}U$	1σ	$^{207}Pb/^{235}U$	1σ	Conc
LV2B																		
15a	rim	33	394	0.05	0.763	0.011	0.0872	0.0011	0.86	0.0634	0.0009	722.5	28.1	539.0	6.4	575.5	6.2	93.7
15b	core	76	764	0.70	0.763	0.012	0.0870	0.0011	0.83	0.0636	0.0009	728.1	30.4	537.8	6.5	575.6	6.6	93.4
16a	rim	85	1123	0.08	0.691	0.009	0.0771	0.0009	0.90	0.0650	0.0008	775.0	26.6	479.0	5.6	533.6	5.7	89.8
16b	rim	75	972	0.08	0.640	0.009	0.0804	0.0010	0.89	0.0577	0.0007	519.6	27.9	498.6	5.8	502.4	5.4	99.2

		Content (ppm)			Isotopic Ratios							Ages (Ma)						
Zircon		Pb	U	Th/U	$^{207}Pb/^{235}U$	1σ	$^{206}Pb/^{238}U$	1σ	rho	$^{207}Pb/^{206}Pb$	1σ	$^{207}Pb/^{206}Pb$	1σ	$^{206}Pb/^{238}U$	1σ	$^{207}Pb/^{235}U$	1σ	Conc
LV15																		
1a	core	48	276	0.38	1.739	0.022	0.1647	0.0019	0.91	0.0766	0.0009	1110.4	23.6	983.0	10.4	1023.2	8.1	96.1
1b	rim	32	439	0.13	0.601	0.008	0.0752	0.0009	0.90	0.0579	0.0007	525.5	26.3	467.7	5.1	477.6	4.8	97.9
2a	core	90	273	0.48	4.973	0.059	0.2922	0.0033	0.95	0.1235	0.0014	2006.8	19.5	1652.5	16.4	1814.8	10.0	90.4
2b	**rim**	**98**	**1372**	**0.09**	**0.584**	**0.007**	**0.0751**	**0.0009**	**0.90**	**0.0565**	**0.0007**	**469.4**	**26.3**	**466.5**	**5.1**	**467.1**	**4.7**	**99.9**
3a	core	68	322	0.38	3.177	0.040	0.1838	0.0021	0.92	0.1254	0.0015	2034.0	20.9	1087.8	11.5	1451.6	9.6	71.4
3b	rim	38	528	0.13	0.594	0.008	0.0749	0.0009	0.88	0.0576	0.0007	513.7	26.9	465.4	5.1	473.6	5.0	98.3
3c	rim	30	378	0.15	0.667	0.009	0.0818	0.0009	0.88	0.0592	0.0007	573.7	26.4	506.6	5.6	518.9	5.2	97.6
4a	core	19	145	0.83	1.014	0.014	0.1105	0.0013	0.85	0.0666	0.0009	823.9	27.7	675.7	7.5	710.9	7.0	95.0
4b	rim	60	841	0.11	0.591	0.007	0.0752	0.0009	0.93	0.0571	0.0007	492.9	25.4	467.2	5.1	471.7	4.6	99.0
5a	core	61	709	0.09	0.845	0.011	0.0883	0.0010	0.91	0.0694	0.0008	911.0	24.4	545.4	6.0	621.9	5.9	87.7
5b	rim	56	680	0.11	0.695	0.009	0.0865	0.0010	0.92	0.0583	0.0007	539.2	25.8	534.8	5.8	535.8	5.2	99.8
6a	core	38	77	0.74	8.680	0.106	0.4085	0.0047	0.94	0.1541	0.0018	2392.2	19.4	2208.1	21.6	2305.0	11.2	96.4
6b	rim	26	361	0.11	0.594	0.008	0.0747	0.0009	0.87	0.0578	0.0007	520.2	28.3	464.1	5.2	473.7	5.1	98.0
6c	rim	83	1173	0.08	0.590	0.007	0.0750	0.0009	0.92	0.0571	0.0007	493.4	25.5	466.2	5.1	470.9	4.6	99.0
7a	core	8	57	0.89	1.088	0.017	0.1194	0.0015	0.78	0.0661	0.0010	808.7	31.9	727.1	8.4	747.4	8.2	97.3
7b	core	25	349	0.10	0.608	0.008	0.0751	0.0009	0.89	0.0588	0.0007	558.1	26.8	466.8	5.2	482.5	5.0	96.7
7c	rim	10	84	0.52	1.015	0.016	0.1154	0.0014	0.76	0.0638	0.0010	734.8	33.7	704.0	8.2	711.4	8.3	99.0
8a	core	30	322	0.43	0.793	0.011	0.0895	0.0010	0.87	0.0643	0.0008	750.5	26.8	552.7	6.2	593.0	6.0	93.2
8b	core	30	329	0.24	0.739	0.010	0.0939	0.0011	0.88	0.0570	0.0007	492.4	27.8	578.6	6.4	561.5	5.7	103.0
8c	**rim**	**55**	**773**	**0.13**	**0.585**	**0.007**	**0.0749**	**0.0009**	**0.92**	**0.0566**	**0.0007**	**476.9**	**25.9**	**465.8**	**5.2**	**467.8**	**4.7**	**99.6**
9a	core	11	97	0.80	0.834	0.013	0.0962	0.0012	0.80	0.0630	0.0009	706.5	31.2	591.8	6.8	616.1	7.0	96.1
9b	core	32	343	0.38	0.740	0.010	0.0903	0.0011	0.87	0.0595	0.0008	585.3	27.6	557.2	6.3	562.7	5.8	99.0
9c	rim	51	673	0.28	0.642	0.008	0.0751	0.0009	0.89	0.0620	0.0008	674.6	26.2	466.8	5.2	503.6	5.2	92.7
10a	core	0	6	0.11	0.554	0.033	0.0495	0.0012	0.41	0.0811	0.0051	1224.4	117.9	311.7	7.4	447.6	21.4	69.6
10b	rim	54	757	0.14	0.592	0.008	0.0752	0.0009	0.90	0.0571	0.0007	494.7	26.7	467.2	5.2	471.9	4.9	99.0
10c	rim	65	946	0.15	0.577	0.007	0.0729	0.0008	0.90	0.0574	0.0007	508.1	25.9	453.4	5.1	462.5	4.7	98.0

Zircon		Content (ppm)			Isotopic Ratios							Ages (Ma)						
		Pb	U	Th/U	$^{207}Pb/^{235}U$	1σ	$^{206}Pb/^{238}U$	1σ	rho	$^{207}Pb/^{206}Pb$	1σ	$^{207}Pb/^{206}Pb$	1σ	$^{206}Pb/^{238}U$	1σ	$^{207}Pb/^{235}U$	1σ	Conc
LV15																		
11a		49	697	0.16	0.585	0.008	0.0733	0.0009	0.87	0.0578	0.0007	523.3	27.9	456.1	5.2	467.4	5.0	97.6
11b		84	1196	0.13	0.599	0.008	0.0739	0.0009	0.86	0.0588	0.0008	560.8	28.1	459.5	5.2	476.7	5.2	96.4
12a	core	27	239	0.53	0.894	0.012	0.1054	0.0012	0.87	0.0616	0.0008	658.7	27.3	645.7	7.2	648.5	6.5	99.6
12b	**rim**	**29**	**407**	**0.18**	**0.585**	**0.009**	**0.0750**	**0.0009**	**0.81**	**0.0566**	**0.0008**	**475.9**	**32.3**	**466.2**	**5.4**	**467.9**	**5.6**	**99.6**
13a		21	305	0.10	0.609	0.011	0.0729	0.0009	0.74	0.0605	0.0011	622.9	37.0	453.8	5.6	482.7	6.7	94.0
13b		**38**	**546**	**0.12**	**0.580**	**0.008**	**0.0753**	**0.0009**	**0.85**	**0.0559**	**0.0008**	**446.0**	**29.2**	**468.1**	**5.4**	**464.3**	**5.2**	**100.8**
13c		33	452	0.13	0.645	0.009	0.0754	0.0009	0.84	0.0620	0.0009	675.2	28.9	468.7	5.4	505.3	5.7	92.8
15a	core	36	63	0.86	10.332	0.137	0.4653	0.0056	0.91	0.1611	0.0020	2467.4	20.8	2462.7	24.5	2465.0	12.2	99.9
15b	core	76	146	0.50	10.159	0.134	0.4715	0.0056	0.91	0.1563	0.0019	2416.1	20.7	2490.3	24.6	2449.3	12.2	101.4
16a		110	1542	0.18	0.606	0.008	0.0755	0.0009	0.88	0.0582	0.0007	538.0	28.1	468.9	5.4	480.8	5.2	97.5
16b		76	1076	0.16	0.589	0.008	0.0749	0.0009	0.88	0.0571	0.0007	494.6	28.0	465.3	5.3	470.2	5.1	99.0
17a	core	61	516	0.79	0.876	0.011	0.1044	0.0012	0.94	0.0608	0.0007	633.4	24.5	640.3	7.2	638.7	6.0	100.3
17b	rim	57	668	0.05	0.801	0.010	0.0916	0.0011	0.93	0.0634	0.0007	722.5	24.1	564.7	6.4	597.1	5.7	94.6
18a	core	19	172	0.71	0.808	0.011	0.0974	0.0012	0.87	0.0602	0.0008	610.7	28.0	599.0	6.9	601.4	6.3	99.6
18b	rim	80	1146	0.12	0.591	0.008	0.0732	0.0009	0.91	0.0585	0.0007	548.7	25.9	455.5	5.2	471.2	4.9	96.7
19a	core	11	125	0.36	0.726	0.011	0.0866	0.0011	0.84	0.0608	0.0009	633.0	29.7	535.5	6.3	554.4	6.3	96.6
19b	rim	37	514	0.16	0.597	0.008	0.0747	0.0009	0.92	0.0580	0.0007	527.9	26.2	464.4	5.3	475.3	4.9	97.7
20a		57	868	0.25	0.526	0.008	0.0669	0.0008	0.85	0.0570	0.0008	492.5	30.2	417.7	4.9	429.4	5.0	97.3
20b		40	555	0.17	0.599	0.008	0.0747	0.0009	0.90	0.0582	0.0007	534.8	27.2	464.6	5.4	476.7	5.1	97.5
20c		61	852	0.13	0.619	0.008	0.0749	0.0009	0.91	0.0600	0.0007	602.1	25.9	465.3	5.4	489.0	5.1	95.2
21a	core	35	100	0.58	5.278	0.067	0.3165	0.0038	0.94	0.1210	0.0014	1970.5	20.4	1772.4	18.5	1865.2	10.8	94.7
21b	core	80	217	0.59	5.497	0.069	0.3292	0.0039	0.95	0.1211	0.0014	1972.6	20.0	1834.6	19.0	1900.1	10.8	96.3
21c	rim	19	237	0.06	0.709	0.010	0.0831	0.0010	0.88	0.0619	0.0008	670.7	27.1	514.6	6.0	544.2	5.8	94.6
21d	core	40	287	0.16	1.689	0.022	0.1342	0.0016	0.93	0.0913	0.0011	1453.1	22.1	811.6	9.1	1004.4	8.2	69.1
22a	core	13	32	1.10	5.448	0.075	0.3238	0.0040	0.90	0.1221	0.0016	1986.5	23.0	1808.0	19.6	1892.4	11.8	95.3
22b	rim	41	537	0.11	0.719	0.010	0.0777	0.0009	0.90	0.0672	0.0008	842.5	25.5	482.5	5.6	550.3	5.7	87.7

Zircon		Content (ppm)			Isotopic Ratios							Ages (Ma)						
		Pb	U	Th/U	$^{207}Pb/^{235}U$	1σ	$^{206}Pb/^{238}U$	1σ	rho	$^{207}Pb/^{206}Pb$	1σ	$^{207}Pb/^{206}Pb$	1σ	$^{206}Pb/^{238}U$	1σ	$^{207}Pb/^{235}U$	1σ	Conc
LV15																		
22c	rim	78	1213	0.06	0.565	0.008	0.0686	0.0008	0.90	0.0598	0.0007	595.1	27.0	427.6	5.0	454.9	4.9	94.0
23a	core	66	229	0.57	4.411	0.056	0.2526	0.0030	0.94	0.1267	0.0015	2052.2	20.3	1452.0	15.5	1714.5	10.5	83.5
23b	zon.1	51	429	0.11	1.510	0.020	0.1170	0.0014	0.92	0.0936	0.0011	1500.3	22.5	713.4	8.1	934.5	7.9	62.3
23c	rim	33	403	0.12	0.745	0.010	0.0874	0.0011	0.90	0.0618	0.0008	668.1	26.4	539.8	6.2	565.0	5.8	95.5
24a	core	27	199	0.54	1.153	0.016	0.1244	0.0015	0.88	0.0672	0.0009	843.8	26.6	756.0	8.6	778.5	7.5	97.1
24b	rim	55	660	0.12	0.691	0.009	0.0870	0.0010	0.91	0.0576	0.0007	514.7	26.0	538.0	6.2	533.5	5.5	100.8
24c	rim	38	482	0.11	0.644	0.009	0.0825	0.0010	0.89	0.0566	0.0007	476.3	27.8	511.2	5.9	505.0	5.4	101.2
25a		73	618	0.72	0.904	0.012	0.1060	0.0013	0.90	0.0619	0.0008	670.4	26.2	649.5	7.4	654.1	6.4	99.3
25b		36	344	0.47	0.811	0.011	0.0982	0.0012	0.88	0.0599	0.0008	598.8	27.4	604.0	6.9	602.8	6.2	100.2
25c		18	178	0.24	0.807	0.012	0.0977	0.0012	0.83	0.0599	0.0009	600.2	30.4	600.7	7.1	600.5	6.7	100.0
26a		39	494	0.18	0.653	0.009	0.0813	0.0010	0.86	0.0583	0.0008	541.8	29.3	503.6	5.9	510.6	5.6	98.6
26b		32	378	0.17	0.703	0.010	0.0874	0.0011	0.86	0.0583	0.0008	541.8	29.4	540.3	6.3	540.6	5.9	99.9
26c		54	633	0.15	0.707	0.010	0.0892	0.0011	0.89	0.0575	0.0007	510.3	27.2	550.6	6.3	542.8	5.7	101.4
27a	core	81	740	0.50	0.893	0.012	0.1033	0.0012	0.90	0.0627	0.0008	697.8	26.1	633.8	7.2	647.9	6.4	97.8
27b	rim	44	518	0.13	0.738	0.010	0.0892	0.0011	0.87	0.0600	0.0008	603.1	27.9	550.8	6.4	561.0	6.0	98.2
27c	rim	65	843	0.12	0.650	0.009	0.0813	0.0010	0.89	0.0580	0.0007	528.2	27.8	504.1	5.8	508.4	5.4	99.2
28a	core	101	919	0.03	1.049	0.014	0.1187	0.0014	0.89	0.0641	0.0008	745.2	26.1	723.0	8.2	728.3	7.0	99.3
28b	rim	62	729	0.09	0.740	0.010	0.0893	0.0011	0.88	0.0601	0.0008	607.2	27.7	551.6	6.4	562.5	6.0	98.1
28c	core	55	436	0.58	1.058	0.015	0.1174	0.0014	0.88	0.0654	0.0009	786.3	26.9	715.6	8.2	732.8	7.2	97.7
29a	core	5	34	0.99	1.064	0.021	0.1190	0.0016	0.69	0.0648	0.0013	769.3	41.4	724.9	9.3	735.7	10.3	98.5
29b	rim	25	329	0.14	0.642	0.009	0.0789	0.0010	0.84	0.0590	0.0008	565.6	29.4	489.8	5.8	503.3	5.8	97.3
29c	rim	22	293	0.21	0.640	0.010	0.0750	0.0009	0.83	0.0620	0.0009	673.2	30.2	466.0	5.5	502.5	5.9	92.7
30a	core	414	858	0.07	13.061	0.176	0.4534	0.0054	0.89	0.2090	0.0026	2897.7	20.3	2410.3	24.2	2684.1	12.7	92.6
30b	**rim**	**36**	**502**	**0.14**	**0.588**	**0.009**	**0.0751**	**0.0009**	**0.82**	**0.0568**	**0.0008**	**482.0**	**32.3**	**466.7**	**5.6**	**469.3**	**5.7**	**99.4**
30c	rim	49	658	0.21	0.604	0.009	0.0751	0.0009	0.85	0.0583	0.0008	541.5	29.9	466.8	5.5	479.7	5.4	97.3

Chapitre 2 – Garnet-phengite-kyanite-quartz pseudomorph after cordierite: record of a high-pressure event in an Ordovician granite (Lévézou massif, French Massif Central)

Table of content

Résumé

Les roches granitiques constituent la majeure partie de la croûte continentale, mais sont connues pour être de piètres enregistreuses du métamorphisme. Les stades les plus tardifs du métamorphisme ou la déformation tendent par ailleurs à effacer toute histoire plus ancienne. Comprendre l'histoire métamorphique des orthogneiss granitiques est ainsi un défi aussi important que difficile à relever. L'étude de pseudomorphoses dans des faciès peu déformés peut être une clé pour déterminer l'histoire métamorphique ces roches, pourtant réputées hostiles.

Le massif du Lévézou, (sud Massif Central) est en parti composé de granites peralumineux ordoviciens, présentant une déformation hétérogène, depuis des faciès porphyriques indemnes de déformation, en passant par des orthogneiss jusqu'aux faciès ultramylonitiques. Cette déformation est parallèle à celle de l'unité voisine dominée par des amphibolites qui préservent de nombreuses lentilles d'éclogites. Les faciès porphyriques, malgré l'absence de déformation apparente, présentent de nombreuses textures métamorphiques. Par exemple, de petits grenats entourent des biotites magmatiques ou des aggrégats de rutiles pseudomorphosent l'ilménite. De rares formes subrectangulaires à muscovite, disthène, grenat et quartz peuvent aussi être observées. Leur forme et leur composition chimique suggèrent qu'elles correspondent à des pseudomorphoses de cordiérite. La modélisation des équilibres de phases (THERMOCALC) réalisée sur la composition de roche totale n'explique pas ces nombreuses textures métamorphiques mais permet de préciser les conditions de mise en place de ce granite à ca. 2 kbar et 670°C.

A l'inverse, le calcul de pseudosections à partir de la composition chimique locale de ces pseudomorphoses de cordiérite suggère qu'elles se sont développées à 15-17 kbar et 650-670°C, *i.e.* sous des conditions métamorphiques du faciès éclogite. Les modélisations suggèrent également que malgré la faible teneur en eau du granite, les pseudmorphoses étaient saturées en eau. Ceci est la conséquence probable d'une altération précoce ayant sans doute permis la recrystallisation de ces cristaux de cordiérites et leur pinitisation. Les conditions P-T sont similaires (15-17 kbar), bien qu'inférieures, à celles estimées sur les lentilles d'éclogites de la bande d'amphibolite avoisinante (18-23 kbar). Cela suggère que ces granites et roches mafiques aient subi le même évènement de haute pression, pendant la subduction Varisque. Ces orthogneiss sont ainsi les rares témoins de la subduction de croûte continentale pendant l'orogenèse Varisque.

Abstract

Granitic rocks constitute the major part of the continental crust, but are known to poorly record metamorphism. Furthermore, late stages tend to erase the record of the early metamorphic history. It is therefore important, although difficult, to understand the metamorphic history of granitic rocks. Studying pseudomorphs in the least deformed rocks may help to unravel the metamorphic history of these rocks, despite their "hostile" reputation.

In the Lévézou Massif (southern French Massif Central), elongated bodies of peraluminous granitic orthogneisses are parallel to a major regional amphibolite band containing abundant lenses of eclogite. These Ordovician granitic orthogneisses display a variable pattern of deformation, from undeformed porphyritic to ultramylonitic facies. The undeformed porphyritic facies displays numerous interesting metamorphic textures, as tiny garnet coronae surrounding magmatic biotite, rutile aggregates pseudomorphing ilmenite or rare rectangular clusters dominated by phengite, kyanite, garnet and quartz. The shape and the bulk composition of the latter suggest that they are pseudomorphs after cordierite. Phase diagrams modelling (THERMOCALC) performed on the whole rock composition does not explain these observations but allows to constrain the emplacement conditions of the granite at ca. 2 kbar and 670°C.

On the other hand, pseudosections calculated for the local bulk composition of the cordierite pseudomorphs suggest that they developed at 15-17 kbar and 650-670°C, *i.e.* under eclogite-facies conditions. Calculations further suggest that despite the H2O-depleted character of a crystallised granite, the pseudomorphs were saturated in aqueous fluid. This was a possible consequence of early alteration that also enhanced the recrystallisation of the cordierite crystals. The inferred P-T conditions are similar albeit slightly lower-pressure (15-17 kbar), to those obtained from the eclogite lenses of the neighbouring amphibolite band (18-23 kbar), implying that both the granites and the mafic rocks have experienced the same high-pressure event, during the early Variscan subduction. These orthogneisses are therefore rare witnesses of the subduction of the continental crust during the early stages of the Variscan orogeny.

1. Introduction

The record and preservation of high-pressure (HP) events is of paramount importance for deciphering mountain building processes. Metabasic and metapelitic rocks commonly preserve characteristic high-pressure assemblages, which make them the perfect material to access to the early stages of the orogeny. Quite the reverse, granitic rocks, which constitute the major part of the continental crust, are known to poorly record metamorphism and commonly remain metastable during HP to UHP metamorphism (Proyer et al. 2003; Petermann et al. 2009, and references therein). Rare cases preserved their prograde history until eclogitic peak-metamorphism with the assistance of deformation (e.g. Monte Mucrone, Western Alps, Oberhänsli et al. 1983; Orlica–Śnieżnik dome, Bohemian Massif, Chopin et al. 2012). The fact remains, however, that deformation commonly goes hand in hand with exhumation and retrogression, which tends to erase the early metamorphic history of rocks. Relics of HP stages are then theoretically best preserved in the least deformed zones (e.g. Malpica-Tuy, Iberian Massif, Ibarguchi 1995). Discrete evidences of HP metamorphism are scarce and can be found as the crystallization of jadeite or coesite in the most exceptional case (e.g. Chopin 1991; Ibarguchi 1995), the crystallisation of muscovite at the expense of biotite.

In the Variscan Belt, numerous pre-orogenic granitic rocks are closely associated with eclogitic terranes. They are supposed to belong to the margin of an opening ocean or back arc basin at ca. 490-470 Ma and occur all along the belt (e.g. Ballèvre et al. 2012) Despite their close association with HP rocks, the metamorphic history of these granites has rarely been investigated (e.g. Ibarguchi 1995; Chopin et al. 2012). In the Lévézou Massif, in the southern part of the French Massif Central (Fig. 1A), the Pinet granitoids are closely associated with the HP terranes and display variable deformation patterns, from undeformed porphyritic to ultramylonitic facies (Fig. III.2.1). Their emplacement has recently been dated at ca. 470 Ma (Lotout et al. 2017 and Part III, chapter 1), In the inner part of the massif, they locally enclose mafic enclaves with HP mineral assemblages (Delor et al. 1985). In this study, we investigate the emplacement and metamorphic P-T conditions experienced by the granite through a petrographical analysis and numerical modelling of phase equilibria.

2. Geological setting

The French Massif Central is classically subdivided into four Gondwana-derived units, based on their petrological characteristics: the Upper Gneiss Unit (UGU), the Leptyno-Amphibolitic Complex (LAC), the Lower Gneiss Unit (LGU) and the Parautochthon Unit (PAU) (e.g. Burg and Matte 1978; Matte 1986, Ledru et al. 1989). LGU and PAU display low grade metamorphism, while the LAC and UGU have recorded high-pressure (HP) and high-temperature (HT) metamorphism, respectively (e.g. Ledru et al. 1989). Since few years (e.g. Lardeaux 2014, Lardeaux et al., 2014), the LAC in the French Massif Central is considered to reflect a hyper-extended margin, where UGU and LGU are allochthonous blocks metamorphosed under various conditions. Following this interpretation, the UGU and LGU are considered to correspond to the more distal and more proximal part of the ordovician Gondwana margin, respectively.

The LAC emplacement in the Lévézou massif is dated at ca. 472 Ma, while HP metamorphism occurred at at ca 360 Ma (Part II, chapter 3). The HP conditions of the LAC have been estimated at 18-23 kbar and 680-780°C (Part II, chapter 3), 16.2 ± 0.3 kbar and 720 ± 30°C (Bouchardon, 1987), 18 kbar and 700 ± 50°C (Joanny et al., 1989) and 12.5-20 kbar and 750-840°C (Nicollet, 1978).

Variably deformed granitic orthogneisses outcrop in both the LGU and the UGU and are calc-alcaline peraluminous ordovician intrusions (Fig. III.2.1, Lotout et al. 2017 and Part III, chapter 1). They show variable microstructures and deformation patterns, ranging from undeformed and porphyritic, through augen-type to ultramylonitic facies. There are no described evidences of HP assemblages in the granites from the UGU, only scarce HP mafic enclaves are locally found (Delor et al. 1985). They were initially considered as xenoliths (Delor et al. 1985).

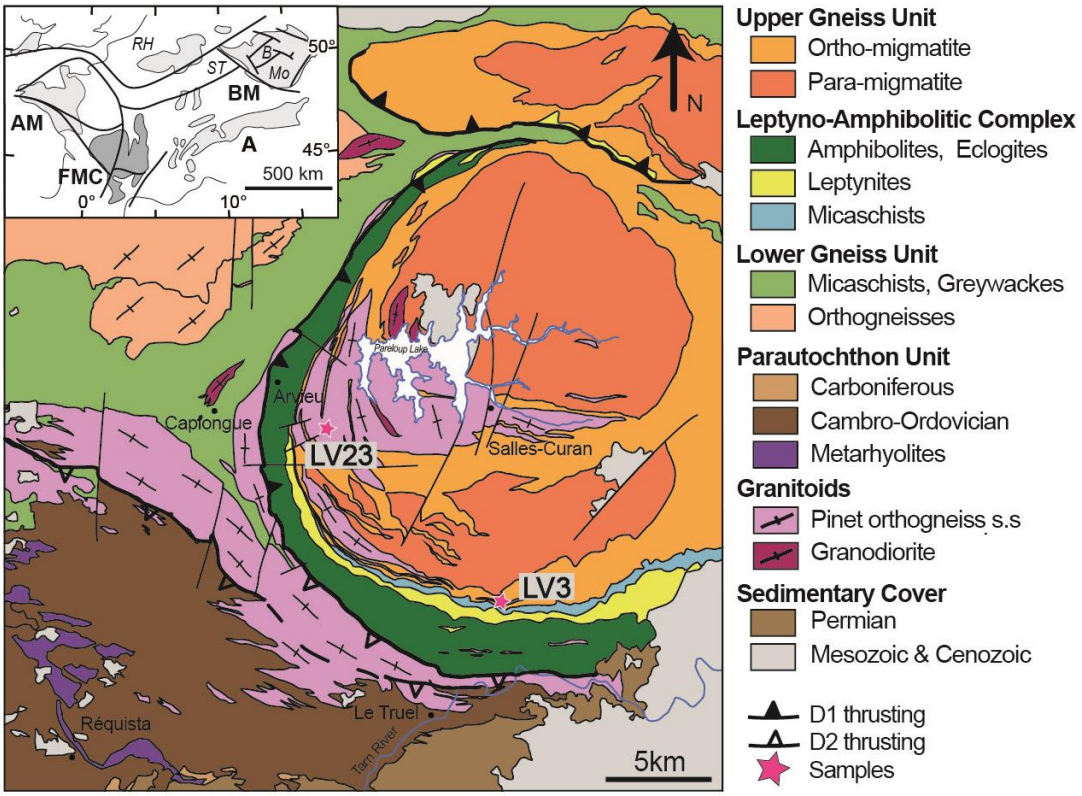

Figure II.2.1 - Simplified geological map of the Lévézou Massif (modified from Lotout et al. 2017), pink stars indicate sample locations from this study: LV3A (44° 5'58.09"N, 2°47'58.19"E), LV23 (44°10'52.07"N, 2°41'19.00"E)

3. Analytical methods

3.1. Chemical analyses

The sample LV3 was first cleaned from any weathered material, then crushed in a jaw crusher and in an agate mortar in order to obtain a fine powder. Major and trace elements analyses were performed by Inductively Coupled Plasma Atomic Emission Spectrometry (ICP-AES) and Inductively Coupled Plasma Mass Spectrometry (ICP-MS), respectively, at the Geochemical and Petrographical Research Center (SARM laboratory, CNRS-CRPG) in Nancy, following the procedure described in Carignan et al. (2001).

3.2. Mineral composition

Mineral analyses were carried out with a Cameca SX100 electron microprobe (Microsonde Ouest, IFREMER, Plouzané, France) operating in a wavelength-dispersive mode (for the complete analytical procedure, see Pitra et al., 2008). Data are summarized in the supplementary section

3.3. Thermocalc modelling

P-T conditions were calculated using the software THERMOCALC (version 3.37; Holland and Powell 1985; Powell and Holland, 1988), with the thermodynamic data set 6.2 (Holland and Powell, 2011; Feb. 2012 upgrade). Pseudosections have been calculated in the model system Na_2O–CaO–K_2O–FeO–MgO–Al_2O_3–SiO_2–H_2O–TiO_2–O (NCKFMASHTO), FeO standing for the total iron, O for the proportion of Fe_2O_3 (=2FeO+O). Solid solution models are from White *et al.* (2014). The muscovite model is from Nahodilová et al. (2014), because it allows the incorporation of titanium in muscovite. Phase abbreviations used are : ab = albite, and = andalousite, bi = biotite, cd = cordierite, ep = epidote, g = garnet, hem = hematite, ilm = ilmenite, jd = jadeite, ksp = K-feldspar, liq = liquid (melt), ma = margarite, mu = muscovite, o = omphacite, pa = paragonite, pl = plagioclase, q = quartz, ru = rutile, sill = sillimanite, sph = titanite (sphene), st = staurolite. Other symbols (mole/atomic proportions) used are: $X_{Fe} = Fe^{2+}/(Fe^{2+}+Mg)$ (garnet, biotite), weight per cent (wt%), mole per cent (mol.%), pfu = per formula unit. The bulk rock composition used to calculate the phase diagrams was corrected for the presence of apatite, not considered in the calculations.

4. Petrography

4.1. Description

Macroscopically, the undeformed facies (samples LV3, LV23) are composed of porphyritic K-feldspar (up to 15 cm), plagioclase, quartz, biotite and muscovite. Even if the rock appears undeformed macroscopically, the thin section observation discloses metamorphic textures. Two types of mineral aggregates are also observed, referred to hereafter as decussate aggregates and rectangular clusters. The specific assemblage of the latter is discussed in its own section.

Subrectangular K-feldspar (X_{Or} = 0.79-1.0) crystals display Carlsbad twins and perthitic exolutions, and contain numerous inclusions of tiny muscovite crystals (up to 0.1 mm). Rims are commonly recrystallized and rarely display myrmekite textures. Locally, K-feldspar crystals (in average 1-2 cm) are recrystallised into granoblastic aggregates of tiny crystals (up to 0.1 mm) with thin flakes of muscovite (up to 0.15 mm), surrounding unrecrystallized K-

feldspar relics (in average ≈1 mm). Plagioclase (X_{An} = 0.19-0.26) is present as (i) large crystals (up to 10 mm), commonly enclosing tiny muscovite (up to 0.1 mm) and locally displaying rim recrystallisation, (ii) unoriented remnants (up to 0.2 mm) of former large crystals (up to 10 mm), and (iii) small unoriented crystals (up to 0.1 mm) localised in aggregates with garnet, muscovite, biotite, quartz and tourmaline (dravite). Quartz forms commonly anhedral unoriented crystals (up to 3 mm) with irregular grain boundaries. It can be also associated with tiny biotite along cleavage planes of large muscovite crystals (Fig. III.2.2E and see below)

Biotite is found in two textural positions. Red-brown biotite (biotite 1) forms subrectangular unoriented thick flakes (up to 2 mm), locally strongly kinked. Biotite 1 is Ti-rich and ferroan (Ti = 0.16-0.23 pfu, X_{Fe} = 0.58-0.65). Locally, it is surrounded by tiny crystals of titanian slighly phengitic muscovite (Fig. III.2.2A, B) or or by a corona of tiny crystals of garnet (up to 0.02 mm, Fig. III.2.2C). Light greenish to colourless biotite (biotite 2) is less titanian and more magnesian (Ti = 0.00-0.02 pfu, X_{Fe} = 0.50-0.59) and occurs in different textural positions (i) as microscopic crystals closely associated with decussate aggregates of muscovite garnet, plagioclase and locally dravite (Fig. III.2.D, G), (ii) as inclusions (up to 0.2 mm, Fig. III.2.2E) in large muscovite crystals, commonly aligned along the cleavage planes, or (iii) as small crystal in apparent crystallographic continuity with muscovite (Fig. III.2.2E)

Muscovite is present in several textural positions. (i) Tiny crystals (up to 0.15 mm) are surrounding biotite 1 in reactional symplectitic coronae-(Ti = 1.1-1.2, Si = 3.05-3.12 pfu, Fig. III.2.2A, B). (ii) Similar crystals (up to 0.15mm) form unoriented inclusions in K-feldspar, or in close association with the granoblastic K-feldspar or plagioclase domains. (iii) Unoriented crystals of muscovite (in average 0.04 mm, up to 0.5 mm) form the major part of decussate aggregates (Ti = 0.002-0.008; Si =3.04-3.19), associated with biotite 2, plagioclase, garnet or dravite. (iv) Rare large crystals (up to 1mm) are also observed systematically associated with biotite 2 and sometimes with tiny garnet crystals (Ti = 0.002-0.008, Si = 3.07-3.14 pfu, Fig. III.2.2E).

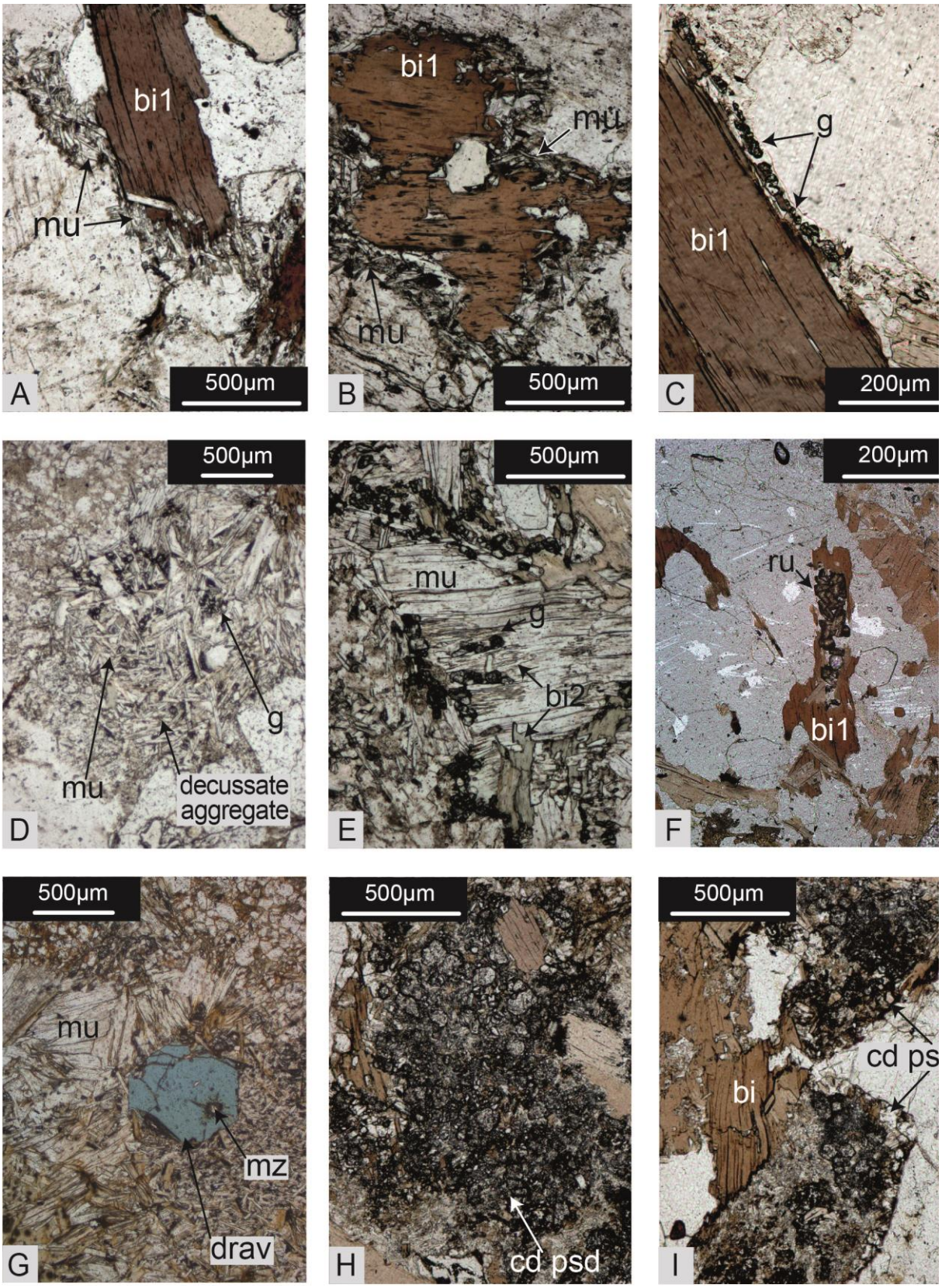

Figure III.2.2 – Photomicrograph of undeformed facies of the Pinet granite. A. B. biotite 1 surrounded by fine muscovite-rutile- quartz symplectites. C. tiny garnet in coronae surrounding biotite 1. D. garnet-muscovite-biotite2-plagioclase-quartz decussate aggregate. E. Large muscovite crystal with quartz and biotite 2 exsolution, associated to garnet. F. rutile aggregate in biotite1. G. Dravite grain in muscovite-garnet-plagioclase-quartz decussate aggregate. H. I. kyanite-garnet –phengite-quartz pseudomorph after cordierite.

Dravite forms unoriented blue strongly pleochroic subhedral crystals (in average 0.5 mm, locally up to 1.5 mm) localised in decussate aggregates of garnet, muscovite, biotite 2, quartz and plagioclase (Fig. III.2.2G). Rutile (up to 0.1 mm) is locally included in biotite and can be associated with ilmenite. It forms generally subrectangular aggregates up to 0.5 mm long (Fig. III.2.2F). Small grains can be found associated with tiny phengitic muscovite and quartz. With the exception of the clusters decribed below, garnet is rare and small (up to 60µm). It is localised in coronitic rims surrounding biotite (Fig. III.2.2C), in decussate aggregates (Fig. III.2.2D) or closely associated with large muscovite (Fig. III.2.2E), and has ferrous composition (X_{alm} = 0.69-0.74, X_{pyr} = 0.09-0.18, X_{spe} = 0.09-0.16, X_{gro} = 0.02-0.04, X_{Fe} = 0.80-0.87). Accessory minerals in the rock are zircon, monazite, apatite, ilmenite, hematite and pyrite.

Decussate aggregates (up to 5mm) are systematically composed of biotite 2, tiny flakes of muscovite, plagioclase quartz and locally garnet or dravite (Fig. III.2.2D). These aggregates are unoriented, and can be surrounded by K-feldspar, biotite 1 or plagioclase.

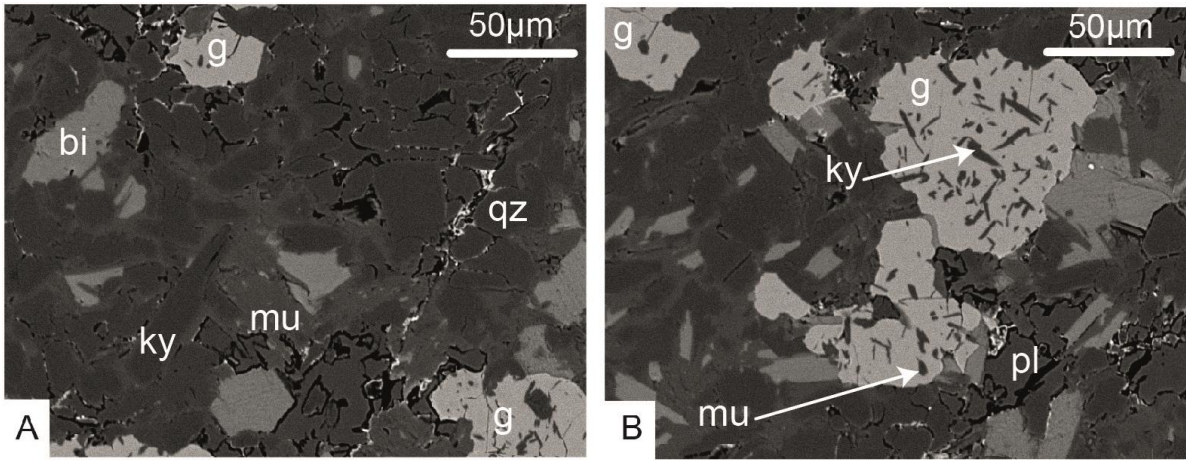

Figure III.2.3 –SEM picture from a part of the kyanite-garnet –phengite-quartz pseudomorph after cordierite seen in Fig. III.2.2H. Inclusions of kyanite and muscovite in garnet are highlited.

Subrectangular clusters (~0.5x1.0 mm) of unoriented very fine grained crystals (~0.01-0.05 mm) occur locally in the samples (Fig. III.2.2H, I and III.2.3). They are composed of muscovite, garnet, kyanite, quartz, biotite, plagioclase and hematite. Slightly phengitic muscovite (up to 0.05 mm, Si up to 3.21 pfu in the matrix, but average Si = 3.1-3.13, Ti = 0.01-0.05 pfu) comprises about 40% of the cluster and also forms inclusions in garnet (up to 0.01 mm). Garnet forms subhedral unzoned crystals (X_{alm} = 0.71-0.74, X_{pyr} = 0.05-0.1, X_{spe} = 0.15-0.2, X_{gro} = 0.01-0.03, X_{Fe} = 0.88-0.93) and represents 15% of the cluster. Kyanite

and quartz occur both as inclusion (up to 0.01 mm) in garnet and in the matrix of the cluster (up to 0.08 mm). They represent 13% and 11% of the cluster, respectively. Biotite only occurs in the matrix (in average 0.2 mm, locally up to 1.5 mm) and forms 10% of the cluster. The chemical composition (Ti = 0.04-0.14 pfu, X_{Fe}= 0.56-0.61) is different from both biotite 1 and biotite 2 described above (Fig. III.2.D, E). Plagioclase (up to 0.03 mm, X_{an} = 0.18-0.21) comprises 7% of the cluster and is exclusively present in the matrix. Hematite (0.5% of the cluster) is localised along grain boundaries of the other minerals and associated with rounded plagioclase grains.

4.2. Interpretation

The multiple textural positions of muscovite (symplectite rims around biotite 1, decussate aggregates, clusters with garnet and kyanite, close association with biotite 2) suggests that it is not a part of the primary magmatic assemblage but rather formed during (several?) subsequent metamorphic event(s).

The subrectangular aggregates of rutile can be interpreted as pseudomorphs of original crystals of illmenite (e.g. Le Bayon et al. 2006). Biotite 2, found in apparent crystallographic continuity with large muscovite crystals, and associated with tiny quartz has a very low Ti content and could be the result of an exsolution from phengitic muscovite (e.g. Nahodilova et al. 2014).

The shape of the subrectangular clusters and the minerals they comprise suggest that they could be pseudomorphs after magmatic cordierite (e.g.. Godard, 2001, 2009), common in peraluminous granites. The local bulk composition for the cluster is SiO_2-53.56%, Al_2O_3-29.44%, TiO_2-0.31%, FeO-7.92%, MnO-1.1%, MgO-1.46 %, CaO- 0.43%, Na_2O- 0.96%, K_2O-4.63%. (weight % oxyde), yielding a formula of $Si_{5.53}$ $Al_{3.59}$ $Ti_{0.02}$ $Fe_{0.68}$ $Mn_{0.1}$ $Mg_{0.23}$ $Ca_{0.05}$ $Na_{0.19}$ $K_{0.61}$ O_{18}. This composition is relatively close to the theoretical chemical composition of cordierite ($(Mg,Fe)_2Al_4Si_5O_{18}$). Kyanite, muscovite and quartz are found in the pseudomorph matrix and also included in garnet. Biotite is dispersed in the pseudomorph, while plagioclase and hematite are commonly associated. Garnet, kyanite, muscovite and quartz appear then as the principal stable assemblage. Biotite, plagioclase and hematite could be the result of a later partial recrystallisation (see Discussion below).

Based on their shape, decussate aggregates could also be pseudomorphs after cordierite. They are composed of variable mineral assemblages (muscovite, biotite 2, plagioclase, quartz and locally dravite and/or garnet).

Consequently, the magmatic paragenesis is interpreted as K-feldspar-plagioclase-quartz-biotite 1-ilmenite-cordierite. A subsequent metamorphic stage lead to (i) the replacement of ilmenite by rutile, (ii) crystallization of muscovite, partly at the expense of biotite 1, (iii) development of garnet-kyanite-muscovite-quartz pseudomorphs after cordierite (iv) development of decussate aggregates, and finally (v) exsolution of biotite 2 and quartz from a former phengitic metamorphic muscovite.

5. Phase diagrams

Pseudosections were first calculated assuming H_2O in excess and 5% of Fe^{3+} out of the total Fe. The validity of these assumptions was then checked using P/T-X pseudosections.

5.1. Whole rock P-T modelling

First, a P-T pseudosection was calculated for the whole rock chemical composition of the sample LV3 (Fig. III.2.4) in order to estimate the conditions of the emplacement of the cordierite-biotite-ilmenite-bearing granite (cf. part 4) and possibly those of the development of the pseudomorph assemblages (mu+g+ky+q) The phase diagram was calculated with H_2O in excess and consequently the phase relations beyond the solidus (marked "+liq" in Fig. III.2.4) are not represented. Quartz, K-feldspar, plagioclase and biotite are stable in all fields (with the exception of the uppermost HP-LT field, which is plagioclase-absent). Cordierite and ilmenite are only stable in the LP-HT part of the diagram. In contrast, muscovite and rutile are stable at higher pressures and/or lower temperatures, but the stability of garnet or kyanite is not predicted in this diagram. Furthermore, muscovite and cordierite cannot be stable at the same P–T conditions in this rock. The inferred primary magmatic assemblage (ksp-pl-q-bi-cd-ilm) corresponds to the stability field at $P<3$ kbar and $T>600$°C. Since this assemblage is inferred to correspond to the crystallisation of the magma, the equilibration conditions must be in the high-temperature part of the field, close to the solidus ($T>660$°C). The formation of the pseudomorph assemblage can not be explained using this

bulk rock composition. Calculations on the specific composition of these pseudomorphs are then needed to be investigated.

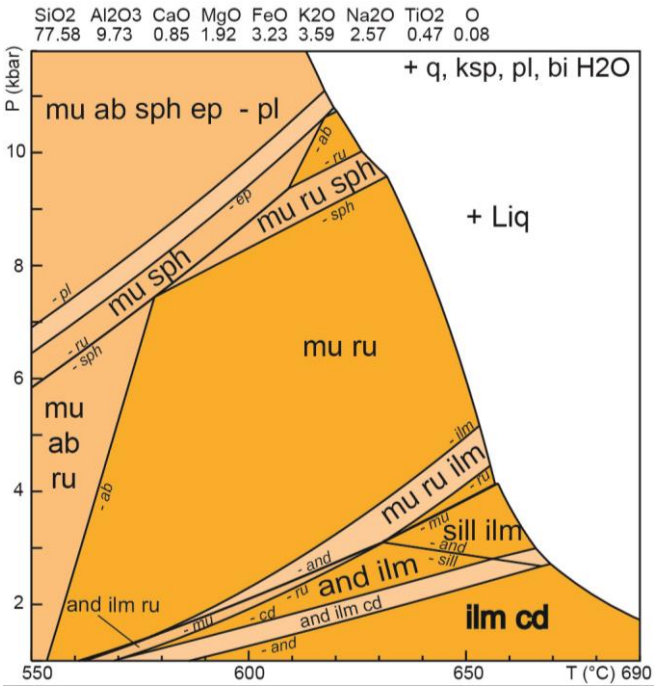

Figure III.2.4 – P-T diagram calculated for the whole rock chemical composition

5.2. Pseudomorph P-T modelling

Subrectangular clusters of muscovite-garnet-kyanite-quartz are interpreted as pseudomorphs after cordierite. To quantify the P–T conditions leading to the pseudomorph development, phase diagrams were then calculated using the local bulk chemical composition of the pseudomorph. The first pseudosection was calculated with H_2O in excess and 5% of Fe^{3+} out of the total Fe. Since it has been suggested by several studies that Na-clinopyroxene may fail to nucleate in granitoid rocks (Oberhänsli et al. 1983; Koons et al. 1987; Chopin et al. 2012), pseudosections have been calculated both with and without jadeite and omphacite (Fig. III.2.5A, B).

In the pseudosection without Na-pyroxenes (Fig. III.2.5A), the garnet-kyanite-muscovite-quartz assemblage is stable in a field ranging from 10.5kbar and 660°C to 18.5kbar and

700°C. It is delimited by the appearance/disappearance lines of paragonite, hematite and liquid at higher pressure, lower pressure and higher temperature respectively. Paragonite is stable in the upper part of the diagram (along a line from 12 kbar and 575°C to 18.5Kbar and 700°C). Si in muscovite ranges from 3.08 to 3.13 pfu. Compositional isopleth for silica in muscovite ranges 3.08-3.13 pfu in the pfu in the g-ky-q-mu±hem fields.

In the pseudosection with Na-pyroxenes (Fig. III.2.5B), the stability field of the garnet-kyanite-muscovite-quartz assemblage is located at 11 to 17.5 kbar and 660 to 700°C. It is delimited by the appearance/disappearance lines of hematite and paragonite at lower temperature, jadeite at higher pressure and liquid at higher temperature. Jadeite is stable in the HP part of the diagram (> 18 kbar) while paragonite and rutile are stable in the LT–HP of the diagram. Compositional isopleths for silica in muscovite are pressure-dependant and range 3.08-3.12 pfu in the garnet-kyanite-muscovite-quartz stability field.

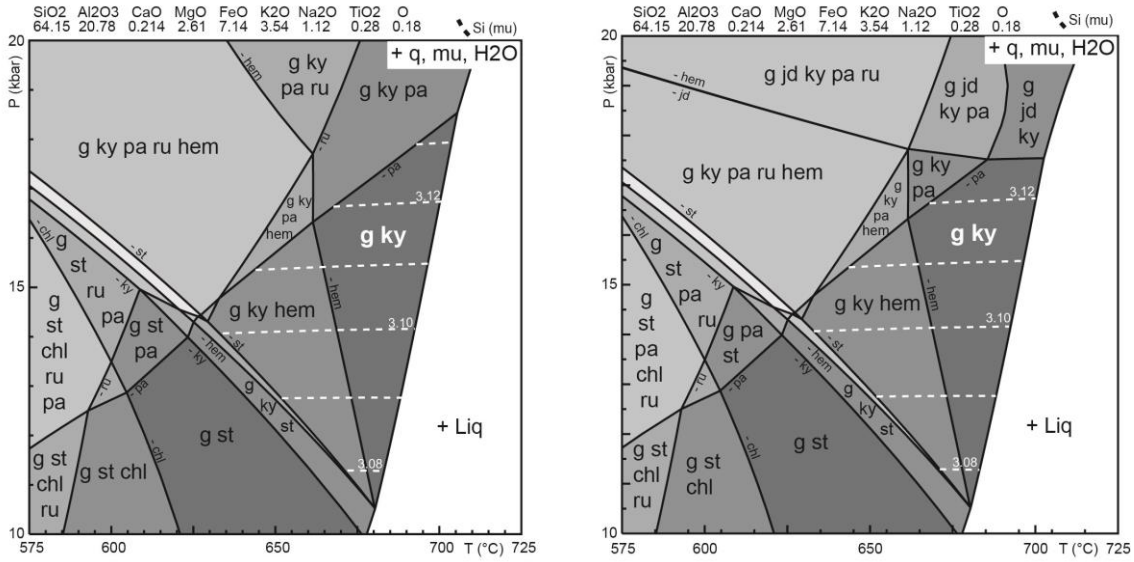

Figure 5 – P-T pseudosection for cordierite pseudomorph. Fields are colored with respect to their variance. Left P-T : without Na pyroxene included in calculation, Right P-T : with Na pyroxene in calculation. Compositionnal isopleths of Si in muscovite are represented.

In both pseudosections, the muscovite-garnet-kyanite-quartz assemblage is stable in similar P-T conditions: from ca. 11 to 18.5 kbar and about 670 to 680°C, i.e. eclogite facies. The stability of jadeite only marginally restricts the stability of the assemblage of interest, by merely ~1 kbar.

Microprobe analyse on muscovite from the pseudomorph showed Si content in muscovite up to 3.21 pfu, and average Si range from 3.1 to 3.13 pfu. The calculated values from the compositional isopleths in the stability field of interest indicates 3.08 to 3.13 pfu. Even if these results match with most of the analysed muscovite, it does not explain the high-Si muscovite. Nevertheless, it is proposed that the kyanite-garnet-muscovite-quartz pseudomorph may have equilibrated at minimum pressure of 15-17 kbar, and temperatures of ca. 670°C.

5.3. Pseudomorph P-M_{H2O} modelling

To test the H2O influence on the stability field of the mineral assemblages, P-X_{H2O} pseudosections (X_{H2O} correspond to the amount of H_2O available) were calculated both with (not shown) and without Na-pyroxene (Fig. III.2.6A). The temperature was fixed at 670°C (about the middle of the g-ky-mu-bearing fields). Results show the same stability field (i.e. 14-17 kbar, Si(mu) isopleth from 3.08 to 3.12) for the muscovite-garnet-kyanite assemblage, until the loss of H_2O saturation, at ~0.65 M(H_2O). Then, Si(mu) = 3.12 isopleth falls from 16.6 kbar (g-mu-ky-q-H2O field, 1-0.75 M(H_2O)) to 11.3 kbar (g-mu-ky-q-pl-bi-ilm-ksp field, 0.45-0.1 M(H_2O); Fig. III.2.6B).

Molar proportions of muscovite garnet and kyanite were also calculated in the P-XH_2O pseudosection without Na-pyroxene, to identify the most appropriate stability field (Fig. III.2.6C). In the muscovite-garnet- kyanite- quartz-H2O stability field, muscovite represents 51 to 54 %, garnet 15 to 16%, kyanite ~10.7 to 11.7%, quartz 16 to 17% and water about 0.03 to 4% (Fig. III.2.5C). Garnet calculated modal proportion is identical to the estimated proportion of ~15%. Similarly, kyanite and quartz estimations at ~13% and 11% are quite similar to calculations (~10.7-11.7% and 16-17%, respectively). Muscovite modal proportion is higher by 10% than estimated. The presence of biotite in the pseudomorph (~10%), is probably the cause of this overestimation.

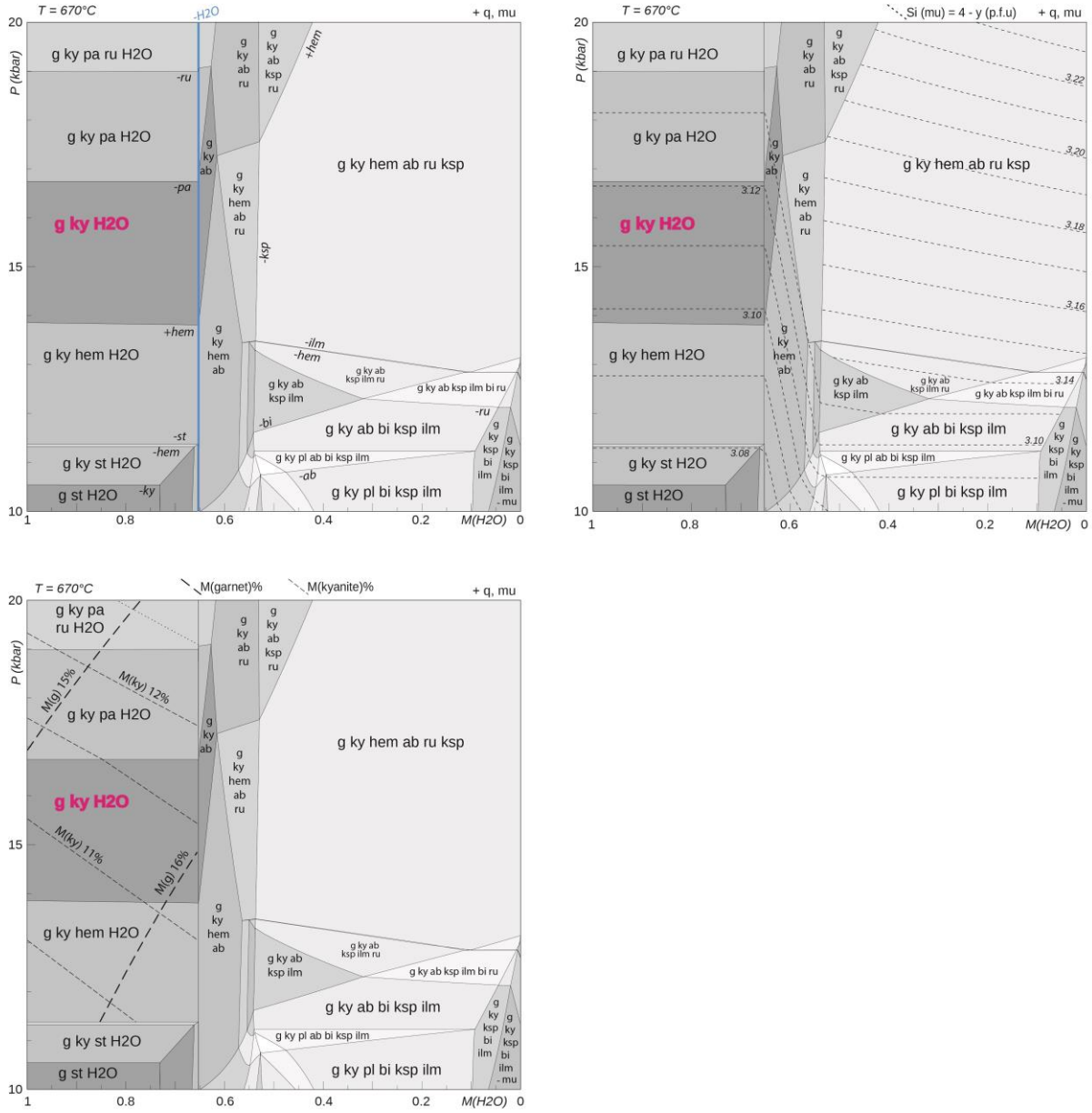

Figure III.2.6 – A. P-X_{H2O} pseudosections, where X_{H2O} correspond to the amount of H_2O available, calculated without Na-pyroxene. B. Si(mu) isoplets. C. Molar proportions of garnet and kyanite.

The H2O amount appears to be a key parameter for both the Si content in muscovite, and the stability of the kyanite-garnet-phengite-quartz assemblage, since the latter disappears in the H_2O-undersaturated part of the pseudosection. Calculated modal proportions, with the partial exception of muscovite, is in perfect agreement with the measured ones.

5.4. Pseumorph P-X_{Fe} modelling

To investigate the influence of the proportion of ferric iron on the stability field of the mineral assemblages, two P-X_{Fe}^{3+} pseudosections were calculated at 670°C, and X_{H2O} = 0.7 and X_{H2O} = 0.4, corresponding to H_2O saturated and undersaturated conditions, respectively (Fig. III.2.7A and B, respectively).

At X_{H2O} = 0.7, the P-X_{Fe}^{3+} diagram shows that hematite is not stable at $XFe^{3+} \leq 0.05$. The mineral assemblage g-ky-mu-q-H2O is stable at P > 10-11 kbar for $XFe^{3+} < 0.05$. The mineral assemblage g-ky-mu-q-hem is stable from ca 11 kbar to 17-15 kbar at XFe^{3+}= 0.05-0.30, respectively.

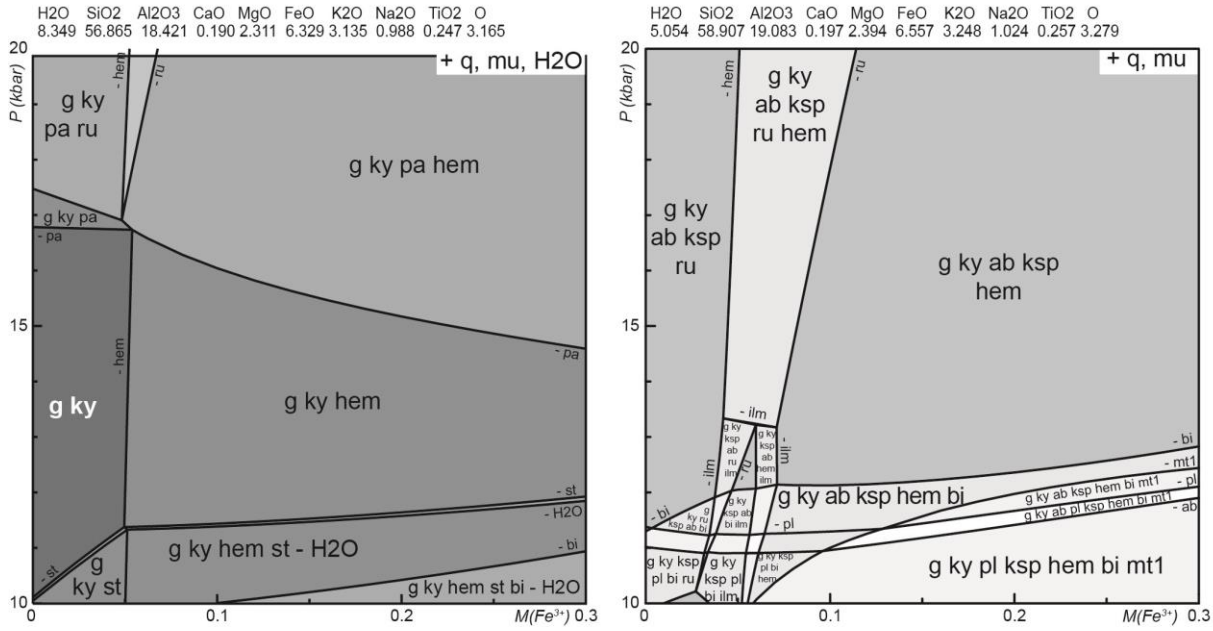

Figure III.2.7- P-X_{Fe}^{3+} pseudosections were calculated at 670°C, and X_{H2O} = 0.7 (A) and X_{H2O} = 0.4 (B)

In the P-X_{Fe}^{3+} diagram at X_{H2o} = 0.4, magnetite appears from XFe^{3+} = 0.07 and is gradually stable until 12 Kbar at XFe^{3+} = 0.3. Illmenite is no longer stable from $XFe^{3} \leq 0.03$. The stable assemblage kyanite-garnet-muscovite-quartz, without additional phases is not observed. The stability of hematite is dependant from the Fe^{2+}/Fe^{3+} ratio. The assemblage of interest kyanite-garnet-phengite-quartz remains stable within the same range of pressure. Consequently, Fe^{2+}/Fe^{3+} ratio is not a key factor and does not restrain the stability field of interest.

5.5. interpretation

The garnet-muscovite-kyanite-quartz assemblage stability field is not affect by the Na-pyroxene presence or the Fe^{2+} /Fe^{3+} balance. Only the amount of water is a determinant parameter. Cordierite crystals $(Mg,Fe)_2Al_4Si_5O_{18}(nCO_2,mH_2O)$ can incorporate a large range of H_2O within its channel structure. THERMOCALC calculation estimates the amount of H_2O in the cordierite (q-ksp-pl-bi-ilm-cd-H2O assemblage, 670°C, 2 kbar) at 0.51 pfu, meaning that the cordierite is not fully H_2O saturated. Besides, cordierite crystals are commonly altered by fluids and pinitized, leading to the development of hydrous minerals. The measured proportion of minerals in the analysed pseudomorph matches the calculated modal proportion, apart from muscovite amount. The calculated Si in muscovite also globally matches the analysed values, except for the highest Si in muscovite values at ~3.21.

Consequently, we interpret the kyanite-garnet-muscovite-quartz assemblage as a high pressure assemblage, equilibrate at least under 15-17 kbar and 670°C condition. This result implies that the pseudomorph after the initial cordierite had been equilibrated under eclogite-facies conditions.

6. Discussion

6.1. Primary magmatic assemblage

The primary assemblage is interpreted as K-feldspar-plagioclase-quartz-biotite-ilmenite-cordierite based on petrographical observation. THERMOCALC modelling on the WR chemistry allow to identify a corresponding stability field at 600-700°C and <3 kbar. We then interpret these P-T conditions as corresponding to the emplacement of the granite, at ca. 470 Ma (Lotout et al. 2017).

6.2. Metamorphic assemblage

All muscovite in the sample are metamorphic, and the various textures combined to the large range of measured Si(mu) values suggests that they possibly crystallized or recrystallized under a large range of P-T conditions.

Numerous metamorphic textures are seen, and can not be infer to any specific P-T conditions. The development of rutile pseudomorph after ilmenite is described in the literature as due to prograde metamorphism (e.g. Le Bayon et al. 2006). Similarly, the development of phengite-rutile-quartz symplectites at the expense of biotite could be the results of local disequilibrium that slightly destabilise biotite on the prograde path, during the P-T evolution. The large crystals of muscovite slightly phengitic display quartz and secondary low Ti-biotite exsolution, and can be interpreted as expelled from a former more phengitic muscovite (e.g. Nahodilova et al. 2014). They are then likely to have grown under higher pressure, and the exsolution then testifies to the subtle retrogression experienced by the undeformed granitic facies.

The kyanite-garnet-phengite-quartz pseudomorph after cordierite is undoubtedly the best witness of a former HP event. The phase equilibria numerical modelling allow to estimate minimum P-T conditions at 15-17 kbar and ~670°C. The biotite and plagioclase observed in this pseudomorph could be due to a slight retrogression. In particular, when H2O saturation is loss, the assemblage g-ky-mu-q-pl-bi is found.

Equilibrium was not attained at the whole rock scale and only local zones did record the metamorphic evolution by developing scarce and various metamorphic texture.

6.3. Tectonic implications

The recorded P-T conditions at ~670°C and minimum 15-17 kbar correspond to the eclogite facies. They are quite similar to the conditions reached by the neighboring HP terranes, at 21-23 kbar and 680-800°C. The presence of the HP pseudomorphs, as well the presence of mafic enclaves displaying HP assemblages (Delor et al. 1985) indicate that the whole granite did experience a high pressure event. At a larger scale, the 15-17 kbar and 670°C indicate that the whole granitic terranes from the inner part of the Lévézou massif experienced a HP pressure

event compatible with a subduction setting. This therefore demonstrates the subduction of continental crust in this massif.

7. Conclusion

The Pinet granite in the inner part of the Lévézou massif emplaced during Ordovician times at ca. 2 kbar and ~670°C. It experienced a high pressure event during the variscan subduction estimated at 670°C and 15-17 kbar as minimum pressures, highlighted by the development of kyanite-garnet-phengite-quartz pseudomorph after cordierite. This result testifies to the subduction of continental crust during the variscan orogeny in the French Massif Central.

Supplementary data - Chemical composition of minerals

	LV3Ai	LV3Ai	LV3Ai	LV3Ai	LV3Ai	LV3Ai	LV3Ai	LV3Ai	LV3Ai	LV3Ai	LV3Ai	LV3Ai	LV3Ai
analysis #	45.00	46.00	47.00	48.00	49.00	104.00	105.00	108.00	204.00	325.00	326.00	330.00	331.00
	large muscovite crystal					muscovite in symplectite surounding biotite				muscovite in decussate aggregate			
SiO2	46.24	46.69	47.07	47.39	47.64	46.17	46.78	45.88	46.21	45.50	45.61	46.33	46.73
TiO2	0.15	0.16	0.14	0.12	0.16	1.13	1.14	1.17	1.20	0.06	0.04	0.11	0.13
Al2O3	35.71	34.94	35.43	34.85	35.17	35.25	33.76	35.12	35.48	34.91	35.23	33.33	32.02
MgO	0.71	0.85	0.86	0.77	0.71	0.61	0.92	0.52	0.63	0.81	0.77	1.18	1.41
FeO	1.01	1.09	1.13	1.07	1.11	1.20	1.22	1.00	1.14	1.14	1.15	1.21	1.34
MnO	0.01	0.00	0.00	0.02	0.01	0.02	0.02	0.03	0.00	0.05	0.00	0.03	0.05
CaO	0.01	0.26	0.00	0.04	0.00	0.18	0.02	0.01	0.00	0.01	0.04	0.03	0.12
Na2O	0.43	0.40	0.39	0.39	0.65	0.51	0.42	0.55	0.51	0.60	0.52	0.45	0.35
K2O	11.26	11.30	11.30	11.31	10.62	11.13	11.00	11.40	11.29	11.24	11.07	11.04	11.06
H2O	4.50	4.51	4.54	4.53	4.55	4.52	4.49	4.50	4.54	4.43	4.45	4.41	4.39
Sum	100.02	100.19	100.87	100.50	100.63	100.73	99.77	100.17	101.00	98.74	98.87	98.12	97.58
Si	3.08	3.10	3.10	3.14	3.14	3.06	3.12	3.06	3.05	3.08	3.07	3.15	3.19
Ti	0.01	0.01	0.01	0.01	0.01	0.06	0.06	0.06	0.06	0.00	0.00	0.01	0.01
Al	2.80	2.74	2.75	2.72	2.73	2.75	2.66	2.76	2.76	2.78	2.80	2.67	2.58
Mg	0.07	0.08	0.09	0.08	0.07	0.06	0.09	0.05	0.06	0.08	0.08	0.12	0.14
Fe2	0.06	0.06	0.06	0.06	0.06	0.07	0.07	0.06	0.06	0.06	0.07	0.07	0.08
Mn	0.00	0.00	0.00	0.00	0.00	0.00	0.00	0.00	0.00	0.00	0.00	0.00	0.00
Ca	0.00	0.02	0.00	0.00	0.00	0.01	0.00	0.00	0.00	0.00	0.00	0.00	0.01
Na	0.06	0.05	0.05	0.05	0.08	0.07	0.05	0.07	0.07	0.08	0.07	0.06	0.05
K	0.96	0.96	0.95	0.96	0.89	0.94	0.94	0.97	0.95	0.97	0.95	0.96	0.96
OH	2.00	2.00	2.00	2.00	2.00	2.00	2.00	2.00	2.00	2.00	2.00	2.00	2.00
Sum	9.02	9.02	9.01	9.00	8.98	9.01	8.99	9.03	9.02	9.06	9.04	9.02	9.02
XNa	0.05	0.05	0.05	0.05	0.09	0.07	0.06	0.07	0.06	0.08	0.07	0.06	0.05
Xfe	0.44	0.42	0.42	0.44	0.47	0.53	0.43	0.52	0.50	0.44	0.46	0.37	0.35

	biotite					
Analysis #	110.00	101.00	202.00	304.00	309.00	312.00
		biotite 1			biotite 2	
SiO2	35.01	35.21	35.29	35.36	35.44	35.63
TiO2	3.76	3.67	3.52	0.24	0.19	0.09
Al2O3	18.86	19.41	19.76	20.37	20.99	21.42
MgO	6.86	6.61	6.87	9.28	9.64	9.37
FeO	21.01	21.20	19.43	19.79	18.18	18.43
MnO	0.12	0.20	0.19	0.32	0.20	0.24
CaO	0.00	0.01	0.06	0.03	0.03	0.03
Na2O	0.04	0.15	0.13	0.12	0.08	0.13
K2O	10.09	9.98	10.10	9.70	10.29	10.03
H2O	3.90	3.94	3.92	3.92	3.94	3.96
Sum	99.66	100.38	99.29	99.12	98.97	99.33
Si	2.69	2.68	2.69	2.70	2.69	2.70
Ti	0.22	0.21	0.20	0.01	0.01	0.01
Al	1.71	1.74	1.78	1.83	1.88	1.91
Mg	0.79	0.75	0.78	1.06	1.09	1.06
Fe2	1.35	1.35	1.24	1.26	1.16	1.17
Mn	0.01	0.01	0.01	0.02	0.01	0.02
Ca	0.00	0.00	0.01	0.00	0.00	0.00
Na	0.01	0.02	0.02	0.02	0.01	0.02
K	0.99	0.97	0.98	0.95	1.00	0.97
OH	2.00	2.00	2.00	2.00	2.00	2.00
Sum	9.74	9.74	9.72	9.85	9.86	9.84
Xfe	0.63	0.64	0.61	0.54	0.51	0.52

	garnet from decussate aggregate				
	11.00	12.00	1301.00	1302.00	1303.00
SiO2	37.72	38.41	37.08	37.49	37.52
TiO2	0.01	0.02	0.01	0.03	0.03
Al2O3	21.23	21.44	20.87	21.48	21.08
MgO	2.75	2.52	2.54	2.40	2.51
FeO	32.50	31.88	31.76	31.61	31.91
MnO	5.36	6.14	6.21	6.07	5.95
CaO	1.11	1.34	1.15	1.12	1.15
Na2O	0.01	0.00	0.00	0.00	0.00
K2O	0.02	0.01	0.02	0.01	0.00
Sum	100.71	101.75	99.64	100.20	100.17
Si	3.02	3.04	3.01	3.01	3.02
Ti	0.00	0.00	0.00	0.00	0.00
Al	2.00	2.00	2.00	2.03	2.00
Mg	0.33	0.30	0.31	0.29	0.30
Fe2	2.17	2.11	2.16	2.12	2.15
Mn	0.36	0.41	0.43	0.41	0.41
Ca	0.10	0.11	0.10	0.10	0.10
Na	0.00	0.00	0.00	0.00	0.00
K	0.00	0.00	0.00	0.00	0.00
Sum	7.98	7.97	8.00	7.97	7.98
XFe	0.87	0.88	0.88	0.88	0.88
Xalm	0.73	0.72	0.72	0.73	0.73
Xpyr	0.11	0.10	0.10	0.10	0.10
Xgro	0.03	0.04	0.03	0.03	0.03
Xspe	0.12	0.14	0.14	0.14	0.14

Cordierite pseudomorph

	muscovite					biotite			garnet		
analysis #	19	24	81	86	216	analysis #	220	226	analysis #	12	45	113
SiO2	50.1	47.5	46.88	46.27	46.58	SiO2	35.26	36.52	SiO2	39.86	37.32	36.8
TiO2	0.15	0.45	0.1	0.55	0.26	TiO2	1.83	1.34	TiO2	0.01	0.03	0
Al2O3	33.56	34.82	36.2	31.27	35.2	Al2O3	20.75	24.02	Al2O3	20.57	21.38	21
MgO	0.74	0.55	0.48	1.9	0.56	MgO	7.81	5.89	MgO	0	0	0.14
FeO	1.54	0.91	0.84	4.27	1.09	FeO	18.61	14.94	FeO	2.01	2.19	2.31
MnO	0.04	0.01	0	0.05	0.03	MnO	0.19	0.14	MnO	29.79	31.93	31.97
CaO	0.01	0.04	0	0	0.03	CaO	0	0.06	CaO	6.77	6.92	6.87
Na2O	0.28	0.49	0.33	0.3	0.46	Na2O	0.05	0.15	Na2O	0.43	0.48	0.62
K2O	11.01	11.19	11.28	10.86	11.02	K2O	10.17	9.9	K2O	0	0	0
H2O	4.62	4.53	4.54	4.42	4.5	H2O	3.92	3.96	H2O	0.45	0.25	0.05
Sum	102.05	100.48	100.64	99.89	99.73	Sum	98.6	96.91	Sum	99.89	100.5	99.77
Si	3.251	3.139	3.091	3.136	3.104	Si	2.696	2.762	Si	3.178	3.006	2.992
Ti	0.007	0.022	0.005	0.028	0.013	Ti	0.105	0.076	Ti	0.001	0.002	0
Al	2.567	2.712	2.813	2.498	2.765	Al	1.87	2.141	Al	1.933	2.03	2.012
Mg	0.071	0.055	0.047	0.192	0.055	Mg	0.89	0.664	Mg	0	0	0.009
Fe2	0.084	0.05	0.046	0.242	0.061	Fe2	1.19	0.945	Fe2	0.239	0.262	0.28
Mn	0.002	0	0	0.003	0.002	Mn	0.013	0.009	Mn	1.987	2.151	2.174
Ca	0.001	0.003	0	0	0.002	Ca	0	0.005	Ca	0.458	0.472	0.473
Na	0.036	0.062	0.042	0.04	0.06	Na	0.008	0.022	Na	0.037	0.041	0.054
K	0.912	0.943	0.949	0.939	0.937	K	0.992	0.955	K	0	0	0
OH	2	2	2	2	2	OH	2	2	OH	0.046	0.026	0.005
Sum	8.932	8.986	8.993	9.077	8.999	Sum	9.764	9.58	Sum	7.877	7.99	8
Xfe	0.038	0.062	0.042	0.041	0.06	Xfe	0.572	0.587	Xfe	0.893	0.891	0.886
Xna	0.54194	0.47619	0.4946237	0.5576037	0.5258621							
									Xalm	0.73	0.73	0.73
									Xpyr	0.09	0.09	0.09
									Xgro	0.01	0.01	0.02
									Xspe	0.17	0.16	0.16

Further discussion

Limit of the high-pressure terranes: First insights from the outer part of the Lévézou Massif

As detailed in the preceding paper "in preparation", the Pinet granite outcropping in the inner part of the massif displays HP pseudomorphs. Since the granites inside and outside the Levezou complex are of the same age and chemical composition (chapitre XXX), this HP overprint must also be sought in the Pinet granite from the outer part of the massif. This question is of paramount importance: if this "outer Pinet granite" did record a HP event, it will modify the limit of the HP terranes and consequently the overall tectonic structure of this region. Preliminary results, which consist in a petrographic description, are presented in this complementary discussion.

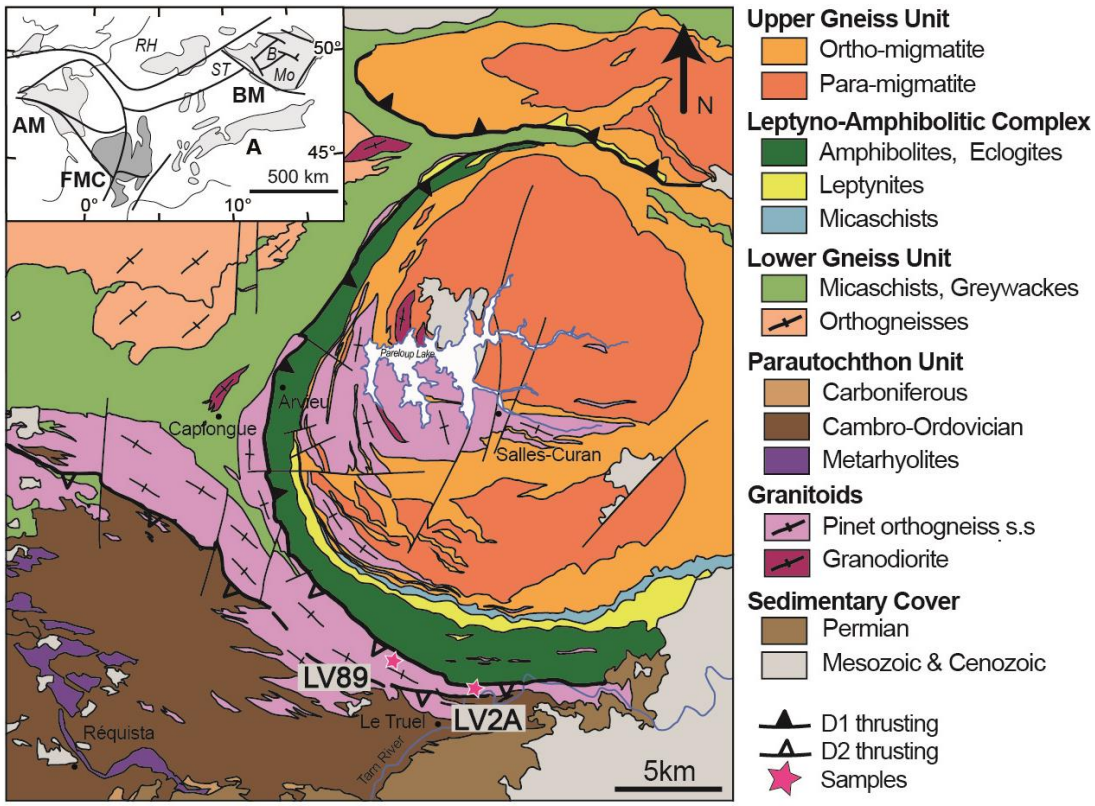

Figure II.2.8 - Simplified geological map of the Lévézou Massif (modified from Lotout et al. 2017), pink stars indicate sample locations from this study.

1. Petrographic observations

Macroscopically the rock (samples LV2A, LV89) is composed of porphyritic K-feldspar (up to 15 cm) usually displaying the rapakivi texture, in a coarse-grained (2-10 mm) matrix of quartz, plagioclase and biotite. It appears isotropic, without any discernible deformational fabric. Nevertheless, the thin section observation reveals a range of metamorphic textures.

K-feldspar forms large subhedral crystals with undulose extinction, locally finely perthitic and typically displaying Carlsbad twins. Locally, the crystals are crossed by curved to linear zones (deformation bands?), up to 0.2 mm thick, where they recrystallize into a mosaic of tiny (≈0.05 mm) grains, in places associated with tiny crystals of muscovite. Rare myrmekite is present at the rim of the crystals. Plagioclase forms subhedral crystals (up to 10 mm) that are generally partly altered to a mixture of tiny crystals of muscovite, but do not recrystallise. Quartz is present as remnants of large anhedral crystals (up to 10 mm) with undulous extinction systematically surrounded by a mosaic of recrystallised grains with irregular grain boundaries.

Biotite is present in two textural positions. Red-brown biotite (biotite 1, Fig. III.2.9A, B, D, E, F) forms unoriented subhedral thick flakes (up to 5 mm) that display undulous extinction and locally are strongly kinked. They are Ti-rich and display a core-to-rim zoning (Ti = 0.15-0.18→0.09-0.14 pfu; X_{Fe} = 0.58-0.63→0.55-0.60). They are locally surrounded by a thin very fine-grained symplectitic rim involving quartz, rutile and muscovite (Fig. III.2.9A, B). Light greenish to colourless biotite (biotite 2) is less titanian and more magnesian (Ti = 0.00-0.04 pfu, X_{Fe} = 0.48-0.55, Fig. III.2.9D, E). It is systematically associated with muscovite. Although it develops locally crystals up to 1 mm long, in most cases it forms small thin flakes (≈0.05-0.20 mm) in decussate aggregates with muscovite. In large muscovite crystals, biotite 2 also forms inclusions that are elongated parallel to the cleavage of the host, suggesting crystallographic continuity (Fig. III.2.9E). Locally a rimward transition from red-brown to greenish biotite can be observed at the scale of a single crystal.

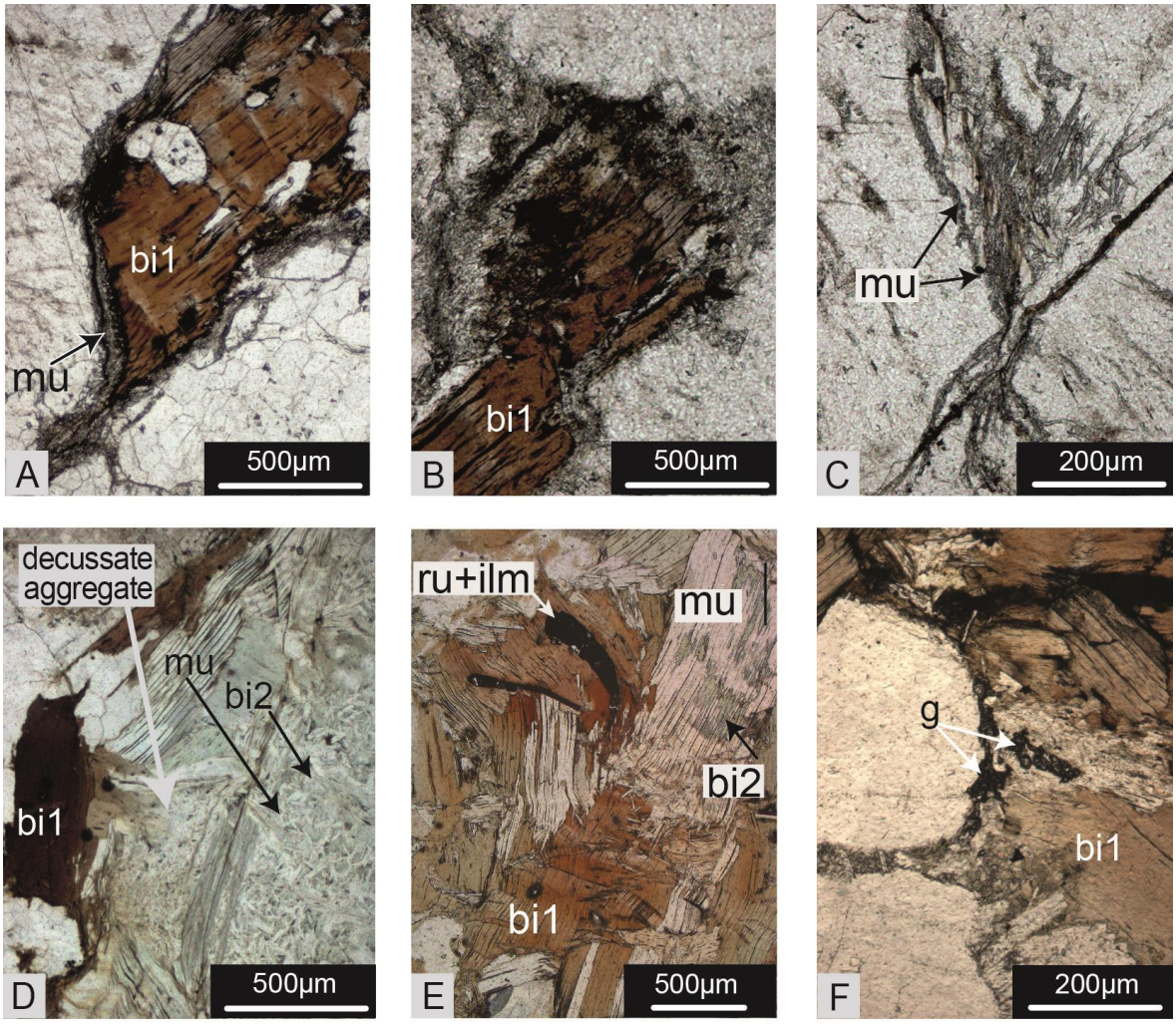

Figure III.2.9 – A, B muscvite-rutile-quartz symplectite surrounding biotite 1. C unoriented crystals of muscovitein K-felspar. D. Decussate aggregate of biotite2 and muscovite. E Muscovite and biotite 2 in apparent crystallographic continuity. F. Garnet associated with muscovite.

Muscovite is present in three textural positions. Tiny unoriented crystals (up to 0.05 mm) partly replace plagioclase and crystallise in the deformation bands of K-feldspar (Fig. III.2.9C); ii) associated with rutile and quartz, they also form rims around crystals of red-brown biotite (Fig. III.2.9A, B). However, most crystals are associated with biotite 2, and locally garnet and quartz, in subrectangular decussate aggregates up to 20 mm long (Fig. III.2.9D). Muscovite crystals up to 1 mm long are localised generally at the rim of the aggregates and commonly have fine inclusions of biotite 2 and quartz, oriented parallel to the cleavage (Fig. III.2.9D, E). They are commonly kinked and show undulous extinction. Crystals in the cores of the aggregates are undeformed, unoriented and significantly smaller (≈0.2 mm). Muscovite is slightly phengitic (Si = 3.04-3.16 pfu, X_{Na} = 0.03-0.08). The crystals

surrounding biotite 1 are systematically more titanian (Ti = 0.03-0.05 pfu) than the others (Ti = 0.00-0.01 pfu).

Garnet forms small rounded grains (up to 30µm), closely associated with muscovite (Fig. III.2.9F). Rutile (up to 0.04 mm), locally associated with muscovite, forms stubby prisms generally in subrectangular aggregates up to 0.5 mm long (Fig. III.2.9E). Accessory minerals include zircon, monazite, apatite, pyrite and hematite.

2. Interpretations

The subrectangular shape of the aggregates of muscovite+biotite 2+quartz±garnet suggests that they result from the pseudomorphism of another "primary" mineral, possibly cordierite (e.g. Godard 2001, 2009). As in the inner granite described above, the subrectangular aggregates of rutile (Fig. III.2.9E) can be interpreted as pseudomorphs of original crystals of illmenite (e.g. Le Bayon et al. 2006). Muscovite is exclusively present in "secondary" textural positions (pseudomorphs, reaction rims around biotite 1, replacing feldspars), suggesting a growth related to a metamorphic overprint of the original granite. Inclusions of biotite 2 and quartz in muscovite can be interpreted as exsolutions from a first metamorphic muscovite that would have been more phengitic (e.g. Nahodilová et al. 2014).

Consequently, it is interpreted that the primary (magmatic) paragenesis comprised K-feldspar, plagioclase, quartz, biotite 1, illmenite and possibly cordierite. A metamorphic event lead to (i) the replacement of ilmenite by rutile, (ii) the development of rutile-phengite-quartz symplectite surounding biotite 1, (iii) the growth of muscovite and destabilisation of cordierite into aggregates containing garnet and high-Si muscovite.

3. Discussion

The major difference between the inner and outer Pinet granite relates to the presence of the HP garnet-kyanite-phengite-quartz pseudomorph after cordierite: they have not yet been observed in the outer Pinet granite. Nevertheless the numerous similarities in all the other

metamorphic textures (reaction rims around biotite 1, decussate aggregates, rare garnet coronae, secondary muscovite) call for a similar P-T evolution.

Different possibilities can be listed:

- Both granite from the inner and outer part of the massif did experience the same metamorphic evolution, which explains the similarities between the metamorphic textures. The apparent absence of clear HP pseudomorphs in the outer part of the massif could result of :
    - The scarcity of the texture. Indeed, in the inner granite, they have been observed in only one sample.
    - The non-preservation of the textures. That could be the result of a higher retrogression of the outer terranes.
    - Slightly different bulk composition, e.g. related to different degree of alteration of the magmatic cordierite, leading to the development of pseudomorphs without garnet and kyanite, despite identical metamorphic PT conditions.
- Granite from the inner and outer part of the massif did not experience the same metamorphic evolution, and the absence of HP pseudomorph in the outer granite is the consequence of different P-T evolution.

Pseudosection modelling, on the local bulk chemistry of the decussate aggregates could help to decipher if they could be the result of the retrogression of former kyanite-garnet-phengite-quartz pseudomorph after cordierite.

Supplementary data – mineral chemical composition

	muscovite								
	62	**71**	**72**	**001**	**005**	**006**	**022**	**104**	**105**
	symplectite surounding bi1			large muscovite			tiny sticks		
SiO2	43.92	46.27	45.72	46.76	46.62	46.31	47.29	46.3	47.59
TiO2	0.92	1.05	0.67	0.01	0.03	0.03	0.07	0.02	0
Al2O3	33.32	34.06	33.21	35.96	35.75	35.91	33.99	35.95	33.54
MgO	0.72	0.73	0.85	0.85	0.75	0.77	1.19	0.69	1.44
FeO	2.71	1.56	1.55	1.15	1.04	1.38	1.85	1.03	1.85
MnO	0	0	0.01	0.01	0.02	0	0.05	0.01	0.03
CaO	0.05	0.02	0.02	0	0	0	0.01	0	0.01
Na2O	0.4	0.43	0.4	0.55	0.4	0.5	0.23	0.54	0.35
K2O	10.84	11.41	11.03	11.28	11.52	11.26	11.51	11.19	11.43
H2O	4.33	4.48	4.39	4.55	4.53	4.52	4.51	4.51	4.52
Sum	97.21	100.02	97.85	101.12	100.66	100.69	100.7	100.26	100.77
Si	3.042	3.095	3.12	3.078	3.085	3.066	3.139	3.073	3.157
Ti	0.048	0.053	0.034	0	0.002	0.001	0.003	0.001	0
Al	2.72	2.685	2.672	2.79	2.788	2.803	2.659	2.812	2.622
Mg	0.074	0.073	0.086	0.084	0.074	0.076	0.117	0.068	0.142
Fe2	0.157	0.087	0.089	0.063	0.057	0.076	0.103	0.057	0.103
Mn	0	0	0	0.001	0.001	0	0.003	0.001	0.002
Ca	0.004	0.002	0.002	0	0	0	0.001	0	0.001
Na	0.054	0.055	0.053	0.07	0.051	0.064	0.03	0.07	0.044
K	0.958	0.974	0.961	0.948	0.973	0.951	0.975	0.948	0.967
OH	2	2	2	2	2	2	2	2	2
Sum	9.056	9.024	9.016	9.035	9.031	9.038	9.03	9.029	9.038
XNa	0.053	0.054	0.052	0.069	0.05	0.063	0.03	0.069	0.044
XFe	0.680	0.544	0.509	0.429	0.435	0.500	0.468	0.456	0.420

	biotite							
	009	**010**	**011**	**016**	**018**	**019**	**020**	**021**
	biotite 1				biotite 2			
SiO2	36.34	35.4	35.97	36.3	35.49	38.65	35.98	36.47
TiO2	2.15	2.22	2.76	2.79	0.72	0.29	0.45	0.33
Al2O3	18.4	18.31	18.41	18.07	18.83	23.27	18.77	19.59
MgO	8.75	9.05	7.58	8.19	9.55	7.27	9.61	9.52
FeO	19.7	19.47	20.58	20.26	19.28	15.58	19.08	18.82
MnO	0.29	0.28	0.25	0.26	0.22	0.23	0.21	0.23
CaO	0.03	0.14	0.04	0.02	0.01	0.09	0.17	0.04
Na2O	0.08	0.06	0.03	0.08	0.06	0.07	0.08	0.12
K2O	10.09	9.46	9.54	9.74	9.9	9.65	8.93	10.35
H2O	3.94	3.89	3.91	3.93	3.87	4.07	3.87	3.95
Sum	99.77	98.29	99.07	99.64	97.93	99.18	97.14	99.41
Si	2.762	2.727	2.757	2.765	2.744	2.848	2.783	2.768
Ti	0.123	0.129	0.159	0.16	0.042	0.016	0.026	0.019
Al	1.648	1.663	1.663	1.622	1.716	2.021	1.711	1.752
Mg	0.991	1.04	0.866	0.93	1.1	0.799	1.108	1.077
Fe2	1.252	1.255	1.319	1.291	1.247	0.96	1.234	1.194
Mn	0.019	0.019	0.016	0.017	0.015	0.014	0.013	0.015
Ca	0.002	0.012	0.004	0.001	0.001	0.007	0.014	0.003
Na	0.011	0.009	0.005	0.012	0.009	0.01	0.012	0.017
K	0.979	0.93	0.933	0.946	0.977	0.908	0.881	1.002
OH	2	2	2	2	2	2	2	2
Sum	9.786	9.783	9.721	9.743	9.85	9.584	9.782	9.847
XFe	0.558	0.547	0.604	0.581	0.531	0.546	0.527	0.526

Chapitre 3 – ^{40}Ar-^{39}Ar dating to investigate post high-pressure events in the Lévézou massif

Table of content

1. Introduction

We have demonstrated in the previous chapters that:

(i) "Pinet type granites" from the Lévézou massif are Ordovician intrusions that experienced a Variscan HP metamorphism, estimated at 15-17 kbar and ~670°C (Part III, chapter 1 & 2).

(ii) Mafic eclogite from the Lévézou massif recorded peak P-T conditions at 21-23 kbar and ~750°C, and were quickly exhumed at 8-9.5 kbar and cooled at ca. 450°C at ca. 352 Ma (Part II, chapter 3).

These two works were dedicated to understanding the eclogite facies metamorphism from a petrological (part II, chapter 3 and part III, chapter 2) and chronological (part II, chapter 3) point of view. After the HP event, the terranes of the Lévézou massif experienced migmatization at various degrees, and were thrusted onto the parautochnous units. The timing of their exhumation is crucial in order to propose a coherent scenario for the Variscan Orogeny in the Lévézou massif.

The evolution of the Lévézou massif, after the HP metamorphic peak, was investigated through a large ^{40}Ar-^{39}Ar study on the various granitic rocks, displaying various degrees of deformation (undeformed, moderately deformed augen mylonites, ultramylonitic facies) and partial melting. Two migmatites with a sedimentary protolith were also analyzed (Fig. III.3.1). Analytical methods describing the single grain step heating procedure are described in the Annexe sections.

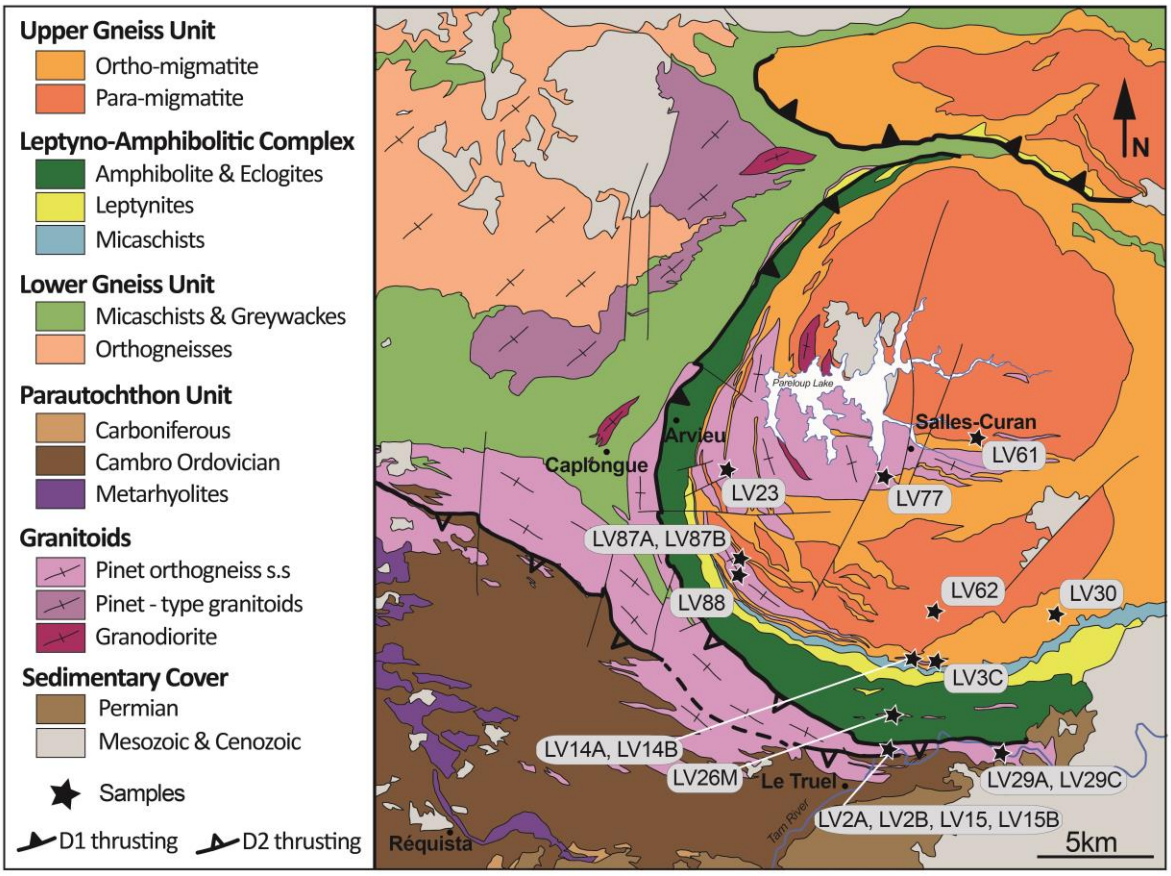

Figure III.3.1 - Schematic map of the Lévézou Massif . Black stars indicates the sample locations

2. Results

2.1. Undeformed granitic facies

The macroscopically isotropic, undeformed Pinet granites occurs both in the inner and the outer part of the Lévézou massif. The primary, magmatic paragenesis of the samples contains porphyritic K-feldspar, plagioclase, quartz, biotite, ilmenite and probably cordierite, inferred from rectangular garnet-kyanite-muscovite-bearing pseudomorphs. Primary biotite is commonly strongly kinked and is locally surrounded by coronae of either small garnet crystals or muscovite±quartz±rutile symplectites (Fig. III.2.2A, B, C). Muscovite is systematically found in a secondary textural position and is inferred to crystallize during metamorphism (see Part III – chapter 1 & 2 for detailed petrographic observation). It commonly encloses exsolutions of secondary biotite (see Fig. III.2.2E). Muscovite and primary biotite were analyzed in all samples.

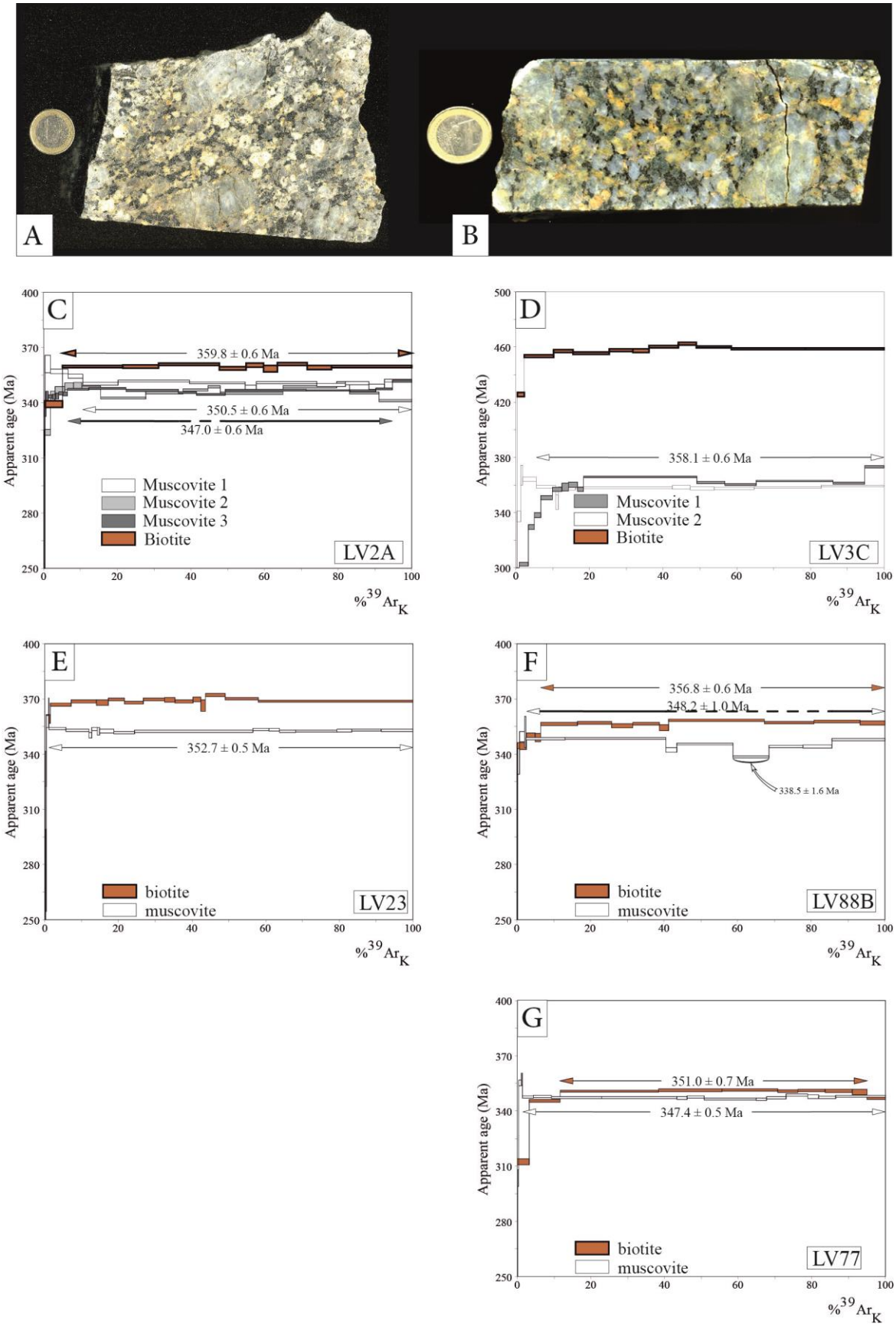

Figure III.3.2 – A, Sample LV3C. B, Sample LV2A. C, D, E, F, G ^{40}Ar-^{39}Ar spectrum for undeformed facies. The corresponding sample is noticed

2.2.1 Outer part of the massif

Sample LV2A (Fig. III.3.2C) – Muscovite analyses were triplicated. Muscovite 1 yields a slight saddle shape spectra that gives a plateau age at 350.5 ± 0.6 Ma for the lower part of the saddle. Muscovite 2 does not provide any plateau or pseudoplateau age and displays a strongly disturbed age spectrum. Muscovite 3 displays a saddle shaped age spectrum, whose lower apparent ages yield a mean age at 347.0 ± 0.6 Ma. Biotite yields an older plateau age at 359.8 ± 0.6 Ma.

2.2.2 Inner part of the massif

Four samples from the inner domain of the massif were selected: LV3C, LV23, LV77 and LV88B, each of them outcropping in distant location (Fig. III.3.1). They all provided muscovite and biotite grains.

Sample LV3C (Fig. III.3.2D) - Muscovite analyses were duplicated. Strongly disturbed Muscovite 1 age spectrum does not allow plateau or pseudoplateau age calculation. Muscovite 2 yields a plateau age at 358.1 ± 0.6 Ma. The biotite does not yield a plateau or pseudoplateau age, and is characterized by old ca. 450-460 Ma apparent ages.

Sample LV23 (Fig. III.3.2E) – Muscovite yields a well defined plateau age at 352.7 ± 0.5 Ma through more than 95% of the released gas. Biotite age spectrum displays higher apparent ages in the range ca. 365-370 Ma.

Sample LV88B (Fig. III.3.2F) – Muscovite grain yields a saddle shaped age spectrum, with higher apparent ages from the sides at 348.2 ± 1.0 Ma and lowest apparent age from the base of the saddle at 338.5 ± 1.6 Ma. Biotite yields an older plateau age at 356.8 ± 0.6 Ma.

Sample LV77 (Fig. III.3.2G) – Muscovite grain yields a well-defined plateau age of 347.4 ± 0.5 Ma (more than 95% of released gas). Biotite provides a hump-shaped age spectrum with an older plateau age at 351.0 ± 0.7 Ma in the high temperature steps.

Biotites from undeformed samples collected either in the inner or outer domains systematically yield plateau ages older than muscovite ones. In this way, apparent age spectrum yielded by biotite from LV3C sample shows450-460 Ma apparent ages just slightly younger than the ca. 470 Ma U-Pb zircon age obtained by Lotout et al. (2017). Together with the fact that muscovite plateau ages are systematically younger than biotite ones, "anomalously old ages" evidenced by biotite ^{40}Ar-^{39}Ar analyses suggest that their K-Ar isotopic system was disturbed by an inherited argon component. In these samples, biotite is part of the primary assemblage, and stays metastable during the metamorphic evolution, including the HP stage, of the terranes. Consequently, in such HP context, it is likely for these minerals to display argon inheritance as shown by Ruffet et al. (1995) or more broadly by Foland (1983). The variation in the recorded inherited "ages" could either be due to the distinct deformation (kink-band) rates of biotites or interactions with potential surrounding symplectites.

Muscovite LV3C excepted, plateau or pseudoplateau ages provided by muscovites range from 347.4 ± 0.5 Ma to 352.7 ± 0.5 Ma. Age at ca. 358 Ma of muscovite LV3C has to be seen in conjunction with the ca. 460 Ma "age" shown by biotite from the same sample, which could suggests that muscovite also trapped a small inherited ^{40}Ar components when it crystallized. In other samples, muscovites are presumed to have crystallized -or for some of them partly to fully recrystallized- during one or different metamorphic stages during exhumation. The saddle shaped age spectra yielded by muscovites LV2A and LV88B could confirm, as shown by Cheilletz et al. (1999), Alexandrov et al. (2002) and Tartèse et al. (2011), the existence of two post ca. 350 Ma disturbing "events", younger than ca. 347 Ma for the first one, and younger than ca. 338 Ma. for the second one. These ages will be refined through the analyses of the other samples (see below).

2.2 Migmatitic facies

The migmatitic facies are mostly found in the inner part of the Lévézou massif, and rarely in the Leptyno-Amphibolitic Complex. Two paramigmatites (LV30, LV62, Fig. III.3.3A) and four orthomigmatites (LV61, LV14A, LV87A, LV87B, Fig. III.3.3B) were sampled in the inner part of the massif. LV26M, an orthomigmatite, was sampled within the Leptyno-Amphibolitic Complex. All samples provided for muscovite and biotite grains.

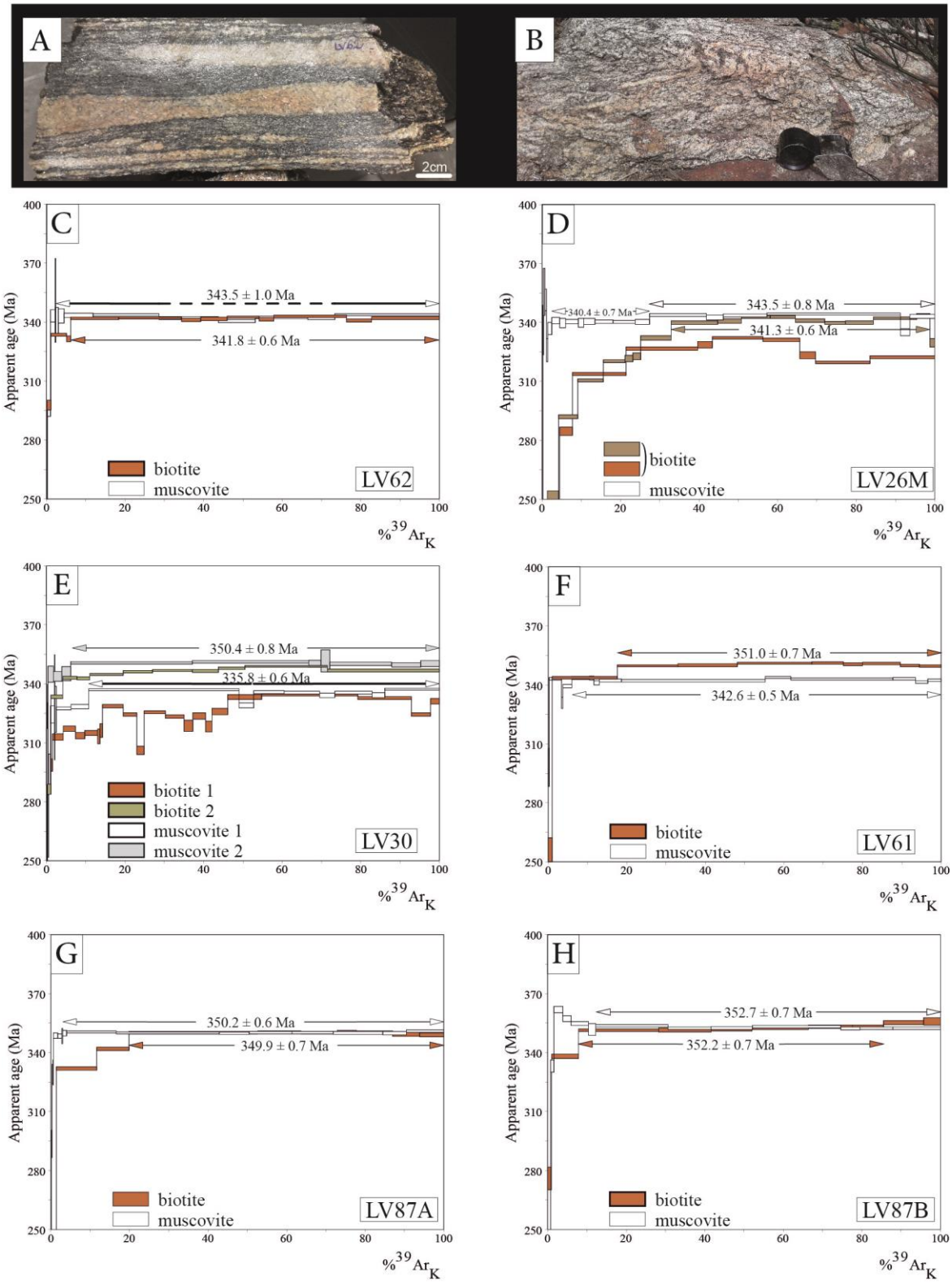

Figure III.3.3 - A, Sample LV62. B, Sample LV61. C, D, E, F, G, H ^{40}Ar-^{39}Ar spectrum for migmatitic facies. The corresponding sample is noticed.

2.2.1 Paramigmatite

Sample LV62 (Fig. III.3.3C) – Muscovite displays a saddle shaped age spectrum with a mean age for the saddle sidewall steps at 343.5 ± 1.0 Ma and a saddle minimum apparent age at ca. 340.5 Ma. This age spectrum shape indicates (see above) that K-Ar isotopic system of muscovite, closed before ca. 344 Ma, was disturbed, through partial recrystallization during a subsequent event, younger than ca. 340 Ma. Biotite yields a plateau age at 341.8 ± 0.6 Ma..

Sample LV30 (Fig. III.3.3E) – Muscovite analyses were duplicated. Muscovite 1 yields a nearly plateau age at 335.8 ± 0.6 Ma when Muscovite 2 yields a plateau age of 350.4 ± 0.8 Ma. Biotite analyses were also duplicated, but did not provide any plateau or pseudoplateau age. Their hump shaped age spectra suggest they were strongly chloritized (Ruffet et al., 1991).

2.2.2 Orthomigmatite

Sample LV26M (Fig. III.3.3D) – Muscovite yields two pseudoplateaux in apparent staircase pattern, at 340.7 ± 0.7 Ma and 343.5 ± 0.8 Ma for the lower and higher temperature step released, respectively which indicate that K-Ar isotopic system of muscovite, closed before ca. 344 Ma, was disturbed during a subsequent event younger than ca. 340 Ma. Biotite analyses were duplicated. Biotite 1 displays a hump-shaped age spectrum, whose high temperature steps allow calculating a pseudoplateau age at 341.3 ± 0.6 Ma. Biotite 2 displays a strongly disturbed hump-shaped age spectrum which did not allow, and does not provide for any plateau or pseudoplateau age calculation. As previously (see above), such shape suggests that analyzed biotite grains were chloritized.

Sample LV61 (Fig. III.3.3F) – Muscovite age spectrum allows calculating a nearly perfect plateau age at 342.6 ± 0.5 Ma. Biotite spectrum displays an apparent staircase pattern whose highest temperature steps provide a plateau age of 351.0 ± 0.7 Ma.

Sample LV87B (Fig. III.3.3H) – Muscovite and biotite provide a plateau ages at 352.7 ± 0.7 Ma and 352.2 ± 0.7 Ma, respectively.

Sample LV87A(Fig. III.3.3G) – Muscovite yields a plateau age at 350.2 ± 0.6 Ma while biotite provides a concordant plateau age at 349.9 ± 0.7 Ma.

Sample LV14A (Fig. III.3.4A, C) – Muscovite analyses were duplicated. They both provide plateau ages at 345.2 ± 0.5 Ma (muscovite 1) and 345.8 ± 0.6 Ma (muscovite 2). Biotite analyses were also duplicated. Biotite 1 yields a pseudoplateau of 344.5 ± 0.8 Ma in the high temperature steps, while biotite 2 age spectrum was too much disturbed to allow calculating plateau or pseudoplateau age. Nevertheless it could be noticed that its apparent ages are in the 350-355 Ma range.

Comparison between LV14A and its adjacent (<1m) alter ego without any melting evidence LV14B (see results below and Fig. III.3.4 A, B, C and D), shows that even if melting could be an overall process it is in the present case localized and its impact on the K-Ar isotopic systems is also localized. Such process could be related to fluid circulations probably governed by deformation. These two samples suggest that such event occurred at ca. 345 Ma. It is also observable through results yielded by muscovites and biotites from samples LV62 and LV26M, despite slightly younger ages at ca. 343.5 Ma which both result of a subsequent disturbing event (ca. 336 Ma, see below), but also with LV61 muscovite age at ca. 343 Ma.

On the other hand, part of results obtained on samples showing melting highlight a previous event in the range 350-353 Ma (LV30, LV87A and LV87B). In the absence of a subsequent disturbing event at ca. 345 Ma, muscovite and biotite age spectra from samples LV87A and B clearly indicate that a first melting/deformation event occurred in the range 350-353 Ma. Furthermore, LV30 sample with a muscovite plateau age at ca. 336 Ma enable to unambiguously date the disturbing event which was detected through muscovite analyses of samples LV62 and LV26M.

Generally, it is admitted that age concordance between minerals with distinct isotopic closure temperatures suggest a rapid cooling at the global scale. In the present case the nearly systematic concordance between muscovite and biotite ages suggests much more likely that these two detected melting events arise locally and are governed by combined effect of temperature, and fluids, with or without deformation. Tartese et al. (2011) in their study of monazites and muscovites from leucogranites showed in detail how isotopic systems may be sensitive to fluid circulations, with hydrothermal resets through recrystallisation, during a cooling event.

In summary, this set of samples allows evidencing three distinct events, the unambiguous first two at ca. 350-353 Ma and ca. 342.5-344.5 Ma with local melting and the

last one, more subtle, at ca. 336 Ma. This last event was also identified in the previous set of undeformed samples.

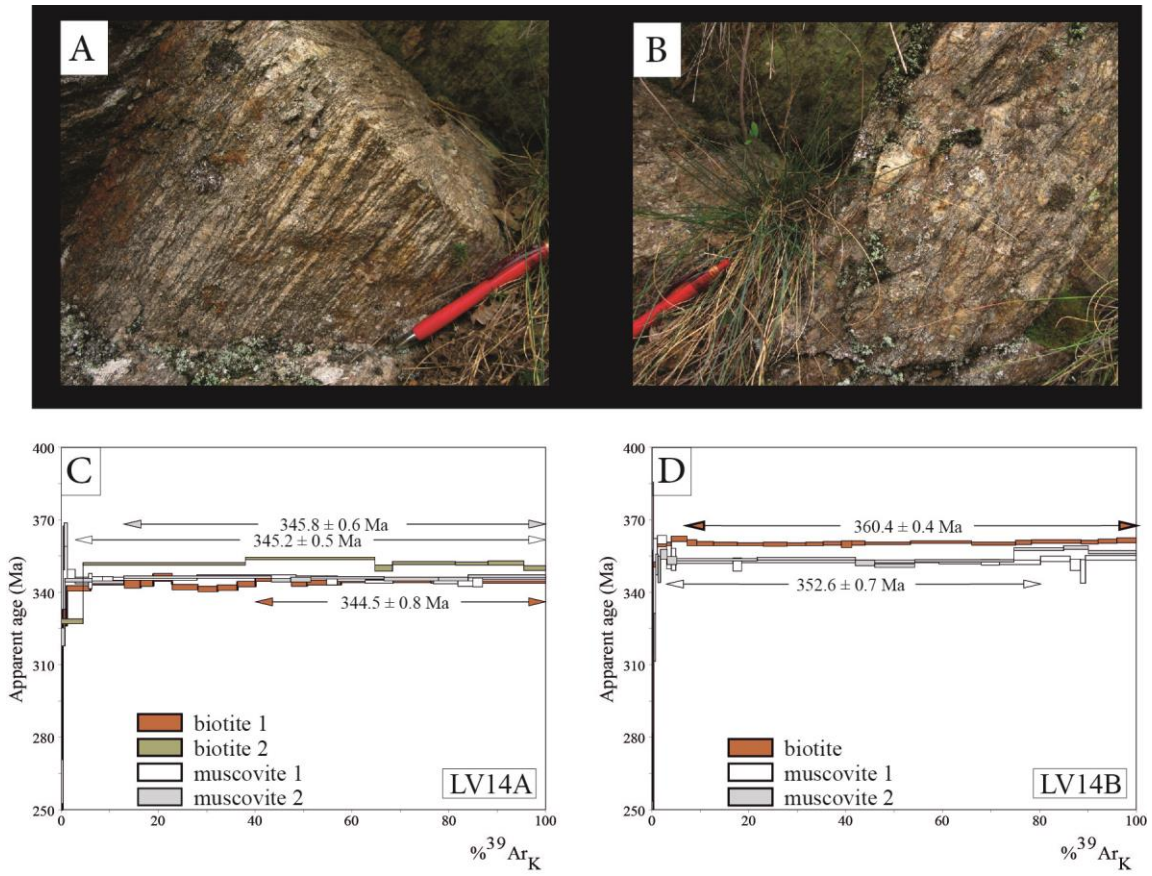

Figure III.3.4 - A, Sample LV14A. B, Sample LV14B. C, D ^{40}Ar-^{39}Ar spectrum for undeformed facies. The corresponding sample is noticed. Note that the red pen did not moved between the pictures.

2.3 Deformed facies

Orthogneisses facies are found within the whole massif. Six samples were selected, one in the inner part of the massif, which locally evolves toward a migmatitic orthogneiss (LV14B, evolving in LV14A, see above) and five samples in the outer part of the massif (LV15, LV15B, LV29A, LV29C, LV2B). Muscovite grains were provided by all the samples, but biotite was either too damaged in LV15, or too chloritized in LV2B to be analyzed.

2.3.1 Inner part of the massif

Sample LV14B (Fig. III.3.B, D4) – Muscovite analyses were duplicated. Muscovite 1 and 2 provide a plateau ages, at 352.6 ± 0.7 Ma and 353.0 ± 0.7 Ma, respectively. Muscovite 2 also shows in the high temperature steps higher apparent ages which unambiguously indicate that this mineral was inherited/crystallized from a previous event (ca. 365 Ma?) and nearly fully reset/recrystallized during a subsequent event, at ca. 353 Ma. Biotite gives a plateau age of 360.4 ± 0.4 Ma.

2.3.2 Outer part of the massif

Rocks of the outer part of the massif show the strongest deformation. The Pinet granite is commonly found under orthogneissic facies (LV29A, LV29C, LV2B) that locally evolves into ultramylonite (LV15, LV15B, Fig. III.3.5A, B and Part III, chapter 1).

Sample LV15 (Fig. III.3.5B, C) – Muscovite analyses were duplicated. Muscovite 1 displays a saddle shaped age spectrum. Saddle sidewall apparent ages yield a mean age at 350.7 ± 1.0 Ma when saddle basement define a pseudo-plateau at 346.1 ± 1.4 Ma. As previously discussed, it indicates that this mineral, crystallized or fully recrystallized at ca. 351 Ma, was partly recrystallized at or after ca. 346 Ma. This interpretation seems confirmed by the perfect plateau age at 346.4 ± 0.9 Ma calculated from muscovite 2 age spectrum.

Sample LV15B (Fig. III.3.5D) – Muscovite displays a hump-shaped spectrum and does not provide any plateau or pseudoplateau age. The summital apparent age could express that this mineral crystallized before ca. 358 Ma. Biotite yields a staircase pattern whose higher steps provide a pseudoplateau age of 356.2 ± 1.2 Ma.

Sample LV29A (Fig. III.3.5E) – Muscovite analyses were duplicated. Muscovite 1 yields a saddle shaped age spectrum with saddle sidewall apparent ages at ca. 351.5 Ma and a saddle minimum apparent age at ca. 347.5 Ma. This age spectrum, very similar to the one yielded by muscovite 1 from sample LV15, is interpreted in the same way. On the other hand, staircase shaped age spectrum displayed by Muscovite 2 suggests that it was disturbed after its initial closure during a subsequent event at or younger than 337.5 Ma.. Biotite yields a plateau age at 350.5 ± 0.4 Ma.

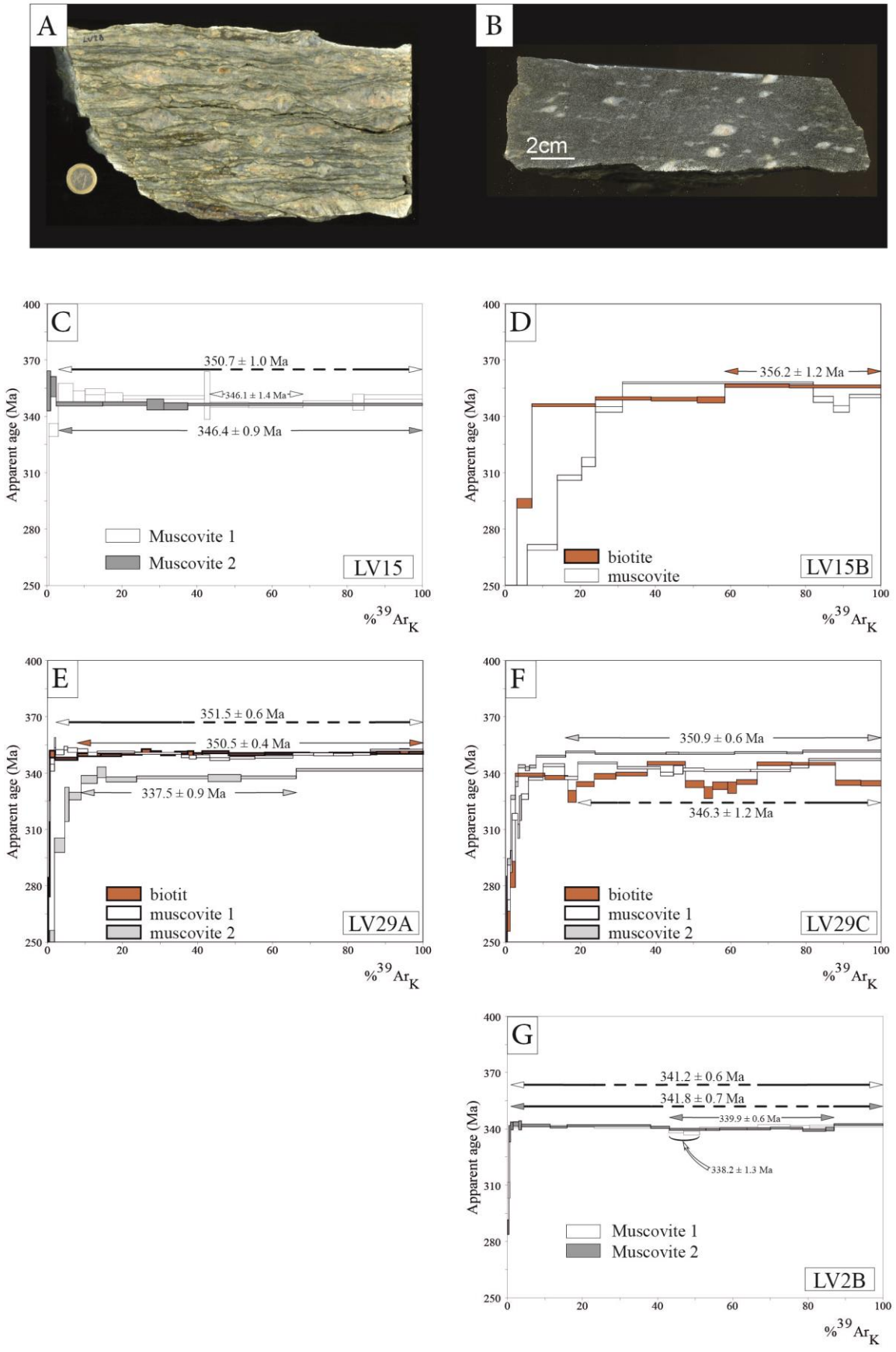

Figure III.3.5 - A, Sample LV2B. B, Sample LV15. C, D, E, F, G ^{40}Ar-^{39}Ar spectrum for undeformed facies. The corresponding sample is noticed.

Sample LV29C (Fig. III.3.5F) – Muscovite analyses were duplicated. Muscovite 1 displays a strongly disturbed saddle shaped age spectrum with saddle sidewall apparent ages at ca. 346.5 Ma and minimum apparent ages for the basement of the saddle at ca. 341 Ma. Once again, such spectrum suggests the subsequent disturbance of a mineral whose isotopic system initially closed at ca 347 Ma. On the other hand Muscovite 2 yields a nearly perfect plateau age at 350.9 ± 0.6 Ma while biotite yields a plateau age at 350.5 ± 0.4 Ma.

Sample LV2B (Fig. III.3.5G) – Both muscovites yield slight but wild saddle shaped age spectra which, as previously, suggest a partial recrystallization of the analyzed muscovites during an event younger than ca. 338 Ma. Initial age of these muscovites would be older than ca. 342 Ma. The amplitude and flatness of the saddles could suggest that the two components are poorly separated or that the post initial isotopic closure of the muscovite grains was nearly complete.

This set of deformed samples evidence three distinct events, two major ones and a more subtle one, which are consistent with previous results from undeformed samples and migmatitic samples. The oldest event, at ca. 350.5-351.5 Ma, is undoubtly the most efficiently characterized, despite the existence and the overlap of the two subsequent events at ca. 346 Ma and at ca 337 Ma or slightly younger. These two last events are generally observed as disturbances on muscovites probably initially crystallized in the early stages (>358 Ma) and whose isotopic system was fully reset during the first and oldest identified event (350.5-351.5 Ma), as suggested by the reminiscence of older phases observed in sample LV15B or LV14B.

3. Two major events with localized melting but no global migmatisation

Granite from the inner part of the massif have experienced a relatively high pressure event (15-17 kbar), based on (i) the garnet-kyanite-phengite-quartz pseudomorph after cordierite in the undeformed granite (Part III, chapter 3) and (ii) the existence of enclaves displaying HP assemblage (Delor et al. 1985). The inherited component for the biotite ages is obvious, and the variability of muscovite plateau ages question a potential trapping of inherited argon. As previously discussed, the age at ca. 358 Ma from Muscovite LV3C could suggest that this muscovite also trapped a small inherited ^{40}Ar components when it crystallized. On the other hand, ages at ca. 353-350 Ma, which are in agreement with the

whole set of dates (deformed and migmatitic samples) from this study, must not be rejected and must be considered as valid dates related to the major deformational stage, contemporaneous with exhumation. Muscovite in the undeformed facies have grown/recrystallized ((re)equilibrated) under different ranges of pressure and temperature after the HP peak and the plateau ages in muscovites in range 350-353 Ma reflect their crystallization/(re)equilibration.

Migmatitic samples yield two distinct dates at 350-353 Ma and ca. 342.5-344.5 Ma. If the 342.5-344.5 Ma age should reflect the migmatization stage, then older ca. 350 Ma signal should have been completely erased, due to recrystallization. Yet, LV61 displays evidence of inheritance at ca. 351 Ma (LV61), indicating that it recrystallized at that time. On the opposite, if the migmatization event occurred at ca. 350 Ma, and a deformational stage occurred at ca. 342.5-344.5 Ma, younger spectra should display inheritance. Yet, LV62 and LV14A display perfect signals, and LV14B shows inheritance. The proximity on the field, between migmatites and orthogneisses, strongly suggests that deformation and fluids enhance the melting. Furthermore, these dates are sufficiently different to suggest two distinct events, and one long–lasting massive melting event is unlikely to happen, since numerous non migmatitic samples are preserved and do not display any isotopic disturbance. We consequently propose that fluid circulation and deformation led to local melting of the samples, but that no massive migmatitic event occurred.

In the neighboring HP terranes, the temperature of ca. 450°C is reached at ca 352 Ma, which is consistent with the results presented in this study. Indeed, closure temperature for biotite and muscovite are commonly admitted to be as high as 450°C and 500°C, respectively (cf isotopic closure in annexe section).

The ca. 350 Ma is the best characterized signal, and is found either in orthogneissic, ultramylonitic or migmatitic samples. It is supposed to correspond to the major deformation event. The mechanism leading to the exhumation process remains unknown: thickening and erosion during collisional stage or exhumation stage assisted by an extensive tectonics.

4. Conclusion

This ^{40}Ar-^{39}Ar study evidence that:

- The melting seems to be localized and enhanced by deformation and fluids,
- Two major deformational episodes occurred, accompanied by localized melting, at ca. 350 and ca. 342.5-344.5 Ma
- Further investigations are needed to characterize the melting mechanism in the orthogneisses.

Partie IV

Discussion Générale

1.

2. Résultats Principaux

a. Du point de vue Varisque

De nombreuses contraintes quantitatives précises sur le métamorphisme de haute pression des massifs de Najac, de la Montagne Noire et du Lévézou, et sur l'évolution post-métamorphisme de haute pression dans le massif du Lévézou ont été présentées dans ce manuscrit. Les résultats majeurs sont résumés brièvement ci-après.

Dans le massif de Najac (Partie II, chapitre 1 ; article accepté à *Lithos*), nous révélons:

- des conditions de 15 à 20 kbar pour des températures de 560 à 630°C pour le pic du métamorphisme éclogitique,
- un âge de ~ 383 Ma pour le début du faciès éclogite,
- un âge de 376.3 ± 3.3 Ma pour le pic du métamorphisme éclogitique,
- un âge de 369 ± 13 Ma pour la rétromorphose.

Les conditions P-T que nous avons déterminées réévaluent à la hausse les précédentes estimations sur le métamorphisme de haute pression proposées dans ce massif (initialement 12 kbar et ≤ 600°C, Delor et al. 1986). Les âges obtenus permettent également de proposer une durée de ~ 6.1 ± 4.3 Ma pour le cheminement prograde en faciès éclogite.

Dans le massif de la Montagne Noire (Partie II, chapitre 2 ; article en préparation pour *EPSL*), nous proposons :

- des conditions P-T de ~ 21 kbar et ~ 750°C pour le pic du faciès éclogite,
- un âge du métamorphisme de haute pression ≥ 360 Ma,
- un âge de la migmatisation à environ 315 Ma.

Nos estimations P-T reconsidèrent à la hausse les précédentes conditions du métamorphisme éclogitique présentées pour ce massif (i.e., ~ 14 kbar et ~ 725°C, Whitney et al. 2015). Par ailleurs, nous contestons l'interprétation de l'âge du métamorphisme de haute pression à 315 Ma faite par Whitney et al. (2015). D'après nos analyses, cet âge correspondrait au stade de la migmatisation de haute température. Bien que l'âge de la haute pression n'ait réellement pu être déterminé, notre étude suggère un âge de 360 Ma ou au-delà.

Dans le massif du Lévézou (Partie II, chapitre 3 ; article en préparation pour *Journal of Petrology et* Partie III), nous proposons :

- une mise en place à ~ 470 Ma des granites dits « Pinet » à des pressions de ~ 2 kbar et températures ~ 670°C,
- un métamorphisme de haute pression enregistré par des pseudomophoses de cordiérite à grenat-phengite-disthène-quartz à 15-17 kbar et ~ 670°C,
- un âge du pic du métamorphisme éclogitique à ~ 358 Ma, pour des pressions et températures de 21-23 kbar et 680-800°C, suivi d'une phase d'exhumation rapide et majeure à 8.5-9 kbar. Une phase de refroidissement de ~50°C/Ma post exhumation majeure s'en suit.

Les conditions P-T proposées pour l'enregistrement du pic de pression dans les éclogites mafiques correspondent aux estimations proposées dans la littérature (i.e., 20 kbar et 720 ± 30°C, Bouchardon 1987). L'âge du métamorphisme de haute pression dans ces roches est estimé à ~ 358 Ma, ce qui va à l'encontre des précédentes hypothèses proposées pour ce massif (e.g. Duguet et Faure, 2004). Le contexte tectonique du granite « du Pinet » est fondamentalement réinterprété, puisque jusqu'alors considéré comme un granite syn-tectonique de la collision .varisque, dont la mise en place était datée à ~ 360 Ma (Pin, 1981). Le protolithe est ainsi daté à 470 Ma et interprété comme le témoin du magmatisme contemporain du rifting Ordovicien. L'âge de son métamorphisme en faciès éclogitique à 15-17 kbar n'a pas été déterminé, mais est estimé à ~ 358 Ma par analogie avec les éclogites environnantes. Nous suggérons ainsi la subduction de blocs continentaux. La migmatisation n'a jamais été datée dans le massif du Lévézou. Cependant, l'étude ^{40}Ar-^{39}Ar menée sur les différents faciès granitiques a permis de suggérer qu'il s'agit, tout du moins dans ces roches, d'un évènement, potentiellement la résultante de déformation.

b. Du point de vue thématique

Les résultats présentés sur les massifs de Najac et de la Montagne Noire remettent en question l'usage systématique des spectres de terres rares comme critère d'identification de l'âge du métamorphisme éclogitique.

D'une part, à haute pression, l'étude réalisée dans le massif de Najac met en évidence l'existence contemporaine de spectres « magmatiques » et « éclogitiques », tous deux présentant les mêmes âges U-Pb, équivalents aux âges Lu-Hf obtenus sur grenat datant le début du faciès

éclogite. Ainsi, à un âge U-Pb sur zircon – datant le début du faciès éclogite – correspondent différents spectres de terres rares.

D'autre part et à l'inverse, l'étude réalisée dans la Montagne Noire met en exergue le phénomène opposé. A différents âges U-Pb obtenus sur des zircons, dont un âge similaire à celui du métamorphisme de BP-HT dans l'ensemble du massif, correspondent des spectres de terres rares censés être caractéristiques du faciès éclogite. Ainsi, à différents âges correspondent un spectre type « éclogitique ».

Il va de soi que ces observations ne remettent pas en cause le bien-fondé et la validité de l'ensemble des études ayant utilisé avec succès les tendances de spectres de terres rares. Néanmoins, l'identification de situations problématiques permet d'alerter sur de potentielles utilisations caricaturales et abusives, et de mettre l'accent sur des phénomènes encore mal compris. La datation des grenats, certes fastidieuse, s'est révélée essentielle dans le massif de Najac pour mieux appréhender les résultats. De la même manière, seule une datation précise des grenats des éclogites de la Montagne Noire permettrait de déterminer l'âge véritable de la haute pression.

3. Implications de ce travail à grande échelle

a. Age de la haute pression

A l'échelle du Massif Central…

Les terrains de Najac et du Lévézou ont révélé des âges datant le pic du métamorphisme de haute pression de ~ 376 Ma et ~ 358 Ma, respectivement. Les grenats des éclogites de la Montagne Noire semblent indiquer un métamorphisme de haute pression à ~ 358 ± 8 Ma (Faure et al., 2014), mais cette date nécessite d'être précisée. Les âges Silurien à Dévonien inférieur, jusque-là globalement bien admis dans l'ensemble du Massif Central n'existent donc pas dans les zones les plus méridionales.

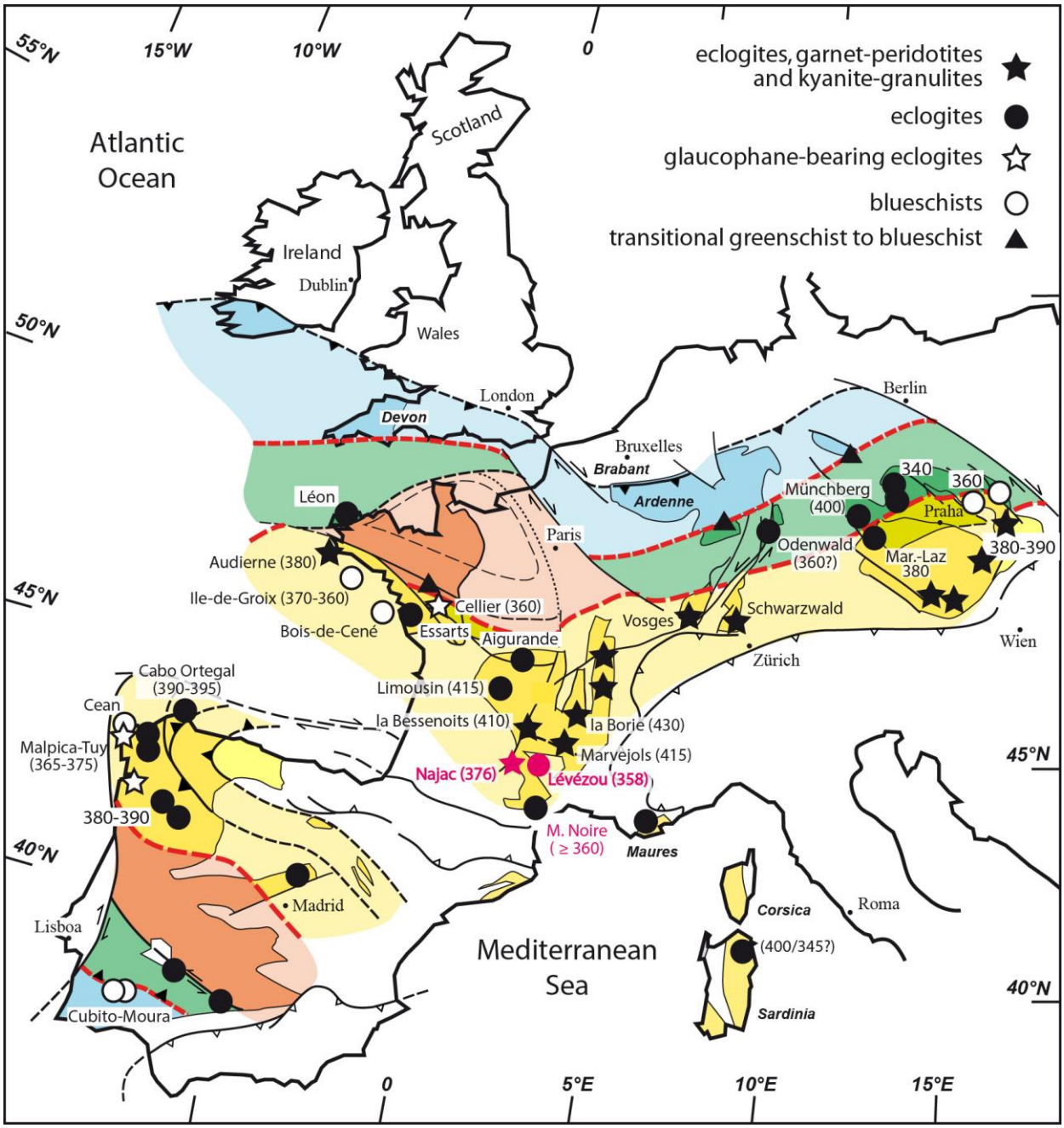

Figure IV.1 - Carte synthétique des âges de la haute pression dans la chaîne Varisque (modifiée d'après Paquette et al

Ce constat induit deux hypothèses immédiates :

(i) Une seule gamme d'âge du métamorphisme de haute pression, au Dévonien supérieur

Cette hypothèse implique que les âges de 430-410 Ma (Lancelot *et al.*1982 ; Ducrot *et al.* 1983 ; Paquette *et al.* 1995 ; Berger *et al.* 2010) ne reflètent pas une réalité géologique et ne correspondent pas au stade de haute pression. Il ne s'agit ainsi, dans cette hypothèse, que de dates, et seuls les âges Dévonien supérieur reflètent l'âge du métamorphisme de haute pression. S'il est aisé d'admettre cette hypothèse pour les âges obtenus par dissolution de populations de zircon (Lancelot et al. 1982 ; Ducrot et al.,1983 ; Paquette et al.,1995), la datation de zircons in situ à ca. 412 Ma réalisée par Berger et al. (2010) reste plus problématique. Néanmoins, le faible nombre de spot analysés dans cette étude (N = 3), permet de questionner la validité géologique de cette date.

(i) Différents âges de la haute pression, au Silurien-Dévonien inférieur et au Dévonien supérieur

Cette hypothèse impliquerait deux épisodes distincts de subduction : un premier épisode de 430 à 410 Ma dans les terrains nord Massif Central et un second épisode de 376 à 358 Ma dans les terrains du sud Massif Central. Considérant la large incertitude pesant sur les âges obtenus par dilution isotopique de fractions de zircons, cette hypothèse, pour être étoffée, nécessiterait de nouvelles datations précises du métamorphisme de haute pression dans les terrains plus au nord du Massif Central.

… A l'échelle de la chaîne Varisque

Si, à la seule échelle du Massif Central, les nouvelles données présentées dans ce manuscrit ne permettent pas d'invalider formellement les datations allant de 430 à 410 Ma, la contextualisation à l'échelle de la chaîne varisque apporte une nouvelle perspective.

Effectivement, une unique tendance apparait clairement (Fig. IV.1), puisque l'ensemble des âges de la haute pression associés à la fermeture de l'océan Médio-Européen s'étalent de 395 à 365 Ma dans le Massif Ibérique, de 380 à 360 Ma dans le Massif Armoricain, et de 390 à 360 Ma dans le Massif de Bohème. Ces nouvelles données sur le métamorphisme de haute pression dans le sud du Massif Central s'inscrivent donc pleinement dans ces gammes d'âges, de 376 Ma (Najac) à ~ 360 Ma (Lévézou).

b. Origine différente des roches mafiques ou exhumation épisodique ?

Au sein de chaque massif varisque, les âges interprétés comme datant la haute pression s'étalent de ~ 390 à ~ 360 Ma révélant ainsi des diachronismes. Les âges présentés dans ce manuscrit présentent la même tendance : les éclogites de Najac et du Lévézou sont diachrones de plus de 15 Ma. Cela implique que ces unités de haute pression ne soient pas positionnées au même niveau dans la « pile tectonique » du Massif Central. Deux hypothèses peuvent être proposées pour justifier d'un tel diachronisme.

(i) Une origine différente

Les roches mafiques sont globalement retrouvées dans les croûtes océaniques, mais peuvent également intruder des croûtes continentales. Ainsi, la subduction de la croûte océanique suivie de la subduction de sa marge continentale (qu'elle soit très amincie ou non) se traduirait par un diachronisme des âges de la haute pression .Une origine différente des roches datées, et donc un positionnement initial différent au sein des plaques qui convergent pourrait éventuellement expliquer le diachronisme observé entre les massifs.

(ii) Une exhumation épisodique

Cette hypothèse implique le fonctionnement continu d'une zone de subduction, au sein de laquelle des écailles métamorphisées en faciès éclogite se désolidarisent de la croûte subductée et s'exhument successivement au cours du temps.

Ces deux hypothèses impliquent de retrouver une zonéographie temporelle, témoignant du fonctionnement de l'ancienne zone de subduction.

4. Perspectives

Ce travail de thèse a permis d'amener de nouvelles informations sur le métamorphisme de haute pression dans le Massif Central. De nombreuses perspectives, pour mieux appréhender la géodynamique Varisque dans le Massif Central, pourraient être développées :

(i) du point de vue Varisque:

- Dans le massif de Najac, il serait judicieux de pouvoir réaliser une étude détaillée des granites dans lesquels sont intercalés les micaschistes de haute pression décrits par Delor *et al.* (1987). Le parallèle avec le massif du Lévézou, où les granites associés au LAG présentent des

textures de haute pression, mériterait d'être testé. Les résultats préliminaires du Zr dans le sphène ou le rutile mériteraient également d'être approfondis pour encadrer de façon plus précise le chemin rétrograde.

- Dans le massif du Lévézou, la datation des différents faciès migmatitiques étudiés dans ce manuscrit par U-Pb sur monazite pourrait permettre de préciser la tectonique générale du massif. L'usage de thermomètres ou baromètres (Zr-in-rutile, Zr-in-Titanite) dans les éclogites permettraient en outre de mieux encadrer le trajet rétrograde. Les conditions pression-température dans le granite affleurant à l'extérieur du massif doivent être caractérisées, puisque fondamentales pour déterminer l'évolution tectonique de l'ensemble du massif Lévézou ainsi que les limites des terrains de haute pression.

- Dans le massif de la Montagne Noire, une datation conjointe en Lu-Hf et Sm-Nd, couplée à des profils d'analyse en éléments traces des grenats, permettrait d'apporter un âge solide du métamorphisme de haute pression. Estimer les conditions de pressions et températures exactes auxquelles la migmatisation a eu lieu apporterait également des contraintes quantitatives sur l'évolution carbonifère de cette zone.

- A l'échelle de l'ensemble du Massif Central,

Il serait judicieux de poursuivre la datation des faciès éclogites, à la fois dans les massifs anciennement datés (Marvejols, La Bessenoit, le Haut-Allier) et dans les massifs n'ayant jamais fait l'objet d'investigation géochronologique de la haute pression (*e.g.* Artense, Lyonnais, Vivarais). Un diachronisme ou une homogénéité de l'âge du faciès éclogite préciserait ainsi la dynamique de la subduction dans cette portion de la chaîne Varisque.

L'examen des granites anté-Varisque associés au LAG en vue de potentielles traces de métamorphisme de haute pression permettrait de déterminer si la subduction de croûte continentale, dans le Massif Central Varisque, était une caractéristique commune et systématique ou exceptionnelle. Cela permettrait alors de reconsidérer la taille des unités métamorphiques, et donc la structuration de la chaîne.

(ii) du point de vue thématique

- Une étude *in situ* et en contexte (*i.e*. directement en lame mince) sur la chimie des éléments traces (REE, Zr) des zircons et des minéraux environnants dans l'échantillon NC5A (massif de Najac) pourrait être envisagée. Elle permettrait de déterminer si des équilibres locaux peuvent être à l'origine de la diversité des spectres de terres rares observés dans les zircons, ou si des vestiges de spectres de terres rares de type « magmatiques » peuvent avoir persisté au sein d'un zircon recristallisé.
- Une étude systématique sur des éclogites empaquetées dans des migmatites permettrait de préciser si le scénario présenté pour les éclogites de la Montagne Noire (zircons ayant une signature éclogitique en terres rares bien qu'enregistrant l'âge de la migmatisation environnante) est un cas isolé ou s'il s'agit d'une situation plus commune.

Conclusions générales

Ce travail de thèse a eu pour objectif de préciser les conditions du métamorphisme de haute pression dans les zones méridionales du Massif Central, tant en apportant des contraintes temporelles que des contraintes de pressions et températures.

Ce manuscrit et les articles soumis ou acceptés qu'il comprend présentent ainsi les premiers âges de la haute pression pour les massifs de Najac et du Lévézou. Le métamorphisme de haute pression, à Najac, est estimé à 15-20 kbar pour des températures de 560-630°C. Le début du faciès éclogitique est daté à ~ 383 Ma, tandis que le pic de métamorphisme de haute pression est atteint à 376.3 ± 3.3 Ma. Les terrains éclogitiques du massif du Lévézou présentent des conditions de pression et température différentes, à 18-23 kbar pour 680-800°C. L'âge du métamorphisme de haute pression y est plus jeune, d'environ 20 Ma par rapport au massif de Najac, puisque le pic du métamorphisme est atteint à ~ 358 Ma. L'exhumation, bien caractérisée, y est rapide : les terrains éclogitiques atteignent 8-9.5 kbar de façon quasi adiabatique. Il s'en suit une phase de refroidissement de près de 50°C/Ma.

Les éclogites de la Montagne Noire n'ont pas permis de préciser un âge solide de l'évènement de haute pression. Les conditions de pression et température du pic de pression y sont estimées à ~ 21 kbar et ~ 750°C.

L'étude géochronologique des massifs de Najac et de la Montagne Noire a mis en évidence de potentiels découplages entre les systèmes de terres rares et le système isotopique U-Pb.

Une étude focalisée sur les granites du massif du Lévézou a mis en évidence qu'il s'agit d'intrusions ordoviciennes ayant subi un métamorphisme de haute pression à ~15-17 kbar et ~670°C lors de l'orogenèse varisque. Ce métamorphisme s'est notamment traduit par le développement de pseudomorphoses de cordiérite à disthène-grenat-phengite-quartz. Il témoigne ainsi de la subduction de la croûte continentale pendant l'orogenèse Varisque.

Ces nouvelles données permettent de remettre en question la géodynamique varisque dans la Massif Central mais ouvrent également de nombreuses perspectives attrayantes pouvant dépasser les frontières varisque, tant d'un point de vue pétrologique (e.g. métamorphisme des granitoïdes) que géochronologique (e.g. lien entre les systèmes isotopiques et les éléments traces

Références bibliographiques

RÉFÉRENCES BIBLIOGRAPHIQUES

Alexandrov P, Ruffet G, Cheilletz A (2002) Muscovite recrystallization and saddle-shaped 40Ar/39Ar age spectra: example from the Blond granite (French Massif Central). Geochimica et Cosmochimica Acta 10:1793-1807.

Ballèvre M, Bosse V, Ducassou C, Pitra P (2009) Palaeozoic history of the Armorican Massif: models for the tectonic evolution of the suture zones. Comptes Rendus Geoscience 341:174-201.

Ballevre M, Fourcade S, Capdevila R, Peucat JJ, Cocherie A, Fanning CM (2012) Geochronology and geochemistry of Ordovician felsic volcanism in the Southern Armorican Massif (Variscan belt, France): Implications for the breakup of Gondwana. Gondwana Research 21:1019-36.

Ballèvre M, Catalán JR, López-Carmona A, Pitra P, Abati J, Fernández RD, Ducassou C, Arenas R, Bosse V, Castiñeiras P, Fernández-Suárez J (2014) Correlation of the nappe stack in the Ibero-Armorican arc across the Bay of Biscay: a joint French–Spanish project. Geological Society, London, Special Publications 405:77-113.

Bard JP, Burg JP, Matte P, Ribeiro A (1980) La chaine hercynienne d'Europe occidentale en termes de tectonique des plaques. Mem. BRGM 108:233-46.

Bellot JP, Roig JY (2007) Episodic exhumation of HP rocks inferred from structural data and PT paths from the southwestern Massif Central (Variscan belt, France). Journal of Structural Geology 29:1538-1557.

Berger J, Femenias O, Mercier JC, Demaiffe D (2005) Ocean-floor hydrothermal metamorphism in the Limousin ophiolites (western French Massif Central): evidence of a rare preserved Variscan oceanic marker. Journal of Metamorphic Geology 23:795-812.

Berger J, Féménias O, Ohnenstetter D, Bruguier O, Plissart G, Mercier JC, Demaiffe D (2010) New occurrence of UHP eclogites in Limousin (French Massif Central): age, tectonic setting and fluid–rock interactions. Lithos 118:365-82.

Bodinier JL, Burg JP, Leyreloup A, Vidal H (1988) Reliques d'un bassin d'arrière-arc subducté, puis obducté dans la région de Marvejols (Massif central). Bulletin de la Société géologique de France 4:21-33.

Bosse V, Féraud G, Ballèvre M, Peucat JJ, Corsini M (2005) Rb–Sr and 40 Ar/39 Ar ages in blueschists from the Ile de Groix (Armorican Massif, France): implications for closure mechanisms in isotopic systems. Chemical Geology 220:21-45.

Bosse V, Feraud G, Ruffet G, Ballèvre M, Peucat JJ, De Jong K (2000) Late Devonian subduction and early-orogenic exhumation of eclogite-facies rocks from the Champtoceaux Complex (Variscan belt, France). Geological Journal 35:297-325.

Bouchardon JL (1987) Evaluation des conditions de pression-température du «top» métamorphique des éclogites du Lévezou (Rouergue, Massif central français). Comptes rendus de l'Académie des sciences 305:271-275.

Briand BE, Piboule MI, Bouchardon JL (1988) Diversite geochimique des metabasites des groupes leptyno-amphiboliques du Rouergue et de Marvejols (Massif Central); origine et implications. Bulletin de la Société Géologique de France 4:489-98.

Burg JP, Matte PJ (1978) A cross section through the French Massif Central and the scope of its Variscan geodynamic evolution. Zeitschrift der Deutschen Geologischen Gesellschaft 429-60.

Burg JP, Matte P, Leyreloup A, Marchand J (1984) Inverted metamorphic zonation and large-scale thrusting in the Variscan Belt: an example in the French Massif Central. Geological Society, London, Special Publications 14:47-61.

Burg JP, Van Den Driessche J, Brun JP (1994) Syn-to post-thickening extension: mode and consequences. Comptes rendus de l'Académie des sciences. Série 2. Sciences de la terre et des planètes 319:1019-32.

Carignan J, Hild P, Mevelle G, Morel J, Yeghicheyan D (2001) Routine analyses of trace elements in geological samples using flow injection and low pressure on-line liquid chromatography coupled to ICP-MS: a study of geochemical reference materials BR, DR-N, UB-N, AN-G and GH. Geostandards and Geoanalytical Research 25:187-98.

Chelle-Michou C, Laurent O, Moyen JF, Block S, Paquette JL, Couzinié S, Gardien V, Vanderhaeghe O, Villaros A, Zeh A (2017) Pre-Cadomian to late-Variscan odyssey of the eastern Massif Central, France: Formation of the West European crust in a nutshell. Gondwana Research 46:170-90.

Cheilletz A, Ruffet G, Marignac C, Kolli O, Gasquet D, Féraud G, Bouillin JP (1999) 40Ar/39Ar dating of shear zones in the Variscan basement of the Greater Kabylia (Algeria). Evidence of an eo-Alpine event at 128 Ma (Hauterivian-Barremian boundary): geodynamic consequences. Tectonophysics 306:97-116.

Chopin C, Henry C, Michard A (1991) Geology and petrology of the coesite-bearing terrain, Dora Maira massif, Western Alps. European Journal of Mineralogy 3:263-91.

Chopin F, Schulmann K, Štípská P, Martelat JE, Pitra P, Lexa O, Petri B (2012) Microstructural and metamorphic evolution of a high-pressure granitic orthogneiss during continental subduction (Orlica–Śnieżnik dome, Bohemian Massif). Journal of Metamorphic Geology 2012 30:347-76.

Delor C, Leyreloup A, Bodinier JL, Burg JP (1986) Découverte d'éclogites à glaucophane dans la klippe de Najac (Massif Central, France): nouveaux témoins océaniques d'un stade haute pression dans la chaîne de collision varisque. Comptes rendus de l'Académie des sciences. Série 2, Mécanique, Physique, Chimie, Sciences de l'univers, Sciences de la Terre 302:739-44.

Delor C, Leyreloup A, Burg JP (1985) Nouveaux arguments pétrologiques en faveur de l'allochtonie du Lévézou (Massif Central français): les enclaves basiques des granites

calco-alcalins et les métacornéennes associées. Comptes rendus de l'Académie des sciences. Série 2, Mécanique, Physique, Chimie, Sciences de l'univers, Sciences de la Terre 301:1037-42.

Dewey JF, Burke KC (1973) Tibetan, Variscan, and Precambrian basement reactivation: products of continental collision. The Journal of Geology 81:683-92.

Demange M. The eclogite-facies rocks of the Montagne Noire, France. Chemical Geology 50:173-88.

Ducrot J, Lancelot JR, Marchand J (1983) Datation U-Pb sur zircons de l'éclogite de la Borie (Haut-Allier, France) et conséquences sur l'évolution anté-Hercynienne de l'Europe occidentale. Earth and Planetary Science Letters 62:385-94.

Duguet M, Faure M (2004) Granitoid emplacement during a thrusting event: structural analysis, microstructure and quartz c-axis patterns. An example from Hercynian plutons in the French Massif Central. Journal of structural geology 26:927-945.

Duthou JL, Chenevoy M, Gay M (1994) Age Rb-Sr, Dévonien moyen des migmatites à cordiérite du Lyonnais (Massif central français). Comptes rendus de l'Académie des sciences. Série 2. Sciences de la terre et des planètes 319:791-6.

Faure M (1995). Late orogenic carboniferous extensions in the Variscan French Massif Central. Tectonics 14:132-53.

Faure M, Cocherie A, Gaché J, Esnault C, Guerrot C, Rossi P, Wei L, Qiuli L (2014) Middle Carboniferous intracontinental subduction in the Outer zone of the Variscan belt (Montagne Noire axial zone, French Massif Central): Multimethod geochronological approach of polyphase metamorphism. Geological Society, London, Special Publications 405:289-311.

Faure M, Cocherie A, Mezeme EB, Charles N, Rossi P (2010) Middle carboniferous crustal melting in the Variscan belt: new insights from U–Th–Pb tot. monazite and U–Pb zircon ages of the Montagne Noire Axial Zone (southern French Massif Central). Gondwana Research 18:653-73.

Faure M, Lardeaux JM, Ledru P (2009) A review of the pre-Permian geology of the Variscan French Massif Central. Comptes Rendus Geoscience 341:202-13.

Faure M, Bé Mézème E, Cocherie A, Rossi P, Chemenda A, Boutelier D (2008) Devonian geodynamic evolution of the Variscan Belt, insights from the French Massif Central and Massif Armoricain. Tectonics 27.

Franke W, Doublier MP, Klama K, Potel S, Wemmer K (2011) Hot metamorphic core complex in a cold foreland. International Journal of Earth Sciences 100:753-85.

Foland KA (1983) 40Ar/39Ar incremental heating plateaus for biotites with excess argon. Isot. Gesci. 1:3-21.

Forestier FH (1961) Métamorphisme hercynien et antéhercynien dans le bassin du Haut-Allier (Massif central français). Doctoral dissertation, Faculté des Sciences de l'Université de Clermont-Ferrand.

Franke W, Cocks LR, Torsvik TH (2017) The Palaeozoic Variscan oceans revisited. Gondwana Research 48:257-84.

Giraud A, Marchand J, Dupuy C, Dostal J (1984) Geochemistry of leptyno-amphibolite complex from haut Allier (French Massif Central). Lithos 17:203-214.

Godard G (2001) The Les Essarts eclogite-bearing metamorphic Complex (Vendée, Southern Armorican Massif, France). Géologie de la France 1:19-51.

Godard G (2009) Two orogenic cycles recorded in eclogite-facies gneiss from the southern Armorican Massif (France). European Journal of Mineralogy 21:1173-1190.

Hayden LA, Watson EB, Wark DA (2008) A thermobarometer for sphene (titanite). Contributions to Mineralogy and Petrology 155:529-40.

Holland TJB., POWELL, R (1985) An internally consistent thermodynamic dataset with uncertainties and correlations: 2. Data and results. Journal of metamorphic Geology 3:343-370.

Holland TJB, Powell R (2011) An improved and extended internally consistent thermodynamic dataset for phases of petrological interest, involving a new equation of state for solids. Journal of Metamorphic Geology 29:333-383.

Ibarguchi JI (1995) Petrology of jadeite metagranite and associated orthogneiss from the Malpica-Tuy allochthon (Northwest Spain). European Journal of Mineralogy 29:403-16.

Janoušek V, Farrow CM, Erban V (2006) Interpretation of whole-rock geochemical data in igneous geochemistry: introducing Geochemical Data Toolkit (GCDkit). Journal of Petrology 47:1255-9.

Joanny V, Lardeaux JM, Trolliard G, M. Boudeulle M (1989) La transition omphacite→diopside+plagioclase dans les éclogites du Rouergue (Massif Central Français): un exemple de précipitation discontinue C.R. Acad. Sci. Paris 309 :1923-1930.

Kohn MJ (2017) Titanite petrochronology. Reviews in Mineralogy and Geochemistry 83:419-41.

Koons PO, Rubie DC, Fruch-Green G (1987) The effects of disequilibrium and deformation on the mineralogical evolution of quartz diorite during metamorphism in the eclogite facies. Journal of Petrology 28:679-700.

Kroner U, Romer RL (2013). Two plates—many subduction zones: the Variscan orogeny reconsidered. Gondwana Research 24:298-329.

Lardeaux JM (2014) Deciphering orogeny: a metamorphic perspective Examples from European Alpine and Variscan belts. Bulletin de la Société Géologique de France 185:281-310.

Lardeaux JM, Ledru P, Daniel I, Duchene S (2001) The Variscan French Massif Central—a new addition to the ultra-high pressure metamorphic 'club': exhumation processes and geodynamic consequences. Tectonophysics 332:143-67.

Lardeaux JM, Schulmann K, Faure M, Janoušek V, Lexa O, Skrzypek E, Edel JB, Štípská P (2014) The moldanubian zone in the French Massif Central, Vosges/Schwarzwald and Bohemian Massif revisited: differences and similarities. Geological Society, London, Special Publications 405:7-44.

Lasnier B (1977) Persistance d'une série granulitique au coeur du Massif Central français, Haut-Allier: les termes basiques, ultrabasiques et carbonatés. Doctoral Dissertation. Université de Nantes; laboratoire de pétrologie et de minéralogie.

Laurent O, Couzinié S, Zeh A, Vanderhaeghe O, Moyen JF, Villaros A, Gardien V, Chelle-Michou C (2017) Protracted, coeval crust and mantle melting during Variscan late-orogenic evolution: U–Pb dating in the eastern French Massif Central. International Journal of Earth Sciences 106:421-51.

Le Bayon B, Pitra P, Ballevre M, Bohn M (2006) Reconstructing P–T paths during continental collision using multi-stage garnet (Gran Paradiso nappe, Western Alps). Journal of Metamorphic Geology 24:477-96.

Ledru PA, Lardeaux JM, Santallier DA, Autran AL, Quenardel JM, Floc'h JP, Lerouge G, Maillet N, Marchand J, Ploquin A (1989) Où sont les nappes dans le Massif central français?. Bulletin de la Société géologique de France 1:605-18.

Lotout C, Pitra P, Poujol M, Van Den Driessche J (2017) Ordovician magmatism in the Lévézou massif (French Massif Central): tectonic and geodynamic implications. International Journal of Earth Sciences 106:501-15.

Malavieille J (1993) Late orogenic extension in mountain belts: insights from the Basin and Range and the late Paleozoic Variscan belt. Tectonics 12:1115-30.

Matte P (1986) Tectonics and plate tectonics model for the Variscan belt of Europe. Tectonophysics 126:329335347-32344374.

Matte P (2001) The Variscan collage and orogeny (480–290 Ma) and the tectonic definition of the Armorica microplate: a review. Terra nova 13:122-8.

Matte P, Burg JP (1981 Sutures, thrusts and nappes in the Variscan Arc of western Europe: plate tectonic implications. Geological Society, London, Special Publications 9:353-8.

Martínez Catalán JR (2011) Are the oroclines of the Variscan belt related to late Variscan strike-slip tectonics?. Terra nova 23:241-7.

Mercier JC, Girardeau J, Prinzhofer A, Dubuisson G (1985) Les complexes ophiolitiques du Limousin : structure, pétrologie et géochimie. Rapport GPF2, thème 3. Doc BRGM, Orléans, 95-3 :35-48.

Mercier L, Johan V, Lardeaux JM, Ledru P (1989) Découverte d'éclogites dans l'Artense (M.C.F.). Implications pour la définition des nappes à l'est du Sillon Houiller. C. R. Acad. Sci., Paris, 308:315-320.

Nahodilová R, Štípská P, Powell R, Košler J, Racek M (2014) High-Ti muscovite as a prograde relict in high pressure granulites with metamorphic Devonian zircon ages (Běstvina granulite body, Bohemian Massif): consequences for the relamination model of subducted crust. Gondwana Research 25:630-48.

Nicollet C (1978) Pétrologie et tectonique des terrains cristallins anté-permiens du versant sud du dôme du Lévezou (Rouergue, Massif central)." Bull BRGM 3:225-263.

Nicollet C, Leyreloup A, Dupuy C (1979) Petrogenesis of high pressure trondhjemitic layers in eclogites and amphibolites from southern Massif Central, France. Trondhjemites, Dacites and Related Rocks 435-463.

Oberhansli R, Hunziker JC, Martinotti G, Stern WB (1983) Geochemistry, geochronology and petrology of Monte Mucrone: an example of eo-Alpine eclogitization of Permian granitoids in the Sesia–Lanzo zone, Western Alps, Italy. Chemical Geology 52:165–184.

Paquette et al., accepté pour publication à Lithos.

Paquette, J.L., 1987. "Comportement des systèmes isotopiques U-Pb et Sm-Nd dans le métamorphisme éclogitique. Chaîne Hercynienne et chaîne Alpine." PhD dissertation, Université Rennes 1.

Paquette JL, Monchoux P, Couturier M (1995) Geochemical and isotopic study of a norite-eclogite transition in the European Variscan belt: Implications for U-Pb zircon systematics in metabasic rocks. Geochimica et Cosmochimica Acta. 59:1611-22.

Piboule M, Briand B (1985) Geochemistry of eclogites and associated rocks of the southeastern area of the French Massif Central: origin of the protoliths. Chemical Geology 50:189-199.

Peterman EM, Hacker BR, Baxter EF (2009) Phase transformations of continental crust during subduction and exhumation: Western Gneiss Region, Norway. European Journal of Mineralogy 21:1097-118.

Pin C (1981) Old inherited zircons in two synkinematic variscan granitoids: “the granite du Pinet” and the “Orthogneiss de Marvejols” (Southern French Massif Central). Neues Jahrbuch für Mineralogie, Abhandlungen 142:27-48.

Pin C (1990) Variscan oceans: ages, origins and geodynamic implications inferred from geochemical and radiometric data. Tectonophysics, 177:215-227.

Pin C, Lancelot J (1982) U-Pb dating of an early Paleozoic bimodal magmatism in the French Massif Central and of its further metamorphic evolution. Contributions to Mineralogy and Petrology 79:1-2.

Pin C, Paquette JL (1998)A mantle-derived bimodal suite in the Hercynian Belt: Nd isotope and trace element evidence for a subduction-related rift origin of the Late Devonian Brévenne metavolcanics, Massif Central (France). Contributions to Mineralogy and Petrology 129:222-38.

Pin C, Vielzeuf DA (1988) Les granulites de haute-pression d'Europe moyenne témoins d'une subduction éo-hercynienne. Implications sur l'origine des groupes leptyno-amphiboliques. Bulletin de la Société Géologique de France 4:13-20.

Pitra P, Boulvais P, Antonoff V, Diot H (2008) Wagnerite in a cordierite-gedrite gneiss: Witness of long-term fluid-rock interaction in the continental crust (Ile d'Yeu, Armorican Massif, France). American Mineralogist 93:315-26.

Poujol M, Pitra P, Van den Driessche J, Tartèse R, Ruffet G, Paquette JL, Poilvet JC (2017) Two-stage partial melting during the Variscan extensional tectonics (Montagne Noire, France). International Journal of Earth Sciences 106:477-500.

Powell R, Holland TJB (1988) An internally consistent dataset with uncertainties and correlations: 3. Applications to geobarometry, worked examples and a computer program. Journal of metamorphic Geology 6:173-204.

Roger F, Teyssier C, Respaut JP, Rey PF, Jolivet M, Whitney DL, Paquette JL, Brunel M (2015) Timing of formation and exhumation of the Montagne Noire double dome, French Massif Central. Tectonophysics 640:53-69.

Rubatto D (2017) Zircon: the metamorphic mineral. Reviews in mineralogy and geochemistry 83:261-95.

Ruffet G, Féraud G, Amouric M (1991) Comparison of 40Ar-39Ar conventional and laser dating of biotites from the North Trégor Batholith. Géochimica et Cosmochimica Acta, 55:1675-1688.

Ruffet G., Féraud G, Ballèvre M, Kienast JR (1995) Plateau ages and excess argon on phengites: a 40Ar-39Ar laser probe study of alpine micas (Sesia zone). Chemical Geolog 121:327-343.

Santallier DA, Briand BE, Menot RP, Piboule M (1988) Les complexes leptyno-amphiboliques (CLA): revue critique et suggestions pour un meilleur emploi de ce terme. Bull Soc Géol Fr 8:3-12.

Tartèse R, Ruffet G, Poujol M, Boulvais P, Ireland TR, Bohn M (2011) Simultaneous resetting of the muscovite K-Ar and monazite U-Pb geochronometers: a story of fluids. Terra Nova 23:390-398. Doi: 10.1111/j.1365-3121.2011.01024.x.

Tomkins HS, Powell R, Ellis DJ (2007) The pressure dependence of the zirconium-in-rutile thermometer. Journal of metamorphic Geology 25:703-13.

de Veslud CL, Alexandre P, Ruffet G, Cuney M, Cheilletz A (2013) A two-stage exhumation in Western French Massif Central: New geochronological evidences of syn-collisional extension. Lithos 175:1-5.

Watson EB, Wark DA, Thomas JB (2006) Crystallization thermometers for zircon and rutile. Contributions to Mineralogy and Petrology 151:413.

Whitney DL, Roger F, Teyssier C, Rey PF, Respaut JP (2015) Syn-collapse eclogite metamorphism and exhumation of deep crust in a migmatite dome: the P–T–t record of the youngest Variscan eclogite (Montagne Noire, French Massif Central). Earth and Planetary Science Letters 430:224-234.

Annexes

Annexe 1 - ^{40}Ar–^{39}Ar Analytical procedure

About half of the presented ^{40}Ar–^{39}Ar results were analyzed by Gilles Ruffet during this PhD.

^{40}Ar–^{39}Ar ages of biotite and muscovite were measured by the step-heating experimental method, which is described in detail by Ruffet et al. (1995) and Ruffet et al. (1997). The step-heating analyses of the selected grains were carried out by an ^{40}Ar–^{39}Ar laser probe (CO_2 Synrad®) at Géosciences Rennes (Université Rennes 1, France) (see following tables). Biotite and muscovitegrains were carefully handpicked under a binocular microscope from 0.25-2 mm fraction of crushed rocks. The samples were wrapped in aluminum foil to form packages (11 × 11 × 0.5 mm) and stacked up to form a pile, within which packages of flux monitors were inserted. Three distinct irradiation were proceed. The stack, placed in an irradiation can, was irradiated at the McMaster reactor (Hamilton, Canada).Irradiation time, total flux and flux gradient precision, are precised in the following tables. Blanks are performed routinely every first or third run and are subtracted from the subsequent sample gas fractions. Analyses are performed on a Map215® mass spectrometer. To define a plateau age, a minimum of three consecutive steps are required, corresponding to a minimum of 70% of the total $^{39}Ar_K$ released, and the individual fraction ages should agree to within 1σ or 2σ of the integrated age of the plateau segment. Pseudo-plateau ages, with less than 70% of $^{39}Ar_K$ released, can also be defined. All presented and discussed ^{40}Ar–^{39}Ar results are displayed at the 1σ level.

Irradiation 21

			J parameter	error J			Mass Discrimination (1+e)	Err Discrimination							
	LV2 A Muscovite		1.75E-02	7.13E-05			1.008709	1.32E-03							
laser power	40Ar	Error 40Ar	39Ar	Error 39Ar	38Ar	Error 38Ar	37Ar	Error 37Ar	36Ar	Error 36Ar	40Ar*/39ArK	Error 40Ar*/ 39ArK	Apparent age (My)	Error Age (My)	Delay to irradiation (day)
300	511.67541	0.79976	26.62219	0.099581	0.617695	0.052554	0.013318	0.029863	1.036453	0.024487	8.055319	0.2796	238.0012	7.816	242.413194
350	1549.119757	1.237911	124.155806	0.180095	1.979526	0.051056	0.032728	0.036618	0.572395	0.023779	11.229257	0.0628	323.7994	2.199	242.433333
390	1155.767158	1.107068	94.624724	0.178638	1.294426	0.053825	0.000001	0.045168	0.114473	0.041918	11.948805	0.1324	342.6969	3.78	242.513194
430	2531.81334	1.402559	204.19983	0.331599	2.847276	0.070401	0.000001	0.060284	0.260709	0.040492	12.115179	0.0639	347.0384	2.269	242.533333
440	2374.32983	1.191617	192.321907	0.127078	2.618776	0.06443	0.000001	0.046318	0.16462	0.044197	12.183855	0.0697	348.8275	2.387	242.553472
460	2117.712058	1.226751	170.860224	0.233001	2.351026	0.087361	0.025508	0.042224	0.167773	0.03605	12.198078	0.0663	349.1977	2.321	242.573611
500	5003.165046	1.95984	410.401253	0.286007	5.576414	0.078115	0.055432	0.037298	0.170626	0.038533	12.157384	0.0334	348.1381	1.774	242.623611
530	11440.64582	3.587897	961.343166	0.527299	12.296712	0.12541	0.067119	0.038983	0.149827	0.025012	11.939762	0.0192	342.4606	1.603	242.643056
550	9582.709736	5.068123	798.691697	0.334826	10.422451	0.140624	0.104182	0.02793	0.090281	0.029353	12.050904	0.0209	345.3624	1.629	242.663194
570	6425.110426	5.479853	532.158079	0.513133	6.999513	0.125379	0.103898	0.03632	0.094532	0.024903	12.10908	0.0263	346.8794	1.687	242.683333
600	3218.149729	1.748414	265.341126	0.207986	3.714844	0.04234	0.000001	0.04143	0.035633	0.01667	12.174694	0.0271	348.5889	1.701	242.713194
660	16085.1319	6.359121	1343.279477	1.19994	17.358188	0.113966	0.00396	0.050678	0.075379	0.022082	12.042364	0.0204	345.1396	1.623	242.733333
700	13861.4153	18.356835	1144.168077	1.341593	15.246088	0.249352	0.000001	0.041866	0.094379	0.022245	12.176039	0.0275	348.6239	1.706	242.753472
740	3447.323183	3.080589	283.192177	0.349684	3.687473	0.124904	0.00709	0.034901	0.000723	0.021157	12.258142	0.0329	350.7607	1.777	242.773611
830	7523.61356	2.603101	627.986719	0.47323	8.089243	0.118081	0.077445	0.039099	0.037853	0.02183	12.048485	0.0213	345.2993	1.633	243.363194
Fusion	8239.607968	6.828513	696.590612	0.601134	9.02669	0.160813	0.061211	0.050257	0.063491	0.028119	11.88601	0.0243	341.0556	1.645	243.383333

			J parameter	error J			Mass Discrimination (1+e)	Err Discrimination							
	LV2 A Muscovite		1.75E-02	7.13E-05			1.008709	1.32E-03							
laser power	40Ar	Error 40Ar	39Ar	Error 39Ar	38Ar	Error 38Ar	37Ar	Error 37Ar	36Ar	Error 36Ar	40Ar*/39ArK	Error 40Ar*/ 39ArK	Apparent age (My)	Error Age (My)	Delay to irradiation (day)
300	224.164127	0.416047	13.705845	0.081568	0.231908	0.03369	0.004773	0.026364	0.423795	0.024338	7.494679	0.5221	222.4136	14.61	243.423611
350	782.459407	0.995104	56.82622	0.117937	0.810369	0.067981	0.003289	0.027872	0.237549	0.034252	12.652875	0.1794	360.9986	4.909	243.433333
390	2418.223784	1.780356	181.781862	0.338976	2.372087	0.074916	0.000001	0.030288	0.561788	0.020474	12.498815	0.0465	357.0098	1.989	243.453472
430	1905.043953	1.030802	151.808543	0.192164	2.025092	0.054701	0.000001	0.032352	0.127056	0.019346	12.39409	0.0445	354.2932	1.95	243.473611
460	4536.768751	2.262273	364.709136	0.44548	4.41899	0.078955	0.000001	0.036088	0.360993	0.01536	12.239173	0.0269	350.2672	1.705	243.503472
480	9070.420379	2.613761	734.195166	0.242606	9.130742	0.111167	0.067877	0.040003	0.368768	0.018432	12.296055	0.0192	351.7465	1.639	243.523611
490	7014.699561	3.171989	570.22971	0.452875	6.961112	0.080253	0.000001	0.031159	0.253713	0.020258	12.258568	0.0227	350.7718	1.666	243.543056
500	1423.340679	0.44693	116.600666	0.146868	1.430842	0.05249	0.000001	0.028601	0.050768	0.015573	12.166111	0.0452	348.3654	1.944	243.563194
540	7631.384072	3.610953	622.921083	0.580582	7.600436	0.130216	0.000001	0.028514	0.160576	0.023916	12.26199	0.0237	350.8608	1.675	243.593056
580	3614.707514	2.581792	295.348001	0.425617	3.780588	0.086666	0.050019	0.026295	0.113681	0.018881	12.214802	0.0318	349.6331	1.759	243.613194
630	2945.667586	1.72145	240.635213	0.318849	3.150717	0.070683	0.017359	0.029583	0.060123	0.020411	12.255403	0.0346	350.6895	1.798	243.633333
700	1951.176068	1.290949	159.834029	0.30052	2.078753	0.10294	0.068722	0.039387	0.066516	0.024254	12.177149	0.0531	348.6528	2.075	243.653472
Fusion	3438.823324	1.138185	279.649849	0.394598	3.625228	0.07443	0.000001	0.033301	0.078181	0.016277	12.302013	0.0297	351.9014	1.742	243.673611

			J parameter	error J			Mass Discrimination (1+e)	Err Discrimination							
	LV15 Muscovite		1.75E-02	7.13E-05			1.008709	1.32E-03							
laser power	40Ar	Error 40Ar	39Ar	Error 39Ar	38Ar	Error 38Ar	37Ar	Error 37Ar	36Ar	Error 36Ar	40Ar*/39ArK	Error 40Ar*/ 39ArK	Apparent age (My)	Error Age (My)	Delay to irradiation (day)
300	140.169095	0.241234	8.121553	0.06354	0.189198	0.033572	0.000001	0.038963	0.381436	0.022591	3.741929	0.814	114.5561	24.15	243.703472
400	510.369717	0.609011	40.774043	0.115958	0.505556	0.035713	0.000001	0.026118	0.146409	0.017553	11.561992	0.132	332.8137	3.773	243.723611
470	774.25761	0.887089	61.291213	0.085977	0.662594	0.054616	0.000001	0.03262	0.084676	0.04145	12.319594	0.1986	352.623	5.397	243.743056
510	638.12001	0.911369	50.932713	0.085688	0.686294	0.030824	0.000001	0.03262	0.067076	0.021574	12.234236	0.1275	350.402	3.666	243.763194
550	1031.42621	0.734512	82.683813	0.185749	1.002294	0.041156	0.000001	0.024513	0.062676	0.01555	12.341641	0.0644	353.1963	2.293	243.773611
600	920.495144	0.852801	74.729357	0.280592	0.945135	0.043006	0.054812	0.036393	0.050763	0.022844	12.215117	0.1021	349.9041	3.081	244.373611
640	4174.622584	2.717252	341.546315	0.29316	4.024246	0.087124	0.032258	0.039113	0.101024	0.025086	12.223449	0.0301	350.1211	1.741	244.393056
680	267.077844	0.325923	21.953357	0.056167	0.289335	0.0425	0.021512	0.036107	0.000001	0.037395	12.262164	0.4966	351.129	13.02	244.413194
800	1978.61723	1.291851	163.296911	0.203617	2.098914	0.085055	0.143087	0.033568	0.077635	0.023406	12.073515	0.048	346.2125	1.984	244.433333
910	2739.742048	1.597326	226.95794	0.242678	2.764679	0.074542	0.007303	0.039215	0.072704	0.033419	12.063466	0.0481	345.9502	1.985	244.463194
1060	2495.414753	0.888419	205.754868	0.26562	2.600459	0.065925	0.061673	0.028905	0.067697	0.027152	12.120958	0.0448	347.4502	1.935	244.493056
1200	607.777446	0.652007	50.111997	0.133898	0.594706	0.04629	0.000001	0.03163	0.015376	0.027786	12.124174	0.1657	347.5341	4.59	244.513194
Fusion	2949.500953	0.757798	242.792968	0.146738	3.028159	0.062763	0.008673	0.029484	0.002297	0.033715	12.230998	0.0442	350.3177	1.935	244.533333

			J parameter	error J			Mass Discrimination (1+e)	Err Discrimination							
	LV3C Muscovite		1.75E-02	7.13E-05			1.008709	1.32E-03							
laser power	40Ar	Error 40Ar	39Ar	Error 39Ar	38Ar	Error 38Ar	37Ar	Error 37Ar	36Ar	Error 36Ar	40Ar*/39ArK	Error 40Ar*/ 39ArK	Apparent age (My)	Error Age (My)	Delay to irradiation (day)
300	133.539048	0.237331	11.047642	0.055686	0.146784	0.037704	0.000001	0.03119	0.185871	0.019464	7.286239	0.5156	216.7536	14.49	244.563194
370	460.763909	0.582635	38.564751	0.120806	0.40954	0.047744	0.000001	0.031525	0.040672	0.018804	11.724958	0.1483	337.0947	4.17	244.583333
420	319.985548	0.201552	24.896842	0.091116	0.197484	0.048431	0.000001	0.026855	0.005471	0.023594	12.878089	0.2801	367.0901	7.407	244.603472
490	1862.791548	0.950308	144.143442	0.145964	1.799684	0.048862	0.000001	0.025484	0.124671	0.024605	12.762586	0.0548	364.108	2.146	244.623611
510	2624.100317	1.309554	206.993903	0.330968	2.596409	0.047299	0.035223	0.03608	0.155186	0.022007	12.550262	0.0414	358.6132	1.918	244.653472
530	410.523817	0.440649	32.370003	0.045386	0.394309	0.040224	0.000001	0.033081	0.071786	0.021655	12.127023	0.1968	347.6099	5.359	244.673611
570	2266.432917	0.996857	179.845303	0.228115	2.293709	0.075685	0.000001	0.03227	0.116486	0.024073	12.502378	0.0458	357.3716	1.981	244.693056
630	13127.34862	3.021606	1048.796103	0.899482	12.802209	0.121811	0.006323	0.032513	0.281886	0.023168	12.526274	0.0212	357.9913	1.68	244.723611
670	2411.483656	1.449966	192.477907	0.285677	2.379053	0.062895	0.000001	0.031447	0.054009	0.029805	12.534912	0.0521	358.2153	2.085	244.753472
750	3249.282121	1.848074	259.975325	0.548812	3.26559	0.074157	0.000001	0.027985	0.070193	0.031041	12.507604	0.0473	357.5072	2.004	244.773611
850	5329.525391	2.520386	427.254395	0.51144	5.301381	0.080352	0.000001	0.037289	0.078276	0.028498	12.508033	0.0302	357.5183	1.769	245.363194
990	9125.927891	3.857136	730.725795	0.422875	8.982581	0.108662	0.006732	0.046439	0.105676	0.029807	12.534396	0.0224	358.2019	1.691	245.383333
Fusion	8427.810291	2.567956	672.676095	0.332985	8.669781	0.202826	0.056632	0.045932	0.089976	0.02745	12.578709	0.0218	359.3503	1.69	245.403472

			J parameter	error J			Mass Discrimination (1+e)	Err Discrimination							
	LV2B Muscovite		1.75E-02	7.13E-05			1.008709	1.32E-03							
laser power	40Ar	Error 40Ar	39Ar	Error 39Ar	38Ar	Error 38Ar	37Ar	Error 37Ar	36Ar	Error 36Ar	40Ar*/39ArK	Error 40Ar*/39ArK	Apparent age (My)	Error Age (My)	Delay to irradiation (day)
300	486.953394	0.626916	35.481251	0.03949	0.575252	0.041622	0.000001	0.03192	0.393504	0.019247	10.600076	0.1623	307.2292	4.538	245.713194
350	1335.487157	1.603368	107.817523	0.088871	1.300293	0.042125	0.023471	0.032897	0.201141	0.02077	11.933941	0.0617	342.4381	2.218	245.733333
390	11922.07948	5.873054	997.16295	0.831844	12.484972	0.073361	0.062422	0.038218	0.488839	0.027075	11.898034	0.0216	341.4993	1.62	245.753472
410	11609.53045	3.926426	981.961229	0.481546	11.949619	0.2156	0.119847	0.030914	0.139488	0.021702	11.865651	0.0185	340.6521	1.591	245.773611
420	2247.096089	0.980793	190.581653	0.137723	2.514905	0.068922	0.037938	0.032081	0.04907	0.024532	11.80079	0.0419	338.9541	1.865	248.383333
450	2523.465799	0.648136	211.378039	0.198957	2.690252	0.044065	0.071018	0.025179	0.2024	0.019533	11.74757	0.0338	337.5597	1.744	248.403472
500	9056.245984	3.31638	766.378205	0.517455	9.606303	0.119112	0.143371	0.032115	0.115548	0.026397	11.857936	0.0208	340.4502	1.61	248.423611
540	5036.431989	1.617056	425.660053	0.753932	5.323505	0.117052	0.082338	0.031097	0.02817	0.017702	11.897794	0.0292	341.493	1.7	248.443056
620	2961.377327	0.902801	250.595483	0.382676	3.065293	0.071686	0.000001	0.019364	0.028596	0.024195	11.866666	0.0371	340.6787	1.8	248.473611
Fusion	11508.89392	2.512354	972.387895	0.280442	11.717791	0.227901	0.050787	0.039287	0.070135	0.02671	11.897943	0.0182	341.4969	1.592	248.493056

			J parameter	error J			Mass Discrimination (1+e)	Err Discrimination							
	LV2A biotite		1.75E-02	7.13E-05			1.008709	1.32E-03							
laser power	40Ar	Error 40Ar	39Ar	Error 39Ar	38Ar	Error 38Ar	37Ar	Error 37Ar	36Ar	Error 36Ar	40Ar*/39ArK	Error 40Ar*/39ArK	Apparent age (My)	Error Age (My)	Delay to irradiation (day)
250	331.821323	0.277558	11.804139	0.047084	0.299051	0.041207	0.071623	0.031745	0.911229	0.02883	5.962239	0.7221	179.1081	20.67	248.543056
310	2251.234369	2.061606	159.792906	0.269971	2.546599	0.089941	0.055751	0.029014	1.306314	0.032066	11.817565	0.0689	339.2648	2.352	248.573611
370	6889.693434	1.300112	542.538834	0.355372	7.90057	0.167126	0.051221	0.031155	0.347779	0.022551	12.602966	0.023	359.7074	1.702	248.583333
400	4116.467234	1.488944	325.949834	0.459497	4.64007	0.047744	0.098921	0.033835	0.140479	0.026156	12.596165	0.0343	359.5313	1.824	248.603472
460	6922.240125	3.475875	547.652945	0.393041	7.865677	0.125985	0.000001	0.038096	0.152713	0.018666	12.647371	0.0226	360.8563	1.703	248.643056
500	3010.961255	1.606194	239.230862	0.372743	3.601154	0.067803	0.085563	0.033804	0.09763	0.018116	12.560157	0.0347	358.5991	1.827	248.663194
560	1986.763025	1.342802	157.860945	0.265309	2.194977	0.098364	0.000001	0.03204	0.025513	0.016987	12.626661	0.0423	360.3205	1.936	248.683333
580	1610.514387	0.773909	127.467772	0.211545	1.927171	0.071985	0.016772	0.042947	0.074536	0.028327	12.555082	0.0704	358.4676	2.419	248.703472
650	3376.589468	1.00438	266.554209	0.368468	3.831248	0.118816	0.000001	0.033465	0.091443	0.014857	12.656636	0.0296	361.0959	1.774	248.733333
750	2765.86888	0.803767	220.285023	0.102369	3.007662	0.080063	0.000001	0.034231	0.047765	0.029334	12.580714	0.0428	359.1314	1.94	248.753472
Fusion	9092.405405	4.802414	724.416339	0.699096	10.110109	0.09206	0.000001	0.035402	0.101935	0.020616	12.598319	0.0233	359.5871	1.704	248.773611

			J parameter	error J			Mass Discrimination (1+e)	Err Discrimination							
	LV3C Biotite		1.75E-02	6.23E-05			1.008709	1.32E-03							
laser power	40Ar	Error 40Ar	39Ar	Error 39Ar	38Ar	Error 38Ar	37Ar	Error 37Ar	36Ar	Error 36Ar	40Ar*/39ArK	Error 40Ar*/ 39ArK	Apparent age (My)	Error Age (My)	Delay to irradiation (day)
300	447.671723	0.567661	17.657468	0.053695	0.399235	0.036531	0.000001	0.035747	1.023554	0.028926	8.697955	0.4884	255.9032	13.44	249.363194
350	1469.495127	0.961653	85.224317	0.09565	1.416723	0.050141	0.000001	0.031132	0.641258	0.012469	15.178676	0.0568	425.4863	2.217	249.383333
410	6171.958919	2.971459	365.638884	0.481299	5.355169	0.128943	0.02841	0.028348	0.882321	0.031723	16.298452	0.0423	453.2414	2.084	249.403472
440	3966.086027	2.126083	237.728317	0.261016	3.426323	0.07524	0.000001	0.034389	0.284058	0.017093	16.45315	0.0373	457.0426	2.038	249.423611
480	7411.471935	2.455567	447.631805	0.433547	6.524587	0.100121	0.023373	0.039593	0.42948	0.032354	16.395131	0.0354	455.6179	2.012	249.463194
520	4775.585101	3.001729	289.138998	0.345902	4.162308	0.049892	0.000001	0.025904	0.155242	0.025241	16.476352	0.0405	457.612	2.076	249.473611
570	3227.989539	1.420207	195.458689	0.25397	2.679355	0.066565	0.03528	0.02548	0.112301	0.025647	16.46602	0.0497	457.3584	2.192	249.493056
650	6141.138335	4.762161	367.749999	0.341981	5.335325	0.107332	0.03353	0.028882	0.29832	0.025825	16.581822	0.0368	460.1981	2.041	249.513194
730	3665.148937	2.868212	219.02105	0.20517	3.160303	0.088264	0.000724	0.029591	0.140033	0.023654	16.66583	0.0439	462.2554	2.13	249.543056
850	7184.435337	2.751244	431.44535	0.301188	6.198303	0.090864	0.030924	0.028819	0.292133	0.018961	16.572953	0.0293	459.9808	1.966	249.563194
1000	15216.23884	4.669211	916.44885	0.635684	13.240403	0.136255	0.000001	0.034191	0.613233	0.029244	16.525464	0.0275	458.8167	1.948	249.583333
Fusion	16110.02594	8.509148	970.12965	0.78115	13.960803	0.221419	0.054124	0.036695	0.671033	0.026666	16.522223	0.0289	458.7372	1.959	249.603472

			J parameter	error J			Mass Discrimination (1+e)	Err Discrimination							
	LV2A muscovite		1.75E-02	7.13E-05			1.008908	1.32E-03							
laser power	40Ar	Error 40Ar	39Ar	Error 39Ar	38Ar	Error 38Ar	37Ar	Error 37Ar	36Ar	Error 36Ar	40Ar*/39ArK	Error 40Ar*/ 39ArK	Apparent age (My)	Error Age (My)	Delay to irradiation (day)
280	386.522352	0.467677	12.831418	0.052085	0.403875	0.037486	0.008382	0.02418	1.016266	0.019005	7.364881	0.4524	218.7856	12.7	4.563194
320	242.028478	0.417313	15.480172	0.055128	0.224126	0.040582	0.028455	0.018649	0.253299	0.01384	11.015813	0.2672	318.1556	7.217	4.583333
370	721.150055	0.793142	56.162015	0.150471	0.82616	0.051981	0.023698	0.021477	0.253566	0.014426	11.641133	0.0851	334.6407	2.685	4.603472
380	855.227904	0.749953	70.898671	0.222463	0.869197	0.061628	0.009103	0.025391	0.044219	0.020909	11.987582	0.0957	343.7097	2.929	4.743056
400	1636.646004	1.203304	137.510994	0.184153	1.686769	0.049438	0.000001	0.022503	0.01498	0.008733	11.975049	0.0305	343.3824	1.722	4.763194
410	1302.014172	0.77095	109.240493	0.248243	1.346517	0.047799	0.037251	0.038397	0.020054	0.014073	11.970311	0.0495	343.2587	2	5.373611
430	1273.27741	0.729382	106.108401	0.170022	1.398636	0.068195	0.020075	0.032169	0.048477	0.017086	11.972575	0.0536	343.3178	2.072	5.393056
480	1725.310496	0.728113	143.590599	0.161931	1.752752	0.063326	0.039317	0.031813	0.03832	0.013884	12.043647	0.0355	345.1731	1.793	5.413194
530	1877.258535	0.547417	155.663344	0.131972	1.953277	0.057853	0.061423	0.028916	0.073503	0.016921	12.0286	0.0372	344.7804	1.815	5.433333
600	8521.128113	3.009639	703.732716	0.463558	9.139525	0.152264	0.062352	0.01393	0.22055	0.016166	12.123932	0.0199	347.2665	1.628	5.463194
630	15139.69521	4.250336	1252.616416	0.66341	15.398325	0.170372	0.125752	0.014596	0.22015	0.014672	12.141734	0.0181	347.7304	1.615	5.483333
660	21190.55591	22.622738	1763.255516	2.713127	21.964425	0.107033	0.090252	0.03391	0.14185	0.010079	12.100231	0.0278	346.6488	1.702	5.513194
690	7172.86571	2.965725	598.73767	0.250723	7.584078	0.11677	0.021802	0.027565	0.064201	0.013819	12.054232	0.0187	345.4492	1.611	5.523611
750	11633.24881	1.748678	974.935389	0.94261	12.153282	0.138131	0.000001	0.029268	0.066042	0.019925	12.017631	0.0206	344.4942	1.623	5.573611
800	32744.0549	15.869277	2725.823285	1.959554	33.875163	0.316778	0.149117	0.024721	0.156028	0.024403	12.101604	0.0193	346.6845	1.62	5.583333
850	17732.1053	3.209762	1476.128285	0.751603	18.592363	0.187418	0.110117	0.029425	0.091328	0.020788	12.100296	0.0177	346.6505	1.608	5.613194
920	10349.44579	3.712453	861.561634	0.67903	10.636392	0.180939	0.038234	0.026167	0.070405	0.022135	12.094371	0.0205	346.496	1.63	5.643056
1050	6616.034093	2.218243	549.221935	0.275978	6.906368	0.132366	0.001605	0.025384	0.03443	0.015798	12.133968	0.0195	347.528	1.625	5.673611
Fusion	7995.277536	5.013573	654.711878	0.575341	8.259827	0.116064	0.016521	0.027503	0.069281	0.015746	12.288605	0.0221	351.5529	1.663	5.703472

			J parameter	error J			Mass Discrimination (1+e)	Err Discrimination				Error	Apparent	Error Age	Delay to
	LV2B muscovite		1.75E-02	7.13E-05			1.008908	1.32E-03							
laser power	40Ar	Error 40Ar	39Ar	Error 39Ar	38Ar	Error 38Ar	37Ar	Error 37Ar	36Ar	Error 36Ar	40Ar*/39ArK	Error 40Ar*/39ArK	Apparent age (My)	Error Age (My)	Delay to irradiation (day)
300	501.356191	0.475274	37.893889	0.16751	0.545323	0.034203	0.010622	0.029482	0.453697	0.017717	9.866855	0.1467	287.5789	4.158	-1.256944
340	494.890911	0.550638	40.216359	0.137685	0.493977	0.030283	0.018264	0.022509	0.093741	0.022093	11.736926	0.1663	337.2807	4.612	-1.236806
360	728.621281	0.80417	60.563856	0.106088	0.636004	0.034504	0.027726	0.0272	0.049873	0.014862	11.897432	0.0774	341.4835	2.53	1.373611
390	1685.244108	0.831821	136.43673	0.114192	1.720499	0.072527	0.02365	0.028716	0.245482	0.017565	11.937826	0.0433	342.5397	1.898	1.393056
410	686.487527	0.26145	56.819769	0.087225	0.694696	0.028809	0.012974	0.030567	0.0536	0.016848	11.914256	0.0899	341.9235	2.799	1.413194
440	8403.136686	4.203519	691.38926	0.390445	8.674291	0.111513	0.078145	0.028612	0.833919	0.017939	11.910636	0.0211	341.8288	1.617	1.433333
450	4735.897052	1.28595	401.486594	0.291427	5.078258	0.085241	0.02129	0.02344	0.030515	0.015359	11.877916	0.0213	340.973	1.616	1.483333
470	23670.34285	6.734924	2001.591194	0.824751	24.705958	0.304279	0.10429	0.039025	0.145015	0.024986	11.909073	0.0172	341.788	1.585	1.493056
480	5368.410052	3.352757	454.696494	0.548727	5.723958	0.073147	0.06459	0.017405	0.060415	0.014455	11.872152	0.0244	340.8222	1.645	1.523611
490	10329.35069	2.847515	878.457715	0.754252	11.040663	0.185067	0.104948	0.019425	0.097002	0.011952	11.830175	0.0194	339.7236	1.594	1.543056
510	3857.747873	2.521902	327.365777	0.356548	4.206759	0.05559	0.046588	0.016842	0.06445	0.009853	11.830962	0.0235	339.7442	1.632	1.733333
550	7639.745358	3.865444	649.149291	0.471168	8.099168	0.111398	0.068188	0.019266	0.06849	0.016848	11.842031	0.0203	340.0339	1.604	1.753472
590	6654.793876	2.467856	565.888228	0.486352	7.139233	0.069511	0.055089	0.03242	0.049189	0.016691	11.838358	0.021	339.9378	1.609	2.363194
670	9139.654457	2.78316	775.6419	0.509707	9.877298	0.119743	0.056261	0.028667	0.077779	0.01983	11.858117	0.0194	340.455	1.597	2.383333
750	6374.091709	3.154409	541.929307	0.302409	6.598987	0.087672	0.110108	0.026411	0.092457	0.021436	11.815985	0.0214	339.3521	1.611	2.403472
850	2432.508676	0.926188	206.154798	0.318236	2.605315	0.062607	0.017741	0.036099	0.045482	0.018685	11.839355	0.0361	339.9639	1.783	2.423611
Fusion	13839.18278	3.815309	1169.740907	0.720011	14.044179	0.154918	0.109198	0.015626	0.031139	0.017697	11.927585	0.0182	342.272	1.594	2.463194

			J parameter	error J			Mass Discrimination (1+e)	Err Discrimination				Error	Apparent	Error Age	Delay to
	LV3C muscovite		1.75E-02	7.13E-05			1.008908	1.32E-03							
laser power	40Ar	Error 40Ar	39Ar	Error 39Ar	38Ar	Error 38Ar	37Ar	Error 37Ar	36Ar	Error 36Ar	40Ar*/39ArK	Error 40Ar*/39ArK	Apparent age (My)	Error Age (My)	Delay to irradiation (day)
290	129.539789	0.266713	8.900648	0.061003	0.196207	0.031081	0.011241	0.018478	0.340548	0.014736	3.559415	0.487	109.1343	14.5	2.513194
350	186.540396	0.33543	18.031058	0.11025	0.28985	0.031517	0.020745	0.034086	0.110174	0.014947	8.660289	0.2483	254.8696	6.913	2.613194
410	820.978168	0.506411	76.180225	0.124948	0.924154	0.037195	0.015952	0.022966	0.11608	0.012072	10.428765	0.0521	302.7731	1.944	2.633333
450	552.449905	0.348263	48.62376	0.139922	0.644261	0.03881	0.010161	0.020012	0.00435	0.010787	11.435877	0.0743	329.4965	2.447	2.653472
500	631.845983	0.681757	53.449936	0.148333	0.672226	0.042584	0.067813	0.014652	0.028416	0.010611	11.770952	0.0695	338.3007	2.363	2.673611
530	1160.505571	0.581505	94.89281	0.15257	1.166019	0.039208	0.013662	0.022209	0.029237	0.01646	12.247942	0.0569	350.7604	2.15	2.713194
550	1016.637681	0.532383	81.680811	0.16468	1.086693	0.051837	0.015304	0.025507	0.020877	0.014379	12.481958	0.0598	356.8419	2.216	2.733333
570	663.671634	0.499867	53.115278	0.221801	0.657019	0.05212	0.024578	0.028676	0.010489	0.016882	12.547741	0.108	358.5478	3.218	2.753472
600	951.1566	0.723732	75.8792	0.220944	0.9542	0.037026	0.0358	0.03314	0.009257	0.014047	12.610254	0.0679	360.1674	2.376	2.773611
620	623.98287	0.60506	49.354769	0.102402	0.652207	0.030683	0.011738	0.018891	0.046057	0.008918	12.483004	0.0624	356.8691	2.265	3.363194
670	11977.74091	3.92884	937.277648	0.612713	11.606747	0.143788	0.044751	0.025561	0.186883	0.009746	12.834018	0.0198	365.9528	1.699	3.383333
720	2903.654496	1.316337	229.21272	0.390408	2.924597	0.040877	0.016881	0.030923	0.079755	0.013474	12.678497	0.033	361.9338	1.816	3.403472
800	3255.119754	1.682038	258.93131	0.289813	3.173027	0.087808	0.023806	0.020847	0.057898	0.016336	12.617201	0.0294	360.3473	1.769	3.453472
950	8074.823988	2.026334	637.98655	0.438617	8.1064	0.091979	0.008659	0.016056	0.121838	0.016206	12.712813	0.0207	362.8214	1.694	3.463194
1100	3303.185239	2.456842	261.937989	0.256822	3.256935	0.057871	0.02837	0.020237	0.060738	0.014368	12.654339	0.028	361.3087	1.758	3.483333
Fusion	2092.327105	1.159098	159.290892	0.141442	2.1124	0.073189	0.035677	0.022538	0.076225	0.011859	13.111994	0.0313	373.1142	1.835	3.503472

		J parameter	error J	Mass Discrimination (1+e)	Err Discrimination
	LV15 muscovite	1.75E-02	7.13E-05	1.008908	1.32E-03

laser power	40Ar	Error 40Ar	39Ar	Error 39Ar	38Ar	Error 38Ar	37Ar	Error 37Ar	36Ar	Error 36Ar	40Ar*/39ArK	Error 40Ar*/39 ArK	Apparent age (My)	Error Age (My)	Delay to irradiation (day)
290	178.084121	0.257094	11.099633	0.044781	0.130441	0.01727	0.053987	0.036119	0.14621	0.015366	12.356939	0.4078	353.5939	10.72	2.467361
350	230.602199	0.321117	17.125531	0.052987	0.204704	0.030518	0.015547	0.041074	0.067141	0.01172	12.444601	0.2047	355.8709	5.544	2.4875
400	1719.9601	0.930129	138.7236	0.162929	1.7343	0.069492	0.0182	0.040234	0.19822	0.017295	12.092465	0.0434	346.707	1.912	2.507639
430	1590.787043	0.565589	131.613704	0.144555	1.632614	0.043537	0.023978	0.041175	0.04456	0.015344	12.094991	0.0401	346.7729	1.863	2.527778
450	618.324458	0.582147	51.097144	0.09766	0.669683	0.041215	0.018988	0.017837	0.022486	0.018505	12.079797	0.1096	346.3764	3.249	2.567361
500	850.583359	1.0337	70.484073	0.172436	0.836114	0.058436	0.011355	0.023715	0.032779	0.015276	12.038991	0.073	345.3113	2.447	2.5875
Fusion	8443.695659	3.078936	701.446489	0.573251	8.700614	0.082008	0.057617	0.031469	0.153529	0.014516	12.080093	0.0204	346.3841	1.628	2.607639

Parameters	(36Ar/37Ar)Ca	0.000279	3	%
	(39Ar/37Ar)Ca	0.000706	4	%
	(38Ar/37Ar)Ca	0.00003	100	%
	(40Ar/37Ar)Ca	0.0006	100	%
	(40Ar/39Ar)K	0.00085	4	%
	(38A/39Ar)K	0.011	91	%
[3]	(36Cli/38Cl)	316	5	%
[1] and [1']	(40Ar/36Ar)Atm	298.56	0.104	%
[1] and [1']	(38Ar/36Ar)Atm	0.1885	0.159	%
[2]	Lambda 40	5.53E-10	1.35E-12	y-1
	Lambda 39	2.58E-03		y-1
	Lambda 37	1.98E-02		d-1
	Lambda 36Cl	2.26E-06		y-1

References:

[1] Lee, JY, Marti, K, Severinghaus, JP, Kawamura, K, Yoo, HS, Lee, JB, Kim, JS (2006). A redetermination of the isotopic abundances of atmospheric Ar. Geochimica Cosmochimica Acta, 70, 4507-4512.

[1'] Mark, DF, Stuart, FM, De Podesta, M (2011). New high-precision measurements of the isotopic composition of atmospheric argon. Geochimica Cosmochimica Acta, 75, 7494-7501.

[2] Renne, PR, Balco, G, Ludwig, RL, Mundil, R, Min, K, . (2011). Response to the comment by W.H. Schwarz et al. on "Joint determination of (40)K decay constants and (40)Ar*/(40)K for the Fish Canyon sanidine standard, and improved accuracy for (40)Ar/(39)Ar geochronology" by PR Renne et al. (2010). Geochimica Cosmochimica Acta, 75, 5097-5100.

[3] York, D, Personnal Communication - McMaster reactor

Regression method: York, D. (1969). Least-squares fitting of a straight line with correlated errors. Earth Planet. Sci. Lett. 5, 320-4.

Ages and errors of Hb3gr and TCs monitors refers to: Rennes, PR, Balco, G, Ludwig, Mundil, R, Min, K, . (2011). Response to the comment by W.H. Schwarz et al. on "Joint determination of (40)K decay constants and (40)Ar*/(40)K for the Fish Canyon sanidine standard, and improved accuracy for (40)Ar/(39)Ar geochronology" by PR Renne et al. (2010). Geochimica Cosmochimica Acta, 75, 5097-5100.

Irradiation 25

	J parameter	error J	Mass Discrimination (1+e)	Err Discrimination
LV14A biotite	9.19E-03	3.79E-05	1.007792	1.32E-03

laser power	40Ar	Error 40Ar	39Ar	Error 39Ar	38Ar	Error 38Ar	37Ar	Error 37Ar	36Ar	Error 36Ar	40Ar*/39ArK	Error 40Ar*/39ArK	Apparent age (My)	Error Age (My)	Delay to irradiation (day)
250	64.061432	0.16068	2.464222	0.02517	0.116694	0.021571	0.000001	0.018865	0.129138	0.010526	10.90302	1.254977	172.581	18.96	179.37708
290	15.457236	0.095473	0.718634	0.0214	0.044338	0.016345	0.000001	0.01962	0.034058	0.009195	7.847873	3.73947	125.86	57.93	179.39722
340	294.189305	0.385386	12.253811	0.083598	0.200814	0.029632	0.000001	0.018408	0.101148	0.008739	21.76091	0.260527	329.489	3.899	179.41736
370	1600.343176	0.586846	65.600342	0.098398	0.975997	0.03961	0.004044	0.018418	0.432798	0.013975	22.63363	0.081573	341.529	1.899	179.4375
390	2177.751846	1.618778	95.079134	0.128314	1.342753	0.032115	0.000001	0.024772	0.076651	0.019728	22.82	0.076548	344.09	1.867	179.47708
400	1014.955453	1.082642	44.597957	0.1248	0.609958	0.029654	0.000001	0.022688	0.020388	0.014963	22.77394	0.123024	343.457	2.286	179.49722
420	851.573829	0.821412	37.059185	0.077987	0.507561	0.034586	0.000001	0.022373	0.035933	0.016598	22.84695	0.144282	344.46	2.512	179.51736
460	1171.939461	0.653058	51.109385	0.214048	0.705572	0.039823	0.000001	0.020778	0.020136	0.012604	22.96561	0.124486	346.088	2.307	179.5375
490	1677.448417	1.632857	73.862766	0.180147	0.929038	0.025638	0.026202	0.017685	0.047488	0.010204	22.67321	0.078127	342.073	1.873	179.57708
510	1222.150174	1.273044	53.710079	0.097363	0.733217	0.037278	0.048525	0.019253	0.052877	0.012331	22.62048	0.087678	341.348	1.949	179.60694
550	1285.783954	1.039121	56.316086	0.115751	0.829889	0.030355	0.070214	0.020653	0.062816	0.00997	22.66128	0.078435	341.909	1.875	179.62708
600	1147.597543	0.98403	50.249341	0.108519	0.698147	0.03711	0.030081	0.018332	0.037428	0.01007	22.77316	0.084657	343.447	1.93	179.64722
680	2276.665486	1.064459	99.275389	0.117667	1.234801	0.0356	0.002707	0.022044	0.060341	0.016276	22.90608	0.063929	345.271	1.779	179.6875
750	1009.201963	0.61053	44.205609	0.109576	0.624464	0.02691	0.013116	0.023333	0.023651	0.015788	22.82474	0.123114	344.155	2.289	179.70694
900	2159.971141	1.248564	94.730192	0.128649	1.18726	0.057303	0.000001	0.023984	0.044455	0.017469	22.81394	0.070381	344.007	1.82	179.72708
1150	5746.867769	2.269002	252.16614	0.273447	3.227368	0.049169	0.054853	0.02136	0.072354	0.015492	22.85658	0.043979	344.592	1.659	179.74722
Fusion	7276.725195	3.599992	319.48708	0.263882	4.248109	0.082319	0.06209	0.021066	0.105842	0.017373	22.82979	0.040683	344.224	1.641	179.76736

			J parameter	error J			Mass Discrimination (1+e)	Err Discrimination							
	LV14A Muscovite		9.19E-03	3.79E-05			1.007792	1.32E-03							
laser power	40Ar	Error 40Ar	39Ar	Error 39Ar	38Ar	Error 38Ar	37Ar	Error 37Ar	36Ar	Error 36Ar	40Ar*/39ArK	Error 40Ar*/39ArK	Apparent age (My)	Error Age (My)	Delay to irradiation (day)
260	204.93451	0.360277	7.999576	0.025929	0.184744	0.027672	0.000001	0.015383	0.242674	0.017192	16.948434	0.633885	261.617878	9.187325	186.7375
300	136.14568	0.258735	5.582292	0.032307	0.072456	0.012788	0.034193	0.017565	0.013638	0.012499	23.863675	0.669525	358.363493	9.260283	186.756944
330	369.037486	0.510533	14.743487	0.056649	0.20297	0.026389	0.000001	0.017406	0.046496	0.017518	24.274789	0.362046	363.95523	5.178524	186.777083
350	942.583665	0.746298	37.622961	0.104635	0.504864	0.038604	0.034261	0.015964	0.279143	0.017341	23.059112	0.155728	347.369982	2.641574	187.377083
355	1421.28959	0.997312	61.792089	0.062405	0.767778	0.049084	0.000001	0.019477	0.0572	0.020123	22.880969	0.103826	344.926793	2.102653	187.397222
360	396.801551	0.463628	17.25595	0.055526	0.185534	0.024665	0.026839	0.016197	0.017583	0.012716	22.854587	0.230706	344.564683	3.523505	187.406944
370	1072.07603	0.905489	45.67541	0.08336	0.604315	0.024333	0.000001	0.013597	0.11524	0.015581	22.889249	0.114704	345.040421	2.206821	187.427083
380	1136.07144	0.61663	49.60244	0.057116	0.630849	0.020249	0.000001	0.018636	0.028774	0.016309	22.883415	0.104763	344.960361	2.111478	187.456944
400	9003.50714	3.535046	392.436098	0.549774	5.014442	0.079064	0.011254	0.013294	0.218886	0.01876	22.929378	0.047492	345.591035	1.680443	187.477083
410	10617.012	12.718771	462.895536	0.540426	5.70239	0.102357	0.057218	0.016307	0.148678	0.017834	22.992116	0.050423	346.451537	1.6996	187.497222
415	3188.66057	1.525384	139.722931	0.16312	1.684009	0.045666	0.000001	0.020695	0.000001	0.014944	22.96956	0.052067	346.142212	1.707767	187.527083
430	1192.04793	0.865606	52.287733	0.105868	0.619585	0.030237	0.000001	0.020935	0.01173	0.023242	22.880567	0.141796	344.921275	2.485501	187.556944
470	2967.03134	1.339924	129.491394	0.143482	1.520437	0.042884	0.057538	0.013118	0.069555	0.015183	22.907327	0.053518	345.288496	1.713098	187.577083
520	2962.15176	1.533628	130.149371	0.134708	1.639084	0.03502	0.003419	0.012537	0.029937	0.010739	22.840639	0.046783	344.373215	1.672152	187.5875
570	4300.16286	1.641515	188.154876	0.096462	2.389245	0.059176	0.04088	0.01579	0.050383	0.01332	22.925891	0.039534	345.543197	1.64102	187.617361
610	2589.98893	0.982448	113.511823	0.110164	1.368579	0.030156	0.040326	0.020644	0.051128	0.017645	22.835527	0.059578	344.303032	1.746916	187.647222
670	1639.34232	1.189059	71.923576	0.133803	1.075897	0.041673	0.000001	0.019875	0.037019	0.015589	22.791252	0.083627	343.695077	1.92194	187.667361
760	1011.16594	0.959853	44.60374	0.074532	0.566085	0.04749	0.023144	0.026726	0.000001	0.019212	22.819668	0.136242	344.085293	2.42472	187.677083
Fusion	6704.72964	3.33846	293.271907	0.28228	3.732458	0.075631	0.057737	0.024295	0.070909	0.019107	22.940851	0.043582	345.748421	1.660981	187.697222

			J parameter	error J			Mass Discrimination (1+e)	Err Discrimination							
	LV14B Biotite		9.19E-03	3.79E-05			1.007792	1.32E-03							
laser power	40Ar	Error 40Ar	39Ar	Error 39Ar	38Ar	Error 38Ar	37Ar	Error 37Ar	36Ar	Error 36Ar	40Ar*/39ArK	Error 40Ar*/39ArK	Apparent age (My)	Error Age (My)	Delay to irradiation (day)
270	87.735914	0.213774	3.953056	0.047879	0.048148	0.021974	0.020574	0.016167	0.074791	0.019848	16.84979	1.479102	260.202	21.31	187.72708
310	580.199331	0.540147	23.291838	0.121881	0.355731	0.032043	0.027599	0.015743	0.122532	0.018281	23.5451	0.263602	354.022	3.933	187.75694
350	2171.908573	1.562996	88.21629	0.124254	1.452419	0.038648	0.031148	0.019284	0.248343	0.017478	23.96222	0.077809	359.709	1.925	187.77708
370	2367.356516	0.989498	95.69376	0.077855	1.592134	0.042836	0.024541	0.016816	0.250537	0.024425	24.13858	0.085354	362.108	1.991	187.7875
380	1480.721194	1.149182	61.53052	0.093337	1.025353	0.031013	0.015214	0.015454	0.042602	0.015972	24.02102	0.091928	360.509	2.04	188.37708
400	2454.263686	1.361808	101.78644	0.129439	1.672049	0.047444	0.009087	0.012344	0.096785	0.012608	23.99232	0.059064	360.119	1.799	188.39722
420	3405.687673	2.033448	142.27008	0.184382	2.308688	0.042947	0.025199	0.019019	0.055494	0.018858	23.98124	0.06068	359.968	1.809	188.41736
440	3764.660533	1.606408	157.56783	0.188555	2.478716	0.031323	0.099172	0.017092	0.044171	0.012332	23.96911	0.049538	359.803	1.744	188.4375
460	3436.891174	1.469059	143.73985	0.254916	2.356624	0.058344	0.034058	0.018703	0.04313	0.014488	23.97988	0.061511	359.949	1.814	188.46736
480	2689.108696	1.16414	112.61163	0.155099	1.805058	0.048736	0.011587	0.016427	0.023531	0.007213	23.97454	0.050463	359.877	1.749	188.4875
510	2578.692134	1.292744	107.85977	0.115755	1.828468	0.045715	0.012203	0.015712	0.031779	0.011156	23.97824	0.052201	359.927	1.759	188.49722
560	2583.348059	1.089556	108.30094	0.15034	1.73001	0.045498	0.035504	0.020985	0.003329	0.011799	24.00127	0.056612	360.24	1.785	188.51736
620	1484.264634	1.431988	62.241293	0.132028	0.974195	0.042815	0.008874	0.021724	0.00474	0.017228	23.98061	0.103014	359.959	2.134	188.54722
700	1988.274898	0.89204	82.813617	0.112469	1.328802	0.051324	0.018365	0.021712	0.043875	0.015502	24.01201	0.072042	360.386	1.886	188.56736
830	6553.578342	2.861715	274.1962	0.248624	4.309871	0.100602	0.000444	0.026777	0.050159	0.018884	24.0033	0.044582	360.268	1.721	188.5875
890	8840.121156	4.897427	369.00748	0.21499	6.011015	0.074996	0.063673	0.022941	0.09791	0.020677	24.03595	0.040658	360.712	1.704	188.60694
930	6416.167274	1.722165	268.20072	0.16255	4.379265	0.056905	0.023008	0.020639	0.081853	0.01994	23.99023	0.041647	360.09	1.706	188.6375
960	2312.702759	1.497173	96.475207	0.11324	1.489892	0.048135	0.007967	0.025471	0.031545	0.015655	24.03308	0.065515	360.673	1.842	188.65694
1050	7144.434621	3.577561	297.49849	0.382917	4.788944	0.052797	0.023104	0.021394	0.116013	0.018593	24.05809	0.049609	361.013	1.749	188.67708
1120	2511.533665	1.013567	104.94764	0.087956	1.636176	0.031361	0.006251	0.020581	0.019218	0.015381	24.03393	0.057684	360.685	1.793	188.69722
1250	2721.341397	1.34748	113.4619	0.155787	1.83282	0.041395	0.026848	0.021876	0.029417	0.016311	24.06632	0.063255	361.125	1.829	188.72708
Fusion	2805.045611	2.537808	116.61958	0.190733	1.919774	0.038085	0.004116	0.022804	0.04887	0.020232	24.08762	0.074932	361.415	1.91	188.74722

			J parameter	error J			Mass Discrimination (1+e)	Err Discrimination							
	LV14B Muscovite		9.19E-03	3.79E-05			1.007792	1.32E-03							
laser power	40Ar	Error 40Ar	39Ar	Error 39Ar	38Ar	Error 38Ar	37Ar	Error 37Ar	36Ar	Error 36Ar	40Ar*/39ArK	Error 40Ar*/39ArK	Apparent age (My)	Error Age (My)	Delay to irradiation (day)
250	56.693724	0.194645	2.97955	0.020583	0.090105	0.024731	0.010376	0.020621	0.053602	0.024906	13.92743	2.43879	217.675	35.93	188.77708
290	37.607051	0.162575	1.59753	0.037786	0.000001	0.026712	0.000001	0.022194	0.002606	0.014147	23.21687	2.640401	349.534	36.18	189.37708
350	314.340436	0.446282	13.029435	0.048641	0.160965	0.024682	0.000001	0.020612	0.02194	0.015164	23.79136	0.353828	357.382	5.081	189.3875
390	745.22246	0.297001	30.675645	0.040143	0.399657	0.024903	0.000001	0.020228	0.035445	0.013289	24.11467	0.134662	361.783	2.443	189.40694
400	331.271369	0.263308	14.113734	0.067951	0.144595	0.026489	0.000001	0.025107	0.002241	0.015702	23.5773	0.34538	354.462	4.975	189.42708
440	347.028519	0.404003	14.697757	0.028921	0.176655	0.021035	0.000001	0.021622	0.012273	0.016642	23.52082	0.33582	353.69	4.852	189.46736
441	4433.503263	1.895948	187.87105	0.203986	2.496177	0.039629	0.025554	0.018741	0.201083	0.018089	23.44065	0.05077	352.595	1.724	189.4875
445	613.570486	0.613452	26.427047	0.037733	0.310864	0.022804	0.000001	0.025217	0.000001	0.017648	23.36801	0.201142	351.602	3.169	189.49722
470	15077.95152	7.121646	644.72372	0.600727	8.182755	0.082076	0.112389	0.021818	0.201542	0.020059	23.44815	0.040628	352.698	1.674	189.51736
480	3229.074635	2.22872	138.38925	0.19981	1.726576	0.052878	0.047723	0.014358	0.024023	0.011343	23.43568	0.054127	352.527	1.743	189.54722
500	1373.278778	0.656462	58.979956	0.094076	0.69723	0.034574	0.038728	0.01616	0.002642	0.015008	23.42484	0.089198	352.379	1.994	189.56736
540	3135.068542	1.666171	134.3717	0.282864	1.600402	0.052588	0.054533	0.014856	0.025429	0.010512	23.42937	0.063697	352.441	1.802	189.5875
620	2254.329743	1.238148	96.353608	0.193966	1.139821	0.035468	0.034809	0.019958	0.005815	0.018534	23.53223	0.080614	353.846	1.929	189.60694
700	806.710949	0.888682	34.664861	0.109737	0.414296	0.024689	0.000001	0.02291	0.00874	0.017145	23.34912	0.166857	351.344	2.772	189.6375
850	341.104245	0.455821	14.733153	0.034901	0.205188	0.021823	0.019911	0.026578	0.007891	0.017298	23.15289	0.349303	348.658	5.033	189.64722
Fusion	3908.044626	1.908026	166.49794	0.092309	1.995727	0.048955	0.0322	0.033771	0.034117	0.034493	23.56542	0.070104	354.299	1.852	189.66736

			J parameter	error J			Mass Discrimination (1+e)	Err Discrimination							
	LV23 Biotite		9.19E-03	3.79E-05			1.007792	1.32E-03							
laser power	40Ar	Error 40Ar	39Ar	Error 39Ar	38Ar	Error 38Ar	37Ar	Error 37Ar	36Ar	Error 36Ar	40Ar*/39ArK	Error 40Ar*/39ArK	Apparent age (My)	Error Age (My)	Delay to irradiation (day)
260	97.076598	0.18876	4.470791	0.062184	0.092974	0.024339	0.000001	0.016788	0.226584	0.015263	7.090868	1.00414	114.1	15.67	189.69722
300	112.965315	0.203034	4.404976	0.039525	0.092391	0.027251	0.000001	0.016022	0.117862	0.023634	18.01754	1.573409	276.931	22.46	189.71736
320	762.693742	0.67827	27.228192	0.095197	0.491231	0.030095	0.003624	0.013026	0.399609	0.014086	23.91872	0.182194	359.13	2.955	189.7375
350	3307.366416	1.595979	133.87841	0.240464	2.277762	0.060852	0.007421	0.016494	0.1699	0.016047	24.49554	0.066685	366.968	1.871	189.75694
372	3998.268728	1.823747	162.04556	0.294196	2.625948	0.032914	0.04905	0.025809	0.125814	0.017821	24.60945	0.065257	368.512	1.867	189.76736
390	1909.003141	1.009421	77.665072	0.1473	1.215471	0.076318	0.000001	0.035777	0.044862	0.026861	24.57142	0.116544	367.997	2.279	189.7875
410	2539.454679	1.290365	103.33159	0.092826	1.691856	0.037298	0.026416	0.01929	0.012127	0.011833	24.70256	0.053074	369.773	1.8	190.37708
440	2975.607856	2.28082	121.68033	0.088702	1.985546	0.049611	0.038067	0.019179	0.019859	0.013734	24.56721	0.052957	367.94	1.792	190.39722
470	3334.926848	1.275418	135.77433	0.129085	2.209323	0.056008	0.025173	0.01846	0.00875	0.014111	24.70402	0.051044	369.793	1.789	190.41736
500	1631.735531	1.109238	66.33939	0.123594	1.122925	0.035235	0.000001	0.019657	0.017446	0.015448	24.68007	0.089791	369.468	2.048	190.4375
540	2819.071804	0.769942	114.887	0.151416	2.018138	0.038864	0.000001	0.019727	0.031844	0.014957	24.61661	0.059976	368.609	1.835	190.46736
570	1244.326039	0.903484	50.542718	0.140864	0.902347	0.038276	0.000001	0.017789	0.014662	0.009446	24.69493	0.095323	369.669	2.094	190.4875
620	793.177439	0.716414	32.165201	0.180547	0.543709	0.038035	0.000001	0.021027	0.040756	0.018948	24.45066	0.223385	366.36	3.443	190.50694
720	3123.976788	1.043354	125.62982	0.225398	2.100183	0.05998	0.012345	0.017323	0.065003	0.017	24.87789	0.068707	372.145	1.902	190.51736
800	5245.758515	3.270257	213.06359	0.197131	3.482953	0.066195	0.052813	0.016333	0.035139	0.013933	24.73377	0.046747	370.195	1.769	190.55694
Fusion	24377.03891	12.596876	994.77116	0.937167	16.835647	0.136194	0.163649	0.035067	0.13127	0.025548	24.62682	0.042477	368.747	1.743	190.57708

			J parameter	error J			Mass Discrimination (1+e)	Err Discrimination							
	LV23 Muscovite		9.19E-03	3.79E-05			1.007792	1.32E-03							
laser power	40Ar	Error 40Ar	39Ar	Error 39Ar	38Ar	Error 38Ar	37Ar	Error 37Ar	36Ar	Error 36Ar	40Ar*/39ArK	Error 40Ar*/39ArK	Apparent age (My)	Error Age (My)	Delay to irradiation (day)
240	178.394873	0.236398	7.699642	0.071724	0.260111	0.027991	0.010468	0.027047	0.234553	0.02071	14.45358	0.798489	225.415	11.75	190.62708
280	188.657767	0.255484	7.554648	0.050157	0.142483	0.0277	0.039994	0.030939	0.08354	0.017378	21.93917	0.68847	331.971	9.633	190.64722
320	775.440115	0.81518	30.172788	0.078348	0.407622	0.025548	0.010305	0.026238	0.212337	0.02282	23.81822	0.234243	357.761	3.571	190.65694
340	257.894419	0.298103	10.326081	0.037696	0.119803	0.021325	0.000001	0.028241	0.029087	0.015377	24.31619	0.445387	364.535	6.262	190.67708
350	5369.39192	1.301199	223.73425	0.2585	2.952651	0.08215	0.02201	0.022965	0.478964	0.011149	23.53136	0.046256	353.848	1.705	190.71736
352	7116.631736	4.129006	302.80476	0.237992	3.751808	0.067396	0.056323	0.019419	0.206525	0.017261	23.45683	0.042521	352.83	1.683	190.72708
354	772.112763	0.852765	32.793874	0.048111	0.437168	0.02161	0.027385	0.018748	0.048697	0.011376	23.26853	0.114609	350.255	2.218	190.74722
370	1773.12674	0.855098	73.546157	0.123341	0.930226	0.043013	0.02031	0.01441	0.189843	0.011066	23.51462	0.069368	353.619	1.845	190.76736
390	738.08918	0.576156	30.888518	0.118696	0.492701	0.029764	0.0304	0.022422	0.067232	0.013427	23.42118	0.160102	352.342	2.698	190.7875
420	5003.398729	1.49067	190.11931	0.280548	2.871359	0.086494	0.022026	0.024185	1.995636	0.021824	23.43031	0.067414	352.467	1.827	193.37708
440	6337.468953	2.555586	266.7418	0.284675	3.606241	0.053156	0.083059	0.025514	0.502296	0.017967	23.36546	0.047057	351.581	1.701	193.39722
460	36493.60423	27.271669	1552.8403	1.125826	19.121621	0.2633	0.156987	0.035521	1.205152	0.028675	23.42743	0.040505	352.428	1.672	193.40694
470	5000.73789	3.136458	213.05628	0.292626	2.746439	0.056858	0.104272	0.025417	0.094306	0.014691	23.49669	0.05145	353.374	1.731	193.42708
490	3264.353821	1.581757	139.4498	0.117309	1.652948	0.078474	0.000001	0.018622	0.037034	0.018591	23.48258	0.054732	353.181	1.749	193.45694
540	4905.056643	1.175449	209.70551	0.190459	2.648983	0.057925	0.005617	0.015383	0.083534	0.019699	23.42541	0.046984	352.4	1.703	193.47708
590	12835.46302	6.096674	549.83594	0.374096	6.82092	0.114831	0.012343	0.020163	0.12858	0.017961	23.42693	0.037793	352.421	1.66	193.49722
700	4503.190841	2.230873	192.67918	0.265816	2.379949	0.07109	0.000001	0.016656	0.050492	0.018902	23.44604	0.054408	352.682	1.745	193.51736
850	9045.220951	2.834214	387.5252	0.228685	4.863568	0.062596	0.117207	0.025595	0.040493	0.014713	23.46287	0.036305	352.912	1.656	193.54722
Fusion	9683.441257	3.395421	414.28506	0.254753	4.982938	0.105586	0.06077	0.019344	0.095561	0.023129	23.45834	0.038756	352.85	1.666	193.56736

			J parameter	error J			Mass Discrimination (1+e)	Err Discrimination							
	LV26 Biotite		9.19E-03	3.79E-05			1.007792	1.31E-03							
laser power	40Ar	Error 40Ar	39Ar	Error 39Ar	38Ar	Error 38Ar	37Ar	Error 37Ar	36Ar	Error 36Ar	40Ar*/39ArK	Error 40Ar*/39ArK	Apparent age (My)	Error Age (My)	Delay to irradiation (day)
240	1296.692941	1.037169	40.798943	0.068768	1.041386	0.041674	0.000001	0.020122	2.364174	0.040344	15.1089	0.309699	235	4.643	193.59722
280	581.50358	0.590991	28.34912	0.053954	0.417304	0.018824	0.000001	0.021841	0.202935	0.013579	18.55954	0.149681	284.641	2.485	193.61736
320	2711.23408	1.369096	122.91947	0.132973	1.711175	0.056099	0.049594	0.023479	0.666326	0.013321	20.62247	0.053441	313.68	1.599	193.6375
350	3620.211229	2.526937	164.28095	0.287708	2.270895	0.077426	0.032834	0.017621	0.354718	0.016443	21.55115	0.059146	326.602	1.683	193.65694
370	756.536183	0.520478	33.680544	0.058456	0.430947	0.026372	0.000001	0.026992	0.105455	0.011678	21.69507	0.113884	328.597	2.161	193.69722
420	2572.813066	1.090403	115.39249	0.147465	1.533473	0.037879	0.013864	0.024772	0.193869	0.011026	21.95142	0.051242	332.144	1.652	193.70694
470	1873.51881	1.12401	84.245623	0.148363	1.193745	0.030313	0.000001	0.020784	0.144134	0.010144	21.88413	0.062174	331.213	1.719	193.72708
550	793.908195	0.513353	36.076474	0.098038	0.455035	0.030736	0.011963	0.019958	0.103412	0.012816	21.315	0.123715	323.325	2.252	193.74722
700	2662.927266	1.030417	123.62909	0.156389	1.68007	0.052042	0.000001	0.022966	0.269368	0.010181	21.04408	0.047976	319.558	1.587	193.76736
Fusion	3222.378554	1.785934	148.5605	0.195343	2.043093	0.045052	0.000001	0.020426	0.300639	0.016728	21.24131	0.054317	322.301	1.636	193.7875

			J parameter	error J			Mass Discrimination (1+e)	Err Discrimination							
	LV29A Biotite		9.19E-03	3.79E-05			1.007792	1.32E-03							
laser power	40Ar	Error 40Ar	39Ar	Error 39Ar	38Ar	Error 38Ar	37Ar	Error 37Ar	36Ar	Error 36Ar	40Ar*/39ArK	Error 40Ar*/39ArK	Apparent age (My)	Error Age (My)	Delay to irradiation (day)
240	365.82681	0.358726	3.793917	0.043296	0.292838	0.033044	0.000001	0.019627	1.112474	0.019746	11.63679	1.59341	183.639	23.93	194.37708
290	122.025409	0.254789	3.003332	0.027561	0.137779	0.02989	0.01725	0.012446	0.354937	0.017115	6.495938	1.674465	104.802	26.25	194.39722
330	902.066409	0.757446	19.2228	0.100261	0.725728	0.028845	0.019488	0.011944	1.917498	0.018564	18.17992	0.347177	279.252	5.101	194.41736
370	1988.446076	1.662286	59.294968	0.20138	1.371639	0.016607	0.000111	0.012003	2.137309	0.013099	23.25236	0.135744	350.043	2.431	194.4375
390	5983.590158	2.29744	247.4246	0.272518	4.628496	0.141687	0.08566	0.022102	1.072137	0.014349	23.07978	0.048668	347.68	1.695	194.46736
400	6018.822429	1.963576	258.97623	0.369782	4.834139	0.055223	0.087235	0.011941	0.146855	0.01343	23.22807	0.048564	349.711	1.701	194.47708
420	5148.377501	3.41444	222.21402	0.256988	3.961779	0.081597	0.072034	0.012387	0.075314	0.012642	23.22162	0.046755	349.623	1.692	194.49722
440	5218.938471	1.186768	224.84902	0.218203	4.090385	0.099741	0.083043	0.015122	0.067294	0.017476	23.27602	0.044757	350.367	1.684	194.51736
460	2277.863998	0.962497	97.851304	0.12308	1.788371	0.037812	0.000001	0.023487	0.020271	0.019311	23.36933	0.072243	351.644	1.859	194.54722
490	2650.79987	1.575835	114.10402	0.181628	2.059725	0.032533	0.000001	0.027316	0.023388	0.01415	23.32223	0.06183	350.999	1.785	194.56736
520	3625.93941	2.151719	156.2513	0.153007	2.718836	0.057703	0.005067	0.027797	0.05216	0.01421	23.25901	0.04866	350.134	1.704	194.5875
540	3282.779576	1.615113	141.54144	0.091524	2.675029	0.092679	0.000001	0.023675	0.01419	0.013341	23.31421	0.045292	350.89	1.689	194.59722
560	1458.602013	0.849689	62.477603	0.06226	1.13094	0.019369	0.026938	0.016357	0.051701	0.021756	23.25846	0.109625	350.127	2.17	194.62708
620	2295.082655	1.029973	98.470336	0.066012	1.775889	0.051328	0.030376	0.020644	0.072446	0.011829	23.24565	0.050708	349.952	1.714	194.64722
710	6684.642992	2.994623	287.08914	0.464662	5.176761	0.070887	0.055324	0.017862	0.105877	0.012895	23.32863	0.051651	351.087	1.723	194.66736
800	9310.27226	4.533525	401.49741	0.36144	7.115725	0.114591	0.084108	0.021188	0.115307	0.016272	23.2565	0.040701	350.1	1.664	194.6875
870	11399.25011	4.647864	491.45538	0.334389	8.813235	0.11544	0.108048	0.023537	0.11665	0.015247	23.27714	0.037017	350.383	1.649	194.71736
930	5169.184752	1.959704	223.1556	0.217289	4.02168	0.059101	0.139891	0.022094	0.038727	0.01588	23.26685	0.04428	350.242	1.681	194.72708
1020	11977.76517	4.364776	516.72371	0.6117	9.563299	0.119243	0.111741	0.021171	0.080788	0.012523	23.28601	0.042673	350.504	1.675	194.74722
1080	5979.956601	2.542587	257.57368	0.291576	4.658929	0.058118	0.013756	0.023384	0.041067	0.013607	23.32071	0.044441	350.979	1.685	194.76736
1180	2221.707962	1.315377	95.617937	0.204385	1.74402	0.051294	0.078463	0.027537	0.007637	0.022931	23.36687	0.092212	351.61	2.017	194.7875
Fusion	3657.453594	1.359134	157.4078	0.145359	2.825781	0.07296	0.03655	0.029964	0.042138	0.016222	23.30919	0.04892	350.821	1.708	195.37708

			J parameter	error J			Mass Discrimination (1+e)	Err Discrimination							
	LV29A Muscovite		9.19E-03	3.79E-05			1.007792	1.32E-03							
laser power	40Ar	Error 40Ar	39Ar	Error 39Ar	38Ar	Error 38Ar	37Ar	Error 37Ar	36Ar	Error 36Ar	40Ar*/39ArK	Error 40Ar*/39ArK	Apparent age (My)	Error Age (My)	Delay to irradiation (day)
260	412.849701	0.388061	10.534168	0.058624	0.474269	0.030905	0.032754	0.022591	0.973101	0.021566	12.554	0.621887	197.351	9.306	195.40694
300	151.486327	0.289688	7.439915	0.030573	0.173759	0.033434	0.00112	0.017857	0.102745	0.016379	16.47151	0.647595	254.771	9.415	195.42708
340	615.475005	0.543497	19.131227	0.105489	0.430738	0.034403	0.077425	0.015104	0.744773	0.024256	21.06091	0.397831	319.799	5.721	195.44722
390	1780.871085	0.936294	60.475869	0.106651	1.098339	0.04294	0.149343	0.025286	1.43701	0.024121	22.72954	0.140311	342.874	2.466	195.46736
410	529.081214	0.554314	21.815158	0.059367	0.272021	0.017838	0.028381	0.020266	0.053464	0.013832	23.70236	0.200382	356.192	3.164	195.49722
440	3106.822686	1.330264	113.79563	0.19773	1.695279	0.057633	0.029618	0.014782	1.619039	0.028053	23.33493	0.098262	351.173	2.069	195.51736
450	1273.048083	0.701508	53.981575	0.039275	0.624695	0.040306	0.037493	0.014403	0.045842	0.011696	23.49128	0.073971	353.31	1.877	195.52708
465	3734.869973	1.988655	141.06085	0.230411	2.047312	0.056853	0.025478	0.020235	1.569153	0.030781	23.40847	0.089215	352.179	1.993	195.54722
475	3376.540818	1.480186	144.10412	0.246147	1.896835	0.026319	0.034669	0.030014	0.095009	0.022667	23.39159	0.069263	351.948	1.838	195.5875
490	3129.582011	0.945284	133.24134	0.187471	1.620373	0.033809	0.075632	0.024493	0.176233	0.019049	23.25718	0.062488	350.109	1.786	195.60694
500	12547.50574	4.296999	532.68061	0.329113	6.807886	0.083603	0.102132	0.026875	0.659189	0.017574	23.34779	0.037626	351.349	1.655	195.62708
510	15205.15867	4.274702	654.86098	0.422175	8.372347	0.103501	0.115822	0.026127	0.19266	0.023907	23.28383	0.036535	350.474	1.647	195.64722
515	2603.223967	1.035919	112.47746	0.078445	1.415931	0.066123	0.061483	0.020506	0.045907	0.012769	23.17761	0.048958	349.02	1.701	195.6875
525	2270.773398	1.30663	98.122179	0.117748	1.185405	0.070585	0.016439	0.021578	0.052787	0.021455	23.13557	0.077277	348.444	1.886	195.70694
550	4469.552114	1.502111	193.14269	0.317509	2.410443	0.050303	0.103343	0.02462	0.081234	0.010241	23.17068	0.051997	348.925	1.718	195.72708
600	6453.311153	7.010014	279.71834	0.306104	3.526283	0.059613	0.10177	0.016533	0.147644	0.020108	23.06762	0.051658	347.513	1.71	195.7375
680	8330.055348	2.182467	360.683	0.473652	4.466831	0.06009	0.095986	0.023359	0.174352	0.020457	23.10465	0.046748	348.021	1.686	195.76736
770	12456.40125	6.479353	538.29214	0.481633	6.682325	0.141471	0.146436	0.027527	0.258925	0.016584	23.15104	0.040198	348.656	1.656	195.7875
830	6765.960584	2.354534	292.14675	0.351025	3.551805	0.096926	0.029791	0.023021	0.054111	0.017493	23.25516	0.04572	350.082	1.688	196.37708
920	6342.149153	3.088849	273.92592	0.478403	3.436459	0.105434	0.020042	0.020615	0.049203	0.011557	23.24996	0.053525	350.011	1.73	196.39722
1040	6500.062707	3.155862	281.30905	0.269744	3.467672	0.098695	0.032684	0.029692	0.014565	0.022099	23.2408	0.045548	349.885	1.686	196.40694
1130	5670.001107	1.394516	244.93378	0.227833	3.029178	0.032885	0.013934	0.021255	0.03656	0.013246	23.25499	0.04106	350.08	1.665	196.42708
Fusion	17353.42849	4.800615	745.38457	0.454524	9.426544	0.154556	0.049863	0.022014	0.058666	0.015305	23.40854	0.034996	352.18	1.648	196.44722

			J parameter	error J			Mass Discrimination (1+e)	Err Discrimination							
	LV30 biotite		9.20E-03	3.80E-05			1.007001	1.31E-03							
laser power	40Ar	Error 40Ar	39Ar	Error 39Ar	38Ar	Error 38Ar	37Ar	Error 37Ar	36Ar	Error 36Ar	40Ar*/39ArK	Error 40Ar*/39ArK	Apparent age (My)	Error Age (My)	Delay to irradiation (day)
260	78.646102	0.198969	2.593684	0.042035	0.000001	0.007101	0.016715	0.034309	0.217984	0.01374	5.961703	1.559672	96.5678	24.6	0.477778
310	72.310165	0.087276	1.950116	0.038573	0.004687	0.00744	0.128751	0.028922	0.246588	0.017447	0.374666	2.623416	6.22313	43.5	0.5375
360	736.803406	0.672721	30.284041	0.16724	0.102822	0.013479	0.227548	0.026255	0.516141	0.019476	19.51693	0.223867	298.649	3.434	0.557639
390	1521.601335	1.593468	59.527498	0.168616	0.033592	0.018104	0.315531	0.036401	1.059152	0.016201	20.53778	0.115529	312.991	2.146	0.627778
400	1636.028638	1.662404	71.450176	0.13878	0.03704	0.014336	0.312492	0.050054	0.541962	0.018372	20.8396	0.096639	317.21	1.966	0.647917
405	1148.633952	0.713939	52.130845	0.109397	0.050601	0.015642	0.31241	0.038247	0.28546	0.017798	20.58665	0.115143	313.675	2.144	0.677778
410	1580.193026	1.778958	72.291034	0.171948	0.000001	0.014617	0.381828	0.042939	0.328828	0.016267	20.68152	0.092256	315.001	1.918	0.697917
415	308.455795	0.827231	14.339572	0.063828	0.000001	0.008915	0.155979	0.026684	0.054245	0.011811	20.55557	0.266086	313.24	3.982	1.377778
430	331.707987	0.391442	15.373135	0.071501	0.002682	0.008326	0.134264	0.031321	0.050311	0.01188	20.77128	0.249141	316.255	3.761	1.407639
480	2555.139538	1.389204	115.37266	0.19303	0.393993	0.032363	0.281813	0.025651	0.25225	0.017869	21.66185	0.067139	328.653	1.747	1.4375
500	1753.603304	0.907938	79.827055	0.109712	0.069097	0.01305	0.235002	0.021684	0.20769	0.01125	21.3599	0.060848	324.459	1.688	1.4875
520	866.286912	1.12124	39.983919	0.109455	0.035298	0.009024	0.295286	0.03219	0.241613	0.0192	20.05059	0.157384	306.16	2.607	1.507639
550	2666.021253	1.913936	121.16598	0.167305	0.061137	0.019531	0.264631	0.01669	0.30031	0.011317	21.43161	0.053667	325.456	1.643	1.527778
580	2305.735548	1.559909	105.5077	0.158253	0.049282	0.015005	0.263316	0.034472	0.259857	0.015075	21.28582	0.063073	323.428	1.7	1.557639
620	1139.776806	0.827608	51.962799	0.103021	0.007566	0.007488	0.187925	0.03028	0.205188	0.035188	20.93285	0.205644	318.511	3.208	1.597917
670	1596.177123	1.454536	72.821814	0.208413	0.046234	0.013521	0.19022	0.02887	0.192193	0.022482	21.29996	0.115232	323.625	2.166	1.617361
730	799.440814	0.422384	36.487107	0.143935	0.008333	0.006506	0.264094	0.031528	0.143446	0.022564	20.91391	0.201844	318.247	3.16	1.6375
850	1988.675454	1.395326	89.741311	0.14015	0.04329	0.012824	0.268431	0.036153	0.261718	0.030777	21.4618	0.111686	325.875	2.135	1.667361
1000	4268.004926	2.306431	191.93461	0.625239	0.103178	0.019885	0.250803	0.024912	0.259522	0.019203	21.99615	0.084149	333.284	1.897	1.697917
1200	12092.30391	4.07617	547.37426	0.431244	0.128058	0.028136	0.246638	0.030957	0.344793	0.018329	22.06082	0.036567	334.179	1.584	2.277778
1400	6761.879854	1.726124	306.25782	0.432617	0.155907	0.022537	0.392902	0.021822	0.288097	0.030506	21.95753	0.052399	332.75	1.662	2.2875
1700	2371.331515	1.613976	108.22903	0.115166	0.066807	0.010646	0.349348	0.034115	0.260939	0.018456	21.35797	0.064968	324.432	1.717	2.307639
Fusion	1106.242403	1.219766	49.970393	0.073301	0.109345	0.028601	0.10585	0.024301	0.076421	0.015247	21.84485	0.102657	331.19	2.059	2.327778

			J parameter	error J			Mass Discrimination (1+e)	Err Discrimination							
	LV30 muscovite		9.20E-03	3.80E-05			1.007001	1.31E-03							
laser power	40Ar	Error 40Ar	39Ar	Error 39Ar	38Ar	Error 38Ar	37Ar	Error 37Ar	36Ar	Error 36Ar	40Ar*/39ArK	Error 40Ar*/39ArK	Apparent age (My)	Error Age (My)	Delay to irradiation (day)
250	49.038863	0.118664	1.971179	0.022335	0.01263	0.009166	0.136953	0.040087	0.13528	0.024127	4.992767	3.581476	81.2198	56.97	1.367361
300	19.570129	0.13463	0.833212	0.023715	0.004098	0.007188	0.000001	0.038538	0.028848	0.024528	13.52819	8.617409	212.14	127.5	1.3875
350	51.438217	0.092154	2.233015	0.028505	0.000222	0.006081	0.045365	0.031669	0.035155	0.024021	18.59487	3.154807	285.596	44.84	1.407639
370	144.104466	0.229296	6.360623	0.02984	0.000001	0.011739	0.186076	0.024573	0.119222	0.023965	17.33633	1.106358	267.627	15.92	1.447917
410	235.811662	0.497976	10.451501	0.050149	0.000001	0.012649	0.232983	0.025399	0.124084	0.023353	19.2507	0.662936	294.89	9.465	1.467361
430	504.271151	0.550562	22.301568	0.098539	0.000001	0.007737	0.101869	0.032341	0.107753	0.022435	21.35655	0.311873	324.412	4.576	1.567361
440	75.944474	0.165239	3.538383	0.037976	0.00072	0.005351	0.046008	0.025191	0.000001	0.02319	21.61363	1.930989	327.984	26.84	1.5875
470	166.312757	0.291377	7.426997	0.078629	0.000001	0.006629	0.093178	0.02603	0.025616	0.020692	21.54171	0.847473	326.985	11.86	1.607639
480	1903.097688	0.584999	85.186029	0.09697	0.0606	0.015284	0.293133	0.047065	0.26633	0.011079	21.58209	0.056366	327.546	1.668	1.647917
500	2198.717236	1.890717	99.674526	0.127574	0.016793	0.011144	0.243097	0.031249	0.192464	0.023952	21.64802	0.083891	328.461	1.88	1.667361
520	19306.22001	11.874114	860.70665	0.59517	0.38411	0.06745	0.4422	0.035446	0.927223	0.024602	22.27167	0.03793	337.093	1.601	1.6875
530	1842.207744	1.135061	83.127049	0.215585	0.056768	0.010328	0.226453	0.031991	0.178515	0.01728	21.68775	0.089662	329.012	1.933	2.2875
560	3928.220991	2.201867	175.82596	0.222482	0.1356	0.027691	0.277731	0.029505	0.196198	0.020747	22.17067	0.055411	335.698	1.691	2.307639
600	4519.671544	2.155103	201.97949	0.096433	0.106878	0.047441	0.253108	0.03131	0.258485	0.026679	22.15831	0.051646	335.527	1.667	2.327778
650	1941.249109	1.321194	87.195294	0.1657	0.048925	0.014201	0.2249	0.031613	0.105727	0.017706	22.06367	0.080312	334.218	1.867	2.367361
740	4698.468117	2.708188	210.72853	0.316254	0.162003	0.012456	0.23003	0.023501	0.210511	0.021099	22.15924	0.055253	335.54	1.689	2.3875
850	1669.715284	1.194727	74.225601	0.153344	0.069758	0.011955	0.233246	0.028914	0.147856	0.017381	22.06937	0.089653	334.297	1.947	2.427778
Fusion	6952.497509	1.657622	311.46501	0.120013	0.529308	0.050397	0.27654	0.024636	0.201464	0.018131	22.28796	0.035949	337.318	1.594	2.447917

			J parameter	error J			Mass Discrimination (1+e)	Err Discrimination							
	LV29C biotite		9.19E-03	3.80E-05			1.007001	1.31E-03							
laser power	40Ar	Error 40Ar	39Ar	Error 39Ar	38Ar	Error 38Ar	37Ar	Error 37Ar	36Ar	Error 36Ar	40Ar*/39ArK	Error 40Ar*/39ArK	Apparent age (My)	Error Age (My)	Delay to irradiation (day)
260	90.411441	0.211609	2.412053	0.029373	0.003616	0.007891	0.071232	0.032147	0.217515	0.031096	11.38178	3.775981	179.955	56.83	1.497917
300	49.035828	0.131931	0.886796	0.039839	0.000689	0.004047	0.091476	0.022585	0.136857	0.023481	10.57091	7.762109	167.71	117.6	1.507639
350	464.70664	0.654993	12.294517	0.042787	0.068282	0.01108	0.147772	0.027631	0.887537	0.016568	16.95627	0.423151	261.959	6.202	1.527778
380	490.556889	0.587426	16.450796	0.087621	0.010831	0.008452	0.160881	0.036865	0.640852	0.026914	18.63874	0.496943	285.996	7.171	1.547917
390	2338.037344	2.184818	97.525349	0.101639	0.000001	0.006043	0.263433	0.044266	0.569933	0.014427	22.43206	0.06619	339.045	1.774	1.5875
395	1753.634096	1.050067	75.74279	0.097257	0.055532	0.013072	0.313661	0.026302	0.25519	0.014824	22.32889	0.073915	337.623	1.827	1.607639
405	646.319269	0.708128	28.370633	0.062278	0.022315	0.009081	0.213947	0.024904	0.129705	0.020695	21.60385	0.222713	327.595	3.422	1.627778
430	1336.689063	1.378807	58.424113	0.081476	0.066004	0.016143	0.348658	0.026506	0.193348	0.016491	22.07124	0.097294	334.066	2.015	1.647917
470	1617.471718	1.451763	70.135915	0.235208	0.182778	0.02045	0.279157	0.033671	0.203953	0.01873	22.37255	0.115279	338.225	2.198	1.6875
510	2384.690171	1.775672	103.3322	0.155578	0.000001	0.009996	0.352248	0.040496	0.274994	0.020503	22.46066	0.076937	339.439	1.856	1.707639
540	2917.288766	1.914524	125.41247	0.221856	0.147833	0.023593	0.325902	0.034059	0.233948	0.019433	22.87809	0.070665	345.182	1.827	2.307639
570	1410.851355	0.537935	61.436765	0.244748	0.095117	0.021204	0.361965	0.024325	0.221638	0.020589	22.06977	0.136318	334.045	2.408	2.327778
620	651.210342	0.403314	28.606804	0.108096	0.005357	0.013957	0.304983	0.023423	0.115485	0.020245	21.74327	0.225734	329.528	3.461	2.347917
670	1145.134046	1.005091	49.719	0.110054	0.021161	0.010995	0.32393	0.024865	0.199665	0.022244	22.01877	0.1453	333.34	2.506	2.367361
730	664.151851	0.407357	28.735242	0.07313	0.02779	0.010934	0.138297	0.02061	0.130728	0.02043	21.94382	0.218623	332.304	3.373	2.417361
850	1567.524186	1.408911	68.076197	0.144391	0.0985	0.019156	0.242746	0.027184	0.240882	0.015372	22.15187	0.090415	335.18	1.956	2.4375
1000	2677.427671	1.223113	114.67036	0.138803	0.227717	0.038073	0.260124	0.021425	0.254616	0.023543	22.8622	0.074737	344.964	1.856	2.457639
1150	3334.368269	2.491711	143.44297	0.083388	0.551981	0.031029	0.255142	0.022986	0.268084	0.01976	22.86053	0.056306	344.941	1.729	2.497917
1300	1893.500842	0.838892	82.564072	0.105774	0.07699	0.01544	0.391115	0.023627	0.271216	0.024822	22.13316	0.098898	334.921	2.032	2.517361
Fusion	1540.880792	1.22023	66.996179	0.157637	0.070535	0.013492	0.337228	0.021882	0.240164	0.017828	22.11181	0.101352	334.626	2.054	2.5375

			J parameter	error J			Mass Discrimination (1+e)	Err Discrimination							
	LV29C muscovite		9.19E-03	3.80E-05			1.007001	1.31E-03							
laser power	40Ar	Error 40Ar	39Ar	Error 39Ar	38Ar	Error 38Ar	37Ar	Error 37Ar	36Ar	Error 36Ar	40Ar*/39ArK	Error 40Ar*/39ArK	Apparent age (My)	Error Age (My)	Delay to irradiation
270	156.784925	0.281992	9.424562	0.060814	0.009651	0.009605	0.11379	0.020628	0.360717	0.018203	5.562112	0.57044	90.1798	9.032	1.577778
300	67.190776	0.13925	4.387495	0.039472	0.000001	0.007378	0.042096	0.025696	0.08203	0.012826	9.955057	0.860964	158.355	13.13	1.597917
350	432.608832	0.484033	21.73582	0.129284	0.076718	0.016624	0.181961	0.025171	0.189886	0.012991	17.48804	0.207761	269.591	3.218	1.617361
380	261.769103	0.54647	12.25087	0.029838	0.004577	0.007419	0.041434	0.026043	0.100214	0.01735	19.12461	0.420759	292.878	6.095	1.657639
430	937.668991	1.025237	41.690182	0.134626	0.031432	0.008754	0.227752	0.034963	0.259527	0.013164	20.82827	0.122486	316.806	2.227	1.677778
450	320.857634	0.592006	13.925	0.069057	0.01211	0.006854	0.041647	0.030982	0.139686	0.011532	20.26949	0.268902	308.993	4.018	1.697917
490	341.721719	0.713348	15.152656	0.050244	0.000001	0.007894	0.146085	0.026995	0.080896	0.024253	21.14846	0.47689	321.268	6.793	5.297917
550	1167.620699	1.390059	51.026374	0.086824	0.000001	0.010511	0.233234	0.021991	0.252417	0.017138	21.59548	0.114098	327.479	2.162	5.317361
580	2514.147174	1.360805	109.97822	0.123034	0.018098	0.015316	0.32168	0.023822	0.277209	0.010998	22.28218	0.052085	336.978	1.675	5.3375
600	3729.690114	1.49394	162.33383	0.257684	0.122011	0.029791	0.201355	0.021486	0.181591	0.016416	22.80768	0.057086	344.214	1.731	5.377778
620	2151.059968	1.879811	94.452481	0.1602	0.034085	0.014667	0.189372	0.020604	0.198483	0.010117	22.31759	0.062112	337.467	1.74	5.397917
650	6792.902141	2.837257	295.63174	0.292544	0.835073	0.063648	0.244955	0.015566	0.237578	0.013709	22.90188	0.041911	345.509	1.652	5.417361
665	7314.232376	1.704747	320.29249	0.439609	0.194695	0.025437	0.30828	0.022196	0.314886	0.022469	22.70695	0.048863	342.83	1.678	5.4375
690	2224.214332	1.003291	97.874173	0.126267	0.041085	0.018698	0.186009	0.032419	0.138417	0.02002	22.46938	0.074242	339.56	1.835	5.477778
740	1551.473675	1.28391	68.727727	0.084909	0.012423	0.013134	0.163221	0.026654	0.024139	0.038555	22.62813	0.17011	341.745	2.798	5.497917
820	3586.870414	2.07065	157.27706	0.252759	0.113671	0.022636	0.247945	0.034685	0.177206	0.019114	22.63478	0.061124	341.837	1.749	5.517361
900	7899.263561	2.464176	348.96374	0.450681	0.25093	0.043259	0.30056	0.040421	0.22011	0.013899	22.60879	0.044325	341.479	1.649	5.5375
1000	6715.590781	1.391458	296.37112	0.382665	0.116441	0.022153	0.221471	0.026815	0.210777	0.014524	22.60846	0.044869	341.475	1.652	5.5875
1200	3089.334913	3.078392	135.14711	0.126188	0.000001	0.005225	0.20345	0.034385	0.12173	0.016035	22.75419	0.056069	343.479	1.722	5.607639
Fusion	12372.46219	3.824629	538.32523	0.488632	0.374545	0.051495	0.336346	0.026589	0.218794	0.019551	23.02365	0.039228	347.18	1.646	5.627778

		J parameter	error J	Mass Discrimination (1+e)	Err Discrimination
	LV26M muscovite	9.19E-03	3.79E-05	1.007001	1.31E-03

laser power	40Ar	Error 40Ar	39Ar	Error 39Ar	38Ar	Error 38Ar	37Ar	Error 37Ar	36Ar	Error 36Ar	40Ar*/39ArK	Error 40Ar*/39ArK	Apparent age (My)	Error Age (My)	Delay to irradiation (day)
270	106.869606	0.21162	4.544032	0.0374	0.000001	0.011531	0.143702	0.024361	0.194738	0.00929	11.15567	0.611759	176.402	9.253	5.447917
310	129.914071	0.186879	4.720228	0.030616	0.000001	0.011177	0.076982	0.025408	0.088436	0.014452	22.23804	0.909407	336.101	12.63	5.457639
340	152.698473	0.296994	6.202124	0.055454	0.000001	0.012557	0.108359	0.028594	0.024288	0.018047	23.6482	0.878699	355.446	12.1	5.477778
360	224.378421	0.390249	9.149074	0.029052	0.016274	0.00737	0.07867	0.025925	0.041842	0.012056	23.35861	0.396455	351.49	5.645	5.527778
380	198.973612	0.2995	8.409283	0.020442	0.008898	0.008721	0.000001	0.023386	0.066955	0.012123	21.49725	0.428114	325.855	6.116	5.547917
400	476.115724	0.774333	20.1284	0.085785	0.002987	0.007808	0.073263	0.022348	0.105134	0.013399	22.29114	0.22309	336.833	3.427	5.567361
410	1002.786423	0.818877	43.446062	0.143297	0.00909	0.00958	0.127056	0.019243	0.097228	0.012676	22.5871	0.119431	340.909	2.245	5.597917
420	709.524521	0.81656	30.979853	0.034955	0.018708	0.008563	0.085447	0.020905	0.059686	0.017633	22.49843	0.17343	339.689	2.832	5.647917
425	1601.888946	0.874014	69.82038	0.139307	0.087733	0.0128	0.163551	0.027436	0.130569	0.01403	22.55541	0.081691	340.473	1.896	5.667361
430	682.165987	0.773815	29.857662	0.077833	0.007317	0.007656	0.05532	0.025097	0.050842	0.014615	22.50785	0.160069	339.818	2.679	5.6875
435	1427.342242	1.086673	62.11375	0.1693	0.121512	0.014514	0.164579	0.01232	0.123198	0.015627	22.55897	0.102718	340.522	2.081	6.247917
450	2216.977537	1.676283	96.701738	0.129817	0.044717	0.006615	0.149675	0.021621	0.175455	0.014988	22.55431	0.065628	340.458	1.774	6.267361
470	2721.12938	1.736664	119.69002	0.152494	0.030294	0.007221	0.177391	0.018435	0.144007	0.014085	22.54054	0.056516	340.268	1.713	6.2875
490	1762.159352	1.106072	77.250507	0.175355	0.021572	0.01023	0.161671	0.017547	0.114129	0.015169	22.53715	0.084373	340.222	1.918	6.307639
520	7107.642016	2.614022	310.65479	0.331221	0.318278	0.034371	0.244171	0.019381	0.258087	0.03308	22.79508	0.050884	343.767	1.692	6.327778
550	2089.811195	1.183499	90.804688	0.236761	0.033717	0.007745	0.158376	0.0148	0.145874	0.017393	22.70414	0.088527	342.518	1.96	6.407639
600	5446.886792	2.700692	237.66542	0.346542	0.136764	0.028792	0.240559	0.02239	0.246315	0.016226	22.77399	0.051062	343.478	1.692	6.427778
700	16566.32484	5.155708	725.59416	0.450333	0.276563	0.045506	0.350231	0.02492	0.382734	0.026914	22.8352	0.036083	344.318	1.621	6.447917
900	1174.080868	0.723811	51.296484	0.154434	0.095756	0.016201	0.235863	0.019708	0.155387	0.018049	22.16145	0.127888	335.044	2.319	6.467361
Fusion	3104.007268	2.035577	135.41125	0.1988	0.054848	0.011869	0.218383	0.018528	0.158338	0.022701	22.73975	0.068782	343.007	1.805	6.4875

Parameters	(36Ar/37Ar)Ca	0.000322	3	%
	(39Ar/37Ar)Ca	0.000788	4	%
	(38Ar/37Ar)Ca	0.000026	100	%
	(40Ar/37Ar)Ca	0.0006	100	%
	(40Ar/39Ar)K	0.00085	4	%
	(38A/39Ar)K	0.011	91	%
[3]	(36Cli/38Cl)	316	5	%
[1] and [1']	(40Ar/36Ar)Atm	298.56	0.104	%
[1] and [1']	(38Ar/36Ar)Atm	0.1885	0.159	%
[2]	Lambda 40	5.53E-10	1.35E-12	y-1
	Lambda 39	2.58E-03		y-1
	Lambda 37	1.98E-02		d-1
	Lambda 36Cl	2.26E-06		y-1

References:

[1] Lee, JY, Marti, K, Severinghaus, JP, Kawamura, K, Yoo, HS, Lee, JB, Kim, JS (2006). A redetermination of the isotopic abundances of atmospheric Ar. Geochimica Cosmochimica Acta, 70, 4507-4512.

[1'] Mark, DF, Stuart, FM, De Podesta, M (2011). New high-precision measurements of the isotopic composition of atmospheric argon. Geochimica Cosmochimica Acta, 75, 7494-7501.

Renne, PR, Balco, G, Ludwig, RL, Mundil, R, Min, K, . (2011). Response to the comment by W.H. Schwarz et al. on "Joint determination of (40)K decay constants and (40)Ar*/(40)K for the Fish Canyon sanidine standard, and improved accuracy for (40)Ar/(39)Ar geochronology" by PR Renne et al. (2010).

[2] Geochimica Cosmochimica Acta, 75, 5097-5100.

[3] York, D, Personnal Communication - McMaster reactor

Regression method: York, D. (1969). Least-squares fitting of a straight line with correlated errors. Earth Planet. Sci. Lett. 5, 320-4.

Ages and errors of Hb3gr and TCs monitors refers to: Rennes, PR, Balco, G, Ludwig, Mundil, R, Min, K, . (2011). Response to the comment by W.H. Schwarz et al. on "Joint determination of (40)K decay constants and (40)Ar*/(40)K for the Fish Canyon sanidine standard, and improved accuracy for (40)Ar/(39)Ar geochronology" by PR Renne et al. (2010). Geochimica Cosmochimica Acta, 75, 5097-5100.

			J parameter	error J			Mass Discrimination (1+e)	Err Discrimination							
	LV87A Muscovite		1.05E-02	4.35E-05			1.009446	1.32E-03							
laser power	40Ar	Error 40Ar	39Ar	Error 39Ar	38Ar	Error 38Ar	37Ar	Error 37Ar	36Ar	Error 36Ar	40Ar*/39ArK	Error 40Ar*/39ArK	Apparent age (My)	Error Age (My)	Delay to irradiation (day)
280	69.150493	0.1678	3.865125	0.017802	0.000001	0.011228	0.023329	0.021625	0.136341	0.0101	8.026359	0.790787	146.738656	13.902921	298.820139
320	80.280829	0.146382	3.700844	0.034396	0.00012	0.011217	0.000895	0.021215	0.131216	0.009705	11.589498	0.801663	208.248629	13.639937	298.839583
360	166.100658	0.280809	7.665059	0.043099	0.012261	0.00972	0.000462	0.023782	0.13507	0.010586	16.726205	0.433211	293.394644	7.139058	298.859722
390	300.940459	0.430959	10.197976	0.020781	0.000001	0.010534	0.020998	0.022747	0.38208	0.009725	18.956026	0.307293	329.143538	5.097724	298.909722
420	131.619194	0.239916	6.371562	0.028229	0.006068	0.010293	0.002623	0.013827	0.039972	0.008346	19.007455	0.401691	329.959767	6.544175	298.929861
430	1233.728082	0.830242	58.703748	0.16493	0.0158	0.011603	0.000001	0.00425	0.199201	0.012754	20.186634	0.091554	348.574297	2.122662	298.95
435	1108.55677	1.235918	54.061536	0.072182	0.000001	0.010229	0.016943	0.013064	0.090756	0.010178	20.181483	0.071902	348.493407	1.926773	298.970139
450	246.863167	0.387998	12.075253	0.021129	0.000001	0.014713	0.000001	0.023408	0.017504	0.009592	20.172943	0.249551	348.359262	4.218917	299.009722
480	1176.070047	0.625549	57.156033	0.071007	0.009835	0.013497	0.000001	0.025864	0.090136	0.013241	20.269792	0.08025	349.87982	2.010347	299.029861
520	13646.24594	8.614477	669.443631	0.458397	0.013193	0.015687	0.138151	0.025384	0.530814	0.023569	20.311852	0.035293	350.539783	1.664501	299.05
550	28097.94467	9.139554	1389.717237	0.937701	0.000001	0.016258	0.226373	0.028883	0.454419	0.022621	20.277816	0.031475	350.005742	1.643457	299.079861
580	8164.871834	7.023922	404.540622	0.422824	0.012087	0.009098	0.063188	0.026948	0.095928	0.009653	20.267923	0.03921	349.850489	1.68334	299.120139
650	11759.78596	10.242399	580.55385	0.844607	0.016376	0.009459	0.072588	0.022707	0.241152	0.009854	20.288638	0.044229	350.175569	1.71489	299.139583
750	11271.58858	8.440342	556.661879	0.538334	0.002137	0.011493	0.06684	0.017765	0.220497	0.010254	20.286345	0.037294	350.139585	1.673679	299.159722
950	13621.85719	17.839484	673.741023	0.866531	0.000001	0.007316	0.121305	0.018541	0.225544	0.014894	20.276038	0.046573	349.977845	1.729392	299.179861
1200	6419.857402	10.939213	317.504434	0.456513	0.000001	0.012236	0.056768	0.022056	0.116283	0.013068	20.268383	0.054232	349.857717	1.783097	299.820139
Fusion	10182.12042	3.432481	502.447986	0.348393	0.000001	0.010513	0.102213	0.02003	0.145003	0.032741	20.337518	0.036643	350.942382	1.673198	299.839583

			J parameter	error J			Mass Discrimination (1+e)	Err Discrimination							
	LV87A Biotite		1.05E-02	4.35E-05			1.009446	1.32E-03							
laser power	40Ar	Error 40Ar	39Ar	Error 39Ar	38Ar	Error 38Ar	37Ar	Error 37Ar	36Ar	Error 36Ar	40Ar*/39ArK	Error 40Ar*/39ArK	Apparent age (My)	Error Age (My)	Delay to irradiation (day)
270	1520.891537	0.793615	23.985963	0.057413	0.00733	0.014479	0.018916	0.028142	4.444245	0.03219	10.233334	0.492027	185.083349	8.501771	299.879861
310	3558.468379	1.359887	176.579432	0.274701	0.004562	0.014111	0.000001	0.02835	0.714068	0.018348	19.127643	0.05359	331.865856	1.716286	299.9
350	2866.33982	1.801387	143.838655	0.198947	0.018051	0.015038	0.000001	0.02976	0.155401	0.020046	19.759685	0.058049	341.856589	1.785625	299.920139
390	11495.97791	13.627459	567.885793	0.491211	0.000001	0.011767	0.0463	0.033789	0.217635	0.017016	20.283333	0.041418	350.092319	1.69721	299.95
420	3861.146114	4.16522	190.965445	0.102882	0.000001	0.00982	0.067987	0.038407	0.055592	0.01001	20.296838	0.040456	350.304224	1.692284	299.989583
470	3262.937254	2.175214	161.501906	0.159856	0.000001	0.011876	0.100556	0.019751	0.054129	0.011328	20.279653	0.041946	350.034575	1.700189	300.009722
540	1723.398275	1.753917	84.364616	0.156587	0.000001	0.014393	0.046483	0.017942	0.087875	0.008921	20.29798	0.060546	350.322152	1.834001	300.029861
650	3244.466699	3.273398	159.415887	0.126487	0.000001	0.01545	0.022912	0.016392	0.117002	0.009851	20.293874	0.042396	350.257727	1.703764	300.05
800	2428.451848	2.143284	119.796066	0.131862	0.000001	0.008454	0.023555	0.021798	0.077316	0.022565	20.240452	0.067934	349.419317	1.893812	300.089583
Fusion	2143.813213	1.182213	105.936676	0.120345	0.000001	0.010586	0.056124	0.029328	0.070541	0.01739	20.213299	0.061681	348.993019	1.838931	300.109722

		J parameter	error J		Mass Discrimination (1+e)	Err Discrimination							
	LV62 Muscovite	1.05E-02	4.34E-05		1.009446	1.32E-03							

laser power	40Ar	Error 40Ar	39Ar	Error 39Ar	38Ar	Error 38Ar	37Ar	Error 37Ar	36Ar	Error 36Ar	40Ar*/39ArK	Error 40Ar*/39ArK	Apparent age (My)	Error Age (My)	Delay to irradiation (day)
270	392.623971	0.522059	3.242325	0.033869	0.01649	0.012818	0.000001	0.007561	1.33084	0.019097	3.090692	1.827638	57.740366	33.605637	300.15
340	247.645066	0.46059	9.996144	0.054013	0.000001	0.012753	0.000001	0.013745	0.277226	0.006274	16.921522	0.225404	295.678983	3.8719	300.159722
380	296.936422	0.314249	14.046142	0.067521	0.00177	0.01106	0.000001	0.008436	0.067418	0.007803	19.903849	0.193048	343.1247	3.399393	300.179861
410	51.108241	0.137751	2.472287	0.026814	0.004026	0.012057	0.000001	0.019821	0.003539	0.011082	20.40874	1.360368	351.035184	21.32529	300.209722
430	178.390259	0.52526	8.535472	0.021363	0.000001	0.009181	0.016174	0.021453	0.041098	0.012627	19.736973	0.449871	340.502509	7.237204	300.839583
480	371.327246	0.59161	17.862681	0.05686	0.000001	0.006305	0.000001	0.030121	0.063941	0.012985	19.902379	0.235555	343.101627	4.005976	300.85
530	1871.707655	0.991886	92.934053	0.100893	0.000001	0.009696	0.005408	0.029361	0.118363	0.018808	19.920287	0.070619	343.382792	1.897375	300.879861
550	4160.034543	1.678986	208.33823	0.137662	0.000749	0.01	0.006306	0.02106	0.132785	0.01619	19.929668	0.038763	343.530071	1.656198	300.889583
600	3756.438987	1.953046	189.814943	0.345212	0.000001	0.014591	0.01978	0.022718	0.072983	0.006223	19.827014	0.047211	341.917842	1.70358	300.939583
650	2327.35745	1.619438	118.014105	0.156545	0.012744	0.013902	0.079548	0.020338	0.063293	0.008501	19.737546	0.045556	340.51153	1.687308	300.959722
740	3316.660858	1.923496	166.73173	0.125227	0.000897	0.015414	0.049483	0.01654	0.108831	0.01436	19.860386	0.041598	342.442125	1.669017	300.979861
1000	1694.99065	0.859646	85.50818	0.036905	0.002707	0.013411	0.079685	0.019365	0.053628	0.008222	19.824425	0.042044	341.877152	1.669678	301
Fusion	6630.056225	2.738674	333.633653	0.243789	0.010488	0.014776	0.088887	0.023016	0.09572	0.009844	19.945009	0.032733	343.770879	1.624742	301.020139

		J parameter	error J		Mass Discrimination (1+e)	Err Discrimination							
	LV62 Biotite	1.05E-02	4.34E-05		1.009446	1.32E-03							

laser power	40Ar	Error 40Ar	39Ar	Error 39Ar	38Ar	Error 38Ar	37Ar	Error 37Ar	36Ar	Error 36Ar	40Ar*/39ArK	Error 40Ar*/39ArK	Apparent age (My)	Error Age (My)	Delay to irradiation (day)
280	199.836164	0.227919	3.917688	0.023676	0.000001	0.015614	0.000001	0.031918	0.602922	0.011928	6.804263	0.969386	124.763491	17.185226	301.059722
330	868.563342	0.402357	36.199371	0.10338	0.005733	0.0141	0.000001	0.030483	0.890286	0.016335	17.04485	0.156092	297.665887	2.851257	301.079861
370	2689.784751	1.771093	134.027836	0.148066	0.000001	0.013634	0.028455	0.035599	0.431695	0.011783	19.290814	0.048149	333.47309	1.679894	301.1
400	682.87645	0.814189	34.63466	0.083106	0.000001	0.017099	0.001577	0.0341	0.083025	0.00767	19.167511	0.096609	331.525571	2.133229	301.120139
450	8417.06268	6.958461	423.717508	0.401017	0.000001	0.008358	0.046145	0.024787	0.27448	0.013614	19.826278	0.038069	341.906277	1.646072	301.159722
480	10921.83586	7.553969	551.831203	0.568065	0.000001	0.007992	0.079781	0.020632	0.205449	0.017285	19.834237	0.037419	342.031331	1.642865	301.179861
500	3236.225862	2.885165	163.668659	0.322162	0.000001	0.01085	0.013774	0.024329	0.080251	0.008609	19.778395	0.053037	341.153752	1.742733	301.2
570	4616.809512	6.247379	233.374001	0.405871	0.001044	0.013587	0.0309	0.020453	0.10279	0.020306	19.804804	0.057198	341.568834	1.776357	301.220139
650	5547.238005	1.961464	279.575269	0.197389	0.006293	0.01038	0.020146	0.02793	0.119669	0.020136	19.865021	0.037638	342.51493	1.645934	301.809722
730	2550.156751	1.507106	128.639478	0.142639	0.000001	0.011752	0.008591	0.021015	0.079159	0.01916	19.792795	0.05707	341.380098	1.774701	301.829861
870	12628.63858	2.983605	636.397671	0.634002	0.010135	0.013438	0.115963	0.016135	0.238493	0.017109	19.887477	0.034478	342.867616	1.630126	301.859722
1000	4382.183748	5.653329	221.916617	0.100608	0.003892	0.012429	0.120091	0.031055	0.124926	0.019861	19.750679	0.046517	340.718023	1.694525	301.879861
Fusion	11695.21824	12.626167	591.199665	0.874288	0.000001	0.012524	0.1027	0.018773	0.205152	0.020952	19.832924	0.046203	342.010699	1.697075	301.920139

			J parameter	error J			Mass Discrimination (1+e)	Err Discrimination							
	LV77 muscovite		1.05E-02	4.34E-05			1.009446	1.32E-03							
laser power	40Ar	Error 40Ar	39Ar	Error 39Ar	38Ar	Error 38Ar	37Ar	Error 37Ar	36Ar	Error 36Ar	40Ar*/39ArK	Error 40Ar*/39ArK	Apparent age (My)	Error Age (My)	Delay to irradiation (day)
290	312.826252	0.542986	8.186872	0.039197	0.000001	0.01008	0.000001	0.028764	0.82982	0.013806	9.130028	0.540469	165.58768	9.398251	301.959722
340	397.007787	0.666268	17.939751	0.037206	0.000001	0.007235	0.000001	0.030134	0.302818	0.016315	17.401681	0.281951	303.542826	4.730615	301.979861
430	1027.06255	0.623377	48.692194	0.122247	0.000001	0.010935	0.004612	0.02943	0.098614	0.011998	20.663904	0.09768	355.181934	2.202021	302
430	381.841528	0.31183	18.220864	0.05627	0.000001	0.011738	0.000001	0.030196	0.019714	0.011837	20.795358	0.214048	357.232173	3.699336	302.029861
440	4077.885555	1.544714	201.364987	0.259207	0.000001	0.009561	0.024741	0.02241	0.156426	0.009482	20.178751	0.041339	347.594973	1.686757	302.079861
450	6766.05947	7.710696	334.541467	0.294663	0.000001	0.012401	0.027517	0.021857	0.206489	0.013796	20.196692	0.041967	347.87611	1.691604	302.1
460	18550.17036	13.968313	923.754446	0.849882	0.000001	0.014058	0.139584	0.030706	0.234164	0.011379	20.16037	0.03623	347.3069	1.656554	302.120139
470	28127.38369	14.873856	1389.744553	0.918957	0.000001	0.018081	0.188219	0.029757	1.12027	0.018776	20.158757	0.032837	347.281619	1.638988	302.139583
480	3717.54152	2.21464	185.220843	0.240678	0.00098	0.014051	0.000001	0.022522	0.050358	0.011397	20.138006	0.04355	346.956344	1.698009	302.189583
520	6372.067612	4.280444	316.232379	0.402895	0.008828	0.012319	0.028209	0.021916	0.124701	0.015724	20.186079	0.042404	347.709814	1.693664	302.209722
560	19107.5069	9.245057	951.540991	0.899033	0.047681	0.011341	0.242714	0.033743	0.417941	0.021677	20.110788	0.035154	346.529608	1.647858	306.820139
600	3951.771889	2.430993	196.878938	0.12393	0.003188	0.007786	0.000001	0.020294	0.077077	0.013154	20.103942	0.038003	346.422252	1.662929	306.859722
680	7193.686082	6.216282	357.681279	0.423363	0.000001	0.008412	0.000001	0.021062	0.136884	0.00899	20.146687	0.040835	347.092425	1.681861	306.889583
800	8092.371659	6.217796	400.496741	0.397072	0.000001	0.008795	0.009701	0.018016	0.152029	0.009776	20.243261	0.037956	348.605637	1.670946	306.909722
950	4048.27598	1.741879	201.345651	0.571936	0.000001	0.010343	0.072918	0.025206	0.053839	0.015645	20.191362	0.06797	347.792592	1.887428	306.95
1200	6226.958826	2.590418	310.069794	0.416912	0.000001	0.010068	0.060234	0.022166	0.071302	0.007942	20.170387	0.039895	347.463895	1.677703	306.970139
Fusion	18447.52064	13.839787	917.732899	0.732821	0.000001	0.014729	0.149924	0.026305	0.147826	0.01658	20.207753	0.035188	348.04941	1.65388	306.989583

			J parameter	error J			Mass Discrimination (1+e)	Err Discrimination							
	LV77 biotite		1.05E-02	4.34E-05			1.009446	1.32E-03							
laser power	40Ar	Error 40Ar	39Ar	Error 39Ar	38Ar	Error 38Ar	37Ar	Error 37Ar	36Ar	Error 36Ar	40Ar*/39ArK	Error 40Ar*/39ArK	Apparent age (My)	Error Age (My)	Delay to irradiation (day)
270	1860.221727	0.606395	68.860473	0.1177	0.000001	0.013162	0.023776	0.025328	2.20541	0.014427	17.949927	0.101085	312.324993	2.143312	307.029861
320	3733.994926	3.292328	182.573449	0.236141	0.017858	0.018118	0.026291	0.029341	0.351759	0.016576	20.048831	0.051065	345.55784	1.743788	307.05
370	11733.53902	5.597633	574.273244	0.389285	0.00734	0.014699	0.142635	0.026559	0.411744	0.012878	20.384032	0.033325	350.809111	1.655086	307.070139
400	7585.084751	5.227574	372.03038	0.587005	0.000001	0.012985	0.093016	0.024956	0.171042	0.014362	20.414669	0.046117	351.288312	1.730318	307.089583
440	6639.177357	2.71246	325.814449	0.326829	0.009102	0.014944	0.099042	0.024865	0.13584	0.01183	20.418409	0.036959	351.346788	1.675909	307.139583
500	2424.26398	1.739045	118.894141	0.077113	0.000001	0.014906	0.043352	0.03217	0.071422	0.015443	20.381092	0.052351	350.763119	1.771333	307.159722
600	3269.470495	1.413116	159.778184	0.104554	0.000001	0.01413	0.039841	0.027454	0.117882	0.012707	20.408869	0.040447	351.197602	1.694937	307.189583
700	3255.179965	2.419215	159.33638	0.184569	0.000001	0.013078	0.077058	0.020027	0.117364	0.016271	20.387243	0.04978	350.859336	1.753445	307.209722
850	1782.306854	0.609322	87.111425	0.230646	0.000001	0.013934	0.000001	0.029502	0.078017	0.021962	20.348635	0.096614	350.255295	2.178503	307.820139
Fusion	2164.120321	1.206475	106.510524	0.227797	0.000001	0.015405	0.000001	0.018158	0.111941	0.011567	20.160868	0.06189	347.314713	1.833785	307.839583

			J parameter	error J			Mass Discrimination (1+e)	Err Discrimination							
	LV87B muscovite		1.05E-02	4.35E-05			1.009446	1.32E-03							
laser power	40Ar	Error 40Ar	39Ar	Error 39Ar	38Ar	Error 38Ar	37Ar	Error 37Ar	36Ar	Error 36Ar	40Ar*/39ArK	Error 40Ar*/39ArK	Apparent age (My)	Error Age (My)	Delay to irradiation (day)
280	878.256102	0.56398	18.123055	0.068954	0.000001	0.008892	0.039866	0.030978	2.337502	0.019115	11.554971	0.383455	207.674665	6.580436	307.879861
310	437.074191	0.336377	19.942049	0.041281	0.000001	0.011425	0.018978	0.028723	0.200534	0.012069	19.208955	0.197632	333.173085	3.47	307.9
360	1057.556289	0.799496	48.763278	0.145208	0.000001	0.009201	0.025031	0.032994	0.140743	0.012735	21.033572	0.109629	361.84709	2.35285	307.929861
370	1035.502024	1.596018	49.366656	0.136242	0.000001	0.010674	0.000001	0.022343	0.067484	0.010216	20.731529	0.096234	357.131758	2.194128	307.95
385	2022.741527	1.381747	98.307473	0.136362	0.000001	0.012631	0.101486	0.019179	0.067755	0.017071	20.575083	0.066458	354.684558	1.897587	307.979861
410	886.775755	0.894018	43.513868	0.071822	0.005079	0.01366	0.080935	0.017995	0.03395	0.02731	20.391009	0.189272	351.800957	3.359482	308.009722
440	8539.197722	7.254894	417.654163	0.365082	0.000001	0.012219	0.073615	0.020498	0.128113	0.022674	20.513188	0.040397	353.715465	1.704735	308.029861
460	5094.951019	2.139144	250.000826	0.199088	0.005981	0.010037	0.123488	0.025674	0.11017	0.017323	20.423495	0.038992	352.310206	1.691391	308.05
500	4871.234181	3.348795	238.669252	0.411235	0.000001	0.013309	0.078905	0.026359	0.116965	0.012358	20.4317	0.049487	352.438794	1.757987	308.079861
560	10387.23187	7.671069	509.195478	0.466175	0.008384	0.011378	0.083628	0.018277	0.140276	0.011938	20.475	0.037103	353.117285	1.683992	308.1
620	2259.486518	1.095766	111.213083	0.057831	0.000001	0.011519	0.110577	0.016163	0.035721	0.01064	20.419053	0.042072	352.240579	1.709163	308.120139
750	3869.775845	1.914371	190.345495	0.14313	0.00728	0.014203	0.080613	0.01689	0.047792	0.019489	20.425182	0.044449	352.336645	1.724235	308.139583
Fusion	5595.789267	2.486565	274.649095	0.189252	0.011821	0.014512	0.109046	0.01983	0.102315	0.022366	20.433093	0.04	352.460628	1.697724	308.159722

			J parameter	error J			Mass Discrimination (1+e)	Err Discrimination							
	LV87B biotite		1.05E-02	4.35E-05			1.009446	1.32E-03							
laser power	40Ar	Error 40Ar	39Ar	Error 39Ar	38Ar	Error 38Ar	37Ar	Error 37Ar	36Ar	Error 36Ar	40Ar*/39ArK	Error 40Ar*/39ArK	Apparent age (My)	Error Age (My)	Delay to irradiation (day)
280	268.963984	0.264576	12.584027	0.022217	0.007082	0.013593	0.006628	0.027807	0.256226	0.014305	15.655241	0.351003	275.986025	5.873988	308.2
340	1856.219421	2.187951	91.135514	0.132601	0.005025	0.015648	0.000001	0.028398	0.312231	0.012951	19.522554	0.065315	338.133803	1.835208	308.220139
370	5463.59027	2.710762	267.589158	0.184386	0.000001	0.013856	0.026697	0.024222	0.192028	0.011819	20.362414	0.035503	351.352584	1.66873	308.829861
390	3575.397406	4.872522	175.11834	0.392494	0.009855	0.012086	0.031435	0.03002	0.122624	0.014529	20.370602	0.065472	351.480981	1.878929	308.85
420	2773.23764	1.271624	135.919991	0.143222	0.003244	0.013089	0.045714	0.025642	0.081412	0.01923	20.394011	0.055522	351.848023	1.799694	308.870139
480	3861.321688	1.409525	189.131463	0.182217	0.000001	0.010888	0.043484	0.026406	0.091588	0.011394	20.434683	0.039445	352.485544	1.694625	308.889583
580	3014.693877	1.823064	147.217334	0.217098	0.000001	0.019237	0.00872	0.030574	0.07924	0.017515	20.472816	0.055918	353.083076	1.806927	308.929861
700	2142.750003	1.498507	104.083345	0.170826	0.000001	0.018937	0.016588	0.025563	0.098579	0.016338	20.469174	0.065984	353.026004	1.888248	308.95
950	2776.392365	1.987626	134.507206	0.246647	0.000001	0.020131	0.000001	0.025168	0.083606	0.018016	20.610314	0.063427	355.235951	1.873795	308.970139
Fusion	1141.193612	1.210515	55.257012	0.131273	0.000001	0.01857	0.020859	0.029605	0.032349	0.019374	20.650873	0.121225	355.87052	2.475958	309

		J parameter	error J			Mass Discrimination (1+e)	Err Discrimination							
	LV61 muscovite	1.05E-02	4.35E-05			1.009446	1.32E-03							
laser power	40Ar	Error 40Ar	39Ar	Error 39Ar	38Ar	Error 38Ar	37Ar	Error 37Ar	36Ar	Error 36Ar	40Ar*/39ArK	Error 40Ar*/39ArK	Apparent age (My)	Error Age (My)	Delay to irradiation (day)
300	300.500846	0.455218	11.311764	0.044459	0.000001	0.009591	0.026292	0.027888	0.384579	0.022712	17.02295	0.603858	298.003591	9.838653	309.05
350	3585.084982	2.272689	176.005854	0.169944	0.000001	0.009087	0.02721	0.028507	0.407849	0.012914	19.852689	0.043914	343.10652	1.686743	309.070139
370	473.363413	0.52961	24.009719	0.055951	0.000001	0.009489	0.014869	0.034139	0.067619	0.012923	19.072524	0.180385	330.783463	3.222477	309.089583
390	2460.876423	1.584763	123.494264	0.163696	0.001309	0.012665	0.039059	0.029387	0.201532	0.013654	19.613857	0.052938	339.342982	1.736723	309.109722
400	5047.267302	4.379305	253.300962	0.341797	0.000001	0.010273	0.042473	0.029951	0.180297	0.015173	19.871956	0.045772	343.409788	1.700041	309.139583
420	1229.135704	1.398665	60.471321	0.105639	0.000001	0.013496	0.090685	0.018529	0.139717	0.004054	19.877864	0.056757	343.50278	1.780518	309.179861
460	1563.074868	0.939731	78.282192	0.228011	0.013378	0.014212	0.044838	0.023978	0.113771	0.005546	19.71878	0.069805	340.997325	1.88424	309.2
500	6369.995042	5.575979	314.253605	0.440952	0.000001	0.00932	0.03108	0.015372	0.674539	0.011059	19.799672	0.045355	342.271747	1.693127	311.820139
550	40458.41811	32.209915	2046.648587	1.966505	0.000001	0.020202	0.194762	0.03843	0.910678	0.012214	19.786532	0.036444	342.064785	1.638076	311.839583
580	7232.46943	4.455539	363.771297	0.217317	0.014994	0.009912	0.079017	0.018625	0.182666	0.016095	19.890981	0.03447	343.709207	1.633782	311.870139
650	28693.26317	14.191619	1450.45808	1.082323	0.000001	0.021533	0.206155	0.032328	0.410162	0.021774	19.850145	0.032245	343.066471	1.619991	311.889583
700	6327.479911	4.039151	319.358622	0.318388	0.004026	0.01016	0.000001	0.020773	0.116098	0.012569	19.850419	0.037489	343.070787	1.647741	311.929861
800	3531.908834	1.70277	179.885133	0.1526	0.000001	0.009083	0.002273	0.026856	0.019116	0.015484	19.745439	0.041672	341.417434	1.666314	311.95
Fusion	3659.895394	1.542179	185.613916	0.20107	0.000001	0.009894	0.000001	0.030983	0.035108	0.015941	19.804922	0.043797	342.354426	1.683224	311.979861

		J parameter	error J			Mass Discrimination (1+e)	Err Discrimination							
	LV61 biotite	1.05E-02	4.35E-05			1.009446	1.32E-03							
laser power	40Ar	Error 40Ar	39Ar	Error 39Ar	38Ar	Error 38Ar	37Ar	Error 37Ar	36Ar	Error 36Ar	40Ar*/39ArK	Error 40Ar*/39ArK	Apparent age (My)	Error Age (My)	Delay to irradiation (day)
280	2301.922716	0.829506	29.876039	0.046975	0.025474	0.013894	0.062683	0.023262	6.540815	0.038718	14.303889	0.517311	253.578277	8.634597	312.020139
330	10789.96501	2.9673	517.161473	0.400027	0.003353	0.014399	0.068077	0.023683	2.03781	0.01962	19.879725	0.037779	343.532059	1.65113	312.039583
360	9672.987875	3.252582	476.658686	0.419683	0.000001	0.014632	0.118655	0.030087	0.287488	0.014207	20.277869	0.034783	349.78723	1.658832	312.059722
390	9452.686798	13.745954	466.299421	0.778178	0.004694	0.014354	0.08449	0.025366	0.216881	0.013236	20.292514	0.053382	350.016901	1.77705	312.079861
430	11930.5081	7.649045	587.863799	0.326758	0.000001	0.016978	0.120678	0.020538	0.198237	0.018508	20.353974	0.033602	350.980436	1.657454	312.129861
480	5058.161418	3.533834	249.059056	0.288443	0.000001	0.016722	0.064784	0.022258	0.095092	0.015316	20.358464	0.042946	351.050814	1.7099	312.15
560	3079.802146	1.649067	151.059678	0.098473	0.000001	0.017076	0.031882	0.03095	0.113177	0.017651	20.328929	0.048316	350.587859	1.743081	312.170139
750	6051.090234	3.432212	295.998982	0.323381	0.025898	0.013506	0.031681	0.028257	0.258081	0.007817	20.343263	0.038745	350.812563	1.684167	312.809722
950	3133.390372	1.049717	154.342125	0.13007	0.000001	0.013001	0.016925	0.019639	0.089676	0.00979	20.285247	0.038487	349.902941	1.679271	312.829861
Fusion	3432.651823	1.983955	168.690875	0.177781	0.000001	0.010995	0.033549	0.022772	0.134379	0.007643	20.275103	0.039943	349.743844	1.687018	312.839583

			J parameter	error J			Mass Discrimination (1+e)	Err Discrimination							
	LV14A muscovite		1.05E-02	4.35E-05			1.009446	1.32E-03							
laser power	40Ar	Error 40Ar	39Ar	Error 39Ar	38Ar	Error 38Ar	37Ar	Error 37Ar	36Ar	Error 36Ar	40Ar*/39ArK	Error 40Ar*/39ArK	Apparent age (My)	Error Age (My)	Delay to irradiation (day)
290	519.341052	0.964497	21.326189	0.090617	0.000001	0.01015	0.037316	0.024402	0.452117	0.015264	18.479924	0.241017	321.533243	4.105472	312.879861
340	3382.306447	3.400713	167.144439	0.178058	0.007033	0.009488	0.053063	0.019633	0.25327	0.012904	19.959493	0.04715	344.964642	1.715122	312.9
370	3804.045306	2.260866	190.124631	0.125512	0.000001	0.006836	0.079038	0.030612	0.175944	0.009203	19.906252	0.036666	344.126732	1.647285	312.920139
390	18159.11217	4.788693	899.024518	0.866741	0.000001	0.008053	0.201962	0.022866	0.98948	0.013484	20.037225	0.034718	346.187302	1.64473	312.939583
400	2352.478086	1.087874	118.099508	0.104114	0.000001	0.011206	0.02971	0.013556	0.045738	0.013064	19.964004	0.046674	345.03563	1.712153	312.979861
430	2382.041193	3.168431	119.472397	0.184229	0.000001	0.011373	0.018697	0.027778	0.046251	0.013436	19.977647	0.059968	345.250272	1.812453	313
	8928.003106	3.102039	445.842202	0.401639	0.000001	0.013448	0.047622	0.021349	0.227506	0.008553	20.026979	0.03385	346.026196	1.639627	313.029861
570	6652.573539	6.08076	333.19242	0.472453	0.000001	0.010418	0.029	0.024238	0.134746	0.019326	19.997284	0.046483	345.559175	1.712758	313.05
700	3545.870009	1.576294	178.082971	0.198209	0.000001	0.013036	0.080238	0.033118	0.050777	0.02092	19.996104	0.050421	345.540607	1.740036	313.089583
Fusion	9447.758313	7.523894	472.484955	0.325119	0.000001	0.012189	0.051446	0.019034	0.126548	0.01135	20.067964	0.034906	346.670581	1.647573	313.120139

			J parameter	error J			Mass Discrimination (1+e)	Err Discrimination							
	LV14A biotite		1.05E-02	4.35E-05			1.009446	1.32E-03							
laser power	40Ar	Error 40Ar	39Ar	Error 39Ar	38Ar	Error 38Ar	37Ar	Error 37Ar	36Ar	Error 36Ar	40Ar*/39ArK	Error 40Ar*/39ArK	Apparent age (My)	Error Age (My)	Delay to irradiation (day)
270	1882.704561	1.282405	83.845551	0.129057	0.000001	0.011552	0.059014	0.026411	1.09109	0.009632	18.884537	0.06671	327.97118	1.816053	313.159722
320	12914.86013	6.809626	632.616537	0.396697	0.00273	0.011541	0.180196	0.022305	0.404489	0.015011	20.392009	0.033193	351.757273	1.658536	313.179861
350	10337.00151	7.327247	503.74066	0.211756	0.000001	0.007578	0.112293	0.020048	0.245739	0.009253	20.538852	0.033028	354.057646	1.666654	313.2
380	1370.386409	0.825917	67.443078	0.140287	0.000001	0.015439	0.070786	0.026014	0.057294	0.012206	20.276408	0.076753	349.944266	1.976524	313.829861
440	4982.65225	3.254268	244.470718	0.264239	0.029995	0.013282	0.038116	0.023836	0.107215	0.013828	20.409421	0.041441	352.030203	1.70454	313.85
520	2623.914116	1.693998	128.56845	0.145486	0.000001	0.011709	0.009072	0.026926	0.070938	0.010145	20.399457	0.046105	351.874031	1.733147	313.870139
700	2836.075606	1.688346	138.936972	0.181682	0.000001	0.015921	0.074469	0.03134	0.085639	0.017352	20.410185	0.055572	352.042174	1.800658	313.889583
Fusion	1709.804436	1.388007	84.221062	0.100601	0.000001	0.013223	0.071612	0.030774	0.06332	0.014388	20.275998	0.066899	349.93783	1.886275	313.909722

			J parameter	error J			Mass Discrimination (1+e)	Err Discrimination							
	LV15B muscovite		1.05E-02	4.35E-05			1.009446	1.32E-03							
laser power	40Ar	Error 40Ar	39Ar	Error 39Ar	38Ar	Error 38Ar	37Ar	Error 37Ar	36Ar	Error 36Ar	40Ar*/39ArK	Error 40Ar*/39ArK	Apparent age (My)	Error Age (My)	Delay to irradiation (day)
300	653.492169	0.79154	53.596265	0.149232	0.000001	0.010999	0.034337	0.030254	0.593868	0.009603	9.102221	0.072056	165.581599	1.469456	313.95
360	1311.944559	1.276227	73.604246	0.091199	0.001216	0.010147	0.000001	0.032451	0.674478	0.019108	15.297865	0.089551	270.195823	1.915139	313.970139
410	1080.209653	0.905147	59.578045	0.062772	0.000001	0.011833	0.026389	0.03632	0.143611	0.01515	17.586602	0.088257	307.360032	1.98434	313.989583
450	608.685552	0.786762	32.916002	0.082142	0.000001	0.014264	0.036267	0.021566	0.065576	0.016082	18.107105	0.156911	315.706317	2.88558	314.029861
530	1371.54484	0.933647	66.453769	0.121317	0.000001	0.00994	0.051468	0.014248	0.219155	0.017036	19.874561	0.090164	343.763412	2.095899	314.059722
670	9800.021138	6.898589	463.505377	0.254091	0.000001	0.011821	0.057948	0.026552	0.83061	0.020105	20.783172	0.037743	358.019278	1.70616	314.070139
750	1013.053459	1.445634	49.408625	0.12365	0.002549	0.011411	0.082223	0.020638	0.090328	0.01262	20.212643	0.101357	349.080972	2.231349	314.1
900	791.111778	1.335479	39.228521	0.035175	0.000001	0.008496	0.015916	0.019549	0.060517	0.012323	19.88703	0.106433	343.959815	2.277784	314.139583
Fusion	1553.31409	1.413971	76.436216	0.06437	0.001425	0.008175	0.050706	0.021783	0.04597	0.011629	20.329981	0.059888	350.922875	1.830822	314.159722

			J parameter	error J			Mass Discrimination (1+e)	Err Discrimination							
	LV15B Biotite		1.05E-02	4.35E-05			1.009446	1.32E-03							
laser power	40Ar	Error 40Ar	39Ar	Error 39Ar	38Ar	Error 38Ar	37Ar	Error 37Ar	36Ar	Error 36Ar	40Ar*/39ArK	Error 40Ar*/39ArK	Apparent age (My)	Error Age (My)	Delay to irradiation (day)
280	113.751209	0.203092	5.77754	0.029211	0.001942	0.00975	0.000001	0.024846	0.206716	0.004365	9.466572	0.323621	171.904114	5.662258	314.820139
330	238.95196	0.301252	15.515182	0.025498	0.001514	0.010068	0.010279	0.028122	0.189118	0.0081	12.015257	0.183985	215.523297	3.264941	314.839583
380	496.213518	0.610023	27.112433	0.100232	0.000001	0.010616	0.000001	0.030932	0.158216	0.010833	16.742975	0.150045	293.750061	2.769777	314.859722
440	2345.854388	1.383764	114.57126	0.165195	0.000001	0.008935	0.021424	0.023695	0.244524	0.008254	20.014348	0.049175	345.963955	1.732849	314.889583
470	2094.513546	1.253504	101.328729	0.161595	0.000001	0.005952	0.000001	0.027702	0.200165	0.007141	20.246801	0.052162	349.617359	1.767101	314.929861
510	1708.963683	1.534243	82.779768	0.11777	0.000001	0.00763	0.026615	0.023938	0.168123	0.008816	20.222659	0.057126	349.238268	1.803263	314.959722
620	1047.273053	0.881841	50.32019	0.135854	0.000001	0.015683	0.030263	0.022212	0.138808	0.01366	20.196244	0.104906	348.823394	2.270878	314.970139
800	2445.439166	1.06572	115.948764	0.170732	0.000001	0.006729	0.043116	0.022162	0.232452	0.012411	20.682378	0.054748	356.443378	1.809805	315
Fusion	3441.135411	0.953963	165.564948	0.182953	0.008454	0.005137	0.047713	0.017336	0.169435	0.009516	20.653236	0.041069	355.987487	1.71722	315.020139

			J parameter	error J			Mass Discrimination (1+e)	Err Discrimination							
	LV88B Biotite		1.05E-02	4.34E-05			1.009446	1.32E-03							
laser power	40Ar	Error 40Ar	39Ar	Error 39Ar	38Ar	Error 38Ar	37Ar	Error 37Ar	36Ar	Error 36Ar	40Ar*/39ArK	Error 40Ar*/39ArK	Apparent age (My)	Error Age (My)	Delay to irradiation (day)
280	116.44151	0.236723	2.519969	0.027204	0.000001	0.014009	0.029319	0.022617	0.324779	0.008716	9.815103	1.137688	177.506787	19.614619	315.059722
320	858.038323	0.661903	39.888689	0.105104	0.000001	0.013735	0.06216	0.019064	0.246378	0.012329	19.963335	0.114142	344.373658	2.365972	315.089583
350	781.977099	1.254549	37.275304	0.107202	0.000001	0.01489	0.061688	0.021166	0.117338	0.010243	20.30996	0.113502	349.8099	2.369312	315.109722
380	509.758171	0.683212	24.45143	0.0468	0.004613	0.017762	0.073455	0.024973	0.07631	0.009578	20.261742	0.139391	349.054651	2.685759	315.139583
420	3292.984852	1.006211	158.700826	0.229602	0.000001	0.009753	0.000001	0.02985	0.091745	0.013967	20.731227	0.049908	356.39486	1.774202	315.170139
450	3046.084743	1.22313	147.043385	0.156565	0.000001	0.011029	0.000001	0.027056	0.048354	0.016186	20.769084	0.049548	356.985431	1.773851	315.189583
490	1884.112663	1.044778	90.876738	0.211809	0.000001	0.008665	0.015092	0.02125	0.070133	0.012414	20.667323	0.070616	355.397486	1.934807	315.220139
550	2381.48195	1.67822	114.8625	0.140033	0.000001	0.01111	0.037163	0.018152	0.063582	0.012976	20.740227	0.052854	356.535279	1.795339	315.820139
650	852.174701	1.621102	41.182552	0.067889	0.000001	0.009486	0.08676	0.017972	0.050325	0.011321	20.607017	0.10253	354.455782	2.253969	315.839583
850	8579.774312	4.708935	412.43933	0.331414	0.000001	0.01175	0.132246	0.014124	0.166205	0.031777	20.853389	0.041203	358.299928	1.726045	315.870139
950	4456.334977	2.173365	215.173325	0.174722	0.000001	0.009979	0.102329	0.015081	0.077351	0.018905	20.782072	0.042714	357.188006	1.730821	315.889583
1200	4141.537956	3.00856	199.284591	0.292274	0.000001	0.014034	0.009411	0.018855	0.079278	0.016395	20.818657	0.050399	357.758497	1.782416	315.929861
Fusion	2227.324301	1.66012	107.163364	0.205107	0.000001	0.014627	0.092629	0.021503	0.081102	0.014916	20.763677	0.066162	356.90109	1.900852	315.95

			J parameter	error J			Mass Discrimination (1+e)	Err Discrimination							
	LV88B Muscovite		1.05E-02	4.34E-05			1.009446	1.32E-03							
laser power	40Ar	Error 40Ar	39Ar	Error 39Ar	38Ar	Error 38Ar	37Ar	Error 37Ar	36Ar	Error 36Ar	40Ar*/39ArK	Error 40Ar*/39ArK	Apparent age (My)	Error Age (My)	Delay to irradiation (day)
290	166.289112	0.20257	6.890636	0.043192	0.000001	0.012116	0.050852	0.025547	0.342039	0.015319	10.31958	0.684601	186.17591	11.767781	316
350	264.801334	0.253003	12.548384	0.052507	0.000001	0.011117	0.000001	0.032981	0.078793	0.01756	19.435205	0.441186	336.059242	7.123302	316.009722
390	657.728854	0.908002	31.37148	0.101804	0.000001	0.009141	0.028247	0.031952	0.094768	0.016421	20.292646	0.18032	349.538747	3.229084	316.039583
420	171.6797	0.159575	8.177338	0.026282	0.000001	0.0098	0.000001	0.029588	0.019585	0.013883	20.451564	0.538577	352.026035	8.569834	316.059722
440	5169.486714	2.530881	255.201902	0.237687	0.000001	0.011694	0.045378	0.023317	0.171522	0.012173	20.217214	0.037847	348.356928	1.669504	316.079861
450	13219.91516	4.987687	655.909173	0.481494	0.000001	0.014402	0.154174	0.028737	0.203826	0.018495	20.223043	0.032902	348.448276	1.643919	316.1
460	1420.143126	0.636487	71.157379	0.147086	0.003205	0.012436	0.089534	0.032204	0.085055	0.012394	19.826247	0.07572	342.219123	1.942593	316.120139
500	7270.298203	3.68032	363.69761	0.332532	0.000001	0.012574	0.114765	0.033259	0.143912	0.011818	20.036663	0.035755	345.525043	1.647279	316.15
550	4611.643841	2.222213	233.939103	0.11192	0.000245	0.007148	0.024136	0.031006	0.217089	0.01127	19.591397	0.034192	338.522177	1.612041	316.179861
630	4429.339245	3.099855	222.188461	0.221495	0.000001	0.007638	0.025705	0.023132	0.101134	0.013808	19.952739	0.040939	344.207204	1.671829	316.2
750	3728.526794	3.990501	187.055082	0.361461	0.000001	0.012323	0.022686	0.024564	0.082751	0.013075	19.954464	0.056026	344.234311	1.776603	318.809722
Fusion	6925.779767	3.484806	344.601785	0.318983	0.000001	0.010537	0.060125	0.029336	0.08186	0.013113	20.183358	0.036363	347.826248	1.659351	318.829861

			J parameter	error J			Mass Discrimination (1+e)	Err Discrimination							
	LV29C Muscovite		1.05E-02	4.33E-05			1.009446	1.32E-03							
laser power	40Ar	Error 40Ar	39Ar	Error 39Ar	38Ar	Error 38Ar	37Ar	Error 37Ar	36Ar	Error 36Ar	40Ar*/39ArK	Error 40Ar*/39ArK	Apparent age (My)	Error Age (My)	Delay to irradiation (day)
290	621.06812	0.412737	40.945036	0.061548	0.000001	0.012324	0.000001	0.033681	0.498843	0.012918	11.747374	0.109961	210.189321	2.093997	318.879861
350	1235.423113	1.101206	68.50602	0.127838	0.000001	0.016738	0.015935	0.036461	0.337068	0.021269	16.751039	0.105698	292.79297	2.160185	318.9
380	1782.38089	1.336016	90.759852	0.168622	0.007583	0.012508	0.001576	0.030159	0.27746	0.01549	18.89441	0.071802	327.054254	1.859198	318.929861
410	1217.73214	0.516791	61.332053	0.097664	0.000001	0.01242	0.00747	0.031314	0.139925	0.013435	19.343205	0.082554	334.146669	1.987006	318.95
430	2880.123452	1.443426	139.443682	0.21427	0.000001	0.014133	0.060008	0.021207	0.427313	0.014468	19.940521	0.054599	343.543241	1.762608	318.989583
440	1684.014628	0.838606	84.161058	0.133748	0.000001	0.014109	0.060492	0.025653	0.095515	0.016414	19.867089	0.073443	342.390681	1.920317	319.009722
470	2781.442134	2.056596	138.136449	0.174097	0.000001	0.016345	0.028934	0.030774	0.170809	0.013302	19.933942	0.050992	343.440002	1.735442	319.029861
500	12333.69755	5.622253	605.90864	0.319003	0.000001	0.017149	0.124663	0.025224	0.475324	0.021012	20.286524	0.032922	348.964059	1.645779	319.059722
520	12345.46146	6.744481	605.150641	0.451456	0.000001	0.012519	0.096125	0.024867	0.256132	0.01856	20.433589	0.034627	351.263215	1.663185	319.1
550	29383.72224	10.62892	1446.738419	0.583473	0.000001	0.015602	0.171196	0.024622	0.418599	0.010091	20.378938	0.029478	350.409175	1.63542	319.120139
570	5372.960177	3.346791	264.38536	0.272638	0.000001	0.013052	0.125615	0.023013	0.092271	0.009651	20.395513	0.038567	350.668244	1.681963	319.139583
650	23100.63959	5.218204	1137.820771	0.576952	0.000001	0.013365	0.162915	0.023835	0.301658	0.018432	20.379612	0.029848	350.419699	1.637099	319.159722
750	21792.97173	8.903711	1071.746637	0.538154	0.000606	0.015794	0.164922	0.025853	0.269908	0.016764	20.415883	0.030632	350.98656	1.642859	319.209722
850	6545.958345	1.647414	322.474333	0.26644	0.000001	0.01048	0.055914	0.026767	0.058645	0.01935	20.402213	0.037036	350.772939	1.673937	319.839583
Fusion	32628.83453	15.438729	1602.982699	0.966695	0.000001	0.017628	0.230057	0.02507	0.224042	0.018106	20.468896	0.031513	351.814758	1.650162	319.870139

			J parameter	error J			Mass Discrimination (1+e)	Err Discrimination							
	LV30 muscovite		1.05E-02	4.35E-05			1.010169	1.33E-03							
laser power	40Ar	Error 40Ar	39Ar	Error 39Ar	38Ar	Error 38Ar	37Ar	Error 37Ar	36Ar	Error 36Ar	40Ar*/39ArK	Error 40Ar*/39ArK	Apparent age (My)	Error Age (My)	Delay to irradiation (day)
280	80.688671	0.141761	3.848827	0.024198	0.002829	0.005584	0.000001	0.017421	0.050535	0.011149	17.334902	0.889104	302.890826	14.368967	320.05
350	339.012515	0.772256	15.980578	0.083936	0.000001	0.008262	0.001641	0.019796	0.078023	0.012211	19.976288	0.262762	344.892982	4.410051	320.070139
370	546.527036	0.692819	24.766591	0.044924	0.001302	0.004736	0.000001	0.021066	0.200205	0.011759	19.904668	0.158539	343.766879	2.931449	320.089583
380	494.83476	0.575188	24.450461	0.04416	0.000001	0.011262	0.014343	0.024633	0.037148	0.018068	19.994447	0.228376	345.178384	3.908421	320.109722
400	7166.17648	3.064815	352.08722	0.179151	0.000001	0.011118	0.042065	0.032818	0.220442	0.016136	20.339947	0.034057	350.60005	1.658178	320.15
410	6816.63123	3.174105	335.741219	0.537591	0.000001	0.010266	0.032816	0.032009	0.109461	0.009765	20.374747	0.044738	351.145243	1.721349	320.170139
425	730.494556	0.400489	36.015781	0.086273	0.000001	0.010842	0.038892	0.027111	0.023351	0.011123	20.321489	0.115695	350.310805	2.39755	320.189583
460	509.017287	0.556098	25.272429	0.034798	0.000001	0.008681	0.044371	0.02509	0.000001	0.030293	20.408171	0.354907	351.668722	5.77637	320.209722
520	3624.738782	4.551715	178.699826	0.224667	0.000001	0.012771	0.094267	0.020101	0.105703	0.01857	20.30545	0.054944	350.059437	1.788654	320.820139
650	1676.059824	1.503339	82.97216	0.139481	0.000001	0.008901	0.088272	0.029106	0.041789	0.011935	20.280045	0.066691	349.661214	1.882967	320.839583
Fusion	1104.569628	0.70366	54.427293	0.140809	0.000001	0.00926	0.064662	0.022116	0.03998	0.011737	20.316016	0.090687	350.22504	2.116551	320.859722

			J parameter	error J			Mass Discrimination (1+e)	Err Discrimination							
	LV30 biotite		1.05E-02	4.35E-05			1.010169	1.33E-03							
laser power	40Ar	Error 40Ar	39Ar	Error 39Ar	38Ar	Error 38Ar	37Ar	Error 37Ar	36Ar	Error 36Ar	40Ar*/39ArK	Error 40Ar*/39ArK	Apparent age (My)	Error Age (My)	Delay to irradiation (day)
290	254.314785	0.4209	7.929382	0.030641	0.006748	0.008345	0.028558	0.02362	0.736211	0.01291	5.695242	0.524955	105.212033	9.434014	320.909722
340	492.947105	0.349775	24.991864	0.056517	0.000001	0.008133	0.030502	0.023562	0.314395	0.011924	16.317873	0.159773	286.454686	2.900695	320.929861
380	1652.083681	1.434113	83.071233	0.111747	0.000001	0.007702	0.016982	0.03216	0.232499	0.00964	19.247659	0.059601	333.403757	1.769827	320.95
400	2032.145443	0.940626	101.2565	0.152814	0.000001	0.008672	0.007548	0.023425	0.131061	0.006915	19.857581	0.048711	343.02615	1.71861	320.970139
420	1870.56779	1.125236	93.455625	0.145336	0.000001	0.008098	0.056633	0.018722	0.119741	0.008216	19.840474	0.051797	342.756954	1.73987	321.009722
460	4787.948442	3.376364	239.35292	0.190171	0.005577	0.004481	0.076872	0.028673	0.177537	0.009306	19.96666	0.037232	344.741627	1.652547	321.029861
500	4207.622916	3.108277	210.031148	0.200092	0.000001	0.009396	0.071096	0.024721	0.112386	0.010743	20.057333	0.039991	346.166415	1.673747	321.059722
560	5739.148228	2.903395	285.872868	0.238065	0.000001	0.007387	0.100994	0.027227	0.16363	0.008703	20.090378	0.035242	346.685384	1.649198	321.070139
640	3734.060456	1.535866	185.752658	0.31226	0.011436	0.013208	0.058168	0.032042	0.129019	0.009039	20.079229	0.047692	346.510313	1.72403	321.120139
750	3808.84618	2.475128	187.997363	0.138256	0.000001	0.007407	0.035742	0.027349	0.170993	0.006852	20.16841	0.037023	347.910276	1.663458	321.139583
1000	11933.32312	3.089482	590.190648	0.268363	0.000001	0.007855	0.124203	0.025686	0.327714	0.00611	20.231095	0.02973	348.893668	1.630901	321.15
Fusion	16099.75418	9.709991	803.396652	1.576187	0.000001	0.010667	0.069119	0.025261	0.287412	0.018872	20.099078	0.049776	346.821985	1.739607	321.2

			J parameter	error J			Mass Discrimination (1+e)	Err Discrimination							
	LV14B muscovite		1.05E-02	4.35E-05			1.010169	1.33E-03							
laser power	40Ar	Error 40Ar	39Ar	Error 39Ar	38Ar	Error 38Ar	37Ar	Error 37Ar	36Ar	Error 36Ar	40Ar*/39ArK	Error 40Ar*/39ArK	Apparent age (My)	Error Age (My)	Delay to irradiation (day)
290	245.826252	0.624349	9.984137	0.024614	0.000001	0.008041	0.008255	0.018091	0.470444	0.011331	11.247126	0.362704	202.4165	6.245508	321.820139
340	234.654707	0.350545	9.87629	0.040717	0.000001	0.009826	0.022977	0.01205	0.192283	0.020524	18.46626	0.614243	321.333653	9.898858	321.839583
380	284.242121	0.363848	13.197329	0.056518	0.000001	0.009877	0.022941	0.013588	0.065975	0.010919	20.373423	0.266696	351.485679	4.467781	321.859722
410	257.702126	0.191702	11.969191	0.023189	0.000001	0.010239	0.000001	0.020384	0.060307	0.013581	20.243549	0.349743	349.448259	5.708478	321.879861
450	817.068174	0.81974	38.169754	0.153896	0.002957	0.010566	0.051477	0.029561	0.134721	0.009504	20.640779	0.126746	355.672649	2.542164	321.909722
490	1059.822184	0.458692	50.60684	0.115692	0.001278	0.013522	0.019995	0.029293	0.115051	0.01415	20.475089	0.105317	353.07897	2.284565	321.939583
540	8999.187368	3.598615	438.335738	0.343255	0.008472	0.010048	0.037907	0.027553	0.29443	0.011923	20.503033	0.034452	353.516671	1.671631	321.959722
550	10918.10822	5.180695	533.73235	0.403074	0.033606	0.015997	0.044699	0.032237	0.176712	0.015582	20.52651	0.034323	353.884298	1.672397	321.979861
560	2153.800119	1.398753	105.256118	0.175442	0.000001	0.013967	0.038607	0.034396	0.085418	0.017679	20.412166	0.070109	352.093025	1.921431	322.059722
610	4444.238832	2.490647	217.982628	0.390906	0.000001	0.01446	0.000001	0.031102	0.09337	0.015003	20.424358	0.052023	352.284102	1.775295	322.079861
700	10998.23161	3.453075	539.943101	0.344249	0.000001	0.017204	0.111203	0.030223	0.132004	0.014275	20.471769	0.032047	353.026971	1.657945	322.1
800	5619.100389	2.724035	270.999194	0.19694	0.000001	0.013718	0.080816	0.031198	0.130121	0.015026	20.778058	0.037776	357.81876	1.705497	322.120139
950	2836.803434	1.412654	136.187726	0.173162	0.000001	0.007161	0.04594	0.025642	0.092665	0.012383	20.818823	0.049503	358.455564	1.779511	322.159722
Fusion	5325.488217	2.10596	258.754498	0.149473	0.000001	0.011095	0.068587	0.027637	0.04864	0.023639	20.705631	0.041357	356.686802	1.721433	322.179861

			J parameter	error J			Mass Discrimination (1+e)	Err Discrimination							
	LV29A muscovite		1.05E-02	4.33E-05			1.010169	1.33E-03							
laser power	40Ar	Error 40Ar	39Ar	Error 39Ar	38Ar	Error 38Ar	37Ar	Error 37Ar	36Ar	Error 36Ar	40Ar*/39ArK	Error 40Ar*/39ArK	Apparent age (My)	Error Age (My)	Delay to irradiation (day)
280	82.190343	0.215933	4.223695	0.02254	0.000001	0.005815	0.046324	0.025043	0.169199	0.013935	8.689635	1.027109	157.711382	17.866517	322.80972
350	155.564946	0.148126	9.926925	0.046931	0.002493	0.008528	0.08119	0.02753	0.074421	0.011506	14.1359	0.385518	249.974433	6.468506	322.82986
400	352.749871	0.351977	19.468176	0.01892	0.006027	0.006501	0.149464	0.030979	0.097151	0.014754	17.308326	0.245216	301.624206	4.165234	322.8
440	169.129653	0.227438	8.635385	0.055091	0.02766	0.012561	0.064766	0.029409	0.046436	0.015322	18.668591	0.573674	323.326361	9.213541	322.87013
490	466.909454	0.715675	24.096627	0.035364	0.000001	0.011642	0.000001	0.023338	0.048666	0.008232	18.94477	0.126933	327.700983	2.490934	322.92013
530	612.756145	0.689583	31.173061	0.079997	0.005011	0.009961	0.018131	0.021866	0.03633	0.011658	19.511668	0.132308	336.647501	2.57349	322.93958
560	338.896972	0.583329	16.878695	0.031335	0.000001	0.008415	0.000001	0.019826	0.02858	0.009443	19.746534	0.187989	340.34112	3.324782	322.95972
600	1176.353744	0.723233	59.823155	0.164043	0.000001	0.00909	0.029802	0.02871	0.070681	0.009337	19.508919	0.082209	336.604237	1.989708	322.97986
630	2725.502084	2.383163	138.665908	0.185969	0.000898	0.012202	0.064602	0.025894	0.121456	0.011165	19.586436	0.049089	337.824172	1.701734	323.02986
670	1263.515757	3.772501	64.168082	0.21026	0.000001	0.012334	0.038474	0.024368	0.07226	0.014328	19.558651	0.114599	337.386992	2.354983	323.0
770	2123.679648	1.244879	108.197607	0.130081	0.000001	0.010293	0.040851	0.023337	0.085432	0.011007	19.578045	0.049742	337.692148	1.705953	323.07013
1000	4886.505586	3.317891	246.718157	0.362449	0.005751	0.012969	0.070801	0.015983	0.124008	0.014183	19.834789	0.045225	341.727112	1.689228	323.08958

Parameters	(36Ar/37Ar)Ca	0.000322	3	%
	(39Ar/37Ar)Ca	0.000788	4	%
	(38Ar/37Ar)Ca	0.000026	100	%
	(40Ar/37Ar)Ca	0.0006	100	%
	(40Ar/39Ar)K	0.00085	4	%
	(38A/39Ar)K	0.011	91	%
[3]	(36Cli/38Cl)	316	5	%
[1] and [1']	(40Ar/36Ar)Atm	298.56	0.104	%
[1] and [1']	(38Ar/36Ar)Atm	0.1885	0.159	%
[2]	Lambda 40	5.53E-10	1.35E-12	y-1
	Lambda 39	2.58E-03		y-1
	Lambda 37	1.98E-02		d-1
	Lambda 36Cl	2.26E-06		y-1

References:

[1] Lee, JY, Marti, K, Severinghaus, JP, Kawamura, K, Yoo, HS, Lee, JB, Kim, JS (2006). A redetermination of the isotopic abundances of atmospheric Ar. Geochimica Cosmochimica Acta, 70, 4507-4512.

[1'] Mark, DF, Stuart, FM, De Podesta, M (2011). New high-precision measurements of the isotopic composition of atmospheric argon. Geochimica Cosmochimica Acta, 75, 7494-7501.

[2] Renne, PR, Balco, G, Ludwig, RL, Mundil, R, Min, K, . (2011). Response to the comment by W.H. Schwarz et al. on "Joint determination of (40)K decay constants and (40)Ar*/(40)K for the Fish Canyon sanidine standard, and improved accuracy for (40)Ar/(39)Ar geochronology" by PR Renne et al. (2010). Geochimica Cosmochimica Acta, 75, 5097-5100.

[3] York, D, Personnal Communication - McMaster reactor

Regression method: York, D. (1969). Least-squares fitting of a straight line with correlated errors. Earth Planet. Sci. Lett. 5, 320-4.

Ages and errors of Hb3gr and TCs monitors refers to: Rennes, PR, Balco, G, Ludwig, Mundil, R, Min, K, . (2011). Response to the comment by W.H. Schwarz et al. on "Joint determination of (40)K decay constants and (40)Ar*/(40)K for the Fish Canyon sanidine standard, and improved accuracy for (40)Ar/(39)Ar geochronology" by PR Renne et al. (2010). Geochimica Cosmochimica Acta, 75, 5097-5100.

Annexe 2 – Isotopic closure temperatures for the K-Ar system

Reproduced with agreement of Gilles Ruffet :

Isotopic mineral ages are commonly interpreted to record cooling below a critical temperature, known as the closure temperature (Tc), or the age of mineral (re)crystallisation, if this occurred at temperatures lower than Tc. The geological implications of isotopic ages in terms of closure temperatures, particularly for the K-Ar isotopic system, should ideally be restricted to crystals unaffected by recrystallisation whether related to deformation or the passage of fluids (Villa, 1998). This is because deformation damages the crystal lattice, enhances Ar diffusion, and promotes the formation of intra-crystalline domains with lower diffusion length-scales and lower closure temperatures. In the presence of fluids, minerals or sub-domains within minerals commonly recrystallize in order to form new crystals that lock in younger ages as far as disturbing process occurs at $T \leq Tc$. On the other hand, since muscovite grains extracted from deformed rocks are generally texturally complex (partially recrystallized, composite grains, etc), and because Tc is strongly dependent on the size of diffusing domains, 39Ar-40Ar analyses of such complex grains can provide informations over a relatively wide range of temperature and time (e.g., Bosse et al., 2000; Hames et al., 2008)

K-Ar isotopic closure temperatures of muscovite (more generally white micas), was first estimated at ca. 350°C by calibration of isotopic ages versus metamorphic grade (Purdy and Jäger, 1976), but are currently debated. Several studies suggest that in the absence of deformation and fluid-enhanced recrystallisation, isotopic closure temperatures may be as high as 500°C for muscovite (Villa, 1998; Bosse et al., 2005) or higher than 550°C (Lister and Baldwin, 1996) for phengite under blueschist facies metamorphic conditions. The new experimental determinations of muscovite diffusion coefficients performed by Harrison et al. (2009) support these conclusions. These authors calculated a muscovite Tc at ca. 425°C but for a rather small effective diffusion radius (100 μm, which corresponds to size of grains used

349

for their experiments) and a rather low 10 °C/Ma cooling rate. From these new muscovite diffusion coefficients and on the model of Harrison et al. (2009), Pitra et al. (2010) calculated closure temperatures for greater diffusion radius (500 and 1000 μm) over a complete range of cooling rates, from 1 to 1000°C/Ma. 500μm and 1000μm radius values generate wide 440-560°C and 460-590°C Tc ranges, respectively (cf. Fig.10 in Pitra et al. (2010)). If we consider

a 250μm effective diffusion radius and a 10-200°C/Ma cooling rate, matching better with studied objects, Tc will vary in the narrower 450-500°C range. Closure temperatures for amphibole, although less debated than those of muscovite, are also difficult to estimate. In addition to the effect of cooling rate and the size of diffusion domains, amphibole diffusivity is also influenced by ionic porosity (Fortier and Giletti, 1989; Dahl, 1996). On the basis of natural hornblende compositions measured by various authors (i.e. Leake, 1978; Robinson et al., 1982), Dahl (1996) suggested a Tc range of 480-560°C, calculated for an effective diffusion radius of 80 μm and a 10°C/Ma cooling rate. If we consider higher cooling rates (e.g. ca. 200°C/Ma), this Tc range could be ca. 520-600°C. Harrison (1981) estimated from measured 40Ar* loss following isothermal-hydrothermal treatments the activation energy and frequency factor of hornblende. With an effective diffusion radius of 80 μm, these diffusion parameters predict closure temperatures between 500°C and 580°C for cooling rates in the range 10 to 500°C/Ma. This closure temperature has been slightly re-estimated at 550-650°C by Villa (1998) using Kamber et al. (1995) estimate. Kamber et al. (1995) compared P-T determinations with Pb-Pb ages on garnets and sphene and proposed that hornblendes, depending on their lattice characteristics, may become closed systems for Ar diffusion as high as 580°C under cooling rates of 0.7 °K/Ma (Villa et al., 1996).

Biotite is also concerned with suggested closure temperature as high as ca. 450°C (e.g., Villa & Puxeddu, 1994), ca. 150°C higher than the commonly admitted temperature.